REPORT NO.
UCB/EERC-89/01
JANUARY 1989

EARTHQUAKE ENGINEERING RESEARCH CENTER

BEHAVIOR OF LONG LINKS IN ECCENTRICALLY BRACED FRAMES

by

MICHAEL D. ENGELHARDT
EGOR P. POPOV

Report to the Sponsors:
National Science Foundation
American Iron and Steel Institute
American Institute of Steel Construction

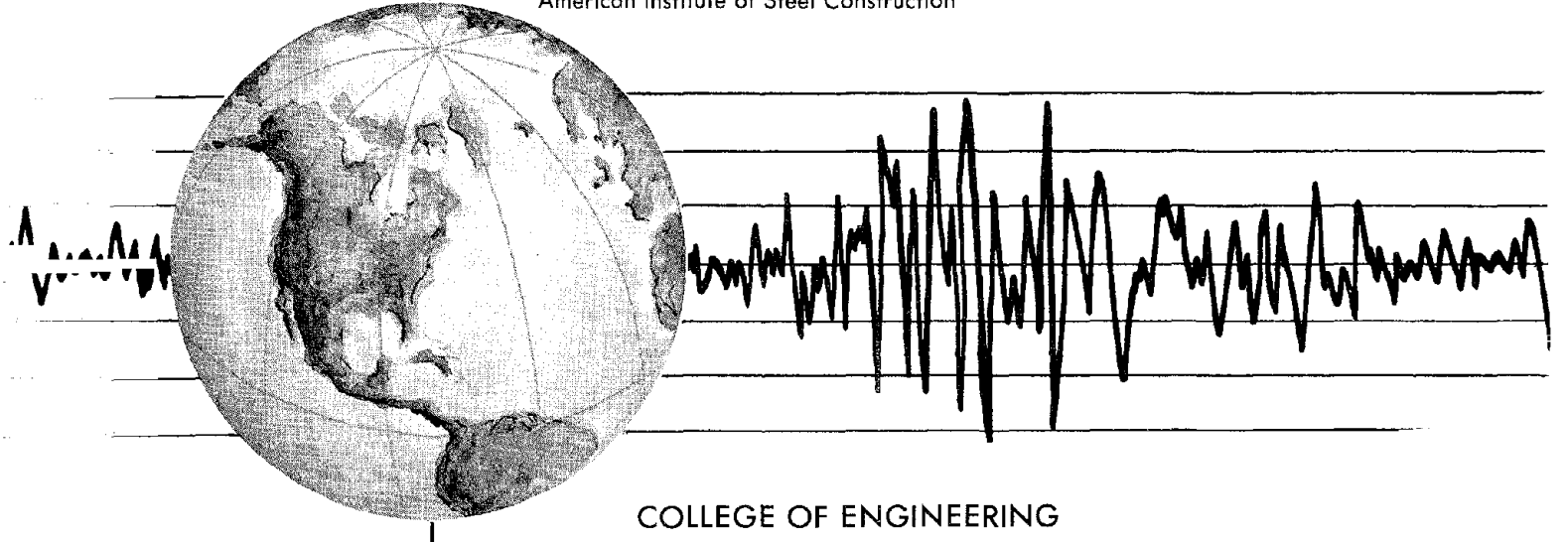

COLLEGE OF ENGINEERING

UNIVERSITY OF CALIFORNIA AT BERKELEY

For sale by the National Technical Information Service, U.S. Department of Commerce, Springfield, Virginia 22161

See back of report for up to date listing of EERC reports.

Behavior of Long Links in Eccentrically Braced Frames

by

Michael D. Engelhardt
and
Egor P. Popov

A Report to the Sponsors:
National Science Foundation
American Iron and Steel Institute
and
American Institute of Steel Construction

Report No. UCB/EERC - 89/01
Earthquake Engineering Research Center
University of California
Berkeley, California
January 1989

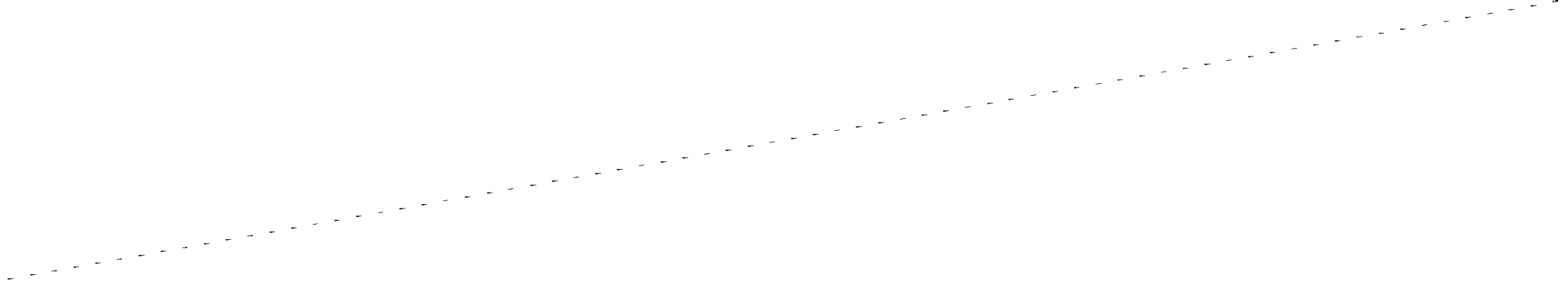

Abstract

This report describes an experimental investigation and associated studies on the behavior of long, flexural yielding links in seismic-resistant Eccentrically Braced Frames (EBFs). EBFs provide ductile behavior under severe earthquake loads by restricting yielding to beam segments called "links". Short, shear yielding links are preferred because of their demonstrated excellent plastic rotation and energy dissipation capacities. Longer, flexural yielding links, however, can offer important architectural advantages and have been used on a number of recently constructed EBFs. Little experimental data has been available on the behavior of long links under cyclic loading.

The central focus of this report is an experimental investigation on fourteen 2/3 scale subassemblages subject to cyclic loads. The subassemblages model a portion of a single-diagonal EBF with the links attached to the columns. The testing program showed that the dominant failure mode for long links attached to columns is fracture of the link flange at the link-to-column connection. Based on this experimental program, the recommendation is made that long links attached to columns not be used in EBFs. The test results suggest, however, that long links located between two braces can provide acceptable performance, although short links are still preferred for best overall performance.

Because of the very high axial force and bending moment typically carried by the beam segment outside of the link, this member can buckle before link inelastic rotation is fully developed, with a consequent loss in the overall system performance. Problems with the beam can be avoided by adhering to capacity design principles. A preliminary design procedure based on capacity design concepts is developed for the beams and braces of an EBF.

Based on the findings of this investigation, combined with the results of previous EBF research, preliminary design recommendations are provided for the use of long links not attached to columns. Included are recommendations on the design yield strength, ultimate strength, plastic rotation capacity and stiffening requirements for long links. The testing program has also demonstrated the suitability of selected brace-to-link connection details for use in EBFs with long or short links.

Acknowledgements

The authors gratefully acknowledge the financial support of the National Science Foundation (current grant no. ECE-8603320) and the American Iron and Steel Institute. The support of Dr. S.-C. Liu of NSF and A.C. Kuentz of AISI over a number of years is much appreciated. The first author is also grateful for the continued financial support of the American Institute of Steel Construction Fellowship Program. The opinions expressed in this report are those of the authors and do not necessarily reflect the views of the sponsors.

The assistance and expertise provided by Prof. Francis Moffitt on the photogrammetric analysis was an important contribution to this project and is much appreciated. Special thanks are accorded to Tim Wickens and Lorraine Lin for their diligent efforts in the laboratory and data reduction phases of this project. The assistance provided by Roy Stephen and the Davis Hall machine shop and electronics shop staff is also appreciated.

Table of Contents

1. INTRODUCTION

1.1 GENERAL

Seismic resistant eccentrically braced frames (EBFs) are a lateral load resisting system for steel buildings that are capable of combining high stiffness in the elastic range with good ductility and energy dissipation capacity in the inelastic range. EBFs can be viewed as a hybrid between conventional concentrically braced frames (CBFs) and conventional moment resisting frames (MRFs), attempting to combine the individual advantages of each system (the stiffness of CBFs and the ductility of MRFs) while minimizing their respective disadvantages (the poor ductility of CBFs and the sometimes inadequate elastic stiffness of MRFs). The distinguishing characteristic of an EBF is that at least one end of every brace is located so as to isolate a segment of beam called a *link*. Figure 1.1 illustrates some common EBFs, with the link lengths identified by the letter e.

Although eccentric bracing is not a new concept for wind bracing, its application to seismic resistant construction is very recent. Extensive research on seismic resistant EBFs began only in the mid 1970's [1,2] while the first major buildings incorporating EBFs as part of their seismic lateral resisting systems were constructed in the early 1980's [3,4]. Since then, application of EBFs in practice has developed rapidly. Requirements covering design and detailing of EBFs have also only recently been put into code format. Detailed provisions covering EBFs have been included in the most recent update of the Structural Engineers Association of California's (SEAOC) *Recommended Lateral Force Requirements* [5], which with minor revisions has been adopted by the *1988 Uniform Building Code* [6]. In its most recent update of the *NEHRP (National Earthquake Hazard Reduction Program) Recommended Provisions for the Development of Seismic Regulations for New Buildings* [7], the Building Seismic Safety Council (BSSC) moved EBF requirements from the appendix to its main body as a fully recognized and approved structural system. The American Institute of Steel Construction (AISC) has also recently drafted tentative seismic provisions for steel buildings [8], including detailed provisions for EBFs.

The viability of eccentric bracing for seismic resistant construction is based largely on the system's stable and predictable inelastic behavior under cyclic lateral load. In a well designed EBF, inelastic activity under severe cyclic loading is restricted primarily to the links, which are designed and detailed to sustain large inelastic deformations without loss of strength. The links act as a ductile fuse, dissipating energy through stable hysteretic behavior, while limiting the forces transmitted to the braces, columns, and beam segments outside of the links. The design goal of restricting yielding to the links is implemented through the application of "Capacity Design" concepts. With this approach, the links are sized for code specified seismic lateral loads. All other frame members, however, are not designed for code level seismic forces, but rather for the forces generated by the fully yielded and strain hardened links. That is, all other members are designed

for the *capacity* of the links. By making the link the weakest element of the frame, the designer can force the yielding to occur in the ductile link elements while preventing non-ductile failure modes such as brace buckling.

Clearly, the link is a critical element affecting the inelastic behavior of EBFs. In turn, a critical factor affecting the inelastic behavior of the link is its length. The link's yielding mechanism, energy dissipation capacity, and ultimate failure modes are all closely tied to its length. For very short links, shear dominates inelastic link behavior, whereas for very long links, flexure dominates. Within an intermediate length range, both shear and flexural yielding significantly affect link behavior.

Previous research on EBFs has included tests on isolated links [9,10,11,12] and on model frames and subassemblages tested pseudo-statically [1,13,14,15,16], on a full-scale six story building tested pseudo-dynamically [17], and on two reduced scale buildings tested dynamically on an earthquake simulator [18,51]. The great majority of EBF research to-date, both experimental and analytical, has been concerned with the short shear yielding links. Previous researchers have pointed out the advantages of short links in stiffness, strength, and energy dissipation capacity [1,9,14], and have recommended the exclusive use of short links in EBFs.

Objective - The seismic resistant EBF system, as conceived and developed over the last decade, is based on the use of short shear yielding links. Nonetheless, a number of recently constructed tall steel buildings have incorporated EBFs with long links, well beyond the range of previous experimental research. Further, the recently developed EBF model codes noted earlier permit the use of long links, despite the lack of experimental research in this length range.

A sometimes important benefit of eccentric over concentric bracing is the greater architectural freedom permitted with EBFs. The offset braces in EBFs provide spaces for doors, windows, or other openings in the frame. By using short shear yielding links, the space made available by the link is not always sufficient to accommodate the needed architectural openings. In such instances, long links offer an important advantage. Architectural and functional constraints calling for large openings in braced bays are the primary incentive for long links in EBFs. As discussed later, varying link length may permit a designer to manipulate frame stiffness within a limited extent. This provides additional potential incentives for long links.

The apparent need for long links in EBFs in certain applications coupled with the lack of experimental data in this length range provides the motivation for this study. Although previous research has demonstrated the superior performance of short links, longer links may still provide acceptable performance in a limited range of EBF applications. The overall objectives of the study described in this report are to provide an assessment of the key issues affecting the use of long links in EBFs, to identify the potential range of applicability of long link EBF systems and to develop preliminary design recommendations for EBFs with long links.

In the remainder of this chapter, some basic characteristics of EBFs are briefly reviewed. Some of the key issues affecting the use of long links are then identified. Finally, the complete scope of this study is described.

1.2 BASIC CHARACTERISTICS OF EBFS

This section reviews some basic characteristics of EBF behavior, with an emphasis on the effects of link length to span length ratio, e/L, on overall frame behavior. The kinematics of a plastically deformed EBF are reviewed to demonstrate the important effect of the e/L ratio on link plastic rotation demand. Static equilibrium of an isolated link is then considered to clarify the concept of a *short* versus a *long* link.

Frame Stiffness

Previous research on EBFs has identified the important effects of the e/L ratio on global frame stiffness and strength. Hjelmstad and Popov [9] demonstrated the effect of the e/L ratio on the elastic stiffness of two simple EBFs, as shown in Fig. 1.2. The plots demonstrate the full range of possible lateral frame stiffnesses, from a moment resisting frame at $e/L = 1.0$, to a concentrically braced frame at $e/L = 0$. Clearly, to obtain the maximum benefit from the bracing, e/L must be kept small. However, as discussed later, e/L cannot be made too small because the plastic rotation demand on the link becomes excessive.

Figure 1.2 suggests the interesting possibility of using link length for manipulating, to a limited extent, the stiffness of a building. For example, in a dual EBF-MRF system, it may be possible to achieve a more equitable sharing of lateral load between the two systems by "tuning" the stiffness of the EBF to be closer to that of the MRF. This same concept could presumably be used to move to fundamental period of vibration of a structure away from a peak in the response spectrum for a particular site. It must be recognized however that the actual variation of stiffness with e/L will typically be considerably less than illustrated in Fig. 1.2, as code imposed drift limitations will require a minimum elastic stiffness.

Frame Strength

In addition to influencing elastic stiffness, the e/L ratio also has an important effect on the strength of an EBF under lateral load. Kasai and Popov [14] computed frame strength as a function of e/L, based on simple plastic theory (no strain hardening and no moment-shear interaction) and based on the assumption that plastic hinges occur only in the links. The result, in slightly modified form, is shown in Fig. 1.3. Frame capacity is normalized by the quantity $2M_p/h$ which represents the strength of an MRF. Frame strength rapidly increases with decreasing e/L, until it is limited by the fully plastic shear capacity of the links. This region of frame behavior is represented by the horizontal lines in Fig. 1.3. The value of e/L at which link shear capacity

controls frame strength depends on the ratio of $(2M_p/V_p)/L$. As discussed later, $e = 2M_p/V_p$ represents the dividing line between a shear yielding and a flexural yielding link for simple plastic theory. $M_p = ZF_y$ is the fully plastic moment of the W section and $V_p = .55F_y dt_w$ is the fully plastic shear capacity. F_y is the steel yield strength, Z is the plastic modulus, d is the overall beam depth, and t_w is the web thickness.

It is evident from Figs. 1.2 and 1.3 that for a given span length L, a small e/L ratio is advantageous for maximizing both stiffness and strength of the frame. However, it must be recognized that the effects of e/L illustrated in Figs. 1.2 and 1.3 represent idealized situations for small frames, assuming constant member sizes as e/L is varied. The actual effects will depend on many factors, including building height and code imposed drift limitations. However, these figures are representative of the significant trends in behavior as e/L is varied.

Energy Dissipation Mechanisms

In EBF design, it is necessary to estimate the plastic rotation demand on the links. This number is then compared to an estimate of the plastic rotation that the links can supply. From a design point of view, a simple but useful technique for estimating link plastic rotation demand is by the use of *Energy Dissipation Mechanisms* (EDMs), constructed by assuming rigid-plastic behavior of the frame members. In traditional static plastic frame analysis, such mechanisms are usually known as *Collapse Mechanisms* [19], since the formation of a mechanism implies failure of the structure. In such cases, the designers goal is to prevent the formation of a mechanism. Under dynamic earthquake loads, however, the formation of a mechanism does not imply failure or collapse, but rather is a means of dissipating earthquake energy input to the structure. In this case, the designer's goal is not to prevent the formation of a mechanism, but rather to control the location of the plastic hinges in the mechanism (through application of capacity design concepts) and to assure that the plastic rotation demands at these hinges are not excessive. Accordingly, *Collapse Mechanism* is not an appropriate term for seismic resistant design.

Figure 1.4 illustrates EDMs for an MRF and for several EBFs. In this figure, a black circular dot indicates a plastic flexural hinge and the cross-hatched lines indicate a plastic shear hinge. These mechanisms assume that plastic hinges, shear or flexural, form only in the links (with the exception of the first story column bases). In each case, θ_p represents the plastic frame drift. For the MRF, the plastic rotation demand at the beam plastic hinges is also θ_p. For the EBFs, however, the plastic rotation demand on the links is much larger than θ_p and can be determined from the geometry of the mechanism as shown in Fig. 1.4. For most EBF types, the plastic rotation demand on the links, γ_p, can be estimated from one of the following two equations:

$$\gamma_p = \frac{L}{e}\theta_p \tag{1.1a}$$

$$\gamma_p = \frac{L}{2e}\theta_p \tag{1.1b}$$

Equation 1.1a is applicable to the EBF types in Figs. 1.4b, c and d containing one link at each floor level. Note that the same equation applies regardless of where the link is placed within the span. Equation 1.1b is applicable to the EBF type in Fig. 1.4c containing two links at each floor level. The reduced link rotation demand for the same frame drift is an advantage of this EBF type.

Based on the simple concept of EDMs, the plastic rotation demand on the link depends only on frame geometry (Eq. 1.1), and is the same whether the link yields in shear or in flexure. The symbol γ has typically been used to denote link rotation, reflecting the importance of shear yielding in supplying plastic rotation of short links. In long links, the plastic rotation is supplied primarily through flexural yielding and therefore the symbol γ may no longer be appropriate. Typically, the symbol θ or θ_p is used to denote rotations at beam flexural hinges. However, to avoid introducing new symbols, γ will be used to represent link rotation, regardless of link length or yielding mechanism.

Figure 1.5 is a plot of link rotation demand, normalized by story drift, versus e/L ratio for the EBF mechanisms illustrated in Figs. 1.4b, c, and d. This plot demonstrates the rapid growth in rotation demand as e/L decreases. Past research has demonstrated that large plastic rotations can be supplied by short shear yielding links [9,11,14,16]. Links can not be made too short, however, or else the rotation demand becomes excessive, even for a shear yielding link. Although longer flexural yielding links may be unable to supply large plastic rotations, as Fig. 1.5 illustrates, the rotation demand is also likely to be less. For example, increasing e/L from 0.1 to 0.2 reduces link rotation demand by one half.

For certain EBF configurations, particularly those with long links, the mechanisms illustrated in Fig. 1.4 may not be achieved. Rather, a mechanism with hinges in the beams and braces, just outside of the links, may control frame behavior in the plastic range. The implications of such a mechanism will be considered later in this report.

Forces in Beams and Links

Typical distributions of bending moment M, shear V, and axial force P in the beams and links of an EBF under lateral load are qualitatively illustrated in Fig. 1.6. Two common eccentric framing arrangements are considered. From this figure, it is clear that the link is subject to high shear force along its entire length, high end moments, and generally low axial force. The beam segment outside of the link, on the other hand, is dominated by high axial force and a large bending moment at the end nearest the link.

Forces acting on an isolated link, and the relationship between shear force and bending moment in the link based on static equilibrium are illustrated in Fig. 1.7. In the case where link end moments are equal, then $M_a = M_b = M$, and the equation of statics reduces to $V\,e = 2M$. If one now assumes simple plastic theory, i.e., no strain hardening and no $M-V$ interaction, it is

simple to derive that a link length of $e = 2M_p/V_p$ is the theoretical dividing line between a link that yields in shear and one that yields in flexure. Thus, based on simple plastic theory, if $e < 2M_p/V_p$, the link shear will reach V_p before both end moments reach M_p, and the link will yield in shear, forming a shear hinge. On the other hand, if $e > 2M_p/V_p$, the link end moments will reach M_p, forming flexural hinges at both ends, before the link shear reaches V_p.

Real behavior of links, however, cannot be adequately characterized by simple plastic theory. Experiments clearly show the importance of strain hardening in links, with ultimate shear strengths on the order of $1.5V_p$ expected for short stiffened links [9,11,13,16]. One implication of this strain hardening is that there is no clear dividing line between a shear yielding and a flexural yielding link. Instead, both shear and flexural yielding occur over a broad range of link lengths. Another important implication of strain hardening is that bending moments considerably in excess of M_p can be developed at the link ends. In order to assure that link behavior is controlled by the more desirable shear yielding mechanism, Kasai and Popov [13] recommend that link length comply with the following equation:

$$e \leq 1.6 \frac{M_p}{V_p} \tag{1.2}$$

This equation is based on the requirement that link end moments should be limited to $1.2M_p$ to avoid high bending strains that may lead to severe flange buckling or to failure of link flange to column welds. Thus, from the statics of Fig. 1.7, if the link end moments are limited to $1.2M_p$ and the link shear is assumed to reach $1.5V_p$, then the limiting link length is $e = 2(1.2M_p)/1.5V_p = 1.6M_p/V_p$. At present, Eq. 1.2 represents the recommended basis for link lengths in EBFs. For the purposes of this report, any link satisfying Eq. 1.2 will be called a *short* link, whereas any link exceeding this limit will be called a *long* link.

To summarize, it is apparent from the above discussion that short links, or more accurately small e/L ratios, have the advantage of providing high frame stiffness and strength. Small e/L ratios incur very high link rotation demands, but the ability of short links to supply these high plastic rotations through shear yielding is well established. Larger e/L ratios, while providing less stiffness and strength, also incur smaller link rotation demands. Finally, it must be recognized that a small e/L ratio does not necessarily imply a short link. The length criteria of Eq. 1.2 depends on beam section properties, whereas the e/L ratio does not. A long link with a small e/L ratio is therefore possible, and thus for certain W sections and span lengths, a long link with a very high rotation demand is possible.

1.3 KEY ISSUES AFFECTING THE USE OF LONG LINKS

In this section, some of the important issues affecting the use of long links in EBFs are identified and briefly discussed. The emphasis is primarily on those issues considered in this study.

Yielding and Failure Mechanisms in Long Links

Before considering the use of long links in EBFs, it is important to recognize the completely different yielding and failure mechanisms in long and short links. In a very short link where little or no flexural yielding occurs, say $e = M_p/V_p$, link post yield behavior is dominated by development of large inelastic shear strains in the link web. Because the shear force is constant over the length of the link (Fig. 1.6), these inelastic shear strains are expected to be fairly uniformly distributed over the length of the link. Further, the occurrence of shear yielding limits the magnitude of the link end moments and precludes the development of high bending strains at the link ends. On the other hand, in a very long link where little or no shear yielding occurs, say $e = 3M_p/V_p$, link post yield behavior is dominated by large, non-uniformly distributed inelastic bending strains concentrated at the link ends, with the remainder of the link staying elastic. There is, of course, an intermediate range of link lengths, perhaps in the area of $1.6M_p/V_p$ to $3M_p/V_p$, where both shear and flexural yielding significantly affect link behavior. This length range can be considered a transition from the shear dominated to the flexurally dominated ranges of behavior.

Because of the completely different yielding mechanisms, one would anticipate that the strength and plastic rotation capacity of short and long links will be limited ultimately by different failure modes. For short links, inelastic shear buckling of the web has been typically observed as the controlling failure mode. Web shear buckling can be substantially delayed by stiffening the web of the link, and much of the past EBF research has been directed towards developing stiffener spacing criteria for short links [20]. For long links, failure mechanisms typically associated with large flexural deformations are anticipated, i.e., some combination of flange buckling, compression web buckling, and/or lateral torsional buckling. In addition, because of the very high bending strains developed at the ends of long links, the possibility of fracture at welded connections at the link ends must be considered as a potential failure mode. An important goal of link design and detailing is to delay various failure modes until sufficient plastic rotation is developed. It is therefore important to recognize the different controlling failure modes in short versus long links. Again, one would expect a transition range of link lengths where both shear and flexural failure modes, perhaps with some interaction, are possible.

Plastic Rotation Capacity of Long Links

The ability of a link to sustain large plastic rotations without loss of strength is a primary requirement of a seismic resistant EBF. As noted above, plastic rotation demands on links can be estimated by the use of EDMs, as in Figs. 1.4 and 1.5, and may be as much as 5 to 10 times greater than the plastic rotation demand on a beam in an MRF. Supplying these large plastic

rotations is a critical issue for EBFs.

The plastic rotation capacity of short links (Eq. 1.2) is well established. Numerous experiments have demonstrated that a properly stiffened short link can sustain plastic rotations up to $\gamma_p = \pm .10$ rad. under cyclic load or up to $\gamma_p = .20$ rad. under monotonic load [9,11,14,16]. Furthermore, this rotation capacity can be accurately and reliably predicted [20].

The plastic rotation capacity of long links, on the other hand, is a very poorly understood problem. Because of the completely different yielding and failure mechanisms in long links, it is apparent that the large rotations typical of short links cannot be expected of long links. Further, there is little experimental data available for long links. A review of past EBF research indicates that of approximately 80 links tested to-date, either as isolated links or as part subassemblages or frames, only six links have exceeded the length criteria of Eq. 1.2. These six were tested by Hjelmstad and Popov [9] as isolated links under conditions of equal end moments. The longest link in this group was a $W12\times22$ section, 36 inches in length (nominal $e = 2.15M_p/V_p$). Even these six links were therefore in the length range still heavily influenced by shear deformations. No previous experimental data are available in the length range dominated by flexural yielding ($e > 3M_p/V_p$).

The limited experimental data available for cyclically loaded beams for MRF applications may be considered to provide some guidance on the plastic rotation capacity of long links. For example, cyclic tests on beam-column subassemblages by Popov and Stephen [21] showed plastic rotations on the order of $\pm .015$ rad. up to about $\pm .03$ rad., with the higher values being achieved with all welded beam-to-column connections. This may suggest that similar rotations are possible in long links, since both long links and beams in MRFs supply plastic rotation by flexural yielding. However, such tests for MRF applications are conducted under conditions of much lower moment gradient than is typical of links, and therefore these data are not directly applicable to the problem of long link rotation capacity.

It is instructive to consider the significance of moment gradient in the problem of flexural rotation capacity by the simple example illustrated in Fig. 1.8. Two simple end loaded cantilevers are considered, one being three times the length of the other. The 20 inch cantilever may be viewed as one-half of a long link, whereas the 60 inch cantilever is perhaps more typical of a beam in an MRF. Each cantilever in Fig. 1.8 is loaded so as to produce a flexural plastic rotation angle of .02 rad., based on the simple bi-linear moment-curvature relationship of Fig. 1.8a. Plastic rotations are computed as the area under the inelastic portion of the curvature diagrams (the cross-hatched areas). This simple example demonstrates a very important point. That is, as the beam length is decreased (and moment gradient is increased), yielding is confined to a smaller region at the end of the beam, resulting in the need for higher curvatures and therefore higher bending strains to supply the same plastic rotation. For this particular example, the maximum curvature

developed in the 20 inch cantilever (the "long link") is nearly double that in the 60 inch cantilever (the "MRF beam") for the same plastic flexural rotation of .02 rad. Note that the length of the yielded zone in the 20 inch cantilever is only about half of that in the 60 inch cantilever.

As beam length decreases, ever higher bending strains are required to develop the same flexural plastic rotations. An important consequence of these higher bending strains is the increased possibility of fracture at welded connections at the member ends. Further, the reduced length of the yielded zone affects the problems of flange buckling and lateral torsional buckling in flexural yielding members. Because of these higher bending strains and shorter yielded lengths, flexural yielding links must be considered as significantly different from flexural yielding beams in MRFs. Rotation capacity predictions based on MRF beam tests cannot be directly applied to long links. Note that at some point as beam length is decreased, shear yielding will commence and will contribute plastic rotations through inelastic shear straining. After this point, any further reduction in member length will *reduce* bending strains by limiting the member end moments.

To summarize, the mechanisms for supplying plastic rotations in long links differs both from that in short links as well as from that in MRF beams. Developing a reasonable estimate of long link plastic rotation capacity based on experiments accurately simulating long link conditions is a central issue affecting long link use in EBFs.

Long Link Stiffening Requirements

As noted earlier, short links typically fail by inelastic shear buckling of the web. This failure mode, first noted in EBF tests by Manheim [15], was a subject of several subsequent experimental investigations on short links [9,11,14]. This work culminated in the development of definitive stiffener spacing criteria by Kasai and Popov [20]. Combining classical plastic plate buckling theory with all available experimental data, a remarkably simple and accurate rule was developed relating stiffener spacing to the available plastic rotation up to the onset of web inelastic shear buckling:

$$a = 29t_w - \frac{d}{5} \qquad \text{for } \gamma_p = \pm .09 \text{ rad} \tag{1.3a}$$

$$a = 38t_w - \frac{d}{5} \qquad \text{for } \gamma_p = \pm .06 \text{ rad} \tag{1.3b}$$

$$a = 56t_w - \frac{d}{5} \qquad \text{for } \gamma_p = \pm .03 \text{ rad or less} \tag{1.3c}$$

In these equations, a is the distance between *equally* spaced stiffeners, d is the beam depth, and t_w is the web thickness. For intermediate values of γ_p, it is appropriate to interpolate. These equations correlate very closely with the available experimental data for short links [20].

Based on the earlier work on short links by Hjelmstad and Popov [9] and Malley and Popov [11], it was observed that stiffeners on only one side of the web are adequate for links of moderate depth. It was also observed that partial depth stiffeners, welded to the web but not to the flanges,

were nearly as effective as full depth stiffeners. The model EBF codes [5,7,8] incorporated the first observation by permitting one sided stiffeners for links less than 24 inches in depth. Deeper sections require two sided stiffeners. The model codes also require that full depth stiffeners, welded to the web and both flanges, be used in all cases. Though the primary function of the stiffeners in a short link is to reinforce the web, full depth stiffeners provide additional restraint against flange buckling and lateral torsional buckling of the link.

Whereas stiffening requirements are now well established for short links, considerably less is known about stiffening long links. Since different forms of local instability are expected for long links, different stiffening criteria are also likely needed. In the very long, purely flexural yielding length range, web shear yielding is not anticipated and therefore stiffening of the web may not be needed. The predominant forms of local instability expected in such long links are flange buckling and lateral torsional buckling, and stiffeners must be located to delay these failure modes.

Limited experimental data indicates that proper stiffening may be effective in delaying local instability of long links. In the previously mentioned test by Hjelmstad and Popov [9] on a long $W12\times22$ link, the addition of stiffeners near the link ends nearly doubled rotation capacity. Recent monotonic tests by Kemp [22] on simply supported beams showed that stiffeners increased rotation capacity by two to four times. Stiffeners in flexural yielding members, in addition to restraining flange buckling, also significantly increase the torsional stiffness of a W section [24] and thereby inhibit lateral torsional buckling. Clearly, such stiffeners must be full depth to be fully effective.

It may be postulated that the most effective location for stiffeners in long links is near the half-wavelength point of the flange buckle. Based on Lay's well known theory on flange buckling [25], the half-wavelength for most W sections is approximately equal to the flange width, b_f, of the section. Therefore, as a first estimate, stiffeners located at about b_f from each end of the link may be appropriate. However, as noted earlier, the significantly shorter yielded length of flange in flexural yielding links as compared to flexural yielding beams changes the nature of the flange buckling problem. Consequently, locating stiffeners at b_f from the link ends can only be considered a starting point in the investigation of long link stiffening requirements.

In the transition range of link lengths of about 1.6 to $3M_p/V_p$, both shear and flexural failure modes are anticipated to varying extents. In this length range, a combination of equally spaced web stiffeners along with flange stiffeners near the link ends are likely needed.

Link Ultimate Strength

The basic philosophy of EBF design requires that inelastic frame activity be confined primarily to the links, which are then designed and detailed to provide the needed strength and plastic rotation capacity. Inherent in this philosophy is the requirement that the remainder of the frame possess adequate strength to permit link strength and rotation capacity to be fully developed.

More specifically, the braces, columns, and beam segments outside of the links must be designed for the maximum forces generated by the fully yielded and strain hardened links, i.e., according to capacity design principles. EBF design therefore requires a reasonable upper bound estimate of link strength, that is the ultimate shear force and end moments that can be achieved by the link.

Numerous experiments on short links have typically shown ultimate shear strengths significantly greater than V_p. This overstrength can be attributed to:

- strain hardening
- effects of composite floor systems
- actual yield strength of steel greater than specified yield strength, particularly in the web of the link.

The actual observed ultimate shear strength of links is frequently 40 to 50 percent greater than V_p, and sometimes in excess of 2 times greater [1,9,14,18].

For design purposes, a value of $1.5V_p$ has been recommended as a reasonable estimate of the ultimate shear force of a short link [1]. The model EBF codes [7,8] have adopted this recommendation and have extended it to links of any length. That is, the model codes recommend that the ultimate strength of a link be taken as 1.5 times its strength based on simple plastic theory. Following this recommendation, the ultimate shear force and end moments in a link can be estimated as follows:

$$For\ e \le 2\frac{M_p}{V_p}: \quad V_{ult} = 1.5V_p \tag{1.4a}$$

$$M_{ult} = \frac{e\,V_{ult}}{2} \tag{1.4b}$$

$$For\ e \ge 2\frac{M_p}{V_p}: \quad V_{ult} = \frac{2M_{ult}}{e} \tag{1.5a}$$

$$M_{ult} = 1.5M_p \tag{1.5b}$$

These equations are based on the following assumptions:

(1) Link end moments will be equal when the link achieves its ultimate strength. (Kasai and Popov [14] have shown that this equalization does not occur for links of length $e < 1.3M_p/V_p$ attached to columns, and have developed estimates of ultimate link end moments for this situation).

(2) The strength of short links is achieved when the shear force reaches $1.5V_p$ (Eq. 1.4a). The corresponding end moments are determined from statics (Eq. 1.4b).

(3) The strength of very long links is achieved when the end moments both reach $1.5M_p$ (Eq. 1.5b). The corresponding shear force is determined by statics (Eq. 1.5a).

(4) There is no interaction between shear and bending at the ultimate limit state. Thus, $e = 2M_p/V_p$ is the dividing line between shear and flexure controlled ultimate strength.

There is insufficient experimental data to judge whether the above assumptions are reasonable for long links. Because of the importance of link ultimate strength in controlling the capacity design of the beams, braces, and columns, developing a reasonable estimate of long link strength must be considered an important issue affecting long link use in EBFs.

Behavior of Beam and Brace Outside Link

As noted above, the basic design philosophy for EBFs requires that the braces, columns, and beam segments outside of the links remain essentially elastic under the forces generated by the fully yielded and strain hardened links. Following this design philosophy, however, may sometimes not be possible for EBFs with long links, and in some cases, even for EBFs with short links.

The problem occurs with the beam segment outside of the link. As illustrated in Fig. 1.6, the beam segment outside of the link typically carries a large axial force when link ultimate strength is fully developed. It is important to recognize the magnitude that this axial force can attain. As an example, Fig. 1.9 illustrates the axial force in the beam of an EBF with a $W21\times50$ beam and link, when the link shear is at $1.5V_p$. Plotted on the vertical axis is P/P_y in the beam, where P is the beam axial force and $P_y = AF_y$ is the fully yielded axial force for the beam. The horizontal axis is the angle between the brace and the beam, a critical factor affecting axial force levels in the beam. For frame geometries with very flat braces, say with a brace-beam angle of 30 to 35 degrees, the beam axial force will reach as high as $.8P_y$ for this frame! In addition to this extraordinarily large axial force, the beam must also carry significant bending moments transferred to it from the end of the link. The magnitude of this bending moment increases as link length increases. In some cases, this combination of high axial force and bending moment may result in yielding or instability of the beam before link ultimate strength is fully developed. This, in turn, may result in a redistribution of bending moment from the beam to the brace, possibly causing yielding or instability in the brace. In such cases, the desired EBF mechanisms illustrated in Fig. 1.4 will not be the controlling mechanism. Rather, a mechanism with hinges in the beams and/or braces will control inelastic frame behavior. Examples of such mechanisms are illustrated in Fig. 1.10. For these mechanisms, significant plastic rotation demands may be imposed on the beam and brace, and the ability of these members to supply these demands must be investigated. Because both the beam and brace typically carry large axial forces, their ability to supply large plastic rotations is doubtful.

Link-to-Column Connection Details

At present, the connection of a short link to a column is required by the model EBF codes [5,7,8] to be all welded. That is, both the flanges and the web of the link must be welded to the column. This requirement is based largely on tests by Malley and Popov [11] in which various end

connection details were investigated for *short* links. Those connections with welded flanges and a welded web showed excellent performance. However, in those specimens with welded flanges and a bolted web, premature flange failures were observed. Apparently, the large shear forces induced bolt slippage in the web connection which then redistributed large forces to the flanges, resulting in sudden flange failures.

Similarly, cyclic tests on flexural yielding beams for MRF applications [21,23] with conventional MRF connection details (full penetration welds at the flanges and a bolted web) frequently show that a primary failure mode is fracture of the beam flange near the flange to column weld. These tests also typically show improved performance when a welded web connection is used in lieu of the more conventional bolted web connection.

As discussed earlier, significantly higher bending strains are anticipated in long links than in either short links or MRF beams. Further, the ultimate shear force in a long link, though not as large as in a short link, is still much larger than in an MRF beam. Consequently, it is apparent that all welded connections are appropriate for attaching long links to columns. However, due to the high bending strains anticipated at the ends of long links, it is not apparent whether or not even an all welded connection will be satisfactory. It is clear, however, that link-to-column connection details are likely to be a critical factor affecting the performance of long links in EBFs.

An additional issue of concern is the behavior of link-to-column web connections. Tests on such connections for MRF applications have often shown poor performance [23,26,27], with fracture occurring in the beam flange or in the flange to column connection plate at rather low values of plastic rotation. For EBFs, only a single test has been conducted to-date on a short link to column web connection [11]. This connection showed satisfactory performance, possibly due to the lower levels of flange strain in short links as compared to MRF beams.

The model EBF codes limit the use of link-to-column web connections to those cases where the plastic rotation demand is less than .015 rad. This low limit reflects the uncertain reliability of these connections. Additional data on link-to-column web connections are needed to determine if an increase in allowable rotation is warranted.

Brace-to-Link Connections

The importance of brace-to-link connections was demonstrated during the testing of a full-scale six story building with eccentric braces in Tsukuba Japan in 1984 [17]. This short link EBF was of the type illustrated in Fig. 1.1b, and used tube braces with a gusseted brace-to-link connection detail. A sketch of this detail is shown in Fig. 1.11. The building was subjected to a simulated major earthquake, using the 1952 Taft earthquake accelerogram scaled to a peak ground acceleration of 0.5g. Pseudo-dynamic test methods were used. The building survived this simulated earthquake in excellent condition with relatively little visible damage. Since the damage was so slight, the test was extended to produce larger frame displacements and to reveal the frames

final failure mechanism. During the extended tests, the gusset plates connecting the braces at the 2nd and 3rd floor links buckled severely in the region shown in Fig 1.11. Negative bending moments in the beam producing large compressive stresses along the free edge of the gusset between the brace and the link may be postulated as the cause of this buckling.

The Tsukuba tests demonstrated that brace connections in EBFs are subject to a significantly different stress environment than brace connections in CBFs. These tests also showed that the proper design of brace connections must be considered an important issue in any EBF design. It is particularly important in long link EBFs where a combination of large axial forces and potentially large bending moments in the brace result in particularly severe requirements on the brace connection.

1.4 SCOPE

This report documents an experimental investigation and associated studies on the behavior of long links in EBFs. Chapter 2 describes the experimental subassemblage as well as modelling and design considerations for the test specimens. Link and connection details are also presented for each of fourteen test specimens in this chapter. The performance, observed damage and failure mechanisms, and overall hysteretic response of each specimen are described in detail in Chapter 3. Some important design implications of the test observations are also discussed in this chapter. Further detailed analyses of the experimental data is conducted in Chapter 4. This includes analysis of the initial yield and ultimate forces developed by the links, comparison of specimen performance based on energy dissipation considerations, detailed studies on beam and brace response, and investigation of the out-of-plane forces developed at the link end lateral supports. Design implications for each of these items are also discussed. Techniques of close range photogrammetry were used to collect data on deformations and strains in the link region of five of the fourteen test specimens. The methods used to collect and reduce this data, and the results of the photogrammetric analyses are presented in Chapter 5. In Chapter 6, preliminary design recommendations are developed for the ultimate strength, plastic rotation capacity and stiffening requirements for long links. Finally, Chapter 7 provides a summary of the key findings of this investigation.

2. EXPERIMENTAL SETUP

2.1 OBJECTIVES

Based on consideration of the issues affecting long link use in EBFs discussed in Chapter 1, an experimental program was designed to investigate a number of important aspects of long link behavior. The objectives of this experimental program were as follows:

(1) develop an improved understanding of the yielding mechanisms and controlling failure modes in long links

(2) collect experimental data on the plastic rotation capacity and ultimate strength of long links

(3) investigate the effectiveness of stiffeners for delaying various failure modes in long links

(4) assess the performance of link-to-column connections, including connections to the column web

(5) investigate the effects of yielding outside of the link on overall strength and rotation capacity

(6) verify selected brace connection details

In order to collect meaningful data on each of the above items, a number of important variables required consideration. The major experimental parameters investigated in this study were as follows:

- link length
- beam section properties
- location of stiffeners
- brace-beam angle
- brace flexural stiffness
- beam lateral support spacing
- link-to-column connection details
- brace-to-link connection details

Because of the rather large number of variables considered in this program, no single variable could be exhaustively investigated. Consequently, it must be recognized that this experimental program only begins to address some of the important issues related to long links. Nonetheless, this program was expected to provide useful data on a rather broad range of potential long link problems as well as provide a basis for preliminary design recommendations for long link EBF systems.

2.2 DESCRIPTION OF SUBASSEMBLAGE

The subassemblage chosen for this experimental program models a portion of a single diagonal EBF (Fig. 1.1a). The location of the subassemblage within the frame is illustrated by the bold lines in Fig. 2.1. An EBF with the links attached to the columns was chosen as the prototype since the behavior of link to column connections was identified as a potentially serious problem for long link EBFs. Portions of the beam and brace outside of the link were also included since the effect of yielding outside of the link was of interest. Boundaries of the subassemblage were chosen to approximately coincide with points of inflection in the frame.

A schematic representation of the testing arrangement is shown in Fig. 2.2, with a more detailed view of the setup shown in Fig. 2.3. As indicated by Fig. 2.2, the brace and the beam are essentially held in place, while the column segment is cycled back and forth. By comparing Fig. 2.2 with Figs. 1.4c or 1.10a, it is apparent that the rigid-plastic kinematics of the subassemblage are identical to that of a single diagonal EBF. The additional linkage between the end of the brace and the end of the beam generates the correct level of axial force in the beam. Two test setups with different overall lengths were used. These are indicated as setup "A" and "B" in Fig. 2.3. This permitted a wide range of link lengths and brace-beam angles to be investigated. A photograph of the test setup is shown in Fig. 2.4.

The dimensions of subassemblage were chosen to model a full size frame at approximately 2/3 scale. The length of the column segments in the subassemblage are based on a nominal 12 ft. prototype story height, with assumed points of inflection at column mid-height. The actual location of points of inflection in columns varies during an earthquake [28]. This is an important issue for column design, but should have little effect on link behavior. The brace segment in the subassemblage corresponds to one-half of the brace in the prototype, with an assumed point of inflection at mid-length. This was a necessary constraint in order to make use of existing test facilities and equipment. In the prototype, brace inflection points are typically located at about 0.6 to 0.8 times the length of the brace from the link. Thus, in order to maintain approximately the correct relative flexural stiffness between the beam and the brace, the point of inflection in the beam was also moved closer to the link. This was accomplished in the subassemblage by introducing a small eccentricity at the beam end connection.

The dimensions of the individual test specimens were not chosen to model specific prototype frames, but rather were chosen to investigate the various geometric parameters of interest, specifically link length and brace-beam angle. However, for each test specimen, a corresponding prototype span length can be determined for the chosen link length and brace beam angle and from the assumed 12 ft. prototype story height. These prototype frame dimensions corresponding to each test specimen are listed in Table 2.1. Note that the prototype span lengths cover a wide range, varying from about 14 ft. to 27 ft.

The testing arrangement was chosen to accurately simulate particular force relationships in the prototype. Those relationships considered specifically in the modelling were as follows:

- the ratio of initial elastic end moments in the link
- the ratio of axial force in the beam to shear force in the link
- the ratio of axial force in the brace to shear force in the link
- the initial elastic distribution of link end bending moment to the beam and brace

Comparison of elastic analyses of the prototype frames to elastic analyses of the subassemblages indicated that the above quantities were accurately simulated in the subassemblages.

Limitations of Subassemblage

The subassemblage chosen for this experimental program has several important limitations which must be considered when interpreting the results of the experiment. These are discussed below.

(1) Composite Floor Deck

A composite floor deck may significantly influence the behavior of an EBF with long links, both in the behavior of the link as well as in the behavior of the beam segment outside of the link. An experimental study by Ricles and Popov [16] indicated that a composite deck had little influence on the ultimate strength and rotation capacity of *short* links. Because of the completely different deformations and forces generated in a long link, there is no reason to assume that this conclusion necessarily applies to long links. A composite floor deck may also have an important effect on the strength and stability of the beam segment outside of the link.

A composite floor deck was not included within the scope of this experimental program for several reasons. First, an understanding of bare steel behavior of long link EBF systems is needed before composite behavior can be properly understood. The present investigation will help to identify those EBF configurations, if any, where bare steel behavior is unacceptable due to excessive yielding outside of the link. This will provide useful input to future studies where composite decks are included. Further, a composite deck is not always present. For example, EBFs around the elevator core of a building may have little or no decking. In addition, industrial structures often have no floor systems. Bare steel behavior is therefore directly applicable to these cases.

(2) Link Axial Force

No axial loads are applied to the links in this experimental program. Experiments by Kasai and Popov [14] on short links indicate a loss in link strength and plastic rotation capacity due to the application of large axial forces to the link. Further, the observed detrimental effects of link axial force increased as link length increased. It is therefore anticipated that long links would suffer significant loss of strength and plastic rotation capacity in the presence of high axial loads. This is not a significant limitation though, since EBF framing can generally be chosen to preclude

large link axial forces.

(3) Brace Buckling

Since the subassemblage models only one half of the full brace length, it is apparent that the possibility of brace buckling cannot be investigated in this test program. A basic premise of EBFs is that braces are designed not to buckle, regardless of the magnitude or distribution of lateral loads on the frame. It is assumed that this premise is adhered to in the prototypes. The possibility of brace buckling has therefore been eliminated as a variable in this experimental program. Note that the subassemblage does properly represent the forces generated in the brace by the link as well as those generated by the effects of beam yielding or instability. In order to properly design a brace to preclude buckling, a realistic estimate of the brace forces are needed. The subassemblage properly models these forces.

2.3 THE TEST SPECIMENS

Fig. 2.5 illustrates a typical test specimen. Each specimen was bolted into the test setup through end plate connections at the brace, beam, and column as shown. A total of 14 tests were conducted in this experimental program. Table 2.2 lists the key dimensions and the beam and brace sections for each specimen. The original testing program called for 12 test specimens. Specimen 11, however, after initial testing was repaired, retested, repaired again, and retested again. The repaired versions of Specimen 11 were designated Specimens 11R1 and 11R2 ("R" for repaired). Link details for each specimen, including stiffener locations and brace connection details are illustrated in Figs. 2.6 to 2.18. Link-column connection details are shown in Figs. 2.19 to 2.27.

Section and Material Properties

Tables 2.3 to 2.5 provide a listing of the nominal section dimensions and properties for the *W* sections and rectangular tube sections used for the beams and braces of the test specimens. All *W* sections were of A36 steel, whereas all tubes were of A500 Grade B steel (nominal $F_y = 46\ ksi$). These tube sections are cold-formed and contain a welded seam running the length of the member. Prior to each test, the actual section dimensions of the beam and brace were measured in a number of locations along the members. The average value of these measured dimensions are listed in Tables 2.6 and 2.7.

After the completion of each test, standard plate type tensile coupons were prepared from portions of the members that were not yielded or damaged. Web coupons for *W* sections were taken from mid-depth of the member. Coupons for the tube sections were taken from the central portion of the tube walls, well away from the corners.

A typical stress-strain diagram from a *W* section coupon is shown in Fig. 2.28 and that from a tube section is shown in Fig. 2.29. All of the stress-strain diagrams from the *W* sections displayed a well defined yield point and yield plateau as in Fig. 2.28. On the other hand, no yield plateau or clearly defined yield point were observed in the tube section coupons. These stress-strain diagrams apparently reflect the work hardening of the steel resulting from the cold forming process. Other investigators [29] have noted that the yield strength of cold formed tubes is typically significantly higher in the corner regions than in the central portions of the walls, due to the greater degree of work hardening in the corners. The yield strengths determined from the tube walls must therefore be considered a lower bound on the actual average yield strength of the tube.

Various parameters measured in the testing of the tensile coupons are listed in Tables 2.8 and 2.9. Some observations on these tables:

- The yield strength of all of the A36 *W* sections (Table 2.8) significantly exceeded 36 ksi. The average yield strength of the web coupons was 51.4 ksi (1.43 times nominal strength) and that of the flange coupons was 45.6 ksi (1.27 times nominal strength)
- The average *W* section web yield strength was 1.13 times the average flange yield strength. The greater degree of overstrength in the web as compared to the flange is significant since it will delay the onset of shear yielding with a consequent increase in the degree of flexural yielding experienced by the link.
- The average ultimate tensile strengths of the W section webs and flanges were 65 ksi and 67.7 ksi, respectively. This is within the specified 58 to 80 ksi tensile strength range for A36
- For the rectangular tube sections (Table 2.9), the average yield strength was 56.9 ksi (1.24 times nominal strength). There was little difference between the average yield strengths of the web and flange coupons. This is expected since the tube is formed from a single plate of uniform thickness. As noted above, the actual average yield strength of the tubes may be somewhat higher than indicated by Table 2.9 due to the anticipated higher yield strength at the tube corners.

Based on the actual measured section dimensions combined with the tensile coupon data, actual section properties were estimated for the *W* sections and tube sections. These are listed in Tables 2.10 and 2.11. These values can only be considered an estimate of the actual section properties since they are based on a limited sampling of section dimensions and tensile coupon data for each member. The estimated properties of the tube sections are likely less accurate than those of *W* sections because of the difficulty in establishing a representative yield stress value for the tubes.

Finally, Table 2.12 lists the link lengths non-dimensionalized by the factor M_p/V_p for each specimen. Due to the difference in flange and web-yield strengths, the actual values of M_p/V_p differ significantly from the nominal values. As a result, the actual non-dimensionalized link lengths are on the order of 10 to 20 percent greater than the nominal values. Thus, the difference in flange and web yield strengths effectively "lengthens" the links and can have the effect of transforming a nominally *short* link into a *long* link.

2.4 TEST SPECIMEN DESIGN CONSIDERATIONS

This section discusses some general aspects of the design basis for the test specimens. Additional remarks concerning specific design issues are included in the discussion of test specimen performance in Chapter 3 of this report.

Link Length

The link lengths were chosen to provide data in the transition zone where both shear and flexural yielding are significant (Specimens 1-4, 7, 8 and 11) as well as in the zone where flexural yielding alone dominates (Specimens 5, 6, and 12). Specimens 9 and 10 were provided with short links in order to study the behavior of short link to column web connections. Based on the estimated actual values of M_p/V_p, link lengths varied from $1.4M_p/V_p$ up to $4.25M_p/V_p$ (Table 2.12).

Beam Sections

Of the beam section properties that may affect long link behavior, the width-thickness ratio of the flange is likely to be the most important, since flange buckling is expected to be an important failure mode in long links. Accordingly, two sections were chosen for the beams of the test specimens: $W12\times16$ and $W12\times22$. These sections represent reasonable upper and lower bounds for flange width-thickness ratio, $b_f/2t_f$ (Table 2.3). The W12×16 is representative of sections with relatively slender flanges whereas the $W12\times22$ has relatively stocky flanges. At the same time, the web slenderness ratio, d/t_w, for these sections are typical of many common larger beam sections. The $W12\times16$ and $W12\times22$ were not chosen to model any particular larger beam sections. Nonetheless, at 2/3 scale, the $W12\times16$ approximately models a $W18\times35$, and the $W12\times22$ approximately models a $W18\times46$.

Stiffeners

Stiffener locations were chosen for each specimen as the testing program proceeded, based on the observed failure patterns in the earlier specimens. Every specimen, however, was provided with full depth, two-sided stiffeners above the brace at the link end, as well as above the other end of the brace connection. All other stiffeners were provided on only one side of the beam. The location and size of stiffeners for each specimen are shown in Figs. 2.6 to 2.18.

Brace-Beam Angle

As noted in Chapter 1, the angle between the brace and the beam in an EBF is an important factor controlling the level of axial force in the beam segment outside of the link. As this angle is decreased, the axial force level in the beam and consequently the potential for beam yielding and instability increases rapidly. The test specimens were designed with brace beam angles varying from about 28 deg. to 51 deg. (Table 2.2). The specimens with particularly small brace-beam angles (Specimens 7, 8, and 11) represent a very severe case of potential beam damage. However, a review of several actual recent EBF designs indicated that brace-beam angles as low as 28 deg. are being used in practice.

Brace Sections

For most of the test specimens, the braces were sized using the beam-column strength and stability equations in Part 2 of the 1978 AISC Specification (Eqs. 2.4-2 and 2.4-3 in Ref. 30). These equations were checked using the estimated axial force and bending moment generated in the brace by the ultimate link shear force and end moment. For this purpose, the ultimate link strength was estimated as follows:

(1) For the nominally short links (Specimens 9, 10, and 11), an ultimate link shear of $1.5V_p$ was assumed. Ultimate link end moments were computed from link statics, assuming end moment equalization ($2M = eV$).

(2) For the very long links (Specimens 5, 6 and 12), ultimate end moments of $1.5M_p$ were assumed, with ultimate link shear determined from statics.

(3) For link lengths in the intermediate range of about $2M_p/V_p$ (Specimens 1, 2, 3, 4, 7, and 8) an ultimate link shear of $1.25V_p$ and ultimate end moments of $1.25M_p$ were assumed.

The first two assumptions above are consistent with the code recommended values of ultimate link strength (Eqs. 1.4 and 1.5). For the intermediate length links, however, following the code recommended ultimate strengths resulted in the need for excessively large brace sections. Further, preliminary analyses of long links [35] indicated that the code specified ultimate link strengths may be too large in the intermediate link length range. Consequently, for these test specimens, a reduced overstrength factor of 1.25 was used for both shear force and bending moment.

The axial force generated in the brace by the ultimate link forces were estimated from the statics of the link-beam-brace connection. The portion of the ultimate link end moment transferred to the brace was then estimated from an elastic analysis. If the analysis of the beam segment outside of the link indicated the likelihood of the beam yielding, the design moment for the brace was increased so that the combined flexural strength of the beam and brace exceeded the assumed ultimate link end moment. The listing of the brace sections in Table 2.2 indicates many

of the test specimens used very heavy brace sections. Those heavy brace sections are primarily a consequence of the large bending moments generated in the braces when long links are used.

For Specimens 7, 8 and 11, the above design procedure was not used for the braces. For these specimens, the braces were sized only for axial force, ignoring the bending moment generated in the brace by the link. These braces were therefore sized in the same way as a brace in an CBF. Consequently, brace sections were chosen that provide high compressive axial strength but only very little bending strength. For these specimens, the combined flexural strength of the brace and beam (reduced for axial force in the members) was generally less than 50% of the assumed ultimate link end moment. Thus, by virtue of these light brace sections combined with very low brace-beam angles, Specimens 7, 8 and 11 were designed to incur severe yielding outside of the link. The intent of these specimens was to determine if yielding in the beam and/or brace could provide a stable energy dissipation mechanism for EBFs.

Specimen Lateral Support System

The lateral support system used for the test specimens is illustrated in Fig. 2.30. Simple teflon coated supports were provided at two locations on the column and also at the end of the brace primarily to support the weight of the subassemblage.

For the link end as well as for the beam segment outside of the link, a somewhat more elaborate lateral support system was devised, as illustrated in Fig. 2.30. This system, which used teflon coatings on all moving surfaces, restrained lateral displacements as well as rotations about the longitudinal axis of the beam. The lateral support at the link end was equipped with a series of four load cells that permitted measurement of the out-of-plane forces developed at the link end support.

The spacing of lateral supports along the link and beam of each test specimen are listed in Table 2.13. For each specimen, a lateral support was always provided at the link end. No additional lateral supports were provided within the link.

The distance from the link end lateral support to the first beam lateral support was initially set at $96(r_y)^{½}$, where r_y is the weak axis radius of gyration of the beam section. This is the support spacing recommended by SEAOC [5] for beams in MRFs. With this spacing, the beam-column stability equation in Part 2 of the 1978 AISC Specification (Eq. 2.4-2 of Ref. 30) was checked using an estimate of the axial force and bending moment generated in the beam by the assumed ultimate link forces. This check showed that a spacing of $96(r_y)^{½}$ did not satisfy the AISC stability equation for some of the specimens, particularly those with very low brace-beam angles. However, a spacing of $96(r_y)^{½}$ was still used in many cases in order to avoid the use of overconservative lateral spacing and to test the actual stability limits of the beam. This spacing was varied for some of the later specimens based on the performance of the earlier test specimens.

The distance to the next beam lateral support for most specimens was controlled by the end of the subassemblage. Only for Specimen 11R2 was an additional lateral support provided between the first beam lateral support and the end of the subassemblage.

Column Section

The stiffness of the column section has an important effect on the initial distribution of elastic bending moments in the link. Very stiff columns result in much higher elastic moments at the column end of the link relative to the brace end of the link. Experiments by Kasai [14] demonstrated that initially unequal end moments have little effect on the ultimate strength and rotation capacity of a short link. The present experiment permitted a similar investigation of the effect of initially unequal end moments in long links and the manner of subsequent moment redistribution within the link. A review of several actual EBF designs, including a 12 story and a 40 story building, indicated that column sections were typically on the order of 1 to 6 times stiffer than the link sections, depending on location within the frame. Based on this range, a $W10\times77$ column section was chosen for the test specimens, providing relative column to link moments of inertia of 4.4 and 2.9 for the $W12\times16$ and $W12\times22$ links, respectively. Use of the $W10\times77$ column therefore resulted in a realistic range of column to link stiffnesses. The same column size was used for all specimens to reduce the number of variables in the test and to simplify the testing apparatus. Elastic analyses of the subassemblages indicated that the initial elastic bending moment at the column end of the link varied from 1.7 to 4.3 times the moment at the brace end of the link.

Link-to-Column Connections

At present, the connection of a short link to a column is required to be all welded [5]. That is, both the flanges and web of the link must be welded to the column. Based on the discussion in Chapter 1, a similar practice is appropriate for long links, due to high shear forces and very high bending strains anticipated at the link end. A fully welded link-to-column connection was therefore used for all test specimens. Details of the link-to-column connections are shown in Figs. 2.19 to 2.27.

With the exception of Specimen 12, all specimens were provided with full penetration welds at the link flanges. Web connections consisted of either a fully welded shear tab or a full penetration weld between the link web and the column. For Specimen 12, an all-around fillet weld was used to connect the link flanges and web to the column flange. Specimens 9 and 10 were provided with link-to-column web connections. All other connections were to the column flange. For connections to the column flange, no continuity plates were provided opposite the link flanges. The SEAOC criteria for MRF connections (Section 4.F.4 of ref. 5) indicated that continuity plates were not required.

For some of the specimens, the link-column connection was reinforced either with "ribs" (Specimens 4, 6, 7 and 8) or with cover plates (Specimens 11R1 and 11R2). The design of these

connections is described in greater detail in Chapter 3.

Brace-Link Connections

Three different types of brace connections were used for the test specimens:

- a direct welded connection for *W* section braces,
- a direct welded connection for tube section braces,
- a stiffened gusset plate connection for tube section braces.

Details of the brace connection for each specimen are illustrated in Figs. 2.6 to 2.18. Factors influencing the choice of these details are discussed below.

Analysis of the test specimens indicated that high brace end moments were anticipated for all specimens. These high end moments, combined with very high axial forces, indicated the need for fully rigid brace connections capable of developing the strength of the brace under combined bending and axial force. Discussions with a fabricator experienced in EBF construction indicated that direct connections are generally more economical than connections involving a number of splice plates. Therefore, for a number of the test specimens, the braces were welded directly to the beams.

For specimens with *W* section braces (Specimens 1, 2, 5, 6 and 12), full penetration welds were used at the brace flanges. The brace webs were connected by either a fully welded shear tab or by means of a full penetration weld directly between the brace web and beam flange. Welded web connections were used because it was found that the brace web strength could not be developed by a bolted web connection. Stiffeners were provided above the brace flanges and were designed according to sect. 1.15.5 of the 1978 AISC Specification [30].

For specimens with tube braces connected directly to the beam (Specimens 3, 4, and 8), the tube was welded all around using the detail shown in Fig. 2.8. For these Specimens, in addition to providing vertical stiffeners above the tube flanges, stiffener plates were also provided above the brace webs as shown in Fig. 2.8. The purpose of these stiffeners was to permit full development of brace web strength without causing excessive "flexing" of the beam flange. It was believed that such flexing may cause an early failure of the brace web weld by causing a highly nonuniform distribution of stress along this weld.

An additional design constraint imposed on the brace connection was the requirement that the intersection of the brace and beam centerlines must fall either at the end of the link or inside the link, but not outside of the link. Analysis of EBFs with the brace-beam centerline intersection inside the link indicated that this eccentricity in the connection produced a moment that was opposite in sign to the link end moment. This produced the desirable effect of reducing the bending moment generated in the beam and brace. On the other hand, when the intersection falls outside of the link, the bending moment generated in the beam and brace is increased. This undesirable

effect was avoided by requiring that the intersection always occur inside the link.

For braces with direct connections to the beam, the above requirement effectively limited the depth of the brace section as follows:

$$d_{brace} \leq d_{beam} \cos\alpha \tag{2.1}$$

Where d_{brace} and d_{beam} are the depth of the brace and beam section, and α is the angle between the beam and brace. For example, for Specimen 1 with a 12 inch beam depth and a brace-beam angle of 48 deg., the permissible brace depth was limited to about 8 inches. This imposed a significant constraint on the choice of brace sections. In order to satisfy the strength and stability requirements for the brace as well as satisfy the above geometric constraint resulted in *W* section braces with a flange width greater than the width of the beam. For Specimens 1 and 2, the brace flange was tapered to match the beam flange width at the connection. For the remaining W section braces, the brace flange was not tapered. For tube section braces with direct connections, in addition to the above constraint on brace depth, the brace width was of course limited to the width of the beam.

As discussed in Chapter 1, a gussetted tube brace to link connection (Fig. 1.11) failed in the Tsukuba tests. Based on an analysis of the failed connection, an improved detail was developed. The edge of the gusset nearest the link was stiffened and the brace end was cut parallel to the beam and located as close to the beam as practical. Both of these measures were intended to reduce the likelihood of gusset buckling. This improved detail was used for Specimens 7, 9, 10 and 11 in order to verify the performance of the connection.

2.5 TEST SPECIMEN FABRICATION

The test specimens were constructed by a commercial steel fabricator in San Francisco, California. The test specimens were fabricated in three stages; first Specimens 1-6, then Specimens 7-9, and then finally Specimens 10-12. This permitted design changes in the later specimens based on the observed performance in the earlier tests. It also permitted reuse of the the $W10\times77$ column sections. Each column section was used two times, with the link connected to a different face of the column for each use. Some fabrication was also performed by in-house personnel at the University of California Structural Engineering Laboratory. This included welding stiffeners to the links for Specimens 2-5, welding the "ribs" at the link-column connection for Specimens 4 and 6, and performing the repairs and modifications to the link-column connection for Specimen 11R1.

The fabricator was required to weld the link-column and brace-beam connections with the column in an upright position and the test specimen oriented with the brace beneath the beam. This was intended to simulate field welding positions. All welding on the test specimens was by

the Shielded Metal Arc ("stick welding") processes using E7018 electrodes. Only visual inspection was provided for the welds. Discussions with a weld inspection specialist indicated that ultrasonic testing would be ineffective for the material thicknesses used in the test specimens.

Several undesirable features were noted in the welding of the first six test specimens that were corrected in the last six specimens. Full penetration welds tended to be "overwelded", with somewhat excessive amounts of weld metal extending above the plate. In addition, web copes made to accommodate the full penetration welds were flame cut and appeared very rough and jagged. Further, back-up strips for the full penetration welds were attached using fillet weld tacks on the side of the strip opposite the weld groove. For the last six specimens, each of these undesirable features were eliminated. Full penetration welds were not permitted to extend more than 1/8 inch above the plate. Grinding was required at flame cut web copes. Back-up strips were permitted to be tacked only within the groove, as recommended by AISC (see Fig. 2.19 in Ref. 31).

2.6 INSTRUMENTATION

As shown in Fig. 2.3, load cells were installed at a number of locations throughout the subassemblage. These load cells permitted determination of axial force, shear force, and bending moment at points within the subassemblage by statics. Also, as shown in Fig. 2.30, load cells were provided at the link end lateral support to measure out-of-plane forces. Based on the calibration data and the observed performance of the load cells, the accuracy of the load cells is estimated as follows:

50 kip cells:	$\pm$.2 kip $\pm$ .5% of load
125 kip cell:	$\pm$.2 kip $\pm$ .5% of load
200 kip cells:	$\pm$1.5 kip $\pm$ 1% of load
300 kip cell:	$\pm$1 kip $\pm$ 1% of load
7 kip cells:	$\pm$.1 kip $\pm$ 2% of load

A variety of displacement transducers were used to monitor deflections and rotations at various locations of the subassemblage. The locations are shown in Fig. 2.31. Rotations were measured by attaching a rigid bar at the point of interest and measuring displacements at the ends of the bars.

For most test specimens, electrical resistance strain gages were applied at number of locations in the link and/or brace connection area. Strain gage locations, installation, and results are discussed later. Further, for Specimens 1, 4, 6, 9 and 12, techniques of close-range photogrammetry were used to monitor deformations of grid lines drawn on the specimens. This technique and the results are described in detail later.

Electronic data (load cells, displacement transducers and strain gages) were recorded on an IBM PC/AT using a data acquisition systems developed at the University of California. For Specimen 1, a low speed data acquisition system was used that required loading of the test specimen to be stopped for each reading. For the remainder of the tests, a high speed system was used that permitted readings to be taken without stopping the loading process. An average of 50 to 60 channels of data were recorded for most specimens.

Subsequent data reduction and plotting was accomplished on a Digital Microvax Workstation using a general purpose data analysis and graphics software package called "S" [32]. This software package was also used for analysis and plotting of photogrammetric data.

3. EXPERIMENTAL PERFORMANCE OF TEST SPECIMENS

3.1 INTRODUCTION

This chapter provides detailed descriptions of the 14 tests performed on the EBF specimens described in Chapter 2. For each test, a brief description is provided of significant events that occurred during the test, such as initiation of yielding, flange buckling, lateral torsional buckling, fracture, etc.. A detailed summary of damage to the specimen is then provided. It should be noted that the occurrence of yielding on a specimen is based on the observed flaking of whitewash painted on the specimen. Whitewash is not always a reliable indicator of yielding and so these observations must be interpreted with caution. More specifically, it was found that whitewash was not effective on the tube brace members nor on any surface where the mill scale was removed by grinding or by other means.

The overall performance of each specimen is displayed in plots of link shear versus link rotation angle γ, and in plots of link shear versus link plastic rotation angle γ_p. In addition, photographs of the specimens during and after testing are presented to clarify the nature and extent of the damage incurred by each specimen. Additional experimental data collected during the tests are presented and analyzed in later chapters.

Figure 3.1 illustrates the manner by which the link rotation angle γ is computed. The angle γ is defined as the relative end deflection of the link divided by the link length. A positive value of γ corresponds to an eastward displacement of the column, as shown in Fig. 3.1. The value of γ defined in this way includes contributions from both elastic and inelastic link deformations, as well as contributions from link end rotations at the column and brace ends of the link. The link end rotations also include an inelastic component for those cases where yielding occurred outside of the link.

A response parameter of greater interest than the total rotation γ is the link plastic rotation angle γ_p. The value of γ_p was computed for each specimen as follows:

$$\gamma_p = \gamma - \frac{V_{link}}{k_e} \tag{3.1}$$

In this equation, γ is the total link rotation angle as defined in Fig. 3.1, V_{link} is the shear force in the link, and k_e is the ratio V_{link}/γ in the elastic range. For each specimen, k_e was estimated from the measured values of V_{link} and γ in the initial elastic test cycles. The value of γ_p computed in this manner includes contributions of inelastic link deformations as well as inelastic link end rotations produced by yielding or inelastic buckling outside of the link.

Figure 3.2 illustrates the sign convention adopted for forces and moments at various locations in a test specimen. This figure also shows the terminology used for portions of a test specimen.

Note that the term "brace connection panel" refers to the portion of the beam directly above the brace. Also, in the description of the tests, the term "beam" refers to the portion of the member north of the brace connection panel.

Test Procedure

All specimens were tested pseudo-statically with slowly applied (i.e. no strain-rate effects) cyclic loads. Testing was controlled by monitoring a plot of load applied to the column (load on the column is equal in magnitude to the shear force in the link) versus column displacement. For a typical test, the specimen was first subjected to several cycles of increasing load in the elastic range. After significant yielding of the specimen was observed, displacements were progressively increased. For most specimens, the cyclically imposed displacements were increased up to the essentially complete failure of the specimen. However, for Specimens 11 and 11R1, testing was stopped after initial failure to permit repair of the specimens.

A history of link rotation for a typical test specimen is shown in Fig. 3.3. Table 3.1 lists the complete history of link rotation and link shear for each test. Note that the value of link shear reported in Table 3.1 is the value at the end of each cycle, and may be less than the peak value for that cycle.

3.2 THE TESTS

3.2.1 Specimen No. 1

Specimens 1 and 2 were of nominally identical design, except for the location of stiffeners. The link lengths were in the intermediate length range (nominal e = $2M_p/V_p$) where significant contributions of shear and flexural yielding are anticipated. These specimens were designed to minimize the likelihood of significant yielding or instability of the beam or brace in order to focus study on the behavior of the link and on the effects of stiffener location on link performance. Link stiffeners for Specimen 1 were equally spaced to satisfy the short link stiffener spacing criteria of Eq. 1.3b.

Test Notes - The response of Specimen 1 is shown in Fig. 3.4. Initial yielding occurred during cycles 5 and 6 with significant yielding observed in the link flanges adjacent to the column. For most of the test specimens, initial yielding was typically observed at this location and can be attributed to the initially high link end moment at the column end of the link. During cycle 8W, initiation of flange buckling was noted at the southeast end of the link, and during cycle 9E, at the southwest end of the link. Flange buckling at the northwest end of the link was first observed in cycle 10W. During cycle 13E, a severe flange buckle developed in the east flange of the brace connection panel outside of the link. Coincident with the formation of this flange buckle was a

small loss of load carrying capacity of the specimen. Each of the flange buckles became more pronounced with each successive loading cycle, and link strength deteriorated with each cycle as is apparent in Fig. 3.4. Even though flange buckling at the southwest, southeast and northwest ends of the link occurred fairly early in the loading sequence, a significant deterioration in the hysteretic loops was not observed until flange buckling occurred in the east flange of the brace connection panel. Flange buckling was never observed at the northeast end of the link.

During cycle 16E, a crack developed in the flange at the southeast end of the link. It appeared that the crack initiated in the central portion of the flange near the point where the web cope meets the flange. This crack spread rapidly across the entire width of the flange. Once the east flange was completely fractured, the shear tab began to fracture. This fracture appeared to initiate near the end of the fillet weld connecting the shear tab to the link web. Upon further loading, this fracture continued along the length of the shear tab. The test was terminated at this point. On the hysteretic loops in Fig. 3.4, a circle is drawn at point where fracture of the link flange occurred. The response of the specimen after formation of the crack is indicated by the dotted lines.

Summary of Damage - Photographs of Specimen 1 after testing are shown in Fig. 3.5. Yielding, as evidenced by flaking of whitewash painted on the back side of the specimen was apparent in the link flanges at both ends of the link, in the east flange of the brace connection panel and throughout the entire link web. The most severe flange buckling occurred in the east flange of the brace connection panel (Figs. 3.5 a, b, and d). The length of this buckle extended over the entire length of the panel (about 10 inches), with the peak occurring 2 to 3 inches from the north end of the link. The web of the brace connection panel was also severely buckled in the region adjoining the flange buckle.

Severe flange buckles were also present in both flanges at the south end of the link (Fig. 3.5c). These buckles extended over the full length of the link's first panel, running from the north edge of the back-up strip at the link flange weld to the edge of the fillet weld at the first stiffener, a length of about 5 inches. These flange buckles terminated at the first stiffener on both sides of the link, even though stiffeners were provided on only one side. The flange buckle at the northwest end of the link was less severe than those at the south end of the link. The length of this buckle extended from the link end to the first stiffener. The buckle at the northwest end of the link was symmetric, with both the top and bottom portions of the flange buckled outwards. The flange buckles at the south end of the link and in the brace connection panel were unsymmetric, with the top and bottom portions of the flange buckled in opposite directions. As noted earlier, no flange buckling was observed at the northeast end of the link.

No web buckling was observed within the central portion of the link. At both the north and south ends of the link minor web distortions were present in the regions adjoining the flange

buckles. These web distortions were apparently associated with the flange buckles. There was no observable damage in the beam, brace or brace connection.

Ultimate failure of Specimen 1 was caused by a fracture in the east flange of the link in the region adjoining the full penetration weld (Fig. 3.5c). The fracture appeared to start at the web cope ("rathole"). As is apparent from Fig. 3.4, this fracture resulted in almost total loss of link load carrying capacity. If the test had not been stopped, the link would have likely completely separated from the column.

3.2.2 Specimen No. 2

Specimen 2 was of nominally identical design to Specimen 1, except for stiffener locations. Within the link of Specimen 2, one stiffener was placed at about 4 inches from each end. This spacing is equal to one flange width and was chosen to delay the onset of flange buckling at the link ends. As noted in Chapter 1, locating stiffeners at b_f from the link ends is motivated by Lay's theory of flange buckling [25]. No additional stiffeners were provided within the link in an attempt to determine if web stiffening is needed in the intermediate link length range. The lack of web stiffening was also motivated by the fact that no sign of shear buckling of the link web was observed in Specimen 1.

For Specimen 2, a partial depth stiffener was also provided at mid-length of the brace connection panel (Fig. 2.7). This stiffener was intended to delay the very severe flange and web buckling observed in the brace connection panel of Specimen 1. A partial depth stiffener was used since all of the damage was concentrated in the upper portion of the panel. The stiffener extended about three-quarters of the beam depth in order to "anchor" the stiffener in the stable lower portion of the brace connection panel.

Test Notes - The response of Specimen 2 is shown in Fig. 3.6. Slight yielding was first observed during cycles 2E and 2W in the link flanges at the south end of the link and in the east flange of the brace connection panel opposite the partial depth stiffener. During cycle 4E, significant yielding was noted in the flange at the southwest end of the link, with slight additional yielding in the flange at the southeast end of the link and in the east flange of the brace connection panel. The initiation of yielding in the flanges at the north end of the link was also observed during this cycle. In cycle 5, the formation of slight yield lines was observed in the beam's east flange. These yield lines were consistently oriented at about 45 deg. to the longitudinal axis of the beam. During cycle 6E, web yielding became apparent in the link end panels and also towards the south end of the link's central panel. In cycles 7E and 7W, significant web yielding was apparent over the full length of the link. Within the central panel of the link, the web yield lines were consistently oriented parallel to the longitudinal axis of the link. Near the end of cycle 9E, a large web buckle formed in the central panel of the link, running diagonally across the

panel. Coincident with the formation of this web buckle was a significant drop in link load carrying capacity. With each successive loading cycle, the web buckle in the central link panel became more severe. Link hysteretic behavior also deteriorated severely as is apparent in Fig. 3.6. Whenever the direction of loading was reversed the location of the web buckle also switched between opposite diagonal corners of the panel. During cycle 14E, a large tear developed in the central portion of the link web. During cycle 15E, this tear continued to grow rapidly, and the test was terminated.

Summary of Damage - Photographs of Specimen 2 after testing are shown in Fig. 3.7. Significant yielding in this specimen occurred over the entire link web, at the link ends, and in the east flange of the brace connection panel. Slight yield lines were also apparent in the east flange of the beam. Otherwise, there was no observable damage in the beam, brace or brace connection. The primary failure mode for Specimen 2 was severe web buckling in the large central panel of the link. No significant flange buckling occurred at the link ends or in the brace connection panel. The absence of buckling in the brace connection panel however cannot necessarily be attributed to the addition of a stiffener in the panel. The load level at which buckling initiated in the brace connection panel of Specimen 1 was never achieved in Specimen 2.

The hysteretic behavior of Specimen 2 (Fig. 3.6) is typical of many previous tests on shorts links subject to cyclic inelastic web-buckling [9]. Each cycle displays a peak load followed by a drop in capacity due to formation of the web buckle. Upon continued loading, capacity once again increases due to the formation of a tension field. Associated with formation of the tension field is the development of flange distortions in the buckled panel (Fig. 3.7b). Load carrying capacity degrades steadily with each cycle until tearing of the web finally occurs.

It was apparent from Specimen 2 that some degree of web stiffening is needed for links in the intermediate length range. It is also interesting to note that a fracture did not occur in the link flange of Specimen 2 as it did in Specimen 1. It appears that the loss of load carrying capacity due to web buckling in Specimen 2 precluded the development of a fracture.

3.2.3 Specimen No. 3

Specimens 3 and 4 were of nominally identical design, except for the location of stiffeners and the modification of the link-to-column connection in Specimen 4. The link lengths for these specimens were again in the intermediate length range (nominal $e = 2M_p/V_p$). As with Specimens 1 and 2, these specimens were designed to prevent significant damage in the beam or brace in order to focus study on the link behavior. The $W12\times22$ sections used for Specimens 3 and 4 had much thicker flanges than the $W12\times16$'s used for Specimens 1 and 2. Link stiffeners were equally spaced for Specimen 3. Based on the observed performance of Specimen 1, stiffener spacing was increased somewhat beyond that required by Eq. 1.3b.

Test Notes - The response of Specimen 3 is shown in Fig. 3.8. Initial yielding of this specimen was noted during cycle 3E with slight yielding in the flanges at the south end of the link, in the east flange of the brace connection panel opposite the stiffeners, and also in the web of the link. Some yielding of the flange at the northwest end of the link was first noted in cycle 4E. In cycle 5E, significant yielding was apparent in the flanges at the south end of the link as well as some additional yielding in the link web. Slight yielding was also apparent in both flanges at the north end of the link. During cycle 8E, the first signs of slight flange buckling were noted at the southwest end of the link. In cycle 8W, the appearance of a very small crack was noted at the west edge of the shear tab near the end of the fillet weld connecting the shear tab to the link web. A slight flange buckle was first noted at the northwest end of the link in cycle 10W. During cycle 12W, a slight flange buckle was observed at the southeast end of the link. The crack in the west end of the shear tab also appeared to grow during this cycle. During cycle 13E, the flange at the southeast end of the link suddenly fractured. Upon reversing the loading in cycle 13W, the flange at the southwest end of the link also suddenly fractured. On the hysteretic loops in Fig. 3.8, circles are drawn at the points where the flanges fractured. The response of the specimen after formation of the first fracture in the east flange is indicated by dotted lines.

Summary of Damage - Photographs of Specimen 3 after testing are shown in Fig. 3.9. Significant yielding on this specimen was apparent in the link web over the entire length of the link. The link flanges showed yielding for about 6-7 inches from each end of the link (Figs. 3.9b and c). The east flange of the brace connection panel also showed heavy yielding, with the more severe yielding in the south half of the panel (Fig. 3.9c). Yielding also was observed in the web of the brace connection panel in the southeast corner of the panel (Fig. 3.9a). The upper portion of the vertical stiffener (the portion extending beyond the horizontal stiffener above the brace) was noticeably bent towards the link. Measurements after testing showed that the length of the brace connection panel increased by about 3/16 in. at the east end of the panel, indicating the severity of yielding in this area. Slight yielding was also noted in the east flange of the beam extending about 3-4 inches north of the brace connection panel (Fig. 3.9c). Other than this yielding, there was no observable damage in the beam, brace or brace connection. No whitewash was applied to the $W10\times77$ column for this specimen. However, it was noted that some mill scale in the web of the column adjoining the link was flaked off, indicating some yielding in the column panel zone. Also, very slight "kinks" were observed in the north flange of the column at points where the link flanges were attached.

Flange buckling occurred at the southeast, southwest and northwest flanges of the link at the various stages of the testing. At the end of the test, buckles remained only in the southeast and northwest flanges, with the southwest buckle straightened in the final loading cycle. The flange buckles were all of the typical unsymmetrical shape. Due to the thicker flanges in the $W12\times22$

section, the buckles were far less severe than in the $W12\times16$ section of Specimen 1. No flange buckling was observed in the northeast flange of the link or in the brace connection panel of Specimen 3. Also, despite some flange buckling within the link of Specimen 3, no degradation of the hysteretic loops was observed. This suggests that flange buckling, if not too severe, produces no significant damaging effect to link performance. No web buckling was observed in this specimen.

Ultimate failure of Specimen 3 was caused by fracture of the link flanges (both east and west flanges) in the region adjoining the full penetration welds (Fig. 3.9d). Both fractures appear to have initiated in the central portion of the flange near the junction of the web cope and the flange. After fracture of each flange, a fracture also immediately ran through the shear tab. The shear tab fractures appeared to initiate at the point of termination of the fillet weld connecting the shear tab to the link web. As with Specimen 1, if the testing had not been stopped, the link would have completely separated from the column.

3.2.4 Specimen No. 4

From the tests completed to this point, it was becoming apparent that fracture of the link at the link-to-column connection was the critical failure mode controlling plastic rotation capacity of the test specimens. As a result, the link-to-column connection in Specimen 4 was reinforced in an attempt to prevent or delay fracture of the link flanges. This was accomplished by welding 4 "ribs" to the link and column flanges as shown in Fig. 2.20. This system of reinforcing ribs was used by Tsai and Popov [33] in tests on moment resisting connections to column webs. The use of these ribs proved very successful in preventing connection failure in their tests.

The intent of the ribs was to move the critical section of the link away from the full penetration welds at the link-to-column connection back to the tips of the ribs. It was believed that the heat affected zone adjacent to the full penetration welds as well as the discontinuities associated with the flame-cut web copes contributed significantly to the flange fractures. The ribs, in effect, were an attempt to move the yielding and largest inelastic strain demands to a portion of the flange less damaged by welding or by web copes.

The ribs were sized somewhat arbitrarily based on the experience of Tsai & Popov [33] so that the area of 2 ribs provided approximately 50 to 60 percent of the area of one flange. The ribs were taped in an attempt to reduce the stress concentrations in the link flange at the rib ends. The lower ribs were placed within the link for the practical consideration of avoiding field overhead welding at the connection. A photograph of the reinforced link-to-column connection is shown in Fig. 3.11a.

The locations of link stiffeners was also changed in Specimen 4. The outermost stiffeners were moved closer to the link ends in order to delay the onset of flange buckling. The remaining central portion of the link was divided in two 12 inch panels. This 12 inch spacing corresponds to

that required by Eq. 1.3c.

Test Notes - The response of Specimen 4 is shown in Fig. 3.10. Initial yielding was observed during cycles 4 and 5 in the south flanges of the link (outside of the rib area) and in the east flange of the brace connection panel. During cycles 6E and 6W yielding became more extensive in the south flanges of the link, with most of the yielding occurring outside of the ribs. In the southeast flange, however, slight yielding was noted within the rib area. During cycles 7 and 8, significant web yielding in the link was noted.

During cycle 11W, the formation of a small "kink" or bend in the link's southeast flange was observed between the end of the ribs and the first stiffener. During cycle 12E, a fracture formed in the southeast flange of the link just beyond the ribs. The fracture appeared to initiate at the tip of one of the ribs. The point at which this fracture occurred is indicated by a circle in the hysteretic plots in Fig. 3.10. During this cycle, web buckles also formed in the center two panels of the link. The buckles ran diagonally across the panels and appeared to be more severe in the south panel. Before the fracture extended over the full width of the flange, the specimen was unloaded and then reloaded in the other direction (west). During the next cycle of eastward loading (cycle 13E), the fracture in the southeast flange extended over the full width of the flange. A fracture also developed in the link web and loading was continued until this tear extended to about mid-depth of the link. Loading was then reversed for one final westward cycle. During this final cycle (13W), the specimen continued to carry significant load for large displacements. Despite these large displacements, no fracture ever developed in the west flange of the link. During this cycle, severe web buckling occurred in the central panel closest to the column. Most of the link deformation was concentrated in this panel during the final cycle.

Summary of Damage - Photographs of Specimen 4 after testing are shown in Fig. 3.11. Significant yielding of this specimen was apparent throughout the link web and in the link flanges at both ends of the link. At the south end of the link, yielding of the flanges occurred primarily beyond the ribs, with only slight yielding between the column face and the rib ends. No significant yielding was observed on the ribs themselves. Severe yielding was again apparent in the east flange of the brace connection panel and in 3 to 4 inches of the beam's east flange beyond the brace connection panel. Other than this yielding, no damage was observed in the beam, brace or brace connection. Some yielding was also apparent again in the column panel zone (Fig. 3.11d).

No flange buckling was observed at either end of the link or in the brace connection panel. Web buckling was apparent in both of the link's central panels, with the most severe buckling occurring the panel closer to the column (possibly due to higher bending moment at the column end of the link).

Ultimate failure of Specimen 4 occurred by fracture of the southeast link flange just beyond the ribs. The ribs were successful in preventing a fracture at the full penetration weld, but

unfortunately only moved the fracture to another location. The plastic rotation developed by Specimen 4 was, in fact, somewhat less than that for Specimen 3 indicating the ribs may have even worsened overall link performance. It was believed that a contributing factor to the disappointing performance of the ribs was the fact that the first stiffener may have been placed to close to the ribs. This stiffener may have forced highly localized flange distortions to occur in a very short length of flange. This is supported by the observation of a "kink" in the flange at the rib end in the loading cycle immediately preceding the fracture. It is interesting to note that the west flange of the link did not fracture as it did in Specimen 3. The performance of Specimen 4 in the final westward loading cycle suggests that significant improvements in link plastic rotation capacity are possible if connection failure can be prevented.

3.2.5 Specimen No. 5

Specimens 5 and 6 were of nominally identical design, except for the location of stiffeners and the modification of the link-to-column connection in Specimen 6. These specimens were in the long link range (nominal $e = 3.15 M_p/V_p$) where flexure is expected to dominate link behavior. $W12\times16$ sections were used for the beam and link for these specimens, the same as for Specimens 1 and 2. Consequently, Specimens 5 and 6 were intended to provide a direct comparison with Specimens 1 and 2 on the effects of increasing link length. As with the previous tests, Specimens 5 and 6 were designed to focus study on link behavior rather than on the effects of beam yielding.

On Specimen 5, one stiffener was placed at 6 inches from each end of the link (Fig. 2.10), a distance corresponding to 1.5 b_f. These stiffeners were intended to provide restraint against local buckling at the link ends. The spacing was increased from b_f (used on Specimens 2 and 4) up to 1.5 b_f in order to avoid constraining local buckles into too small of a region. No additional stiffeners were provided within the link because significant web yielding was not anticipated for this link length.

Test Notes - The response of Specimen 5 is shown in Fig. 3.12. Initial yielding of this specimen was observed during cycles 3E and 3W, in the south flanges of the link, in the web at the link ends, and in the northeast flange of the link. Slight yielding was also observed in the south flange of the brace near the brace-to-link connection. During cycle 4E and 4W, yielding was first noted in the east flange of the brace connection panel and at the northwest end of the link. The first signs of flange buckling were apparent at the southwest end of the link in cycle 6E and at the southeast end in cycle 6W. During cycle 8W, a crack was observed at the west end of the shear tab at the termination of the fillet weld between the shear tab and the link web. A similar crack was noted at the east end of the shear tab in cycle 9E, in addition to the initiation of a slight flange buckle at the northeast end of the link. During cycle 9W, the crack at the west end of the shear tab grew in length. The formation of a crack was also observed in the center of the

southwest link flange, opposite the junction of the web cope and the flange. During cycle 10W, the crack in the southwest flange spread over nearly the full width of the flange. This point is indicated by a circle on the hysteretic loops in Fig. 3.12. During the reverse, final loading cycle (11E), the southeast flange of the link ruptured over the full width of the flange. This point is indicated by the other circle on the hysteretic loops. Immediately upon fracture of the flange, a buckle formed in the east flange of the brace connection panel. Upon continued application of load, the crack at the east end of the shear tab began to grow along the length of the tab. The flange buckle in the brace connection panel became more severe, and some out-of-plane displacement of the east flange was observed in the region of the brace connection panel. The test was stopped at this point.

Summary of Damage - Photographs of Specimen 5 after testing are shown in Fig. 3.13. Yielding was apparent in the link flanges, extending about 5-6 inches from each end of the link. Significant web yielding was also present at the link ends (Fig. 3.13b and d). The pattern of this web yielding resembled that typical of a moment hinge, i.e. extending further near the flanges than at mid-depth of the section. No flange or web yielding was observed in the large central panel of the link. As anticipated, general shear yielding of the link had not occurred. It was apparent that link yielding occurred only at the very ends of the link, with the remainder of the link staying elastic. Outside of the link, there was severe yielding in the east flange of the brace connection panel, concentrated primarily in a 6 inch length at the south end of the panel (Fig. 3.13c). Some web yielding was also observed in the southeast corner of the brace connection panel (Fig. 3.13b). Very slight yielding was present in the east flange of the beam, extending about 4 ft. beyond the brace connection panel. No yielding was observed in the west flange of the brace connection panel or beam. Slight yielding was also present in the south flange of the $W10\times26$ brace, in the region immediately adjacent to the link. No yielding was observed in the column panel zone for this specimen.

Severe unsymmetric flange buckling occurred in both flanges at the south end of the link. These buckles extended from the north edge of the backup strip to the edge of the fillet weld at the first stiffener, a length of about 4 to 4.5 inches. There was also a minor buckle in the northeast flange of the link, but only in the upper half of the flange. The downward out-of-plane displacement at the northeast end of the link apparently straightened out the lower portion of this buckle. Very slight web buckles were also present at both ends of the link in the regions adjacent to the flange buckles.

A severe flange buckle was also present in the east flange of the brace connection panel (Fig. 3.13b). This buckle extended over a length of about 10 inches at the south end of the panel. A portion of the web adjacent to the flange buckle was also distorted. Some out-of-plane displacement of the specimen's east flange was also apparent in the region of the brace connection panel

(Fig. 3.13c). The flange in the brace connection panel was deflected upwards (about 1 inch at its peak) and the east flange at the north end of the link was deflected downwards (about .5 inches at its peak). No out-of-plane displacement was noted in the west flange of the specimen. The flange buckling and out-of-plane displacement in the brace connection panel were not observed until after the southeast flange of the link ruptured. This rupture apparently caused a significant redistribution of moment towards the brace end of the link, and initiated local buckling in the brace connection panel.

Ultimate failure of Specimen 5 was caused by the fracture of the link flanges at the south end of the link. Both fractures appeared to initiate at mid-depth of the flange near the junction of the web cope and the flange. Well before these flange cracks were first observed, the formation of cracks at both the east and west ends of the shear tab were noted. These cracks appeared to initiate at the termination of the shear tab to link web fillet weld. These welds terminated at the flame cut edges of the link web copes. The discontinuities in this region combined with the stress concentration at the end of the fillet weld likely contributed to crack initiation in the shear tabs. The formation of the shear tab cracks may have redistributed load to the link flanges, thereby contributing to the flange failures. This suggests that the connection performance may be improved by terminating the fillet weld well away from the edge of the link web or web cope.

Finally, it is interesting to compare the hysteretic loops for Specimen 5 (Fig. 3.13) with those of Specimen 1 (Fig. 3.4). These specimens are very similar, except for link length. Specimen 1 is in the intermediate length range where inelastic shear deformations contribute significantly to link plastic rotation, whereas the long link of Specimen 5 must rely almost completely on flexure to supply link rotation. Comparison of the loops for these specimens graphically illustrates the very large loss in strength and plastic rotation capacity associated with increasing link length. It is also useful to recall that if these specimens were constructed with short links, plastic rotations of $\pm$ .10rad without loss of strength would be anticipated.

3.2.6 Specimen No. 6

Specimen 6 was of nominally identical design to Specimen 5, except for stiffener locations and modifications to the link-to-column connection. In an attempt to delay fracture of the link flange, the link-to-column connection in Specimen 6 was reinforced with ribs in a manner similar to Specimen 4. However, building on the experience of Specimen 4, two changes were made in the connection for Specimen 6. First, the taper on the ribs was increased to further reduce the stress concentration in the link flange at the tips of the ribs. Secondly, the first stiffener was located further from the ends of the ribs. This was intended to avoid excessively constraining flange deformations into too small a region beyond the tips of the ribs. At the north end of the link, a single stiffener was located 6 inches from the end of the link, the same as for Specimen 5.

A partial depth stiffener was also provided in the brace connection panel. This stiffener was placed 6 inches outside of the link in the region where severe flange buckling was observed in Specimen 5. As with Specimen 2, this partial depth stiffener was intended to delay and limit the extent of local buckling in the brace connection panel.

Test Notes - The response of Specimen 6 is shown in Fig. 3.14. Initial yielding of this specimen was observed in cycles 3E and 3W in the south flanges of the link and in the east flange of the brace connection panel. During cycle 4W, slight yielding was noted in the south flange of the $W10\times26$ brace adjacent to the link. Small localized "kinks" appeared in the south flanges of the link near the tips of the ribs during cycles 5E and 5W. Clear signs of flange buckling in the link's south flanges became apparent in cycles 6E and 6W. During cycle 11E, a buckle appeared in the east flange of the brace connection panel, in the region between the link end and the partial depth stiffener. Coincident with the formation of this buckle was a noticeable drop in the specimens load carrying capacity. The formation of small cracks in the link's southeast flange at the tips of the ribs was also observed in this cycle. During cycle 11W, a flange buckle first appeared at the northwest end of the link. During cycles 12, 13, and 14, the flange buckles at the link's southeast, southwest and northwest flanges as well as in the brace connection panel continued to grow more pronounced. The cracks in the link's southeast flange at the rib ends gradually grew in length with each successive eastward loading cycle. During cycle 15E, the southeast flange finally ruptured completely. This point is indicated by a circle on the hysteretic loops in Fig. 3.14. Upon continued application of load, the link web began to tear, beginning at the flange rupture and extending to nearly mid-depth of the link. The test was stopped at this point.

Summary of Damage - Photographs of Specimen 6 after testing are shown in Fig. 3.15. Significant yielding was apparent on this specimen at the link ends and in the brace connection panel. The link flanges were yielded to about the first stiffener at each end of the link. At the link's southeast end, significant yielding occurred only beyond the ribs. At the link's southwest end, on the other hand, flange yielding began at the face of the column. At this location, the ribs are inside the link, and so the link flange is at the section's extreme fiber. At the east end of the connection, the ribs are outside the link, and the ribs are at the section's extreme fiber. The west flange of the link is therefore likely subject to higher stresses than the link's east flange in the region immediately adjacent to the column, as evidenced by the yielding pattern. Further, whereas yielding of the east flange begins abruptly at the rib ends, it appears to be distributed more uniformly in the west flange, with no apparent abrupt discontinuity of the yielding pattern at the rib ends. The rather abrupt change in the yielding pattern in the east flange at the rib ends may have contributed to the formation of the fracture at this location.

Some yielding of the web at both ends of the link was present in a pattern similar to that of Specimen 5. At the south end of the link, however, there was no apparent web yielding in the

region between the face of the column and the ends of the ribs. No yielding was observed in either the flanges or the web in the large central panel of the link.

Severe yielding was apparent in the east flange of the brace connection panel, extending from the end of the link to about one inch north of the partial depth stiffener. There was also significant yielding in the web of the brace connection panel, in the southeast corner of the panel. As with Specimen 5, slight yielding was also present in the south flange of the $W10\times26$ brace, in the region immediately adjacent to the link, and approximately opposite the web cope in the brace. No significant yielding was noted in the beam or in the column panel zone for this specimen.

Very severe unsymmetric flange buckles formed in the link's south flanges and in the east flange of the brace connection panel. A somewhat less severe unsymmetric flange buckle was present at the link's northwest end. No flange buckle ever formed at the link's northeast end. The flange buckles at the south end of the link extended approximately from the ends of the ribs to the first stiffener. At the southwest end of the link, the buckled portion of the flange began to separate from the rib to flange weld (Fig. 3.15d). The buckle at the northwest end extended about 4.5 inches from the end of the link. Web buckling was also present at the link ends in the regions adjoining the flange buckles.

The very severe buckle in the east flange of the brace connection panel extended from the link end to the partial depth stiffener (Fig. 3.15b). The web of the panel was also severely buckled in this region. The partial depth stiffener was apparently quite effective in limiting the extent of local buckling in the panel. It is interesting to note that no deterioration in the hysteretic loops was observed until the formation of the brace connection flange buckle, despite the earlier flange buckling at the link's south end. As with Specimen 5, some out-of-plane displacement of the specimen's east flange was present in the region of the brace connection panel (Fig. 3.15c). The extent and severity of this out-of-plane displacement, however, was less than that observed in Specimen 5. The partial depth stiffener may have provided additional restraint against this displacement.

Ultimate failure of Specimen 6 occurred by fracture of the link's southeast flange at the ends of the ribs. Cracks first formed at the tip of each rib. These cracks gradually spread to the outside of the flange. Complete failure finally occurred when the two cracks joined in the central portion of the flange. The formation of this fracture was significantly more gradual than in previous specimens.

Comparison with Specimen 5 indicates that the ribs significantly extended the life of Specimen 6. The fact that a fracture still ultimately occurred reflects the highly concentrated bending strains developed at the ends of a long link.

3.2.7 Specimen No. 7

Specimen 7 was provided with a $W12\times16$ link of intermediate length (nominal $e = 2.1M_p/V_p$). The link length and section of Specimen 7 were therefore nearly identical to that of Specimens 1 and 2. The link-to-column connection of Specimen 7 was provided with reinforcing ribs of the same design as for Specimen 6 (Fig. 2.22). For Specimens 1 to 6, the link web was connected to the column through a welded shear tab. For Specimen 7, as well as Specimens 8, 9, 10, and 11, the web was welded directly to the column by a full penetration weld. As with Specimen 6, the first stiffener in the link of Specimen 7 was located well away from the rib ends to avoid excessively constraining flange deformations. At the south end of the link, the first stiffener was located 5 inches from the link end. This distance corresponds to $1.25b_f$, and was chosen to be intermediate between the spacings of b_f and $1.5b_f$ used on previous specimens. One additional stiffener was placed between the two end stiffeners to avoid the web buckling failure observed in Specimen 2.

In the brace connection panel, a partial depth stiffener was located 5 inches from the end of the link in order to control local buckling in this region. The 5 inch distance was chosen once again to correspond to $1.25b_f$. Because of the very long length of the brace connection panel for this specimen, an additional partial depth stiffener was provided midway between the first partial depth stiffener and the north end of the panel.

The most important feature of Specimen 7 was the fact that it was designed to incur severe yielding and damage in the beam segment outside of the link. The very shallow brace-beam angle on this specimen, about 28.4 deg., was chosen to generate very large axial forces in the beam. Further, the brace section was sized only for the ultimate axial force generated in the brace, assuming the brace connection behaves as a "pin" and transfers no moment to the brace. The brace section was therefore chosen to provide high axial compressive strength with no concern for available flexural strength or stiffness. An analysis of this specimen prior to testing showed that because of the low flexural stiffness of the brace, approximately 95% of the link end moment would be initially transferred to the beam. This high moment in the beam combined with high axial force was expected to produce severe yielding in the beam. Further analysis of this specimen showed that the combined flexural strengths of the beam and brace, reduced for the presence of axial force in the members, was less than 50% of the estimated ultimate link end moment. Consequently, severe damage outside of the link was anticipated.

Test Notes - Plots of link shear force versus link rotation angle for Specimen 7 are shown in Fig. 3.16. In the final half cycle of testing, the displacement transducer at the north end of the link went out of range. Consequently, it was not possible to compute link rotation after this point. The plots in Fig. 3.16 are terminated at the point where the displacement transducer went out of range. In order to show the complete history of this specimen, a plot of link shear versus column

displacement (= displacement of south end of link) is shown in Fig. 3.17. The plots in Fig. 3.16 are missing only the last few data readings after failure of the specimen.

Initial yielding of Specimen 7 was visible during cycle 4E in the link's southeast flange, just beyond the ribs, and in the east flange of the beam at the north end of the brace connection panel. During cycles 5, 6, and 7, significant yielding developed in both flanges at the south end of the link, with moderate yielding visible in the east flange of the beam. Initiation of flange buckling at the southeast end of the link, beyond the ribs, was noted during cycle 8W.

During cycle 9E, a flange buckle formed in the east flange of the beam at about 1 ft. north of the brace connection panel. In addition, downwards out-of-plane displacement was clearly visible in the east flange of the beam. The peak of the out-of-plane displacement was at about the same point as the flange buckle. Flange buckling was also noted in the link's southwest flange during this cycle. During cycle 10E, the flange buckle and out-of-plane displacement of the beam's east flange became significantly more pronounced. The beam's east flange was displaced downwards about 2 inches at its peak. No displacement of the beam's west flange was visible. The specimen's load carrying capacity began to drop during this cycle. A photograph looking towards the beam's east flange at cycle 10E is shown in Fig. 3.18a.

During cycles 11 and 12, the out-of-plane displacement of the beam's east flange became progressively more severe, and the specimen's load carrying capacity continued to degrade. During the westward loading cycles, the beam straightened somewhat, but some residual out-of-plane displacement was always visible.

During cycle 13E, the formation of two cracks became visible in the link's southeast flange, at the tips of the ribs. In this cycle, the beam's east flange was displaced downwards about 3 inches at its peak. In cycle 14E, the cracks in the link's southeast flange spread over nearly the full width of the flange. The flange finally ruptured completely during cycle 15E. This point is indicated by a circle on the hysteretic loops in Fig. 3.16. A tear also formed in the web of the link, starting at the flange fracture. The test was stopped shortly after this point.

Summary of Damage - Photographs of Specimen 7 after testing are shown in Fig. 3.18. Severe yielding was visible in both flanges at the link's south end, extending from the column face to about the first stiffener. Unlike Specimen 6, some yielding of the southeast flange was visible within the rib area on Specimen 7. Some yielding was also evident on the ribs themselves. The web of the link was also severely yielded at the link's south end (Fig. 3.18d). At the north end of the link, minor yielding was evident in the east flange, extending about 4 inches from the end of the link. Only very slight yielding was noticeable in the west flange and in the web at the north end of the link. In the remaining central portion of the link, no flange yielding and only very slight web yielding was visible. Flange buckling within the link occurred only in the south flanges. These unsymmetric buckles extended from the ends of the ribs to the edge of the fillet weld at the

first stiffener. Slight web buckling was also apparent at the south end of the link in the regions adjacent to the flange buckles.

Within the brace connection panel, minor yielding was evident along the entire east flange. Very slight yielding was also noticeable in the web of the panel adjacent to the east flange. No flange buckles formed within the brace connection panel.

Within the beam, yielding was visible in the east flange for a distance of about 70 inches beyond the brace connection panel. The most severe yielding in the east flange was visible at about 10 inches north of the brace connection panel (at the peak of the out-of-plane buckle) and at the beam lateral support. These areas of severe yielding correspond to out-of-plane flexural plastic hinges of the east flange developed during lateral torsional buckling of the beam. Some yielding was also noticeable in the beam's west flange and in the beam web in the region of severe out-of-plane displacement.

The most significant feature of the beam was its severe lateral torsional buckling. The most severe twisting of the beam occurred at about 10 inches north of the brace connection panel. At this location, after testing, the beam's east flange was deflected downwards about 5 inches and the west flange was deflected downwards about one inch. At this same location, a flange buckle, about 4.5 inches in length, was visible in the top half of the flange. No flange buckle was present in the lower half of the flange. After rupture of the link's southeast flange, the lateral torsional buckling of the beam caused the link's east flange to deflect upwards. At the point of rupture, the link's east flange was deflected upwards about 2 inches. A view looking towards the east flange of the specimen is shown in Fig. 3.18c.

No flaking of whitewash was observed on the brace. However, as noted earlier, the use of whitewash did not appear to be an effective indicator of yielding on the cold formed tube members. Upon completion of testing of Specimen 7, the tube brace member was noticeably bent just beyond the brace connection gusset plate (Fig. 3.18e). This permanent deformation indicates the likelihood of brace yielding beyond the gusset plate.

Some minor damage was also apparent in the brace connection. A very slight crack was noticeable where the gusset plate meets the south flange of the brace. The weld connecting the gusset plate to the brace was continued around the edge of the gusset. The crack formed at the edge of this weld, and is visible in Fig. 3.18f. At the point where the gusset plate meets the north flange of the brace, a small indentation was visible in the brace flange. This indicates that the gusset "punched" into the brace wall. The stiffener along the south edge of the gusset plate showed slight yielding extending for a length of about 10 inches from the link.

Although lateral torsional buckling of the beam caused severe deterioration of the specimen's hysteretic loops, ultimate failure was once again caused by fracture of the link flange. As with Specimen 6, cracks initiated in the link's southeast flange at the tips of the ribs, and then gradually

spread over the width of the flange.

As noted earlier, the links for Specimens 1 and 7 were very similar. The primary difference between these specimens was that Specimen 1 was designed to restrict yielding primarily to the link region, whereas Specimen 7 was designed to permit significant yielding in the beam segment outside of the link. By comparing the hysteretic loops for Specimens 1 and 7, it is apparent that a very large loss of strength and plastic rotation capacity resulted by permitting yielding in the beam in this case. The very large axial forces in the beam produced severe instability, and thereby prevented the development of significant plastic rotations in the beam.

3.2.8 Specimen No. 8

Specimen 8 was designed to incur severe yielding and damage in the beam segment outside of the link, similar to the manner in which Specimen 7 was designed. As with Specimen 7, Specimen 8 was provided with a very shallow brace-beam angle (29 deg.). The brace was also designed for axial force only, resulting in a brace section with rather low flexural stiffness and strength.

The $W12\times22$ link in Specimen 8 was in the intermediate length range, with nominal $e = 2.15M_p/V_p$. The link-to-column connection detail was similar to Specimen 7 and was provided with reinforcing ribs. Stiffeners were provided at a distance of about $1.25b_f$ from the north end of the link and from the rib ends at the south end of the link. The remaining central portion of the link was stiffened to provide three equal length panels, according to the criteria of Eq. 1.3b. No partial depth stiffener was provided in the brace connection panel since flange buckling had not been observed in the panel of the previous $W12\times22$ specimens.

An additional interesting feature of the Specimen 8 design was that the brace and beam centerlines intersected a distance of about 5 inches inside the link (Fig. 2.13). As noted earlier, it was expected that this eccentricity would produce a moment that would resist the link end moment. An elastic analysis of Specimen 8 indicated that the 5 inch eccentricity between the centerline intersection and the link end reduced the bending moment transmitted to the beam and brace by as much as 50 percent!

Test Notes - The response of Specimen 8 is shown in Fig. 3.19. Initial yielding of this specimen was first visible during cycle 4E in the south flanges of the link and in the south link web panel. In cycle 7E, some yielding of the link's north panel was first noted as well as slight yielding of the beam's east flange. In cycle 7E, a small deformation of the southeast link flange was observed at the tips of the ribs. This deformation had the appearance of the ribs "punching" into the link flange. By cycle 9E, significant web yielding had propagated over the entire length of the link. During cycle 10E, minor flange yielding was first observed at the north end of the link. Additional yielding was also observed in the south end of the beam's east flange. During cycles 10W and 11W, the deformations in the link's southeast flange became more pronounced and were

closer in appearance to conventional flange buckles.

During cycle 14E, minor lateral torsional buckling of the beam was first visible, with the east flange deflected upwards. The beam's out-of-plane displacement became progressively more severe in cycles 15E and 16E, and the specimen's load carrying capacity began to drop. Measurements at cycle 16E indicated that the beam's east flange was buckled upwards about 3.75 inches at its peak, and the west flange was buckled upwards about 1.5 inches. The peak of the buckle was located about 42 inches north of the link end. The formation of small cracks in the link's southeast flange at the tips of the ribs was also noted during cycle 16E. During cycle 17E, a sudden drop of load was accompanied by the sudden upwards displacement of the beam's east and west flanges. The east flange was deflected 6 inches upwards and the west flange, 4.5 inches. The lateral torsional buckling of the beam had become almost purely lateral buckling. Slight growth of the cracks in the link's southeast flange was also evident. During cycle 18E, the specimen's load carrying capacity dropped rapidly, as the beam buckle grew larger. Even though the specimen may have been able to sustain some additional applied deformation, the test was stopped after this cycle to avoid damaging the test equipment.

Summary of Damage - Photographs of Specimen 8 after testing are shown in Fig. 3.20. In the link of Specimen 8, severe yielding was visible over the entire length of the link web, including the portion in the rib area. Yielding was also apparent in the link flanges at both ends of the link. In the southeast flange, severe yielding was concentrated in the region just beyond the ribs (Fig. 3.20c), although signs of flange yielding were visible up to about 12 inches from the column face. Significant yielding was also apparent in the ribs themselves at the southeast end of the link. At the southwest flange, yielding extended about 14 inches beyond the column face, with the most severe yielding immediately adjacent to the column. No significant yielding was visible in the ribs at the southwest end of the link. Yielding in the link's north flanges was only very slight, and extended to approximately the first stiffener. Flange buckling in the link occurred only in the southeast flange and was very minor. No other local buckling was apparent anywhere within the link.

Within the brace connection panel, slight yielding was apparent over the full length of the east flange and in the east half of the web. No yielding was visible in the horizontal stiffeners above the brace or in the brace itself. No flange or web buckling was present anywhere in the brace connection panel.

In the beam's east flange, yielding was visible at the center and ends of the buckled region. Some yielding was also noticeable in the beam web adjacent to the brace connection panel. The buckle in the beam, which began as a lateral torsional buckle, was an almost purely lateral buckle by the final load cycle. The buckle extended from about the north end of the brace connection panel to the beam lateral support, a distance of about 69 inches. The peak of the buckle was

located at about 44 inches north of the link end. At the peak, the east flange was deflected upwards about 6.75 inches and the west flange, about 6 inches. The shape of the buckle (Fig. 3.20b) reflects the dominating influence of axial force in the beam. Less torsional displacement occurred in the beam of Specimen 8 than in Specimen 7 possibly because of the reduction in beam bending moment resulting from the eccentricity between the link end and the beam-brace center-line intersection.

As with Specimens 6 and 7, cracks formed in the link's southeast flange at the ends of the ribs (Fig. 3.20c). However, for Specimen 8, testing was stopped before the cracks spread over the flange width.

3.2.9/10 Specimen Nos. 9 and 10

The primary objective of Specimens 9 and 10 was to obtain data on the performance of *short* link-to-column web connections. As noted in Chapter 1, only a single test had previously been conducted on such a connection. This test, by Malley and Popov [11], showed satisfactory performance. However, moment resisting connections to the column web in MRF applications have frequently shown poor performance [23, 26, 27]. Because of the uncertain reliability of these connections and because only a single test was available for EBF applications, current codes [5, 7, 8] limit link plastic rotations to ± .015 rad. when links are connected to the column web. The purpose of Specimens 9 and 10 was to increase the experimental data base for short link-to-column web connections, and to determine whether an increase in the allowable link rotation beyond ± .015 rad. was justifiable.

Specimen 9 was provided with a short (nominal $e = 1.2M_p/V_p$) W12×22 link and Specimen 10 with a short (nominal $e = 1.5M_p/V_p$) W12×16 link. The link-to-column connection details are shown in Figs. 2.23 and 2.24. As suggested in Ref. 27, the connection plates were made somewhat thicker than the beam flanges and were extended beyond the column. Further, the lower connection plate was thicker than the upper plate. As noted in Tsai and Popov [33], this practice promotes a sound full penetration weld by compensating for small variations in beam depth. The link web copes at the full penetration welds were ground smooth to reduce stress concentrations. Care was also taken to avoid "overwelding" by strictly limiting to 1/8 inch the amount by which the full penetration welds extended above the flanges. The link webs were directly welded to the vertical connection plate by full penetration welds. The welding sequence required welding the flanges before the web to limit welding residual strains in the flanges. Stiffeners in the links were equally spaced to satisfy the short link stiffening criteria of Eq. 1.3b.

Test Notes: Specimen 9 - The response of Specimen 9 is shown in Fig. 3.21. Significant yielding of this specimen was apparent during cycles 5 and 6 throughout the link web and in the link's south flanges. During cycle 8E, minor bending of the link's southwest flange was visible.

Significant yielding in the east flange of the brace connection panel was noted in cycles 8E and 8W. During cycle 9W, bending was visible in the link's southeast flange. During cycle 10E, a small crack was visible in the link-to-column connection. The crack was located between the connection plate and the run-out portion of the full penetration weld on the east side of the connection. The crack is visible in the photograph in Fig. 3.22a. Downward, out-of-plane displacement of the beam's east flange was also visible in cycle 10E. During cycle 10W, the beam straightened out. A small crack also became visible in the west end of the connection. This crack was again located at the junction of the connection plate and the run-out portion of the full penetration weld. During cycle 11E, the crack in the east portion of the connection ran completely across the connection plate. This point is indicated by the circle on the hysteretic plots in Fig. 3.21. Coincident with the formation of this fracture, the out-of-plane displacement of the beam's east flange became significantly more severe. Testing was stopped at this point.

Summary of Damage: Specimen 9 - Photographs of Specimen 9 after testing are shown in Fig. 3.22. The link web was completely yielded over its entire length. The link's south flanges were yielded for a length of 4-5 inches from the connection plates. The north flanges were yielded for a length of about 3 inches from the link end, and the yielding did not appear to be as severe as in the south flanges. There also appeared to be significant yielding in the east connection plate, concentrated in the central portion of the plate adjacent to the link flange. The extent of yielding was difficult to judge in the west connection plate, but appeared to be less severe than in the east plate. Both flanges at the link's south end showed some distortion, extending a length of about 3 inches beyond the connection plate. Both the top and bottom portions of the flange were uniformly bent in the same direction. This flange distortion did not have the appearance of the usual flange buckling observed in previous tests. No other flange or web buckling was visible in the link of Specimen 9.

In the brace connection panel, severe yielding was visible in the east flange for a length of about 7 inches at the south end of the panel. The web was also yielded in the south half of the panel.

No yielding was apparent in the brace. However, in the brace connection, slight yielding was apparent in the short vertical stiffener and the long diagonal stiffener at the south edge of the gusset plate.

Within the beam, yielding was visible in the east flange and in the web for a distance of about 18 inches from the north end of the brace connection panel. Lateral torsional buckling of the beam extended from the link end lateral support to the beam lateral support (Fig. 3.22c). The peak of the buckle occurred at about 30 inches north of the link end lateral support. At this location, the beam's east flange was deflected downwards about 2.75 inches and the west flange was deflected downwards about .5 inches. After rupture of the link-to-column connection, the lateral

torsional buckling of the beam caused the link's east flange to deflect upwards.

Ultimate failure of Specimen 9 was caused by fracture of the east connection plate at the link-to-column connection (Fig. 3.22d). This crack initiated at the junction of the connection plate and the portion of the full penetration weld that extends beyond the link flange. This crack spread quickly across the connection plate. Examination of the cracked region after testing indicated that incomplete penetration near one end of the full penetration weld may have contributed to initiation of the crack. Instability of the beam may have also contributed to the connection failure. The loss of stiffness associated with the lateral torsional buckling of the beam may have increased the bending moment carried at the column end of the link. Also, the downwards deflection of the beam's east flange would have produced additional tension in the upper portion of the link flange at the location of crack initiation, possibly hastening the failure. However, it should be noted that severe lateral torsional buckling of the beam was not observed until after complete rupture of the link flange connection. This severe buckling was apparently in response to the redistribution of bending moment towards the brace end of the link after failure of the connection.

After rupture of the flange connection occurred, the link web also fractured along the edge of the web's full penetration weld. This fracture extended to about mid-depth of the link when testing was stopped.

Test Notes: Specimen 10 - The response of specimen 10 is shown in Fig. 3.23. Significant yielding of this specimen was visible in cycles 5 and 6, throughout the web of the link and in the link's south flanges. During cycle 7E and 7W, slight flange buckling was observed in the link's southeast and southwest flanges. During cycle 8E, very minor out-of-plane displacement was visible in the east flange of the beam. In cycle 9E, the start of a crack was noted in the link's southeast flange. The crack appeared at the bottom of the flange, adjacent to the full penetration weld. This crack grew in length in cycle 10E, as shown in Fig. 3.24a. The flange completely ruptured during cycle 11E. This point is indicated by the circle on the hysteretic plots in Fig. 3.23. Upon continued application of load, a flange buckle developed in the east flange of the brace connection panel, and the out-of-plane displacement of the beam's east flange became significantly more severe. Testing was stopped at this point.

Summary of Damage: Specimen 10 - Photographs of Specimen 10 after testing are shown in Fig. 3.24. Within the link, severe yielding was visible over the entire web, and for a length of 3-4 inches in the flanges at both ends of the link. After testing, the only visible flange buckling was at the southwest flange of the link. The flange was symmetrically bent in a pattern very similar to that observed in Specimen 9. No signs of web buckling were visible anywhere within the link. At the link-to-column connection, some yielding was evident in both flange connection plates, as well as in the web connection plate.

Within the brace connection panel, severe yielding was visible over the entire east flange and in the southeast corner of the web. Moderate yielding was also visible in the west flange for a length of about 3 inches at the south end of the panel. An unsymmetric flange buckle was present in the east flange at the south end of the panel. The length of the buckle was about 7 inches. There was an additional buckle in the east flange of the panel at about 12 inches north of the link. Only the lower half of the flange was buckled, and appeared to be a consequence of the beam's lateral torsional buckle.

Within the brace connection itself, severe yielding was evident in the southeast corner of the gusset plate. Slight yielding of the gusset plate was also visible in the region adjoining the 2" wide diagonal stiffener. Yielding was also visible in the short vertical stiffener and for about 6 inches of the diagonal stiffener. As with Specimen 7, a small crack was present at the point where the gusset plate meets the south flange of the brace. The slit cut into the brace flanges to accommodate the gusset plate extended somewhat beyond the gusset. This excess slit was filled in with weld metal, and it was at this location that the crack was visible.

In the beam, moderate yielding was apparent in the east flange for a length of about 6 inches beyond the brace connection panel. Slight yielding was visible for the remainder of the east flange to about 6 inches north of the beam lateral support. These yield lines were consistently oriented at 45 deg. to the beam's longitudinal axis. No significant yielding was apparent in the beam web or west flange. Lateral torsional buckling of the beam was present from the link end lateral support to the beam lateral support. The peak of the buckle occurred at about 12 inches north of the link end, within the brace connection panel. At the peak, the east flange was deflected upwards about 1.5 inches, and the west flange was deflected upwards about .5 inches.

Ultimate failure of Specimen 10 was caused by fracture of the link's southeast flange. The fracture initiated at the bottom of the flange and traveled upwards. The fracture appeared to be completely within the base metal of the link flange, with no evidence of weld defects. After rupture of the flange, the link web also fractured along the edge of the web's full penetration weld. This fracture extended to about mid-depth of the link when testing was stopped.

3.2.11 Specimen No. 11

As with Specimens 7 and 8, Specimen 11 was designed to incur severe yielding and damage in the beam segment outside of the link. Specimen 11 was provided with a very shallow brace-beam angle (28 deg.) and with a brace section designed for ultimate axial force only. An analysis of this specimen showed that the low flexural stiffness of the brace would cause almost the full link end moment to be carried by the beam. This high moment combined with high axial force in the beam was intended to produce severe yielding of the beam. Further, the combined flexural strength of the beam and brace, reduced for the estimated ultimate axial force in these members,

was less than 50% of the estimated ultimate link end moment. Thus, a significant loss in overall strength due to beam yielding was expected for this specimen. The location of the beam's first lateral support was also moved significantly closer to the link end lateral support in an attempt to delay instability in the beam.

With a nominal $e = 1.65M_p/V_p$, the link length for Specimen 11 was at the beginning of the long link range. Link stiffeners were equally spaced according to the short link criteria of Eq. 1.3b. No additional stiffeners were provided within the brace connection panel, since no local buckling was observed in the panel of any previous $W12\times22$ specimen.

Test Notes - The response of Specimen 11 is shown in Fig. 3.25. Initial yielding of this specimen was observed in cycle 3E in the east flange of the beam, opposite the stiffener at the north end of the brace connection panel. In cycle 3W, yielding was first noted in the south flanges of the link. In cycle 4E, slight yielding of the link web was visible in the south half of the link. During cycle 5E, additional significant yielding of the beam's east flange was apparent in the region surrounding the north end of the brace connection panel, as well as at the beam lateral support. Very significant web yielding was also evident in the south panel of the link. During cycle 6W, web yielding was visible over the entire length of the link. Yielding in the east flange of the beam and brace connection panel continued to increase in severity, and very slight yielding was first noted at the link's north flanges. Slight yielding was also observed in the diagonal stiffener attached to the brace connection gusset plate. During cycle 8E, very mild flange buckling was observed at the southwest end of the link. Slight upward out-of-plane displacement of the east flange was visible near the north end of the brace connection panel. Also during cycle 8E, the start of a crack was visible in the link's southeast flange. The crack was in the center of the flange, adjacent to the full penetration weld. During cycle 8W, a similar small crack was observed in the link's southwest flange. During cycle 9E, some additional out-of-plane displacement of the beam's east flange was apparent. The crack at the link's southeast flange began to spread across the width of the flange. This point is indicated by the circle on the hysteretic loops in Fig. 3.25. Before the crack spread over the entire width of the flange, load was removed from the specimen, and the test was stopped. Testing was terminated at this point to permit repair and modification of the link-to-column connection so that the specimen could be retested.

Summary of Damage - Photographs of Specimen 11 after testing are shown in Fig. 3.26. Within the link, yielding was apparent over the entire web, but more severe in the south half of the link (Fig. 3.26a). Significant yielding was also visible in the link's south flanges, extending 5 to 6 inches from the column face. Yielding in the southeast flange appeared somewhat more severe than in the southwest flange. Only very slight yielding was visible in the link's north flange, extending only about 1 inch inside the link. During the course of the test, very mild flange buckling was observed only in the link's southwest flange. No local buckling was observed

anywhere else within the link.

In the east flange of the specimen outside of the link, severe yielding was apparent in the north half of the brace connection panel, for about 5 inches north of the brace connection panel, and immediately above the beam lateral support. Slight yielding of the beam's east flange extended as far as 6 ft. north of the link end. Within the brace connection, moderate yielding was visible in the diagonal stiffener attached to the gusset plate. Slight yielding of the column panel zone was also visible.

Slight lateral torsional buckling of the beam was evident between the link end lateral support and the beam lateral support. The peak of the buckle appeared to be at about midway between the supports. At the peak, the east flange of the beam was deflected upwards only about In the specimen's tube brace member, a slight bend was visible just beyond the gusset plate, indicating some permanent deformation in the brace.

At the end of the test, cracks had formed in both the southeast and southwest link flanges. The cracks initiated in the center of the flanges, adjacent to the full penetration welds. The crack in the southeast flange is visible in Fig. 3.26c. Testing was stopped before either crack spread over the full width of the flange.

3.2.11R1 Specimen No. 11R1

After completion of the testing of Specimen 11, the specimen was repaired and modified for retesting. The repaired specimen was designated as 11R1.

The link-to-column connection of Specimen 11 was repaired and extensively modified for Specimen 11R1. The repair and modifications are detailed in Fig. 2.26. The repair involved completely cutting out the damaged connection, and cutting the link back to sound, undamaged steel. This shortened the link by about .75 inches. In the new connection, the link flanges were connected to the column by full penetration welds and reinforced by triangular cover plates. For the web connection, a heavy shear tab was full penetration welded to the column and fillet welded to the link web, in a manner similar to Specimens 1-6.

Repairs were accomplished while the specimen remained bolted in the test setup. This precluded access from the bottom of the specimen. Consequently, the link flange full penetration welds were both welded from the outside of the section as shown in Fig. 2.26. For the same reason, both cover plates were welded to the outside surface of the flanges.

Design of the modified connection was based on the observed performance of the previous specimens. Most of the previous specimens without reinforcing ribs failed by fracture of the link flange. These fractures typically occurred in the region adjacent to the full penetration weld, where the section had been damaged by the heat of the full penetration weld and by the presence

of the web cope. The intent of the reinforcing ribs (Specimens 4, 6, 7 and 8) was to move the link's critical section away from this damaged area, back to an area of sound steel. The ribs were very successful in preventing fracture at the full penetration weld. Unfortunately, each specimen with ribs still developed fractures, with the cracks initiating in the link flange at the tips of the ribs. However, it appears that the ribs were successful in delaying fracture, permitting the development of additional plastic rotation.

In observing the development of cracks in the specimens with ribs, it appeared that the abrupt change in the link stiffness and strength at the ends of the ribs contributed to crack initiation. Prior to fracture, link flange deformations were typically visible at the rib ends. These deformations had the appearance of the ribs "punching" into the flange, producing highly localized strains at the rib ends.

In Specimen 11R1, the cover plates were intended to reinforce the connection and to move the link's critical section away from the full penetration weld and web cope. Thus, the cover plates serve the same basic purpose as the ribs. However, the use of cover plates rather than the vertical ribs was intended to provide a less abrupt change in stiffness and strength. The triangular shape was expected to provide an even more gradual transition. A stress concentration was still anticipated at the tip of the triangle. However, the tip is located directly above the web and it was hoped that this location would provide greater resistance to fracture of the flange.

The weld connection was made through a welded shear tab. A very thick shear tab was chosen (approximately double the web thickness) in an attempt to stiffen the web region and draw stress away from the flanges. For the fillet welds at the top and bottom of the shear tab, care was taken to terminate the welds well away from the web copes and the end of the link. A photograph of the new connection is shown in Fig. 3.28a.

In addition to the repair and modification of the link-to-column connection, a full depth stiffener was added to the brace connection panel as shown in Fig. 2.17. Some slight lateral torsional buckling of the beam was noted towards the end of the Specimen 11 test. The stiffener was located near the peak of the buckle to provide additional torsional stiffness to the section. It was hoped that beam instability could be delayed, so that the modified link-to-column connection could be thoroughly tested.

Test Notes - Prior to testing, whitewash was reapplied to the specimen. Nonetheless, the occurrence of yielding in this specimen was difficult to judge in areas that were heavily yielded in the previous test. In these areas, such as the link web, most of the mill scale on the surface had flaked off in the first test, and so whitewash was not a particularly effective indicator of yielding. However, in other areas, such as the link flanges, the whitewash appeared to be effective.

The response of Specimen 11R1 is shown in Fig. 3.27. During cycle 4W, some yielding was visible in the link's south flanges, just beyond the cover plates. Very slight yielding was also noted

within the cover plate on the east flange. During cycles 5, 6, and 7, further yielding of the south flanges was visible, in addition to slight additional yielding within the east cover plate. During cycle 11E, very sudden out-of-plane buckling occurred between the beam lateral support and the lateral support at the north end of the subassemblage. The testing was stopped at this point to once again permit repair of the specimen.

Summary of Damage - Photographs of Specimen 11R1 after testing are shown in Fig. 3.28. Within the link, the only yielding indicated by flaking of whitewash was in the south flanges. In the southeast flange, yielding was concentrated in a region of about 5 inches beyond the triangular cover plate. Some yielding was also visible in the cover plate itself and in the region of the flange above and below the cover plate. From these yielding patterns, it appears that the cover plate was quite successful in providing a gradual reduction in yielding from the tip of the cover plate towards the column face. In the west flange, a similar pattern of yielding was visible, though somewhat less severe than in the east flange. Photographs of these flanges after testing are shown in Fig. 3.28b and c. Significant additional yielding was also visible in the column panel zone of this specimen. The only other flaking of whitewash visible on the specimen was at the peak of the beam buckle.

Failure of Specimen 11R1 was caused by buckling of the beam. The buckle was located between the beam lateral support and the lateral support at the north end of the subassemblage. A view of the buckled region is shown in Fig. 3.28d. The shape of the deformed beam reflected almost purely lateral buckling. Both the east and west flanges of the beam were displaced upwards about 3.5 inches at the peak of the buckle. The peak was located at about 40 inches north of the beam lateral support.

Other than the buckle in the beam, little deformation was visible anywhere else in the specimen. Consequently, the decision was made to repair the buckled region and retest the specimen.

3.2.11R2 Specimen No. 11R2

After completion of the testing of Specimen 11R1, the specimen was repaired and retested. The repaired specimen was designated as 11R2.

The primary damage to Specimen 11R1 was a severe lateral buckle in the beam. The specimen was removed from the test setup, and the beam was straightened. This was accomplished by applying lateral force to the beam with a hydraulic jack at various locations until the beam appeared fairly straight. Some minor out-of-plane distortions were still visible, however, upon completion of the straightening process. The specimen was then remounted in the test setup. An additional beam lateral support was provided at the location where the peak of the buckle was observed in the previous test. This additional lateral support was constructed by placing a 2×3×3/16 angle above and below the beam. The angles as well as the tips of the beam flanges

were coated with teflon to minimize friction at the support.

Test Notes - Whitewash was not reapplied to Specimen 11R2 before testing. Any flaking of the existing whitewash on this specimen therefore represents additional yielding beyond that experienced in the previous two tests. As with Specimen 11R1, the whitewash was not an effective indicator of yielding in all areas of the specimen.

The response of Specimen 11R2 is shown in Fig. 3.29. At cycle 3E for Specimen 11R2, the previous peak displacement (at the point of beam buckling) from the test of Specimen 11R1 was achieved. There were no signs of beam instability at this point. However, during cycle 4E, slight out-of-plane displacement of the beam's east flange was visible between the link end lateral support and the first beam lateral support. Additional yielding was also apparent at the link's south flanges in the region beyond the cover plates. During cycle 4W, additional yielding of the column panel zone was noted, and some shear deformation of the column panel zone was visible. During cycles 5E and 5W, very slight flange buckling was observed in the link's south flanges in the region between the column face and the tips of the cover plates. During cycles 6E and 7E, the out-of-plane displacements of the specimen's east flange became progressively more severe. Between the link end support and the beam's first lateral support, the beam flange was buckled downwards. Between the first and second beam lateral supports, the beam's east flange was buckled upwards. During cycle 7W, a small buckle formed in the brace connection gusset plate. The buckle was located at the free edge of the gusset, between the diagonal stiffener and the brace. Lateral torsional buckling of the beam became even more severe in cycle 8E. During cycle 8W, the buckle in the brace connection gusset plate also became more severe. A photograph of this buckle is shown in Fig. 3.30a. During cycle 9E, a small crack formed on the free edge of the gusset plate, at about one inch from the end of the diagonal stiffener. A very slight crack was also observed in at the southeast end of the link. The crack was located in the upper portion of the triangular cover plate, adjacent to the full penetration weld. The lateral torsional buckling of the beam became even more severe during this cycle. Towards the end of cycle 9E, the specimen's load carrying capacity began to drop significantly. The link end lateral support began to fail at this point. The load cells in this lateral support (Fig. 2.30 - Section A-A) began to buckle, indicating enormous out-of-plane forces at the link end. The testing was stopped at this point.

Summary of Damage - Photographs of Specimen 11R2 after testing are shown in Fig. 3.30. Within the link, additional significant yielding was apparent in the south flanges, extending a distance of about 12 inches from the column face. Significant yielding was also visible in the triangular cover plates, particularly at the east flange. Yielding of the southeast flange is shown in Fig. 3.30c. A very small crack was present in the upper portion of the east cover plate, immediately adjacent to the full penetration weld. A slight flange buckle was visible at the southwest end of the link, extending about 5 inches from the column face. The overall view of the link region after

testing (Fig. 3.30b), shows remarkably little deformation within the link.

Within the brace connection panel, additional yielding was visible in the east flange and was more severe in the upper portion of the flange at one of the peaks in the lateral torsional buckle. Yielding was also apparent in the west flange, at the north end of the panel.

The brace-to-link connection suffered considerable damage towards the end of the test. Yielding was apparent in the diagonal stiffener for almost its full length. The most severe yielding in the stiffener was concentrated in the region starting about 3 inches from the link, and extending about 9 inches in length. Yielding patterns in the gusset plate were not as clearly evident from the whitewash. However, it appeared that yielding occurred in the portion of the gusset between the brace and the diagonal stiffener. There appeared to be little or no yielding in the north portion of the gusset between the brace and the beam. As noted earlier, during the final two westward loading cycles, a buckle formed in the edge of the gusset between the brace and the diagonal stiffener (Fig. 3.30a). During the final eastward loading cycle, this buckle straightened out, and a small crack formed in the gusset. The crack started at the edge of the gusset at about 1 inch from the end of the diagonal stiffener. The crack extended approximately .5 inches into the gusset. The buckle in the gusset indicates that this connection could be improved by moving the end of the diagonal stiffener as close as possible to the brace, while still leaving sufficient clearance for welding.

As with the other gussetted brace connections (Specimens 7, 9 and 10), a small crack was visible in the south flange of the brace, at the junction of the gusset plate and the brace. It appeared that the slit cut in the brace flanges to accommodate the gusset extended about 1/2 inch beyond the end of the gusset. This excess portion of the slit was filled in with weld metal, and the crack was visible within this filled in region. From this observation, it would appear to be advisable not to fill in the end of the slit with weld metal.

Small fractures were also visible in the gusset plate just beyond the ends of the brace flanges. On the far side of the specimen, the tube brace separated from the brace to gusset fillet weld (Fig. 3.30d). The separation started at the end of the brace and extended for a length of about 6 inches. Examination of this region indicated that poor quality of the fillet weld may have contributed to this separation.

The primary failure mode for Specimen 11R2 was severe lateral torsional buckling of the beam outside of the link (Fig. 3.30e). In the segment of beam between the link end support and the first beam lateral support, the east flange was displaced downwards about 3.5 inches at the peak, and the west flange was displaced downwards about 1.5 inches. The peak of this portion of the buckle was located at about 16 inches north of the link end, within the brace connection panel. Between the first and second beam lateral supports, the beam's east flange was displaced upwards about 2.5 inches at the peak, and the west flange was displaced upwards about 1.5 inches. During

the final loading cycle, both the link end lateral support as well as the second beam lateral support (the new support added for this specimen) began to fail, indicating the development of very large out-of-plane forces.

A major objective of Specimen 11R2 was to test the modified link-to-column connection detail. The performance of the connection indicates that the triangular cover plates were very successful in reinforcing the connection and in providing a smooth transition into the reinforced region. Though this single test cannot be considered conclusive, it appears that the use of the triangular cover plates can significantly delay fracture and thereby significantly enhance the overall connection performance.

3.2.12 Specimen No. 12

Specimen 12, with a nominal link length of $3.6M_p/V_p$, was the longest link tested in this experimental program. At the link-to-column connection, both the link flanges and web were directly welded to the column with continuous fillet welds (Fig. 2.27). No web copes or any other openings were cut into the link. A similar connection tested by Tsai and Popov [23, 34] for MRF applications showed excellent performance. The intent of this specimen was to provide an indication of long link performance when fracture is not the controlling failure mode. This case is of interest when links are located within the span, not connected to a column.

A single stiffener was located 6 inches from each end of the link. This distance was chosen to correspond to $1.5b_f$. The purpose of these stiffeners was to provide restraint against flange buckling and lateral torsional buckling of the link. A relatively steep brace-beam angle was used (39 deg.) to limit axial force in the beam and relatively conservative spacing of beam lateral supports was provided in an attempt to delay instability of the beam.

Test Notes - The response of Specimen 12 is shown in Fig. 3.31. Initial yielding of Specimen 12 was noted in cycle 3E in the flanges at the south end of the link. Slight flange yielding was also visible opposite all stiffeners in the link and brace connection panel. During cycle 4E, significant flange yielding was apparent at both ends of the link. Yielding was also observed in the south flange of the $W8\times21$ brace, in the region immediately adjacent to the link. This yielding was most visible in the portion of the brace flange directly opposite the web cope at the brace connection. Additional yielding was also noted in the east flange of the brace connection panel, primarily opposite the stiffeners. During cycle 6W, flange buckling was first noted at the southeast and northwest ends of the link. After cycle 6W, flange yielding extended for a length of 9 to 10 inches from the column face at the link's south end. At the link's north end, flange yielding extended 8 inches from the link end at the west flange and 6 inches from the link end at the east flange. During cycle 7E, minor lateral torsional buckling was observed both in the beam and within the link. The beam straightened during cycle 7W, but lateral torsional buckling of the link

became more severe. The link's southeast flange was displaced upwards and its northwest flange was displaced downwards. During cycle 8E, lateral torsional buckling of the beam became very severe, although no significant loss in overall load carrying capacity was observed. During cycle 8W, the beam once again straightened, but the lateral torsional buckling of the link became progressively more severe. With increasing displacement in cycle 8W, the overall load carrying capacity of the specimen began to drop. Some damage to the link end lateral support was also observed, indicating the development of very large out-of-plane forces. The test was terminated at this point to avoid further damage to the test setup.

Summary of Damage - Photographs of Specimen 12 after testing are shown in Fig. 3.32. After testing, yielding in the link's east flange extended for a length of about 19 inches at the south end and 13 inches at the north end. At both ends, the yielding appeared to be more severe in the lower half of the flange. In the link's west flange (Fig. 3.26b), yielding extended for a length of about 13 inches at the south end and 16 inches at the north end. For the west flange, yielding appeared more severe in the upper half of the flange. Moderate yielding of the link web was visible at both ends of the link, extending approximately to the stiffener at each end.

Within the brace connection panel, yielding was apparent in the east flange, over the full length of the panel. Yielding of the web was visible in approximately the eastern one-third of the panel, with the yielding more severe adjacent to the link. The west flange of the brace connection panel showed no signs of yielding.

On the $W8\times21$ brace, severe yielding was apparent in the south flange, extending approximately 4 inches beyond the full penetration weld at the brace connection. No other signs of distress were visible in the brace connection. Within the beam, moderate yielding was visible in the east flange for a length of about 2 ft. beyond the brace connection panel. In the west flange, only very slight yielding was visible for a length of about 8 inches beyond the brace connection panel.

Flange buckling was present at the northwest and southeast ends of the link. The flange buckle at the southeast end of the link (Fig. 3.32d) was somewhat more severe than at the northwest end, but both flange buckles were rather mild. No signs of web buckling or additional flange buckling was apparent anywhere else in the specimen.

The primary failure modes of Specimen 12 were severe lateral torsional buckling of the link in the west load cycles and severe lateral torsional buckling of the beam in the east load cycles. Lateral torsional buckling of the link was also observed in the east load cycles, but was much less severe than in the west load cycles. In the east load cycles (beam in compression), the buckling of the beam reduced the overall load carrying capacity of the specimen (Fig. 3.31), and apparently reduced the deformation demands on the link, resulting in less severe link buckling. For the very severe lateral torsional buckling of the link observed in the west load cycles, the southeast and northwest flanges (the flanges in compression) were displaced out-of-plane. The southeast flange

was displaced upwards (Fig. 3.32c) and the northwest flange downwards (Fig. 3.32b). The peak out-of-plane deflections occurred at about 15 to 18 inches from the link ends. It appears that the stiffeners located at 6 inches from the link ends provided substantial restraint against lateral torsional displacements. Moving the stiffeners somewhat further from the link ends might have provided even greater restraint.

A remarkable feature of the Specimen 12 test was the excellent performance of the fillet welded link-to-column connection. Despite the very severe cyclic loading program, the connection suffered no significant distress. This may be due to the lack of web copes or any other openings in the link web as well as possibly a smaller and less severe heat affected zone in the link flanges. Such connections may have application in cases where erection and fabrication techniques permit the link-to-column connections to be shop welded.

3.3 DISCUSSION OF TEST RESULTS

This section summarizes and discusses the experimental performance of the 14 test specimens. The discussion is based on the observations of specimen performance detailed in the previous section and on the link shear versus rotation hysteretic loops for each test. Further detailed data analysis and discussion are also provided in Chapters 4 and 5.

Table 3.2 summarizes the observed failure modes for each specimen. The ultimate failure and cause for termination of testing for each specimen is represented by the "primary" failure modes. The "additional" failure modes listed in this table contributed to loss of strength or rotation capacity, but were not directly responsible for the specimen's ultimate failure.

It is apparent from this testing program that the controlling failure mode for long links attached to columns is fracture of the link flange at the link-to-column connection. This failure mode reflects the very high bending strains developed at the ends of long links as well as the deficiencies of the link-to-column connection. For the conventional link-to-column connection (full penetration welds at the flanges with a welded web connection), the fractures occurred in the link flange immediately adjacent to the full penetration weld. Crack initiation was usually observed at the junction of the web cope and the flange. The web copes are needed to accommodate the full penetration welds, but appear to be very damaging to the connection by promoting the initiation of a crack. The flange fractures can therefore likely be attributed to the combination of very high bending stresses, damage to the flange due to the heat of the full penetration weld, and the damaging effects of the web copes. After initiation of a crack was first observed, the fracture typically spread rapidly across the full width of the flange. After rupture of the flange, the web connection also then typically failed rapidly by fracture of the link web and/or shear tab. For the specimens that failed in this manner, if the testing had not been terminated the links would have

completely separated from the columns. In an actual structure, in addition to the loss of the link, such a failure could also potentially lead to column instability. The fact that fracture is the controlling failure mode poses serious consequences for EBFs with long links attached to columns. Such a failure mode is highly undesirable because it cannot be reliably predicted and represents a sudden and complete failure of the link.

The addition of vertical reinforcing ribs, when properly implemented, appeared to delay fracture of the link flange. This is evident by comparing Specimens 5 and 6. The specimens with ribs, however, still ultimately failed by fracture with cracks initiating in the link flange at the tips of the ribs. After crack initiation, the fractures spread across the width of the link flange much more gradually than in the specimens without ribs. This is possibly because the link flange steel is less damaged by the heat of welding in the region near the rib ends as compared to the region immediately adjacent to the full penetration weld. As demonstrated by Specimen 4, it is important not to place a stiffener too close to the ends of the ribs. Otherwise, flange deformations are constrained into too small of a region, thereby contributing to initiation of a crack.

In contrast to the other specimens, the link-to-column connections in Specimens 11R2 and 12 performed well under the very severe cyclic loading program. The primary feature of the connection for Specimen 11R2 was the addition of triangular cover plates to the link flanges. The shape of these cover plates provided a gradual transition in stiffness and strength into the reinforced region of the connection, providing substantial resistance against the formation and propagation of a crack in the link flange. Although this single test cannot be considered conclusive, the use of triangular cover plates appears to be a promising technique for significantly improving connection ductility. In Specimen 12, the link was connected to the column by all-around fillet welds, with no web copes or other openings cut into the link. This connection provided excellent performance, possibly because the damaging web copes were not present. It is also possible that the fillet welds do less damage, subjecting the steel to less heat than a full penetration weld. Such a fillet welded connection may have useful application when fabrication and erection procedures permit shop welding of the link-to-column connection. Further experimental verification of both of the successful connections used in Specimens 11R2 and 12 would be desirable.

None of the test specimens used a bolted web connection between the link and the column. However, it is clear from the test results that a bolted web connection is not suitable for long links. Experiments by others [11,23,34] have clearly shown that connections with bolted webs are more prone to flange fractures than connections with welded webs. This behavior has been attributed to slippage of bolted web connections under large cyclic loads and the subsequent redistribution of load to the flange, resulting in rupture of the flange. Since fracture of the flange is already the controlling failure mode for long link-to-column connections, it is clear that a bolted web would only hasten the failure.

The plastic rotation capacity of each test specimen is listed in Table 3.3. This table reports values of $\bar{\gamma}_p$, defined as the maximum plastic rotation measured from the last point of zero load. Figure 3.35 illustrates the definition of $\bar{\gamma}_p$. The parameter $\bar{\gamma}_p$ was chosen because it is believed to represent the best overall measure of the link's inelastic deformation capacity. For symmetric cyclic response, the plastic rotation capacity γ_p can be estimated as one-half of $\bar{\gamma}_p$. Note, however, that the response of these specimens was not always completely symmetric. Lack of symmetry in overall response can be largely attributed to lack of symmetry in the response of the beam segment outside of the link. The response of the beam differed depending on whether it was in compression or tension, particularly after the initiation of instability in the beam.

Up to three values of $\bar{\gamma}_p$ are tabulated for each specimen. The first is the value of $\bar{\gamma}_p$ at the limit of stable hysteretic behavior. This is the maximum rotation at which link strength begins to deteriorate. Next is the value of $\bar{\gamma}_p$ at which the link shear force drops below $V_{yield\,(SPT)}$. $V_{yield\,(SPT)}$ is defined as the lesser of V_p or $2M_p/e$, and represents the value of shear force at which the link is predicted to yield based on simple plastic theory (SPT). $V_{yield\,(SPT)}$ is also the code [7,8] specified value of link shear yield design strength. $V_{yield\,(SPT)}$ was computed using the actual estimated values of M_p and V_p listed in Table 2.10. The final tabulated value of $\bar{\gamma}_p$ is the rotation when link failure occurred by fracture, if applicable.

In examining Table 3.3, it is useful to recall that a properly stiffened *short* link can supply $\bar{\gamma}_p$ of .20 rad. with stable hysteretic behavior ($\pm$ .10 rad. for symmetric cyclic loading). The significantly smaller plastic rotation capacities of long links is evident from this table. However, as noted in Chapter 1, the rotation demand may also be less on a long link than on a short link by virtue of the kinematics of an EBF (Eq. 1.1). The very large number of specimens that failed by fracture is also apparent from this table. It is also interesting to note that Specimens 7 and 11 never achieved $V_{yield\,(SPT)}$, the code specified link yield strength. This is a consequence of the large strength loss resulting from yielding and instability of the beam segment outside of the link in these specimens.

In evaluating the plastic rotation capacities of the test specimens, the important question is whether or not these rotations are adequate to meet the demands placed upon such a link in a real structure subjected to a real earthquake. Answering this question is difficult since a realistic estimate of actual link rotation demand is required. Rotation demands on a link will depend on many factors, including the characteristics of the structure, the location of the link within the structure, and the characteristics of the ground motion. Such an estimate of link rotation demand over a range of different structures and ground motions can best be achieved by inelastic dynamic analyses with realistic modelling of long link response. Unfortunately, such analyses are not yet available for EBFs with long links. Such inelastic dynamic analyses must be considered a high priority for future research on long link EBF systems.

In order to obtain some perspective on the adequacy of the plastic rotation capacity of the test specimens, it is useful to examine an estimate of the plastic frame drift developed in the corresponding prototype structures. This can be accomplished by the simple EBF kinematics represented by Eqs. 1.1. The appropriate relationship for a single diagonal EBF is $\theta_p = \gamma_p/(L/e)$. Using this relationship, the maximum plastic story drift, θ_p, under cyclic loading for the prototype span to link length ratios, L/e, are listed in Table 3.4. For each specimen, θ_p is based on a value of γ_p taken as one-half of $\bar{\gamma}_p$ for stable hysteretic behavior. Thus, the values in Table 3.4 provide an approximation of the plastic story drift which the prototypes could supply without loss of strength.

The next difficult question to be addressed is whether or not the plastic frame drifts in Table 3.4 are acceptable. As a guide, NEHRP [7] generally limits *total* (elastic plus plastic) story drift to 1.5 percent. Further, in the dynamic analyses of a six-story EBF with *short* links designed according to the NEHRP guidelines, Ricles and Popov noted total story drifts up to nearly 1.5 percent for the 1966 Parkfield earthquake record [28]. NEHRP also recommends a deflection amplification factor, C_D, of 5 for EBFs. This factor is intended to represent the ratio of ultimate story drift to the drift at yield. A value for C_D equal to 5 implies that 80 percent of the total story drift will be due to inelastic deformation. Based on this reasoning, a rough estimate of the required plastic story drift may be taken as 1.2 percent (.012 rad.), i.e., 80 percent of .015 rad.

Comparing the plastic frame drifts in Table 3.4 against a required plastic drift of about 1.2 percent, it may be concluded that the performance of the test specimens ranged from clearly unacceptable (Specimens 2, 5, 7, 8,11 and 11R1) up to marginally acceptable (Specimens 1, 3, 4 and 12). Overall, the inelastic deformation capacities of the specimens can be judged as being rather poor.

As noted earlier, fracture is a highly undesirable failure mode. It cannot be reliably predicted and results in a very sudden and complete failure. This testing program has provided clear indication that fracture is the controlling failure mode for long links attached to columns with conventional EBF details (full penetration weld at flanges and welded web). Further, these fractures occur at levels of inelastic rotation that are judged to be marginal at best. Based on this evidence, it is recommended that long links attached to columns **not** be used in EBFs. The use of an improved link-to-column connection detail, such as that of Specimen 11R2, may represent a possible exception to this recommendation. However, such connection details require further experimental verification before they can be used with confidence.

There is no evidence that long links cannot be used when located within a span between two braces, as in Fig. 1.1b. There was no sign of fracture at the brace end of the link for any of the test specimens, despite the presence of large welds associated with the brace connection. Further, the majority of the test specimens could have likely supplied significantly larger plastic rotations in

the absence link flange fracture. However, as before, a realistic estimate of link rotation demand based on inelastic dynamic analyses would be desirable to better judge the suitability of EBFs with long links within the span.

Apart from the dominating influence of the connection failures, a number of additional useful observations can be made on the behavior of long links based on these tests. The transition from shear to flexurally controlled behavior with increasing link length is readily apparent from the observed behavior of the test specimens. For the very long links (Specimens 5,6 and 12), the flexurally dominated behavior was clearly evident. For the remainder of the specimens, a combination of shear and flexural yielding was typically observed. There are, of course, no clear boundaries between the various ranges of behavior. In the development of the model EBF codes [5,7,8], the length range of 1.6 to $2.6M_p/V_p$ was taken as the transition from shear to flexural yielding links. From the observed behavior of the test specimens, this appears to be a reasonable approximation. However, several of the test specimens fairly close in length to $2.6M_p/V_p$ still showed a strong influence of inelastic shear deformation. Thus, the transition to predominately flexural behavior may occur at a length somewhat greater than $2.6M_p/V_p$.

The effects of length on link strength and rotation capacity are also evident from these tests. The overall loss of strength and rotation capacity with increasing link length are clearly demonstrated by comparing the response of Specimens 1 and 5. The major difference between these two specimens was the length of their links. Specimen 1 was in the transition length range with significant contributions of plastic shear deformation to link rotation. Specimen 5, on the other hand, was in the length range of dominant flexural yielding, with little or no shear contribution. The response of these two specimens are plotted to the same scale in Fig. 3.33. The large loss of strength and plastic rotation capacity due to the increased link length in Specimen 5 are clearly evident. It is also useful to again recall that with a properly stiffened short link, these same specimens would have been capable of supplying plastic rotations of $\pm$ .10 rad. and develop an ultimate strength of about 110 kips ($1.5V_p$). Further, no cyclic deterioration in strength would be expected for a short link, as was the case for Specimen 1. Clearly, there is a significant penalty in both strength and plastic rotation capacity when long links are used.

The transition from shear to flexural behavior is clearly visible in the observed yielding patterns in the test specimens. Shear yielding of the web, observed in the specimens within the transition length range, develops over the full length and height of the link web. Flexural yielding, on the other hand, is highly concentrated at the link ends, primarily within the flanges. The transition from shear to flexural behavior is also evident from the development of local instabilities in the specimens, i.e., web buckling, flange buckling, and lateral torsional buckling. Specimen 2 clearly demonstrated that inelastic shear buckling of the link web is still an important failure mode in the transition length range. Stiffening of the web is still needed within this length range,

although stiffener spacing can likely be increased as link length increases. It is also evident that no web stiffening is required in very long links. For these links, general shear yielding of the web does not occur and therefore inelastic shear buckling of the web also does not occur.

The $W12\times16$ specimens, i.e., those with slender flanges, suffered severe flange buckling during the tests. The flange buckling typically initiated in the link flanges adjacent to the column, presumably because of the initially higher bending moment at the column end of the link. In the more advanced stages of loading, these specimens also typically developed very severe flange buckling *outside* the link in the brace connection panel. This buckling occurred only in the flange opposite the brace, not in the flange to which the brace was connected. The development of this flange buckling in the brace connection panel is likely the result of interaction of bending moment and axial force in the panel. In the flange at the top of the panel (the east flange of the test specimens), the bending moment generated at the link end and the axial force generated in the beam produce direct stresses of the same sign. That is, for one direction of loading, the bending moment and axial force both produce compression in the top flange, whereas in the other direction of loading, they both produce tension in the top flange. In the flange at the bottom of the panel (the west flange of the test specimens), the stresses produced by bending moment and axial force are of opposite sign and therefore tend to cancel. The top flange of the brace connection panel is therefore subjected to significantly higher stresses, both in tension and compression, than the bottom flange of the panel. The bottom flange of the brace connection panel, of course, also benefits from the stiffening effect of the brace welded to the beam.

The flange buckle in the brace connection panel was typically more severe than flange buckling within the link. Even though flange buckling always occurred first within the link, a significant loss of strength was not usually observed until the development of flange buckling outside the link in the brace connection panel. Further, flange buckling within the $W12\times16$ links did not appear to initiate any significant out-of-plane displacements of the link. On the other hand, flange buckling in the brace connection panel did appear to initiate out-of-plane displacements of the flange, possibly due to the high axial force environment outside of the link. Thus, flange buckling in the brace connection panel was significantly more harmful to overall performance than flange buckling within the link.

The $W12\times22$ specimens, i.e., those with very stocky flanges, typically experienced only very mild flange buckling within the link and no flange buckling outside of the link in the brace connection panel. Further, no deterioration of hysteretic behavior resulted from this mild flange buckling. Rather, as demonstrated by Specimen 12, lateral torsional buckling is the dominant form of local instability for a very long link with stocky flanges.

It is apparent that as link length increases, the forms of local instability produced in the link change from those related to shear deformation (shear buckling of the web) to those related to

flexural deformations (flange buckling and lateral torsional buckling). Further, the type of flexural local instability developed depends on the slenderness of the flange. Flange buckling is dominant for slender flanges whereas lateral torsional buckling is dominant for stocky flanges. A combination of flange and lateral torsional buckling would be anticipated for flanges of intermediate slenderness.

For short links, proper web stiffening can successfully delay the onset of web buckling until very large ($\pm$ .10 rad.) plastic rotations are achieved. Further, the occurrence of web buckling in a well stiffened short link is considered to define failure of the link, as tearing of the web usually occurs soon after buckling [14]. In contrast, it is apparent from these tests that flange buckling cannot be as successfully delayed by stiffening. However, also in contrast to short links, the onset of flange buckling within the link is not a particularly serious event. As observed in the $W12\times16$ specimens, flange buckling must be very severe before link strength begins to deteriorate. Even then, flange buckling causes gradual loss in link strength rather than a large and sudden drop in capacity. As stiffeners are placed closer to the link ends, the onset of flange buckling is delayed, although not substantially. Further, once a flange buckle forms, it is constrained to a region between the stiffener and the link end. Making this distance too small can result in a highly localized buckle with very large local curvatures within the flange. This may in turn contribute to the formation of a fracture at the link-to-column connection. From the test observations, it would appear that locating stiffeners closer than b_f to the link end may be disadvantageous for this reason. For the links with thin flanges, it also appears that the link end stiffeners may be effective in preventing the flange buckling from escalating into lateral torsional buckling of the link. This may, in fact, be the most important contribution of these stiffeners.

For the $W12\times22$ links, flange buckling was very mild, with lateral torsional buckling the dominant form of local instability as link length increases. Judging from the performance of Specimen 12, the link end stiffeners appeared to provide substantial restraint against lateral torsional buckling. It was also evident from this specimen that the stiffeners should not be too close to the link ends in order to be effective in this capacity.

Based on the above observations, a preliminary recommendation can be made to locate stiffeners within long links at a distance of $1.5\,b_f$ from each end of the link. For links with thin flanges, these stiffeners will help control flange buckling and help prevent the flange buckling from developing into lateral torsional buckling. At the same time, the flange buckles will not be constrained into too small of a region. For links with stocky flanges, these end stiffeners should provide substantial restraint against lateral torsional buckling.

For links in the transition length range, in addition to providing stiffeners at $1.5\,b_f$ from the link ends, stiffening of the web within the link is also required to prevent web buckling, as demonstrated by Specimen 2. Based on the test observations, providing equally spaced stiffeners

according to the criteria of Eq. 1.3b is conservative.

An additional important issue is the need for stiffening *outside* of a long link within the brace connection panel. As discussed above, very severe local buckling developed in the brace connection panel of several $W12\times16$ specimens. This included severe flange buckling in the top flange of the panel, web buckling of the upper portion of the panel, and in the later stages of loading, out-of-plane displacement of the top flange. The addition of a partial depth stiffener, while not preventing local buckling, appeared to limit its extent (compare Specimens 5 and 6). For the $W12\times22$ specimens, even though severe yielding was observed in the brace connection panel, no local buckling ever developed. For these specimens, an additional stiffener would have served no useful purpose.

Development of local buckling in the brace connection panel apparently depends strongly on the flange slenderness ratio of the beam section. It may also depend on other factors such as the length of the panel and on the brace-beam angle. Based on these limited test observations, no general recommendation can be made on stiffening of the brace connection panel. Further work is needed to understand the distribution of stresses within the panel to determine under what circumstances local buckling may develop. A conservative approach, of course, is to always stiffen the brace connection panel outside of a long link. Based on the test observations, a reasonable location for this stiffener is a distance of $1.5\,b_f$ from the link end, or one-half of the panel length, whichever is less. This stiffener need only be partial depth as demonstrated by Specimen 6.

For all test specimens, stiffeners within the link as well as the partial depth stiffeners within the brace connection panels were all one-sided. These one-sided stiffeners were very effective in controlling local buckling. At present, the EBF codes [5,7,8] permit one-sided stiffeners for beam sections less than 24 inches in depth, and require two-sided stiffeners for deeper sections. Based on these tests, this rule appears reasonable for long links.

One of the objectives of this testing program was to investigate the effects of significant yielding in the beam segment outside of the link. Specimens 7, 8 and 11 (including 11R1 and 11R2) were specifically designed to incur severe yielding and damage in their beams. This was accomplished by providing very low brace-beam angles, resulting in the development of very large axial forces in the beams. In addition, brace sections with low values of flexural stiffness were chosen. Consequently, almost the entire link end moment was initially transferred to the beam, with only very little taken by the brace. These high moments combined with high axial forces assured severe yielding in the beams. Capacity design principles were also violated for these specimens. The combined flexural strengths of the brace and beam, reduced for axial force, was much less than the estimated ultimate link end moments.

Examining the response of Specimens 7, 8, 11R1 and 11R2 indicates that these specimens suffered significant loss of strength and plastic rotation capacity as a result of severe yielding and

instability in their beams. This loss is graphically illustrated by comparing the response of Specimens 1 and 7. These specimens had identical beam sections and nearly identical link lengths. However, Specimen 1 was designed to restrict yielding primarily to the link, whereas Specimen 7 permitted significant yielding in the beam. The response of these two specimens are plotted together to the same scale in Fig. 3.34. The very large loss of strength and plastic rotation capacity in Specimen 7 is evident.

The loss of strength and rotation capacity in Specimens 7, 8, 11R1 and 11R2 can be attributed to the development of severe instability in their beams. This instability resulted from the combination of very high bending moments and very high axial forces. The beam axial force, in particular, appears to be the prime factor in the development and subsequent severity of the instability. The spacing of lateral supports, of course, has an important influence on beam stability. However, even in Specimen 11R2 where relatively close spacing of lateral supports was provided, severe lateral torsional buckling of the beam still developed.

It is interesting to speculate what influence a composite deck would have had on the performance of these specimens. As discussed earlier in this section, the top flange of the beam is generally much more highly stressed than the bottom flange. Consequently, beam instability initiates with out-of-plane displacements of the top flange. It is the top flange, of course, that would also most benefit from the stabilizing effect of a composite deck. It may therefore be postulated that a composite deck would have improved the performance of those specimens that failed by beam instability. However, because of the extremely severe nature of the instability, the very large out-of-plane displacements, and the apparent development of large out-of-plane forces (as evidenced by damage to lateral supports), it is not at all clear that a composite deck would significantly improve performance. The effects of a composite deck on the behavior of beams in EBFs may be a useful area of future research.

Based on the performance of Specimens 7, 8, 11R1 and 11R2, it must be concluded that significant yielding in the beam segment outside of the link is not an effective energy dissipation mechanism in EBFs. The high axial force in the beam produces severe instability and precludes the development of significant plastic rotations in the beam. The performance of these specimens also suggests that very low brace-beam angles should be avoided in EBFs in order to limit axial force levels in the beam. Other test specimens with steeper braces experienced minor yielding in their beams, but without the development of instability in the beam (for example, Specimens 1 to 6). This indicates that minor yielding of the beam may be acceptable if axial force levels are not excessive.

An additional objective of this testing program was to provide limited experimental verification of selected brace connection details. Three different details were used: a direct welded connection for *W* section braces (Specimens 1, 2, 5, 6 and 12), a direct welded connection for tube

braces (Specimens 3, 4 and 8), and a stiffened gusset plate connection for tube braces (Specimens 7, 9, 10, 11, 11R1 and 11R2). The direct welded connections for both the *W* section and tube section braces performed well, surviving the severe cyclic loading programs without any visible distress. The gusset plate connections also behaved well, and appeared to develop substantial moment resisting capacity. The gussetted brace connection in Specimen 11R2, however, suffered some damage in the final loading cycles, with some buckling of the gusset plate and the partial failure of a brace to gusset weld. Severe lateral torsional buckling of the beam for this specimen appeared to be a primary cause of the brace connection damage by subjecting the brace to extraordinarily large bending moments, both in-plane and out-of-plane of the specimen. A poor brace to gusset weld also contributed to the damage.

Based on the observed performance of the brace connections, the direct welded *W* and tube section connections appear to be suitable for any EBF application. They are particularly suitable when large bending moments are anticipated in the brace, as may be the case with long links. The stiffened gusset plate connection also provides good performance. However, it may be prudent to limit the use of this connection detail to those applications where the brace moments are not excessive. For most EBFs, brace moments will not be excessively large as long as significant yielding of the beam is not permitted. Additional testing of this connection detail would be desirable to better define its limits under combined bending moment and axial force in the brace.

Specimens 9 and 10 were constructed with *short* links attached to the web of the column. These short link should have been capable of supplying up to ± .10 rad. of plastic rotation. Instead, both specimens failed prematurely by fracture at the link-to-column web connection. At the point of fracture, Specimens 9 and 10 developed plastic rotations of only ± .04 rad. and ± .03 rad., respectively. As noted in the test descriptions, incomplete penetration of the flange weld may have contributed to the fracture of Specimen 9. Nonetheless, these specimens tend to confirm the questionable reliability of connections to the column web and confirm that link-to-column web connections are best avoided. Further, based on these tests, there appears to be little justification for increasing the current code [5,7,8] specified rotation limit of ± .015 rad. for a link attached to a column web.

Finally, it should be noted that the links in these tests were not subjected to axial load. However, it is reasonably clear that the addition of significant axial loads would be very damaging to long links. The important failure modes for long links, i.e., flange fracture, flange buckling, and lateral torsional buckling are all a result of very high bending stresses at the link ends. Stresses produced by link axial forces would directly add to these very high bending stresses and would certainly hasten the failure of the links.

3.4 SUMMARY

Following is a summary of the key observations and implications of the testing program described in this chapter.

1. The dominant failure mode for long links attached to columns using conventional EBF details (full penetration weld at the flanges and a welded web connection) is fracture of the link flange at the link-to-column connection. This is a highly undesirable failure mode because it cannot be reliably predicted and represents a sudden and complete failure of the link.
2. Because fracture is the controlling failure mode and because these fractures occur at levels of plastic rotation that are judged to be marginal at best, it is recommended that long links attached to columns **not** be used in EBFs. However, there is no evidence that long links cannot be used when located within a span between two braces.
3. The addition of vertical reinforcing ribs at the link-to-column connection, when properly implemented, can delay fracture and improve plastic rotation capacity. These links, however, still fail by fracture of the link flange at the ends of the ribs.
4. Significantly improved connection performance was achieved by reinforcing the link flanges with triangular cover plates. This promising technique warrants further development and testing.
5. Excellent connection performance was also achieved by connecting the link to the column with all around fillet welds and by avoiding the use of web copes in the link.
6. Additional important failure modes for long links are flange buckling and lateral torsional buckling. Flange buckling dominates for links with slender flanges and lateral torsional buckling dominates for links with stocky flanges. For links with slender flanges, very severe flange buckling can also occur immediately outside of the link, within the brace connection panel.
7. Inelastic shear buckling of the link web is still an important failure mode for links in the intermediate length range of combined shear and flexural yielding. Web stiffening is still required within this length range, although spacing can likely be increased from that used for short links. Web stiffening is not needed in very long links.
8. As link length is increased within the transition length range, both strength and plastic rotation capacity are significantly decreased.
9. The initiation of flange buckling in a stiffened long link is not a particularly serious event. Flange buckling within the link must become very severe before link strength begins to deteriorate. Flange buckling outside of the link within the brace connection panel appears to be more harmful to overall performance than flange buckling within

the link.

10. Locating stiffeners near the ends of long links delays the onset of flange buckling, although not substantially. Placing stiffeners too close to the link ends may be disadvantageous by constraining flange buckles into too small of a region. Stiffeners near the link ends also appear to provide significant restraint against lateral torsional buckling of the link.

11. Based on the test observations, a preliminary recommendation is made to locate stiffeners at $1.5b_f$ from each end of the link. At this distance, the stiffeners help control flange buckling and restrain lateral torsional buckling, but do not excessively constrain flange buckling. For links within the transition length range, in addition to providing stiffeners at $1.5b_f$ from the link ends, stiffening of the web is also required to prevent inelastic web shear buckling. Spacing these additional stiffeners according to the short link criteria of Eq. 1.3b appears conservative.

12. No general recommendation can be made yet for stiffening the brace connection panel outside of a long link. However, a conservative approach is to always provide a stiffener within the panel. A reasonable location for this stiffener is a distance of $1.5b_f$ from the link end or one-half of the panel length, whichever is less. This stiffener need not be full depth.

13. One sided stiffeners were used within the links of these test specimens. It appeared that little improvement would have been gained by using two-sided stiffeners. The present code rule of permitting one-sided stiffeners for sections less than 24 inches in depth appears reasonable for long links.

14. Permitting significant yielding in the beam segments outside of the links resulted in a large loss of strength and plastic rotation capacity. The combination of bending moment and high levels of axial force produce severe instability of the beam. These tests support the capacity design philosophy for EBFs that requires restricting yielding primarily to the links. Minor yielding of the beam may be acceptable if axial force levels in the beam are not excessive.

15. The brace connections tested in this program performed well. No distress was visible in any of the direct welded *W* and tube section brace connections. The gusset plate connections also performed well, although one of these connections suffered some damage (Specimen 11R2).

16. The two tests on short links connected to the column web showed poor performance. These tests tend to confirm the questionable reliability of such connections and indicate that link-to-column web connections are best avoided in EBFs.

4. FURTHER ANALYSIS OF EXPERIMENTAL DATA

The hysteretic response loops combined with the descriptions and photographs of damage presented in Chapter 3 provide an overall picture of the performance of the EBF test specimens. In this chapter, the assessment of specimen performance is supplemented by further detailed analyses of experimental data. The primary emphasis will be to examine design implications of this data. However, an additional goal in examining the experimental data is to develop an improved understanding of long link behavior. Such an understanding is needed ultimately for realistic modelling of long links, both for the analysis of local link behavior and for the analysis of global frame behavior. Description and analysis of the photogrammetric data is presented in Chapter 5.

4.1 LINK YIELD AND ULTIMATE SHEAR FORCES

Link Yield Shear Strength

Following the basic design procedure for EBFs discussed in Chapter 1, links are sized so that the link shear force generated by code specified lateral loads does not exceed the link shear yield strength. "Link shear yield strength" refers to the value of shear force required to cause general yielding of the link, whether by shear yielding of the link web or by flexural yielding of the link ends. The link shear yield strength is therefore an important parameter in EBF design.

Values for link shear yield strength can be predicted analytically using moment-shear (M-V) interaction surfaces developed within the framework of perfect plasticity [39]. These interaction surfaces typically show a substantial reduction in shear strength in the presence of large bending moment as well as a reduction in flexural strength in the presence of high shear force. However, the large body of experimental data on *short* links indicates essentially no M-V interaction at the yield limit state. Accordingly, Kasai and Popov [13] have recommended neglecting M-V interaction for determining the yield strength of short links. Thus, at the yield limit state, the shear strength can be taken as V_p, regardless of the magnitude of bending moment in the link, and the flexural strength can be taken as M_p, regardless of the magnitude of shear force in the link. Neglecting M-V interaction permits significant simplifications in both the design and analysis of EBFs.

The key question here is whether or not M-V interaction can be neglected in predicting the yield strength of long links. In Chapter 3, $V_{yield\,(SPT)}$ was defined as the link shear yield strength based on simple plastic theory (SPT), i.e. based on neglecting M-V interaction. $V_{yield\,(SPT)}$ is computed as follows:

$$V_p \quad \text{for } e \leq 2\,\frac{M_p}{V_p} \tag{4.1a}$$

$$\frac{2M_p}{e} \text{ for } e \geq 2\frac{M_p}{V_p} \tag{4.1b}$$

These equations indicate that a link of length $e \leq 2M_p/V_p$ will yield when the shear force reaches V_p, whereas links of length $e \geq 2M_p/V_p$ yield when the bending moment reaches M_p at both ends.

Values of $V_{yield(SPT)}$ are listed for each test specimen in Table 4.1. The actual estimated values of M_p and V_p listed in Table 2.10 were used for computing $V_{yield(SPT)}$. Further, for those links with ribs at the link-to-column connection (Specimens 4, 6, 7, and 8), the value of e used in Eq. 4.1b was reduced by the length of the ribs. For those specimens, initial flexural yielding was observed to occur outside of the ribs, i.e., in the unreinforced portion of the link.

In order to determine whether or not it is appropriate to neglect M-V interaction in long links, the values of $V_{yield(SPT)}$ listed in Table 4.1 can be compared with the experimentally observed values of shear force at first significant yield of the links. In order to facilitate this comparison, the link shear versus link rotation plots for each specimen are shown in Fig. 4.1 together with lines indicating the values of $\pm V_{yield(SPT)}$ for that specimen. In examining these plots, it is apparent that establishing a representative value of shear force at first significant yield is difficult for these specimens. For most specimens, a clearly defined yield point cannot be uniquely identified. A value of link shear yield strength was therefore subjectively estimated for each specimen near the point where significant hysteretic loops begin to form. These values are listed in Table 4.1. Also listed in this table is the ratio of the estimated link shear yield strength to the value of $V_{yield(SPT)}$.

In examining Table 4.1 and Fig. 4.1, it appears that most specimens yielded somewhat earlier than predicted by $V_{yield(SPT)}$. However, the difference is not large in most cases, with yielding typically occurring at shear forces of 90 to 95 percent of $V_{yield(SPT)}$. The most notable exceptions are Specimens 7, 8 and 11, where first significant yield occurred well before $V_{yield(SPT)}$. These three specimens were designed to incur severe yielding in the beam segment outside of the link. This early yielding can be attributed to moment-axial force interaction in the beam. These three specimens demonstrate that overall frame strength will be controlled by the beam rather than by the link in an EBF where significant beam yielding is permitted.

For the usual case where yielding is restricted primarily to the links, the data in Table 4.1 and Fig. 4.1 indicate the possibility of mild M-V interaction at the yield limit state of long links. However, from a design point of view, this interaction is not significant, especially considering the uncertainty in establishing a representative yield point for these long links. Thus, for design purposes, it appears that neglecting M-V interaction is a reasonable simplification for predicting the yield strength of long links. Eqs. 4.1a and b can therefore be considered to provide a reasonable estimate of link shear yield strength for design of any length link.

Link Ultimate Shear Strength

The ultimate shear force developed by the link controls the maximum axial forces generated in the brace, beam and columns of the EBF. Following capacity design principles, these members must be designed for the maximum forces generated by the link. Developing a reasonable estimate of ultimate link shear force is therefore an important issue in EBF design. Underestimating ultimate link shear may lead to non-ductile failure modes such as brace or beam buckling. On the other hand, overestimating ultimate link shear may result in very heavy braces and columns in order to satisfy capacity design requirements, and may therefore be very costly.

As noted in Chapter 1, for design purposes the ultimate strength of short links has generally been taken as 1.5 times the yield strength. Thus, the ultimate shear strength of short links is estimated as $1.5V_p$. If it is assumed that the lack of M-V interaction observed at the yield limit state can be extended to the ultimate strength limit state, then the ultimate shear strength of long links can be estimated simply as $1.5 \times V_{yield(SPT)}$, where $V_{yield(SPT)}$ is given by Eq. 4.1. This approach has been adopted by some of the model EBF codes [7,8].

In order to examine the validity of the above approach, it is useful to compare the measured values of ultimate shear force developed by the test specimens against the corresponding values of $1.5 \times V_{yield(SPT)}$. These values are listed in Table 4.1. In addition, lines corresponding to $\pm 1.5 \times V_{yield(SPT)}$ are shown on the hysteretic response plots in Fig. 4.1.

By examining Table 4.1 and Fig. 4.1, it is clear that an overstrength factor of 1.5 significantly overestimated the ultimate shear force developed in most of the test specimens. From the last column of Table 4.1, it is apparent that most specimens achieved ultimate shear strengths on the order of only 1.2 to 1.3 times $V_{yield(SPT)}$. Thus, whereas it is reasonable to neglect M-V interaction when predicting the *yield* strength of long links, it appears that M-V interaction must be considered in some manner when predicting the *ultimate* strength of long links. It may be conjectured that since most specimens failed by fracture at the link-to-column connection, higher ultimate strengths would have been achieved if these fractures had not occurred. However, by examining the plots in Fig. 4.1, it appears that the rate of strength increase due to strain hardening in the final loading cycles was generally small. Consequently, even without failure by fracture, a significant increase in ultimate strength would appear unlikely for most of the test specimens.

Some additional observations can be made from Table 4.1 and Fig. 4.1. First, it appears that an overstrength factor that varies with link length may be appropriate in the intermediate link length range, rather than just a single factor. Further, whereas an overstrength factor of 1.5 is too large in the intermediate length range, it appears to be appropriate for very long links, as evidenced by Specimen 12. Finally, it is apparent from Specimens 1, 5 and 6 that cyclic flange buckling will limit the strength of long links with slender flanges. Thus, for long links, ultimate strength also depends on the flange slenderness ratio.

4.2 LINK END MOMENTS

The magnitude and distribution of bending moments developed within the links is of interest for several reasons. First, whereas the strength of short links is limited by the maximum shear force that can be developed by the link, the strength of long links is limited by the maximum bending moments that can be developed within the link. Further, following capacity design principles, the maximum link end moments determine the design moments for the adjoining members. Thus, as with ultimate shear force, it is important to be able to develop a reasonable estimate of ultimate link end moments.

Distribution of Link End Moments

Plots of link end moments are shown for each test specimen in Fig. 4.2. The sign convention for link end moments is shown in Fig. 3.2. Three different plots are provided for each specimen. In the first plot for each specimen, the moment at the column end of the link and at the brace end of the link are plotted against the link rotation angle, γ. These plots show the development of link end moments throughout the course of each test. In these plots, the moment at the brace end of the link (dotted lines) are opposite in sign to the convention of Fig. 3.2 in order to facilitate comparison with the moment at the column end of the link. In the second plot for each specimen, the variation of link end moment with link shear force is illustrated. In the third plot, the moment at the column end of the link is plotted against the moment at the brace end of the link. For all of these plots, the bending moment at the column end of the link is computed at the column face. For links attached to the column web (Specimens 9 and 10), this moment is computed at the junction of the link and the continuity plates.

These plots all show some common features. For each loading cycle, the bending moment was initially higher at the column end of the link than at the brace end of the link, as would be anticipated from an elastic frame analysis. For most specimens, the initial elastic bending moment measured at the column end of the link was on the order of 2 to 3 times the moment at the brace end of the link. Exceptions to this were Specimens 7 and 11, 11R1 and 11R2 for which the initial ratio of end moments was on the order of 6 to 7.

As loading progressed in each cycle, yielding occurred at the column end of the link, and bending moment redistributed, to varying degrees, to the brace end of the link. In experiments on redistribution of end moments in short links, Kasai [13] observed equalization of end moments for links of length greater than about $1.3M_p/V_p$. Based on this experience, complete equalization of end moments would have been anticipated for each of the 14 test specimens. In examining Fig. 4.2, the degree of moment equalization can be best judged from the plots of moment at the column end of the link versus moment at the brace end of the link. Complete moment equalization is indicated by the diagonal line drawn on these plots.

For many of the test specimens, moment equalization was nearly, but not completely achieved. Virtually every specimen shows a rather interesting pattern of redistribution indicating that moment equalization was more complete in the west loading cycles (the left portion of the plots in Fig. 4.2) than in the east loading cycles. In the east loading cycles, large compressive axial forces were generated in the beam segment outside of the link. These large compressive forces were apparently responsible for some loss of flexural stiffness in the beam, thereby attracting less moment to the brace end of the link. Thus, for the same link shear force, the moment at the column end of the link was typically higher in the east loading cycles than in the west loading cycles. This phenomenon may also explain why fractures at the link-to-column connection typically occurred during the east loading cycles.

The link end moment plots for Specimens 7, 8 and 11 (including 11R1 and 11R2) are in sharp contrast to the other test specimens. For these specimens, the ultimate link end moments were far from equal, with the moment at the column end of the link remaining much larger than at the brace end of the link throughout the entire loading history. These are the specimens that were designed to incur severe yielding and damage in the beam segment outside of the link. It appears that the yielding and instability outside of the link prevented the complete redistribution of moment within the link. As a result, the bending moment at the column end of the link was much larger than for specimens where yielding was restricted primarily to the link region. This is particularly evident by comparing Specimens 1 and 7. These specimens had nearly identical links. Specimen 1, however, was designed to restrict yielding primarily to the link region, whereas the design of Specimen 7 permitted severe yielding outside of the link. In comparing the link end moment plots for these two specimens, it may be seen that at a link shear force of, for example 50 kips, the bending moment at the column end of the Specimen 1 link was limited to about 900 inch-kips. For the same 50 kip shear force, the bending moment at the column end of the Specimen 7 link was as high as 1250 kips. The inability of the Specimen 7 link to properly redistribute bending moments away from the column end of the link certainly contributed to the failure of the link-to-column connection.

The Specimen 7 link end moment plots show that the lack of moment equalization is significantly more severe for the direction of loading that puts the beam into compression. Clearly, this effect is due to instability of the beam and the consequent loss of flexural stiffness at the brace end of the link. However, it is also clear that moment equalization cannot be expected even when beam instability does not occur, as evidenced by the loading direction for which the beam is in tension. This point is further illustrated by examining the link end moment plots for Specimens 11, 11R1 and 11R2. The degree of moment equalization is just as poor when the beam is in tension as when it is in compression. This indicates that even if instability of the beam can be prevented by lateral bracing and/or a composite deck, yielding in the beam may still inhibit the

proper redistribution of bending moments within the link. The link end moment plots for Specimens 7 and 11R2 also suggest that the very large difference in the initial elastic link end moments for these specimens contributed to their inability to equalize end moments. This is particularly evident in the west loading cycles (beam in tension) for Specimen 7, where the difference in end moments appears to have been too large for the link to overcome.

From the above discussion, it is apparent that a design permitting significant yielding within the beam outside of the link can result in adverse behavior not only of the beam, but also of the link itself. This observation has important ramifications for the design of EBFs with *short* links attached to columns. If redistribution of link end moments is inhibited by the occurrence of significant yielding outside of the link, then the bending moment at the link-to-column connection will grow to levels characteristic of long links. This may, in turn, result in premature failure of the link-to-column connection.

As a final observation, many of the plots in Fig. 4.2 show somewhat erratic behavior in the final loading cycle. This behavior results from the occurrence of fracture at the link-to-column connection and the subsequent sudden redistribution of bending moment to the brace end of the link. It is useful to note that despite these large bending moments at the brace end of the link, no signs of fracture were observed at the brace end of the link, even though there is substantial welding present at this end of the link (for the brace connection). This indicates that fracture of the link flanges is not likely to be a controlling failure mode when long links are not attached to columns.

Ultimate Link End Moments

As noted above, the magnitude of the ultimate link end moments defines the ultimate strength of a long link, as well as the capacity design moments for the columns, beams and braces of an EBF. The ultimate link end moments measured for each of the 14 tests are listed in Table 4.2. For those specimens that failed by fracture at the link-to-column connection, the bending moments listed in this table are the maximum values measured prior to the occurrence of the fracture. After fracture, the moments at the brace end of the link are no longer representative of actual link behavior when fracture is not the controlling failure mode.

For links with reinforced link-to-column connections (Specimens 4, 6, 7, 8, 11R1 and 11R2), bending moments at the column end of the link are reported both at the column face and at the end of the reinforced region. The final column of numbers in Table 4.2 is the ratio of the maximum ultimate link end moment measured in the unreinforced portion of the link to the value of M_p for that section. This final column is therefore most representative of the ultimate moment capacity of the links.

As discussed in Section 4.1, the ultimate strength of links for design purposes has been taken as 1.5 times the yield strength based on simple plastic theory (no M-V interaction). This approach

would predict ultimate end moments of $1.5M_p$ for links of length greater than $2M_p/V_p$. It is apparent from Table 4.2 that many links, particularly in the intermediate length range, generated ultimate link end moments significantly less than $1.5M_p$. As noted earlier, it appears that an overstrength factor of 1.5 is therefore too large in the intermediate length range and that M-V interaction cannot be neglected when predicting ultimate strength in this length range. However, for very long links with stocky flanges, such as Specimen 12, an overstrength factor of 1.5 appears reasonable. In this very long length range, shear force evidently no longer significantly affects ultimate flexural strength. For very long links with slender flanges, such as Specimens 5 and 6, the development of severe cyclic flange buckling appears to limit ultimate end moments to substantially less than $1.5M_p$.

In examining the ultimate moments at the column end of the link, it is again evident that the ultimate moments generated in the east loading cycles (positive moments) are generally greater than those for the west loading cycles (negative moments). This tends to confirm that fractures at the link-to-column connection generally occurred in the east loading cycles due to the somewhat higher moments generated at the column end of the link during these cycles.

For specimens with reinforcement at the link-to-column connection, Table 4.2 indicates that very large moments can be generated at the column face, within the reinforced portion of the link. For example, in Specimen 11R2, the ultimate moment at the column face is 20 percent greater than in the unreinforced portion of the link. This increase in bending moment delivered to the column from the link should be considered in the column design.

As noted in Chapter 3, the triangular cover plates added to the link of Specimen 11R2 were very successful in preventing fracture at the link-to-column connection. As indicated in Table 4.2, an ultimate moment of 2000 inch-kips was generated at the tips of the cover plates, corresponding to 1.55 times M_p of the link. At the column face, this moment increased to 2400 inch-kips. Based on the known yield stress of the cover plates, the value of M_p for the reinforced section of the link at the column face is estimated as 1850 inch-kips. Thus, the 2400 inch-kip moment at the column face corresponds to 1.3 times M_p of the reinforced section. This indicates that there is no need to reinforce the link to such a degree that no yielding occurs at the column face. From a design point of view, it would appear reasonable to choose the width and thickness of the cover plates to limit bending moments at the column face to perhaps 1.1 to 1.2 times M_p of the combined (W section plus cover plates) section. Note also that the rather small cover plates used in Specimen 11R2 increased M_p of the section by more than 40 percent. This indicates that the cover plates need not be very thick in order to be effective.

A large number of links in this testing program failed by fracture at the link-to-column connection. In examining Table 4.2, it appears that quite a large number of these failures (Specimens 1, 5, 6, 7, and 11) occurred at a bending moment on the order of about $1.2M_p$. As discussed in

Chapter 1, the length limit for *short* links is set at $1.6M_p/V_p$. This is based on limiting the link end moment to $1.2M_p$, with assumed equalization of end moments. The experience of this testing program would therefore suggest that even short links, approaching the length limit of $1.6M_p/V_p$, may be in danger of link-to-column connection failure. As noted earlier, complete moment equalization may not necessarily be achieved for links attached to columns. Therefore, bending moments in excess of $1.2M_p$ may be developed even by short links attached to columns.

In Chapter 3, the recommendation was made that link lengths in excess of $1.6M_p/V_p$ should not be used next to columns. The above discussion suggests that it may be prudent to lower this length limit somewhat in order to assure reliable performance of link-to-column connections. A review of past EBF research indicates very little experimental evidence is available in the length range of about 1.3 to 1.6 M_p/V_p for links attached to columns, using realistic connection details with full penetration flange welds. Additional experimental work in this length range is needed to better define the maximum safe length for links attached to columns.

Moment-Rotation Relationships at Link Ends

Rotations were measured at both ends of the links using rigid bars attached to the link ends and then measuring displacements at the ends of the bars, as shown in Fig. 2.31. In Fig. 4.3, rotations at the column end of the link are plotted against the bending moment at the column end of the link. Clockwise rotations are defined to be positive when the specimen is viewed from above, as in Fig. 2.3. For a number of the specimens, the displacement transducers used to measure rotations went out of range prior to the completion of the test. For these specimens, the moment-rotation plots are terminated at that point. For such cases, the limit of the plot is identified in Fig. 4.3.

The item of interest in Fig. 4.3 is the rather significant hysteretic behavior for some of the text specimens, particularly those with $W12\times22$ links. The inelastic activity revealed by these plots can be attributed to yielding of the column panel zone. Those specimens showing significant inelastic hysteretic behavior in Fig. 4.3 (Specimens 3, 4, 8, 11R2, and 12) correspond with the specimens where panel zone yielding was observed during the course of the testing. These specimens indicate that column panel zone behavior can be an important design issue for EBFs. This is particularly true if long links with reinforced link-to-column connections are used, since such links can develop very high end moments. The degree to which column panel zone yielding should be permitted is still an unresolved issue. Recent studies [34] indicate that panel zone yielding may be advantageous in MRFs, providing a stable energy dissipation mechanism. However, there are still unresolved questions on the full effects of panel zone yielding. Specifically, the effects on the behavior of welded beam-to-column connections as well as on overall column stability are not yet fully understood [34]. These issues and questions concerning panel zone behavior can be as important to EBFs as they are to MRFs. It is useful to note that panel zone yielding reduces

inelastic deformation demands on beams in MRFs [34]. This indicates that long links attached to columns in EBFs may provide acceptable performance if the inelastic deformation demands on the link-to-column connection can be reduced by panel zone yielding. Experimental investigation of EBFs designed for significant panel zone yielding is needed, however, before such a design approach could be reliably implemented.

In Fig. 4.4, rotations at the brace end of the link are plotted against the bending moment at the brace end of the link. As before, clockwise rotations are defined to be positive when the specimen is viewed from above. Also, as before, plots are terminated at the point where displacement transducers measuring rotations went out of range.

Most of the plots in Fig. 4.4 show significant inelastic activity outside of the link. These hysteretic plots indicate that yielding outside of the link, primarily in the brace connection panel and beam, may contribute significant energy dissipation capacity. The moment-rotation response for specimens that experienced significant instability of the beam (Specimens 7, 8, 11R1, 11R2 and 12) clearly show a loss of flexural stiffness at the brace end of the link due to the beam instability. The plot for Specimen 7 indicates that very little energy was dissipated by the beam after the initiation of lateral torsional buckling in the beam. The plots for Specimens 8, 11R2, and 12, on the other hand, show significant energy dissipation outside of the link even after the initiation of beam instability. It is also interesting to note that many of the specimens that did not experience instability outside of the link show a rather one-sided hysteretic response in Fig. 4.4. These specimens show more yielding outside of the link in the west load cycles (beam in tension) than in the east load cycles. The cause for this unsymmetric yielding response is considered later in the discussion of beam and brace response.

4.3 ENERGY DISSIPATION OF TEST SPECIMENS

Quantifying the ability of structural components and joints to dissipate energy through plastic deformations is of interest for several reasons. First, energy methods can provide a useful approach for analysis and design of earthquake resistant structures [53]. The basic approach of such methods is to balance the earthquake energy input to a structure against the structure's elastic vibrational energy (elastic strain energy and kinetic energy) and the energy dissipated by equivalent viscous damping and hysteretic damping (plastic deformations) [52]. For code based EBF designs, energy dissipation under severe earthquake ground motions is provided largely by hysteretic damping, i.e. by the development of plastic deformations [18, 28]. Knowledge of the energy dissipation capacity of structural components is therefore needed for the implementation of energy based design methods.

Energy dissipation calculations also provide a useful basis for comparing the overall performance of the various test specimens. In Chapter 3, the test specimens were compared on the basis

of their plastic rotation capacities. In making such comparisons, it is difficult to define a meaningful criteria for measuring plastic rotation capacity. In Table 3.3, for example, various criteria were chosen for establishing the limit of a specimen's useful plastic rotation. These criteria included the limit defined by stable hysteretic behavior and the limit defined by the point where link shear drops below a specified value. Neither of these limits, however, has a clear physical significance since a specimen can typically still resist applied loads after the limit is exceeded. Comparisons based on energy dissipation capacity are more meaningful. Energy dissipation, based on the area enclosed by load-deformation response loops, can incorporate the effects of various post yield behaviors, including deteriorating hysteretic response. Energy dissipation capacity therefore provides a useful index for comparing the overall performance of the test specimens up to the end of testing for that specimen. For most specimens, testing was continued until the useful load carrying capacity was essentially exhausted. Energy dissipation calculations for the test specimens therefore provide a reasonable basis for performance comparisons.

The total energy dissipated by plastic deformation for each test specimen is displayed by the barplot in Fig. 4.5. Total dissipated energy was computed as the area enclosed by the hysteretic loops in the plots of force applied to the column versus displacement of the column. Considering the entire subassemblage, the end of the column connected to the hydraulic ram is the only reaction point that undergoes significant inelastic displacement in the direction of the reaction force. The above method therefore provides a good overall estimate of total dissipated energy. It also includes all sources of energy dissipation within the specimen.

To provide a meaningful comparison, it is useful to separate the specimens with $W12\times16$ links and beams from those with $W12\times22$ links and beams. Even though the brace sections of the specimens varied, very little yielding was generally observed in the braces, and it is unlikely that brace yielding contributed significantly to energy dissipation. Separating the specimens according to the beam and link section is therefore appropriate. In addition, it is necessary to normalize the computed energy dissipation in some manner to account for differences in the measured yield stress of the beam and link sections (see Table 2.8). It is apparent from Table 2.8 that the flange yield stress is significantly less than the web yield stress for all of the link and beam sections. Normalizing energy dissipation for the effects of varying yield stress values is therefore not a straightforward process. However, in examining the data in Table 2.8, it may be seen that even though flange and web yield stresses vary widely, the ratio of web to flange yield stress is reasonably constant for a given section. This is particularly true for the $W12\times16$ sections, for which the ratio of web to flange yield stress was about 1.15 for all sections. The ratio of web to flange yield stress for the $W12\times22$ sections was not as constant, with values of about 1.1 for Specimens 8, 9, 11 and 12 and about 1.2 for Specimens 3 and 4.

Assuming a relatively constant ratio of web to flange yield stress, it is possible to normalize the dissipated energy according to the measured yield stress of the web or of the flange. The measured web yield stress was chosen as the basis for normalization. Accordingly, the total dissipated energy shown in Fig. 4.5 for each specimen was normalized as follows:

$$E_{normalized} = E_{total} \times \frac{36ksi}{F_{y\,web}} \tag{4.2}$$

The normalized dissipated energy for each of the $W12\times16$ specimens is shown in Fig. 4.6, and for the $W12\times22$ specimens in Fig. 4.7. Based on the above discussion, the elimination of the effects of varying yield stress by the above normalization process is expected to be reasonable for all test specimens, but may be somewhat less accurate for the $W12\times22$ specimens.

In examining the normalized energy dissipated by the $W12\times16$ specimens (Fig. 4.6), several useful observations can be made. The primary difference between Specimens 1 and 5 was link length. The Specimen 1 link was in the intermediate length range of combined shear and flexural yielding whereas the Specimen 5 link was in the length range of predominant flexural yielding. Specimen 1 dissipated nearly 4 times as much energy as Specimen 5 at the point of failure, indicating a significant loss of total energy dissipation capacity with increasing link length. Comparing Specimens 1 and 2 demonstrates a large loss of energy dissipation capacity due to the occurrence of severe web buckling in Specimen 2. Recalling that Specimen 1 suffered severe flange buckling both inside and outside of the link, Fig. 4.6 supports the observation in Chapter 3 that flange buckling is significantly less damaging to link performance than is web buckling. Next, comparing Specimens 1 and 7 demonstrates a large loss of energy dissipation capacity due to the development of severe lateral torsional buckling in the beam of Specimen 7. This observation indicates that cyclic buckling of the beam segment outside of the link was a poor energy dissipator for this specimen. The energy dissipation capacity of Specimen 10 was also rather poor, despite its short, shear yielding link. This poor performance was due to the early failure of the link-to-column web connection in this specimen. Finally, it is useful to compare Specimens 5 and 6. The important difference between these specimens was that the link-to-column connection was reinforced with ribs in Specimen 6. Even though both Specimens 5 and 6 ultimately failed by fracture of the link flange, Fig. 4.6 shows that Specimen 6 dissipated more than twice the energy of Specimen 5. This indicates that reinforcing ribs at the link-to-column connection, if properly implemented, can significantly improve the performance of long links.

The normalized dissipated energy of the $W12\times22$ specimens are shown in Fig. 4.7. Comparing Specimens 3 and 12 again indicates a loss of energy dissipation capacity with increasing link length. In comparing these specimens, it should be recalled that the Specimen 12 test was terminated due to the development of very large out-of-plane forces at the link end lateral support associated with lateral torsional buckling of the link and beam. If a much stronger lateral support

had been provided, some additional energy dissipation would have been possible. However, it is also evident that if a link-to-column connection failure could have been prevented in Specimen 3 as it was in Specimen 12, additional energy would also have been dissipated by Specimen 3. Thus, it must still be concluded that the total energy dissipation capacity of a very long, predominantly flexural yielding link is significantly less than that of a link in the intermediate length range of combined shear and flexural yielding.

The primary difference between Specimens 3 and 4 was the addition of reinforcing ribs at the link-to-column connection. Figure 4.7 confirms the observation in Chapter 3 that the addition of ribs did not improve link performance in this case. As discussed in Chapter 3, this result is likely due to the placement of a stiffener too close to the rib ends. This defect was remedied in Specimen 8, which was also provided with reinforcing ribs. The ability of Specimen 8 to dissipate energy, however, was abruptly terminated by the occurrence of severe buckling in the beam of this specimen. Specimen 9 was provided with a short, shear yielding link. The rather poor energy dissipation capacity of this specimen, as with Specimen 10, was due to the early failure of the link-to-column web connection. Finally, the large energy dissipation capacity of Specimen 11R2, as compared to Specimens 11 and 11R1, should be noted. The impressive gain in energy dissipation can be attributed to the excellent performance of the repaired link-to-column connection (with triangular cover plates) as well as the addition of a beam lateral support. It must be recalled that Specimens 11, 11R1, and 11R2 were designed to incur severe yielding and damage in the beam by violating capacity design concepts. As a result, Specimen 11R2 ultimately failed by severe lateral torsional buckling of the beam and the consequent development of very large link end lateral forces. If this specimen had been designed to restrict yielding primarily to the link, significantly larger energy dissipation would likely have been possible by virtue of the excellent performance of the modified link-to-column connection.

The normalized energy dissipation capacities of the test specimens shown in Figs. 4.6 and 4.7 may not provide a completely unbiased comparison of test specimen performance. The reason for this is because the specimens were not subjected to identical deformation histories. Even though deformations were generally applied symmetrically to the test specimens, the number of load cycles at a given level of link plastic rotation as well as the increase in link plastic rotation from one cycle to the next varied for each specimen. Thus, the normalized energy dissipation capacities shown in Figs. 4.6 and 4.7 may tend to favor those specimens subjected to a larger number of load cycles. This is particularly true if specimen failure is not due to accumulated plastic deformation but rather is due to the occurrence of some threshold level of force. Such may be the case for the specimens that failed by instability of the beam. Severe buckling of the beam is likely due to the occurrence of a critical level of axial force and bending moment in the beam rather than the

amount of accumulated plastic deformation prior to achieving the critical loads.

In an attempt to overcome the above deficiency as well as provide additional insight into test specimen performance, energy dissipation is presented in Figs. 4.8 to 4.11 in a different manner. In these figures, energy dissipation is plotted as a function of cumulative link plastic rotation, which may be expressed as $\Sigma|\gamma_p|$. These plots demonstrate how energy dissipation increases with increasing plastic rotation throughout the specimen's load history. The plots in Figs. 4.8 and 4.9 show total, unnormalized, energy dissipation. For Figs. 4.10 and 4.11, energy dissipation is normalized according to Eq. 4.2 to minimize the effects of differing yield stresses among the test specimens. As before, results for the $W12\times16$ specimens are separated from those of the $W12\times22$ specimens. In order to distinguish the various lines plotted in Figs. 4.8 to 4.11, the end point of each line is indicated by a small circle, with the corresponding specimen number marked nearby.

The plots in Figs. 4.8 to 4.11 are useful because they indicate the amount of energy dissipated for an increment of link plastic rotation angle. These plots therefore provide an indication of how effectively a specimen dissipated energy at any point in its loading history. It should be noted that a perfectly plastic system would plot as a straight line in these figures. A system that hardens, i.e., increases in strength with increasing plastic deformation would plot as a line curving upwards. Correspondingly, a degrading system, i.e., one that loses strength with increasing plastic deformation would plot as a line curving downwards.

Examining the plots of normalized dissipated energy for the $W12\times16$ specimens (Fig. 4.10), several observations can be made. In the early loading cycles, all of the $W12\times16$ specimens dissipated energy at about the same rate with respect to the applied γ_p. Even though the longer links (Specimens 5 and 6) yielded at much lower values of shear force than the shorter links (see Table 4.1), the amount of energy dissipated for a given increment of γ_p was about the same. This may be understood by recognizing that for a given value of γ_p, a longer link undergoes larger relative end displacement than a shorter link. With increasing cumulative plastic rotation, most of the lines initially curve upwards, reflecting the influence of hardening in the early loading cycles. However, at the later loading cycles, most of the lines plotted in Fig. 4.10 curve downwards, reflecting the influence of local instability and the associated loss of strength. It also appears from Fig. 4.10 that rate at which energy dissipation decreases varies with the type of local instability. The more rapid loss of energy dissipation for Specimen 2 as compared with Specimens 1 or 6 indicates that web buckling is more harmful to the link than is flange buckling.

The effects of flange and web buckling on energy dissipation are more clearly indicated in Fig. 4.12. The total, unnormalized, dissipated energy as a function of cumulative link plastic rotation is plotted for Specimens 2 and 6. Specimen 2 suffered severe web buckling inside the link, whereas Specimen 6 experienced severe flange buckling, first inside the link and then later outside of the link within the brace connection panel. The points at which significant flange and web

buckling were first observed for these specimens are shown in Fig. 4.12. Despite the very early occurrence of flange buckling within the link of Specimen 6, the rate of energy dissipation with increasing plastic rotation was still very high. This supports the observation in Chapter 3 that the initiation of flange buckling within a long link is not a particularly significant event. The energy dissipation capacity of Specimen 6 does not begin to deteriorate until flange buckling occurs in the brace connection panel outside of the link. It is also apparent from Fig. 4.12 that the occurrence of web buckling in Specimen 2 resulted in an almost immediate decrease in energy dissipation capacity, indicating again that it is more important to prevent web buckling in a link than it is to prevent flange buckling.

As a final observation on Fig. 4.10, it is interesting to note that Specimen 7, despite severe yielding in the beam segment outside of the link, dissipated energy as effectively as the other specimens in the early loading cycles. However, after the occurrence of lateral torsional buckling in the beam, the ability of Specimen 7 to dissipate energy with increasing deformation was almost completely lost. This supports the previous observation that cyclic buckling in the beam segment was a very poor energy dissipation mechanism for this specimen. However, Fig. 4.10 also indicates that yielding in the beam can effectively dissipate energy prior to instability.

Examining the plots of normalized dissipated energy for the $W12\times22$ specimens in Fig. 4.11, some additional observations can be made. First, by comparing Specimen 9 (a short link) with Specimen 12 (a very long link), it appears that the longer links dissipate significantly more energy for an increment of plastic rotation angle than the shorter links. This may be explained by the significantly thicker flanges on the $W12\times22$ sections resulting in large energy dissipation by flexural yielding. Fig. 4.11 also indicates much less influence of flange buckling for the $W12\times22$ sections. It is useful to recall that both Specimens 8 and 11R2 were designed to sustain severe yielding in the beam. Fig. 4.11 shows that these specimens very effectively dissipated energy up to their points of failure. Failure occurred by sudden buckling of the beam in Specimen 8 and by failure of the link end lateral support in Specimen 11R2 due to severe lateral torsional buckling of the beam. Despite lateral torsional buckling of the beam in Specimen 11R2, virtually no loss in the rate of energy dissipation is apparent up to the end of the test. The same observation can be made for Specimen 12, for which testing was also terminated due to impending failure of the link end lateral support. This indicates that lateral support strength may be critical for long links, particularly for sections with stocky flanges.

To summarize, Figs. 4.8 to 4.11 indicate that prior to the occurrence of a non-ductile failure mode, such as connection failure, long flexural yielding links dissipate as much, or more energy as a short shear yielding link for a given increment of link plastic rotation angle. However, as indicated by Figs. 4.6 and 4.7, the total energy dissipation of shorter links is still significantly superior to longer links simply because the shorter links can generally sustain much larger plastic rotations

without the occurrence of a non-ductile failure mode. Similarly, combined flexural and axial yielding outside of the link can effectively dissipate energy. The total energy dissipation capacity due to beam yielding, however, is limited by the early occurrence of beam instability or by the development of excessively large out-of-plane forces at lateral supports.

As noted earlier in the discussion of link end moments, the link end moment-rotation plots in Figs. 4.3 and 4.4 suggest that areas outside of the link contributed to the energy dissipation capacity of the test specimens. To gain further insight into this question, the distribution of energy dissipation among various portions of a test specimen was estimated for Specimens 1, 3 and 8. The results are shown in Figs. 4.13 to 4.15. Energy dissipation in the column, due primarily to panel zone yielding, was estimated as the area enclosed by the moment-rotation loops in Fig. 4.3. The combined energy dissipation of the brace connection panel, the beam and the brace was estimated as the area enclosed by the moment-rotation loops in Fig. 4.4 combined with the area enclosed by the plot of link shear force versus displacement at the brace end of the link. As noted earlier, this portion of the energy dissipation is due primarily to yielding in the brace connection panel and the beam. The plots in Figs. 4.13 to 4.15 are continued only to the point where displacement transducers measuring link end rotations went out of range. Further, the computed energy dissipation is not normalized according to the section's yield stress since only the relative distribution of energy dissipation within a specimen is of interest.

The plots in Figs. 4.13 to 4.15 show that portions of the test specimens outside of the links contributed significant energy dissipation capacity. Energy dissipated by column panel zone yielding, as anticipated, is larger for the $W12\times22$ specimens than for the $W12\times16$ specimens due to the larger end moments generated by the $W12\times22$ links. These larger end moments produce larger shear forces in the column panel zone. The plots also show that yielding outside of the brace end of the link contributed rather substantial energy dissipation capacity. Based on test observations, this yielding was confined primarily to the brace connection panel in Specimens 1 and 3. For Specimen 8, significant yielding in both the brace connection panel and beam contributed to this portion of the energy dissipation.

Figures 4.13 to 4.15 indicate that limited yielding outside of the link can contribute to overall energy dissipation in an EBF and can help reduce demands on the link itself. However, permitting too much yielding outside of the link can result in non-ductile failure modes outside of the link. This is demonstrated by the severe flange buckling developed in the brace connection panel of Specimen 1 and the severe lateral buckling of the beam in Specimen 8. Local flange buckling in the brace connection panel, of course, is far less serious than overall buckling of the beam. These plots, along with observations made during testing, also demonstrate that the brace connection panel plays an important role in EBFs with long links.

4.4 BEAM AND BRACE RESPONSE

The behavior and design of the beams and braces are an important issue for EBFs. These members typically are subjected to a combination of high axial force and bending moment. Consequently, the occurrence of significant yielding or instability of these members prior to the full development of link strength is a possibility that must be recognized in the EBF design process. As demonstrated by the experimental observations in Chapter 3, problems associated with excessive yielding or instability of the beam can be very detrimental to the overall strength and inelastic deformation capacity of an EBF. In this section, the forces developed within the beams and braces of the test specimens are examined in order to provide further insights into the behavior of the test specimens. Some of the design implications of this behavior are also considered.

The sign convention used for force resultants in the beam and brace of the test specimens is shown in Fig. 3.2. For axial force, tension is considered positive for both the beam and the brace. As indicated, positive bending moments produce tension in the beam's east flange and in the brace's north flange, respectively. Unless noted otherwise, the bending moment in the beam, M_{beam} is computed at the north edge of the brace connection panel, as shown in Fig 3.2. The bending moment in the brace, M_{brace} is computed at the point where the brace meets the brace connection panel, i.e. at the west face of the brace connection panel. The bending moment and axial force within the brace connection panel itself are indeterminate, in that they cannot be determined by statics from the reaction forces on the subassemblage. The axial force in the beam reduces to zero in some manner over the length of the brace connection panel, since there is nominally no axial force within the link for this experimental setup. Bending moment, on the other hand, increases over the length of the brace connection panel, from a value of M_{beam} at the north end of the panel up to the value of the link end moment at the south end of the panel. Outside of the brace connection panel, axial forces remain constant over the length of the beam and the brace whereas bending moments decrease linearly from their values at the boundary of the brace connection panel (see Fig. 1.6).

Axial forces, bending moments and shear forces in the beam and brace were computed by statics from the load cells installed within the subassemblage (Fig. 2.3). This redundant system of load cells permitted two independent determinations of any stress resultant, thereby providing a check on the experimental data. These checks indicated that the computed axial forces in the beam and brace were reliable. However, for some test specimens, computing accurate values of bending moment and shear force was found to be difficult. The reason for this difficulty is that the bending moments and shear forces in the beam and brace are dependent primarily on the difference between various load cell measurements that are of nearly equal magnitude. For example, the shear force and bending moment in the beam can be computed from the east-west components of the two 200 kip load cells at the north end of the subassemblage (see Fig. 2.3).

Whereas the forces in these load cells may be very large, perhaps on the order of 100 to 200 kips, the sum of their east-west components (which are opposite in sign) is a very small force, perhaps on the order of 5 to 10 kips. Even though the error within any single load cell is very small, on the order of 2 percent of the load, the error in the difference between two load cells may be quite large. As a result, beam and brace bending moments are presented only for those specimens for which various consistency checks indicate reliable data. The accuracy of the beam and brace axial forces reported herein is estimated to be comparable to the accuracy of the load cells, on the order of 2 to 3 percent of the reported force. Errors in the beam and brace bending moments are larger because of the reason discussed above, and are estimated to be on the order of 10 to 15 percent. It should be noted that no such difficulties were encountered in computing link shear forces and bending moments, which are estimated to be accurate also within 2 to 3 percent of the computed values.

4.4.1 Beam and Brace Axial Forces

The axial forces generated in the beam and brace are plotted against the shear force in the link for each test specimen in Fig. 4.16. These plots clearly indicate that the ratio of beam or brace axial force to link shear force remains essentially constant throughout the specimen's entire loading history. This linear relationship remains constant despite yielding within the link, yielding outside of the link or even instability of the beam. This constant relationship can also be predicted from simple analytical arguments [35] where it can be shown that the ratio of beam or brace axial force to link shear force depends primarily on the brace-beam angle.

The fact that there is a constant linear relationship between beam and brace axial force and link shear force is useful for EBF design. The axial force to shear force ratio can be taken from an elastic frame analysis. This ratio can then be applied to an estimate of ultimate link shear force in order to predict the ultimate axial force in the beam and brace. This ratio can also be estimated from a simple analysis, considering the statics of the link-beam-brace joint [35]. Note that for a given brace-beam angle, larger ultimate axial forces are generated in the beam and brace by a short link than by a long link, since the ultimate shear strength is greater for a short link than for a long link. Long links, of course, can generate much larger bending moments in the beam and brace.

The maximum axial force measured in the beam and brace of each test specimen is listed in Table 4.3. Also listed is the corresponding maximum value of P/P_y in the member. Table 4.3 and the plots of Fig. 4.16 clearly demonstrate the very large axial forces that can be developed within the beams of an EBF. Notice that values of P/P_y in the beam approach 0.8 in extreme cases (Specimen 11R2). It should be recalled that Specimens 7, 8, 11R1 and 11R2 all suffered significant damage in their beams. From Table 4.3, it may be seen that P/P_y in the beams of these

specimens were all in excess of 0.5. The value of P/P_y, by itself, may not be a reliable indicator of potential beam damage. However, the test results indicate that designers should be particularly cautious when anticipated ultimate values of P/P_y in the beam exceed 0.5 to 0.6.

4.4.2 Beam and Brace Bending Moments

In this section, various data pertaining to beam and brace response are examined in detail for Specimens 3, 6, 7, 8, 11R2 and 12. These were chosen to be representative of specimens for which no significant beam damage was observed (3 and 6) as well as specimens where very severe beam damage occurred (7, 8, 11R2). Only those response parameters that could be computed reliably are presented.

Specimen 3

Figure 4.17 shows the bending moment in the beam and brace plotted against γ, the link rotation angle. This plot shows that the brace carried a substantial portion of the link end moment. It also appears that the brace carried a somewhat larger moment in the east loading cycles (positive γ) as compared to the west loading cycles. The distribution of link end moment between the beam and the brace is more clearly visible in Fig. 4.18, where the beam and brace moments are plotted against the bending moment at the brace end of the link. This plot also shows that with increasing load for the east cycles (left portion of plot), there is a small, but noticeable redistribution of bending moment from the beam to the brace. In the east load cycles, the beam is in compression. Even though no signs of beam instability were visible during the testing of Specimen 3, the compressive axial forces caused a noticeable loss in beam flexural stiffness with a concurrent increase in the brace moment. No such redistribution is noticeable for the west loading cycles, i.e. when the beam is in tension. It is also interesting to note that in the final east loading cycle, this redistribution of moment is no longer visible. In this final cycle, the link-to-column connection failed, causing a rather sudden increase in bending moment at the brace end of the link and therefore an increase in the beam and brace moments. However, along with this increase in moment was a decrease in link shear resulting from the connection failure. This lower link shear force generated lower axial force in the beam. Consequently, the beam was able to carry a larger portion of the link end moment in the final cycle after the link-to-column connection failure, as indicated in Fig. 4.18.

The sum of the beam and brace bending moment is plotted against the moment at the brace end of the link in Fig. 4.19. This plot shows that the beam and brace carried about 85 percent of the link end moment at the boundaries of the brace connection panel. This indicates a drop in bending moment over the length of the brace connection panel.

Figure 4.20 shows the bending moment in the beam plotted against the axial force in the beam. Also shown, in dotted lines, is the P-M interaction surface for a fully yielded cross-section based on perfect plasticity. This surface was computed using the measured section dimensions and yield strength data for the $W12\times22$ beam section. It should be noted that a linear relationship between bending moment and axial force in the beam is not expected in general, even when inside the yield surface. This is because moment and axial force are not, in general, applied proportionately to the beam. The axial force in the beam grows directly in proportion to the link shear (Fig. 4.16) whereas the bending moment increases with the link end moment. Since link end moment does not necessarily increase in direct proportion to link shear (Fig. 4.2), the beam axial force also need not increase in direct proportion to beam moment. Figure 4.20 shows that when the beam was in tension, its response was very close to, but generally inside of the yield surface. This indicates there was no general yielding of the beam segment outside of the brace connection panel. On the compression side, the maximum beam response remained well away from the yield surface, with the loss of beam flexural stiffness with increasing compressive axial force again apparent. This plot also confirms the previous observation that the beam's increased ability to carry moment after the failure of the link-to-column connection resulted from a decrease in beam axial force.

Finally, in Fig. 4.21, the beam bending moment is plotted against the rotation measured at the north end of the brace connection panel. Positive rotation is defined as clockwise when the specimen is viewed from above, as in Fig. 2.3. This plot also indicates there was no general yielding of the beam beyond the brace connection panel. The loss of beam flexural stiffness resulting from the compressive axial forces in the beam is also visible in the lower portion of this plot.

It is interesting to compare the moment-rotation response at the brace end of the link for Specimen 3 (Fig. 4.4) with the beam moment-rotation response shown in Fig. 4.21. Figure 4.4 shows that there was significant yielding outside of the link for Specimen 3. The lack of inelastic response visible in Fig. 4.21 indicates that virtually all of the significant yielding outside of the link was concentrated within the brace connection panel.

Many of the moment-rotation plots for the brace end of the link (Fig. 4.4), including that of Specimen 3, show a rather one-sided response. Significantly more yielding is apparent in the west load cycles (beam in tension) than in the east load cycles (beam in compression). The reason for this one-sided response at the brace end of the link can be understood from the beam and brace bending moment response. When the beam was in tension, there was no redistribution of moment to the brace, despite rather significant yielding in the brace connection panel. However, when the beam was in compression, it attracted a smaller share of the link end moment (Fig. 4.18), resulting in less yielding in the brace connection panel.

Specimen 6

The bending moment in the beam and brace of Specimen 6 are plotted against link rotation in Fig. 4.22. This plot shows that the brace carried a very large portion of the link end moment for this specimen. For the west loading cycles, the beam and brace moments were nearly equal, whereas for the east loading cycles, the brace carried an even larger moment than the beam. Specimen 6 therefore shows a similar response as Specimen 3 in which the beam carries less moment when in compression. This observation is confirmed by Fig. 4.23 where the redistribution of moment from the beam to the brace for the east load cycles is apparent. As with Specimen 3, even though the data shows a noticeable loss of flexural stiffness in the beam due to the presence of compressive axial force, no signs of instability were visible in the beam during the course of the test. However, the above data indicate that the beam of Specimen 6 may have been on the verge of lateral torsional buckling.

Figure 4.24 shows the axial force and bending moment in the beam together with the P-M yield interaction surface for the $W12\times16$ beam section. This plot shows that the beam was well away from general yielding. Figure 4.25 confirms that no significant yielding occurred within the beam when it was under axial tension. This figure also clearly shows the rather substantial loss of flexural stiffness in the beam when it was under axial compression, and also further indicates that the beam was likely nearing instability.

It may be concluded that the satisfactory performance of the beam and brace observed during the testing of Specimen 6 was primarily due to the large flexural stiffness and strength of the brace. The brace attracted a large portion of the link end moment, thereby substantially relieving the bending moment in the beam. Further, as the beam lost flexural stiffness due to its apparently impending instability, the brace was capable of picking up additional moment, thereby permitting the link end moment to continue increasing.

Specimen 7

Only very limited data on beam and brace moments could be reliably computed for Specimen 7. However, it is useful to examine this limited data since the beam of specimen 7 failed by severe lateral torsional buckling.

The plot of beam bending moment versus link rotation in Fig. 4.26 clearly shows the beam's inability to develop bending moment for the east load cycles, i.e. when the beam is under compression. Even in the early load cycles before any sign of instability was visible, the beam carried significantly less moment in the east load cycles than in the west load cycles. After the development of significant lateral torsional buckling, the beam's ability to carry bending moment deteriorated rapidly. In the later loading cycles, the beam suffered almost complete loss of flexural stiffness and strength.

Comparison of Fig. 4.26 with the plot of moment versus rotation at the brace end of the link for Specimen 7 (Fig. 4.4) indicates that there was likely some redistribution of bending moment from the beam to the brace in the east load cycles. However, because of the very low flexural stiffness and strength of the brace, little additional moment was generated at the brace end of the link. Thus, the large loss of flexural stiffness in the beam resulted in a large loss of flexural stiffness at the brace end of the link. The inability of the brace end of the link to develop bending moment, in turn, inhibited the redistribution of bending-moment away from the column end of the link. This certainly contributed to failure of the link-to-column connection.

Fig. 4.27 shows moment in the beam plotted against moment at the brace end of the link. This plot also indicates a redistribution of moment from the beam to the brace in the east loading cycles. However, it appears again that the combined flexural stiffness of the brace and the buckled beam were insufficient to attract bending moment away from the column end of the link.

Specimen 8

This specimen provides additional data for a case where the beam suffered severe instability during the course of the test. Unlike Specimen 7, where the beam failed by lateral torsional buckling, the beam in Specimen 8 failed by predominantly lateral buckling. That is, the failure largely reflected column weak-axis type buckling, with relatively little twisting of the cross-section. Severe buckling of the beam also occurred much later in the loading sequence in Specimen 8 as compared to Specimen 7.

Figure 4.28 illustrates the development of beam and brace moments during the course of the test. In the west load cycles, the bending moment developed at the beam end is much larger than that in the brace, as would be predicted by an elastic analysis. However, as observed in previous specimens, there appears to be a redistribution of moment from the beam to the brace in the east load cycles (beam in compression), well before any signs of beam instability were visible. The rather large difference in the bending moment carried by the beam when in compression as opposed to tension is also clearly visible in Fig. 4.28.

The distribution of bending moment between the beam and the brace is shown in Fig. 4.29. This plot confirms that the beam carried significantly larger moments than the brace for the west load cycles, with no noticeable redistribution of moment between the beam and the brace. In the east load cycles, however, the magnitude of the moments carried by the beam and brace grew closer with increasing load.

Figure 4.30 shows the sum of the beam and brace moments plotted against the moment at the brace end of the link. This plot indicates that the beam and brace were subjected to only about 50 percent of the link end moment. This should be compared to Fig. 4.19 (Specimen 3) which showed, for a similar brace connection, that the beam and brace were subjected to about 85 percent of the link end moment. An important difference between these specimens is that the brace

and beam centerlines intersected approximately 5 inches inside of the link for Specimen 8 (Fig. 2.13). For Specimen 3, on the other hand, this intersection occurred only about .5 inches inside of the link. As noted in Chapter 2, locating the brace-beam centerline intersection inside of the link was expected to reduce the bending moment generated in the beam and brace. Figure 4.30 confirms that this eccentricity in the brace connection was, in fact, very effective in reducing the beam and brace bending moments. The rather significant reduction of bending moment in the beam also likely contributed to the lack of flexural influence observed in the buckled shape of the beam.

The beam moment and axial force are plotted together with the P-M yield interaction surface in Fig. 4.31. In tension, it appears that the beam nearly reached the yield surface, but was probably not subjected to extensive yielding. The moment-rotation plot for the beam end (Fig. 4.32) also indicates only limited yielding of the beam segment beyond the brace connection panel. Comparison of Fig. 4.32 with the moment-rotation response at the brace end of the link for Specimen 8 (Fig. 4.4) indicates that most of the yielding outside of the link occurred within the brace connection panel in the west load cycles (beam in tension). As with Specimen 3, it appears that despite rather extensive yielding within the brace connection panel when the beam was in tension, no noticeable redistribution of moment occurred from the beam to the brace. The lower portion of Fig. 4.32 also shows the almost complete loss of flexural stiffness in the beam upon the development of instability.

Specimen 11R2

After the beam buckled in Specimen 11R1, the beam was straightened and provided with an additional lateral support. This repaired specimen, designated 11R2, failed by very severe lateral torsional buckling in the beam. The link end as well as one of the beam lateral supports also failed on this specimen.

The development of beam bending moment with increasing link rotation is shown in Fig. 4.33. This plot shows that the beam carried less moment in the east load cycles, starting with the earliest cycles in the test. This corresponds with observations of beam out-of-plane displacement very early in the test. The early development of lateral torsional buckling for this specimen can be attributed to the extraordinarily high levels of axial force in the beam combined with residual deformations in the beam after its repair and straightening. However, despite the early development of out-of-plane displacement, the beam continued to carry a rather consistent level of bending moment for a number of cycles. This is in contrast to Specimen 7, where severe cyclic deterioration of the beam's flexural capacity was observed. The better post-buckling performance of the Specimen 11R2 beam can be attributed to the thicker flanges of the $W12\times22$ section as well as the close spacing of lateral supports. The plot in Fig. 4.33 suggests that additional inelastic deformation and energy dissipation would have been possible for Specimen 11R2 if stronger lateral

supports had been provided.

The plot of link end moment versus beam moment in Fig. 4.34 shows a similar pattern to that of Specimen 7 (Fig. 4.27). When the beam is in compression, the loss of flexural stiffness resulting from instability causes a redistribution of moment from the beam to the brace. However, because of the low flexural stiffness and strength of the brace, its ability to carry additional moment is rather limited. Consequently, the brace end of the link suffers a large loss of flexural stiffness. This is apparent in the moment-rotation response for the brace end of the link in Specimen 11R2, shown in Fig. 4.4. As before, this loss of stiffness prevents the redistribution of bending moment from the column end of the link towards the brace end of the link.

The moment versus axial force plot together with the P-M yield interaction surface for the Specimen 11R2 beam is shown in Fig. 4.35. Unlike the previous specimens, this plot shows the beam response extending beyond the yield interaction surface for the direction of loading that places the beam in tension. This indicates that general yielding occurred in the beam segment beyond the brace connection panel. The moment-rotation response at the beam end, shown in Fig. 4.36, also indicates yielding of the beam in combined bending and tension. Despite the yielding of the beam, however, there was no apparent redistribution of moment to the brace. From the plot of link end moments for Specimen 11R2 (Fig. 4.2), it appears that after yielding of the beam, little additional moment was attracted to the brace end of the link. That is, as the beam yielded, the brace did not pick up additional moment and therefore the link's ability to redistribute moment away from the column and towards the brace was significantly impaired. Thus, for this specimen, it appears that the combined flexural stiffness of the brace (in compression) and the yielded beam (in tension) was less than the flexural stiffness of the yielded column end of the link.

Specimen 12

Specimen 12 suffered from severe lateral torsional buckling of the beam for the east load cycles, and severe lateral torsional buckling of the link in the west load cycles. Testing on Specimen 12 was stopped due to the impending failure of the link end lateral support.

Beam and brace moments are plotted against the link rotation angle for Specimen 12 in Fig. 4.37. The brace carried a large portion of the link end moment for this specimen. As observed in previous specimens, the beam carried more moment than the brace in the west load cycles. However, in the east load cycles (beam in compression) there is a significant redistribution of moment from the beam to the brace. This redistribution is also clearly visible in Fig. 4.38.

Despite the rather severe lateral torsional buckling observed in the beam, Figs. 4.37 and 4.38 show that the beam maintained a high level of flexural stiffness and strength for several cycles after the initiation of instability. However, Fig. 4.37 indicates that the beam's capacity was beginning to deteriorate quite rapidly in the final east loading cycle of the test. Nonetheless, as was the case with Specimen 11R2, additional energy dissipation would likely have been possible if sufficiently

strong lateral supports could have been provided.

Even though the beam suffered a loss of flexural stiffness due to lateral torsional buckling, the redistribution of bending moment within the link was not significantly impaired. This can be attributed to the relatively large flexural stiffness and strength of the brace. As the beam's moment carrying capacity decreased with increased buckling, the brace was able to pickup additional moment. Consequently, the bending moment at the brace end of the link could continue to grow.

The moment-axial force response for the Specimen 12 beam is shown in Fig. 4.39, along with the P-M yield interaction surface. This plot shows that large bending moment, rather than axial force, dominated the response of the beam. Even though significant yielding was observed within the brace connection panel in Specimen 12, Fig. 4.39 indicates that general yielding did not occur in the beam segment beyond the brace connection panel.

Discussion of Results

From the above data on beam and brace response, it appears that the behavior of these members, in general, is quite complex. However, a number of useful observations can be made based on this data.

First, it should be noted that the test specimens that performed well with respect to beam and brace behavior were those provided with brace sections of high flexural stiffness and strength. For these specimens, the brace carried a large portion of the link end moment. In some cases, Specimen 6 for example, the brace carried as much moment as the beam. The ability of the brace to attract and carry these large moments is important in EBFs with long links, as it significantly reduces the demands on the beam. Consequently, EBFs with long links will, in general, require very heavy brace sections.

Under increasing compressive axial force, the beams of the test specimens often showed a significant loss of flexural stiffness, typically well before any signs of instability were observed. In some cases, as with Specimens 3 and 6, this loss of stiffness was apparent, even though instability of the beam was never observed during the test. For specimens provided with flexurally stiff and strong brace sections, the bending moment lost by the beam was picked up by the brace. This permitted the link end moment to continue to grow which, in turn, permitted the link to further strain harden and dissipate energy. These specimens demonstrated that a loss of flexural stiffness in the beam can trigger a redistribution of bending moment to the brace, providing the brace possesses adequate flexural stiffness.

From the moment-axial force diagrams for the beams, it appears that the stability interaction surface lies inside the yield interaction surface. That is, under compressive axial forces, the beam

is likely to buckle well before general yielding can occur in the region beyond the brace connection panel. This is likely to be true for many W sections that may be typically used for beams and links in EBFs. For these sections, there is a large difference between the yield axial force, P_y, and the buckling load, P_{cr}. Consequently, even with rather close spacing of lateral supports, instability is still likely to control the strength of the beam when it is under axial compression. The presence of a composite deck, however, may significantly influence this observation, as will be discussed later.

The beam response data indicate that, except for Specimen 11R2, no general yielding of the beam segment occurred beyond the brace connection panel under combined bending and tension. Many of the link end moment-rotation response curves (Fig. 4.4) show that significant yielding occurred outside of the link, particularly for load cycles placing the beam in tension. The beam response data indicate that this yielding was largely restricted to the brace connection panel. This agrees with yielding patterns observed on the test specimens.

Both Specimens 7 and 11R2 suffered severe lateral torsional buckling in the beam. Because of the very low flexural stiffness of the brace members in these specimens, very little bending moment could be redistributed to the brace from the buckled beam. Consequently, the growth of bending moment at the brace end of the link after buckling of the beam was severely limited. The continued redistribution of link end moment away from the column face was therefore effectively prevented.

A similar behavior was also observed when the beam segment beyond the brace connection panel in Specimen 11R2 yielded in combined bending and tension. Because of the very low flexural stiffness of the brace, little or no redistribution of moment from the beam to the brace was observed. If a brace with larger flexural stiffness had been provided, the brace would have likely picked up significant additional moment. Further, for cases where the link is located within the span between two braces, the stiffness of the link end supports will be more nearly equal. For such cases, a significant redistribution of bending moment from the yielded beam to the brace is also more likely than a redistribution from the beam to the opposite end of the link.

Even the rather severe yielding of the brace connection panel in combined bending and tension, observed in many of the test specimens, did not appear to trigger a redistribution of moment from the beam to the brace. Based on the plots of link end moments (Fig. 4.2), yielding of the brace connection panel also did not significantly inhibit link end moment equalization. However, such yielding can prevent complete equalization from taking place. This may be seen, for example, in the link end moment plots for Specimen 3 in Fig. 4.2. These plots show that link end moments did not completely equalize. In general, it appears then that yielding of the brace connection panel in combined bending and tension poses no serious consequences on overall behavior. The only note of caution in this regard is that the bending moment at the column end of the link may be somewhat higher than would be expected from an assumption of complete

moment equalization.

Yielding of the brace connection panel in combined bending and compression, on the other hand, may pose somewhat more difficult problems. Even if overall beam instability is prevented, severe local buckling may still occur within the brace connection panel. Such local instability was observed in Specimens 1, 5 and 6. As discussed in Chapter 3, the loss of strength and inelastic deformation resulting from local buckling in the brace connection panel can be limited by stiffening the panel.

Finally, Specimen 8 demonstrated that locating the intersection of the brace and beam centerlines inside of the link can significantly reduce the bending moment generated within the beam and brace. The use of such an eccentricity in the brace-to-link connection may prove to be a useful tool for EBF designers.

4.4.3 Beam Stability Computations

Many interaction equations have been proposed for predicting instability under combined axial compression and bending [36]. It was not the purpose of this experimental program to evaluate stability interaction equations for beam-columns. Nonetheless, since instability was observed within the beam segment of several test specimens, it is instructive to examine beam response in light of a stability interaction equation. Accordingly, the maximum bending moments and axial forces developed within the beams of selected specimens were checked in a stability interaction equation for beam-columns.

The specimens that are considered here are the same as in the previous section, i.e., Specimens 3, 6, 7, 8, 11R2 and 12. It is useful to recall that during the course of testing, severe instability of the beam was observed in Specimens 7, 8 and 11R2, whereas no signs of instability were observed in Specimens 3 and 6. Instability of the beam in Specimen 12 was also observed, although it was not as severe as in Specimens 7, 8 and 11R2.

The stability interaction equation that will be employed here is that provided in the 1986 *Load and Resistance Factor (LRFD) Design Specification* [37]. This specification is chosen to be representative of the most up-to-date recommended U.S. practice for steel building construction. Interaction under combined bending and axial compression is covered by Eq. H1-1a in the LRFD specification. For a resistance factor of $\varnothing = 1$, this equation can be written as follows:

$$\frac{P_u}{P_n} + \frac{8}{9}\frac{M_u}{M_n} \leq 1.0 \tag{4.3}$$

The various terms are defined in detail in the LRFD specification. Briefly however, P_u and M_u represent the maximum axial force and bending moment in the member. P_n is the nominal compressive strength under axial load in the absence of bending moment, computed on the basis

of effective length, and M_n is the nominal flexural strength in the absence of axial load.

The estimated value of the terms in the above equation are summarized for the selected specimens in Table 4.4. It must be recognized that considerable uncertainty exists in each of these terms. Consequently, the data in Table 4.4 should not be used to judge the validity of Eq. 4.3. Rather, this data is presented as a basis for discussing some of the important issues related to stability of beams in EBFs. In the following paragraphs, each of the terms in Eq. 4.3 are discussed in greater detail as they pertain to the test specimens.

First, it should be noted that the buckled shape of the beams, in all cases except Specimen 8, included participation of the brace connection panel. That is, both the beam segment beyond the brace connection panel as well as the brace connection panel itself buckled out-of-plane. This may be seen from the photographs of the buckled beams in Chapter 3. Specimen 8 was an exception. Buckling in this case was restricted primarily to the beam segment outside of the brace connection panel. This may be due to the short brace connection panel on this specimen as well as the different buckling mode (lateral rather than lateral torsional) of the beam. For the remainder of the specimens, however, the brace connection panel must be included with the beam segment beyond the panel as part of the beam-column.

The term P_u in Eq. 4.3 is the axial force in the beam-column. As noted earlier, whereas the axial force is constant in the beam segment beyond the brace connection panel, it is indeterminate within the brace connection panel itself. The axial force reduces to zero in some unknown manner over the length of the brace connection panel. Consequently, there is some uncertainty on the value of axial force to be used in stability computations. For the present purposes, the axial force in the beam segment beyond the brace connection panel (see Section 4.4.1) was chosen as a reasonable representative value of P_u for use in Eq. 4.3. It is certainly an upper bound on axial force.

The term M_u in Eq. 4.3 essentially represents the maximum bending moment in the beam column. For members restrained against sidesway (for which EBF beams qualify), the LRFD specification computes M_u as follows:

$$M_u = B_1 M_{nt} \tag{4.4}$$

where M_{nt} is the first order moment within the member and B_1 is the amplification factor:

$$B_1 = \frac{C_m}{(1 - P_u/P_e)} \geq 1 \tag{4.5}$$

This familiar factor also appears in the stability interaction equation used in Part 2 of the 1978 AISC specification [30]. (See Refs. 30 or 37 for definitions of C_m and P_e). However, the requirement that B_1 must always be taken to be at least 1.0 is a new provision in the LRFD specification. For the test specimens listed in Table 4.4, the computed value of B_1 was always less than 1.0.

Consequently, a value of B_1 equal to unity was used in computing M_u for all of the test specimens.

Like the axial force, bending moment is also indeterminate within the brace connection panel. The moment increases in some unknown manner over the length of the panel. Therefore, there is also some uncertainty on the value of bending moment to be used in the stability computations. A lower bound is the moment at the junction of the brace connection panel and the beam. An upper bound is the link end moment. Neither of these values, however, seem reasonable for use in stability computations. Therefore, a value of bending moment for use in Eq. 4.3 was computed as follows. The moment at the south end of the brace connection panel (immediately adjacent to the link) was taken as the moment at the north end of the panel plus the shear force in the beam multiplied by the length of the panel. This was then taken as M_u for use in Eq. 4.3. Note that this approach simply assumes that the moment gradient within the brace connection panel is the same as in the beam segment beyond the panel. This is also a convenient assumption for design purposes, since the moment computed in this manner is the same as would be predicted by a frame analysis based on centerline-to-centerline dimensions. For such an analysis, the brace connection panel would effectively have zero length.

The above method for computing M_u was used for all specimens listed in Table 4.4, except for Specimen 8. For Specimen 8, the bending moment at the north end of the brace connection panel was taken as M_u, since the brace connection panel was not part of the buckled shape.

For the beams that buckled during the test (Specimens 7, 8, 11R2 and 12 in Table 4.4), the values of P_u and M_u are the concurrent maximum values for the cycle of loading during which significant out-of-plane displacement was first observed. For Specimens 3 and 6, for which no buckling was observed, the values of P_u and M_u listed in Table 4.4 are the concurrent maximum values measured during the course of the test.

The term P_n in Eq. 4.3 represents the nominal compressive strength of the member under axial compression, i.e., the column buckling load. P_n is computed based on an effective length, KL, and also depends on the yield strength of the steel. For the specimens examined in Table 4.4, effective length factors, K, on the order of 0.6 to 0.7 were used. These values were estimated from the observed buckled shapes. The effective length factor was then applied to the distance from the link end lateral support to the first beam lateral support. The only exception to this was Specimen 8, for which the unbraced length was taken from the north end of the brace connection panel to the first beam lateral support, reflecting the buckled shape of this specimen.

When evaluating the effective length factor, K, for out-of-plane buckling of the beam, it is useful to note that the link served essentially as a "fixed" support for the beam. This is reflected in the buckled shapes of the beams, prior to failure of the link-to-column connections. After these connections failed, by rupture of the link flange, the links typically rotated, causing the beam support to behave more as a "pin." It must also be recognized that the effective length factors listed in

Table 4.4 were chosen somewhat subjectively. The uncertainty in the actual effective length results in substantial uncertainty in the value of P_n.

Computation of the buckling load, P_n, is also dependent on the yield stress of the steel. For the beam sections used in the test specimens, there is a rather large difference in the yield strengths of the web and the flanges (Table 2.8). It is not entirely clear, therefore, what values of yield strength should be used for computing the buckling load. For the purposes of Table 4.4, the flange yield strength was chosen for computing values of P_n. Since the flanges are relatively more important than the web in resisting buckling about the weak axis, it was believed that the flange yield strength is more representative for the purpose of estimating the buckling load. However, uncertainty in the representative value of yield strength results in further uncertainty in the buckling load P_n. With the above assumptions, the values of P_n listed in Table 4.4 were computed according to sect. E2 of the LRFD specification.

The final term in Eq. 4.3 is M_n, the flexural strength of the member is the absence of axial force. M_n was computed according to sect. F1 of the LRFD specification. For each specimen in Table 4.4, M_n was computed to be equal to M_p of the section.

With each of the terms computed as described above, the left side of Eq. 4.3 was evaluated for each specimen under consideration. The results are listed in Table 4.4. A value for Eq. 4.3 greater than 1.0 presumably indicates instability of the member.

In examining the final two columns of Table 4.4, it must again be emphasized that substantial uncertainty exists in most of the terms used in evaluating Eq. 4.3. Nonetheless, some useful observations can be made from this table. First, the beams of Specimens 3 and 6 did not buckle during the test. The value of about .95 computed from Eq. 4.3 for these specimens appears to predict this result. Further, since this value is close to 1.0, the stability interaction equation indicates the beams may have been approaching instability. This is supported by the beam response data in Section 4.4.2, which showed a substantial loss of beam flexural stiffness as the maximum loads were approached. Thus, at least in the case of Specimens 3 and 6, it appears that Eq. 4.3 combined with the various assumptions discussed above provided reasonable results.

For Specimens 7, 8 and 12, the values computed for Eq. 4.3 using the estimated maximum loads at buckling were .90, .93 and .85 respectively. Thus, for these specimens, the buckling load predicted by Eq. 4.3 appears to be somewhat too high. However, in light of the uncertainties involved, the error does not appear to be excessive. The discrepancy between the predicted and measured maximum loads for Specimens 7, 8 and 12 may, in part, also be the result of yielding of the brace connection panel and beam in the loading cycles prior to buckling. This cyclic yielding causes a reduction in the effective tangent modulus of the material due to the Bauschinger effect on the material. The reduction in the buckling load due to the Bauschinger effect has been observed in cyclic buckling tests on axially loaded struts [38].

The predictions of Eq. 4.3 appear to correlate well with the measured maximum loads for the beam of Specimen 11R2. It is not clear why previous yielding of the beam would not have reduced the buckling load, as may have been the case for Specimens 7, 8 and 12. However, it should be noted that the brace connection panel formed an unusually large part of the buckled member for Specimen 11R2. The unbraced length was 39 inches and the length of the brace connection panel was 26 inches. Thus, the brace connection panel accounted for 2/3 of the buckled member. For the other specimens in Table 4.4, the brace connection panel accounted for a much smaller portion of the buckled member. Consequently, the rather large uncertainties involved in estimating the actual forces within the brace connection panel are particularly important for Specimen 11R2.

To summarize, the above discussion indicates that there are numerous uncertainties in estimating the maximum loads for the beam of an EBF using stability interaction equations. These uncertainties are associated with predicting the actual bending moment and axial force within the brace connection panel, estimating the effective length factor for the member, and estimating a representative yield stress value. These uncertainties affected stability predictions for the test specimens and would certainly affect stability predictions for any real structure. Despite these numerous uncertainties, however, it appears that the LRFD stability interaction equation combined with the various assumptions discussed earlier provided a reasonable, though somewhat unconservative prediction of maximum load under combined bending and axial compression. The limited data also suggest that early yielding in the brace connection panel and beam may somewhat reduce the actual buckling load. This indicates a conservative approach is warranted in stability design for beams in EBFs when no composite deck is present.

4.4.4 Beam and Brace Design

In this section, some design implications of the observed response of the beams and braces are considered in greater detail. From a design point of view, the results of this experimental program have confirmed the importance of adhering to the *capacity design* approach for the beams and braces in EBFs. This approach requires that the beam and brace outside of a link possess adequate strength to develop the ultimate strength of the link. Because of the high axial forces carried by the beam and brace, both the overall strength and inelastic deformation capacity of an EBF will suffer if this requirement is violated. The experimental data and observed behavior indicate that limited yielding of the beam is acceptable, particularly if restricted to the brace connection panel. However, the majority of yielding must still be forced to occur within the link for best overall performance of an EBF.

Whereas the specific design requirements for the beam and brace may become somewhat involved, the overall intent of the capacity design approach for these members can be simply

expressed by the following equation:

$$M^*_{p\,beam} + M^*_{p\,brace} \geq M^{ult}_{link} \tag{4.6}$$

In this equation, M^{ult}_{link} is the maximum bending moment that can be generated at the link end. The terms on the left hand side of Eq. 4.6 are the flexural strength of the beam and brace reduced for the presence of axial force in the member. In the general case, this reduction may be due to either yielding or instability. Equation 4.6 simply states that the combined flexural strength of the beam and brace must exceed the ultimate link end moment. In the actual application of this equation, some reduction of link end moment over the length of the brace connection panel may be used to advantage in reducing the required flexural strength of the beam or brace under certain circumstances. This will be discussed in greater detail later in this section.

When considering design requirements for the beam and brace in greater detail, it is necessary to consider the circumstances under which stability may control the design of the member. First, it should be recognized that when the beam is in tension, the brace will be in compression. Likewise, when the beam is in compression, the brace will be in tension. Therefore, stability will not simultaneously control the design of both members.

The observed experimental behavior has clearly shown that instability can control the strength of the beam. For EBFs in which the brace is connected at the link to the lower flange of the beam, as simulated in the experimental setup, the top flange of the beam is critical for stability. That is, for the direction of loading that places the beam in axial compression, the bending moment in the beam is such as to produce additional compression in the upper flange, whereas it relieves the compression in the lower flange. Thus, it is the upper flange that would be expected to buckle out-of-plane. This behavior was clearly visible in the buckled shapes observed in the beams of the test specimens.

Since it is the upper flange that is critical for instability, it is reasonable to assume that a composite concrete deck attached to the top flange will provide substantial restraint against buckling of the beam. A composite deck will also benefit the beam by carrying a portion of the axial load, thereby reducing stress levels in the beam. From a design point of view, therefore, it would appear reasonable to assume that stability will not control the strength of the beam in an EBF when a composite concrete deck is present. Rather, the maximum strength of the beam will be controlled by yielding under combined tension and bending. For this case, a composite deck will be subject to tension, and therefore cannot be relied upon to contribute to the strength of the beam.

On the other hand, if a composite concrete deck is not present, the possibility of buckling must be considered in the design of the beam, particularly with regard to locating lateral supports. As indicated in Section 4.4.3, the brace connection panel will in general buckle along with the

beam. That is, the connection of the brace on the bottom flange of the beam cannot be relied upon to restrain out-of-plane buckling of the top flange of the beam. Thus, in stability computations, unbraced length should be measured starting at the link end lateral support. Also, as noted earlier, yielding in the brace connection panel and the beam may somewhat reduce the buckling load of the beam. A rather conservative approach to stability design of the beam is therefore warranted in cases where no composite deck is present.

A final case which should be considered for the beam is the situation where the brace is connected at the link to the upper flange of the beam. That is, the brace is connected to the same flange that supports the composite deck. For this case, the bottom flange of the beam is subject to combined compression from axial force and bending moment. The bottom flange will therefore be most likely to buckle out-of-plane. In this situation, the composite deck cannot be relied upon to provide lateral support, since it will not be connected to the compression flange. The deck will still likely benefit the beam, however, by reducing stress levels in the beam. Some judgment will be required when locating beam lateral supports for this situation.

Stability must, of course, always be considered in the design of the brace, since the brace is not supported by a deck and, in general, is laterally supported only at its ends. As demonstrated by the brace response data in Section 4.4.3, the braces in EBFs may carry large bending moments. It is important to include these moments in stability computations. Further, the possibility of redistribution of bending moment from the beam to the brace must also be considered. As noted earlier, when the brace is under compression, the controlling design case for the brace, the beam will be under tension. The response of the test specimens indicates that yielding of the brace connection panel in combined bending and tension does not appear to trigger a redistribution of moment from the beam to the brace. Thus, from a design point of view, it appears that the possibility of a redistribution of moment to the brace need only be considered if general yielding in combined bending and tension extends beyond the brace connection panel. The drop in bending moment over the length of the brace connection panel can therefore be used to advantage in this situation. Further, since the beam is under tension, the influence of a composite deck on the beam's yielding strength can be reasonably neglected.

Suggested Capacity Design Approach for Beams and Braces

In order to clarify and summarize the discussion and observations on beam and brace response, a preliminary suggested approach for the design of beams and braces in EBFs is outlined in this section. It is apparent that several aspects of beam and brace behavior require further investigation. However, until such further research is available, the approach outlined below is believed to provide a reasonable basis for beam and brace design.

Capacity design, as represented in principle by Eq. 4.6, represents the overall basis for the suggested design approach. The requirements imposed by Eq. 4.6 are supplemented by the observations and discussions of beam and brace behavior provided thus far in Section 4.4 of this report. The suggested design approach is outlined below in several steps and each step is provided with comments. Note that it is assumed that a preliminary frame geometry and member sizes have been chosen. The steps below can then be used to check the adequacy of the beam and brace.

1. Estimate the ultimate link shear force, V_{link}^{ult}, and the ultimate link end moment, M_{link}^{ult}, for the end of the link adjacent to the beam and brace under consideration.

   Comments: As discussed in Chapter 1, ultimate link forces have often been taken as 1.5 times the strength based on simple plastic theory. Equations 1.4 and 1.5 provide estimates of link ultimate shear force and end moment based on this assumption. However, as noted in Sections 4.1 and 4.2, an overstrength factor of 1.5 appears to be too large in the intermediate link length range of combined flexural and shear yielding. This issue is discussed further in Chapter 6 of this report. V_{link}^{ult} and M_{link}^{ult} represent the capacity design forces that will control the design of the adjoining beam and brace. Note that if the brace connection has been designed with an eccentricity so that the brace and beam centerlines intersect inside of the link, then the value of M_{link}^{ult} can be reduced by the moment produced by this eccentricity. This may substantially reduce the moment that must be carried by the beam and brace.

2. Estimate the axial force generated in the beam, P_{beam}, and in the brace, P_{brace} by the ultimate link shear force.

   Comments: As discussed in Section 4.4.1, the ratio of axial force in the brace to shear force in the link remains essentially constant in both the elastic and inelastic ranges of behavior for an EBF. Therefore, this ratio can be taken from an elastic analysis and used to simply scale up the brace axial force to a level corresponding to the ultimate link shear force. Alternatively, P_{brace} can be estimated by considering the statics of the link-beam-brace joint, where it should be recognized that shear force in the beam segment outside of the link also contributes to axial force in the brace. The same techniques can be used to estimate the ultimate axial force in the beam, P_{beam}. At this point, it is also useful to check the ratio P/P_y for the beam. If this ratio is in excess of say, 0.5 to 0.6, some difficulties may be anticipated in satisfying capacity design requirements for the beam and brace.

3. Estimate $M_{beam}^{elastic}$, the portion of the ultimate link end moment carried by the beam, assuming that the beam and brace remain elastic.

Comments: $M_{beam}^{elastic}$ can be approximated from an elastic frame analysis. The ratio of bending moment in the beam to bending moment in the link can be taken from an elastic analysis, and then used to scale up the moment in the beam to a level corresponding to the ultimate link end moment. For example, if an elastic analysis shows that 90% of the link end moment is carried by the beam, then $M_{beam}^{elastic}$ can be estimated as $0.9 \times M_{link}^{ult}$. Note that $M_{beam}^{elastic}$ will be used to check stability of the beam for the case where no composite deck is present. Accordingly, $M_{beam}^{elastic}$ should reflect the moment immediately outside of the link. That is, $M_{beam}^{elastic}$ should not be reduced to account for the drop in bending moment that occurs over the length of the brace connection panel. If the brace-to-link connection is assumed to behave as a "pin," then $M_{beam}^{elastic}$ will be equal to M_{link}^{ult}, and the beam by itself will be required to carry the entire link end moment. It should also be noted that at large frame displacements, the elastic distribution of link end moment to the beam and brace may vary from that predicted by an elastic analysis, even if no yielding occurs in the beam or brace. Such effects have been observed in inelastic analyses of EBFs [9,28] and appear to be most significant in the first story brace. Thus, it must be recognized that the above procedure for estimating $M_{beam}^{elastic}$ is only an approximation and should be applied with judgement.

4a. If the beam is not provided with a composite deck: Provide lateral supports for the beam that will satisfy beam-column stability criteria. Stability should be checked for a moment of $M_{beam}^{elastic}$ (from step 3) and P_{beam} (from step 2).

Comments: Examples of beam-column stability interaction formulas are Eq. 2.4-2 in the 1978 AISC Specification [30] and Eq. H1-1a in the 1986 LRFD Specification [37]. As discussed earlier, unbraced length should be measured from the link end lateral support, since the brace connection panel will in general buckle along with the beam. Some judgment will be required in choosing an effective length factor, K, for out-of-plane buckling of the beam. For the beams tested as part of this experimental program, effective length factors of about 0.6 to 0.7 appeared to reasonably reflect the buckled shapes. It should be noted that for EBF geometries that generate very high axial forces in the beams, satisfying a stability interaction equation may be very difficult or even impossible. In such cases, measures must be taken to reduce stress levels in the beam. Possible remedial measures may include use of a heavier brace (to draw moment away from the beam), or changes in frame geometry and/or link length. In extreme cases, the use of cover plates may be required on the beam.

4b. If the beam is provided with a composite deck: Assume the deck will prevent instability of the beam's upper flange. Provide lateral bracing at a reasonable interval for the lower flange.

Comments: This assumption is based on the observation that the top flange is critical for stability in EBFs in which the brace enters the beam at the link from below. For these cases, it is assumed that a composite deck attached to the top flange will effectively prevent out-of-plane displacement of the flange. Even though the bottom flange will, in general, be subject to much lower compressive stress than the top flange, lateral support of the lower flange at some reasonable interval would seem to be prudent. Further, for EBFs in which the brace enters the beam from above, the lower flange of the beam will be subject to the highest compressive stresses and will be the critical flange for instability. For these situations, a more conservative approach for lateral support of the lower flange is warranted.

5. Estimate $M_{brace}^{elastic}$, the portion of the ultimate link end moment carried by the brace, assuming that the beam and brace remain elastic.

Comments: $M_{brace}^{elastic}$ can be approximated from an elastic frame analysis in the same manner as described for $M_{beam}^{elastic}$ in step 3. If the analysis is based on member centerline-to-centerline dimensions, $M_{brace}^{elastic}$ may be reduced to account for the drop in brace moment from the brace-beam centerline intersection to the edge of the beam.

6. Estimate the moment in the brace in the event that the beam yields and redistributes moment to the brace. This may be estimated approximately as follows:

$$0.9 M_{link}^{ult} - M_{p\,beam}^{*}$$

Comments: The above equation provides a reasonable upper bound estimate for the moment generated in the brace in the event that general yielding of the beam occurs in combined tension and bending and consequently redistributes moment to the brace. As noted in the discussion on experimental observations, a significant redistribution of moment away from the beam does not appear to occur until yielding extends beyond the brace connection panel. The factor of 0.9 above assumes a drop in bending moment equal to 10 percent of the link end moment over the length of the brace connection panel. This is based on some typical values of moment gradient in the beam and some assumed typical lengths for the brace connection panel. A more accurate analysis can, if desired, be performed based on the actual brace connection panel length and beam moment gradient. The term $M_{p\,beam}^{*}$ in the above equation is the plastic moment of the beam, reduced for axial force. The calculation of $M_{p\,beam}^{*}$ should be based on a yield interaction formula using the ultimate axial force in the beam, P_{beam}, estimated in step 2 above. Note that the use of a stability interaction formula is not required, since the beam is under axial tension for this loading case. "Exact" yield interaction computations under combined bending and axial force are described in many

publications on plastic design, for example, Refs. 19 and 39. Approximate yield interaction formulas are also available. Examples are Eq. 2.4-3 in Ref. 30 and Eq. H1-1a (for tension) in Ref. 37. These approximate formulas are generally conservative and will therefore give a smaller value of $M^*_{p\,beam}$, and consequently a higher brace design moment. Thus, it may be to the designer's advantage to use the exact interaction relationships.

7. Check the adequacy of the brace using beam-column stability criteria. Stability should be checked using the ultimate axial force in the brace (step 2), combined with the larger of the bending moments computed in steps 5 and 6 above.

   Comments: Examples of stability interaction formulas suitable for design were noted in step 4a above. In applying these formulas, some judgment will be required in estimating effective length factors for in-plane and out-of-plane buckling for the brace.

Some additional comments are required on the above capacity design check for the beam and brace. First, inelastic dynamic analyses of EBFs by Ricles and Popov [28] have shown that very large bending moments can be developed at the bottom of the first story story brace, when the brace and column are "fixed" to the foundation. These large moments would also be anticipated by studying EBF energy dissipation mechanisms (Figs. 1.4 and 1.10). These mechanisms show a plastic hinge in the column and brace at the base of the frame. Thus, the procedure outlined above may underestimate the bending moment in the first story brace of an EBF, particularly if a high degree of fixity is provided by the column-brace-baseplate connection detail. Accordingly, a conservative design is warranted for the first story brace. Second, it is assumed that gravity load effects are relatively small in comparison with the capacity design forces on the beam and brace, and will not substantially affect the response of these members. If this is not the case, a contribution of gravity load moment and axial force in the beam and brace should be included in the design check. Further, it has generally been the philosophy that capacity design forces represent an extreme loading condition. Therefore, members designed to resist these large forces are typically designed with no additional factor of safety. Following this philosophy, the stability and yielding interaction formulas used to check the beam and brace would normally be applied at a factor of safety of 1.0 (or a resistance factor of $\varnothing=1$ for LRFD equations). This, of course, is a matter open to judgment.

The capacity design check for the beam and brace outlined in the steps above are based on several important assumptions. Additional research is warranted in several areas to verify these assumptions. For example, the actual effects of a composite deck on the stability of the beam under combined bending moment and large axial compression is an area that requires

investigation. Further studies on the redistribution of moment resulting from yielding of the beam are also needed. The above design approach assumes that yielding of the beam outside of the brace connection panel will cause a redistribution of moment to the brace. However, as indicated by the experimental data, if the brace is not adequately stiff, bending moment may simply redistribute within the link, away from the end connected to the yielded beam. Additional investigation is required therefore on the consequences of yielding in the beam of an EBF. Further investigation is also needed to better predict the bending moments that may develop at the base of the first story brace, as discussed above.

4.5 FORCES AT LINK END LATERAL SUPPORT

4.5.1 Experimental Data

In this section, experimental data on the out-of-plane forces developed at the link end lateral support are presented and discussed. Details of the link end lateral support system used for the test specimens are shown in Fig. 2.30, Section A-A. This system permitted free movement in the plane of the test specimen, but provided very stiff support for resisting out-of-plane displacement. Out-of-plane forces were measured using a truss-like arrangement of four load cells, as shown in Fig. 2.30. The end of each load cell was provided with a bearing that permitted free rotation about any axis, thereby preventing the development of bending moments in the load cells. Consequently, the out-of-plane forces at the points of attachment to the test specimen could be computed by summing the vertical components of the forces measured in the load cells.

The resultant out-of-plane forces at the link end are designated as "P1" and "P2", as shown in Fig. 4.40. P1 is the force near the lower flange, i.e., the flange connected to the brace, and P2 is the force near the top flange. Positive values of P1 and P2, shown in Fig. 4.40, correspond to tension in the link end load cells.

The development of link end out-of-plane forces during the course of testing is shown for each specimen in Fig. 4.41. In this figure, values of P1 and P2 are plotted against the link rotation angle, γ. P1 is plotted as a solid line and P2 as a dashed line for each specimen. The maximum values for P1 and P2 developed during the course of testing for each specimen are summarized in Table 4.5. Also listed is the value of $P_{y\,flange}$, which is defined as $b_f\, t_f\, F_{y\,flange}$. $P_{y\,flange}$ is sometimes referred to as "beam flange strength" in building codes and forms the basis for code specified strength requirements for lateral supports [5, 6, 7, 8]. Both SEAOC [5] and NEHRP [7] require a minimum strength for link end lateral supports equal to 1.5 percent of the beam flange strength, i.e., $0.015 \times P_{y\,flange}$.

4.5.2 Discussion of Test Results

In examining the plots of Fig. 4.41 as well as the data listed in Table 4.5, it is evident that rather large out-of-plane forces developed at the link end lateral support for the majority of the test specimens. For comparison with code provisions, the last column of Table 4.5 lists the ratio of the maximum out-of-plane force to the value of beam flange strength for each specimen. In virtually every case (except Specimen 11), the lateral support forces exceeded the code specified value of 1.5 percent of the beam flange strength. Many specimens developed forces on the order of 6 to 8 percent of the beam flange strength, and in some cases, in excess of 10 percent. It is clear that the code provisions significantly underestimated the lateral support strength requirements for these test specimens.

In order to gain some insight into the mechanisms that may be responsible for generating the large link end lateral forces, the development of these forces is briefly examined for each specimen below, with reference to the plots in Fig. 4.41.

Specimen 1 - A rapid growth in lateral support forces began with cycles 13E and 14E and progressively worsened for the east load cycles. This growth in forces coincides with the observed development of flange buckling outside of the link, in the brace connection panel. Lateral support forces were much lower in the west load cycles. (West load cycles correspond to negative link rotation angles in Fig. 4.41). Recall that flange buckling did not occur outside of the link for the west load cycles, since the region was in tension.

Specimen 2 - The large lateral support forces observed in the final 4 to 5 loading cycles appear to coincide with the development of severe web buckling in the central panel of the link. However, rather large lateral support forces were already developed several cycles before web buckling was observed. As with Specimen 1, substantially larger lateral support forces developed in the east load cycles than during the west cycles.

Specimen 3 - There was a gradual but steady growth in lateral support forces over the course of the test. This growth began well before any form of local buckling was observed in the specimen. Maximum lateral support forces were of comparable magnitude for both directions of loading.

Specimen 4 - In a manner similar to Specimen 3, the lateral support forces for Specimen 4 grew in magnitude rather gradually over the course of the test. A sudden increase in these forces occurred during cycle 12E, which appeared to coincide with the fracture of the link flange at the link-to-column connection and the formation of web buckling within the link. The maximum lateral support forces in both Specimens 3 and 4 were smaller than for Specimens 1 and 2, despite the significantly larger in-plane forces (link shear force and bending moments) developed in Specimens 3 and 4.

Specimen 5 - A sudden increase in link end lateral support forces is apparent in the final loading cycle. This increase appears to coincide with the failure of the link-to-column connection and the concurrent development of flange buckling in the brace connection panel.

Specimen 6 - This specimen showed a large and steady growth in lateral support forces throughout the test. Substantial forces developed well before any local buckling was observed within the test specimen. However, the development of very large lateral support forces in the latter portion of

the test appears again to be associated with the development of severe local buckling in the brace connection panel. Note also the lateral support forces continued to grow rapidly in the final cycles of the test, even though the overall load carrying capacity of the specimen was deteriorating rapidly.

Specimen 7 - The large lateral support forces measured for this specimen coincide with the development of severe lateral torsional buckling of the beam. It is interesting to note that the largest lateral support forces developed during the west load cycles, when the buckled beam was straightening under tensile axial load.

Specimen 8 - The largest lateral support forces occurred in the final loading cycles as the beam buckled. However, despite the very severe buckling of the beam, the lateral support forces were significantly less than for Specimen 7, after buckling of its beam. Also, in contrast to Specimen 7, the lateral support forces in Specimen 8 were larger when the beam was buckling in compression rather than straightening in tension.

Specimen 9 - Prior to the final loading cycle, there was a large and steady growth in the lateral support forces for the west loading cycles, with virtually no lateral support force developed during the east loading cycles. No significant local buckling was observed in this specimen until the final cycle. The very large lateral support forces developed in the final east loading cycle coincide with the failure of the link-to-column connection and the concurrent sudden development of lateral torsional buckling in the beam. It should be noted that Specimen 9 was provided with a short link, indicating that very large link end lateral support forces are possible for short as well as for long links. It may be argued that the final large spike in P1 and P2 should be discounted, since it occurred after the failure of the link-to-column connection. However, even discounting the final cycle, the maximum lateral support force was on the order of 6 percent of the beam flange strength. This is four times larger than the code specified value.

Specimen 10 - The growth of lateral support forces in the east loading cycles appears to be associated with the rather mild lateral torsional buckling experienced by the beam of this specimen. Unlike Specimen 9, lateral support forces were rather small during the west loading cycles. However, like Specimen 9, there was a sudden increase in lateral support force in the final east cycle, after failure of the link-to-column connection. If this final cycle is discounted, the maximum lateral support force was approximately 4 percent of the beam flange strength.

Specimen 11 - The very low lateral support forces are a result of the early termination of testing for this specimen.

Specimen 11R1 - The lateral support force P2 shows a large spike in the final east load cycle, coinciding with the rather sudden buckling of the beam. It is interesting to note that the portion of the beam that buckled was not the span adjacent to the link end. Nonetheless, buckling of the remote span still generated a large out-of-plane force at the link end lateral support.

Specimen 11R2 - The development of very large lateral support forces in this specimen appears to reflect the very severe lateral torsional buckling of the beam. Large lateral forces were generated in both the east loading cycles, during which the beam buckled, and during the west cycles, for which the beam was in tension. During the final loading cycle, the load cells at the link end lateral support failed, with one of the load cells buckling. The plot of P1 and P2 for Specimen 11R2 in Fig. 4.41 is therefore terminated prior to the failure of the load cells.

Specimen 12 - The moderate levels of lateral support force developed prior to the final load cycle appear to grow in conjunction with the observed lateral torsional buckling of the beam. The very large spike in these forces in the final west load cycle, particularly in the force P1, appears to be a consequence of the very severe lateral torsional buckling observed within the link. During this final cycle, an end bearing connected to one of the load cells measuring the force P1 began to bend and deform. This, in effect, reduced the stiffness of the lateral support, thereby permitting substantial (perhaps .5 inches) out-of-plane displacement of the link end. This effective loss of support stiffness appears to have contributed to the very rapid growth in the lateral support forces in the final load cycle.

From the above discussion of the individual test specimens, no clear pattern has emerged on the mechanisms responsible for the development of large link end lateral forces. However, a number of useful observations can be made. First, it is evident that various forms of local buckling can trigger the growth of large lateral support forces. Local buckling in the brace connection panel appears to be particularly detrimental in this regard, as evidenced by Specimens 1 and 6. Severe lateral torsional buckling of the beam segment outside of the link, as might be anticipated, can also result in large lateral support forces. Even larger out-of-plane forces at the link end appear to result from severe lateral torsional buckling of the link itself, as seen in Specimen 12. Severe web buckling within the link also appears to generate rather large lateral support forces. Flange buckling within the link seems to be least detrimental in triggering large lateral support forces.

It must be recognized that very large forces are transferred between the link, beam and brace in the vicinity of the link end lateral support. It may be postulated that any misalignment or out-of-plane displacement in this region will generate an out-of-plane component of the various forces meeting at the link end. Local buckling may contribute to this problem by causing further misalignment and out-of-plane displacement. This observation suggests that link end lateral supports must be very stiff in order to minimize out-of-plane displacements, and thereby minimize the out-of-plane component of the forces meeting at the link end. The need for stiff lateral supports was also indicated by Specimen 12, where a reduction in support stiffness resulted in inordinately large out-of-plane forces.

Local buckling may also contribute to the development of large lateral forces through an additional mechanism. After the occurrence of severe local buckling, the cross-section of the beam or link is no longer completely symmetric. Consequently, the shear center of the cross-section may no longer coincide with the centroid. This, in turn, may generate a tendency for the cross-section to twist.

Local buckling apparently played an important role in the development of large out-of-plane forces in many of the test specimens. However, this was not always the case. In Specimen 9, large lateral support forces were generated even though virtually no local buckling was observed in the specimen. In this case, however, these large forces developed only in the west load cycles. For this direction of loading, the brace is in compression. Any out-of-plane misalignment between the brace and the link would therefore have caused both the brace axial force and the link shear force to tend to push the lower beam flange (the flange to which the brace is connected) out-of-plane. In the opposite direction of loading, on the other hand, the tension axial force in the brace tends to stabilize the lower flange. Such a mechanism may have been responsible for the observed pattern of link end lateral forces in Specimen 9.

Both Specimens 9 and 10 demonstrated that the development of large lateral support forces is not a problem restricted solely to long links. Both of these short link specimens developed rather large out-of-plane forces.

It should also be noted that, in general, both the force P1 and the force P2 were of comparably large magnitude for most of the test specimens. This indicates that both the top and bottom link flanges must be thoroughly braced. In tests on links with composite floors, Ricles and Popov [16] concluded that the composite deck cannot, by itself, be counted upon to supply adequate link end lateral support. The plots in Fig. 4.41 support this conclusion. Thus, even with a composite deck, a transverse member connected at or near the bottom flange should be provided to support this flange.

The experimental data suggest that the lateral support forces may not necessarily correlate with beam flange strength. Sections with very heavy flanges may, in fact, be subject to lower

lateral support forces because these sections are less prone to local buckling. This may be seen by comparing Specimens 1 and 2 (light and slender flanges) with Specimens 3 and 4 (heavy and stocky flanges). Consequently, specifying the required lateral support strength as a percentage of the beam flange strength may not represent the most rational approach for designing link end lateral supports. An alternative approach may be to specify the required lateral support strength as a percentage of the ultimate shear force in the link. However, it is not clear from this limited experimental data whether or not this approach would provide a reasonable bound on lateral support forces. It appears that several mechanisms may contribute to the development of large link end lateral support forces. Consequently, developing a simple model for bounding these forces may be quite difficult.

4.5.3 Design Implications

From a design point of view, it is perhaps most important to recognize that strong and stiff lateral support must be provided at both the top and bottom flanges at the link ends. As far as specific strength requirements are concerned, it is clear that the code specified value of 1.5 percent of the beam flange strength is inadequate. However, it is not clear what this value should be, or even if it should be related to beam flange strength.

Despite these numerous uncertainties, it would appear that an increase in the code specified lateral support strength is warranted. Maintaining beam flange strength as a basis for lateral support strength, despite its potential shortcomings, the data in Table 4.5 and in Fig. 4.41 can be used as a basis for estimating an increased lateral support strength requirement. In evaluating this data, some of the extreme values of lateral support force measured after failure of the link-to-column connection or after buckling of the beam can perhaps be discounted, assuming the designer will guard against these failure modes. The measured values can be somewhat further reduced to account for the fact that the lateral force measurement points were not located directly at the flanges, but rather somewhat inside of the flanges (see Figs. 4.40 and 2.8 Section A-A). This location will cause an increase in the measured force when that force is the result of torsional moments at the link end.

In light of the above adjustments, the authors recommend a *minimum* lateral support strength of 6 percent of the beam flange strength, i.e. $0.06 \times b_f\, t_f\, F_{y\,flange}$. This should be considered a minimum requirement, with recognition that lateral forces can be larger under certain circumstances. In particular, long links with stocky flanges, which may suffer from severe lateral torsional buckling of the link appear to have the potential to generate much larger link end lateral force. The above minimum strength requirement should be applied to short links as well as long links.

Based on the experimental data, no specific recommendations can be made on a minimum stiffness requirement for link end lateral supports. However, it is clear that stiff supports are

required. It is also apparent that a simple analytical model for bounding the required strength and stiffness of link end lateral supports is needed.

As a final comment on design of link end lateral supports, it should be noted that while these supports must provide stiff resistance to out-of-plane displacement, they should not excessively restrain in-plane displacement of the link end. Restraint against in-plane displacement may result in significant additional axial load in the diagonal brace. Accordingly, the use of transverse members framing into both sides of the link end should be avoided. A lateral support member framing into the link end from only one side is preferred.

4.6 STRAIN GAGE DATA

A number of the test specimens were provided with strain gages at various locations within the specimen. In this section, the gage types and installation are briefly described and selected data obtained from these gages are examined.

For most of the test specimens, strain gages were provided within the link, and for a few specimens, additional gages were also provided at selected locations within the brace connection panel or on the brace connection itself. Within the link, strain rosettes were typically provided at several locations along the length of the link, at mid-depth of the section. A rosette was always provided at identical locations on both sides of the web. Rosettes with 2 gages oriented 90 deg. apart were used, and were placed on the link web so that each individual gage was oriented at 45 deg. from the link centerline. The engineering shear strain was then computed as the difference in the normal strains measured by the two gages, and averaged with the shear strain computed from the corresponding rosette on the opposite side of the web.

For Specimen 1, single element gages were located on the flanges at the link ends in an attempt to measure normal strains in the link flanges. However, these gages typically showed erratic behavior, with a considerable amount of drift evident in the output under cyclic load. It was concluded that cyclic strains in the flanges at the link ends were too large to be measured reliably with strain gages. Consequently, the link flanges were not gaged in the remaining test specimens.

Strain gages were obtained from the Micro-Measurements Division of the Measurements Group Inc. The rosettes used for the link webs were Micro-Measurements Nos. EA-06-125TD-120 and EA-06-125RA-120, and the single element gages were No. EA-06-125AD-120. Gages were attached to the specimen using Micro-Measurements M-Bond AE-15 epoxy adhesive, which required curing under pressure and elevated temperature.

The gages listed above are not high elongation, post-yield gages, but are simply general purpose strain gages. Discussions with technical personnel at Micro-Measurements indicated that high

elongation gages are best suited to high monotonically applied strains and generally show poor performance under large cyclic strains. Under cyclic load, the foil elements of the strain gage incur fatigue damage, resulting in a permanent change in the unstrained resistance of the gage [40]. This damage is evidenced as "drift" in the strain readings from the gage. The stain gage manufacturer indicated that no presently available gage is capable of reliably measuring very high cyclic strains, but that for moderate cyclic strains, the general purpose gages show less drift than the high elongation gages. The general purpose gages were therefore used for the test specimens.

Examination of the strain gage data indicated that most gages began to exhibit drift or other erratic and questionable behavior at about ± 3 to ± 4 percent cyclic normal strain. The orientation of the rosettes measuring shear strain in the link web was such that the normal strains in the individual gages of the rosette was equal to one-half of the engineering shear strain. Consequently, shear strains could generally be reliably measured up to about ± 6 to ± 8 percent (± .06 to ± .08 rad), which was adequate for most specimens.

In the remainder of this section, data obtained from selected strain gages are examined in order to obtain additional insights into the behavior of the test specimens. In cases where strain gage data showed significant drift or other questionable behavior, plots are terminated at the point where the questionable behavior begins. Plots which are terminated prior to the end of the test are appropriately identified.

Specimen 1

The link of Specimen 1 was instrumented with strain rosettes along the length of the link centerline. The location of the rosettes are listed in Table 4.6. A rosette was located at approximately mid-length of each panel within the link.

Figure 4.42 shows the link shear plotted against the link shear strain for strain rosette nos. 1 and 3. Strain rosette no. 1 is located in the first panel adjacent to the column, whereas rosette no. 3 is located at approximately mid-length of the link. These plots show some features that were typical of link shear force versus shear strain plots for many of the test specimens. First, theses plots typically show a sharp, well defined yield point, permitting fairly accurate determination of the shear force at first yield at the location of the rosette. A value of shear force at first yield for each of the five rosettes on the link of Specimen 1 are listed in Table 4.6. It is apparent that shear yielding occurred much earlier at the end of the link near the column than in the remainder of the link. It is useful to to compare the measured shear yield values listed in Table 4.6 with the values predicted from simple theory. Using the simple strength of materials formula for shear stress, $\tau = (VQ)/(Ib)$, combined with the yield stress under pure shear based on the von Mises yield criterion, $\tau_y = .577F_y$, a value of shear force at first yield can be computed. This calculation is shown in Table 4.6, using measured section dimensions and web yield stress values. As shown,

the predicted shear force at first yield at mid-depth of the section is 67 kips. This compares well with the measured shear yield force of 66 kips at rosette location no. 3. This rosette, located at about mid-length of the link, is in a region of low bending moment. The earlier yielding at strain rosette no. 1, in a region of high bending moment near the link end, suggests a fairly significant influence of bending moment on the initiation of shear yielding. The influence of interaction between shear and bending stresses is also evident in the plots of Fig. 4.42, where substantially larger inelastic shear strains are developed at the link end near the column as compared with mid-length of the link.

In Fig. 4.43, the distribution of shear strain along the length of the link centerline is plotted at various instants in the loading history. The points plotted in this figure are the readings from the five strain rosettes listed in Table 4.6. In Fig. 4.43a, values of shear strain at the peak deformation of several eastward loading cycles are plotted, whereas in Fig. 4.43b, the shear strain measured at the peak deformation of several westward cycles are shown. Figure 4.43a shows a rather clear pattern of relatively uniform shear strain over the central portion of the link, with shear strain levels increasing towards the link ends. This plot also suggests a rather strong interaction between bending and shear stresses at the link ends. This interaction appears to be stronger at the link end adjacent to the column as compared to the link end adjacent to the brace. This may be due to several reasons. First, the bending moment was generally somewhat larger at the column end of the link than at the brace end of the link for the east loading cycles. Secondly, the apparent bending-shear interaction may be affected by flange buckling at the link ends. As flange buckling develops, it may be postulated that the web carries a greater share of the bending moment on the section. Consequently, a greater apparent degree of interaction may result in the web of the section after severe flange buckling occurs. Thus, the plot in Fig. 4.43a may also reflect the more severe flange buckling observed at the column end of the link.

In contrast to the eastward loading cycles, the shear strain distribution for the west loading cycles, shown in Fig. 4.43b, indicated little or no bending-shear interaction at the column end of the link. This may be due to the fact that moment equalization in the link was more complete in the west loading cycles. Consequently, for the same applied link rotation angle, the bending moments at the column end of the link is lower in the west load cycles than in the east cycles.

In Fig. 4.44, the plastic shear strain at rosette no. 3 is plotted against the plastic link rotation angle, γ_p. This plot is intended to provide an indication of the relative importance of plastic shear strain in supplying plastic link rotation throughout the specimen's loading history. The numbers shown on this plot correspond to load cycle numbers. Plastic shear strain at the rosette location was estimated as the total shear strain measured by the rosette minus the elastic component of the shear strain. The elastic component was estimated as the shear force divided by the slope of the shear force versus shear strain plot in the initial elastic cycles in Fig. 4.42b.

In the early loading cycles, Fig. 4.44 indicates that a small amount of plastic link rotation, perhaps ± .01 rad., was developed before any shear yielding occurred in the central portion of the link. This is visible as short, nearly horizontal lines near the origin in Fig. 4.44. This initial portion of the plot can be attributed to the occurrence of combined flexural and shear yielding at the link ends prior to the occurrence of general shear yielding within the link. Plastic shear strain at rosette no. 3 is a significant portion of the plastic link rotation angle beginning at about load cycle 8. For the following load cycles, the contribution of plastic shear strain to link rotation remains relatively constant, although some reduction in this contribution is visible towards the end of each load cycle. This effect may be due to the increasing severity of flange buckling inside of the link during these cycles. Beginning with load cycle 13, there is a sudden reduction in the contribution of plastic shear strain. This sudden reduction corresponds with the development of severe local buckling in the east flange of the brace connection panel, and the concurrent drop in the specimen's load carrying capacity. Figure 4.44 shows that this effect is initially more severe in the east loading cycles, which is the direction of loading that produced local buckling in the brace connection panel. As the specimen's load carrying capacity dropped in the final loading cycles, the shear force in the link was increasingly less than the maximum strain hardened shear force developed earlier in the specimen's loading history. Consequently, little or no additional shear yielding was possible after overall strength began to deteriorate significantly. Figure 4.44 therefore indicates that in the final loading cycles, almost all of the plastic link rotation was due to bending deformations at the column end of the link and within the buckled brace connection panel. During load cycle 16, the contribution of plastic shear strain is almost completely terminated, corresponding with the failure of the link-to-column connection.

The data plotted in Fig. 4.44 supports previous observations that even rather severe flange buckling inside of the link is not particularly detrimental to overall link behavior. Local buckling within the brace connection panel, on the other hand, is very damaging to overall performance. Finally, it should be noted that the plastic shear strain plotted in Fig. 4.44 should not be considered equal to the portion of the plastic link rotation due to shear deformation. The values plotted in this figure represent the plastic shear strain at a single point within the link. As demonstrated by Fig. 4.43, the shear strain distribution is not uniform along the length of the link. It will be shown in Chapter 5 that shear strain also varies considerably over the depth of the web. Figure 4.44 can therefore only provide an indication of the relative importance of plastic shear strain at various points throughout the specimen's loading history.

Specimen 2

Specimen 2 was similar to Specimen 1, except for the location of stiffeners. Recall that the link of Specimen 2 had a large unstiffened panel, approximately 20 inches in length (Fig. 2.7),

and ultimately failed by severe web buckling in this panel. This large central panel was instrumented with four shear strain rosettes along the link centerline. The data from these rosettes provide an opportunity to compare measured shear deformations at the initiation of web buckling with the analytical predictions of web buckling developed for short links.

A formula for predicting the initiation of web buckling in *short* links has been developed by Kasai and Popov [20]. The predictions of this formula compare closely with the experimentally observed initiation of web buckling in short links, as demonstrated in Ref. 20.

The formula for predicting web buckling in short links is as follows [Eq. 14 in Ref. 20]:

$$\bar{\gamma}_B = 8.7 K_s(\alpha) \left[\frac{1}{\beta}\right]^2 \tag{4.7}$$

where:

$$\alpha = \frac{a}{b}$$

$$\beta = \frac{b}{t_w} = \frac{(d - 2t_f)}{t_w}$$

α = stiffener spacing

d = overall depth of section

t_f = flange thickness

$$K_s(\alpha) = \begin{cases} 8.98 + \dfrac{5.60}{\alpha^2} & (\alpha \geq 1) \\ 5.60 + \dfrac{8.98}{\alpha^2} & (\alpha \leq 1) \end{cases}$$

In the above equation, $\bar{\gamma}_B$ represents the link rotation at the onset of web buckling, measured from the farthest point of zero shear during the previous loading history.

The above formula was developed for short links, where shear deformation dominates overall link rotation. Consequently, it may be postulated that web buckling will occur in longer links when the link rotation resulting directly from shear deformation reaches the value of $\bar{\gamma}_B$ in Eq. 4.7. Using the measured section dimensions for Specimen 2, with a value of a = 20 inches for the center panel of the link, Eq. 4.7 results in a value of $\bar{\gamma}_B$ = 0.034 rad.

During the testing of Specimen 2, web buckling was first observed in the central panel of the link during load cycle 9. Since shear strain rosettes were provided on both sides of the web, it is also possible to determine the initiation of web buckling from the rosette readings. The shear strain measured by rosettes on opposite sides of the link web, at identical locations in the link's central panel, are shown in Fig. 4.45. This plot shows that strain readings on opposite sides of the

web began to differ during cycle 8W, indicating that web buckling initiated in cycle 8W. The average shear strain along the link's central 20 inch panel, based on the four shear strain rosettes in this panel, was 0.030 rad. This value was measured from the point of zero shear force at the start of cycle 8W up to the peak deformation for cycle 8W. Photogrammetric data from Specimen 1, which was identical to Specimen 2 in link length and section, indicates that the average shear strain over the full depth of the web is approximately equal to 77 percent of the shear strain at mid-depth of the section (the location of the rosettes), for the central portion of the link. This data is presented in Chapter 5. Using additional arguments discussed in Chapter 5, the link rotation angle due to shear deformation in the link web is estimated as 90 percent of the average shear strain taken over the depth of the web, for a $W12\times16$ section. Based on these approximations, the rotation of the central panel of the Specimen 2 link due to shear deformation is estimated as $0.9\times0.77\times0.030 = 0.021$ rad. That is, at the onset of web buckling, the estimated panel rotation due to web shear deformation , measured from the last point of zero load, is approximately 0.021 rad. This is significantly less than the value of $\bar{\gamma}_B = 0.034$ rad. predicted by Eq. 4.7. This rather large discrepancy indicates that the above approach for predicting web buckling in long links may not be valid. That is, applying the web buckling predictions for short links to the estimated portion of the link rotation due to shear did not successfully predict web buckling for this test specimen. The error is on the unconservative side, with web buckling occurring significantly earlier than predicted.

The above discrepancy may be due to several reasons. First, there is some uncertainty involved in estimating the portion of link rotation due to shear deformations in the web. However, it should be noted that the total link rotation for cycle 8W, including all sources of deformation, is $\bar{\gamma} = 0.029$ rad., which is still only 85 percent of the value of $\bar{\gamma}_B$. Thus, even if the entire link rotation is attributed to shear deformation, which certainly is not the case, web buckling still occurred earlier than predicted by Eq. 4.7.

Another, perhaps more likely reason for the discrepancy between the predicted and observed web buckling is the influence of bending moment on web buckling. The higher levels of bending moment developed in long links may cause the initiation of web buckling to occur sooner than in short links. In any event, from the above data it appears that it may not be possible to predict web buckling in long links by simple extrapolation of Eq. 4.7 by the methods used above.

Specimen 3

The location of shear strain rosettes along the length of the link centerline for Specimen 3 are listed in Table 4.7. A rosette was located at about mid-length of each panel within the link. Also listed are the measured values of shear force at first yield at each of the rosette locations. As with Specimen 1, these values were taken from plots of shear force versus shear strain at the rosette.

The theoretical value of yield shear force at mid-depth of the section, based on the strength of materials shear stress distribution and the von Mises yield criterion (see calculations in Table 4.7) is 92 kips. This agrees well with the measured first yield shear force of 90 kips at the rosettes in the central portion of the link. First shear yield at the rosettes nearer the link ends occurred at much lower values, again indicating significant interaction between shear and bending stresses at the link ends.

The effects of this interaction are also apparent in Fig. 4.46, where the distribution of shear strain along the length of the link centerline is plotted at various instants in the loading history. The points plotted in this figure represent the shear strain at each of the four rosettes at the point of maximum link rotation for the indicated cycles. As with Specimen 1, these plots show a pattern of increasing shear strain towards the ends of the link, and provide clear evidence of reasonably strong bending-shear stress interaction. Thus, whereas the global link response, as evidenced by the plots of link shear force versus link rotation angle (Fig. 4.1), shows little or no M-V interaction at initial yield, it is apparent from Figs. 4.43 and 4.45 that the interaction of bending and shear stress is very important locally at the link ends.

In Fig. 4.47, the plastic shear strain at rosette no. 2 is plotted against the plastic link rotation angle. Like the corresponding plot for Specimen 1 (Fig. 4.44), this plot provides an indication of the relative contribution of plastic shear strain to overall plastic link rotation throughout the specimens loading history. In the early inelastic load cycles, plastic link rotation is developed with no shear yielding in the central portion of the link. As with Specimen 1, this corresponds to the short horizontal lines near the origin of the plot in Fig. 4.47, and can be attributed to early combined shear-flexural yielding at the link ends. Significant plastic shear strains are first developed at rosette no. 2 in load cycle 7. During cycles 8 to 12, the contribution of plastic shear strain to overall link rotation appears to remain essentially constant. The deterioration in plastic shear strain due to flange buckling seen in Specimen 1 is not visible in Specimen 3, reflecting the significantly milder flange buckling experienced by the Specimen 3 link. The development of plastic shear strain is abruptly terminated during load cycles 13E and 13W, corresponding with the failure of the link-to-column connection. It is interesting to note that the contribution of plastic shear strain is somewhat less in cycle 7 than in the following load cycles. A possible explanation for this observation is that shear yielding may not have yet propagated over the full depth of the web during this cycle. Consequently, inelastic shear deformations near mid-depth of the section would have been constrained by the elastic portions of the web near the top and bottom of the cross-section.

Specimen 4

During the testing of Specimen 4, web buckling was observed in the two interior panels of the link. In this section, the web buckling predictions of Eq. 4.7 will be compared to the experimentally observed initiation of web buckling, in a manner similar to Specimen 2. During the test, both of the central 12 inch long panels of the link experienced web buckling. The observed buckling was more severe in the panel nearer the column, and so this panel will be investigated below.

Based on the measured section dimensions for Specimen 4, and taking a = 12 inches for the buckled panel, Eq. 4.7 predicts web buckling at $\bar{\gamma}_B$ = 0.067 rad.

The actual initiation of web buckling was observed during load cycle 12E. This observation is confirmed by measurements from shear strain rosettes on opposite sides of the web of the buckled panel. Measuring from zero to peak load in cycle 12E, the measured shear strain at mid-depth and mid-length of the buckled panel (averaging near side and far side gages) was 0.055 rad. Based on photogrammetric data for Specimen 4 (see Chapter 5), the average shear strain over the entire web of the panel being investigated is equal to about 93 percent of the shear strain at the location of the rosette. Also, as will be discussed in Chapter 5, the link rotation angle due to shear deformation is estimated as 90 percent of the average shear strain in the web for the $W12\times22$ section. Thus, at the initiation of web buckling, the rotation of the panel due to shear deformation is estimated as $0.9\times0.93\times0.055 = 0.046$ rad. This, again, is substantially less than the predicted $\bar{\gamma}_B$ = 0.067 rad. Note that the total link rotation for cycle 12E was $\bar{\gamma}$ = 0.081 rad.

As with Specimen 2, it appears that attempting to predict web buckling in a long link by the above approach was not successful for Specimen 4. That is, applying Eq. 4.7 to the estimated portion of the link rotation due to shear deformation does not appear to successfully predict web buckling in long links. The error is again on the unconservative side, with web buckling occurring earlier than predicted.

Specimen 5

Specimen 5 was an example of a very long link (nominal $e = 3.15M_p/V_p$), where flexure dominates post-yield behavior. Shear yielding is not anticipated at this length, and test observations for Specimen 5 indicate general shear yielding of the link web did not occur.

A series of five shear strain rosettes were located along the centerline of this link. The locations are listed in Table 4.8. The shear strain measured at each rosette location is plotted against link shear force in Fig. 4.48. Rosette nos. 2, 3 and 4, which were all located in the large central panel of the link, show purely elastic response, confirming the observation that general shear yielding of the link web did not occur for this specimen. The link section properties and material yield strengths for Specimen 5 are the same as for Specimen 1. As shown in Table 4.6, initial shear

yielding is anticipated at mid-depth of this section at a shear force of about 67 kips based on the simple strength of materials solution. Thus, the maximum shear force for this specimen of 49 kips was well away from the initiation of shear yielding in the central portion of the link.

Rosette nos. 1 and 5 were located near the column and brace ends of the link, respectively. In contrast to the rosettes in the central portion of the link, the plots of Fig. 4.48 show substantial shear yielding near the link ends. Initial shear yielding at rosette location no. 1 occurs at a shear force of about 30 kips. In Specimen 1, a similarly located rosette showed initial shear yielding at about 49 kips (Table 4.6). The earlier yielding in Specimen 5 can likely be attributed to the higher bending moments in the longer link.

Figure 4.48 again provides clear evidence of significant interaction between bending and shear stresses at the link ends. For a very long link, as with Specimen 5, even though general shear yielding of the link web does not occur, it appears that shear has an important effect on the yielding patterns developed at the link ends.

Specimen 9

Specimen 9 was an example of a short link (nominal $e = 1.2M_p/V_p$), where shear is expected to dominate post-yield behavior. Shear strain rosettes were provided at the center of each of the three panels of the link. Table 4.9 lists the locations of these rosettes, along with the measured value of shear force at initial yielding at each location. As before, these values were read from plots of shear force versus shear strain at the rosette. Also shown in Table 4.9 is the theoretical value of yield shear force, computed in the same manner as for the previous specimens. The theoretical shear yield value of 80 kips agrees closely with the measured yield values at all three locations. This indicates that there was little or no effect of shear-bending interaction on the initiation of shear yielding at any of the rosette locations, reflecting the lower levels of bending moment in short links.

In Fig. 4.49, the distribution of shear strain along the length of the link centerline is plotted at the peak of several load cycles. These plots show mild interaction between shear and bending stress near the link ends. The shear strain distribution appears to be considerably more uniform in Specimen 9 as compared with Specimen 3 (Fig. 4.46), both of which were $W12\times22$ links. Shear strains in the Specimen 9 link also appear to be higher at the column end of the link for the east load cycles, and larger at the brace end of the link for the west load cycles. This observation most likely reflects the pattern of link end moment equalization for this specimen (Fig. 4.2). Moments tended to equalize more completely in the west load cycles. Consequently, the moment at the brace end of the link was larger in the west load cycles than in the east load cycles, for the same applied link rotation. Conversely, the moment at the column end of the link was larger in the east load cycles than in the west cycles, for the same applied link rotation.

The plastic shear strain at rosette no. 2 is plotted against the plastic link rotation angle, γ_p, in Fig. 4.50. This plot differs from the corresponding plots for Specimens 1 and 3 (Figs. 4.44 and 4.47) in that there is little evidence of a significant initial contribution of flexural yielding in Specimen 9. Figure 4.50 suggests that the contribution of shear yielding to overall plastic link rotation was relatively constant throughout the specimen's loading history, up to the point of the link-to-column connection failure. There is evidence of some deterioration in the contribution of shear yielding in the later loading cycles, which may be attributed to the development of minor yielding and instability outside of the link.

Specimen 9 was provided with a rectangular tube brace and a gussetted brace-to-link connection. The brace connection detail is shown in Fig. 2.14. As discussed in Chapter 1, the potential for buckling of the gusset plate is an important design issue for this type of connection. The type of failure observed in the Tsukuba EBF test (Fig. 1.11) was guarded against in the present tests by the addition of a stiffener along the edge of the gusset nearest the link, as shown in Fig. 2.14. An additional issue of concern is whether or not the edge of the gusset located between the brace and the beam requires stiffening. No stiffener was provided along this edge of the gusset in the present tests. An elastic finite element analysis of the failed Tsukuba connection detail indicated that stress levels along this back edge of the gusset (the edge between the beam and the brace) were generally very low compared to the edge of the gusset between the brace and the link.

In order to obtain data on the stress levels at the gusset plate edges, several strain gages were installed on the brace connection in Specimen 9. The location of these gages are shown in Fig. 4.51. Gages nos. 1 and 2 were located on the diagonal stiffener attached to the edge of the gusset between the brace and the link. At each of these locations, two individual gages were installed near the edges of the stiffener, and the individual measurements were then averaged. Gage nos. 3 and 4 were attached directly to the edge of the gusset between the brace and the beam. All gages on the brace connection were single element gages, providing a measurement of normal strain at each location.

The measured normal strain at each of the brace connection gage locations are plotted against the link rotation angle in Fig. 4.52. It is clear from these plots that the normal strain levels in the diagonal stiffener are much larger than along the back edge of the gusset. In fact, the strain levels at gage locations 1 and 2 are on the order of 10 times larger than at gage locations 3 and 4 (note the different vertical scales in the plots of Fig. 4.52). Along the diagonal stiffener, strain levels are substantially higher at the end of the stiffener closest to the link, i.e., at gage location no. 1. These strains are well beyond yield. In contrast, strain levels at gages location nos. 3 and 4 are below yield.

The data presented in Fig. 4.52, along with the excellent performance of the connection during testing, support the approach of not providing a stiffener on the back edge of the gusset. The

high strain levels in the diagonal stiffener, on the other hand, reflect the high stress levels developed along the front edge of the gusset, and indicate that stiffening of this edge of the gusset is justified. This data also shows substantial yielding can be expected in the diagonal stiffener. Consequently, the width-thickness ratio of this stiffener should be kept small enough to permit yielding without the development of local flange type buckling in the stiffener. Choosing $b/t \leq 52/(F_y)^{1/2}$ should therefore be a minimum requirement for this stiffener [Table C-B5.1 of Ref. 37], where b is one-half of the overall width of the stiffener, and t is the thickness of the stiffener.

The gussetted brace-to-link connection in Specimen 10 was gaged in a manner similar to Specimen 9. These gages showed similar results to those plotted in Fig. 4.52

4.7 SUMMARY

Chapter 4 has provided further detailed analyses of experimental data for the 14 EBF test specimens. Following is a brief summary of some of the key observations and issues discussed in this chapter.

(1) The occurrence of initial significant yielding of the links showed minor influence of M-V interaction. This effect was small, particularly since the links did not exhibit a well defined yield point. For design purposes, neglecting M-V interaction for predicting the yield strength of long links appears to be a reasonable simplification and is consistent with the approach used for short links. Consequently, the shear force required to produce initial significant yielding can be adequately predicted for any length link by Eqs. 4.1a and b.

(2) The test specimens (7, 8, 11, 11R1 and 11R2) which significantly violated capacity design principles in the beam segment outside of the link showed first yielding well before the other specimens. These specimens demonstrated that overall frame strength will be controlled by the beam rather than by the link in an EBF where the beams are not designed for the capacity of the links.

(3) The ultimate shear force developed by most of the links was on the order of 1.2 to 1.3 times the initial shear yield strength. The overstrength factor of 1.5 used for predicting the ultimate strength of short links therefore appears to be too large for long links, particularly those in the intermediate length range of combined shear and flexural yielding. However, for very long links with stocky flanges, such as Specimen 12, an overstrength factor of 1.5 to account for strain hardening appears to again be appropriate. Thus, whereas it is reasonable to neglect M-V interaction when predicting the initial yield strength of long links, it appears that M-V interaction must be considered when predicting the ultimate strength of long links. Cyclic flange buckling will limit the strength of long links with slender flanges. The ultimate strength of long links will therefore, in general, depend on the link length (to account for

varying degrees of M-V interaction) and on the flange slenderness ratio.

(4) For most of the links tested, equalization of end moments was nearly, but not completely achieved. End moment equalization was generally not as complete for the direction of loading that placed the beam segment outside of the link into compression. The large compressive axial forces in the beam were apparently responsible for some loss of flexural stiffness in the beam, even though no signs of instability were visible. Because of this loss of stiffness, less moment was attracted to the brace end of the link, and moment equalization was not as complete.

(5) In specimens where the beam was not designed for the ultimate strength of the link, the moment at the column end of the link remained much larger than at the brace end of the link throughout the entire loading history. The loss of stiffness at the brace end of the link associated with yielding and instability of the beam effectively inhibited equalization of link end moments. The inability to equalize link end moments resulted in increased bending moments at the column end of the link, contributing to the premature failure of the link-to-column connection in Specimens 7, 8 and 11.

(6) The ultimate link end moments generated for most of the test specimens were significantly less than $1.5M_p$, indicating again that an overstrength factor of 1.5 to account for strain hardening may be too large for long links, particularly those in the intermediate length range. However, for very long links with stocky flanges, such as Specimen 12, ultimate end moments on the order of $1.5M_p$ may be anticipated. For very long links with slender flanges, such as Specimens 5 and 6, severe cyclic flange buckling limited end moments to substantially less than $1.5M_p$.

(7) The total energy dissipation capacity of the very long, predominately flexural yielding links was significantly less than that for the links in the intermediate length range of combined shear and flexural yielding. For the same applied plastic rotation angle, γ_p, long flexural yielding links can dissipate as much or more energy as short shear yielding links. However, because shorter links can generally sustain much larger plastic rotations without the occurrence of a non-ductile failure mode, the total energy dissipation capacity of short links is still generally significantly superior to that of longer links. The two short links which were tested, Specimens 9 and 10, showed rather poor total energy dissipation capacity due to the early failure of their link-to-column web connections.

(8) Web buckling inside of the link resulted in a greater loss of energy dissipation capacity than flange buckling inside of the link. Flange buckling outside of the link, within the brace connection panel, also resulted in a greater loss of energy dissipation capacity than flange buckling inside of the link.

(9) The addition of reinforcing ribs at the link-to-column connection, when properly implemented as in Specimen 6, significantly increased total energy dissipation capacity. Likewise, the addition of triangular cover plates at the link-to-column connection in Specimen 11R2 also greatly increased the total energy dissipation capacity.

(10) Yielding outside of the link, in the column panel zone and in the brace connection panel and beam, contributed substantial energy dissipation capacity in a number of the test specimens. Limited yielding outside of the link can therefore contribute significantly to the overall energy dissipation capacity of an EBF and can reduce inelastic deformation demands on the link. Permitting too much yielding outside of the link, however, can result in non-ductile failure modes outside of the link, such as severe flange buckling in the brace connection panel or lateral torsional buckling of the beam.

(11) The ratio of axial force in the beam or brace to the shear force in the link remained essentially constant throughout each specimen's loading history. For design purposes, this ratio can therefore be estimated from an elastic frame analysis and used to estimate the ultimate axial force in the beam and brace.

(12) The ultimate axial forces developed in the beams of the test specimens varied from about 0.3 to $0.8P/P_y$, demonstrating the large axial forces that can be developed in the beams of an EBF. Test observations indicate that designers should be particularly cautious when the anticipated ultimate values of P/P_y in the beam exceeds a value of about 0.5 to 0.6.

(13) The test specimens that performed well with respect to beam and brace behavior were those in which the brace carried a large portion of the link end moment. In some cases, the brace carried as much or more bending moment as the beam. The ability to attract and carry these large bending moments requires a brace of high flexural stiffness and strength. Achieving satisfactory performance of EBFs with long links may often require the use of very heavy brace sections.

(14) A loss of flexural stiffness in the beam can trigger a redistribution of link end moment from the beam to the brace. The ability of the link end moment to continue increasing after this point is dependent on the ability of the brace to attract and carry additional bending moment.

(15) In the absence of a composite concrete deck, beam strength will generally be controlled by stability rather than by yielding. For specimens that experienced instability of the beam, the buckled shape of the beam generally included participation of the brace connection panel. For stability design of the beam, the brace connection panel should be included with the beam segment beyond the panel when computing effective length.

(16) For EBFs in which the brace is connected at the link to the lower flange of the beam, the beam's upper flange will be subjected to combined bending and axial compressive stresses, and will be the critical flange for stability. For such arrangements, a composite deck will likely be very beneficial in maintaining the stability of the beam.

(17) Even severe yielding of the brace connection panel under combined bending and axial tension did not trigger a redistribution of bending moment from the beam to the brace. In general, such yielding restricted to the brace connection panel appears to pose no serious consequences on overall EBF behavior.

(18) Locating the intersection of the brace and beam centerlines inside of the link, as in Specimen 8, significantly reduced the bending moment generated in the beam and brace. For this specimen, the beam and brace were subjected to only about 50 percent of the link end moment. The use of such an eccentricity in the brace-to-link connection may provide a useful design tool for reducing the detrimental effects of large link end moments on the beam and brace behavior. It may be particularly advantageous in EBFs with long links by permitting the use of lighter brace sections.

(19) The experimental observations and data have confirmed the importance of adhering to the *capacity design* approach for the beams and braces in EBFs. Limited yielding outside of the link may be acceptable and perhaps even advantageous, particularly if restricted to the brace connection panel. However, the beam and brace must still possess adequate strength to permit full development of link strength. The overall intent of the capacity design approach for the beam and brace is expressed by Eq. 4.6. A preliminary suggested capacity design procedure for the beam and brace is outlined in Section 4.4.4.

(20) Large out-of-plane forces were measured at the link end lateral support for the majority of the test specimens. Many specimens developed link end lateral forces on the order of 4 to 5 times greater than typical code specified lateral support strength requirements, and in some cases, in excess of 10 times greater. Experimental observations indicate that a variety of mechanisms contribute to the development of these large lateral support forces. Large out-of-plane forces are possible at the ends of both short and long links.

(21) Based on the limited experimental data from this testing program, a *minimum* link end lateral support strength equal to 6 percent of the beam flange strength, i.e., $0.06 \times b_f \, t_f \, F_{y\,flange}$ is recommended. This should be considered a minimum requirement, with recognition that lateral support forces may be larger under certain circumstances. Both the top and bottom flange at the link ends must be braced. The experimental data also confirm the importance of providing stiff resistance to out-of-plane displacement at the link ends.

5. ANALYSIS OF PHOTOGRAMMETRIC DATA

Techniques of close-range photogrammetry were used to collect data on deformations and strains in the link region of five of the fourteen test specimens. These were Specimens 1, 4, 6, 9 and 12. The basic procedure consisted of drawing a grid of lines on the specimen and taking photographs of the specimen at various stages of loading. Measurements were then made from the photographs to determine the position of the gridline intersections and to subsequently compute displacements, strains and rotations. The basic objective of this work was to develop an improved understanding of local behavior within the link region. The resulting data are also intended to provide a useful basis of comparison for analytical predictions of local link behavior. The photographs provide data on deformations throughout the entire link region at a particular instant of loading, and thus provide a far more complete picture of link behavior than can be obtained from strain gages or other measurement techniques. Unlike strain gages, however, the photographs do not provide a continuous record of deformation throughout a specimen's loading history. Photogrammetry has been used successfully in the past to measure deformations in the column panel zone in steel moment resisting frames [41, 42].

In this chapter, the procedures and equipment used to collect the photogrammetric data are described. The processing and reduction of this data and the computation of displacements, strains and rotations are then discussed. This is followed by a presentation of the photogrammetric data in the form of various plots. Finally, the photogrammetric data is used to estimate the components of link rotation (shear, bending, and support rotation) for selected specimens at particular instants of loading.

5.1 TEST PROCEDURES

Photographs were taken with a Wild P30 terrestrial photogrammetry camera mounted above the link region of the test specimen. The camera was located at about 8 ft. above the plane of the link web and was supported by a steel frame especially constructed for this purpose. The steel support frame was grouted to the test floor in order to provide a steady, rigid support for the camera. The 8 ft. distance was chosen to provide a sufficiently large field of view to accommodate the longest link of the test program.

The Wild P30 camera is normally used as part of a phototheodolite for applications in terrestrial photogrammetry [43]. The phototheodolite is typically mounted on a tripod with the camera's focal plane in a vertical orientation. The present application required the camera to be oriented with the focal plane in a horizontal position, permitting photographs to be taken looking down on the specimen. Consequently, a special mounting device was constructed to support the camera in a horizontal position and to permit proper leveling and adjustment of the camera in this position. Portions of a Kelsh plotter [43] were modified to act as the mounting device for the Wild P30

camera, which permitted rotation and tilt of the camera in a horizontal position. A level bubble was also installed on the camera to permit proper leveling of the camera in its final position prior to each photograph. The mounting device together with the camera were attached to the top of the steel support frame. Figure 5.1 shows the steel support frame and the camera in position above a test specimen.

The Wild P30 camera is provided with a fixed focus lens. To permit proper focusing on the test specimen, an additional lens was added to the front of the camera. The photographs were taken on 10cm. × 15cm. glass plates (Kodak Spectroscopic type IVN plates.)

The test specimens were prepared by sandblasting the surface of the steel and then by ruling a grid of lines on the surface. The gridpoints, defined by the intersection of the gridlines, provided the basis for the photogrammetric measurements. The lines were drawn with a Rapidograph technical pen, supplied with a size 0 diamond tipped point. A grid of lines was drawn on the link web of each of the photogrammetric test specimens, with lines typically spaced at 1 inch intervals, or in some cases at ½ inch intervals. For some specimens, a grid was also drawn on the web of the brace connection panel. The grids were drawn to cover as much of the web area as possible, but were interrupted at stiffeners and sometimes at the location of strain gage rosettes on the link web. For those specimens with a shear tab at the link-to-column connection, the web gridlines did not extend into the shear tab region. In addition to the web gridlines, a single line of grid points was drawn at approximately mid-depth of the link flanges on Specimens 6, 9 and 12. Figure 5.2 shows the link region of Specimen 9 after preparation for photographing.

In addition to the gridlines drawn on the specimen, four reference target points were located within the camera's field of view. These target points were located in the plane of link web, but were supported independently off the test floor. The target points remained stationary and undisturbed throughout the entire test for any given specimen. These targets served as control points for the photographs, permitting the gridpoint locations for each photograph to be referenced to a common coordinate system. The targets also permitted corrections to be made for the effects of any possible tilting of the camera which may have occurred from one photograph to the next. Two target points can be seen in Fig. 5.2. Prior to each test, the distance was measured between target points as well as between selected gridpoints. These measurements were used later to establish the approximate scale of the image on the photographic plates.

Approximately 5 to 7 photographs were taken for each of the five photogrammetric test specimens. Lighting for the photographs was provided by two 500 watt 3200°K photofloods, located approximately 3 to 4 ft. from the test specimen. An exposure time of 5 seconds was determined by trial and error. For each specimen, the first photograph was always taken at the test start, with the specimen in its initial unloaded undeformed position. Thereafter, photographs were taken at various stages of loading. Typically, a photograph was taken at the beginning of a load cycle, with no

applied load on the deformed test specimen. Another photograph was then taken at the end of the same load cycle, with the specimen under load at its peak deformation for that cycle. With this photo sequence, it was possible to compute deformations with respect to the initial undeformed state of the specimen, and also with respect to the state of the specimen in its last unloaded, but deformed, position.

5.2 REDUCTION OF PHOTOGRAMMETRIC DATA

After the photographic plates were exposed and developed for each specimen, the next step was to read the gridpoint locations on the plates. The data from each plate was then transformed into a common coordinate system. In this section, the reading and transformation of the photogrammetric data is briefly described.

Reading of Photogrammetric Data

The location of the gridpoints and target points were measured on each photographic plate using a Kern MK-2 comparator. With this device, plane rectangular coordinates of any point on the plate can be read with respect to an arbitrary coordinate system defined by the comparator. The least count of the Kern MK-2 comparator is 1 micrometer (0.001mm). That is, the location of points on the plate can be read with a precision of 0.001mm. It was found that the repeatability of multiple measurements for a given gridpoint on the web was on the order of $\pm$ 5 micrometers. Gridpoints located on the link flange were found to be somewhat more difficult to read. The flange gridpoints were located in a different plane than the web points and were not as sharply focused. It is estimated that flange gridpoints could be read from the plate with an accuracy of about $\pm$ 10 micrometers.

The gridpoints for each specimen were identified using an arbitrary numbering system. The number of gridpoints was rather large for most specimens, ranging from about 300 points for Specimen 4 up to approximately 1000 points for Specimen 6. Reading these points with the comparator is a manual, time consuming process. Consequently, not all plates were read for each specimen and not all gridpoints were read for each plate. Rather, only the plates and gridpoints which were expected to provide the most useful data were read with the comparator. Because of the large number of gridpoints, each point was generally read only once. The target points, however, were read several times and the resulting coordinates averaged in order to obtain improved accuracy for these points.

The result of the comparator reading process is the coordinates of the gridpoints and target points for each plate. The location of the origin and orientation of the axes for the coordinate system is arbitrary and is different for each plate. This initial arbitrary coordinate system for each plate is referred to as the *comparator coordinate system*. Coordinates of points in this system are designated $(r_{x\,i}, r_{y\,i})$, where i is the gridpoint or target number.

After the comparator coordinates are read from each plate for a particular specimen, the coordinates are transformed to a single common coordinate system for the specimen, in the scale of the actual test specimen. The scale and choice of the final common coordinate system are established from the first plate of each test specimen. Comparator coordinates of points on subsequent plates are then transformed to this new coordinate system defined by the first plate. Consequently, the data reduction procedures are different for the first plate than for the subsequent plates of each test specimen. These individual procedures are described below:

Data Reduction for Plate No. 1 of Each Specimen

The first photographic plate for each test specimen was taken with the specimen in its initial unloaded and undeformed position. The first step in data reduction for this plate is to scale the comparator coordinates for grid and target points to the scale of the actual test specimen. A scale factor for the plane of the link web is established from the measured distances between the real target points compared to the distances between the target point images on the plate. The comparator coordinates for web gridpoints and target points are then simply multiplied by this scale factor. For specimens with gridpoints on the flanges, a separate scale factor is established from distances measured between selected flange gridpoints on the actual specimen prior to testing. The comparator coordinates of the flange gridpoints are then multiplied by this scale factor. At this stage, all coordinates are also converted from units of micrometers to units of inches for convenience.

After the above scaling and unit conversion, the coordinates of the gridpoints and targets are designated as $(r'_{x\,i}, r'_{y\,i})$, where $r'_{x\,i} = S\, r_{x\,i}$, $r'_{y\,i} = S\, r_{y\,i}$ and S is a combined scale and unit conversion factor. As noted above, S is slightly different for flange gridpoints than for web gridpoints and target points.

The scale between the image on the photographic plate and the actual test specimen was approximately 1 to 14.8 for web and target points and approximately 1 to 14.6 for flange gridpoints. The link flanges of all test specimens were 4 inches wide. Therefore, the plane containing the flange gridpoints was 2 inches closer to the camera than the plane of the web and target points, accounting for the slightly different scale. It should be noted that the accuracy to which the scale factor is determined is of little importance. The final quantities of interest, strains and rotations, are dimensionless and therefore independent of scale. Consequently, the scale factor has no effect on the accuracy of these quantities. The coordinates are scaled only as a matter of convenience.

The scaled comparator coordinates $(r_{x\,i}, r_{y\,i})$ are still defined in a coordinate system that is of arbitrary orientation with respect to the test specimen. The next step is to translate and rotate this coordinate system to a final, more convenient coordinate system. This final coordinate system is chosen so that the x-axis is parallel to the centerline of the undeformed link, and the location of the origin is arbitrarily chosen so that all coordinates are positive in sign. This final coordinate system will be referred to as the *specimen coordinate system*, and the coordinates of gridpoints and

target points are designated as (x_i, y_i) in this system.

Data Reduction for Subsequent Plates

The comparator coordinates for gridpoints on all subsequent plates for a specimen are transformed to the specimen coordinate system defined by plate no. 1 of that specimen. As the first step in this process, the comparator coordinates $(r_{x\,i}, r_{y\,i})$ of all points on the plate are scaled and converted to inches using the identical scale factors determined from plate no. 1. This results in the scaled comparator coordinates $(r'_{x\,i}, r'_{y\,i})$ for each point on the plate.

The scaled comparator coordinates $(r'_{x\,i}, r'_{y\,i})$ are transformed into the specimen coordinates (x_i, y_i) using an *eight-parameter transformation* [43]. The use of the eight-parameter transformation also adjusts the coordinates of the gridpoints for the effects of any change in camera tilt which may have occurred after photographing plate no. 1. Coordinates are therefore transformed to a common coordinate system in a common plane.

The eight-parameter transformation can be written as follows [43]:

$$x_i = \frac{a_1 r'_{x\,i} + b_1 r'_{y\,i} + c_1}{a_0 r'_{x\,i} + b_0 r'_{y\,i} + 1} \tag{5.1a}$$

$$y_i = \frac{a_2 r'_{x\,i} + b_2 r'_{y\,i} + c_2}{a_0 r'_{x\,i} + b_0 r'_{y\,i} + 1} \tag{5.1b}$$

In this equation, $(r'_{x\,i}, r'_{y\,i})$ are the scaled comparator coordinates for point i, and (x_i, y_i) are the final transformed coordinates for the same point. The constants $a_0, b_0, \cdots c_1, c_2$ are the eight parameters controlling the transformation. These eight parameters are determined from the coordinates of the four target points. For each target point, the coordinates $(r'_{x\,i}, r'_{y\,i})$ are substituted into the right hand side of Eqs. 5.1a and b. On the left hand side of these equations, the coordinates (x_i, y_i) of the same target point on plate no.1 are substituted. Repeating this process for each of the four target points results in a system of 8 linear equations that can be solved for the eight unknown parameters. After these eight parameters are established, Eqs. 5.1a and b can be used to transform all gridpoints on the plate from the scaled comparator coordinates $(r'_{x\,i}, r'_{y\,i})$ to the final coordinates (x_i, y_i).

After the above transformation is accomplished, a final correction is applied to the flange gridpoints. Because the flange gridpoints are in a different horizontal plane than the web gridpoints, the location of the flange points are offset with respect to the web points on the photographs. To correct for this effect, the coordinates of the flange gridpoints are translated so that the flanges appear in the correct position with respect to the web of the section. This correction is done in an approximate manner using the known dimensions of the section. Since this is an approximate correction, the resulting accuracy of distances between points on the flange and points

on the web is rather poor. This is of little consequence, however, since strains and rotations will be computed independently for web points and flange points. The system of photogrammetric measurement used for these tests does not permit accurate determination of the relative displacement of a point in one horizontal plane measured with respect to a point in a different horizontal plane.

The end result of the transformations and corrections described above are the specimen coordinates (x_i, y_i) of each gridpoint; on each photographic plate. These coordinates are all defined with respect to a single common coordinate system defined for each test specimen.

5.3 COMPUTATION OF DISPLACEMENTS, STRAINS AND ROTATIONS

After initial reduction of the photogrammetric data as described in section 5.2 was completed, this data was used to determine various response parameters of interest for the test specimens. The major objective of this stage of the analysis was to compute and plot the following response parameters:

- undeformed and deformed gridpoint locations
- shear strain in the web of the link and/or brace connection panel
- average rotation of web gridlines
- rotation of lines defined by flange gridpoints (Specimens 6, 9 and 12)
- extensional strain in flanges of link and brace connection panel

Each of these items are computed using the gridpoint coordinates (x_i, y_i) defined in the specimen coordinate system. Further, all displacements, strains and rotations are computed with respect to the test specimen moving from a *reference state* to a *final state*. The *final state* is typically defined by the gridpoint coordinates for the specimen at the point of peak deformation, under load, for a particular load cycle. The corresponding *reference state* can be taken either as the initial unloaded undeformed state of the specimen or as the unloaded, but deformed state of the specimen at the start of the load cycle. Whenever results of this analysis are presented, the applicable reference and final states will be identified.

The computation of displacements, strains and rotations as well as the plotting of these quantities were all accomplished using the Unix based computer program "S" [32]. This program permitted reasonably simple and efficient analysis and plotting of the rather large quantity of photogrammetric data. All analysis and plotting were accomplished on a Digital Microvax Workstation.

In the following sections, the methods used to compute displacements, strains and rotations are briefly described. The results of the analyses are presented in plots in Section 5.4.

Displacements

In the specimen coordinate system, the x-axis is parallel to the centerline of the undeformed link, and the y-axis is therefore normal to the undeformed link centerline. The displacement of gridpoint i in a direction parallel to the x-axis, as the specimen moves from the reference state to the final state, is defined as u_i. The displacement of the same point parallel to the y-axis is defined as v_i. These quantities can be expressed as follows:

$$u_i = x_{i\,final} - x_{ref} \tag{5.2a}$$

$$v_i = y_{i\,final} - y_{i\,ref} \tag{5.2b}$$

where $x_{i\,ref}$ is the x coordinate of gridpoint i in the reference state, and so on.

For plots showing the deformed gridpoint locations, the displacements u_i and v_i were added to the coordinates of the gridpoint i for the specimen in its initial undeformed unloaded state. Further, for plotting purposes, the displacements were typically amplified in order to more clearly show the overall deformation patterns. Thus, for plots showing deformed grids, the gridpoint i is plotted at the coordinates $(x_{i\,initial} + \alpha u_i, y_{i\,initial} + \alpha v_i)$, where $x_{i\,initial}$ and $y_{i\,initial}$ are the coordinates of the point in the initial undeformed unloaded state of the specimen, and α is the displacement amplification factor, usually taken as 5 for most plots. Note that with this approach, the deformed grid plots do not typically show the gridpoint locations in the specimen's final state. Rather, these plots show the deformations developed within the specimen in moving from the reference state to the final state.

Shear Strains

Shear strains were estimated from gridpoint displacements throughout the web of a specimen by using some basic techniques developed for finite element analysis [44]. With this approach, the web grids were treated as a finite element mesh consisting of 4-node isoparametric elements. In this application, the "nodes" correspond to the gridpoints. These basic finite element techniques, as applied to the photogrammetric data, are briefly reviewed below.

An "element" is defined as the quadrilateral formed by 4 neighboring web gridpoints. A typical element in the reference state is shown in the specimen coordinate system in Fig. 5.3a. For convenience, the gridpoints are numbered from 1 to 4 as shown. The elements formed by the gridpoints are typically close to but not exactly rectangular, since the reference state may be defined for the specimen in an unloaded, but deformed (due to residual plastic deformation) position.

Following the approach used for isoparametric finite elements, the element shown in Fig. 5.3a is transformed to a square element in a normalized coordinate system defined by the variables ξ and η, as shown in Fig. 5.3b. The sides of the element are located at $\xi = \pm 1$ and $\eta = \pm 1$. The coordinate mapping between the normalized and the specimen coordinate systems is accomplished

by means of standard shape functions [44] as follows:

$$x(\xi,\eta)=\sum_{i=1}^{4} N_i(\xi,\eta)\,x_i \tag{5.3a}$$

$$y(\xi,\eta)=\sum_{i=1}^{4} N_i(\xi,\eta)\,y_i \tag{5.3b}$$

where (ξ,η) are the normalized coordinates of any point within the element in Fig. 5.3b and (x,y) are the specimen coordinates of the corresponding point in Fig. 5.3a. As before, (x_i,y_i) are the coordinates of the 4 gridpoints in the specimen coordinate system, taken in the reference state. The four shape functions are defined as:

$$N_i=\frac{1}{4}(1+\xi\xi_i)(1+\eta\eta_i) \quad i=1,2,3,4 \tag{5.4}$$

where ξ_i and η_i are the normalized coordinates of gridpoint i in Fig. 5.3b.

Using these same shape functions, the displacement of any point within the normalized element is computed as:

$$u(\xi,\eta)=\sum_{i=1}^{4} N_i(\xi,\eta)\,u_i \tag{5.5a}$$

$$v(\xi,\eta)=\sum_{i=1}^{4} N_i(\xi,\eta)\,v_i \tag{5.5b}$$

where u_i and v_i are the displacements of gridpoint i in the specimen coordinate system, in moving from the reference state to the final state, as defined by Eqs. 5.2a and b.

The engineering shear strain at point (ξ,η) is then computed as:

$$2\epsilon_{xy} = \frac{\partial u}{\partial y}+\frac{\partial v}{\partial x} \tag{5.6}$$

which, in terms of Eq. 5.5, results in:

$$2\epsilon_{xy} = \sum_{i=1}^{4}\frac{\partial N_i(\xi,\eta)}{\partial y}u_i + \sum_{i=1}^{4}\frac{\partial N_i(\xi,\eta)}{\partial x}v_i \tag{5.7}$$

The term ϵ_{xy} is the tensor definition of shear strain, and $2\epsilon_{xy}$ therefore represents the engineering shear strain. The term $2\epsilon_{xy}$ is used here because the usual symbol for engineering shear, γ, is used for link rotation in the present context.

The partial derivatives of the shape functions in Eq. 5.7 are computed as follows:

$$\frac{\partial N_i}{\partial x} = \frac{1}{|J|}\left(\frac{\partial N_i}{\partial \xi}\frac{\partial y}{\partial \eta}-\frac{\partial N_i}{\partial \eta}\frac{\partial y}{\partial \xi}\right) \tag{5.8a}$$

$$\frac{\partial N_i}{\partial y} = \frac{1}{|J|}\left(\frac{\partial N_i}{\partial \eta}\frac{\partial x}{\partial \xi}-\frac{\partial N_i}{\partial \xi}\frac{\partial x}{\partial \eta}\right) \tag{5.8b}$$

where $|J|$ is the determinant of the Jacobian matrix, computed as:

$$|J| = \frac{\partial x}{\partial \xi}\frac{\partial y}{\partial \eta} - \frac{\partial y}{\partial \xi}\frac{\partial x}{\partial \eta} \tag{5.9}$$

Thus, using Eq. 5.7, the shear strain can be computed for any point within the element defined by the normalized coordinates (ξ,η). Since linear shape functions are used to interpolate displacements in Eqs. 5.5a and b, the shear strain computed by Eq. 5.7 will be independent of ξ and η. That is, the above computations result in a constant value of shear strain for any point within the element.

Shear strains were computed by Eq. 5.7 from web gridpoint displacements. The computed shear strain for each element was assumed to be most characteristic of the shear strain at the center of the element, defined by $\xi=0, \eta=0$. By Eqs. 5.3, the element center in the specimen coordinate system is at the average of the x and y coordinates of the 4 corner gridpoints. Thus, a value of shear strain was computed for each web "element" by Eq. 5.7 and assigned to a location corresponding to the center of the element for purposes of plotting shear strains.

Rotations

The rotation of a nominally vertical line on the cross section of the specimen, as the specimen moves from the reference state to the final state, provides an indication of the contribution of bending to the total deformation. In the present context, a "vertical" line refers to a gridline that is originally drawn normal to the link centerline. Because of the influence of large inelastic shear strains, warping of the link cross section occurs as the link deforms. That is, the "plane sections remain plane" hypothesis cannot, in general, be applied to links, particularly short and intermediate length links.

Because the cross section does not remain plane as it deforms, the manner in which rotation of the line should be defined is not entirely clear. However, for the present purposes, the rotation of a vertical web gridline will be computed simply as the average of the rotations determined from the individual gridpoints that make up the line. Some of the terms used in computing rotations are illustrated in Fig. 5.4. This figure shows a typical vertical gridline in the reference state, and the same line in the final state. This vertical gridline would originally have been a straight line on the initial undeformed specimen. However, due to the influence of cross sectional warping, the gridline will not, in general, be a straight line in either the reference or final configurations.

With reference to Fig. 5.4, the average rotation of a gridline is computed as follows:

$$\theta_{avg} = \frac{1}{n}\sum_{i=1}^{n}\frac{y_{i\,final} - y_{avg}}{u_{avg} - u_i} \tag{5.10}$$

where n is the number of gridpoints on the line, $y_{i\,final}$ is the y coordinate of point i in the final state and u_i is the x - direction displacement of point i as defined in Eq. 5.2a. The quantities u_{avg} and y_{avg} are defined in Fig. 5.4. Each term in the summation in Eq. 5.10 represents a

measure of rotation for a hypothetical line extending from mid-depth of the web gridline to an individual gridpoint. Eq. 5.10 therefore represents some average measure of gridline rotation.

For specimens which were also provided with flange gridpoints, a separate computation was performed to determine the rotation of vertical lines defined by the flange gridpoints. For this case, a line is defined by only two points: a point on the top flange and a corresponding point (with the same nominal x coordinate) on the bottom flange. These rotations were also computed using Eq. 5.10.

Extensional Strain in Flange

For specimens with gridpoints on the flanges, the extensional strains developed in the flanges as the specimen moved from the reference state to the final state were computed. The engineering definition of extensional strain was employed for this purpose. Thus, the extensional strain developed between two gridpoints was simply computed as the change in distance between the two gridpoints in moving from the reference to the final state, divided by the distance between the gridpoints in the reference state. This provides an average measure of the extensional strain in the region between the two gridpoints.

The flange gridpoints were drawn at approximately mid-depth of the flange. The computed extensional strain therefore does not represent the maximum strain at the outer edges of the flanges. It should also be recognized that extensional strain may vary considerably over the width of the flange. Consequently, the gridpoints provide a measure of the extensional strain at only one edge of the flange. This strain may differ substantially from the average extensional strain over the width of the flange.

Errors in Photogrammetric Data

There are several potential sources of error in the photogrammetric data. As previously discussed, some error is introduced when reading gridpoints on the photographic plates with the comparator. Based on experience with the comparator, this error was estimated as $\pm$ 5 micrometers for web gridpoints and $\pm$ 10 micrometers for flange gridpoints at the scale of the photograph. Based on an approximate scale of 1:15, the corresponding errors in the specimen coordinate system are $\pm$ .003 in. and $\pm$ .006 in. Errors in gridpoint coordinates can also result from out-of-plane displacements of the test specimen [42]. Such errors may become particularly important, for example, after local buckling of the web. No attempt is made here to quantify this source of error. However, in Section 5.4, those cases where out-of-plane buckling may have substantially affected the photogrammetric data are identified. Most of the photographs were taken before severe local buckling occurred within the test specimens.

A rigorous error analysis to determine how errors in gridpoint coordinates affect the accuracy of the computed strains and rotations was not attempted. However, some indication of the

accuracy of the final computed quantities can be obtained from examination of this data.

A reasonable estimate of the accuracy of photogrammetrically computed shear strains can be obtained by comparison with the corresponding shear strains measured by strain gage rosettes on the link web. Such comparisons are shown for several cases for Specimens 1 and 4 in Tables 5.1 and 5.2. As discussed in Section 4.6, shear strain rosettes were located along the link centerline, typically at about mid-length of each panel of the link. (See Table 4.6, for example). The 3rd and 4th columns of Tables 5.1 and 5.2 provide a direct comparison of shear strains at nominally identical locations on the link web. In many cases the photogrammetric grid was interrupted at the location of the rosette to accommodate the rosette or its lead wires. For these cases, the photogrammetric shear strain at the rosette location was estimated as the average shear strain computed from "elements" surrounding the rosette location. Since shear strain gradients are typically rather low within the web, this local averaging should introduce little error.

Examination of the data in Tables 5.1 and 5.2 indicates, in general, very good agreement between the photogrammetric and rosette shear strains. In most cases, these quantities agree within 0.001 to 0.002 rad. In a few cases, however, this difference is as large as 0.006 rad. Note that the rosette shear strain measurements are also subject to some error, and so the differences cannot be attributed solely to photogrammetric errors. However, based on the data in Tables 5.1 and 5.2, the shear strains determined by these two independent means tend to corroborate one another.

Based on the above data, the error in photogrammetric shear strains is estimated in general to be on the order of $\pm$ .003 rad, though it may be somewhat higher in some instances. For the rather large shear strains developed within the web of short and intermediate length links, perhaps on the order of .02 to .10 rad, this can be considered an acceptable level of error.

For photogrammetrically computed rotations, no independent check on the data was available. However, some indication of the quality of this data can be obtained by studying the plots of rotation versus distance along the link. See for example, Fig. 5.36. These plots generally show a rather smooth, continuous variation of rotation along the length of the link, providing good confidence in the accuracy of the computed rotations. Based on these plots, the error in the photogrammetric rotations is estimated to be on the order of $\pm$ 0.002 rad. This is again considered an acceptable level of error, since the computed rotations were typically on the order of 0.02 to 0.06 rad.

In contrast to shear strains and rotations, the photogrammetrically computed flange extensional strains generally showed somewhat erratic behavior. This behavior is visible in the flange strain plots, for example Fig. 5.24. As discussed earlier, greater difficulty was encountered in reading flange gridpoints as compared to web gridpoints on the photographic plates. This was particularly true towards the outer edges of the plates. Unfortunately, this area of the plates generally

coincided with the link ends, which of course are the regions of the link of greatest interest for flange strains. However, some of the erratic behavior in the flange strain plots may, in fact, reflect the actual behavior of the specimen. This is particularly true in regions of flange buckling or in regions where a substantial variation of bending strain exists over the width of the flange. In any event, the flange strain plots suggest rather poor confidence in this data, with errors perhaps on the order of ± 2 percent strain. Consequently, the flange strain data must be interpreted with caution.

5.4 RESULTS OF PHOTOGRAMMETRIC ANALYSIS

Photogrammetric data was collected for Specimens 1, 4, 6, 9 and 12. The links of Specimens 1 and 4 fell in the intermediate length range of combined shear and flexural yielding, the links for Specimens 6 and 12 were in the very long range of predominately flexural yielding, and the link of Specimen 9 was in the short length range of predominate shear yielding. These specimens therefore represent a wide range of possible link behavior. Gridlines were drawn on the webs for all of these specimens. Gridpoints were also drawn on the flange edges for Specimens 6, 9 and 12.

In this section, the results of the photogrammetric analysis are presented as plots showing displacements, shear strains, rotations and flange strains. As described in Section 5.3, these quantities are computed for the specimen moving from a given *reference state* to a given *final state*. Accordingly, the appropriate reference state and final state are noted on each plot.

In plots showing undeformed and deformed gridline locations, gaps sometimes are present in portions of the grids. These gaps correspond to strain gage locations or to locations where gridpoints were not visible on the photographic plates due to obstructions caused by other instrumentation. For all plots presented in this section, the test specimens are oriented so that the column end of the link is on the left.

In the presentation of shear strain data, reference is made to panel locations on the specimens. A panel is the region between two stiffeners. Panel designations for each specimen are shown in Fig. 5.5. In the remainder of this section, the results of the photogrammetric data analysis are presented for each of the five test specimens.

Specimen 1

The web gridlines for Specimen 1 are shown in the initial undeformed position in Fig. 5.6 and in the deformed configuration at several stages of loading in Fig. 5.7. At cycle 4W, shown in Fig. 5.7a, inelastic activity was not yet visible in the overall response of the specimen. Therefore, Fig. 5.7a represents essentially elastic deformations. The other deformed grids in Fig. 5.7 correspond to later loading cycles after significant link yielding had occurred. In each of the plots showing deformed gridlines, the initial undeformed grid is shown in dotted lines for purposes of comparison.

The deformed grid in Fig. 5.7a shows a large influence of shear on the elastic deformations. Shear deformation is evidenced by the parallelogram shaped elements, as well as by the lack of rotation of initially vertical gridlines.

The deformed grids for the yielded links, Fig. 5.7b and c, show a combined influence of shear and bending. The influence of bending is evidenced by the rotation of initially vertical gridlines. Flange buckling in the link of Specimen 1 was first observed in cycle 8W and was quite severe by cycle 13. The influence of flange buckling is evident in the upper portion of panel 1 in Fig. 5.7c. The photogrammetrically measured gridpoint displacements in this region are therefore likely influenced by out-of-plane displacements of the web, since localized web buckling accompanied the flange buckling. This plot, however, clearly shows the effect of severe flange buckling, with the upper portion of panel 1 essentially smaller in width than the lower portion of the panel, resulting in highly localized rotation of the link. All three deformed grids shown in Fig. 5.7 also indicate that shear deformations are largest near mid-depth of the section and tend to decrease near the flanges.

The distribution of shear within the link web is illustrated in Figs. 5.8 to 5.10. Figure 5.8 shows shear strain contours for two cases, both of which show similar trends. Larger shear strains are apparent within the link end panels, with the highest strains occurring in the end panel adjacent to the column. It also appears that shear strains are highest near mid-depth of the section all along the link.

The average web shear strain is plotted along the length of the link in Fig. 5.9. Each point on this plot represents an average of the shear strains for a single vertical line of elements running over the height of the web. The lines drawn on this plot are fit to the points by regression analysis, and are provided to more clearly illustrate shear strain variations. This plot illustrates that shear strains are quite uniform over the central portion of the link, and increase towards the link ends. This agrees with observations from strain gage measurements in Fig. 4.43a.

The effects of bending-shear interaction at the link ends are clearly visible in Fig. 5.9. It is also interesting to note that shear strains appear to drop rather suddenly at the very ends of the link. This is particularly evident at the brace end of the link. This effect can be attributed to warping restraint at the link ends. The essentially elastic regions beyond the link ends restrain the development of inelastic shear strain within a small region near the link ends. The effects of warping restraint appear to be highly localized at the link ends, and dissipate rather rapidly in the regions away from the very ends of the link. Figure 5.9 also shows very high shear strains in the region adjacent to the column for cycle 13E. These strains must be interpreted with caution, since web distortions associated with flange buckling in this region may have introduced additional errors into the photogrammetric data. It should be noted, however, that strain gage measurements showed a similar trend of very high shear strains near the column end of the link for the later

loading cycles (Fig. 4.43a). Thus, the high shear strains shown in Fig. 5.9 near the column end of the link, may in fact be representative of the actual web behavior. As discussed in Section 4.6, it may be postulated that the occurrence of severe flange buckling will cause the web to carry a larger share of the link end moment, which in turn may result in a greater apparent effect of bending-shear interaction.

The plots in Fig. 5.10 show distributions of average shear strain over the depth of the web for each of the 5 link panels. Each point on these plots represents an average of the shear strains for a single horizontal line of elements within the panel. The lines drawn on the plots were established by regression. For the points representing load cycle 7E, the rather low levels of shear strain appear to be fairly uniform over the depth of the web. In contrast, however, the plots for cycle 13E clearly show a pattern of the highest shear strain occurring near mid-depth of the section and then decreasing towards the flanges. These distributions are somewhat similar in appearance to the parabolic elastic shear strain distribution normally expected in the web of a *W* section. Note that these plots represent strain distributions only. No conclusions can be drawn on the distribution of shear stresses from this data.

Finally, Fig. 5.11 shows the average rotation of vertical web gridlines, plotted along the length of the link. Each point on this plot represents the average rotation of a single vertical web gridline, as described in Section 5.3. These plots provide an indication of the influence of bending on link deformation. Figure 5.11 shows that rotations develop very rapidly at the link ends, and then remain virtually constant over the central portion of the link. This rather clearly demonstrates that inelastic bending deformations are concentrated at the link ends. It is also evident from this plot that bending deformations are significantly more severe at the column end of the link than at the brace end of the link, as evidenced by the more rapid change in rotation. The column face apparently acts as a much more rigid support for the link than does the brace connection panel. Deformations developed within the brace connection panel appear to substantially reduce bending deformations developed at the link end. This substantiates the observation in Chapter 4 that limited yielding within the brace connection panel may be quite beneficial to the link.

Specimen 4

The web gridlines for Specimen 4 are shown in the undeformed state in Fig. 5.12, and at two different stages of deformation in Fig. 5.13. The deformed grids again clearly show the combined influence of bending, evidenced by rotation of gridlines, and of shear, evidenced by the parallelogram shaped deformations of the initially rectangular elements. As with Specimen 1, the deformation patterns show a greater influence of shear near mid-depth of the section.

Shear strain deformation patterns are illustrated in Figs. 5.14 to 5.16. The contours in Fig. 5.14 and the plot in Fig. 5.15 again show a clear pattern of higher shear strains near the link ends.

The shear strain distribution shown in Fig. 5.15, in contrast to Specimen 1 (Fig. 5.9), indicates that the influence of bending on shear strain extended over a rather large portion of the link. The influence of warping restraint at the link ends is also clearly visible in Fig. 5.15.

The variation of shear strain over the depth of the web, plotted in Fig. 5.16, shows somewhat erratic behavior at the lower strain levels for cycle 8E. However, at the larger strain levels of cycle 11E, parabolic shaped distributions are again apparent. The shear strain distribution in the panel adjacent to the brace (panel 4) appears to be somewhat skewed towards the upper portion of the plot. That is, the shear strains are somewhat larger towards the side of the link attached to the brace. The same behavior is also visible in panel 5 of Specimen 1 (Fig. 5.10). The shear force carried by the link must ultimately be transferred to the brace. These plots appear to show the influence of shear being "drawn" towards the brace in the region near the end of the link.

The average rotation of web gridlines are plotted for two different load cycles in Fig. 5.17. The development of bending deformations appears to be not as concentrated at the link ends as for Specimen 1 (Fig. 5.11). The nominal link lengths for Specimens 1 and 4 were both about $2M_p/V_p$. The different bending deformation patterns developed between these two links can likely be attributed to the different flange thicknesses. The thicker flanges and the resulting lack of flange buckling in Specimen 4 apparently permitted inelastic bending deformations to propagate for a large distance from the link ends.

Specimen 6

Specimen 6 was an example of a very long link (nominal $e = 3.15M_p/V_p$) with slender flanges. At this length, flexure is expected to dominate link behavior. Photogrammetric data was collected for gridpoints on the web of both the link and brace connection panel as well as for gridpoints on the edges of the flanges of the link and brace connection panel. The gridlines for Specimen 6 in the initial undeformed state are shown in Fig. 5.18. A single gridline was drawn along the length of each flange, at about mid-depth of the flange thickness. These two lines have been omitted in Fig. 5.18 for clarity.

The deformed grids for Specimen 6 are shown for 3 different conditions related to load cycle 10E in Fig. 5.19. Figures 5.19a and b show the grid deformations at the start and end of cycle 10, computed with respect to the initial undeformed state of the specimen. These two plots therefore reflect the actual appearance of the specimen at these two points in the load history, except that displacements are amplified by a factor of 5. Note that the plot in Fig. 5.19a corresponds to the unloaded state of the specimen at the start of cycle 10E. This grid therefore shows residual, permanent deformations in the specimen after completion of load cycle 9W. The deformed grid in Fig. 5.19c shows displacements of the specimen as it moved from the state in Fig. 5.19a to that of Fig. 5.19b, i.e., in moving from zero to peak load (and deformation) during load cycle 10E.

In contrast to Specimens 1 and 4, the plots in Fig. 5.19 show little influence of shear on the overall deformation patterns. The plots also show the important influence of flange buckling on overall link behavior. It is evident from these plots that link rotations were supplied by localized deformations at the link ends. Deformations are concentrated in a particularly short length at the column end of the link. At the other end of the link, it is apparent that a substantial portion of the link rotation is supplied by deformations in the brace connection panel. This is particularly evident in Figs. 5.19b and c, where it can be seen that flange buckling occurs in the east flange of the brace connection panel in preference to the link.

The plots in Fig. 5.19 also show highly localized flange deformations at the tips of the reinforcing ribs located at the link-to-column connection. In Chapter 3, the observation was made that the abrupt change in strength and stiffness at the tips of the ribs contributed to the fracture of the link flange at this location. The flange deformations plotted in Fig. 5.19 substantiate this observation. For the highly concentrated and localized deformations developed at the column end of a long link, a reinforcing scheme that provides a more gradual transition into the reinforced region of the connection is preferred. The triangular cover plates used to reinforce the link-to-column connection of Specimen 11 is an example of such a scheme.

Even though flange buckling appears to be very severe in the amplified deformation plots of Fig. 5.19, the flange buckling on the actual specimen still appeared to be quite mild at this stage of loading. For comparison, a photograph of the column end of the link at the start of cycle 10E is shown in Fig. 5.20, corresponding to the plot of Fig. 5.19a. Flange buckling in this photograph appears fairly mild, particularly in comparison with flange buckling developed in subsequent load cycles (see Fig. 3.15d). Further, whereas the plots of Fig. 5.19 show flange buckling in the east flange of the brace connection panel, this buckling was not yet visible on the actual specimen. However, in the very next load cycle (cycle 11E), the flange buckling in the brace connection panel became very severe, and the overall load carrying capacity of the specimen dropped suddenly. Thus, Fig. 5.19 shows Specimen 6 at its point of maximum load carrying capacity. The plots substantiate earlier observations that flange buckling inside of a long link is much less detrimental than flange buckling immediately outside of the link within the brace connection panel.

Figure 5.21 shows average web shear strain plotted along the length of the link and brace connection panel. As before, each point on this plot represents an average of the shear strains computed for a single vertical line of elements on the web. As expected for a long link, this plot shows very low, essentially elastic levels of shear strain over the large central panel of the link. However, near the link ends, rather large inelastic shear strains are developed within the link web. This agrees with strain gage observations made for Specimen 5 (Fig. 4.48). Evidence of warping restraint at the link ends is also visible in Fig. 5.21. The plot of Fig. 5.21 indicates that inelastic shear strains have an important effect on the local behavior at the ends of even very long links.

The distribution of shear strain over the depth of the web is plotted for the various panels of Specimen 6 in Fig. 5.22. These plots show somewhat erratic behavior due to the generally low levels of shear strain, for which the effect of photogrammetric data errors are relatively larger. Mild out-of-plane web displacements near the link ends may have also contributed to somewhat larger photogrammetric errors. Nonetheless, some useful trends can be spotted within these plots. It is apparent that shear strains are very low within the central panel of the link (panel 2) and increase towards the link ends (panels 1 and 3). A remarkable feature of the plot for panel 1 is that shear strains are smallest near mid-depth of the section. This is exactly opposite to the behavior observed in Specimens 1 and 4. Somewhat larger shear strains are also visible in the brace connection panel, in the region immediately outside the link (panel 4).

Gridline rotations are plotted along the length of the link and brace connection panel in Fig. 5.23. The average rotation of web gridlines, as well as the rotation of flange gridpoints are both plotted on this figure. It can be seen that web and flange rotations are essentially the same, indicating little influence of cross sectional warping within the link. This plot also shows that rotations were highly concentrated at the column end of the link. In contrast, at the other end of the link, rotational deformations are less concentrated, and are developed over portions of both the link end and brace connection panel. It appears, in fact, that at the brace end of the link, greater rotations were developed within the brace connection panel than within the link.

Extensional strains computed from gridpoints on the flanges are plotted in Fig. 5.24. As discussed in Section 5.3, the effect of photogrammetric data errors appear to be significantly larger for flange strain computations. Consequently, these plots should be interpreted with caution, and viewed primarily for qualitative trends. As anticipated, these plots show very low levels of bending strain in the central portion of the link, and rather high levels at the link ends. At the column end of the link, a sudden drop in bending strain is apparent within the region of the reinforcing ribs, as expected. At the brace end of the link, Fig. 5.24b indicates that strains in the east flange are higher in the brace connection panel than in the link. This agrees with observations of flange buckling in this region. At the west flange, on the other hand, strains appear to be higher in the link than in the brace connection panel. The brace is welded to the west flange of the panel, thereby reinforcing this flange. The different behavior of the east and west flanges of the brace connection panel are also likely influenced by axial forces developed outside of the link, as discussed in Chapter 3.

Specimen 9

Specimen 9 was provided with a short (nominal $e = 1.2M_p/V_p$), predominately shear yielding link. Photogrammetric data was collected for this specimen from gridpoints on the web of the link, and on the flanges of the link and brace connection panel. Gridline and gridpoint locations for the initial undeformed configuration are shown in Fig. 5.25.

Deformations developed during load cycle 9E are plotted in Fig. 5.26. Large shear deformations of the web are evident in the parallelogram shaped elements, as well as in the absence of rotation of vertical gridlines. Comparing this with the deformed grid of Specimen 6 (Fig. 5.19) graphically illustrates the different mechanisms that supply rotation in very short versus very long links.

Figure 5.26 shows some localized deformations of the west flange in the panel adjacent to the column. This deformation was also visible during the course of testing (Fig. 3.22b). However, as described in Chapter 3, this flange distortion did not have the appearance of conventional unsymmetric flange buckling. Rather, the entire width of the flange was bent in the same direction. Figure 5.26 also shows a rather abrupt change in direction of the flanges at the junction of the link and brace connection panel, giving the appearance of a "kink" in the flanges. However, as will be discussed later, there is no evidence that this localized flange deformation had any detrimental effects on the flanges or on the specimen as a whole.

The distribution of shear strain over the link web is illustrated in Figs. 5.27 to 5.29. These plots show very large shear strains, with a fairly uniform distribution over most of the link. Shear strain levels increase near the column end of the link but not at the brace end of the link. This behavior is also evident from strain gage measurements (Fig. 4.49), and most likely reflects unequal link end moments, as discussed in Section 4.6. Somewhat surprisingly, the shear strain plot in Fig. 5.28 shows little evidence of warping restraint at the link ends, as was observed in previous specimens. The distribution of shear strain over the depth of the web, Fig. 5.29, shows a similar parabolic shape as was observed for Specimens 1 and 4.

The average rotation of web gridlines as well as the rotation of flange gridpoints are plotted in Fig. 5.30. The large difference in rotation between web and flange points indicates very severe warping of the link cross section. The plot of flange point rotation shows a very smooth transition between the link end and the brace connection panel. There is no abrupt change in rotation at the location of the kink observed in the plot of Fig. 5.26.

Extensional strains computed from gridpoints on the flanges are plotted in 5.31. These plots show very low strain levels throughout most of the link and brace connection panel, with strain levels increasing near the column. It also appears that strain levels in the east flange increase towards the end of the brace connection panel adjoining the beam. This likely reflects the influence of combined bending and axial force in the beam. Finally, there is no indication of higher flange strain levels at the junction of the link and the brace connection panel. Thus, whereas the deformed grid of Specimen 9 shows a kink in the flange at the brace end of the link, Figs. 5.30 and 5.31 indicate no localized increase in flange strain levels.

Specimen 12

Specimen 12 was another example of a very long link, with a nominal $e = 3.6M_p/V_p$. Specimen 12 was therefore in a similar length range as Specimen 6, with somewhat similar behavior anticipated. The link of Specimen 12, however, had much thicker flanges and therefore did not develop severe flange buckling, as was the case with Specimen 6.

The undeformed grid for Specimen 12 is shown in Fig. 5.32. Photogrammetric data was collected for gridpoints on the link web and flanges and on the brace connection panel flanges. The deformations developed during load cycle 7W are plotted in Fig. 5.33. The predominance of bending and the concentration of deformations near the link ends are readily apparent. Flange buckling is visible in the amplified deformation plot at the southeast and northwest flanges of the link. The actual flange buckling observed on the link at this stage of the loading was very mild. There was, however, some lateral torsional buckling of the link at this stage. The out-of-plane displacements associated with this buckling are not readily visible in Fig. 5.33.

Shear strain distribution within the link is represented by the plots in Figs. 5.34 and 5.35. The trends are similar to Specimen 6. Very small, essentially elastic shear strains are developed within the large central portion of the link. Larger, inelastic values of shear strains, however, are developed at the link ends. The influence of warping restraint at the link ends is also, again, clearly evident in Fig. 5.34. The average shear strain distributions plotted over the depth of the web, Fig. 5.35, also show a similar trend as Specimen 6, with the lowest shear strains occurring at mid-depth of the cross section.

The rotation of flange gridpoints and the average rotation of web gridlines are plotted in Fig. 5.36. In contrast to Specimen 9 (Fig. 5.30), the web and flange rotations are essentially equal, indicating little influence of cross sectional warping, except possibly near the link ends. Figure 5.36 also, again, clearly demonstrates that rotation at the brace end of the link is supplied by bending deformations both in the link and in the brace connection panel. This plot graphically illustrates how the brace connection panel reduces bending deformations in the link by supplying a share of the inelastic rotation demand. A similar reduction in bending deformations could presumably be achieved at the column end of the link by permitting the column panel zone to supply a significant share of the inelastic deformation demand.

The flange strains plotted in Fig. 5.37 show, as anticipated, low strain levels throughout the central portion of the link, and high strain levels at link end regions. In the east flange in the region near the brace end of the link, Fig. 5.37b indicates that higher strains are developed in the brace connection panel than in the link. Similar behavior was observed for Specimen 6 (Fig. 5.31b).

5.5 ESTIMATED LINK ROTATION COMPONENTS

In this section, the photogrammetric data, combined with other experimental measurements, will be used to estimate the components of link rotation due to link shear deformation, link bending deformation and link end support rotations. Such a division is of interest because different failure mechanisms and rotational capacities can be associated with each of these components.

The division of total link rotation into components can be expressed as follows:

$$\bar{\gamma} = \bar{\gamma}^{SR} + \bar{\gamma}^{bend} + \bar{\gamma}^{shear} \tag{5.11}$$

where $\bar{\gamma}$ is total link rotation, $\bar{\gamma}^{SR}$ is the component due to support rotation, both at the column and brace ends of the link, $\bar{\gamma}^{bend}$ is the component due to link bending deformations, and $\bar{\gamma}^{shear}$ is the component due to link shear deformations. Each quantity in Eq. 5.11 includes both elastic and plastic contributions. Consequently, Eq. 5.11 can be further subdivided as follows:

$$\bar{\gamma}_{el} = \bar{\gamma}_{el}^{SR} + \bar{\gamma}_{el}^{bend} + \bar{\gamma}_{el}^{shear} \tag{5.12a}$$

$$\bar{\gamma}_{p} = \bar{\gamma}_{p}^{SR} + \bar{\gamma}_{p}^{bend} + \bar{\gamma}_{p}^{shear} \tag{5.12b}$$

where the subscript *el* refers to the elastic component and the subscript *p* refers to the plastic component in each term. The bar above each quantity indicates that the quantity is measured from the last point of zero shear force on the link, up to the current point under consideration. This definition is illustrated in Fig. 5.38. Measuring deformations with respect to the initial undeformed configuration of the link has little physical significance in the present context.

The component $\bar{\gamma}^{SR}$ can be computed from the link end rotations and from the location of the link inflection point, by treating the link as two cantilever beams connected at the link's point of inflection. If $\bar{\theta}_c$ and $\bar{\theta}_b$ are defined as the rotations of the column and brace ends of the link, respectively, (measured from the last point of zero link shear) and d_c and d_b as the distance from the column and brace ends of the link to the point of inflection, with $d_c + d_b = e$, then

$$\bar{\gamma}^{SR} = \frac{\bar{\theta}_c\, d_c + \bar{\theta}_b\, d_b}{e} \tag{5.13}$$

For the point of inflection located at the midpoint of the link, the above equation simplifies to:

$$\bar{\gamma}^{SR} = \frac{\bar{\theta}_c + \bar{\theta}_b}{2} \tag{5.14}$$

For the test specimens considered in this section, end moments were sufficiently equalized to permit the use of Eq. 5.14 with little error. The quantities $\bar{\theta}_c$ and $\bar{\theta}_b$ can be determined from link end rotation measurements or can be estimated from photogrammetrically computed rotations.

After $\bar{\gamma}^{SR}$ is subtracted from the total link rotation $\bar{\gamma}$, the remaining rotation can be attributed to deformations developed within the link. Dividing this remaining rotation into components due to link bending deformations and link shear deformations is not necessarily a

straightforward process. In the presence of severe cross sectional warping and large shear strains that vary over the depth of the section, the physical interpretation of bending and shear deformation is no longer entirely clear.

One approach for separating beam deflections due to bending and shear is provided by sandwich beam theory [45]. Sandwich beam construction consists of two thin high strength layers, called the faces, separated by a thick layer of low strength material called the core. The faces, analogous to the flanges of a *W* section, are assumed to carry normal stresses only, whereas the core, analogous to the web, is assumed to carry shear stress only. Further, the distribution of shear strain over the depth of the core is assumed to be constant. A *W* section under combined shear and bending violates each of these assumptions. Nonetheless, an approach analogous to sandwich beam theory, using averaged web shear strain values, will be used here to differentiate between shear and bending deformations of the link. As will be seen, the resulting rotation computations provide reasonable results.

For sandwich beam theory, curvature of the cross section, from which bending deflections are computed, is defined with respect to a line passing through a point at mid-depth of each flange. Three of the test specimens (Nos. 6, 9 and 12) were provided with gridpoints at mid-depth of the flanges. The rotations computed from these points will be used as the basis for computing link deflection due to bending. With reference to a plot of flange gridpoint rotations, for example Fig. 5.30, the total area under this plot taken over the length of the link can then be interpreted as the link rotation resulting from both link bending and link end support rotations. This can be expressed as follows:

$$\bar{\gamma}^{SR} + \bar{\gamma}^{bend} = \int_e \bar{\theta}_f \, dx \tag{5.15}$$

where $\bar{\theta}_f$ is the rotation of the flange gridpoints measured from the last point of zero link shear and e is the link length. The value of $\bar{\gamma}^{SR}$ determined by Eq. 5.14 can then be subtracted from this quantity to obtain an estimate of $\bar{\gamma}^{bend}$.

Link rotation due to shear deformation is computed in a manner analogous to sandwich beam theory by assuming that the core shear strain of the sandwich beam is equal to the average shear strain of the link web computed from the photogrammetric data. Thus, with reference to a plot of average web shear strain, for example Fig. 5.28, the link rotation due to shear is estimated as follows:

$$\bar{\gamma}^{shear} = \lambda \int_e 2\bar{\epsilon}_{xy\,avg} \, dx \tag{5.16}$$

where $2\bar{\epsilon}_{xy\,avg}$ is the shear strain at any section of the link, averaged over the depth of web. The bar over this symbol again indicates that the shear strain is measured from the last point of zero shear force on the link. As noted earlier, $2\epsilon_{xy}$ is used to represent engineering shear strain since

the symbol γ is reserved for link rotation here. The factor λ in Eq. 5.16 relates the shear strain in the core to the shear deformation of the entire sandwich beam section. From the assumed geometry of the deformed sandwich beam, this factor can be estimated as follows [45]:

$$\lambda = \frac{d - t_f}{h_{web}} \tag{5.17}$$

where the numerator is the distance between mid-depth of the flanges, and the denominator is the depth of the web. If h_{web} is taken as the clear distance between the web-flange fillets of a W section, then λ is approximately 0.9 for both the $W12 \times 16$ and $W12 \times 22$ sections used for the test specimens.

In evaluating the integrals in Eqs. 5.15 and 5.16, the area was computed under a line fit to the photogrammetric data by regression analysis. These lines are shown on each of the appropriate plots. In many cases, the photogrammetric data did not extend to the very ends of the link. For such cases, data was extrapolated to the link ends, introducing a small uncertainty to the integrals.

The sum of the quantities computed by Eqs. 5.15 and 5.16 should account for the entire link rotation. This sum can therefore be compared to the value of $\bar{\gamma}$ measured independently by displacement transducers attached to the test specimens.

In order to estimate the plastic components of $\bar{\gamma}^{bend}$ and $\bar{\gamma}^{shear}$, the corresponding elastic link rotations can be estimated from simple theory and subtracted out of the total (elastic + plastic) rotations. From simple beam theory, elastic link rotation due to bending can be computed as:

$$\bar{\gamma}_{el}^{bend} = \frac{V}{3EI} \frac{(d_c^3 + d_b^3)}{e} \tag{5.18}$$

where V is the shear force on the link, e is the link length, and d_c and d_b are as previously defined. The elastic link rotation due to shear can be estimated by:

$$\bar{\gamma}_{el}^{shear} = \frac{V}{A_s G} \tag{5.19}$$

where A_s is the effective shear area and G is the elastic shear modulus. A detailed derivation for effective shear area is available from Cowper [46]. However, for most W sections, $A_s = d\, t_w$ provides an adequate approximation.

After estimating elastic bending and shear rotations, the plastic rotations are simply:

$$\bar{\gamma}_p^{bend} = \bar{\gamma}^{bend} - \bar{\gamma}_{el}^{bend} \tag{5.20}$$

$$\bar{\gamma}_p^{shear} = \bar{\gamma}^{shear} - \bar{\gamma}_{el}^{shear} \tag{5.21}$$

The sum of the quantities computed by Eqs. 5.20 and 5.21 should account for all plastic deformations developed within the link. Subtracting this sum from the overall plastic link rotation $\bar{\gamma}_p$ thus provides an estimate of $\bar{\gamma}_p^{SR}$, the link rotation due to plastic link end support rotations. The value

of $\bar{\gamma}_p$ can be evaluated from $\bar{\gamma}$ measured by displacement transducers and from the measured overall elastic stiffness of the link (Eq. 3.1). Values of $\bar{\gamma}_p^{SR}$ arise from yielding outside of the link, for example in the column panel zone or in the brace connection panel.

Using the process described above, link rotation components were computed for selected load cycles for Specimens 1, 4, 6, 9 and 12. The results of these computations are summarized in Tables 5.3 to 5.7.

Within the upper box in each table, the values of $\bar{\gamma}$ and $\bar{\gamma}_p$ computed from displacement transducers are listed. The next box lists the values of $\bar{\gamma}^{SR}+\bar{\gamma}^{bend}$ and $\bar{\gamma}^{shear}$ determined from photogrammetric data using Eqs. 5.15 and 5.16. The sum of these two quantities, as shown in the tables, should nominally be equal to the value of $\bar{\gamma}$ listed in the upper box. Since flange gridpoints were not available for Specimens 1 and 4, the integral in Eq. 5.15 was evaluated using the average web gridline rotations (Figs. 5.9 and 5.15) instead of the flange rotations. This introduces an additional level of approximation for these specimens.

In examining Tables 5.3 to 5.7, remarkably close agreement can be seen between the sum of the link rotation components determined by Eqs. 5.15 and 5.16 (the "Total" in the middle box) and the link rotation determined independently by displacement transducers (the value of $\bar{\gamma}$ listed in the upper box). This close agreement suggests that Eqs. 5.15 and 5.16 provide a reasonable approach for splitting total link rotation into bending and shear components. This agreement is also quite close for Specimens 1 and 4, even though bending deflections were computed from average web rotations instead of flange rotations. This suggests that the average rotation of the web was nearly equal to the rotation of the flanges in these intermediate length links.

In the lower box of Tables 5.3 to 5.7, link rotations are further subdivided. The link rotation due to link end support rotations, $\bar{\gamma}^{SR}$, was estimated using Eq. 5.14. This was then subtracted from the value of the integral in Eq. 5.15 to obtain an estimate of $\bar{\gamma}^{bend}$. Consequently, each of the individual rotation components, $\bar{\gamma}^{shear}$, $\bar{\gamma}^{bend}$ and $\bar{\gamma}^{SR}$ could be identified, and are listed in the first column. Next, $\bar{\gamma}^{shear}$ and $\bar{\gamma}^{bend}$ were divided into elastic and plastic components by Eqs. 5.18 to 5.21. The value of $\bar{\gamma}_p^{SR}$ was then taken as the difference between the sum of $\bar{\gamma}_p^{shear}$ and $\bar{\gamma}_p^{bend}$ and the total plastic rotation angle, $\bar{\gamma}_p$, as listed in the upper box. Finally $\bar{\gamma}_{el}^{SR}$ was computed as $\bar{\gamma}^{SR}-\bar{\gamma}_p^{SR}$.

The item of greatest interest in Tables. 5.3 to 5.7 is the division of plastic link rotation angle into the estimated plastic components of shear, bending and link end support rotations. This division is shown in the last column within the lower box of these tables. As might be anticipated, shear dominates the short link (Specimen 9), bending dominates the long links (Specimens 6 and 12), and significant amounts of both plastic shear and bending are evident for the intermediate links (Specimens 1 and 4). For the very long links of Specimens 6 and 12, where purely flexural yielding is expected, it is interesting to note that approximately 10 to 15 percent of the plastic link

rotation can still be attributed to inelastic shear deformations. These shear deformations arise from large inelastic shear strains developed at the link ends due to bending-shear interaction.

It is also of interest to note the rather large contribution of shear to the plastic rotations of Specimens 1 and 4. The nominal link length for both specimens was $2.0 M_p/V_p$. The link lengths based on actual section properties, however, were 2.25 and $2.3 M_p/V_p$ for Specimens 1 and 4, respectively (Table 2.12). As discussed in Chapter 1, the transition to predominately flexural yielding is currently assumed to occur at a length of about $2.6 M_p/V_p$. Specimens 3 and 4 were therefore close to this transition point. Yet, Tables 5.3 and 5.4 indicate that inelastic shear deformations accounted for 50 to 70 percent of the plastic link rotation. This observation suggests that the transition to predominately flexural yielding occurs at a length somewhat greater than $2.6 M_p/V_p$. Finally, Tables 5.3 to 5.7 confirm that yielding outside of the link can contribute substantially to plastic link rotation.

6. PRELIMINARY RECOMMENDATIONS FOR LONG LINK ULTIMATE STRENGTH, ROTATION CAPACITY AND STIFFENING

In this chapter, preliminary design recommendations are developed for the ultimate strength, rotation capacity and stiffening requirements of long links. In Chapter 1, the recommendation was made that long links ($e > 1.6M_p/V_p$) attached to columns should not be used in EBFs due to the poor reliability of long link-to-column connections. Consequently, the recommendations developed in this chapter are intended to apply to EBFs with the link located between two braces.

It is not possible to develop definitive design criteria based on the limited data provided by this experimental program. Considerable further investigation is required for long links before such criteria can be finalized. The preliminary recommendations developed in this chapter are therefore based largely on the authors' judgment and interpretation of the available data. They are intended to provide some guidance to designers until further research results are available.

6.1 LINK ULTIMATE STRENGTH

The ultimate shear force and end moments developed by the link control the capacity design forces for the beams, braces and columns in an EBF. Developing a reasonable estimate of link ultimate strength is therefore an important issue in achieving both a safe and economical EBF design. Underestimating these forces may result in a premature non-ductile failure in a member outside of the link. Overestimating the ultimate link forces, on the other hand, can result in unnecessarily heavy braces and columns.

The ultimate shear strength and ultimate end moments of the link are related by equilibrium. If end moments are assumed to equalize when the link ultimate forces are developed, and no external forces are assumed to act between the link ends, then by statics:

$$e\,V_{ult} = 2M_{ult} \tag{6.1}$$

where V_{ult} is the ultimate link shear force and M_{ult} is the ultimate link end moment. The experimental end moment data presented in Chapter 4 showed that long link end moments nearly equalized in cases where severe yielding or instability was prevented in the beam segment outside of the link. If capacity design principles are adhered to for the beam and the brace, equalization of end moments would appear to be a reasonable assumption for long links attached to columns or located within the span, particularly in the absence of a composite deck. In the present development, it will be assumed that ultimate end moments are approximately equal. Further, the effects of a composite deck on link strength and end moment equalization will not be considered in the present analysis.

As discussed in Section 1.3, the ultimate shear strength of short links is usually taken as:

$$V_{ult} = 1.5\, V_p \tag{6.2}$$

For the case of equal end moments, the corresponding ultimate end moment is then determined by Eq. 6.1. Some experiments have shown strain hardening somewhat in excess of $1.5\, V_p$ [9]. However, for practical design purposes, $1.5\, V_p$ appears to be a reasonable estimate of short link shear strength to account for strain hardening.

In order to estimate the strength of long links, two things are needed. First, an estimate of the ultimate moment that can be developed in the absence of large shear forces. This defines the strength of very long links. Secondly, an assumption on the nature of moment-shear interaction at the link's ultimate limit state is needed. This defines the strength of intermediate length links, where both shear and flexure have a strong influence on the link's inelastic behavior.

To address the issue of the ultimate bending moment that can be achieved by a *W* section in the absence of large shear forces, the available experimental data for very long links as well as for beams in MRFs can be examined. In the present experimental program, the longest links were provided in Specimens 5, 6 and 12. Based on actual measured section properties, the link lengths were approximately $3.4 M_p/V_p$ for Specimens 5 and 6, and $4.25 M_p/V_p$ for Specimen 12. The Specimen 12 link, a section with stocky flanges, developed an ultimate end moment of $1.55 M_p$. Further growth in link end moment for this specimen was prevented by the development of severe lateral torsional buckling in the link, and to a lesser extent, in the beam. The links of Specimens 5 and 6, on the other hand, developed ultimate end moments only on the order of about $1.2 M_p$. The slender flanges on these sections were subject to severe flange buckling, particularly in the brace connection panel. For very long links with slender flanges, located within the span between two braces, it is likely that the ultimate link end moment will be controlled by the development of flange buckling in the adjoining brace connection panels. By comparing Specimen 12 with Specimens 5 and 6, it is evident that long link strength is dependent on flange slenderness, and to a certain extent, on the details of the brace connection panel.

The reinforced link of Specimen 11R2 was in the intermediate length range, with an estimated actual $e = 1.9 M_p/V_p$. Because of the severe lateral torsional buckling developed in the beam of the specimen, the degree of end moment equalization was very poor for this link (see Table 4.2 and Fig. 4.2). Consequently, the moment gradient (equal to the shear force) in this link was much lower than would have been achieved in the case of moment equalization. Because of this lower moment gradient, the behavior of the Specimen 11R2 link can be considered to be characteristic of a much longer link. The ultimate moment of $1.55 M_p$ developed by this link can therefore be considered an additional data point for very long links.

Cyclic loading tests on beams for MRF applications provide additional data on the maximum bending moment that can be developed by a W section. In cyclic loading tests on $W18\times50$ and $W24\times76$ cantilevers, Popov and Stephen [21] reported values of M_{ult}/M_p up to 1.6. A cyclic load test on a welded H section by Ballio and Calado [48] developed $M_{ult} = 1.45M_p$. Additional cyclic tests on beam column subassemblages by Popov et al [47] showed ultimate moments up to $1.45M_p$. Recent tests by Tsai and Popov [34, 23], also on beam-column subassemblages, showed ultimate bending moments up to $1.3M_p$.

Based on the available experimental data, it appears that $M_{ult} = 1.5\,M_p$ provides a reasonable estimate of the ultimate moment due to strain hardening under cyclic loading, in the absence of very large shear force. Thus, for the present development, the ultimate flexural strength of very long links will be taken as:

$$M_{ult} = 1.5\,M_p \tag{6.3}$$

Based on the available data, this value appears to be most reasonable for sections with stocky flanges, and will be quite conservative for sections with slender flanges. Insufficient data are available at present to define the variation of ultimate bending moment with flange slenderness. Further research is needed on the development of flange buckling in the brace connection panel outside of long links before such a variation can be defined. Consequently, Eq. 6.3 will be adopted here for very long links, regardless of flange slenderness ratio. The corresponding ultimate shear force, for assumed equal ultimate end moments, is then defined by Eq. 6.1.

Equations 6.2 and 6.3 can be considered to represent the bounding strengths of a very short and a very long link, respectively. Establishing an estimate of ultimate strength in the intermediate length range, where links are significantly affected by both shear and moment, requires an assumption of moment-shear interaction at the link ultimate state. Kasai and Popov [13] suggest neglecting M-V interaction throughout the entire inelastic range for *short* links, reflecting the apparent lack of interaction at the yield limit state. As described in Section 1.3, this approach has been extended to links of any length by model EBF codes [7, 8]. For assumed equal end moments, the resulting link ultimate shear force and end moments, for any length link, is given by Eqs. 1.4-1.5. Figures 6.1 and 6.2 are plots of link ultimate shear force and ultimate end moments, respectively, as a function of non-dimensionalized link length, $e\,/\,(M_p/V_p)$. Equations 1.4 and 1.5 are plotted as dashed lines in these figures.

While neglecting M-V interaction in the strain hardening range is a reasonable approach for short links [13], it may not be appropriate for links in the intermediate length range. As discussed in Chapter 4, the experimental data on ultimate shear force and end moments for specimens with links in the intermediate length range suggest rather significant M-V interaction. The strain gage data presented in Section 4.6 and the photogrammetric data in Chapter 5 also provide evidence of significant bending-shear interaction at the link ends. These intermediate length links, however,

showed little influence of M-V interaction on the initial yield strength, similar to the behavior observed in short links. The lack of observed interaction at initial yield in short links has been postulated to be a result of very rapid strain hardening after initial yield [13]. The same argument can be extended to links in the intermediate length range. When link ultimate strength is developed, however, a rather low strain hardening rate would be anticipated. Consequently, it is reasonable to expect some influence of M-V interaction on ultimate link forces.

The approach adopted here to predict link ultimate strength will be to simply expand an M-V interaction curve based on perfect plasticity to the ultimate shear force and bending moment defined by Eqs. 6.2 and 6.3. As noted above, a rather low rate of strain hardening is anticipated when link ultimate strength is achieved. At this point, the response of the link can be viewed as being nearly perfectly plastic, but with the yield stress increased due to previous strain hardening. This view provides at least partial justification for expanding a yield surface based on perfect plasticity. The remaining justification is provided by the simplicity of this approach. This approach of course, can only be considered an approximation. The actual state of stress at the link end is likely to be quite complex, affected not only by M-V interaction, but also by the influence of warping restraint and local buckling. Further, different portions of the link cross-section will be subject to different stress and deformation histories, and will therefore be subject to differing degrees of strain hardening. Nonetheless, this approach does provide a useful first approximation to link ultimate strength.

An M-V interaction curve was developed by Hjelmstad and Popov [9] for the analytical modeling of perfectly plastic links. This same interaction curve, expanded to the ultimate limit state will be used here. This interaction curve is based on the following assumptions:

(1) No transverse normal stresses exist in the member

(2) The flanges carry no shear stress

(3) Normal and shear stresses in the web obey the von Mises yield criterion: $\sigma^2 + 3\tau^2 = \sigma_0^2$. In the present context, σ_0 is taken as $1.5\,\sigma_y$, where σ_y is the initial yield stress in simple tension.

The resulting interaction curve, for the case where the link carries no resultant axial force, can be expressed as follows:

$$m^* \sqrt{1-v^2} + v^2 = 1 \qquad 0 \le m^* \le 1 \tag{6.4a}$$

$$v = 1 \qquad m^* \le 0 \tag{6.4b}$$

where:

$$m^* = (1-2\omega)\,m - 2\omega \tag{6.5}$$

$$\omega = \frac{2 b_f t_f}{(d - t_f)\,t_w} \tag{6.6}$$

In the usual context of perfect plasticity, m and v represent the ratio of moment to fully plastic moment and shear force to fully plastic shear force. However, in the present development, m and v are taken as follows:

$$v = \frac{V_{ult}}{1.5\,V_p} \tag{6.7a}$$

$$m = \frac{M_{ult}}{1.5\,M_p} \tag{6.7b}$$

where $1.5\,V_p$ and $1.5\,M_p$ represent the assumed maximum shear and moment for the limiting cases of a very short and a very long link. The sign of v and m are always taken as positive in Eq. 6.4.

The parameter ω depends on the dimensions of the W section. A survey of all W sections listed in the AISC manual [30] indicates ω varies from about 0.75 to 3.2. However, for the sections commonly used as beams, ω varies from about 0.8 to 1.25. Within this range, the parameter ω has little influence on the form of the M-V interaction curve defined by Eq. 6.4, and so as a further simplification, $\omega = 1$ will be used. The interaction curve of Eq. 6.4 then simplifies to:

$$(3m-2)\sqrt{1-v^2} + v^2 = 1 \qquad \frac{2}{3} \le m \le 1 \tag{6.8a}$$

$$v = 1 \qquad 0 \le m \le \frac{2}{3} \tag{6.8b}$$

Next, the assumption of equal end moments will be imposed on Eq. 6.8. For this purpose, it is convenient to work in terms of non-dimensionalized link length, which will be represented by the parameter ρ as follows:

$$\rho = \frac{e}{(M_p/V_p)} \tag{6.9}$$

With the assumption of equal ultimate end moments, Eq. 6.1, can then be written as:

$$\rho v = 2m \tag{6.10}$$

Substituting Eq. 6.10 into Eq. 6.8 provides the final result:

$$v = 1 \qquad 0 \le \rho \le \frac{4}{3} \tag{6.11a}$$

$$\left(\frac{3\rho v - 4}{2}\right)\sqrt{1-v^2} + v^2 = 1 \qquad \rho \ge \frac{4}{3} \tag{6.11b}$$

These equations provide the ultimate link shear force for any non-dimensionalized link length ρ, based on the ultimate M-V interaction curve of Eq. 6.8 and based on the assumption of equal ultimate end moments. Once the ultimate link shear is determined by Eq. 6.11, the corresponding ultimate end moments are determined by Eq. 6.10.

Equation 6.11a indicates $V_{ult} = 1.5 V_p$ for $e \leq 1.33 M_p/V_p$, reflecting no influence of ultimate M-V interaction for this length range. For links beyond this length, ultimate strength is influenced by M-V interaction, as represented by Eq. 6.11b. For any non-dimensionalized link length $\rho > 4/3$, this non-linear equation can be solved iteratively for the ultimate link shear force.

The solution to Eq. 6.11 is plotted as a solid line in Figs. 6.1 and 6.2. Comparing these with the lines representing no M-V interaction at ultimate (the dashed lines) indicates that the assumed M-V interaction has its greatest influence in the intermediate length range. There is no apparent influence in the very short length range, and only little influence in the very long length range. Also plotted in Figs. 6.1 and 6.2 are the ultimate link shear and end moment measured in the present experiment, as well as from previous cyclic link tests [9,11,14,16]. In plotting these points, actual section and material properties based on coupon tests were used in determining V_p and M_p. These estimated actual values of V_p and M_p were then used for computing V_{ult}/V_p, M_{ult}/M_p and $e/(M_p/V_p)$. Consequently, the points in Figs. 6.1 and 6.2 reflect only the effects of strain hardening on link ultimate strength. Further, for the current specimens with reinforcing ribs at the link-to-column connection, the length of the ribs was deducted from the total link length in determining $e/(M_p/V_p)$. This reflects the observation that little inelastic activity occurred within the rib area of these links.

A number of useful observations can be made from Figs. 6.1 and 6.2. First, in the very short length range, it can be seen that several links have exceeded the assumed ultimate shear strength of $1.5 V_p$. Thus, in this length range, $V_{ult} = 1.5 V_p$ does not necessarily provide an upper bound on link overstrength due to strain hardening. A number of links in the short length range also fall considerably short of $1.5 V_p$. These points represent unstiffened or lightly stiffened links, where ultimate strength was limited by severe web buckling. These links, tested in the early stages of link stiffening investigations, are not representative of current recommended practice [20].

In the intermediate length range, it appears that the curve representing M-V interaction provides a reasonable bound on link strength. An exception to this is the point representing Specimen 11R2 in Fig. 6.2, which appears to significantly exceed the strength prediction of Eq. 6.11. However, as noted earlier this specimen violated, to a great degree, the assumption of equal ultimate end moments inherent in Eq. 6.11. The ultimate end moment developed by this specimen was therefore characteristic of a much longer link.

A number of the specimens from the present test program failed prematurely at the link-to-column connection, and therefore somewhat higher ultimate strengths might be anticipated if the same links had been located between two braces. However, at their points of failure, the rate of strain hardening was generally low for these specimens, as can be seen in Fig. 4.1. Thus, even if failure of the link-to-column connection had not occurred, a significant increase in link ultimate strength would probably not have been achieved.

Based on the available experimental data presented in Figs. 6.1 and 6.2, it appears that the curves based on ultimate M-V interaction (Eq. 6.11) provide a reasonable first approximation for link ultimate strength. Since an iterative solution is required, Eq. 6.11 is not particularly suited for design purposes. Consequently, a simplified approximation to Eq. 6.11 is needed for EBF design. In developing such an approximation, it is convenient to divide link lengths into three ranges; one corresponding to very short, predominately shear yielding links; a second corresponding to intermediate length, combined shear and bending links; and a final range corresponding to very long, predominately flexural yielding links. At present, the limit of a short link is taken at $e = 1.6M_p/V_p$. Based on the available data plotted in Fig. 6.1, this appears to be a reasonable dividing line between short and intermediate length links.

The transition from intermediate to very long links is somewhat more difficult to define. At present, for purposes of computing allowable rotation capacity, the model EBF codes [5, 7, 8] define this transition length at $e = 2.6M_p/V_p$. The photogrammetric data presented in Chapter 5 showed very large contributions of inelastic shear deformation for link lengths fairly close to $2.6M_p/V_p$. This data indicates that the transition to predominately flexural yielding occurs at a link length somewhat greater than $2.6M_p/V_p$.

To obtain further insight into the transition length to predominately flexural yielding, it is instructive to examine the experimental data on the inelastic behavior of wide-flange beams by Sawyer [49]. These tests were conducted on simply supported beams, monotonically loaded at midspan. The span lengths of several of Sawyer's test specimens were short enough to be characteristic of a link, and these specimens were subject to significant shear yielding. Further, Sawyer's novel instrumentation system permitted separating inelastic deflections due to shear from inelastic deflections due to bending. Based on the reported section and material properties, it was possible to compute an equivalent link length for each specimen. Such an equivalent link length would have the same moment gradient as developed in the simply supported beams. Sawyer's Specimen 10 had a span length corresponding to an equivalent link length of $2.43M_p/V_p$. Based on Sawyer's data, approximately 40 percent of the inelastic rotation of this beam was due to inelastic shear deformations. Sawyer's Specimen 13, with an equivalent link length of $2.8M_p/V_p$, supplied approximately 33 percent of the total inelastic rotation by shear. Inelastic shear deformation accounted for approximately 20 percent of the total inelastic rotation in Sawyer's Specimen 16, with an equivalent link length of about $3M_p/V_p$. Thus, Sawyer's data tends to confirm that significant shear yielding extends to link lengths somewhat beyond $2.6M_p/V_p$.

For the present purposes, the transition from intermediate to very long links will be taken at $e = 3M_p/V_p$. This is a somewhat arbitrary choice, but reasonably reflects the available experimental data.

Based on the assumed transition lengths of $1.6M_p/V_p$ and $3M_p/V_p$, the following equations are proposed for a preliminary estimate of link ultimate end moments:

$$M_{ult} = \frac{3}{4} e\, M_p \qquad \text{for } e \leq 1.6\frac{M_p}{V_p} \tag{6.12a}$$

$$M_{ult} = 1.2M_p \qquad \text{for } e = 1.6\frac{M_p}{V_p} \tag{6.12b}$$

$$M_{ult} = 1.5M_p \qquad \text{for } e \geq 3\frac{M_p}{V_p} \tag{6.12c}$$

For link lengths between $1.6M_p/V_p$ and $3M_p/V_p$, interpolate between Eq. 6.12b and 6.12c. The corresponding ultimate shear force is then simply computed as:

$$V_{ult} = 1.5V_p \qquad \text{for } e \leq 1.6\frac{M_p}{V_p} \tag{6.13a}$$

$$V_{ult} = \frac{2M_{ult}}{e} \qquad \text{for } e \geq 1.6\frac{M_p}{V_p} \tag{6.13b}$$

where M_{ult} is determined from Eq. 6.12.

The above equations are also plotted in Figs. 6.1 and 6.2. It may be seen that Eqs. 6.12 - 6.13 are identical to the present code approach (Eqs. 1.4-1.5) for $e < 1.6M_p/V_p$ and for $e > 3M_p/V_p$. However, between these two link lengths, Eqs. 6.12 - 6.13 provide for significantly lower ultimate link shear and end moments, resulting in lower capacity design forces to be applied to the braces, beam segments outside of the links, and the columns of an EBF.

It must be emphasized that Eqs. 6.12 - 6.13 provide an estimate of link ultimate strength due to strain hardening only, and are intended to apply to links with approximately equal ultimate end moments. The presence of a composite deck can affect both the magnitude of the link end moments, as well as the equalization of end moments [16, 18]. Further, the actual yield strength of the link may exceed the specified yield strength. This factor is not represented in Figs. 6.1 and 6.2, since actual material properties were used in plotting the experimental points. Designers must consider the possibility that the other frame members may not possess a comparable increase in the actual yield strength. Thus, Eqs. 6.12 - 6.13 must be applied with judgment when estimating the capacity design forces for the braces, beams and columns.

6.2 LINK PLASTIC ROTATION CAPACITY

In this section, a preliminary estimate is developed for the plastic rotation capacity of long links not attached to columns. Developing such an estimate based on the results of the present experimental program is quite difficult, since the majority of the test specimens failed by fracture at the link-to-column connection. Several others failed by severe buckling of the beam segment

outside of the link, where capacity design principles were intentionally violated. Consequently, considerable judgment is required in developing an estimate of rotation capacity for cases where link-to-column connection failure or beam buckling are not the controlling failure modes.

The plastic rotation capacities, $\bar{\gamma}_p$, measured for each of the 14 test specimens, are listed in Table 3.3. Recall that $\bar{\gamma}_p$ represents the total plastic rotation measured from the last point of zero applied shear force on the link. For approximately symmetric cyclic response, the plastic rotation capacity γ_p can be estimated as one-half of $\bar{\gamma}_p$.

When interpreting the data in Table 3.3, several factors must be considered. First, all indications from this test program are that fracture of the link flange will not be a controlling failure mode for long links not attached to a column. In the absence of such a fracture, most of the test specimens would have likely developed significant additional rotation capacity. Further, in the absence of a link flange fracture, long link behavior can be characterized by a gradually deteriorating hysteretic response at large cyclic deformations. This deterioration can be attributed to flange buckling in the brace connection panel for sections with slender flanges, and to lateral torsional buckling of the link for sections with stocky flanges. Consequently, no single measure of plastic rotation capacity can be identified as representing failure of the link, and considerable judgement is therefore required in establishing a meaningful estimate of plastic rotation capacity. Ultimately, such difficulties can perhaps best be resolved by measuring link performance in terms of energy dissipation capacity rather than in terms of plastic rotation capacity.

To obtain an indication of the rotation capacity of very long links, it is useful to examine the performance of Specimen 12. This very long link (actual $e = 4.25 M_p/V_p$) did not fail at the link-to-column connection, and can therefore be considered fairly representative of a link located between two braces. As shown in Table 3.3, this link was capable of supplying γ_p on the order of $\pm$ .025 rad for stable hysteretic response, and on the order of $\pm$ .04 rad up to the point where link strength dropped below the initial yield value. Specimen 6 was also provided with a very long link (actual $e \approx 3.4 M_p/V_p$). Even though this specimen failed at the link-to-column connection, its response was well into the range of deteriorating strength at the point of failure. This specimen therefore also provides a reasonable indication of the performance that might be anticipated for a very long link located between two braces. As shown in Table 3.3, Specimen 6 developed γ_p of about $\pm$ .016 rad at the limit of stable hysteretic behavior, and about $\pm$ .027 rad at the point where link strength dropped below the initial yield value. Cyclic tests on flexurally yielding cantilever beams for MRF applications show plastic rotations in excess of $\pm$ .03 rad at the limit of stable hysteretic behavior for cases where beam-to-column connection failures did not occur [21,34]. As discussed in Section 1.3, data from such MRF tests must be interpreted with caution when applied to long links. Nonetheless, this data does provide an additional reference point from which to judge the capabilities of very long links.

Based on the measured rotation capacities for the very long links listed in Table 3.3, and also based on examination of experimental data from cyclic tests on beams in MRF applications, it is believed that $\gamma_p = \pm .025$ rad provides a reasonable estimate of the plastic rotation capacity of very long links. For well stiffened short links, on the other hand, plastic rotations up to $\gamma_p = \pm .10$ rad are possible [9,14]. In the intermediate length range, a linear interpolation between .10 rad and .025 rad would appear reasonable as a first approximation for rotation capacity in this length range. Using the same arguments as in Section 6.1, the intermediate length range can be taken as $1.6M_p/V_p$ to $3M_p/V_p$.

Because of the uncertainties involved in predicting the rotation capacity of long links based on this very limited experimental data, as well as the uncertainties in predicting the actual rotation demands on a link of any length, a somewhat reduced allowable plastic rotation capacity is recommended for design purposes. To account for these uncertainties, a design rotation capacity equal to approximately 80 percent of the rotation capacity limits noted above is recommended. Thus, for design purposes, the following plastic rotation capacities are suggested:

$$\gamma_p = \pm .08\ rad \qquad \text{for } e \leq 1.6\frac{M_p}{V_p} \tag{6.14a}$$

$$\gamma_p = \pm .02\ rad \qquad \text{for } e \geq 3\frac{M_p}{V_p} \tag{6.14b}$$

with the plastic rotation capacity for links of length 1.6 to $3M_p/V_p$ estimated by interpolation. Note that for link lengths greater than $1.6M_p/V_p$, the above limits are intended only for links not attached to columns.

Inelastic dynamic analysis of a six-story EBF with short links designed according to the tentative AISC seismic provisions [8], with an allowable plastic rotation of $\pm$ .08 rad, showed satisfactory performance under a variety of severe ground motions [50]. No such dynamic analyses have yet been conducted for EBFs with long links.

It is again emphasized that the above rotation capacity limits for long links are based on extrapolation of very limited experimental data. Additional experimental data for long links not attached to columns is needed before rotation limits can be established with confidence. Further, inelastic dynamic analyses of EBFs with long links under realistic ground motions is needed to better define actual rotation demands.

6.3 STIFFENER REQUIREMENTS

In this section, preliminary recommendations are developed for locating stiffeners in long links. Observations from the present series of tests, summarized in Section 3.3 of this report, have provided some initial indications of where stiffeners should be placed in long links. The limited

data provided by these tests, however, are not adequate to develop definitive stiffening recommendations for long links. Consequently, the recommendations provided below reflect the authors' judgement based on very limited available data, and are not intended to serve as final design recommendations.

The purpose of stiffening links in EBFs is to delay various forms of local instability and thereby permit full development of the link's plastic rotation and energy dissipation capacities. The type of local instability which the stiffeners must delay depends on link length and the associated yielding and failure mechanisms. For very short links, shear buckling of the web is the dominant form of local instability. For very long links, flange buckling and/or lateral torsional buckling of the link and the brace connection panel are generally the controlling forms of local instability. For links in the intermediate length range, a combination of all of the above forms of local instability, possibly with some interaction, is possible. In the following discussion, it is again convenient to separate links into the three length categories of short, intermediate and very long links. As before, the dividing lines between these categories will be taken at $1.6M_p/V_p$ and $3M_p/V_p$.

Short Links ($e \leq 1.6 M_p/V_p$)

Stiffening requirements to delay web buckling in short links are well established, both experimentally and analytically [14,20]. The initiation of web buckling can be reliably predicted by Eq. 4.7 [20]. For design purposes, the distance between equally spaced stiffeners within a short link for any required plastic rotation up to $\pm$ .09 rad can be computed using Eqs. 1.3 [20]. A possible issue of concern is whether or not local buckling can develop within the brace connection panel outside of a short link. The relatively lower end moments developed in short links suggest that flange buckling outside of the link is not likely to be a controlling failure mode. Further, there is no experimental evidence showing that such buckling can occur outside of short links. The photogrammetric data analysis for Specimen 9 (a short link) also confirms that stress levels are rather low in the flange of the brace connection panel in the region immediately adjacent to the link end. Thus, based on the available data, there appears to be no need to stiffen the brace connection panel in the region immediately outside of a short link. However, as discussed later, stiffeners should still generally be provided at the back end of the brace connection panel.

Very Long Links ($e > 3 M_p/V_p$)

The test observations as well as the photogrammetric data show that plastic rotations in very long links are developed as a result of yielding in the region near the link ends, both inside and outside of the link. For sections with slender flanges, the tests show that severe flange buckling is possible both inside and outside of the link. Flange buckling in the brace connection panel immediately outside of the link is significantly more detrimental to overall strength and plastic

rotation capacity of an EBF than is flange buckling inside of the link. Sections with stocky flanges, such as the W12×22 sections tested here, tend to develop severe lateral torsional buckling in preference to flange buckling. No flange buckling was observed in the brace connection panel of any of the W12×22 test specimens.

In Chapter 3, the preliminary recommendation was made to locate stiffeners inside of the link at a distance of $1.5\,b_f$ from each end of the link. Additional stiffeners inside of the link may provide some further benefits by increasing the torsional rigidity of the link. Based on the available data, however, locating a single stiffener near each end of the link, inside of the link, appears to be sufficient. The more difficult issue is whether or not to provide an additional stiffener outside of the link. The specimens that suffered from severe flange buckling in the brace connection panel benefited from the addition of a stiffener outside of the link. The specimens with stocky flanges, on the other hand, in which no flange buckling was observed in the brace connection panel, would not have likely shown any better performance with an additional stiffener in the panel. The need for a stiffener outside of the link evidently depends on a number of factors, including link length and flange slenderness ratio, and perhaps also on the length of the panel as well as on the brace-beam angle. Based on the limited available data, it is not possible to determine the combination of conditions that will result in severe flange buckling in the brace connection panel.

In the judgement of the authors, a conservative approach is justified in this case. The test results clearly show that once local buckling initiates in the very highly stressed region outside of a long link, strength and energy dissipation capacity of the system rapidly deteriorate. It is therefore recommended that a stiffener be provided outside of any long link, within the brace connection panels. As noted in Section 3.3, a reasonable location for this stiffener is at a distance of about $1.5\,b_f$ from the link end, or one-half of the brace connection panel length, whichever is less. The use of a partial depth stiffener appears to be adequate at this location. The stiffener should be welded to the flange opposite the brace, and extend at least about 3/4 of the depth of the web.

Intermediate Length Links ($1.6\,M_p/V_p < e \leq 3\,M_p/V_p$)

Links in the intermediate length range are subject to a combination of failure modes seen both in very short and very long links. The intermediate length range represent a transition from shear dominated to flexurally dominated behavior, and the types of local buckling developed in these links reflect this transition. A combination of the stiffening requirements for very long and for short links is therefore appropriate in the intermediate length range.

Considering first the region outside of the link, Specimen 1 showed that very severe flange buckling can occur within the brace connection panel outside of an intermediate length link. It therefore appears to be prudent to provide a partial depth stiffener within the brace connection

panels in the same location as noted above for very long links.

Inside of an intermediate length link, locating a stiffener at $1.5\,b_f$ from each end of the link is needed to control flange buckling and lateral torsional buckling in the same manner as for very long links. In the remaining central portion of the link, some additional stiffening is needed to control inelastic shear buckling of the web. As demonstrated by Specimens 2 and 4, web buckling can still occur in the intermediate length range. Moreover, the occurrence of web buckling appears to be substantially more detrimental than the occurrence of flange buckling in an intermediate length link. Consequently, it is important to provide adequate stiffening against web buckling in this length range. It would seem reasonable to provide a transition in the spacing of web stiffeners, starting with the spacing used for short links at at length of $1.6\,M_p/V_p$, and gradually increasing this spacing so that no additional web stiffeners are provided beyond a length of $3\,M_p/V_p$. Such a transition in stiffener spacing reflects the reduction in inelastic shear strain as link length approaches $3\,M_p/V_p$.

To accomplish a transition in the spacing of web stiffeners in the central portion of an intermediate length link, the following approach is suggested. At the lower limit of $1.6\,M_p/V_p$, provide web stiffeners at the same spacing as for short links. That is, within the region between the outer flange stiffeners, (the stiffeners located nominally at $1.5\,b_f$ from the link ends), provide equally spaced web stiffeners according to the criteria of Eq. 1.3, using the total estimated link plastic rotation demand γ_p. For links of length $3\,M_p/V_p$, provide one additional intermediate web stiffener midway between the outer flange stiffeners. For links of length 1.6 to $3\,M_p/V_p$, determine the spacing of intermediate web stiffeners simply by interpolating between the spacing required at $1.6\,M_p/V_p$ and that required at $3\,M_p/V_p$. This rule is somewhat arbitrary, but appears to reflect the observed trends in link behavior in a reasonable manner.

For some W sections with very wide flanges, the spacing of the intermediate web stiffeners according to the above rule is less than $1.5\,b_f$. For these sections, the flange stiffeners located nominally at $1.5\,b_f$ from the link ends should be placed closer to the link ends so that the spacing does not exceed that of the web stiffeners. This will help guard against web buckling in the panels immediately adjacent to the link ends.

The preliminary stiffener spacing criteria suggested above for intermediate and very long links are summarized in Fig. 6.3. The well established stiffener spacing criteria by Kasai and Popov [20] for short links are also shown in this figure for completeness.

At present, the model EBF codes [5,7,8] require stiffeners to be provided on both sides of the web for W sections that are 24 inches in depth or greater. For sections less than 24 inches in depth, stiffeners on only one side of the web are permitted. Based on the present tests, this rule appears to be reasonable for long links. The stiffeners located at the link ends, however, must

always be provided on both sides of the web [1]. The sketches in Fig. 6.3 also show stiffeners at the back end of the brace connection panel, that is at the end of the brace connection panel farthest from the link end. For brace connections in which the brace flanges are directly welded to the beam, these additional stiffeners aid in the full development of the brace strength. Examples of such connections are shown in Fig. 2.11 or 6.3 for W section braces, and in Fig. 2.8 for rectangular tube section braces. For the gusset plate type connection shown in Fig. 2.14, the need for stiffeners at the back end of the brace connection panel is a matter open to judgement. In the opinion of the authors, these stiffeners help prevent lateral torsional buckling in this region of combined bending and axial force. Thus, the use of two-sided stiffeners at the back end of the brace connection panel is recommended for any brace connection detail.

Finally, it should be noted that the sketches shown in Fig. 6.3 show only W section braces with a direct welded brace-to-link connection. This is not intended to indicate a preference for this type of brace or brace connection, nor is it intended to preclude other brace connection details. Good performance was observed for all three brace connection details tested as part of this investigation (direct welded W section, direct welded tube section, and gusseted tube section connections). Many other suitable brace connection details can certainly be devised. It is also noted that for the direct welded brace connection shown in Fig. 2.8, the horizontal stiffeners located above the brace webs could be extended and welded to the opposite flange of the beam. This would certainly control flange buckling in the brace connection panel, and thus the partial depth stiffener recommended above could be eliminated.

Example:

The following example is intended to illustrate the application of the above suggested stiffener spacing criteria.

Link: W18×40 $\quad e = 66" \quad = 2.6 M_p/V_p$

Stiffen for estimated plastic rotation demand: $\gamma_p = \pm .035$ rad.

This link length falls within the intermediate length range. Determine the stiffnener locations from Fig. 6.3b.

Inside link:

Compute a: For $\gamma_p = \pm .035$ rad. $\quad a \approx 13"$ by interpolation between Eq. 1.3b and 1.3c. (These are the second and third equations shown on Fig. 6.3a).

Compute: $\frac{3}{2}\left[\frac{M_p}{V_p} - b_f\right] \approx 29"$

Compute a^*:

$$a^* = \begin{cases} 13" \text{ at } e = 1.6\dfrac{M_p}{V_p} \\ 29" \text{ at } e = 3\dfrac{M_p}{V_p} \end{cases}$$

By interpolation, $a^* = 24.5"$ at $e = 2.6\dfrac{M_p}{V_p}$

Compute: $1.5b_f = 9" < a^*$

Therefore: $b = 9"$

Inside of the link, provide a stiffener at 9" from each end of the link. Within the remaining central 48" panel, provide stiffeners at a minimum spacing of $a^* = 24.5"$. Thus, provide one additional stiffener at midlength of the link, resulting in two 24" panels in the central portion of the link.

Outside link:

Say brace connection panel length, L, is equal to 20". Thus, provide partial depth stiffeners at a distance of $1.5b_f = 9"$ ($< L/2$) from the link ends. The depth of the web on the W18×40 is: $d - 2t_f = 16.8"$. Take the depth of stiffeners $> .75 \times 16.8" = 12.6"$, say 13".

The results of the above computations are illustrated in Fig. 6.4. Since the overall depth of the W18×40 section is less than 24", the stiffeners need be provided on only one side of the web. Note that the stiffeners located at the link ends, immediately above the brace flanges, must be provided on both sides of the web. Also provide two-sided stiffeners above the other brace flanges, at the far ends of the brace connection panels.

7. SUMMARY

This report has documented the results of an experimental investigation and associated studies on the behavior of long links in seismic-resistant EBFs. The experimental program focused on the behavior of long links attached to columns, for EBF configurations such as shown in Fig. 1.1a. However, much of what was learned also provides guidance for the design of EBFs with long links located between two braces (Fig. 1.1b) and also for the design of EBFs with short links.

For the purposes of this project, a long link was defined as any link whose length exceeds $1.6M_p/V_p$. However, in terms of inelastic behavior, links can more naturally be divided into three length categories:

- short links: $e \leq 1.6M_p/V_p$
- intermediate length links: $1.6M_p/V_p < e \leq 3M_p/V_p$
- very long links: $e > 3M_p/V_p$

Shear dominates the inelastic behavior of short links, and flexure dominates for very long links. The intermediate length links are significantly affected by both shear and flexure in the inelastic range, and represent a transition between the shear and flexurally dominated ranges of behavior. In addition to different yielding mechanisms, the behavior of short and very long links are characterized by distinctly different inelastic rotation capacities and failure mechanisms, with the intermediate length links, again, representing a transition. There are no clearly defined boundaries between these three ranges of link behavior. However, the dividing lines of $1.6M_p/V_p$ and $3M_p/V_p$ appear to reasonably reflect the experimentally observed inelastic behavior of links.

Research on seismic-resistant EBFs has been continuing since the mid-1970's. Previous research has concentrated on EBFs constructed with short links, and has provided ample evidence of their excellent strength, stiffness, inelastic deformability and energy dissipation capacity. There are, however, some important incentives for using longer links in EBFs. The most important of these at present appears to be the architectural advantage offered by longer links. Long links permit larger openings in braced bays than are possible if link lengths are restricted to $e \leq 1.6M_p/V_p$. This, in turn, may permit the use of an EBF where a braced bay would otherwise not be possible due to interference with doors, windows and other architectural features of the building. Long links have been used on a number of recently constructed EBFs, attesting to the need for this system by the building construction industry.

The need for longer links in certain applications combined with the lack of previous experimental research on long links has provided the motivation for this current investigation. The overall objectives of this study were to provide an assessment of the important issues affecting the use of long links in EBFs, to identify the potential range of application of long link EBF systems, and to develop preliminary recommendations for the design of long links in EBFs.

Detailed summaries of the findings and observations from this program of investigation are provided at the ends of Chapters 3 and 4 of this report. Repeated below are those items which are deemed to represent the most important findings of this research program.

1. The controlling failure mode for long links attached to columns is fracture of the link flange at the link-to-column connection. The occurrence of these fractures cannot be reliably predicted and represents a complete and sudden failure of the system. Further, these fractures occur at levels of inelastic rotation which do not appear adequate for application in severe seismic environments. Based on the evidence from this experimental program, it is recommended that **long links ($e > 1.6 M_p/V_p$) attached to columns should not be used in EBFs.**

2. While not suitable for use next to columns, the available evidence indicates that long links can provide substantial inelastic rotation and energy dissipation capacity when located within the span between two braces. The available data indicate that short shear yielding links still provide superior performance under severe cyclic loading, and should be the first choice in EBF design. However, if properly implemented, it appears that acceptable performance can be achieved for EBF configurations with a long link located between two braces.

3. The beam segment outside of the link is a potentially vulnerable area of an EBF. The combination of very high axial force and bending moment typically carried by this member can result in buckling of the member well before link strength and inelastic rotation capacity are developed. This is an important concern for EBFs with short or long links. Problems with the beam can be avoided by adhering to capacity design principles.

4. This investigation has confirmed the importance of the *capacity design* approach for the beams and braces of an EBF. Limited yielding outside of the link may be acceptable and perhaps even advantageous, particularly if restricted to the brace connection panel. However, the beam and brace must still possess adequate strength to permit full development of the link's inelastic rotation capacity. Otherwise, the overall performance of the system may be substantially degraded. A preliminary suggested capacity design procedure for the beams and braces of an EBF is outlined in Section 4.4.4 of this report. This procedure is intended for any EBF, regardless of configuration or link length.

5. Two tests were conducted on short links attached to the column web as part of this investigation. In both cases, premature failures of the link-to-column web connection were observed. These tests tend to confirm the questionable reliability of connections to the column web. Until additional experimental data are available for such connections, it is recommended that designers avoid link-to-column web connections, for any link length.

6. Three different brace-to-link connection details were tested as part of this experimental program: a direct welded detail for *W* section braces, a direct welded detail for tube section braces, and a stiffened gusset plate detail for tube section braces. All three details performed well.

7. Several unconventional link-to-column connection details were investigated in this test program. The most promising detail is one in which the link flanges are reinforced with triangular cover plates (Fig. 2.26). A long link provided with this detail survived a very severe cyclic loading program without failure of the connection. Although this single test cannot be considered conclusive, the use of such triangular cover plates appears to be a very promising technique for significantly improving connection performance, and warrants further investigation. The development of improved link-to-column connection details may ultimately permit the safe use of long links attached to columns in EBFs.

8. The shear force at which significant yielding first occurred in the long links showed minor influence of M-V (bending-shear) interaction. This effect, however, was small and not particularly significant from a design point of view, considering that the links did not exhibit a well defined yield point. For design purposes, neglecting M-V interaction for estimating the yield strength of long links appears to be a reasonable simplification and is consistent with the approach used for short links. Consequently, for design purposes, the shear force required to produce initial significant yielding of a link can be taken as V_p for $e \leq 2M_p/V_p$ and as $2M_p/e$ for $e \geq 2M_p/V_p$. These yield strengths are the basis for sizing the links in an EBF. Neglecting M-V interaction at initial yield simplifies the design process and results in more economical designs for EBFs with long links.

9. Whereas it is reasonable to neglect M-V interaction at initial yield, the data from these experiments suggest that M-V interaction may have a significant influence on the ultimate shear force and end moments developed in intermediate length links. Because of this influence, the overstrength factor of 1.5 typically used to estimate the ultimate strength of short links may be too large for links in the intermediate length range. For very long links, on the other hand, an overstrength factor of 1.5 again appears to provide a reasonable estimate of link ultimate strength. Based on a simplified analysis, combined with the available experimental data, a preliminary estimate of the ultimate strength of long links was developed, and is represented by Eqs. 6.12 - 6.13. Link ultimate strength controls the capacity design forces for the braces, columns, and beam segments outside of the links. The revised ultimate strength estimates provided by Eqs. 6.12 - 6.13 should result in more economical designs for EBFs with intermediate length links, when compared to the approach of using a constant overstrength factor for any length link.

10. Based on extrapolation of the experimental data from the present tests as well as examination of other pertinent experimental data, a preliminary estimate was developed for the design plastic rotation capacity of long links not attached to columns. This preliminary estimate is represented by Eq. 6.14.

11. Observations from this experimental program provided some initial indications of where stiffeners should be placed in long links in order to delay and mitigate the effects of local buckling in

long links. Based on these observations, combined with previous experimental results for links, preliminary stiffener spacing criteria were developed for long links. These criteria are discussed in Section 6.3, and are summarized in Figs. 6.3b and c.

12. Large out-of-plane forces were measured at the link end lateral support in this experimental program. Many specimens developed link end lateral forces on the order of 4 to 5 times greater than typical code specified lateral support strength requirements, and in some cases, in excess of 10 times greater. These large out-of-plane forces developed at the ends of both short and long links. Based on the limited experimental data from this testing program, a minimum link end lateral support strength equal to 6 percent of the beam flange yield strength is recommended. Both the top and bottom flanges at the link ends must be laterally supported. The experimental data also confirm the importance of providing stiff resistance to out-of-plane displacement at the link ends.

As a closing note, it should be emphasized that many of the above observations and design recommendations are based on the authors' judgement and interpretation of very limited data. It is fully recognized that many of these recommendations will change in time as further research on seismic-resistant EBFs becomes available.

REFERENCES

1. Roeder, C. W. and E. P. Popov, *Inelastic Behavior Of Eccentrically Braced Steel Frames Under Cyclic Loadings,* Report No. UCB/EERC-77/18, Earthquake Engineering Research Center, University of California, Berkeley, CA, 1977.
2. Roeder, C. W. and E. P. Popov, "Eccentrically Braced Frames for Earthquakes," *Journal of the Structural Division*, vol. 104, no. 3, ASCE, March 1978.
3. Libby, J. R., "Eccentrically Braced Frame Construction - A Case History," *Engineering Journal*, AISC, 4th Qtr, 1981.
4. Merovich, A. T., J. P. Nicoletti, and E. Hartle, "Eccentric Bracing in Tall Buildings," *Journal of the Structural Division*, vol. 108, no. 9, ASCE, September 1982.
5. SEAOC, *Recommended Lateral Force Requirements,* Seismology Committee, Structural Engineers Association of California, Sacramento/San Francisco/Los Angeles, CA, 1988.
6. ICBO, *Uniform Building Code,* International Conference of Building Officials, Whittier, CA, 1988.
7. BSSC, *NEHRP (National Earthquake Hazards Reduction Program) Recommended Provisions for the Development Of Seismic Regulations for New Buildings,* Building Seismic Safety Council, Federal Emergency Management Agency, Washington, D.C., 1985.
8. AISC, *Tentative Seismic Provisions,* American Institute of Steel Construction. (To be published 1989)
9. Hjelmstad, K. D. and E. P. Popov, *Seismic Behavior of Active Beam Links In Eccentrically Braced Frames,* Report No. UCB/EERC-83/24, Earthquake Engineering Research Center, University of California, Berkeley, CA, 1983.
10. Hjelmstad, K. D. and E. P. Popov, "Cyclic Behavior and Design of Link Beams," *Journal of the Structural Division, ASCE*, vol. 109, no. 10, ASCE, October 1983.
11. Malley, J. O. and E. P. Popov, *Design Considerations for Shear Links in Eccentrically Braced Frames,* Report No. UCB/EERC-83/24, Earthquake Engineering Research Center, University of California, Berkeley, CA, 1983.
12. Malley, J. O. and E. P. Popov, "Shear Links in Eccentrically Braced Frames," *Journal of the Structural Division*, vol. 110, no. 9, ASCE, September 1984.
13. Kasai, K. and E. P. Popov, "General Behavior of WF Steel Shear Link Beams," *Journal of the Structural Division*, vol. 112, no. 2, ASCE, February 1986.
14. Kasai, K. and E. P. Popov, *A Study of Seismically Resistant Eccentrically Braced Frames,* Report No. UCB/EERC-86/01, Earthquake Engineering Research Center, University of

California, Berkeley, CA, 1986.

15. Manheim, D. N., *On the Design of Eccentrically Braced Frames,* Thesis, D.Eng, Department of Civil Engineering, University of California, Berkeley, CA, February 1982.

16. Ricles, J. M. and E. P. Popov, *Experiments on EBFs with Composite Floors Eccentrically Braced Frames,* Report No. UCB/EERC-87/06, Earthquake Engineering Research Center, University of California, Berkeley, CA, 1987.

17. Roeder, C. W., D. A. Foutch, and S. C. Goel, "Seismic Testing of Full-Size Steel Building - Part II," *Journal of the Structural Division, ASCE*, vol. 113, no. 11, November 1987.

18. Whittaker, A. S., C. M. Uang, and V. V. Bertero, *Earthquake Simulation Tests and Associated Studies of a 0.3-Scale Model of a Six Story Eccentrically Braced Steel Structure,* Report No. UCB/EERC-87/02, Earthquake Engineering Research Center, University of California, Berkeley, CA, 1987.

19. ASCE, *Plastic Design in Steel; A Guide and Commentary,* Manual No. 41, American Society of Civil Engineers, 1971.

20. Kasai, K. and E. P. Popov, "Cyclic Web Buckling Control for Shear Link Beams," *Journal of the Structural Division*, vol. 112, no. 3, ASCE, March 1986.

21. Popov, E. P. and R. M. Stephen, *Cyclic Loading of Full-Size Steel Connections,* Bulletin No. 21, American Iron and Steel Institute, February 1972.

22. Kemp, A. R., "Factors Affecting the Rotation Capacity of Plastically Designed Members," *The Structural Engineer*, vol. 64B, no. 2, June 1986.

23. Popov, E. P. and K. C. Tsai, *Performance of Large Seismic Steel Moment Connections Under Cyclic Loads*, Proceedings: Structural Engineers Association of California Convention, San Diego, October 1987.

24. Fujii, K. and H. Ohmura, "A Study of Rigidity and Strength in Torsion of H-Beam Stiffened with Transverse Stiffeners," *Proceedings, Japan Society of Civil Engineers*, vol. 2, no. 1, April 1985.

25. Lay, M. G., "Flange Local Buckling in Wide-Flange Shapes," *Journal of the Structural Division*, vol. 91, no. ST6, ASCE, December 1965.

26. Popov, E. P. and R. B. Pinkney, *Behavior of Steel Building Connections Subjected to Inelastic Strain Reversals- Experimental Data,* Bulletin No. 14, American Iron and Steel Institute, November 1968.

27. Driscoll, G. C. and L. S. Beedle, "Suggestions for Avoiding Beam-to-Column Web Connection Failure," *Engineering Journal*, AISC, 1st Qtr, 1982.

28. Ricles, J. M. and E. P. Popov, *Dynamic Analysis of Seismically Resistant Eccentrically Braced Frames,* Report No. UCB/EERC-87/07, Earthquake Engineering Research Center, University of California, Berkeley, CA, 1987.

29. CIDECT, *Construction with Hollow Steel Sections,* International Committee for the Development and Study of Tubular Construction (CIDECT), 1984. (English version by British Steel Corporation)

30. AISC, *Manual of Steel Construction, 8th Ed.,* American Institute of Steel Construction, 1980.

31. AISC, *Engineering for Steel Construction,* American Institute of Steel Construction, 1984.

32. Becker, R. A. and J. M. Chambers, *S: An Interactive Environment for Data Analysis and Graphics,* Wadsworth Statistics/Probability Series, 1984.

33. Tsai, K. C. and E. P. Popov, *Two Beam-To-Column Web Connections,* Report No. UCB/EERC-86/05, Earthquake Engineering Research Center, University of California, Berkeley, CA, 1986.

34. Tsai, K. C., *Steel Beam-Column Joints in Seismic Moment Resisting Frames,* Ph.D. Dissertation, Department of Civil Engineering, University of California, Berkeley, CA, 1988.

35. Engelhardt, M. D., *Long Links in Eccentrically Braced Frames: A Preliminary Assessment,* CE299 Report, Department of Civil Engineering, Division of Structural Engineering, Mechanics and Materials, University of California, Berkeley, CA, 1987.

36. Galambos, T. V., *Guide to Stability Design Criteria for Metal Structures,* John Wiley and Sons, 4th Edition, 1988.

37. AISC, *Load and Resistance Factor Design Specification,* American Institute of Steel Construction, 1986.

38. Black, R. G., W. Wenger, and E. P. Popov, *Inelastic Buckling of Steel Struts Under Cyclic Load Reversals,* Report No. UCB/EERC-80/40, Earthquake Engineering Research Center, University of California, Berkeley, CA, 1980.

39. Neal, B. G., *The Plastic Methods of Structural Analysis,* Chapman and Hall, Ltd., 1977.

40. *Fatigue Characteristics of Micro-Measurements Strain Gages,* Technical Note No. 508, Micro-Measurements Division, Measurements Group Inc., Raleigh, NC, 1982.

41. Krawinkler, H., V. V. Bertero, and E. P. Popov, *Inelastic Behavior of Steel Beam-to-Column Subassemblages,* Report No. UCB/EERC-71/7, Earthquake Engineering Research Center, University of California, Berkeley, CA, 1971.

42. Moffitt, F. H., *Photogrammetry Applied to Experimental Stress Analysis*, Proceedings; American Society of Photogrammetry, Fall Convention, San Francisco, 1971.

43. Moffitt, F. H. and E. M. Mikhail, *Photogrammetry,* Harper and Row, 1980.

44. Zienkiewicz, O. C., *The Finite Element Method, 3rd Ed.,* McGraw-Hill, 1977.

45. Plantema, F. J., *Sandwich Construction,* John Wiley and Sons, 1966.

46. Cowper, G. R., "The Shear Coefficient in Timoshenko's Beam Theory," *Journal of Applied Mechanics*, vol. 33, no. 6, ASME, June 1966.

47. Popov, E. P., N. R. Amin, J. J. Louie, and R. M. Stephen, "Cyclic Behavior of Large Beam -Column Assemblies," *Earthquake Spectra*, vol. 1, no. 2, February 1985.

48. Ballio, G. and L. Calado, "Steel Bent Sections Under Cyclic Loads - Experimental and Numerical Approaches," *Costruzioni Metallichi*, no. 1, 1986.

49. Sawyer, H. A., "Post-Elastic Behavior of Wide-Flange Steel Beams," *Journal of the Structural Division*, vol. 87, no. ST8, ASCE, December 1961.

50. Popov, E. P., M. D. Engelhardt, and J. M. Ricles, *Eccentrically Brace Frames: U.S. Practice,* 3rd U.S.-Japan Workshop on the Improvement of Building Structural Design and Construction Practices, Tokyo, Japan, July 29-30, 1988, Applied Technology Council.

51. Yang, M. S., *Seismic Behavior of an Eccentrically X-Braced Steel Structure,* Report No. UCB/EERC-82/14, Earthquake Engineering Research Center, University of California, Berkeley, CA, 1982.

52. Bertero, V. V., *Ductility Based Structural Design*, 9th World Conference on Earthquake Engineering, Tokyo, 1988.

53. Akiyama, H., *Earthquake Resistant Limit-State Design for Buildings,* University of Tokyo Press, 1985.

Table 2.1 - Prototype Frame Dimensions

Spec. No.	Prototype Link Length (inches)	Prototype Span Length (feet)	Prototype Brace-Beam Angle (deg)	Prototype L/e
1,2	42	15	48.2	4.3
3,4	50	14	51.2	3.4
5,6	66	25	33.2	4.5
7	44	26	28.4	7.1
8	54	27	29.0	6.0
9	30	16	43.5	6.4
10	32	16	44.1	6.0
11,11R1,11R2	41	27	28.0	7.9
12	90	23	39.3	3.1

Note: All prototype story heights are 12. ft.

Table 2.2 - Test Specimens - Dimensions and Sections

Specimen Number	Beam Section	Link Length (inches)	Brace Section	Brace-Beam Angle (deg.)	Test Setup
1,2	W12x16	28	W8x21	48.2	A
3,4	W12x22	33	TS 7x4x5/16	51.2	A
5,6	W12x16	44	W10x26	33.2	B
7	W12x16	29	TS 4x5x1/4	28.4	B
8	W12x22	36	TS 6x4x1/4	29.0	B
9	W12x22	20	TS 6x6x1/4	43.5	A
10	W12x16	21	TS 6x6x1/4	44.1	A
11	W12x22	27.5	TS 5x5x5/16	28.0	B
11R1,11R2	W12x22	26.75	TS 5x5x5/16	28.0	B
12	W12x22	60	W8x21	39.3	B

Notes: All columns are W10x77
All W sections are A36 steel (nominal $F_y = 36\,ksi$)
All Tube sections are A500 Gr B steel (nominal $F_y = 46\,ksi$)

Table 2.3 - Nominal Section Dimensions - W Sections

Section	d (in.)	b_f (in.)	t_w (in.)	t_f (in.)	$\frac{b_f}{2t_f}$	$\frac{d}{t_w}$
W12x16	11.99	3.99	.220	.265	7.5	54.5
W12x22	12.31	4.03	.260	.425	4.7	47.3
W8x21	8.28	5.27	.250	.400	6.6	33.1
W10x26	10.33	5.77	.260	.440	6.6	39.7

Table 2.4 - Nominal Section Properties - W Sections

Section	A (in^2)	Z (in^3)	P_y $(kips)$	V_p $(kips)$	M_p $(in-k)$	M_p / V_p (in)
W12x16	4.71	20.1	170	52	724	13.9
W12x22	6.48	29.3	233	63	1055	16.6
W8x21	6.16	20.4	222	-	734	-
W10x26	7.61	31.3	274	-	1127	-

Notes: $P_y = A\,F_y$
$V_p = .55\,d\,t_w\,F_y$
$M_p = Z\,F_y$
P_y, V_p, M_p based on nominal $F_y = 36\ ksi$.

Table 2.5 - Nominal Section Properties - Tube Sections

Section	A (in^2)	Z (in^3)	P_y $(kips)$	M_p $(in-k)$
7x4x5/16	6.23	13.8	287	635
4x5x1/4	4.09	5.90	188	271
6x4x1/4	4.59	9.06	211	417
6x6x1/4	5.59	11.9	257	547
5x5x5/16	5.61	9.70	258	446

Notes: $P_y = A\,F_y$
$M_p = Z\,F_y$
P_y, M_p based on nominal $F_y = 46\ ksi$.

Table 2.6 - Measured Section Dimensions
W Sections

Specimen Number	Section	d (in.)	b_f (in.)	t_w (in.)	t_f (in.)
1	W12x16	11.89	3.99	.217	.255
1	W8x21	8.24	5.24	.254	.377
2	W12x16	11.89	4.00	.217	.268
2	W8x21	8.33	5.28	.263	.382
3	W12x22	12.31	3.98	.266	.420
4	W12x22	12.31	3.98	.265	.418
5	W12x16	11.89	3.99	.217	.268
5	W10x26	10.41	5.72	.279	.377
6	W12x16	12.00	4.02	.212	.264
6	W10x26	10.40	5.72	.276	.372
7	W12x16	11.89	3.99	.218	.268
8	W12x22	12.28	4.13	.284	.382
9	W12x22	12.28	4.12	.282	.380
10	W12x16	11.88	4.00	.220	.268
11,11R1,11R2	W12x22	12.28	4.11	.283	.381
12	W12x22	12.28	4.11	.284	.382
12	W8x21	8.31	5.22	.285	.397

Table 2.7 - Measured Section Dimensions
Tube Sections

Specimen Number	Section	height (in.)	width (in.)	wall thickness (in.)
3	7x4x5/16	7.01	4.01	.354
4	7x4x5/16	7.01	4.00	.349
7	4x5x1/4	4.00	5.16	.226
8	6x4x1/4	6.01	4.02	.232
9	6x6x1/4	5.98	6.01	.235
10	6x6x1/4	5.99	5.99	.235
11,11R1,11R2	5x5x5/16	4.99	4.99	.295

Table 2.8 - Tensile Coupon Data - W Sections

Specimen Number	Section	Location	F_y (ksi)	F_{ult} (ksi)	ϵ_{sh}	ϵ_{ult}	% Elon.	Notes
1	W12x16	flange	46	61	.035	.21	28.4	(1)
1	W12x16	web	53	65	.033	.16	22.5	(1)
1	W8x21	flange	48	70	.023	.21	24.5	
1	W8x21	web	50	70	.029	.18	25.6	(1)
2	W12x16	flange	45	59	.037	.22	28.4	
2	W12x16	web	52	64	.032	.10	23.1	
2	W8x21	flange	39	59	.024	.22	28.1	
2	W8x21	web	48	62	.028	.20	26.0	
3	W12x22	flange	46	66	.026	-	24.2	(2)
3	W12x22	web	57	70	.030	.18	21.4	
4	W12x22	flange	47	65	.026	.18	23.5	(1)
4	W12x22	web	56	70	.035	.19	20.6	
5	W12x16	flange	45	60	.029	.21	27.1	(2)
5	W12x16	web	52	64	.033	.19	22.6	
5	W10x26	flange	50	71	.022	.22	27.0	
5	W10x26	web	53	73	.028	.21	25.6	(1)
6	W12x16	flange	52	69	.022	.20	23.6	(1)
6	W12x16	web	60	73	.025	.14	21.4	
6	W10x26	flange	51	73	.025	.21	24.5	
6	W10x26	web	53	73	.026	.20	23.5	
7	W12x16	flange	44	59	.026	.22	25.0	
7	W12x16	web	51	63	.034	.19	22.6	
8	W12x22	flange	42	65	.018	.21	26.4	(2)
8	W12x22	web	46	67	.025	.21	27.2	
9	W12x22	flange	42	66	.014	.21	25.2	
9	W12x22	web	47	68	.026	.21	27.2	
10	W12x16	flange	44	60	.030	.22	25.9	(1)
10	W12x16	web	51	63	.027	.19	22.8	
11/R1/R2	W12x22	flange	44	67	.018	.23	23.0	(2)
11/R1/R2	W12x22	web	48	67	.027	.23	27.8	
12	W12x22	flange	43	66	.016	.21	26.4	(2)
12	W12x22	web	47	66	.029	.21	26.8	
12	W8x21	flange	47	71	.016	.20	24.3	
12	W8x21	web	49	73	.022	.21	24.9	

Notes: (1) Necking and fracture occurred outside extensometer
(2) Extensometer removed during necking
Coupon preparation and testing per ASTM E8
F_y based on lower yield point
F_{ult} is maximum stress
ϵ_{sh} is the strain at the onset of strain hardening
ϵ_{ult} is the strain at F_{ult}
ϵ_{sh} and ϵ_{ult} based on an initial 2 inch gage length
% elongation based on an initial 8 inch gage length

Table 2.9 - Tensile Coupon Data - Tube Sections

Specimen Number	Section	Location	F_y (ksi)	F_{ult} (ksi)	ϵ_{ult}	% Elon.	Notes
3	7x4x5/16	flange	57	61	.18	24.6	
3	7x4x5/16	web	52	60	.19	27.5	
4	7x4x5/16	flange	56	61	.16	25.0	
4	7x4x5/16	web	53	61	.18	27.2	
7	4x5x1/4	flange	55	64	-	23.1	(1)
7	4x5x1/4	web	54	62	.15	26.5	
8	6x4x1/4	flange	63	73	.081	26.4	
8	6x4x1/4	web	64	72	.065	15.6	
9	6x6x1/4	flange	57	62	.051	16.4	
9	6x6x1/4	web	56	61	.074	19.8	
10	6x6x1/4	flange	55	63	.17	24.3	
10	6x6x1/4	web	56	62	.16	25.8	
11/R1/R2	5x5x5/16	flange	59	64	.14	22.0	
11/R1/R2	5x5x5/16	web	59	63	.15	24.2	

Notes: (1) Extensometer removed during necking
Coupon preparation and testing per ASTM E8
Coupons showed no well defined yield point or yield plateau;
F_y estimated from stress-strain plot
F_{ult} is maximum stress
ϵ_{ult} is the strain at F_{ult}
ϵ_{ult} based on an initial 2 inch gage length
% elongation based on an initial 8 inch gage length

Table 2.10 - Estimated Actual Section Properties
W Sections

Specimen Number	Section	A (in^2)	Z (in^3)	P_y $(kips)$	V_p $(kips)$	M_p $(in-k)$	M_p / V_p (in)
1	W12x16	4.58	19.30	228	75	937	12.5
1	W8x21	5.93	19.38	288	-	937	-
2	W12x16	4.68	19.89	228	74	944	12.8
2	W8x21	6.10	20.07	256	-	816	-
3	W12x22	6.47	29.05	331	103	1432	13.9
4	W12x22	6.44	28.91	330	100	1437	14.4
5	W12x16	4.68	19.86	228	74	943	12.7
5	W10x26	7.08	28.50	362	-	1444	-
6	W12x16	4.63	19.88	260	84	1089	13.0
6	W10x26	7.00	28.15	362	-	1449	-
7	W12x16	4.69	19.90	224	73	925	12.7
8	W12x22	6.50	28.62	286	88	1240	14.1
9	W12x22	6.46	28.41	287	89	1240	13.9
10	W12x16	4.72	19.96	225	73	928	12.7
11	W12x22	6.47	28.45	298	92	1289	14.0
12	W12x22	6.49	28.58	305	90	1266	14.1
12	W8x21	6.37	20.72	303	-	982	-

Notes: Properties are based on measured dimensions and tensile coupon yield strengths for flange and web

$P_y = A_{flange} F_{y\,flange} + A_{web} F_{y\,web}$

$V_p = .55\, d\, t_w F_{y\,web}$

$M_p = Z_{flange} F_{y\,flange} + Z_{web} F_{y\,web}$

Table 2.11 - Estimated Actual Section Properties
Tube Sections

Specimen Number	Section	A (in^2)	Z (in^3)	P_y $(kips)$	M_p $(in-k)$
3	7x4x5/16	6.97	15.35	380	837
4	7x4x5/16	6.89	15.18	375	827
7	4x5x1/4	3.81	5.57	207	304
8	6x4x1/4	4.30	8.54	273	542
9	6x6x1/4	5.27	11.26	298	636
10	6x6x1/4	5.27	11.25	292	624
11/R1/R2	5x5x5/16	5.32	9.22	314	544

Notes: Properties are based on measured dimensions and average tensile coupon yield strengths for flange and web
$P_y = A\, F_{y\ average}$
$M_p = Z\, F_{y\ average}$

Table 2.12 - Non-dimensionalized Link Lengths

Specimen Number	e (inches)	$e/(M_p/V_p)$ (nominal M_p/V_p)	$e/(M_p/V_p)$ (estimated actual M_p/V_p)
1	28	2.0	2.25
2	28	2.0	2.20
3	33	2.0	2.40
4	33	2.0	2.30
5	44	3.15	3.45
6	44	3.15	3.40
7	29	2.1	2.30
8	36	2.15	2.55
9	20	1.2	1.45
10	21	1.5	1.65
11	27.5	1.65	2.00
11R1,11R2	26.75	1.6	1.90
12	60	3.6	4.25

Table 2.13 - Spacing of Lateral Supports

Spec. No.	L_{b1} (in.)	$\frac{L_{b1}}{r_y}$	L_{b2} (in.)	$\frac{L_{b2}}{r_y}$	L_{b3} (in.)	$\frac{L_{b3}}{r_y}$	L_{b4} (in.)	$\frac{L_{b4}}{r_y}$
1	28	36	74	96				
2	28	36	74	96				
3	33	39	81	96				
4	33	39	81	96				
5	44	57	74	96	46	60		
6	44	57	74	96	46	60		
7	29	38	74	96	61	79		
8	36	43	81	96	47	55		
9	20	24	81	96	16	19		
10	21	27	58	75	38	49		
11	27.5	32	39	46	97	115		
11R1	26.75	31	39	46	97	115		
11R2	26.75	31	39	46	40	47	57	67
12	60	71	81	96	23	27		

Notes:

L_{b1} =distance from column face to link end lateral support (=e)

L_{b2} =distance from link end lateral support to first beam lateral support

L_{b3} =distance from first beam lateral support to second beam lateral support

L_{b4} =distance from second beam lateral support to third beam lateral support

$\frac{L_b}{r_y}$ based on nominal r_y

$W12x16$: r_y = .773 *inches*

$W12x22$: r_y = .847 *inches*

Table 3.1 - Link Rotation and Load Histories

CYCLE	Spec. No. 1			Spec. No. 2			Spec. No. 3			Spec. No. 4		
	γ (rad)	γ_p (rad)	V_{link} (kips)	γ (rad)	γ_p (rad)	V_{link} (kips)	γ (rad)	γ_p (rad)	V_{link} (kips)	γ (rad)	γ_p (rad)	V_{link} (kips)
1E	.002	0	14	002	0	15	.003	0	16	.002	0	15
1W	-.002	0	-15	-.002	0	-15	-.002	0	-14	-.002	0	-16
2E	.004	0	30	.004	0	29	.005	0	31	.004	0	30
2W	-.004	0	-29	-.004	0	-30	-.004	0	-29	-.004	0	-31
3E	.005	0	39	.005	0	39	.007	0	45	.006	0	45
3W	-.006	0	-39	-.006	0	-40	-.006	.001	-44	-.006	.001	-46
4E	.007	0	51	.007	0	48	.009	.001	60	.009	.001	57
4W	-.007	0	-48	-.007	0	-50	-.008	.001	-58	-.007	.001	-60
5E	.009	.001	59	.009	.001	57	.013	.003	73	.012	.001	73
5W	-.009	-.001	-55	-.009	0	-59	-.010	.001	-72	-.009	.002	-73
6E	.014	.006	54	.013	.005	61	.018	.006	81	.016	.004	83
6W	-.001	-.002	-63	-.013	-.003	-66	-.019	-.007	-84	-.015	-.003	-88
7E	.019	.010	66	.020	.010	66	.021	.008	90	.023	.011	86
7W	-.019	-.009	-67	-.020	-.011	-63	-.023	-.011	-87	-.022	-.009	-94
8E	.019	.009	68	.020	.011	68	.029	.015	93	.030	.017	96
8W	-.018	-.009	-68	-.019	-.010	-69	-.030	-.017	-90	-.029	-.016	-95
9E	.024	.014	71	.027	.018	62	.036	.023	95	.038	.024	100
9W	-.023	-.014	-63	-.024	-.015	-64	-.037	-.024	-96	-.036	-.021	-102
10E	.030	.020	73	.034	.026	57	.036	.022	98	.037	.023	103
10W	-.030	-.019	-74	-.032	-.023	-61	-.037	-.023	-96	-.036	-.021	-102
11E	.037	.026	77	.034	.026	57	.043	.029	99	.045	.030	104
11W	-.037	-.026	-77	-.033	-.025	-54	-.044	-.030	-98	-.043	-.028	-110
12E	.045	.034	79	.036	.028	53	.050	.036	102	.053	.039	100
12W	-.045	-.034	-78	-.033	-.025	-50	-.051	-.037	-102	-.066	-.052	-101
13E	.054	.043	74	.048	.041	52	.074	.062	80	.037	.026	78
13W	-.054	-.042	-78	-.044	-.037	-52	-.127	-.12	-51	-.143	-.129	-98
14E	.062	.053	66	.059	.053	43						
14W	-.063	-.053	-72	-.054	-.048	-45						
15E	.075	.067	52	.093	.090	23						
15W	-.073	-.064	-63									
16E	.086	.083	22									

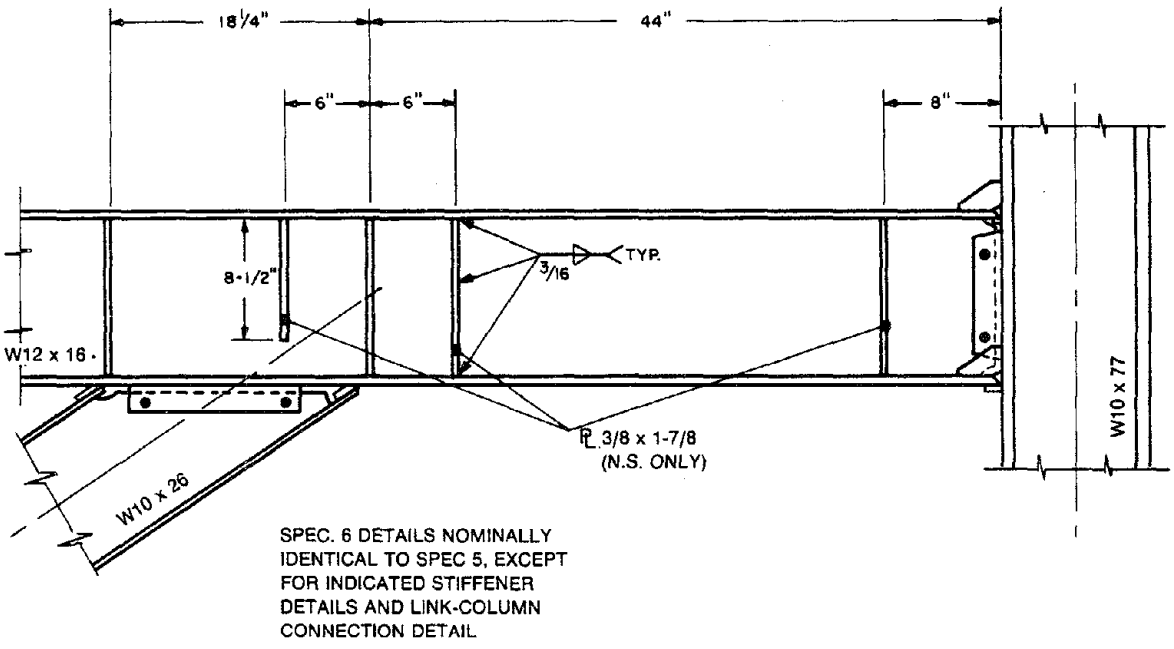

Fig. 2.11 Link Details - Specimen 6

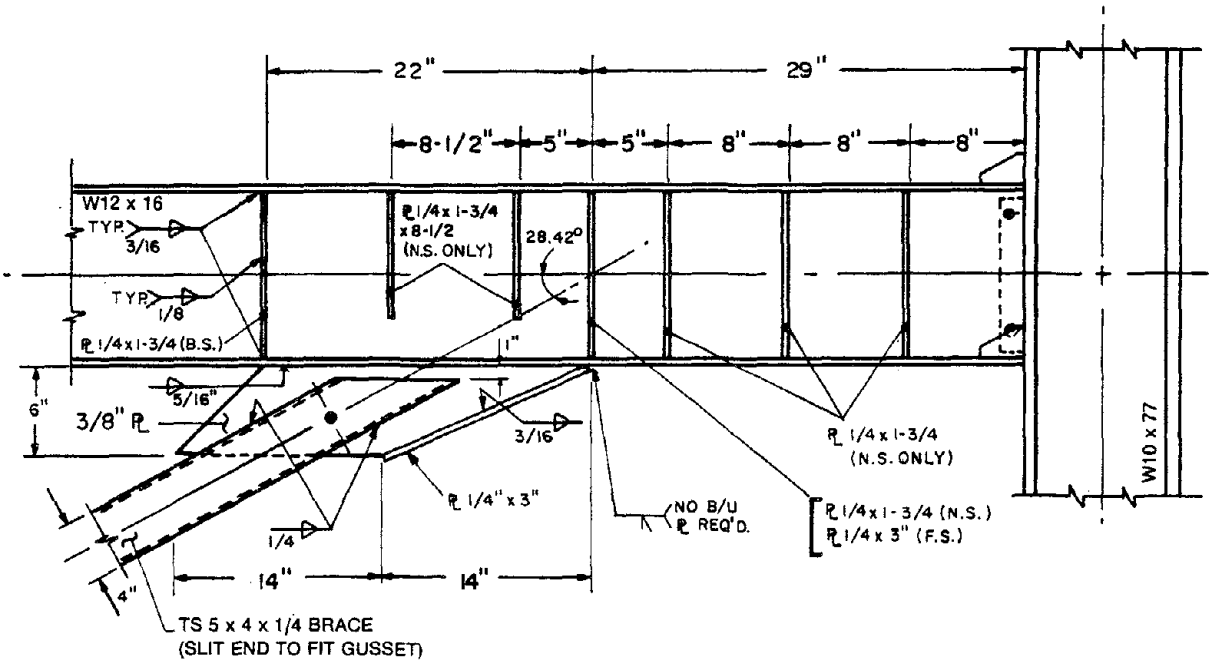

Fig. 2.12 Link Details - Specimen 7

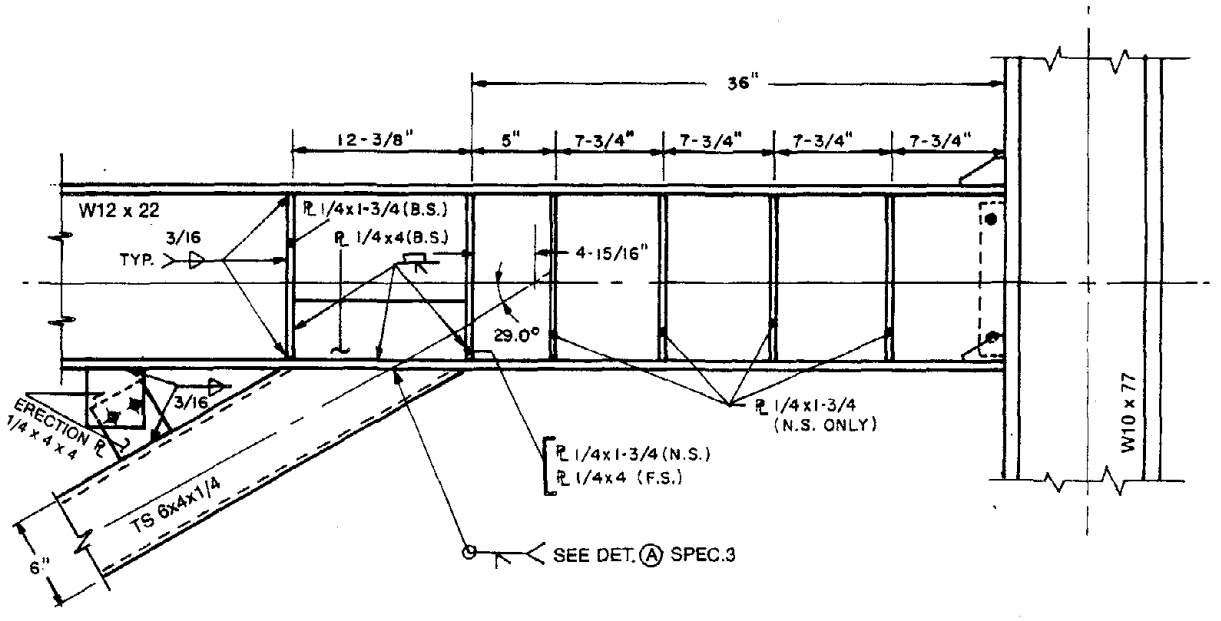

Fig. 2.13 Link Details - Specimen 8

Table 3.1 - Link Rotation and Load Histories (cont)

CYCLE	Spec. No. 5			Spec. No. 6			Spec. No. 7		
	γ (rad)	γ_p (rad)	V_{link} (kips)	γ (rad)	γ_p (rad)	V_{link} (kips)	γ (rad)	γ_p (rad)	V_{link} (kips)
1E	.002	0	9	.002	0	10	.002	0	11
1W	-.003	0	-10	-.003	0	11	-.002	0	-11
2E	.005	0	20	.005	0	20	.002	0	10
2W	-.005	0	-20	-.005	0	-21	-.004	0	-20
3E	.007	0	30	.007	0	29	.004	0	20
3W	-.008	-.001	-30	-.007	0	-29	-.004	0	-20
4E	.001	.002	38	.010	.001	40	.006	0	29
4W	-.001	-.002	-38	-.009	0	-39	-.005	0	-29
5E	.015	.004	45	.014	.003	47	.006	0	30
5W	-.013	-.002	-45	-.013	-.001	-48	-.008	0	-39
6E	.018	.007	46	.017	.004	53	.008	0	38
6W	-.016	-.004	-47	-.016	-.003	-52	-.008	0	-39
7E	.018	.007	47	.020	.006	55	.011	.001	49
7W	-.016	-.004	-47	-.019	-.005	-54	-.011	-.001	-49
8E	.022	.010	47	.023	.008	57	.011	0	49
8W	-.019	-.007	-48	-.022	-.008	-55	-.016	-.005	-51
9E	.025	.013	46	.027	.013	57	.018	.006	58
9W	-.022	-.010	-47	-.026	-.012	-56	-.017	-.005	-56
10E	.029	.017	47	.031	.017	56	.022	.011	52
10W	-.027	-.017	-38	-.029	-.015	-56	-.020	-.008	-59
11E	.074	.069	21	.035	.021	54	.022	.010	53
11W				-.033	-.019	-56	-.023	-.011	-60
12E				.039	.026	48	.025	.015	50
12W				-.036	-.023	-53	-.024	-.013	-55
13E				.042	.030	47	.029	.019	46
13W				-.040	-.028	-49	-.029	-.017	-57
14E				.046	.035	44	.029	.020	44
14W				-.044	-.033	-45	-.033	-.022	-54
15E				.079	.072	29	-	-	28

Table 3.1 - Link Rotation and Load Histories (cont)

CYCLE	Spec. No. 8		
	γ (rad)	γ_p (rad)	V_{link} (kips)
1E	.003	0	20
1W	-.003	0	-20
2E	.003	0	20
2W	-.007	0	-39
3E	.006	0	40
3W	-.007	0	-42
4E	.011	.001	60
4W	-.011	-.001	-58
5E	.010	0	59
5W	-.013	-.002	-64
6E	.014	.002	67
6W	-.013	-.002	-65
7E	.017	.005	71
7W	-.016	-.004	-70
8E	.016	.004	74
8W	-.019	-.007	-72
9E	.021	.008	73
9W	-.018	-.006	-75
10E	.024	.011	75
10W	-.022	-.009	-75
11E	.024	.010	79
11W	-.024	-.012	-77
12E	.028	.014	79
12W	-.025	-.011	-79
13E	.032	.018	81
13W	-.029	-.015	-81
14E	.032	.017	83
14W	-.035	-.021	-82
15E	.036	.022	84
15W	-.035	-.021	-84
16E	.041	.028	75
16W	-.043	-.029	-85
17E	.028	.016	67
17W	-.053	-.039	-86
18E	.008	0	44

Table 3.1 - Link Rotation and Load Histories (cont)

CYCLE	Spec. No. 9			Spec. No. 10			Spec. No. 12		
	γ (rad)	γ_p (rad)	V_{link} (kips)	γ (rad)	γ_p (rad)	V_{link} (kips)	γ (rad)	γ_p (rad)	V_{link} (kips)
1E	.003	0	20	.003	0	16	.005	0	20
1W	-.003	0	-20	-.003	0	-14	-.005	0	-19
2E	.006	0	40	.006	0	30	.007	0	29
2W	-.005	0	-39	-.005	.001	-29	-.007	0	-29
3E	.009	0	59	.009	.001	45	.011	.001	39
3W	-.008	0	-59	-.007	.001	-43	-.010	0	-39
4E	.014	.002	77	.013	.002	59	.017	.005	45
4W	-.011	0	-76	-.008	.002	-57	-.017	-.005	-47
5E	.021	.009	80	.020	.008	65	.021	.008	50
5W	-.021	-.008	-84	-.017	-.004	-67	-.022	-.009	-50
6E	.026	.012	92	.020	.007	69	.028	.015	51
6W	-.026	-.012	-96	-.023	-.010	-70	-.028	-.014	-55
7E	.034	.019	100	.026	.013	71	.036	.022	53
7W	-.035	-.020	-101	-.029	-.016	-73	-.036	-.021	-58
8E	.042	.026	106	.032	.018	78	.044	.030	53
8W	-.043	-.027	-107	-.034	-.021	-76	-.069	-.056	-50
9E	.050	.034	107	.038	.024	78			
9W	-.051	-.034	-112	-.042	-.027	-79			
10E	.059	.042	108	.045	.030	80			
10W	-.060	-.042	-115	-.047	-.032	-83			
11E	.073	.065	57	.099	.091	44			

Table 3.1 - Link Rotation and Load Histories (cont)

CYCLE	Spec. No. 11			Spec. No. 11R1			Spec. No. 11R2		
	γ (rad)	γ_p (rad)	V_{link} (kips)	γ (rad)	γ_p (rad)	V_{link} (kips)	γ (rad)	γ_p (rad)	V_{link} (kips)
1E	.003	0	15	.003	0	15	.014	.002	73
1W	-.003	0	-15	-.003	0	-15	-.009	.003	-73
2E	.005	0	30	.005	0	29	.019	.005	86
2W	-.005	0	-29	-.005	0	-28	-.010	.003	-84
3E	.008	0	44	.007	0	44	.025	.010	91
3W	-.007	.001	-44	-.007	0	-44	-.022	-.006	-104
4E	.011	.001	58	.009	0	59	.030	.014	95
4W	-.009	.001	-58	-.009	.001	-59	-.027	-.010	-102
5E	.018	.006	70	.011	0	66	.034	.018	97
5W	-.013	-.001	-70	-.010	.001	-70	-.030	-.013	-108
6E	.019	.007	73	.013	.001	75	.040	.023	104
6W	-.019	-.006	-76	-.013	0	-81	-.036	-.019	-105
7E	.024	.010	77	.016	.003	80	.047	.032	98
7W	-.023	-.009	-78	-.016	-.002	-87	-.043	-.026	-106
8E	.027	.014	79	.019	.005	87	.056	.041	94
8W	-.026	-.012	-82	-.019	-.005	-91	-.064	-.047	-107
9E	.031	.018	78	.022	.007	91	.055	.043	72
9W	-.007	.005	-71	-.023	-.008	-95			
10E				.025	.011	92			
10W				-.025	-.010	-97			
11E				.025	.010	95			

Notes for Tables 3.1:

The values of γ and γ_p listed above are the maximum for each cycle.

V_{link} is the link shear force at the end of the cycle and is not necessarily the maximum value for that cycle.

Table 3.2 - Failure Modes for Test Specimens

Spec. No.	Primary Failure Modes	Additional Failure Modes
1	fracture of link flange at link-column connection	flange buckling in brace connection panel; flange buckling in link adjacent to column
2	web buckling in central panel of link	
3	fracture of link flange at link-column connection	
4	fracture of link flange at link-column connection at ends of reinforcing ribs	
5	fracture of link flange at link-column connection	flange buckling in brace connection panel; flange buckling in link adjacent to column
6	fracture of link flange at link-column connection at ends of reinforcing ribs	flange buckling in brace connection panel; flange buckling in link adjacent to ribs
7	fracture of link flange at link-column connection at ends of reinforcing ribs; lateral torsional buckling of beam	
8	lateral torsional buckling of beam (primarily lateral buckling)	formation of cracks in link flange at ends of reinforcing ribs
9	fracture in flange connection plate at link- column web connection	lateral torsional buckling of beam
10	fracture of link flange at link-column web connection	lateral torsional buckling of beam
11	fracture of link flange at link-column connection	
11R1	lateral torsional buckling of beam (primarily lateral buckling)	
11R2	lateral torsional buckling of beam; failure of link end lateral support	
12	lateral torsional buckling of link; failure of link end lateral support	lateral torsional buckling of beam

Table 3.3 - Plastic Rotation Capacities of Test Specimens

Spec. No.	$\bar{\gamma}_p$ (rad.)		
	stable hysteretic loops	$V_{link} < V_{yield(SPT)}$	fracture at link-to-column connection
1	.08	.10	.12
2	.025	.025	-
3	.073	.073	.073
4	.068	.068	.068
5	.028	.028	.028
6	.033	.055	.067
7	.017	0	.037
8	.043	.063	-
9	.08	.08	.08
10	.062	.062	.062
11	.03	0	.03
11R1	.023	.023	-
11R2	.085	.085	-
12	.053	.083	-

Table 3.4 - Estimated Plastic Frame Drift
For Prototype Structures

Specimen	θ_p (percent)
1	.9
2	.3
3	1.1
4	1.0
5	.3
6	.7
7	.1
8	.4
9	.6
10	.5
11	.2
11R1	.15
11R2	.5
12	.8

Notes: $\theta_p = \gamma_p / (L/e)$
$\gamma_p = \frac{1}{2}\,\bar{\gamma}_p$ for stable hysteretic loops (Table 3.3)
L/e = span to link length ratio of prototype (Table 2.1)

Table 4.1 - Link Yield and Ultimate Shear Forces

Spec. No.	$V_{yield(SPT)}$ (kips) [1]	$1.5\times V_{yield(SPT)}$ (kips) [2]	$V_{yield(exp)}$ (kips) [3]	$V_{ult(exp)}$ (kips) [4]	$\frac{V_{ult(exp)}}{V_{yield(exp)}}$ [4]/[3]	$\frac{V_{yield(exp)}}{V_{yield(SPT)}}$ [3]/[1]	$\frac{V_{ult(exp)}}{1.5\times V_{yield(SPT)}}$ [4]/[2]	$\frac{V_{ult(exp)}}{V_{yield(SPT)}}$ [4]/[1]
1	67	101	62	79	1.27	.93	.78	1.18
2	67	101	62	71	1.15	.93	.70	1.06
3	87	131	84	112	1.33	.97	.85	1.29
4	96	144	89	110	1.24	.93	.76	1.15
5	43	65	41	49	1.20	.95	.75	1.14
6	53	80	47	59	1.26	.89	.74	1.11
7	71	107	47	61	1.30	.66	.57	.86
8	75	113	60	89	1.48	.80	.79	1.19
9	89	134	82	120	1.46	.92	.90	1.35
10	73	110	67	85	1.27	.92	.77	1.16
11	92	138	65	86	1.32	.71	.62	.93
11R1	92	138	83	97	1.17	.90	.70	1.05
11R2	92	138	89	113	1.26	.97	.82	1.22
12	42	63	44	62	1.41	1.05	.98	1.47

Notes:

$V_{yield(SPT)}$ = lesser of V_p or $2M_p/e$ (e measured from rib ends for specimens 4, 6, 7 and 8)

$V_{yield(exp)}$ = absolute value of measured shear force at first significant yield (estimated)

$V_{yield(exp)}$ = absolute value of measured ultimate shear force

Table 4.2 - Ultimate Link End Moments

Spec. No.	Moment at Column (in-k) [1]		Moment at End of Reinforced Region (in-k) [2]		Moment at Brace (in-k) [3]		$\frac{\lvert \text{Max. Link Moment} \rvert}{M_p}$ [4]
1	-1100	+1135			-1060	+1150	1.21
2	-1065	+1105			-870	+940	1.17
3	-1875	+1945			-1555	+1710	1.35
4	-1910	+1910	-1580	+1595	-1545	+1680	1.11
5	-1060	+1160			-1070	+1155	1.23
6	-1340	+1470	-1165	+1290	-1170	+1260	1.18
7	-1190	+1300	-1020	+1140	-500	+660	1.23
8	-1950	+2070	-1690	+1830	-1160	+1300	1.48
9	-1285	+1400			-890	+1110	1.13
10	-935	+960			-800	+875	1.03
11	-1560	+1615			-800	+800	1.25
11R1	-1950	+1950	-1560	+1570	-635	+645	1.22
11R2	-2385	+2400	-1930	+2000	-500	+685	1.55
12	-1965	+1870			-1590	+1730	1.55

Notes:
The sign convention for link end moments is shown in Fig. 3.2

For specimens that failed by fracture at the link-to-column connection, the moments listed above are the maximum values prior to the occurrence of fracture.

For [2], moment is computed at 3 inches from column face for specimens 4, 6, 7 and 8 and at 4 inches from column face for specimens 11R1 and 11R2.

For [4], | Max. Link Moment | is taken as the maximum absolute value of [1] for specimens 1, 2, 3, 5, 9, 10, 11 and 12, and is taken as the maximum absolute value of [2] for specimens 4, 6, 7, 8, 11R1 and 11R2.
M_p is taken from Table 2.10

Table 4.3 - Ultimate Beam and Brace Axial Forces

Spec. No.	P_{beam} (kips)		P_{brace} (kips)		$\frac{P_{beam}}{P_{y\ beam}}$		$\frac{P_{brace}}{P_{y\ brace}}$	
1	-84	+91	-123	+120	-.37	+.40	-.43	+.42
2	-70	+74	-109	+105	-.31	+.32	-.43	+.41
3	-102	+112	-169	+156	-.31	+.34	-.44	+.41
4	-101	+107	-162	+156	-.31	+.32	-.43	+.42
5	-91	+99	-113	+105	-.40	+.43	-.31	+.29
6	-109	+112	-130	+127	-.42	+.42	-.36	+.35
7	-120	+120	-139	+138	-.54	+.54	-.67	+.67
8	-165	+179	-205	+191	-.58	+.63	-.75	+.70
9	-133	+142	-193	+183	-.46	+.49	-.65	+.61
10	-98	+100	-136	+134	-.44	+.44	-.47	+.46
11	-171	+177	-200	+194	-.57	+.59	-.64	+.62
11R1	-192	+197	-224	+217	-.64	+.66	-.71	+.69
11R2	-208	+233	-262	+236	-.70	+.78	-.83	+.75
12	-93	+104	-124	+114	-.30	+.34	-.40	+.38

Notes:
$P_{y\ beam}$ and $P_{y\ brace}$ from Tables 2.10 and 2.11

+ = tension

Table 4.4 - Beam Stability Computations
(Based on LRFD Stability Interaction Formula)

Spec. No.	Estimated Maximum Loads		Estimated Resistance			Stability Check	Instability Observed in Member ?
	P_u (kips)	M_u (in-k)	$K_y L$ (inches)	$P_n = A_g F_{cr}$ (kips)	M_n (in-k)	$\frac{P_u}{P_n} + \frac{8}{9}\frac{M_u}{M_n}$	
3	100	900	.6×74	260	1430	.94	No
6	109	465	.6×74	190	1090	.95	No
7	120	195	.6×74	168	925	.90	Yes
8	160	350	.6×69	237	1240	.93	Yes
11R2	205	400	.7×39	270	1290	1.03	Yes
12	90	790	.6×81	305	1265	.85	Yes

See section 4.4 for definition of terms and methods of computation

Table 4.5 - Maximum Out-of-Plane Forces at Link End Lateral Support

Spec. No.	Max $\|P_1\|$ (kips) [1]	Max $\|P_2\|$ (kips) [2]	$P_{y\ flange}$ (kips) [3]	$\frac{\text{Max } \|P\|}{P_{y\ flange}}$ [4]
1	4.8	3.7	47	.10
2	2.1	2.6	48	.054
3	0.9	1.4	77	.018
4	1.1	2.1	78	.027
5	1.4	1.3	48	.029
6	2.0	4.4	55	.080
7	3.0	2.4	47	.064
8	1.2	1.4	66	.021
9	4.2	6.2	66	.094
10	3.8	3.4	47	.081
11	.4	.5	69	.007
11R1	1.6	4.0	69	.058
11R2	> 9.0	>9.5	69	> .14
12	14.8	5.6	68	.22

Notes:

P_1 and P_2 are the measured link end lateral forces as shown in Fig. 4.40

$P_{y\ flange} = b_f t_f F_{y\ flange}$ (b_f and t_f from Table 2.6 and $F_{y\ flange}$ from Table 2.8)

Max. $|P|$ for [4] = maximum of [1] and [2]

Values of P_1 and P_2 reported for specimen 11R2 are the maximum values prior to failure of the link end load cells

Table 4.6 - Shear Strain Rosettes on Link
of Specimen 1

Strain Rosette	Distance from Column Face (inches)	Shear Force at First Yield (kips)
1	4.26	49
2	9.32	62
3	14.58	66
4	19.93	63
5	25.32	62

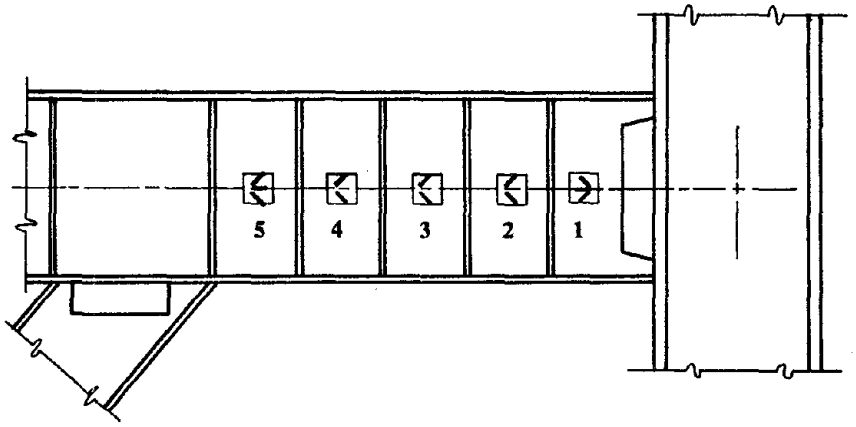

Notes:

(1) All rosettes located along link centerline

(2) Theoretical shear force at first yield based on strength of materials shear stress distribution and von Mises yield criterion:

$$\frac{.577 \times F_{y\,web}}{\frac{Q}{I\,b}} = \frac{.577 \times 53\,ksi}{\frac{9.65\,in^3}{98\,in^4 \times .217\,in}} = 67\,kips$$

Table 4.7 - Shear Strain Rosettes on Link of Specimen 3

Strain Rosette	Distance from Column Face (inches)	Shear Force at First Yield (kips)
1	5.27	72
2	12.43	90
3	20.71	90
4	28.94	75

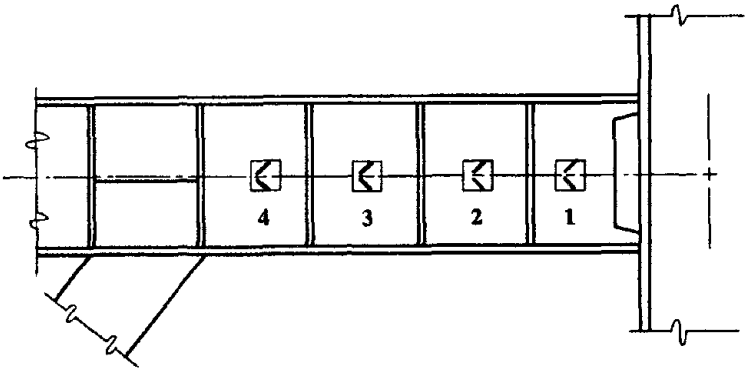

Notes:

(1) All rosettes located along link centerline

(2) Theoretical shear force at first yield based on strength of materials shear stress distribution and von Mises yield criterion:

$$\frac{.577 \times F_{y\,web}}{\frac{Q}{I\,b}} = \frac{.577 \times 57\,ksi}{\frac{14.53\,in^3}{153\,in^4 \times .266\,in}} = 92\,kips$$

Table 4.8 - Shear Strain Rosettes on Link of Specimen 5

Strain Rosette	Distance from Column Face (inches)
1	3.98
2	14.06
3	22.06
4	30.13
5	41.32

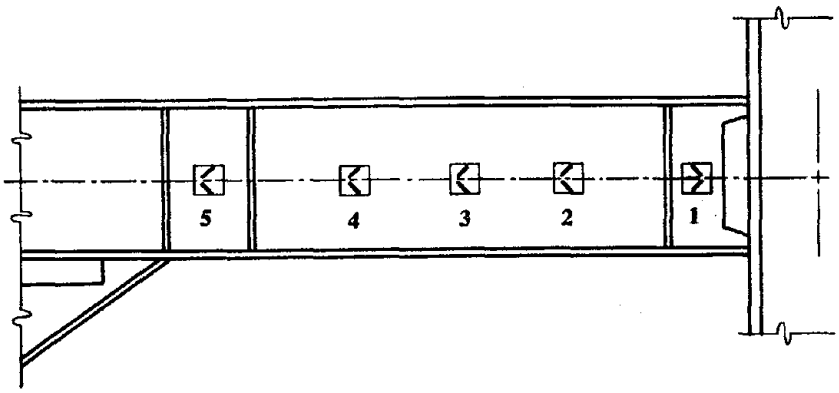

Note:
All rosettes located along link centerline

Table 4.9 - Shear Strain Rosettes on Link
of Specimen 9

Strain Rosette	Distance from Column Face (inches)	Shear Force at First Yield (kips)
1	4.80	80
2	11.02	78
3	17.54	78

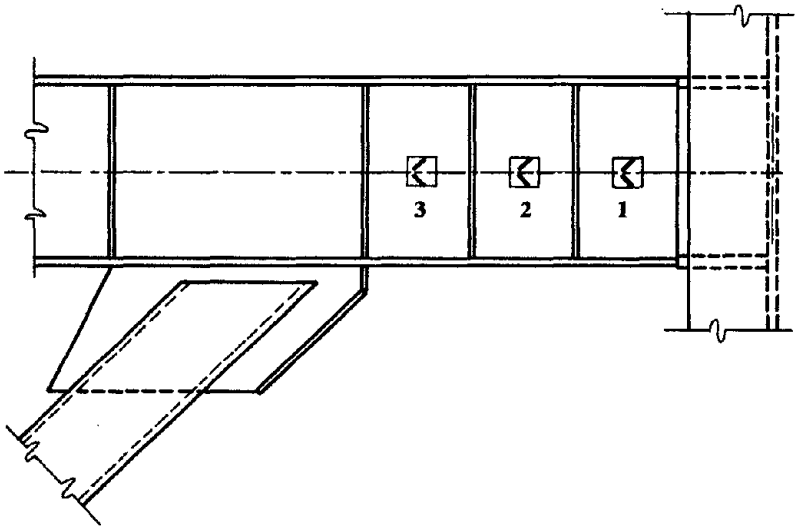

Notes:

(1) All rosettes located along link centerline

(2) Theoretical shear force at first yield based on strength of materials shear stress distribution and von Mises yield criterion:

$$\frac{.577 \times F_{y\,web}}{\frac{Q}{I\,b}} = \frac{.577 \times 47\,ksi}{\frac{14.21\,in^3}{149\,in^4 \times .282\,in}} = 80\,kips$$

Table 5.1 - Specimen 1 - Comparison of Shear Strains Computed from Photogrammetric Data with Shear Strains Measured by Strain Gage Rosettes

Reference State: Unloaded Specimen at Start of Test
Final State: Peak Deformation at End of Cycle 11W

Strain Rosette [1]	Distance from Column Face (in.) [2]	Shear Strain from Rosette [3]	Shear Strain from Photogrammetry [4]	Difference [4]-[3]
R1	4.26	.067	.067	0
R2	9.32	.018	.020	.002
R3	14.58	.018	.019	.001
R4	19.93	.024	.022	-.001
R5	25.32	.044	.043	-.001

Reference State: Unloaded Specimen at Start of Cycle 7E
Final State: Peak Deformation at End of Cycle 7E

Strain Rosette [1]	Distance from Column Face (in.) [2]	Shear Strain from Rosette [3]	Shear Strain from Photogrammetry [4]	Difference [4]-[3]
R1	4.26	.032	.031	-.001
R2	9.32	.0074	.0096	.002
R3	14.58	.0035	.0077	.004
R4	19.93	.0068	.0050	-.002
R5	25.32	.035	.029	-.006

Table 5.1 - Specimen 1 - Comparison of Shear Strains Computed from Photogrammetric Data with Shear Strains Measured by Strain Gage Rosettes (cont)

Reference State: Unloaded Specimen at Start of Cycle 13E
Final State: Peak Deformation at End of Cycle 13E

Strain Rosette [1]	Distance from Column Face (in.) [2]	Shear Strain from Rosette [3]	Shear Strain from Photogrammetry [4]	Difference [4]-[3]
R1	4.26	*	.13	-
R2	9.32	.048	.046	-.002
R3	14.58	.039	.041	.002
R4	19.93	.043	.042	-.001
R5	25.32	.075	.076	.001

* Gage Inoperative

Table 5.2 - Specimen 4 - Comparison of Shear Strains Computed from Photogrammetric Data with Shear Strains Measured by Strain Gage Rosettes

Reference State: Unloaded Specimen at Start of Cycle 8E
Final State: Peak Deformation at End of Cycle 8E

Strain Rosette [1]	Distance from Column Face (in.) [2]	Shear Strain from Rosette [3]	Shear Strain from Photogrammetry [4]	Difference [4]-[3]
R1	3.62	.030	.023	-.007
R2	11.06	.028	.029	.001
R3	22.97	.028	.031	.003
R4	31.06	.030	.031	.001

Reference State: Unloaded Specimen at Start of Cycle 11E
Final State: Peak Deformation at End of Cycle 11E

Strain Rosette [1]	Distance from Column Face (in.) [2]	Shear Strain from Rosette [3]	Shear Strain from Photogrammetry [4]	Difference [4]-[3]
R1	3.62	.043	.040	-.003
R2	11.06	.047	.047	0
R3	22.97	.045	.044	-.001
R4	31.06	.058	.058	0

Table 5.3a - Specimen 1 - Link Rotation Components
Load Cycle 7E (from last point of zero load)

[Intermediate Length Link - actual $e \approx 2.25 M_p / V_p$]

Link Rotation Measured by Displacement Transducers:

$\bar{\gamma} = .022\ rad$

$\bar{\gamma}_p = .013\ rad$

Link Rotation (elastic+plastic) by Integration of Averaged Photogrammetric Data:

Support rotation + link bending: (computed from web gridpoints)	.013 rad
Link shear:	.009 rad
Total:	.022 rad

Estimated Link Rotation Components:

Rotation Source	Rotation(rad)		
	elastic+plastic	elastic	plastic
Link Shear	.0087	.0022	.0065 (50%)
Link Bending	.0052	.0014	.0038 (29%)
Support Rotations	.0084	.0056	.0027 (21%)
Total	.022	.009	.013 (100%)

Table 5.3b - Specimen 1 - Link Rotation Components
Load Cycle 13E (from last point of zero load)

[Intermediate Length Link - actual $e \approx 2.25 M_p / V_p$]

Link Rotation Measured by Displacement Transducers:

$\bar{\gamma} = .087\ rad$

$\bar{\gamma}_p = .077\ rad$

Link Rotation (elastic+plastic) by Integration of Averaged Photogrammetric Data:

Support rotation + link bending: (computed from web gridpoints)	.047 rad
Link shear:	.042 rad
Total:	.089 rad

Estimated Link Rotation Components:

Rotation Source	Rotation(rad)		
	elastic+plastic	elastic	plastic
Link Shear	.042	.003	.039 (52%)
Link Bending	.025	.002	.023 (31%)
Support Rotations	.020	.007	.013 (17%)
Total	.087	.012	.075 (100%)

Table 5.4a - Specimen 4 - Link Rotation Components
Load Cycle 8E (from last point of zero load)

[Intermediate Length Link - actual $e \approx 2.3 M_p / V_p$]

Link Rotation Measured by Displacement Transducers:

$\bar{\gamma} = .041\ rad$

$\bar{\gamma}_p = .027\ rad$

Link Rotation (elastic+plastic) by Integration of Averaged Photogrammetric Data:

Support rotation + link bending: (computed from web gridpoints)	.018 rad
Link shear:	.022 rad
Total:	.040 rad

Estimated Link Rotation Components:

Rotation Source	Rotation(rad)		
	elastic+plastic	elastic	plastic
Link Shear	.022	.003	.019 (70%)
Link Bending	.008	.002	.006 (22%)
Support Rotations	.011	.009	.002 (8%)
Total	.041	.014	.027 (100%)

Table 5.4b - Specimen 4 - Link Rotation Components
Load Cycle 11E (from last point of zero load)

[Intermediate Length Link - actual $e \approx 2.3 M_p / V_p$]

Link Rotation Measured by Displacement Transducers:

$\bar{\gamma} = .067\ rad$

$\bar{\gamma}_p = .052\ rad$

Link Rotation (elastic+plastic) by Integration of Averaged Photogrammetric Data:

Support rotation + link bending: (computed from web gridpoints)	.029 rad
Link shear:	.036 rad
Total:	.065 rad

Estimated Link Rotation Components:

Rotation Source	Rotation(rad)		
	elastic+plastic	elastic	plastic
Link Shear	.036	.003	.033 (63%)
Link Bending	.018	.002	.015 (29%)
Support Rotations	.013	.009	.004 (8%)
Total	.067	.014	.052 (100%)

Table 5.5 - Specimen 6 - Link Rotation Components
Load Cycle 10E (from last point of zero load)

[Very Long Link - actual $e \approx 3.4 M_p / V_p$]

Link Rotation Measured by Displacement Transducers:

$\bar{\gamma} = .043\ rad$

$\bar{\gamma}_p = .029\ rad$

Link Rotation (elastic+plastic) by Integration of Averaged Photogrammetric Data:

Support rotation + link bending:	.038 rad
Link shear:	.006 rad
Total:	.044 rad

Estimated Link Rotation Components:

Rotation Source	Rotation(rad)		
	elastic+plastic	elastic	plastic
Link Shear	.006	.002	.004 (14%)
Link Bending	.025	.003	.022 (76%)
Support Rotations	.013	.010	.003 (10%)
Total	.044	.015	.029 (100%)

Table 5.6 - Specimen 9 - Link Rotation Components
Load Cycle 9E (from last point of zero load)

[Short Link - actual $e \approx 1.45 M_p / V_p$]

Link Rotation Measured by Displacement Transducers:

$\bar{\gamma} = .078$ *rad*

$\bar{\gamma}_p = .061$ *rad*

Link Rotation (elastic+plastic) by Integration of Averaged Photogrammetric Data:

Support rotation + link bending:	.022 rad
Link shear:	.057 rad
Total:	.079 rad

Estimated Link Rotation Components:

Rotation Source	Rotation(rad)		
	elastic+plastic	elastic	plastic
Link Shear	.057	.003	.054 (87%)
Link Bending	.009	.001	.008 (13%)
Support Rotations	.013	.013	0 (0%)
Total	.079	.017	.062 (100%)

Table 5.7 - Specimen 12 - Link Rotation Components
Load Cycle 7W (from last point of zero load)

[Very Long Link - actual $e \approx 4.25 M_p / V_p$]

Link Rotation Measured by Displacement Transducers:

$\bar{\gamma} = -.059\ rad$

$\bar{\gamma}_p = -.044\ rad$

Link Rotation (elastic+plastic) by Integration of Averaged Photogrammetric Data:

Support rotation + link bending:	-.054 rad
Link shear:	-.006 rad
Total:	-.060 rad

Estimated Link Rotation Components:

Rotation Source	Rotation(rad)		
	elastic+plastic	elastic	plastic
Link Shear	-.006	-.002	-.004 (9%)
Link Bending	-.037	-.004	-.033 (75%)
Support Rotations	-.017	-.010	-.007 (16%)
Total	-.060	-.016	-.044 (100%)

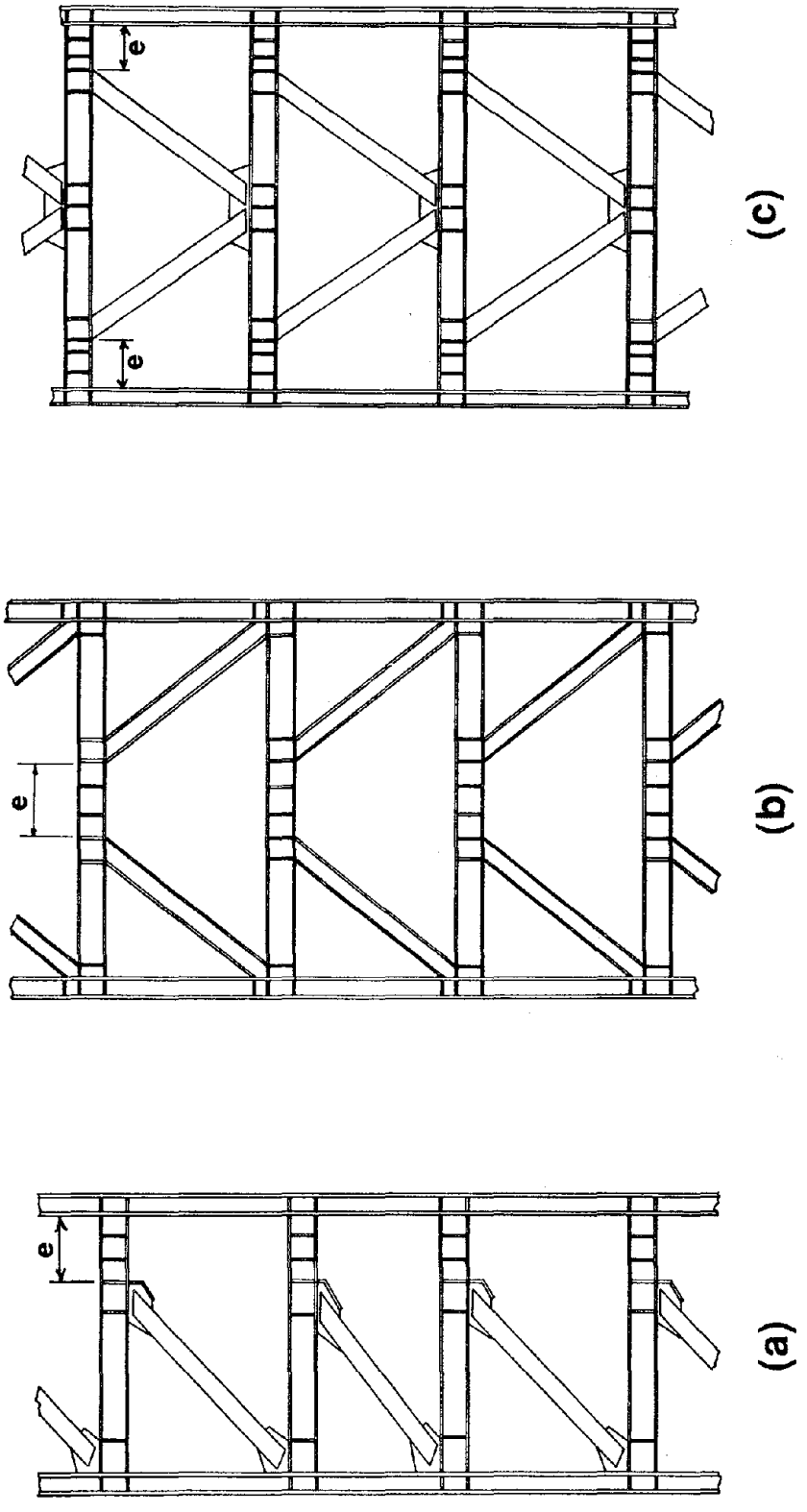

Fig. 1.1 Typical EBFs

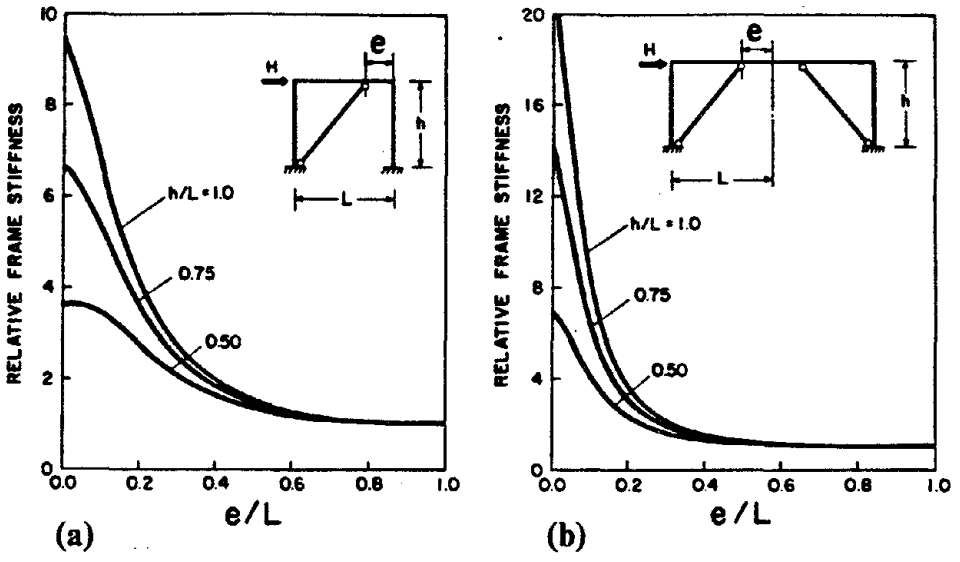

Fig. 1.2 Variation of Elastic Lateral Stiffness with *e/L* for Two Simple EBFs [9]

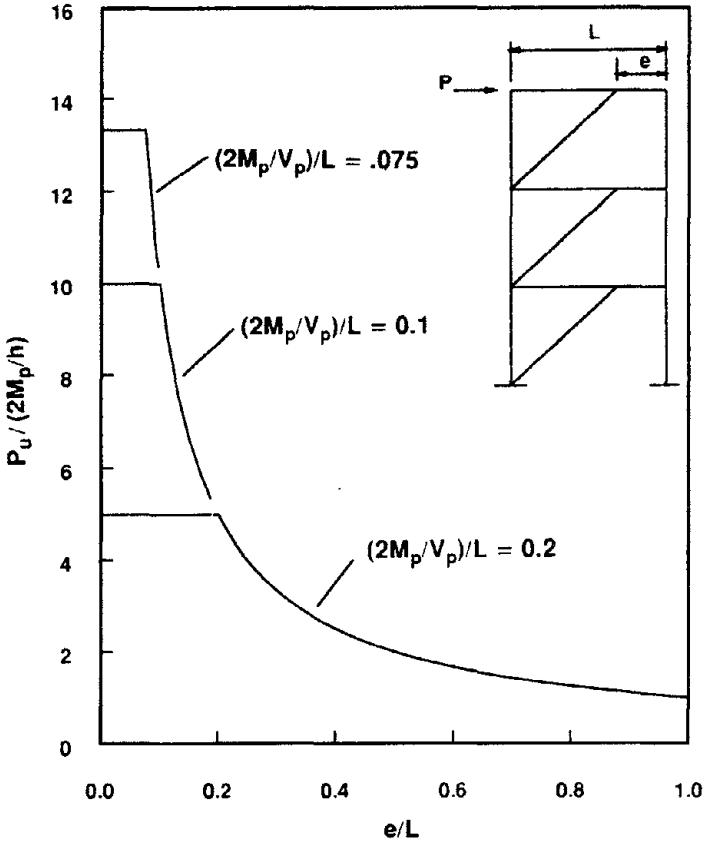

Fig. 1.3 Variation of Frame Plastic Strength with *e/L* [14]

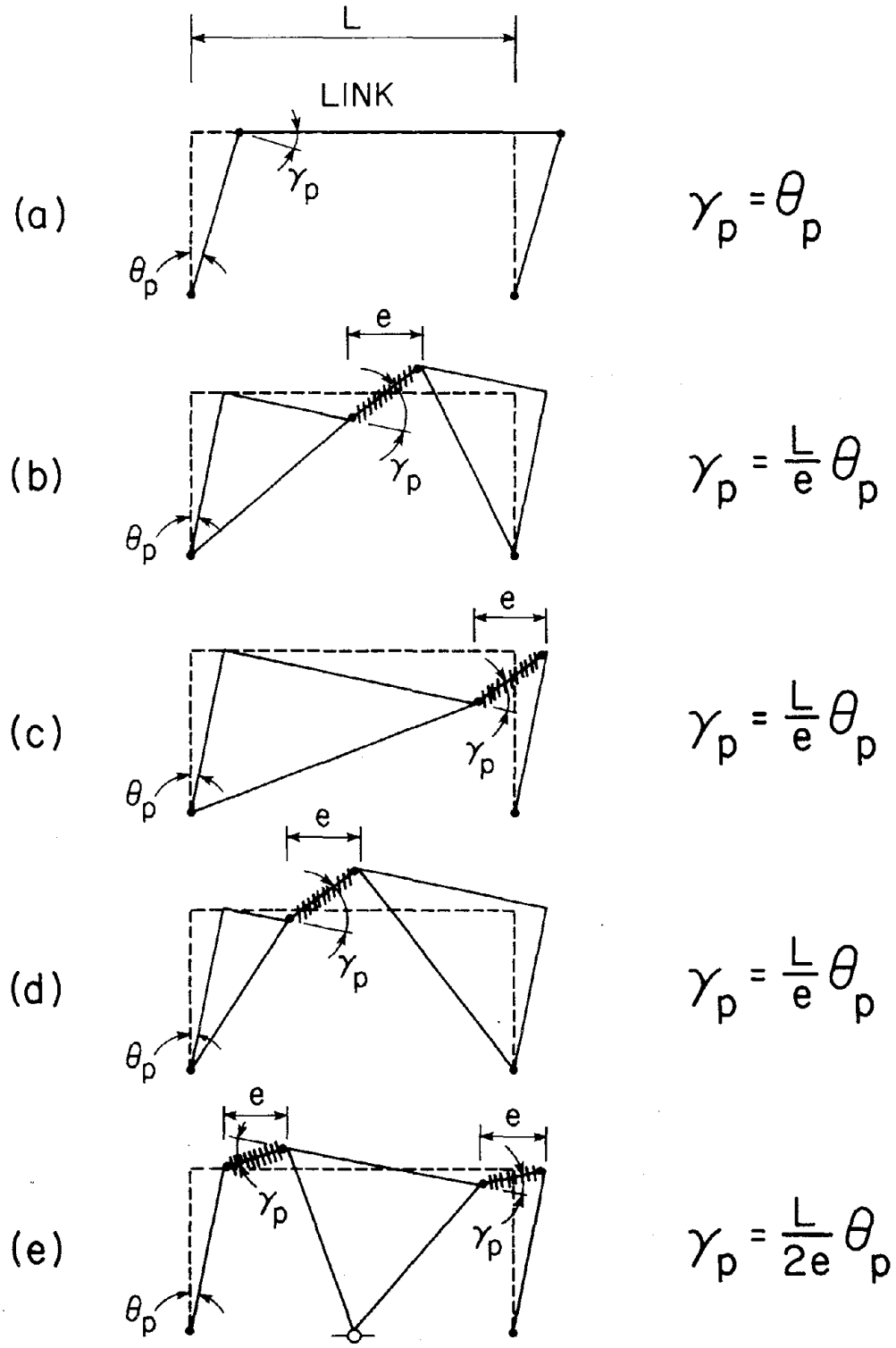

Fig. 1.4 Energy Dissipation Mechanisms

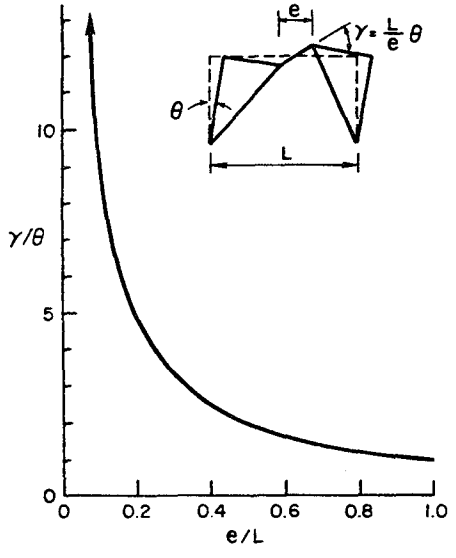

Fig. 1.5 Variation of Link Plastic Rotation Demand with *e/L*

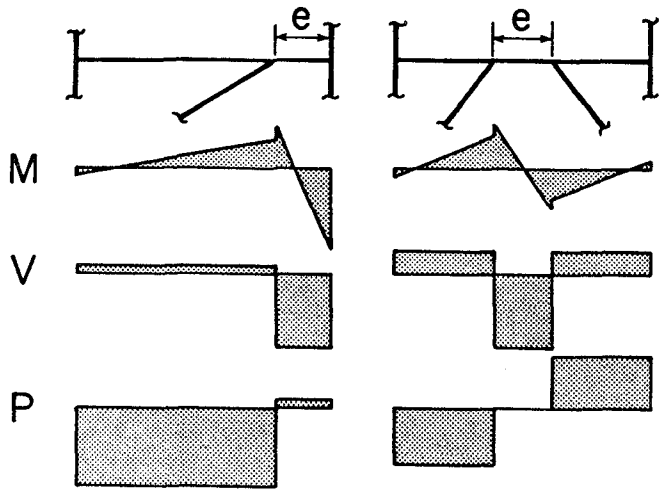

Fig. 1.6 Typical Force Distributions in Beams and Links of EBFs Under Lateral Load

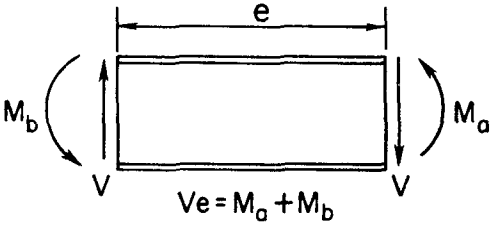

Fig. 1.7 Static Equilibrium of Link

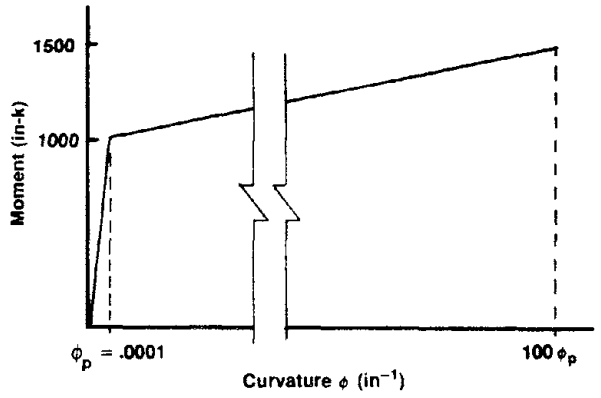

(a) Assumed Moment Curvature Relationship

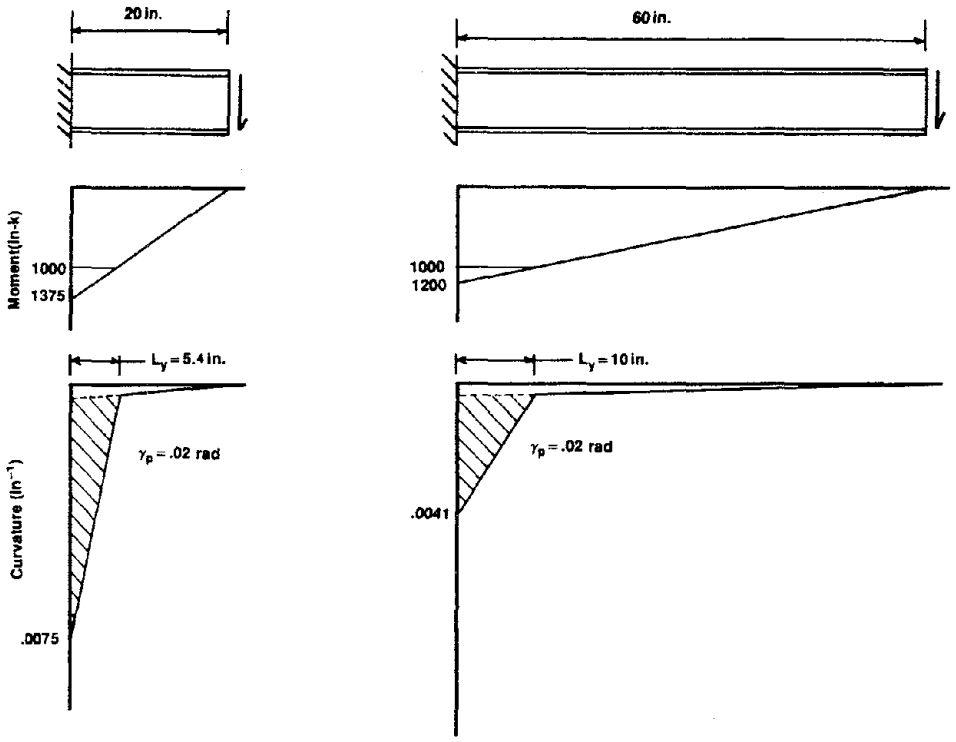

(b) 20 inch Cantilever

(c) 60 inch Cantilever

Fig. 1.8 Example Illustrating Effect of Moment Gradient on Flexural Rotation Capacity

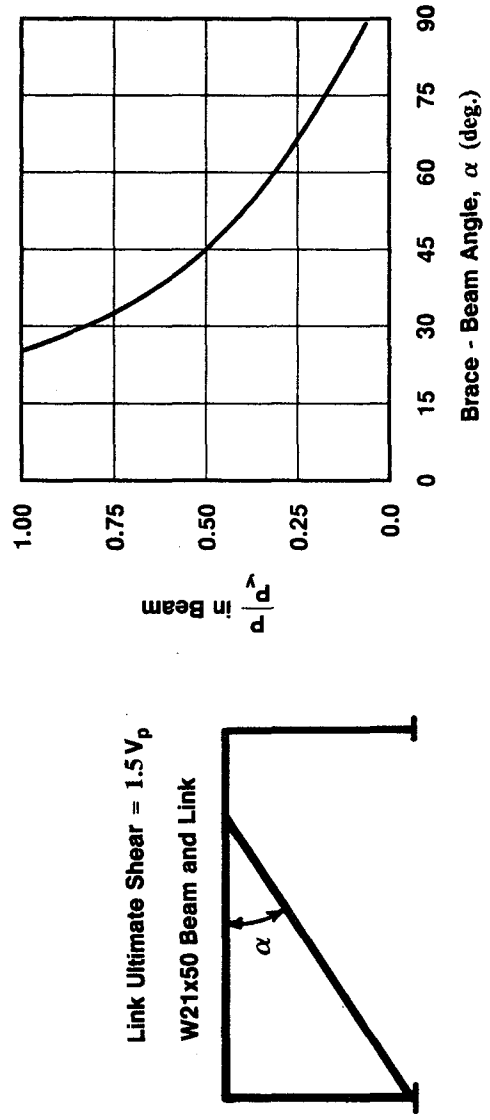

Fig. 1.9 Beam Axial Force Example

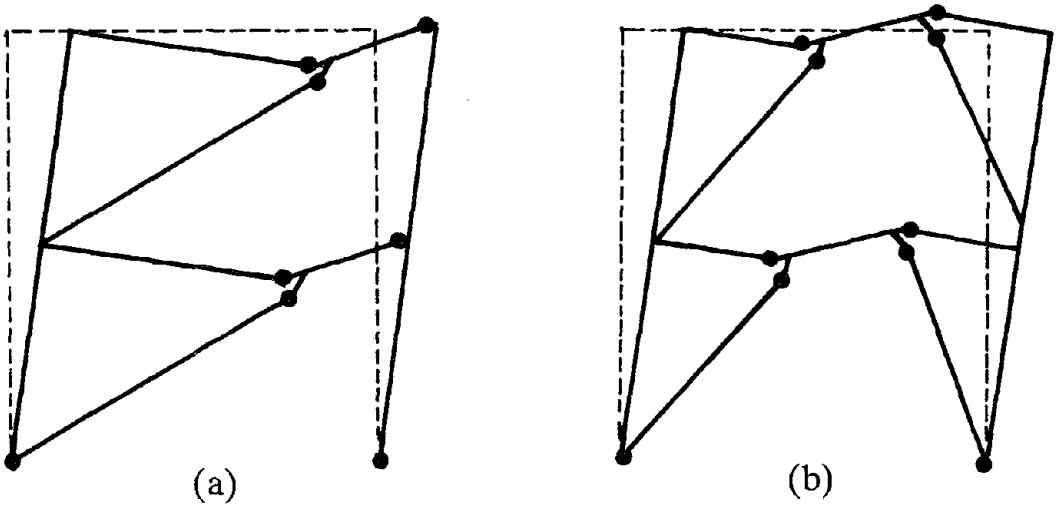

Fig. 1.10 EBF Mechanisms with Hinges in Beams and Braces

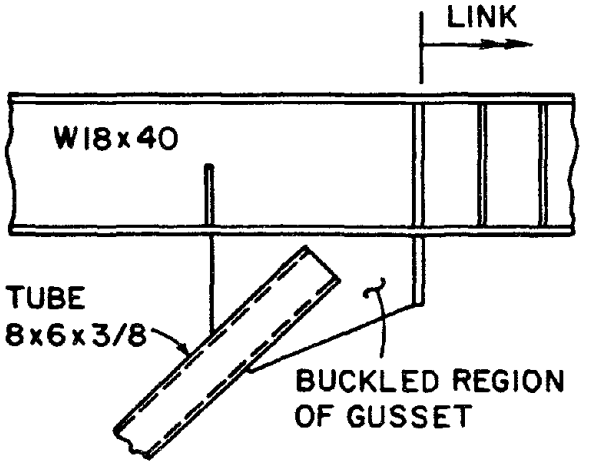

Fig. 1.11 Detail of Tsukuba Brace Connection

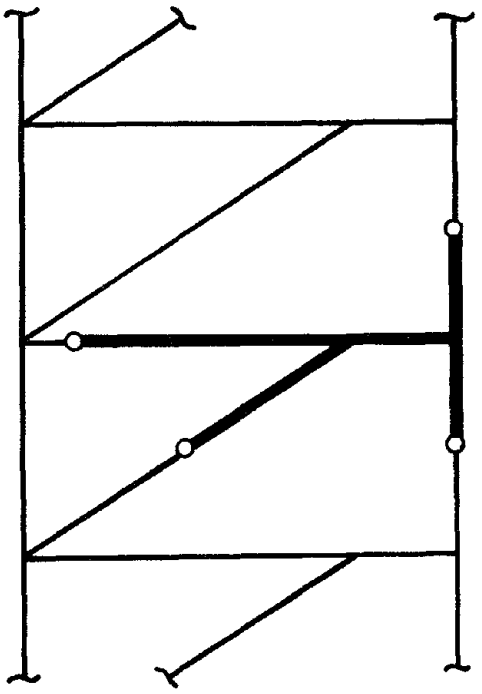

Fig. 2.1 Location of Subassemblage in Frame

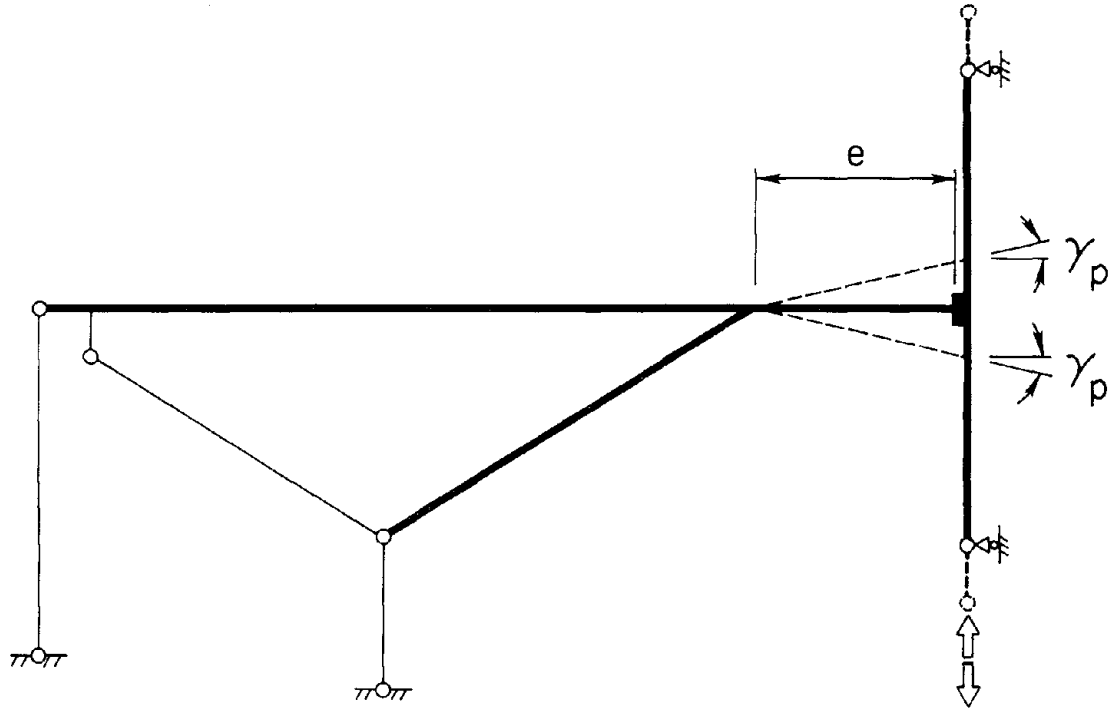

Fig. 2.2 Schematic of Test Setup

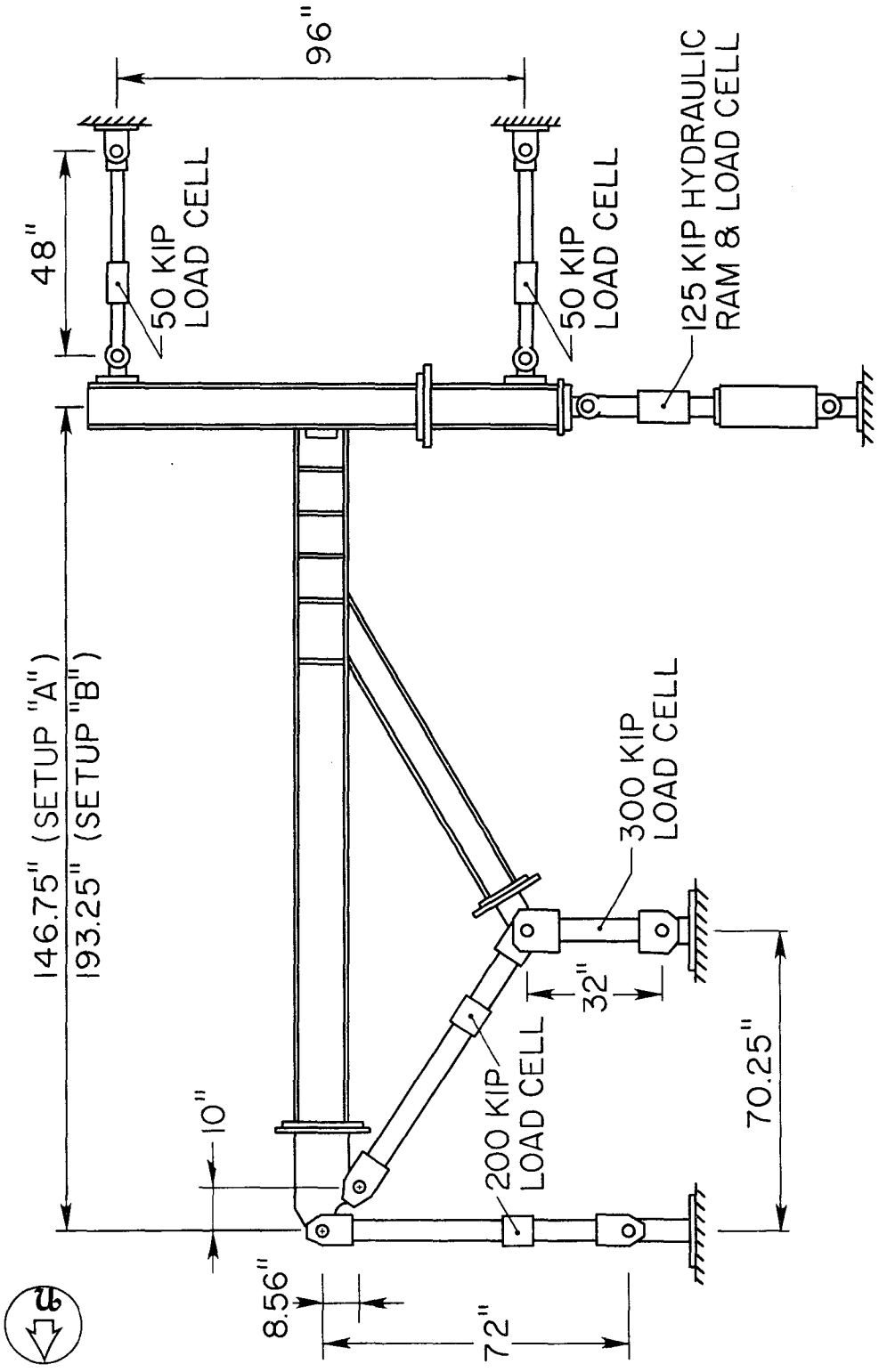

Fig. 2.3 Details of test Setup

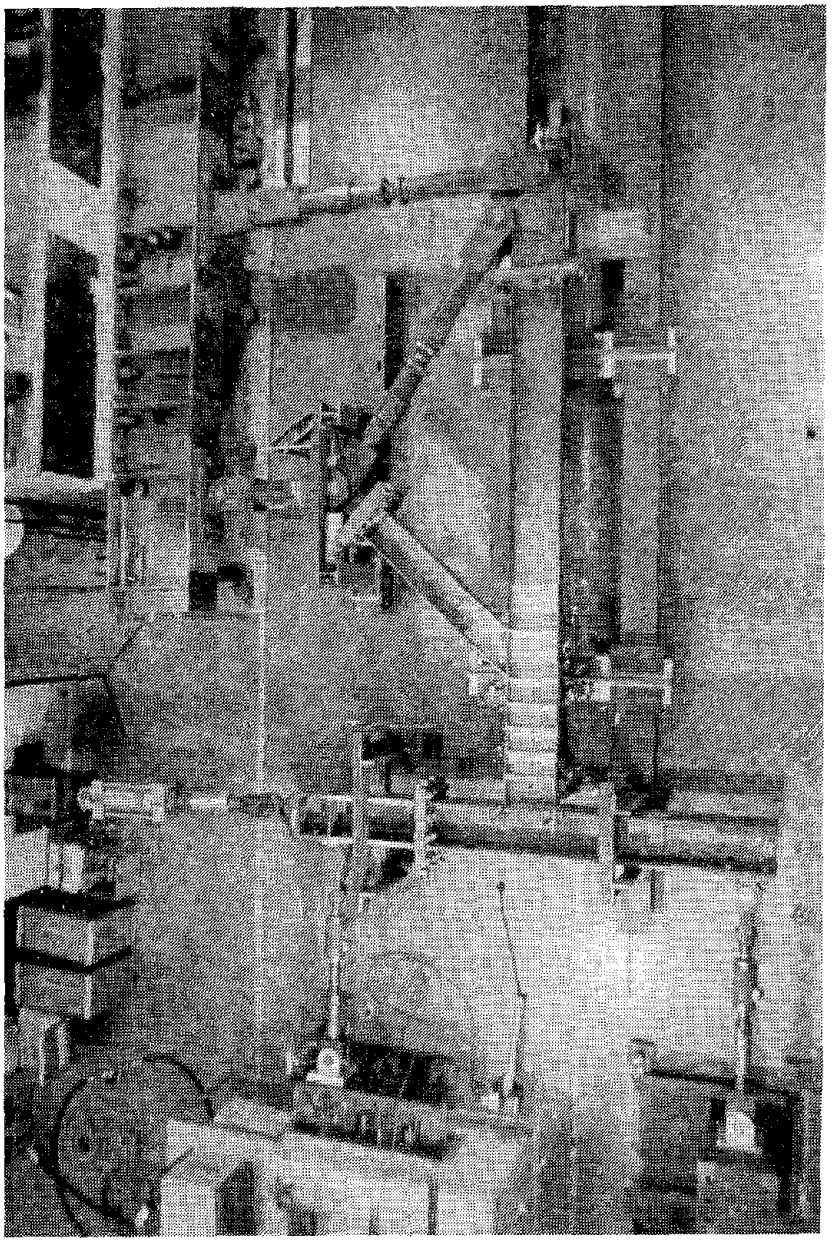

Fig. 2.4 Overall View of Test Setup

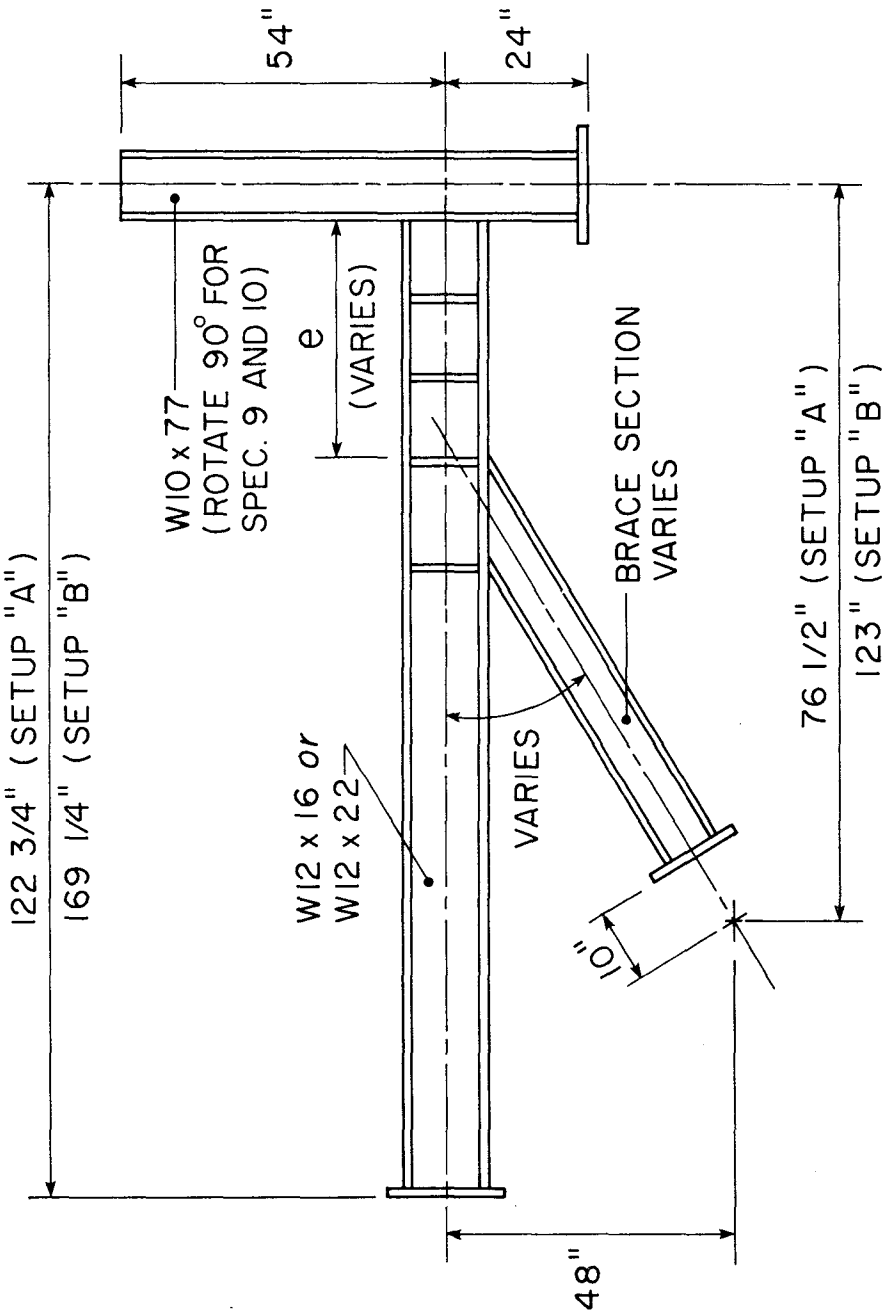

Fig. 2.5 Typical Test Specimen

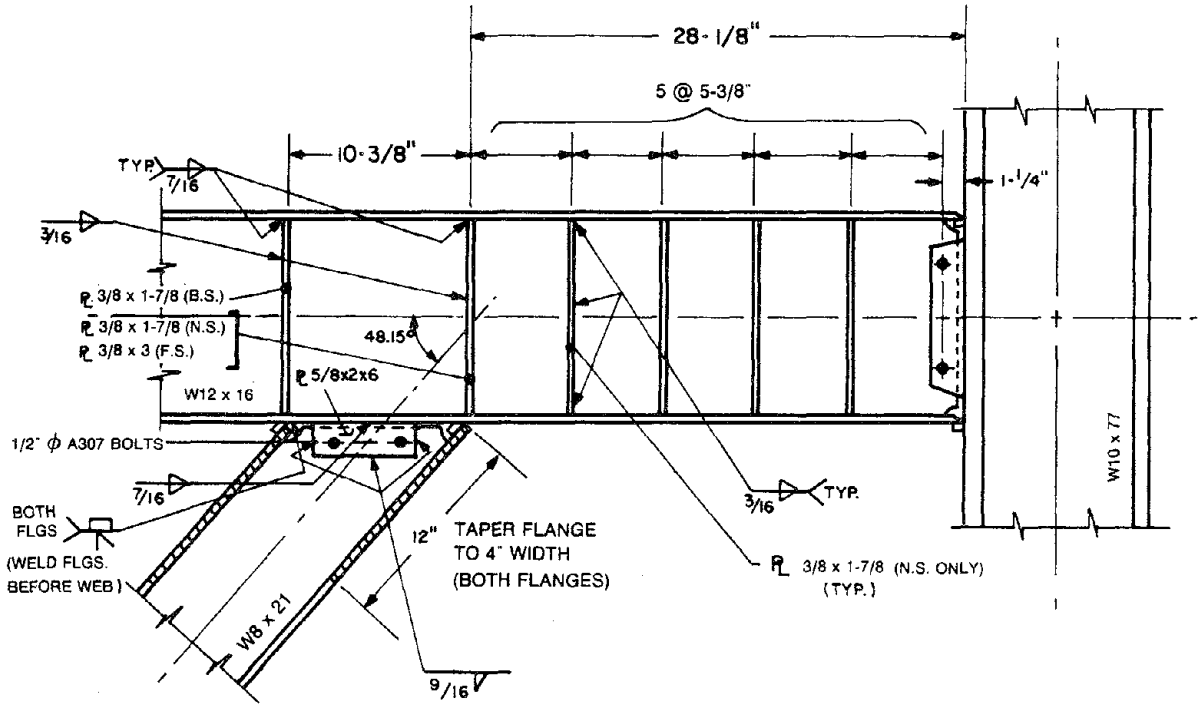

Fig. 2.6 Link Details - Specimen 1

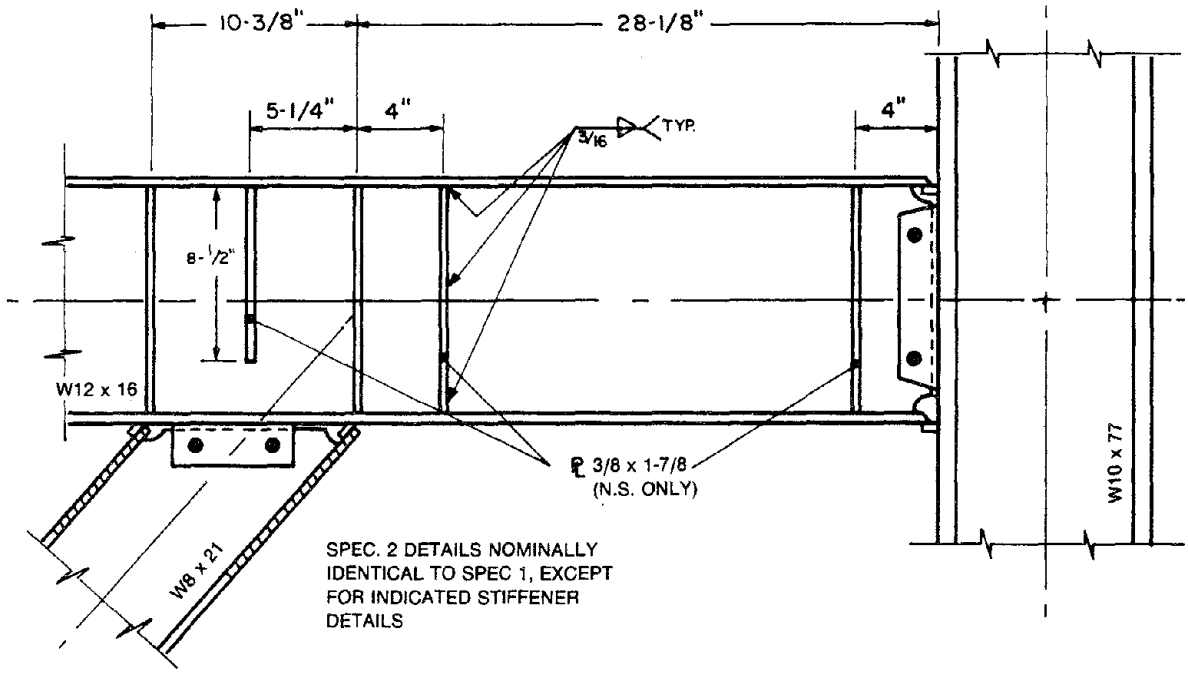

Fig. 2.7 Link Details - Specimen 2

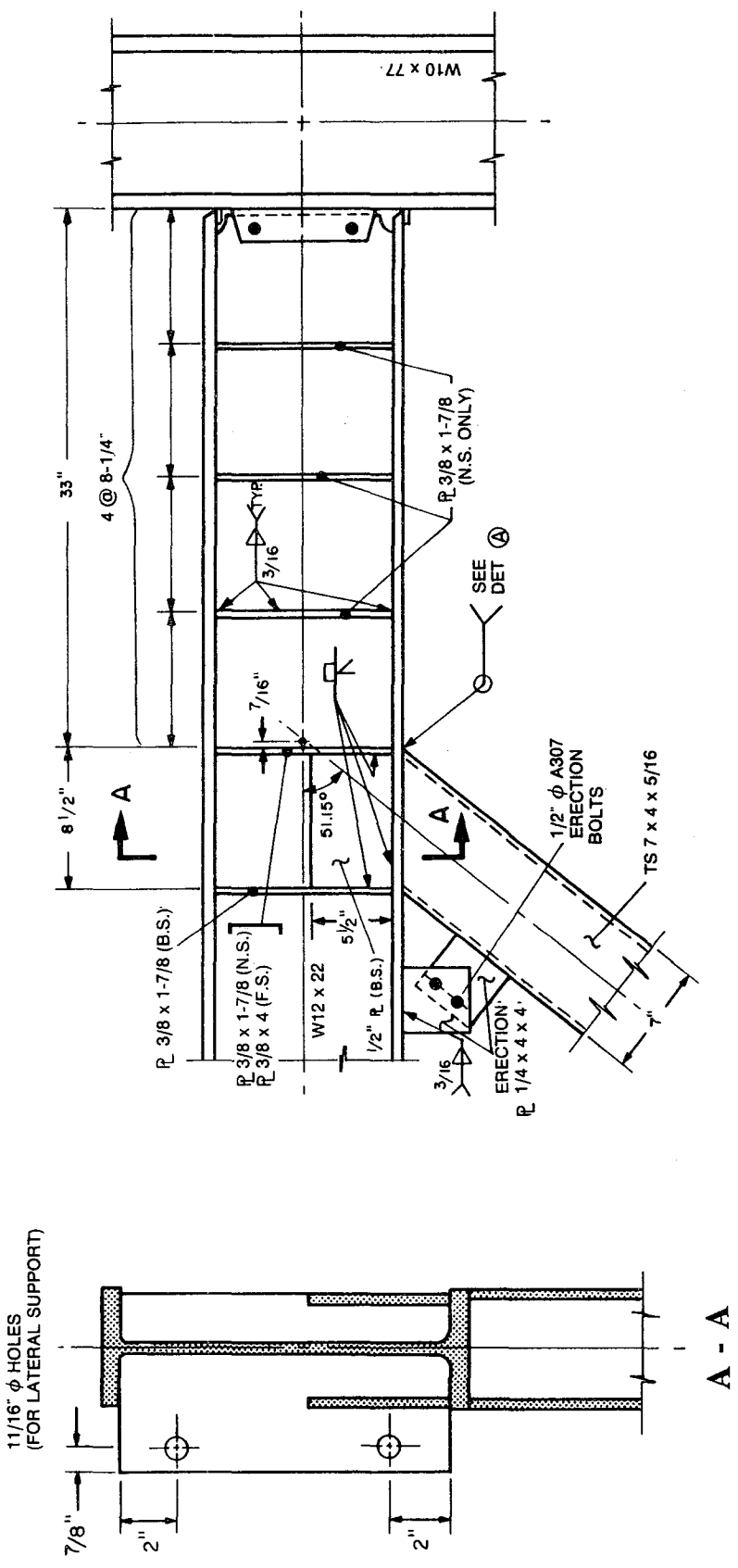

Fig. 2.8 Link Details - Specimen 3

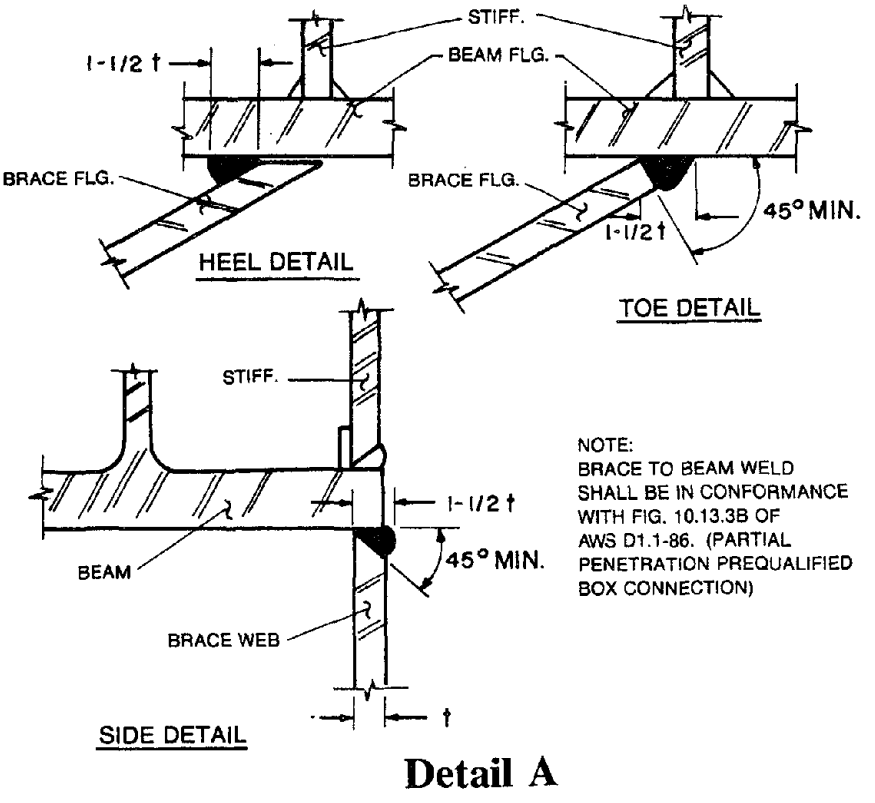

Fig. 2.8 Link Details - Specimen 3 (cont.)

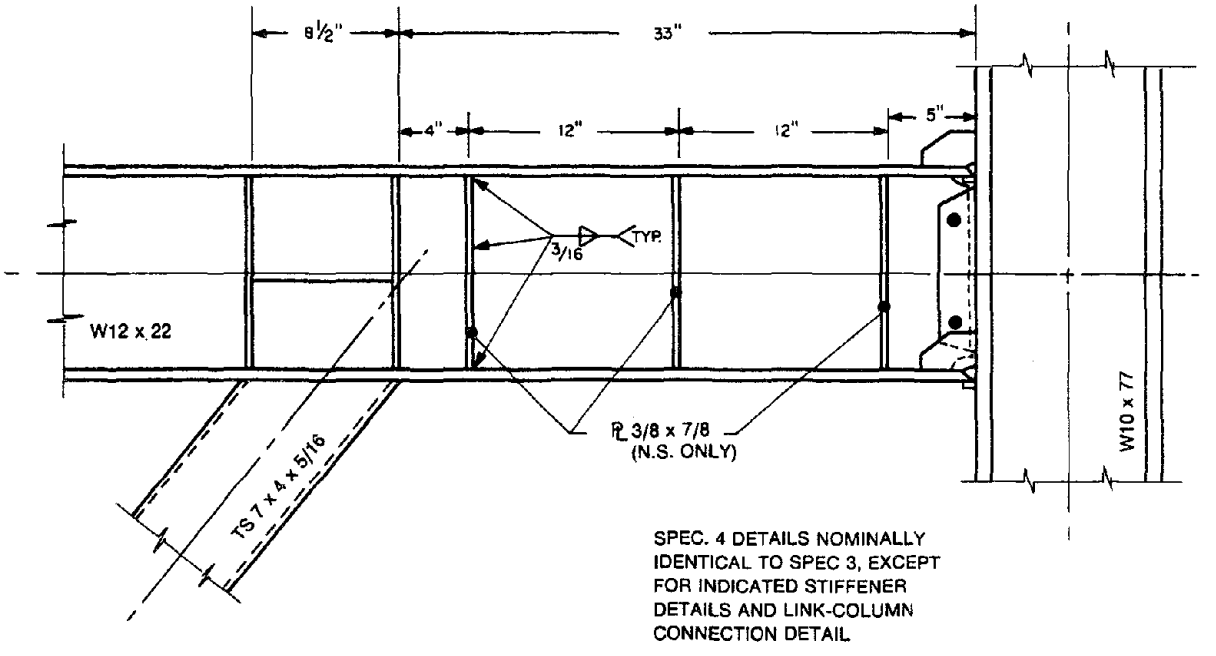

Fig. 2.9 Link Details - Specimen 4

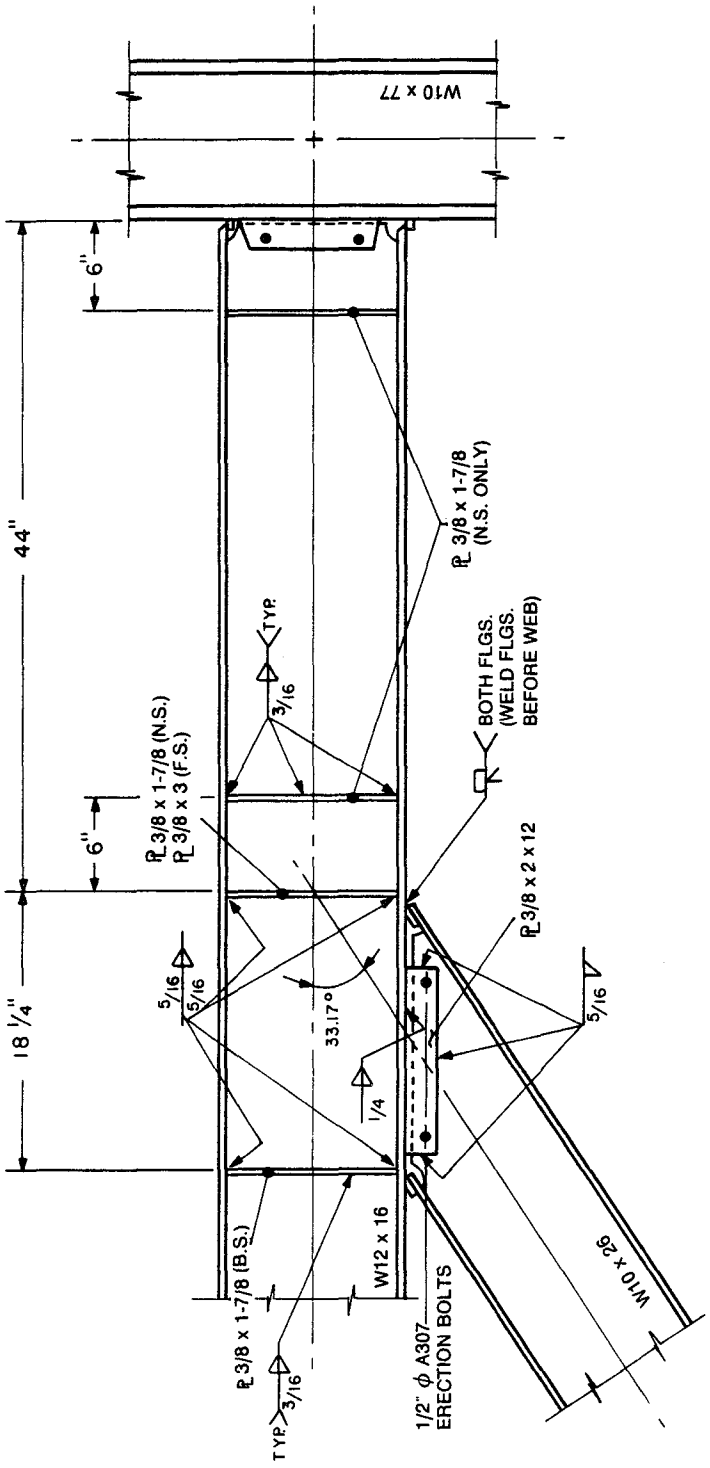

Fig. 2.10 Link Details - Specimen 5

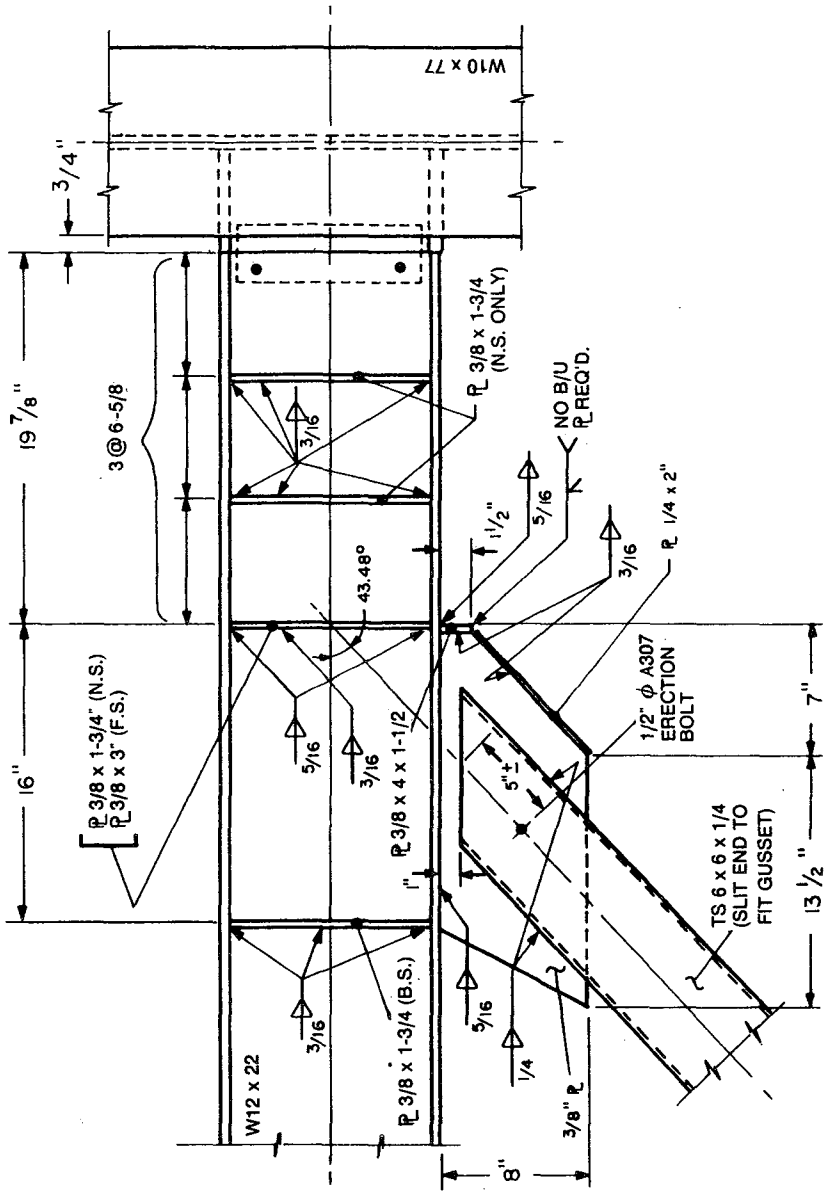

Fig. 2.14 Link Details - Specimen 9

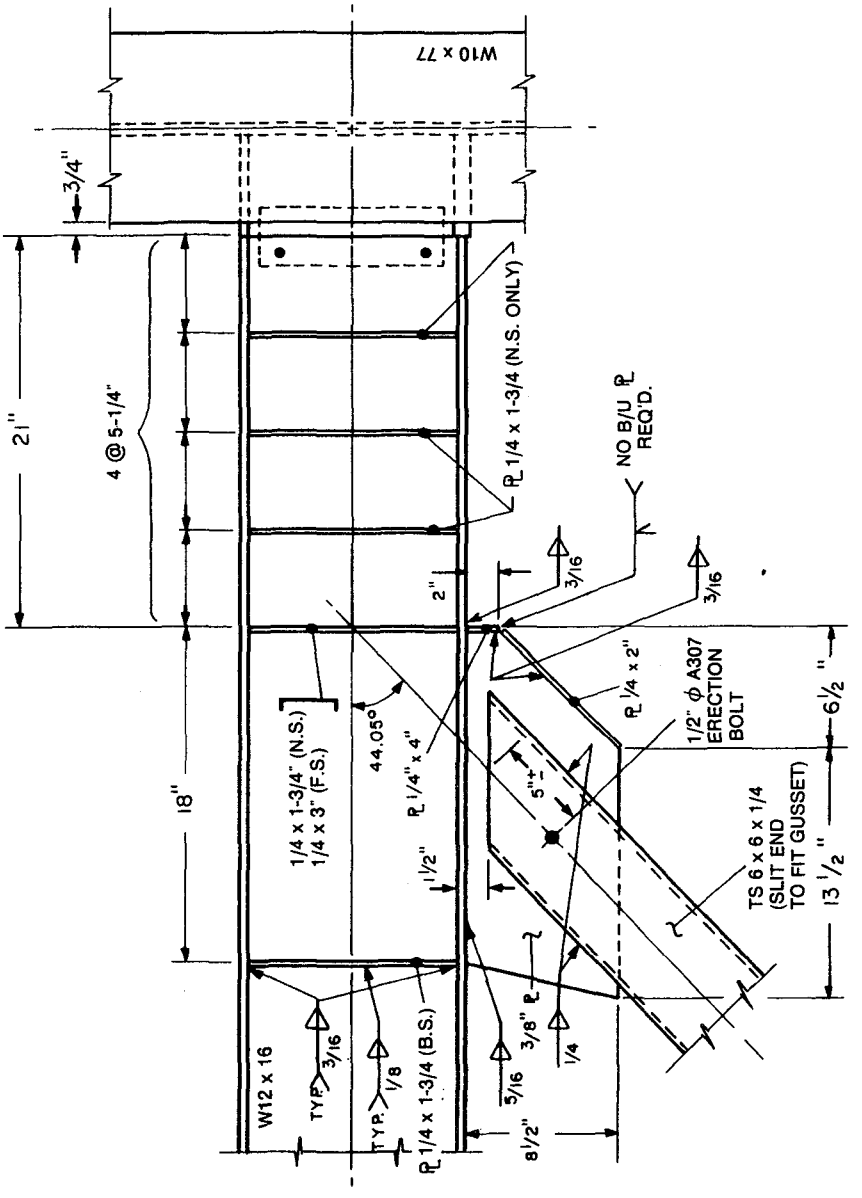

Fig. 2.15 Link Details - Specimen 10

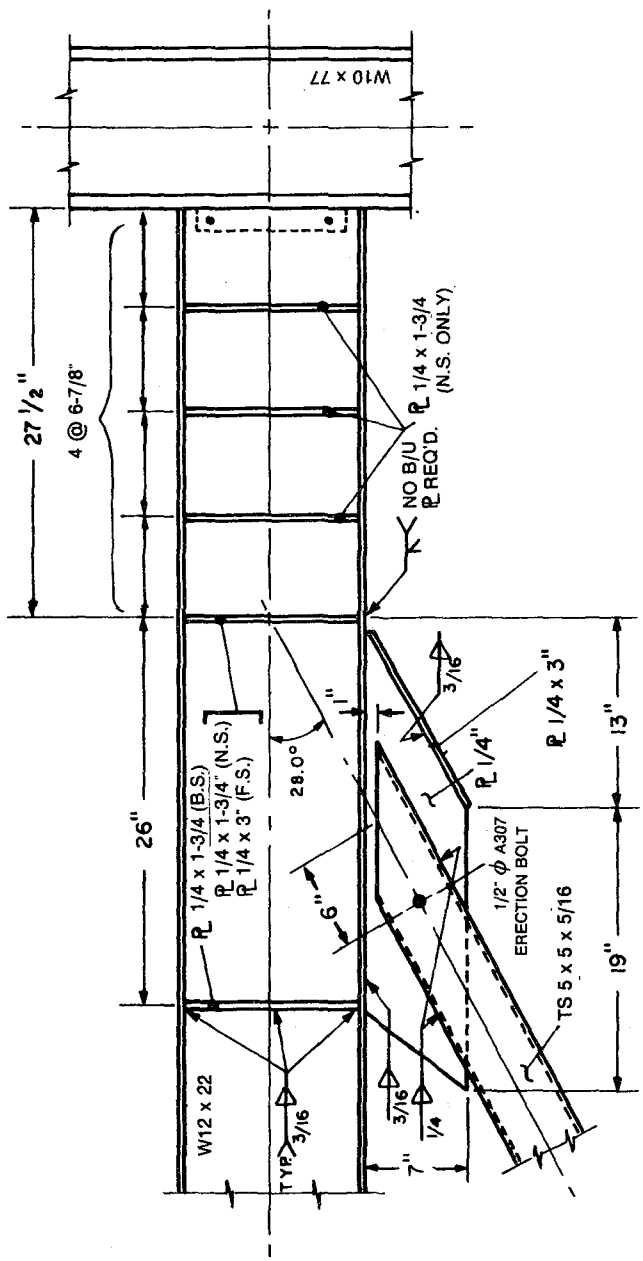

Fig. 2.16 Link Details - Specimen 11

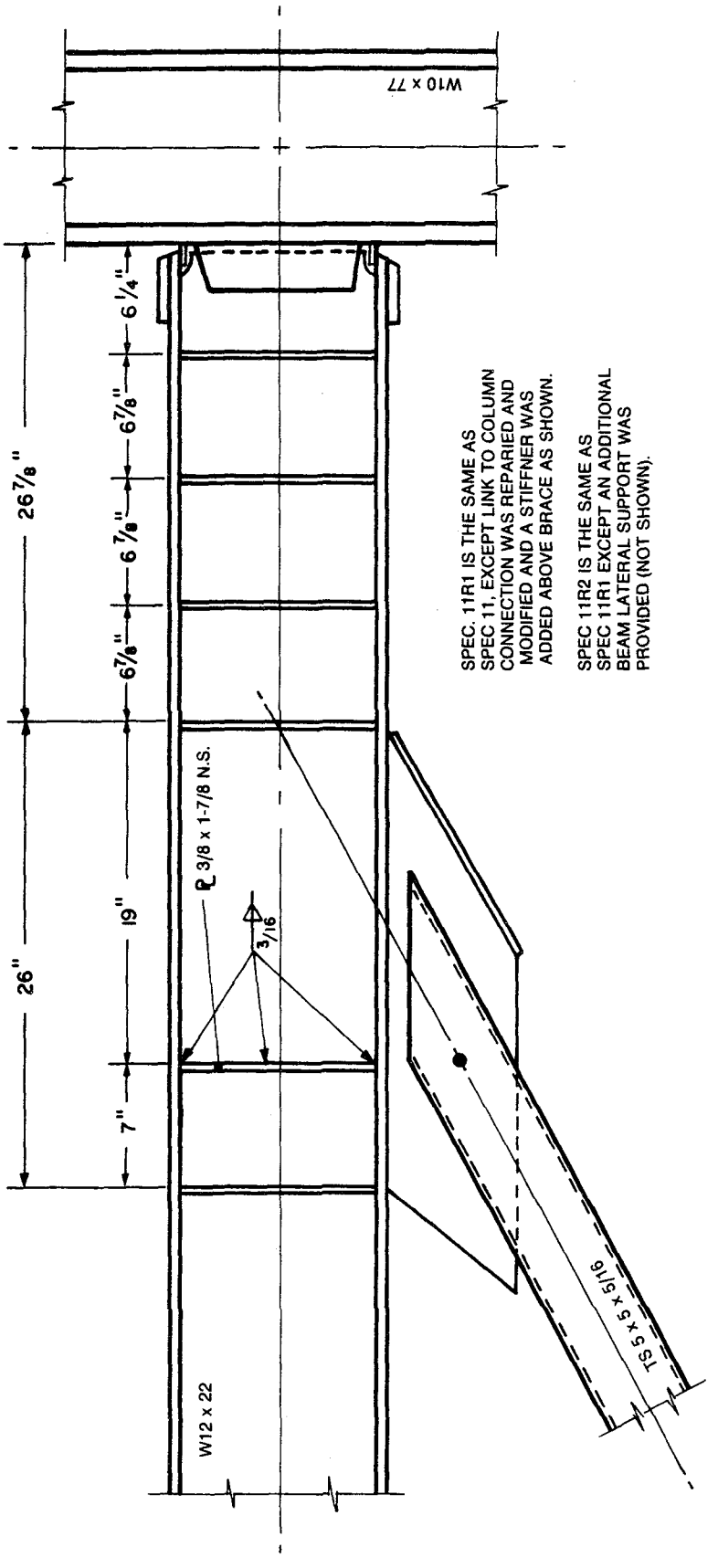

Fig. 2.17 Link Details - Specimens 11R1 and 11R2

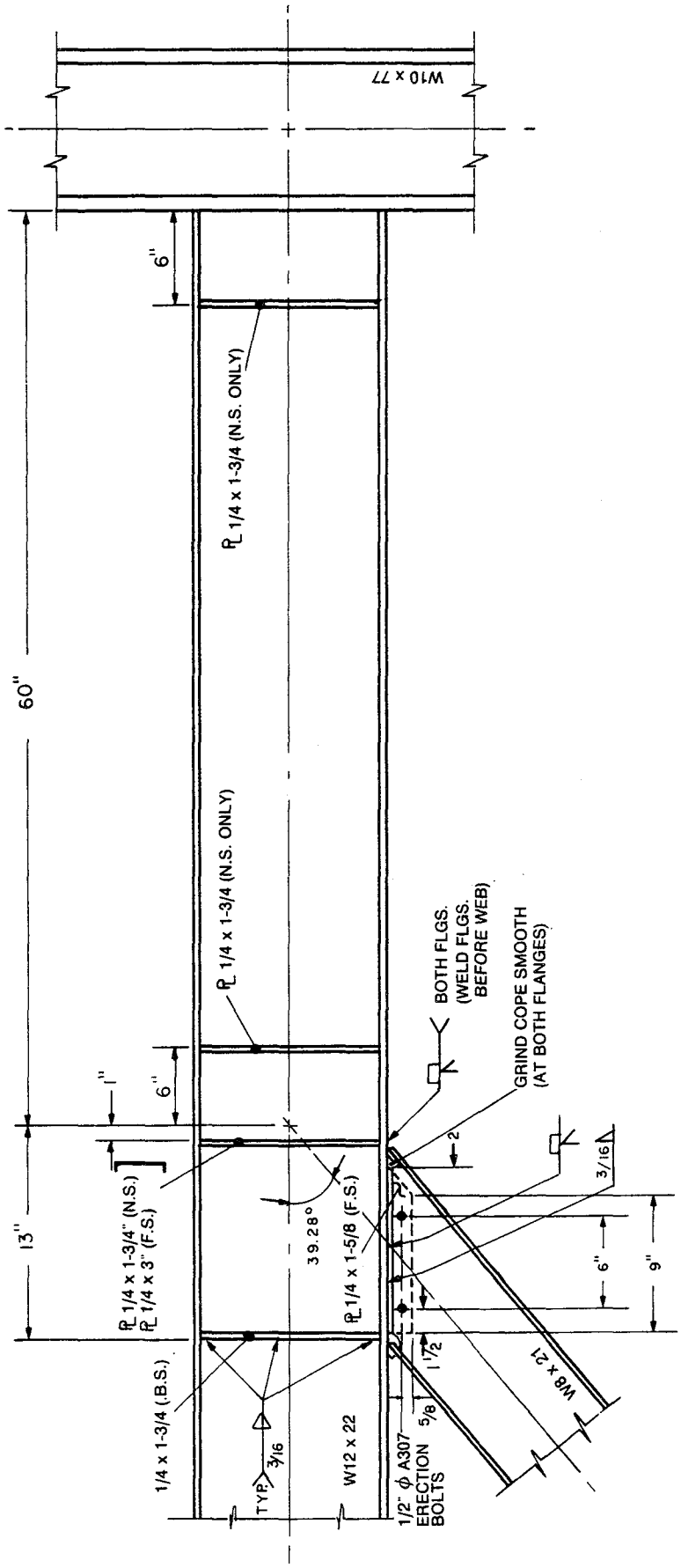

Fig. 2.18 Link Details - Specimen 12

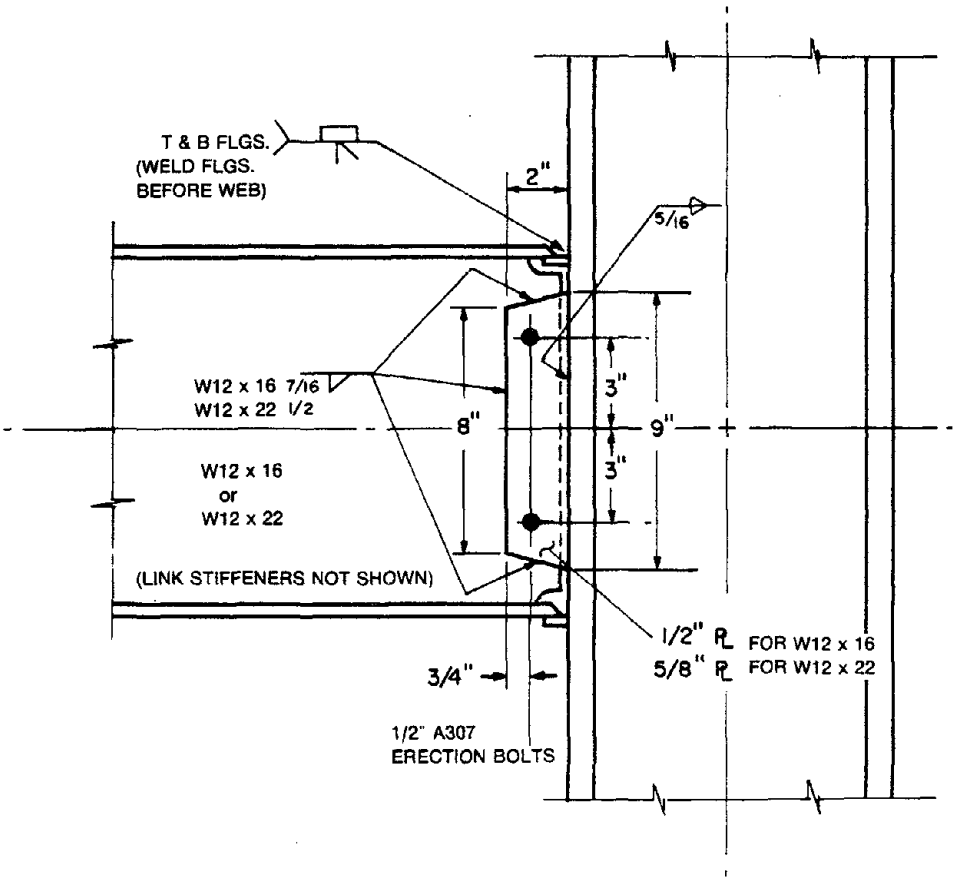

Fig. 2.19 Link-Column Connection Details
Specimens 1, 2, 3 and 5

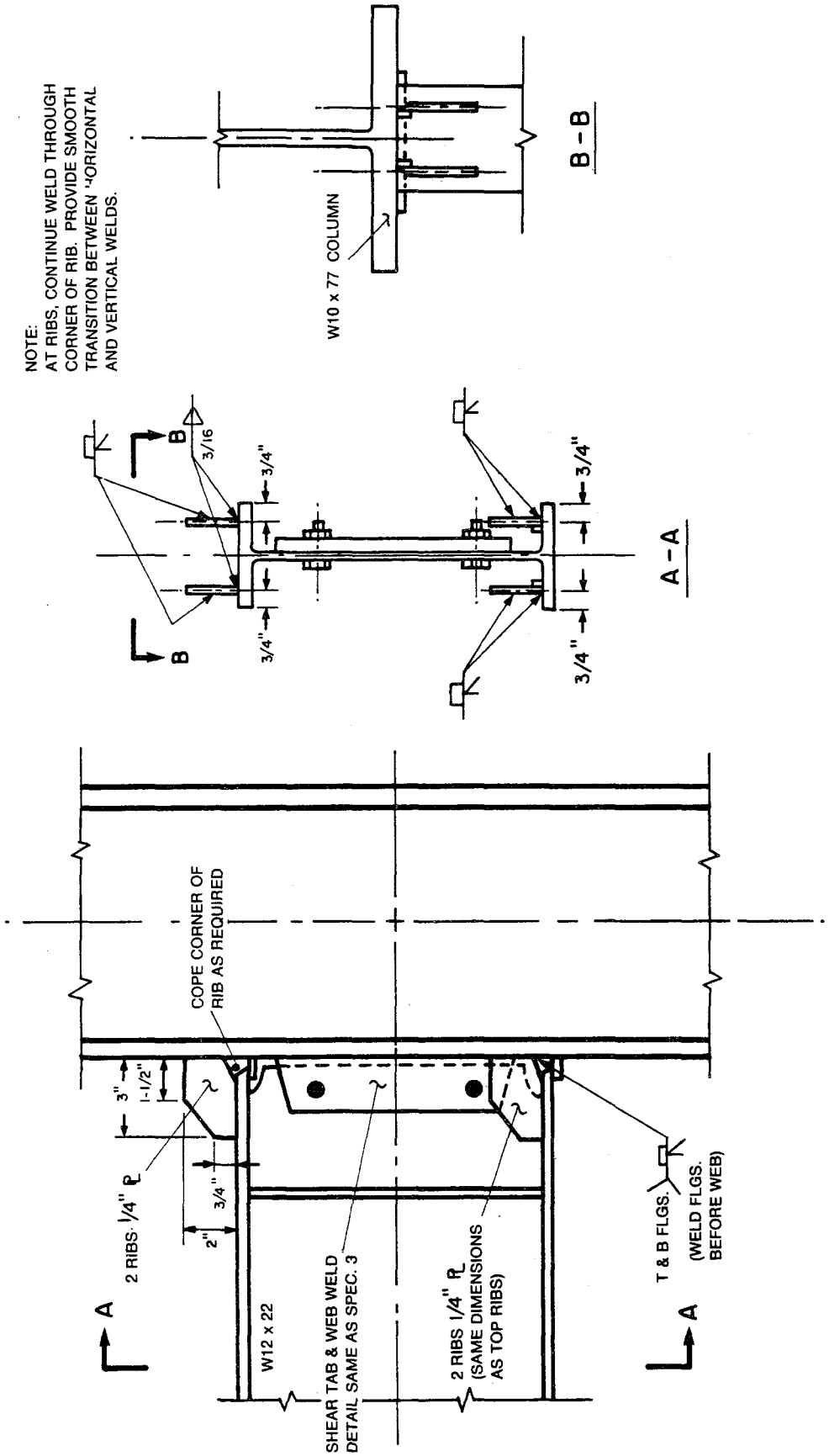

Fig. 2.20 Link-Column Connection Details - Specimen 4

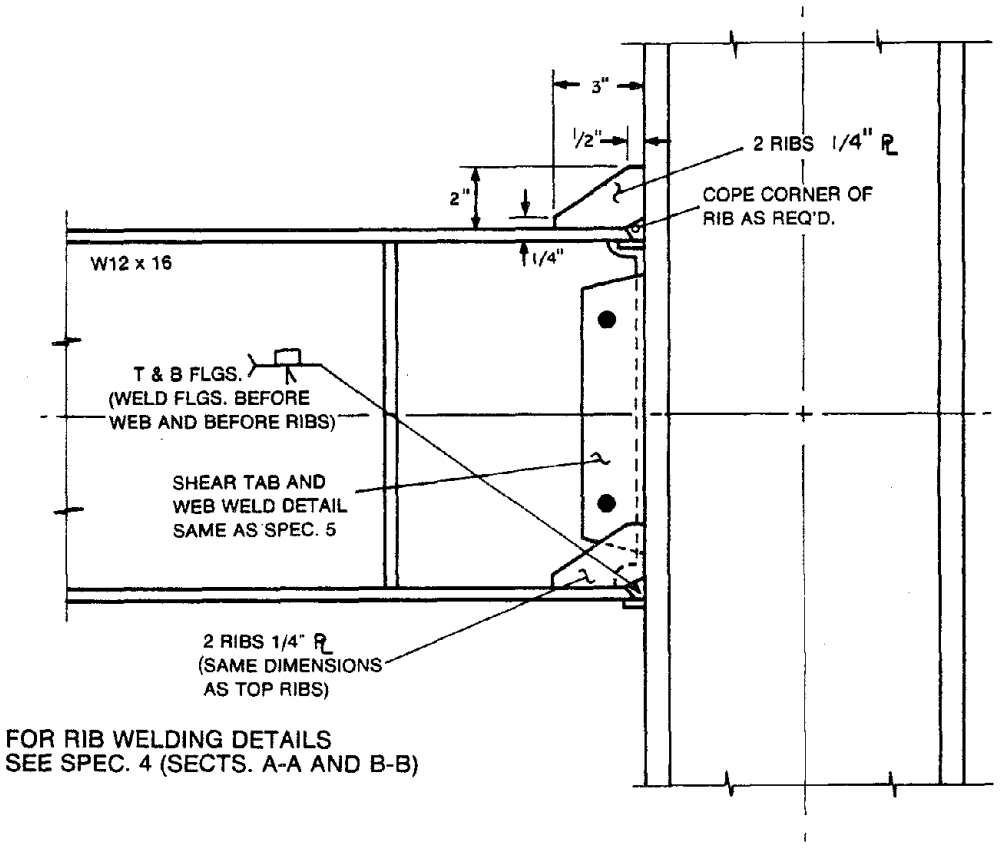

Fig. 2.21 Link-Column Connection Details - Specimen 6

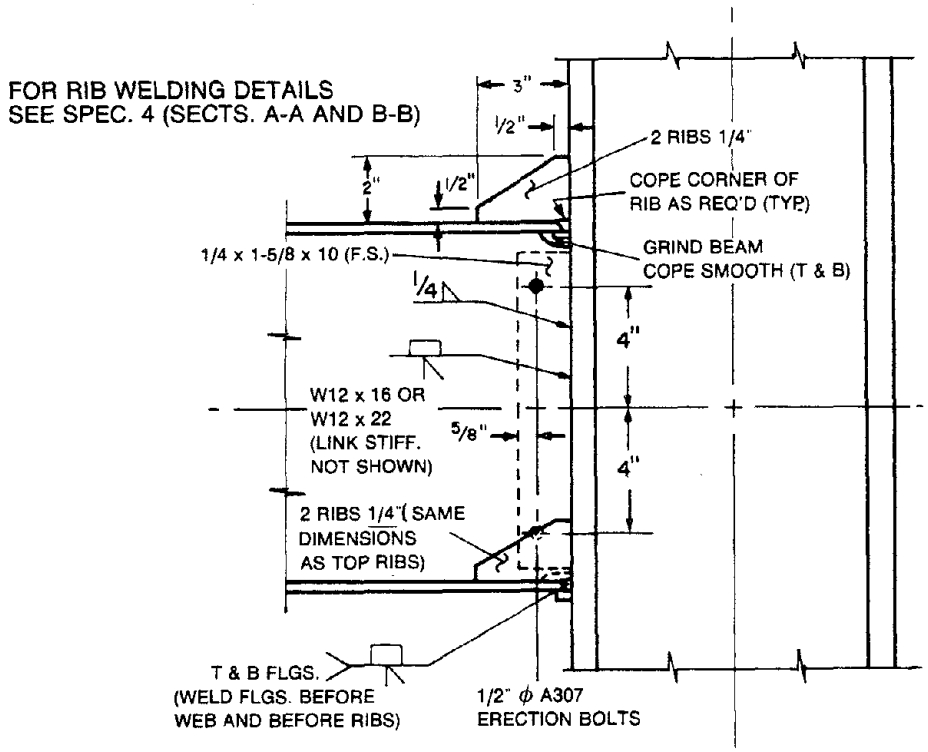

Fig. 2.22 Link-Column Connection Details - Specimens 7 and 8

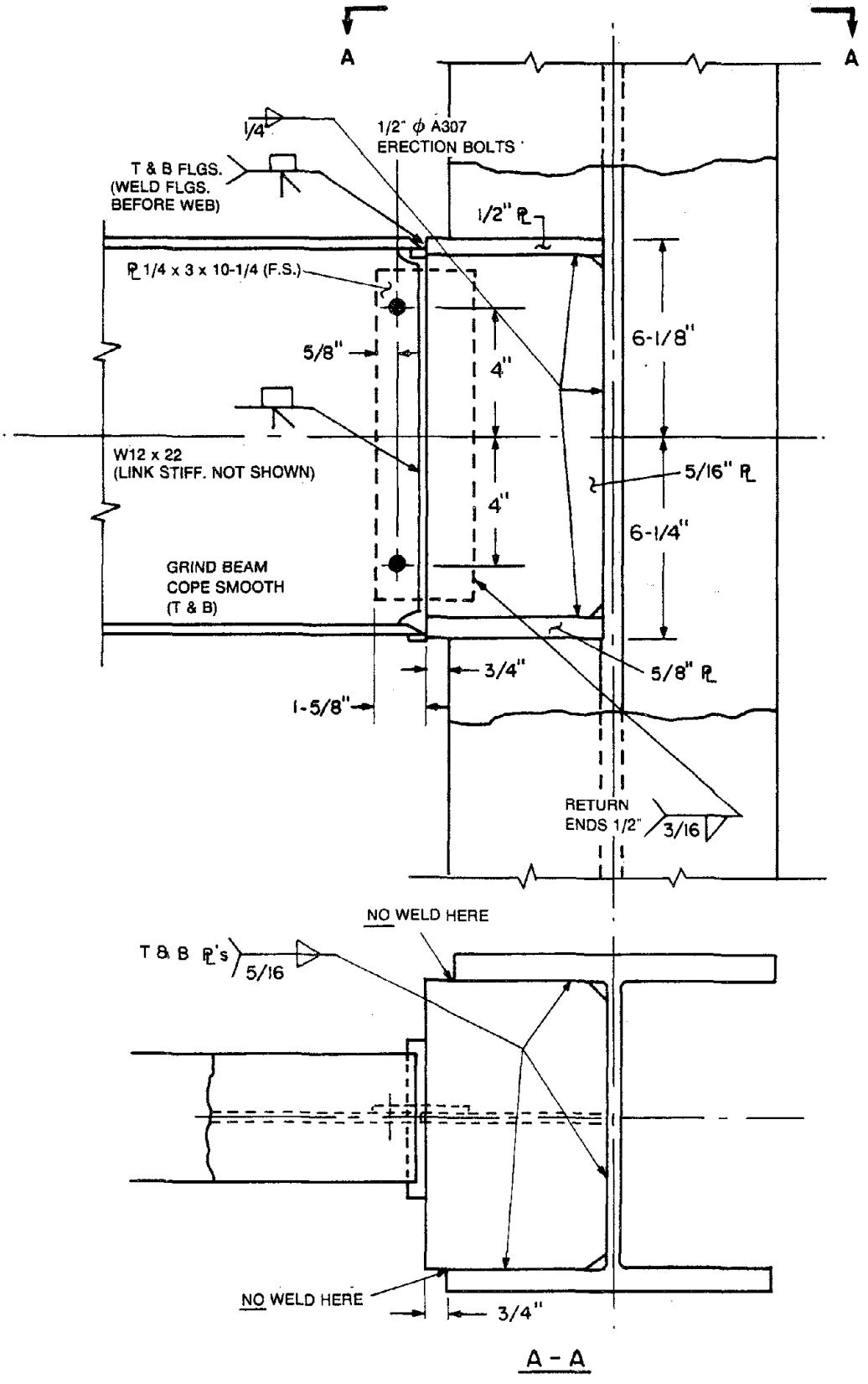

Fig. 2.23 Link-Column Connection Details - Specimen 9

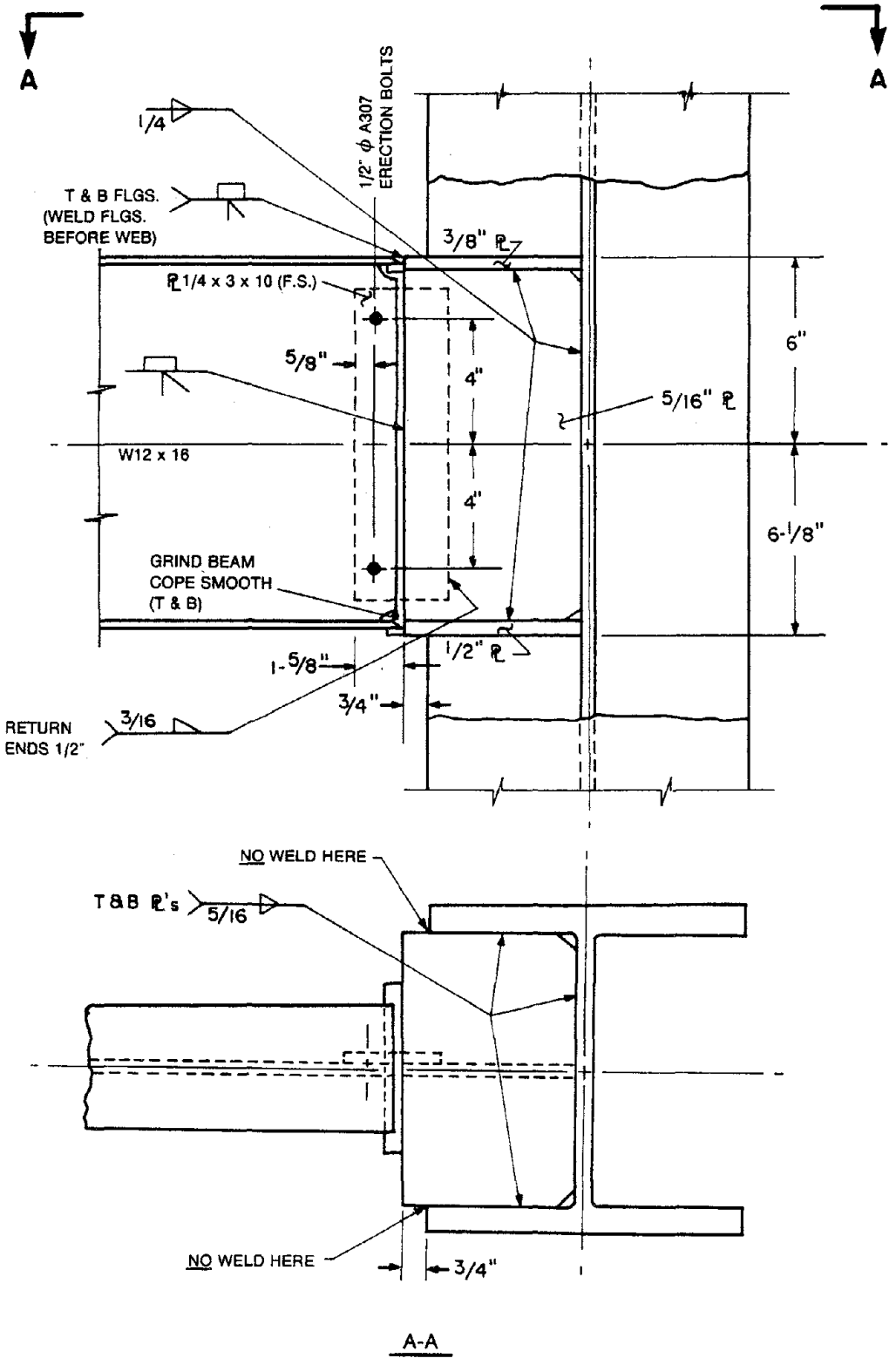

Fig. 2.24 Link-Column Connection Details - Specimen 10

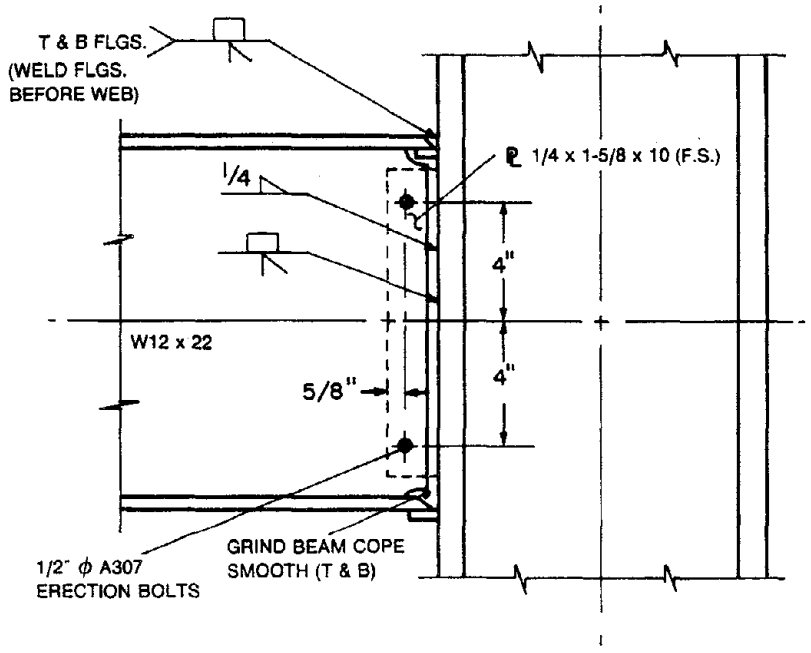

Fig. 2.25 Link-Column Connection Details - Specimen 11

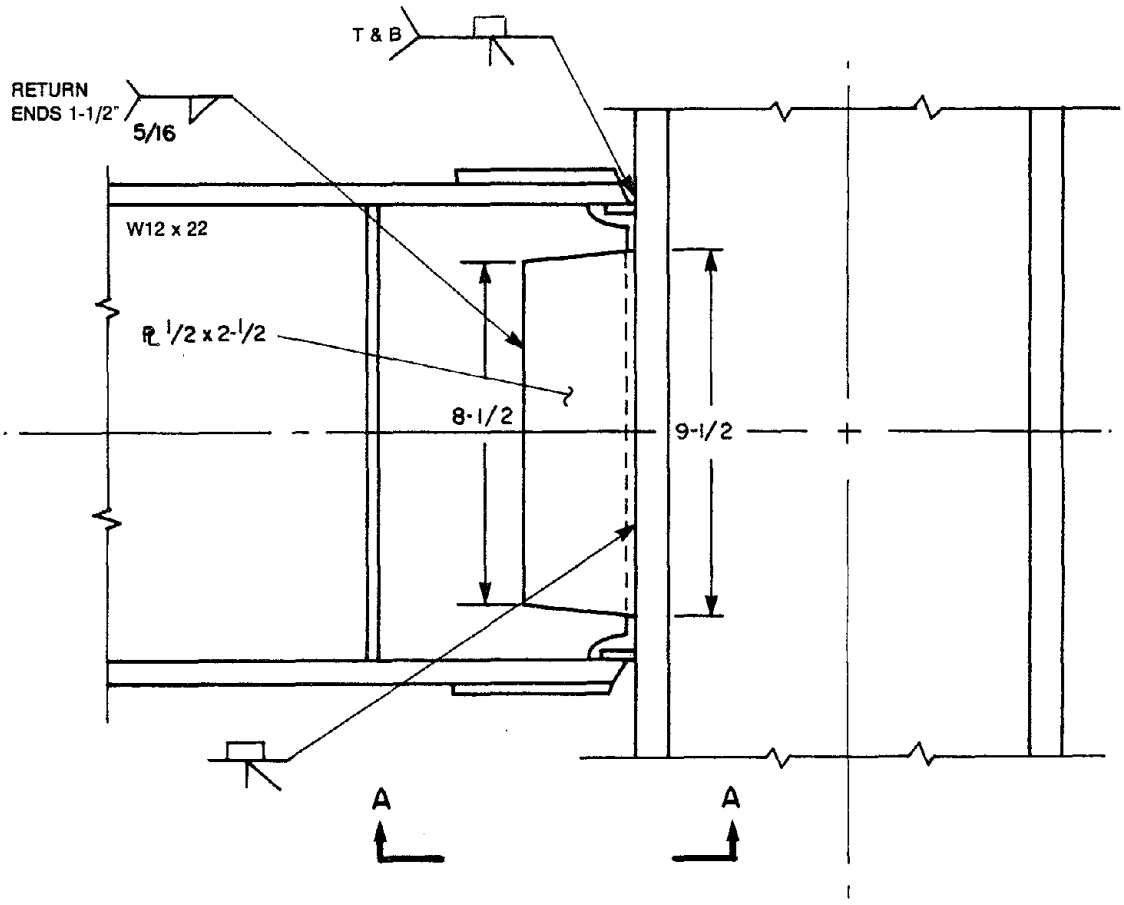

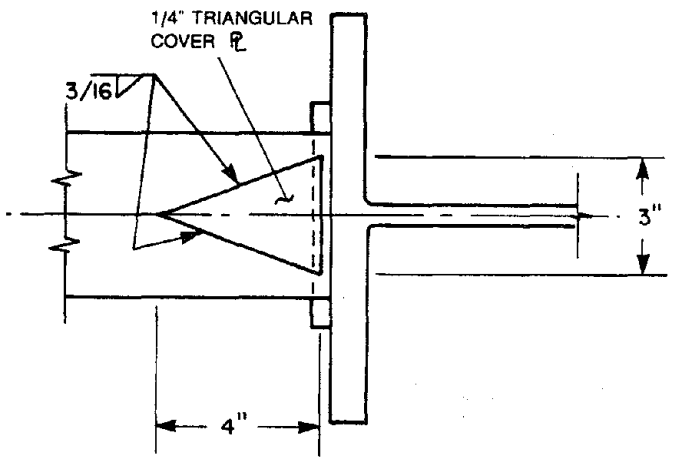

A-A (USE SAME DETAIL T & B)

Add'l Notes:
Material for triangular cover plates was taken from the web of Spec. 4.
All repairs were done with the specimen in place in the test setup.

Repaired Spec. 11 is designated Spec. 11R1 and 11R2

Link to Column Connection Repair and Welding Sequence:

1 - **Flame cut link end to separate from column**
2 - **Grind smooth web and flanges of link. Grind chamfer into link flanges for full pen. weld preparation.**
3 - **Flame cut copes into link web to accommodate back-up strips for flange full pen. welds. Grind copes smooth.**
4 - **Full pen. weld link flanges to column flange.**
5 - **Fillet weld triangular cover plates to link flange.**
6 - **Full pen. weld cover plates to column flange.**
7 - **Full pen. weld shear tab to column flange.**
8 - **Fillet weld shear tab to link web.**

Fig. 2.26 Link-Column Connection Details - Specimens 11R1 and 11R2

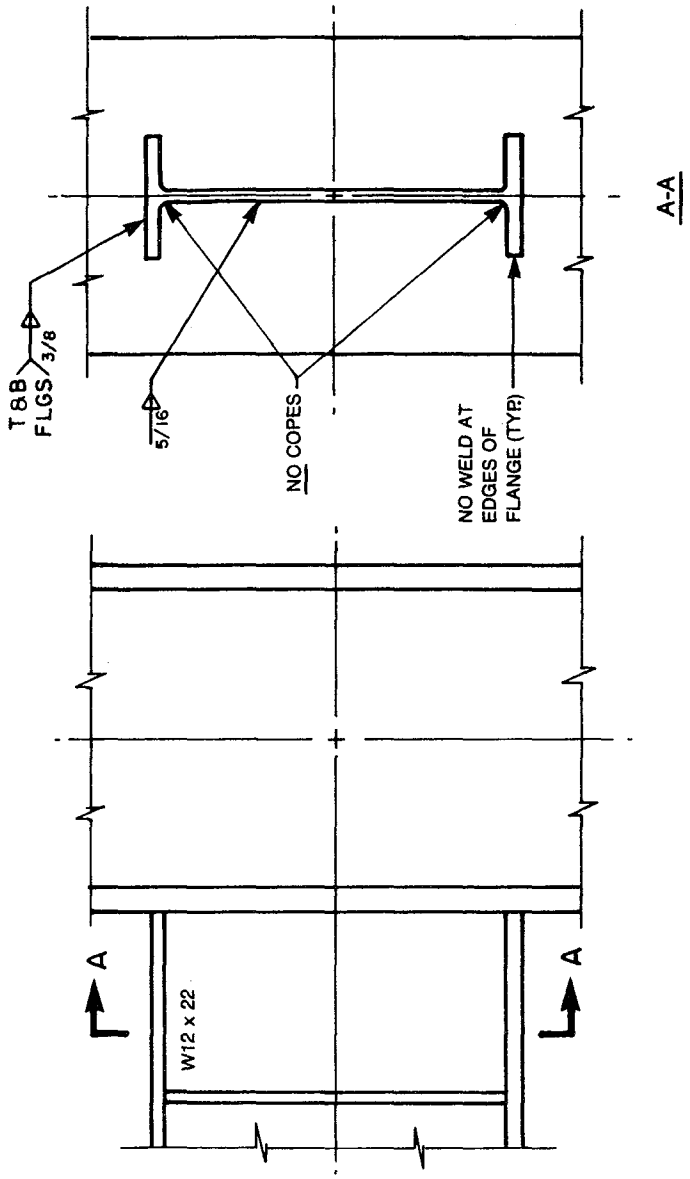

Fig. 2.27 Link-Column Connection Details - Specimen 12

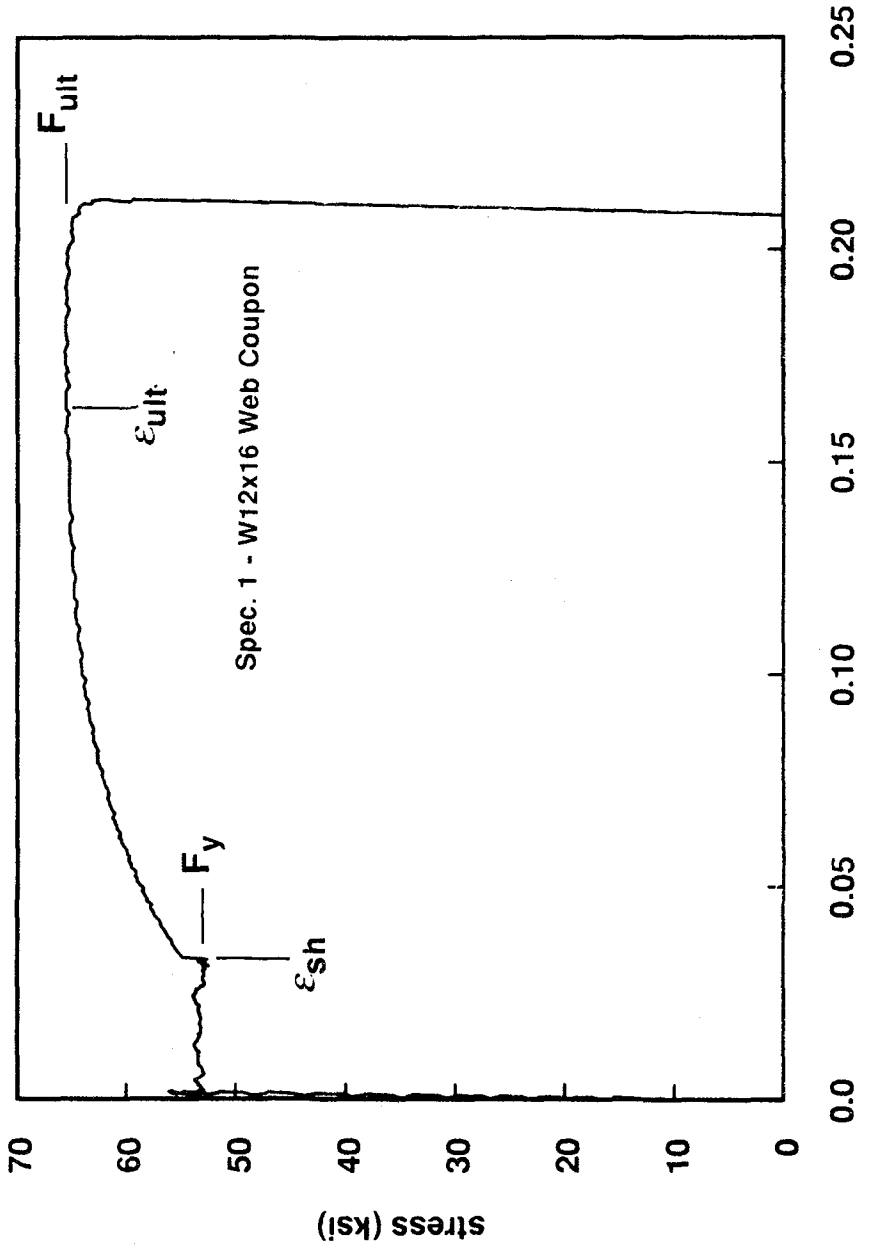

Fig. 2.28 Typical Stress-Strain Diagram for a *W* Section Coupon

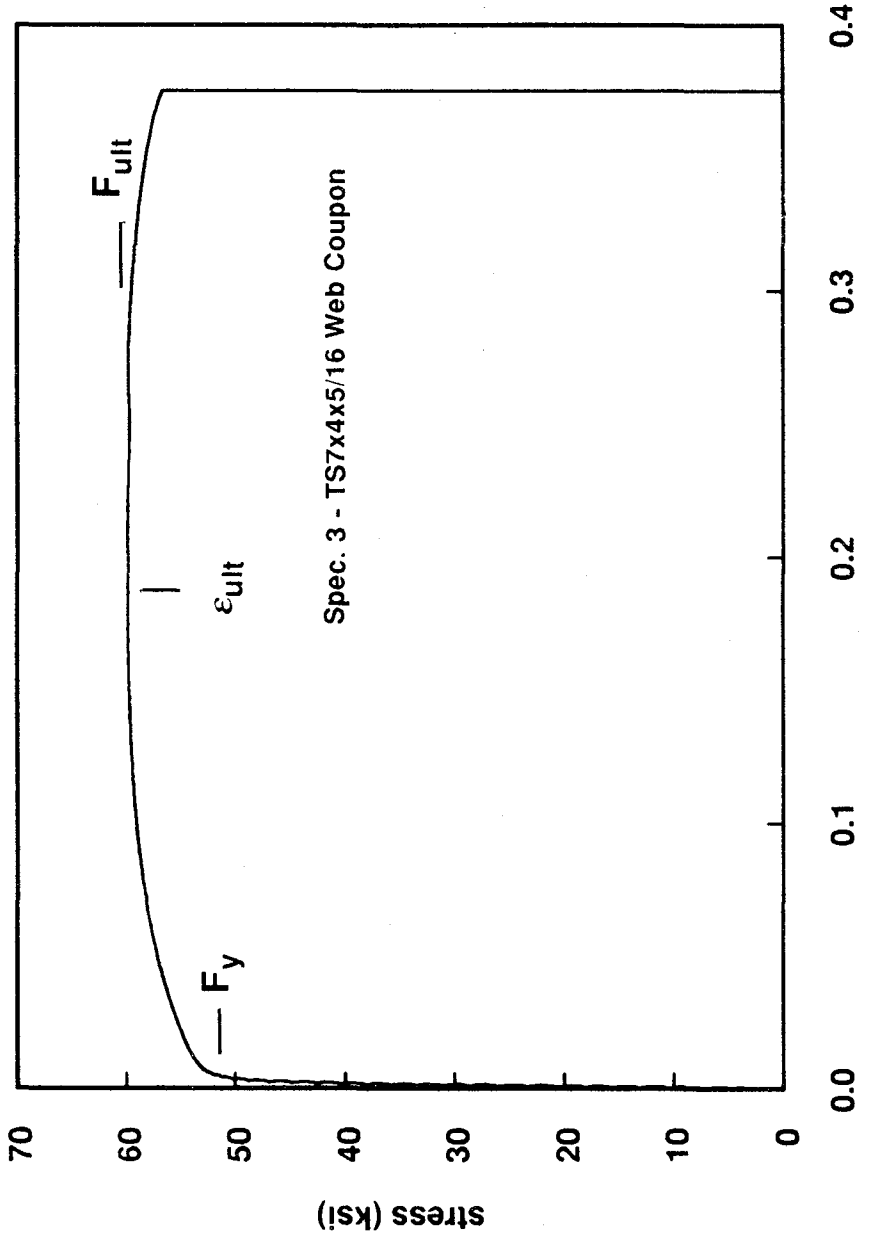

Fig. 2.29 Typical Stress-Strain Diagram for a Tube Section Coupon

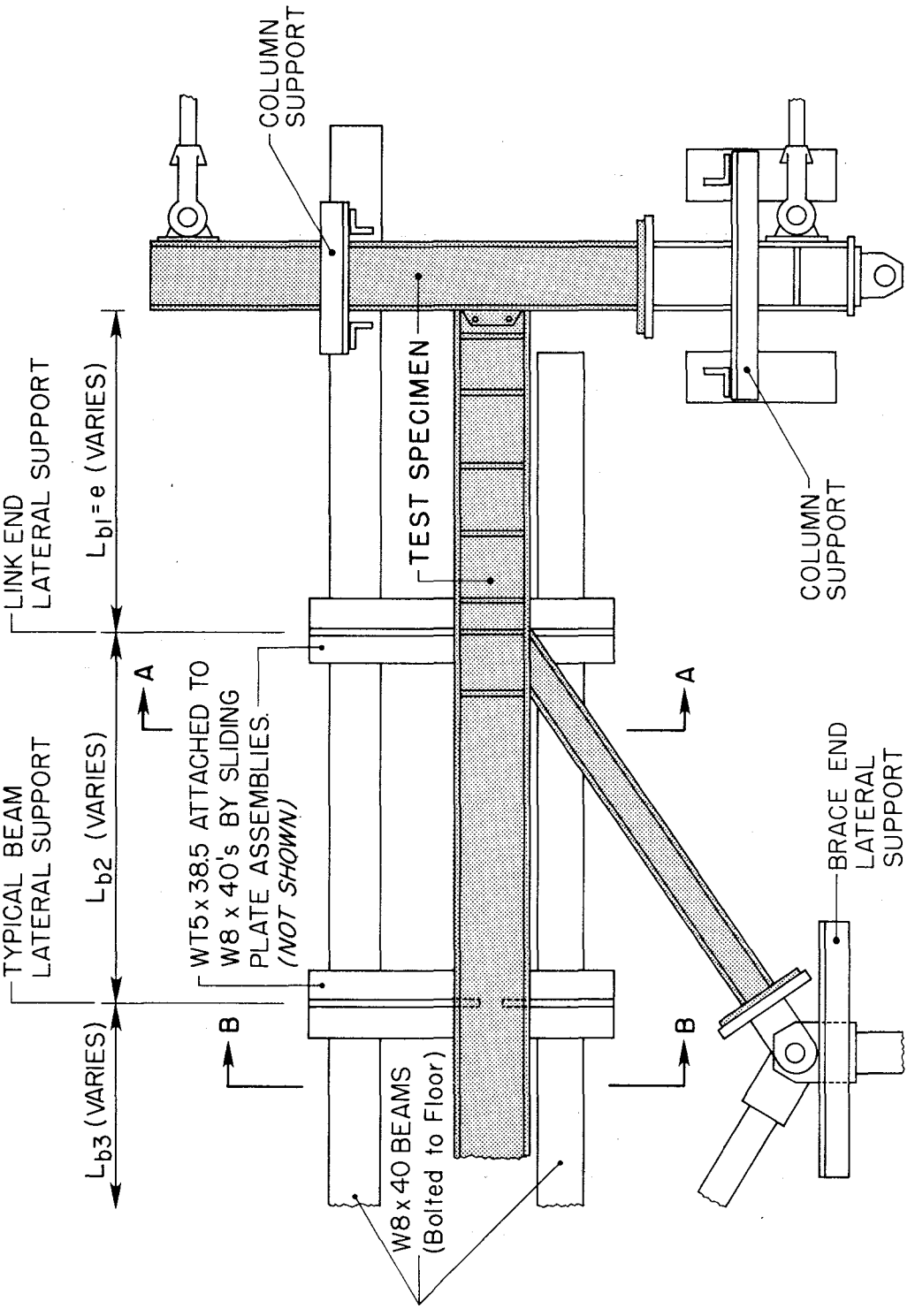

Fig. 2.30 Lateral Support System

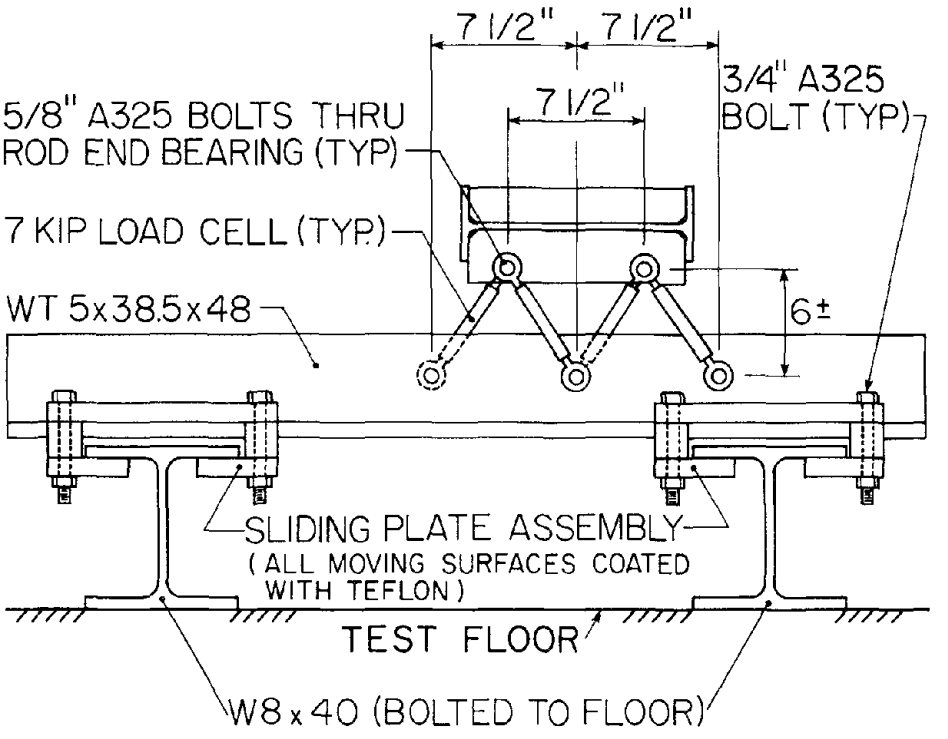

SECTION A - A

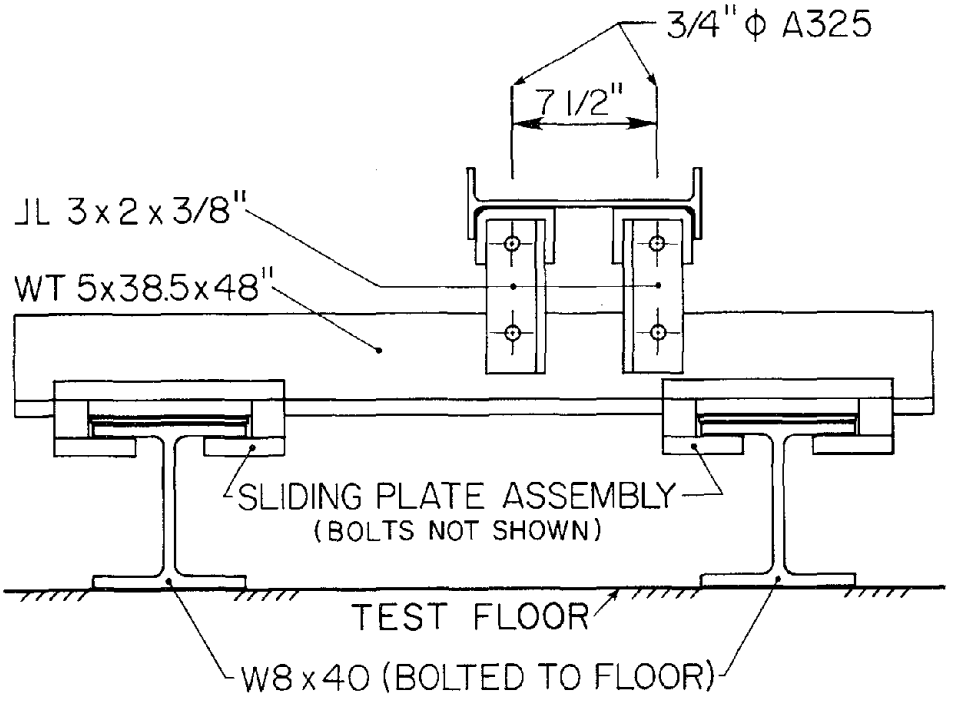

SECTION B - B

Fig. 2.30 Lateral Support System (cont.)

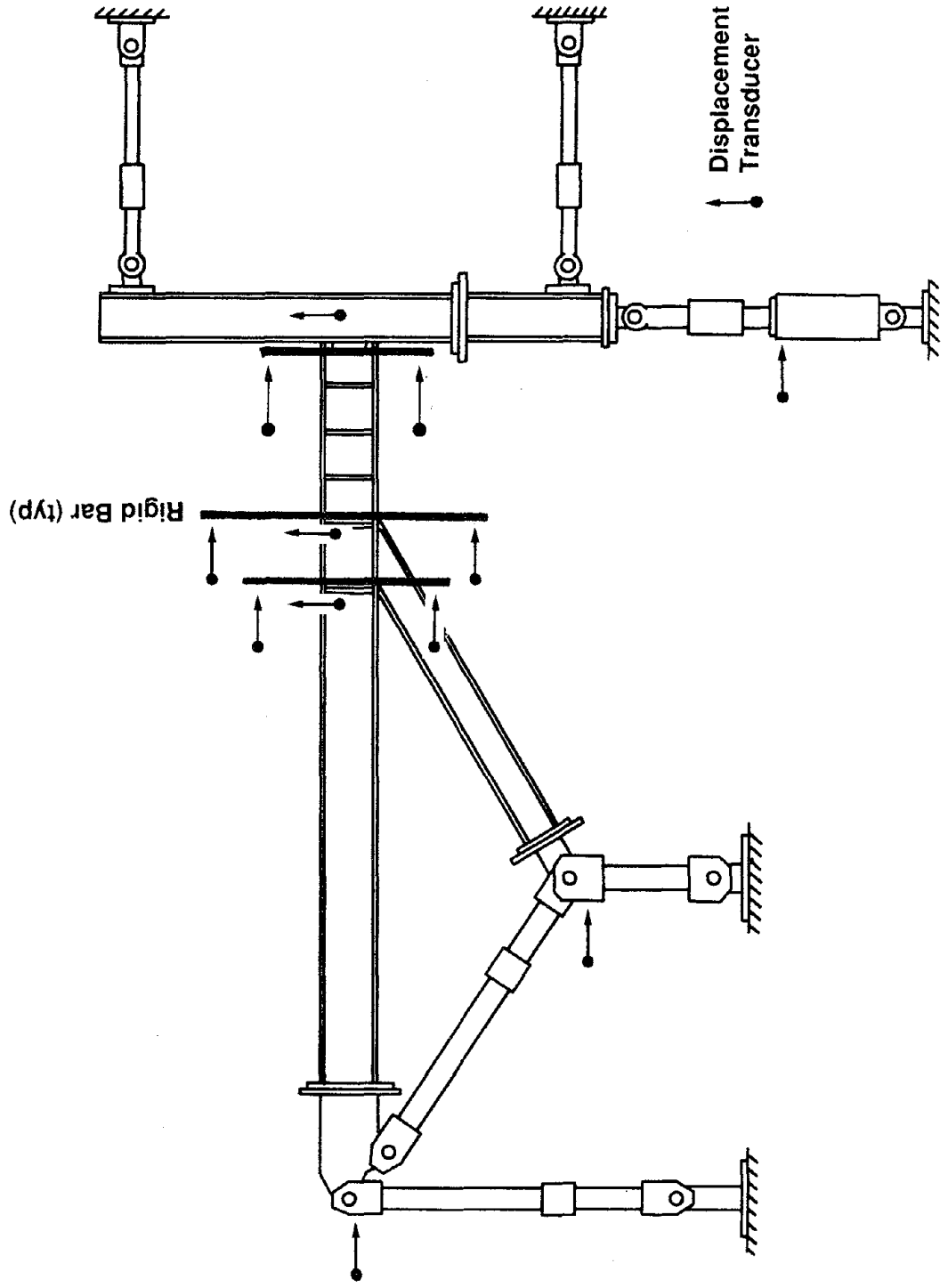

Fig. 2.31 Location of Displacement Transducers

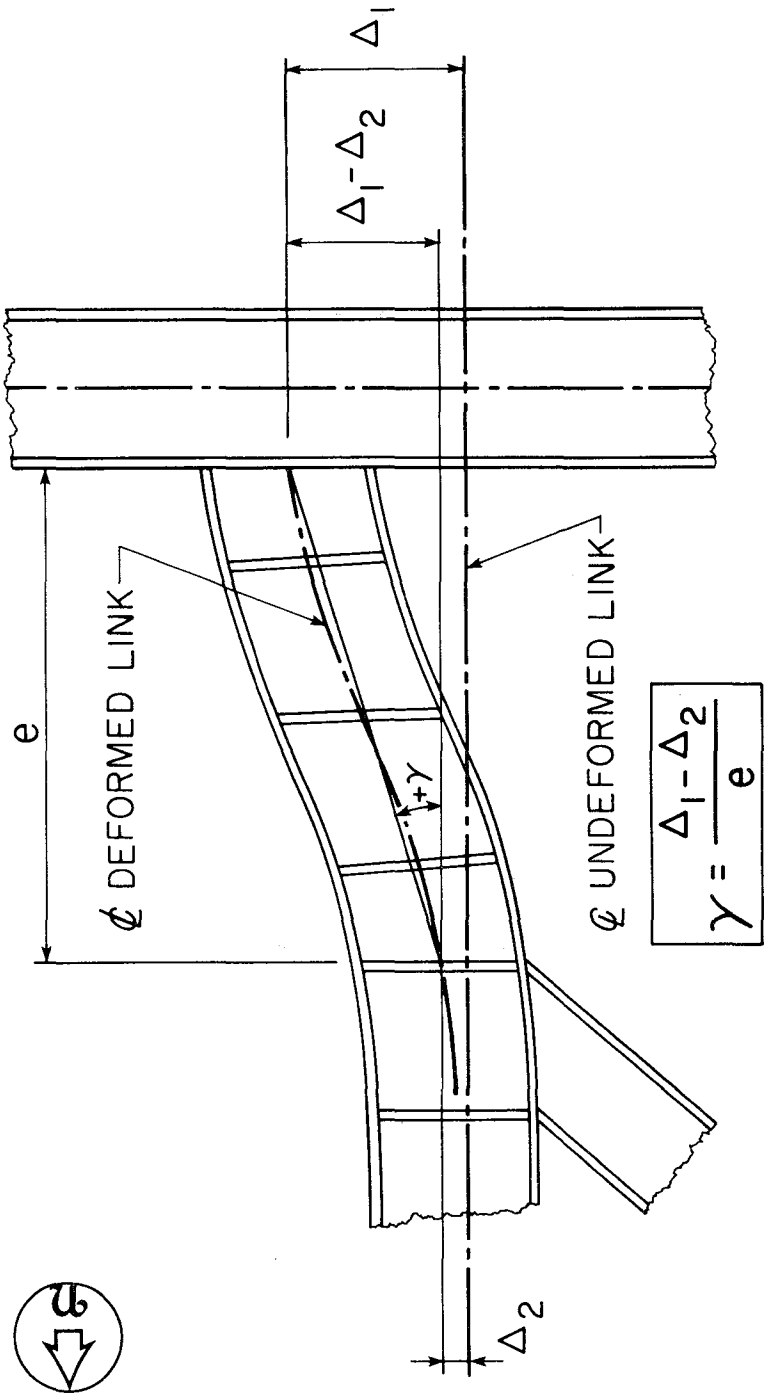

Fig. 3.1 Definition of Link Rotation Angle γ

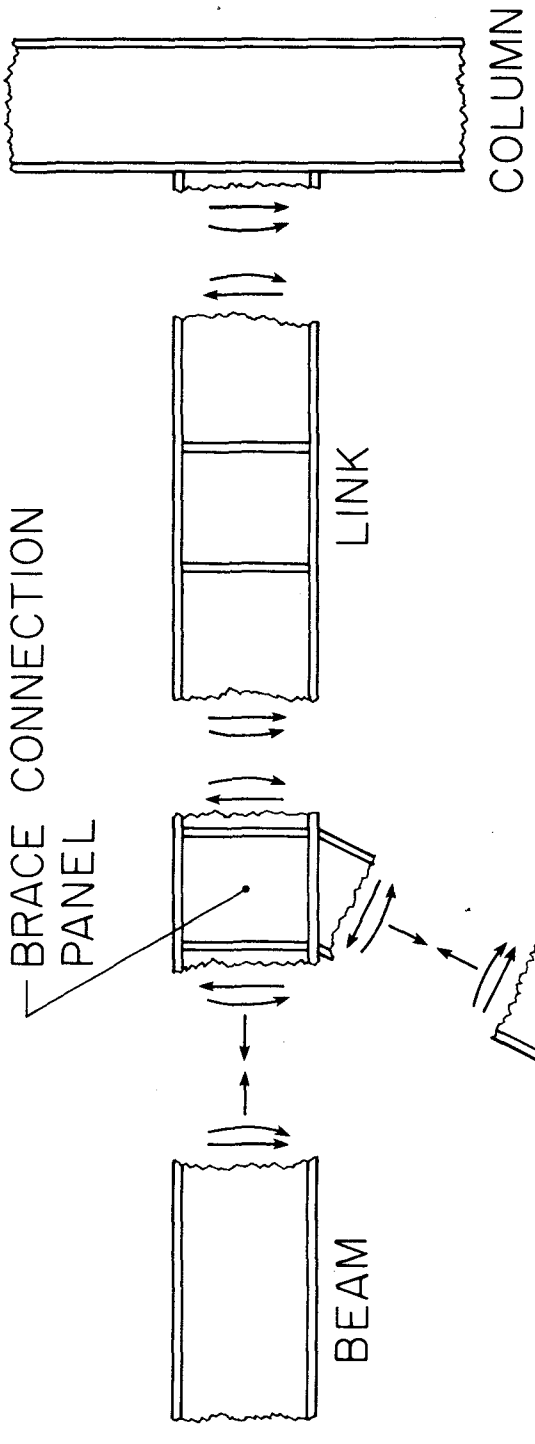

Fig. 3.2 Definition of Positive Force Resultants

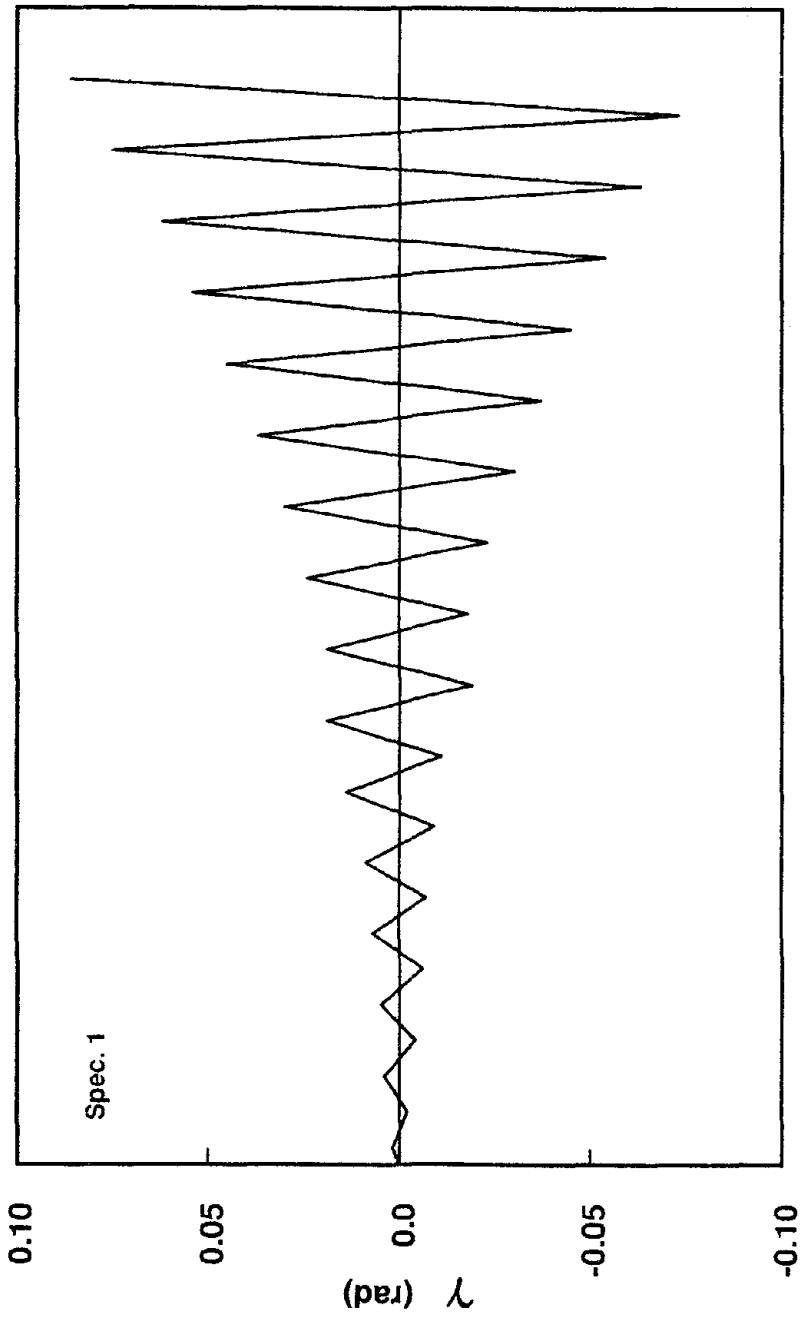

Fig. 3.3 Typical Link Rotation History

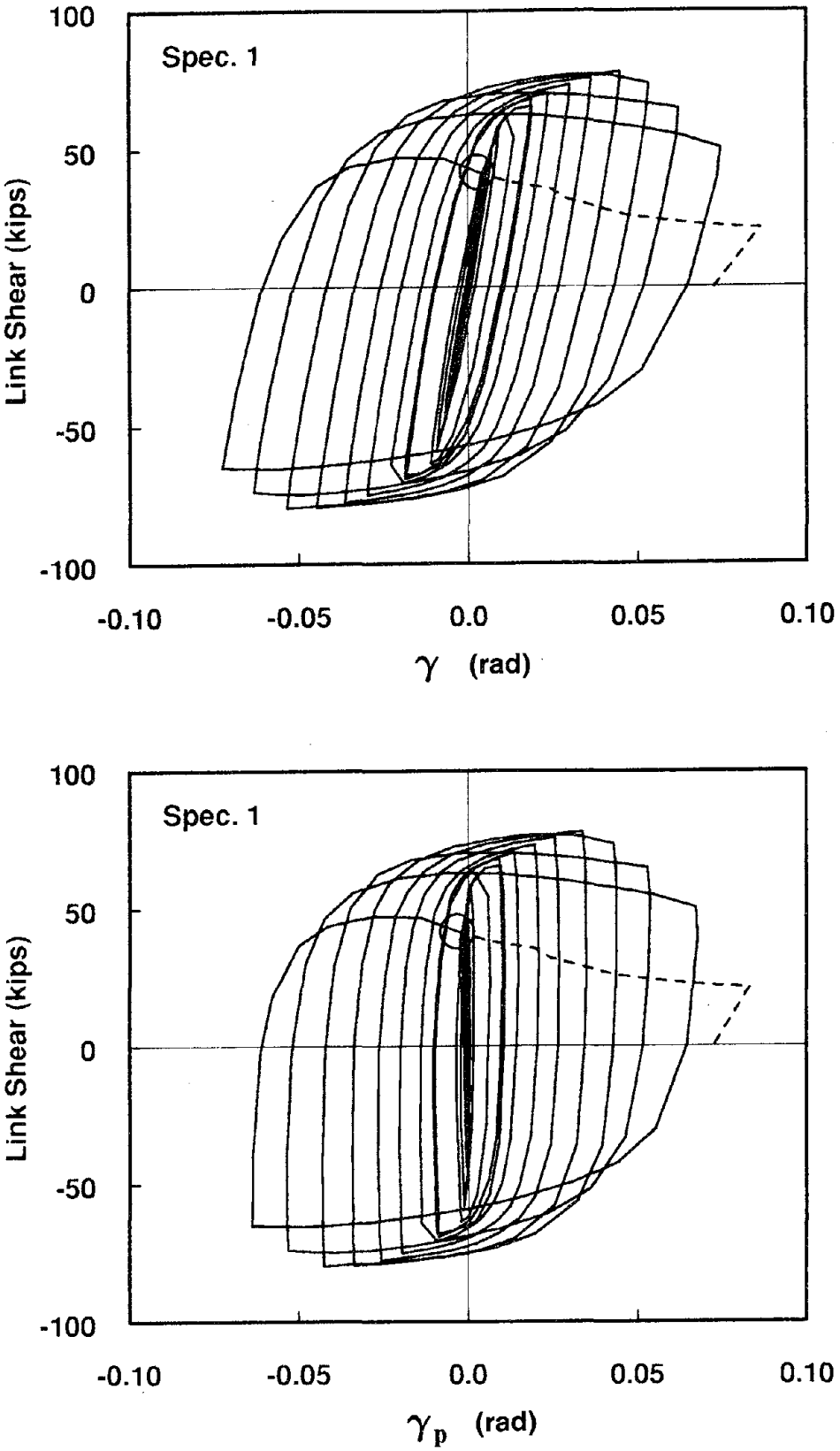

Fig. 3.4 Link Shear vs. Rotation Angle - Specimen 1

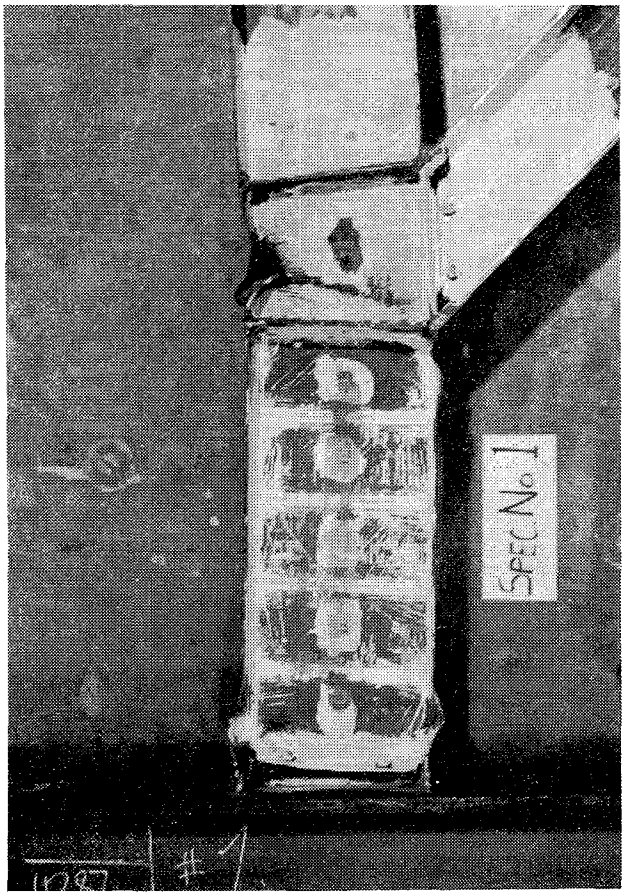

(b) Link Region (Far Side) - After Testing

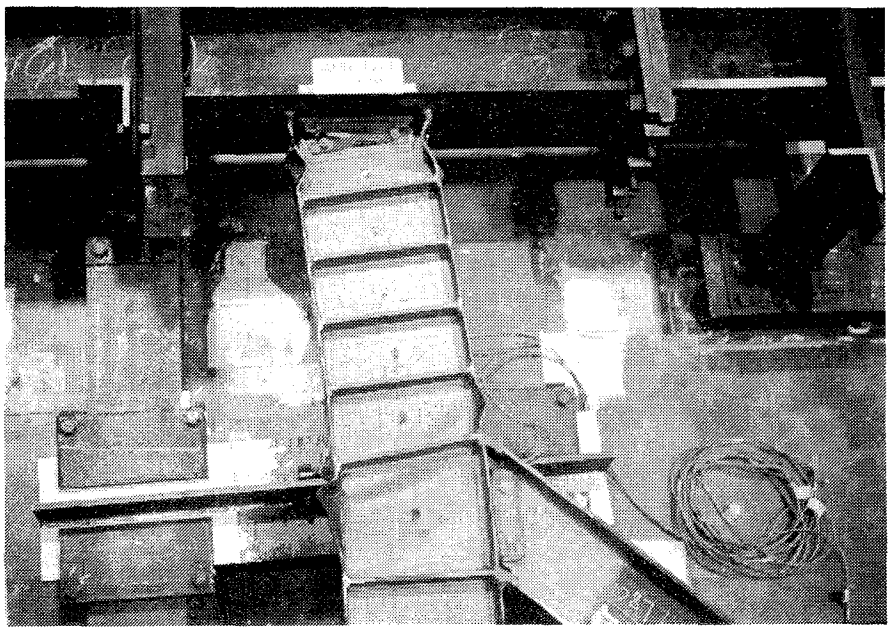

(a) Link Region (Near Side) - After Testing

Fig. 3.5 Specimen 1

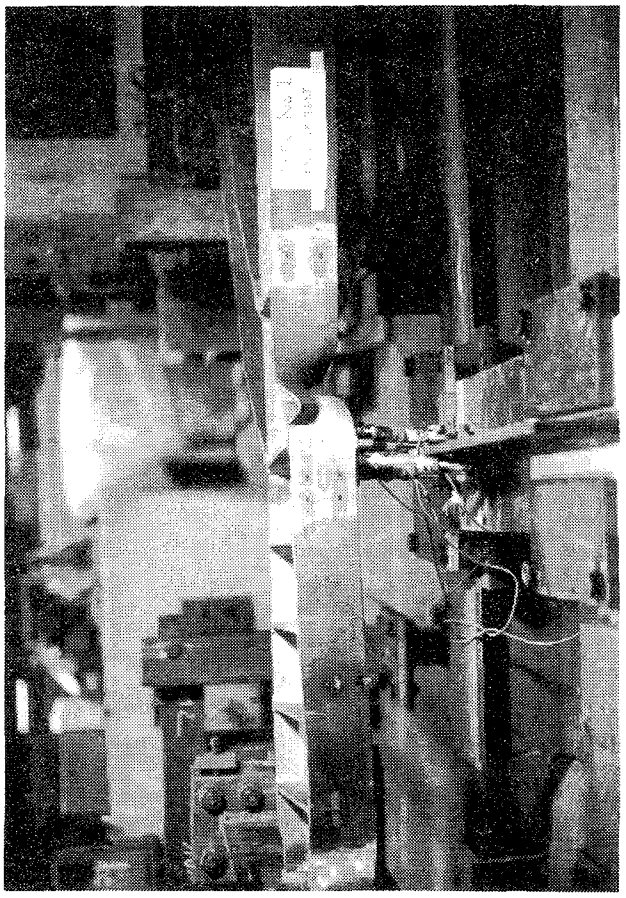

(d) East Flange of Link and Brace Connection Panel - After Testing

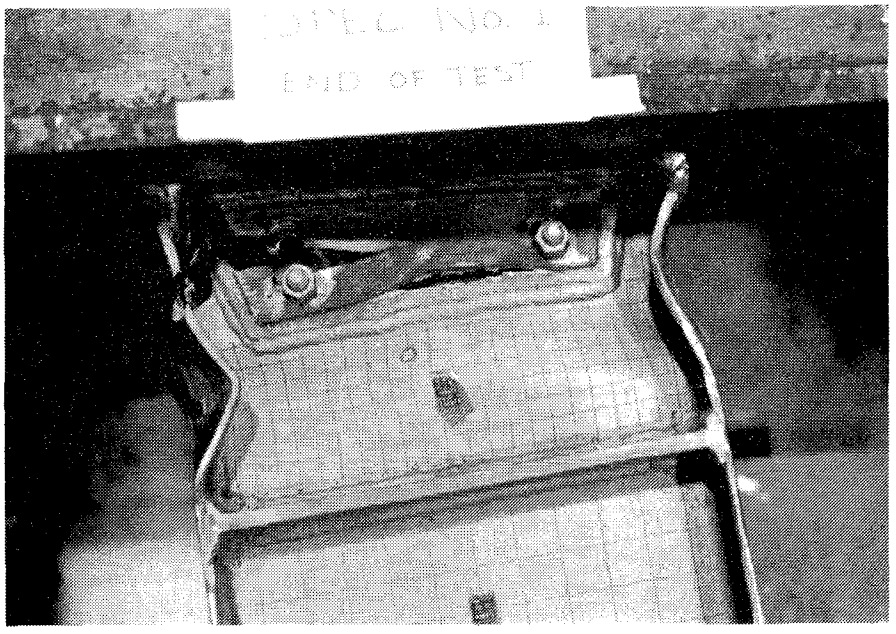

(c) Link-Column Connection - After Testing

Fig. 3.5 Specimen 1 (cont.)

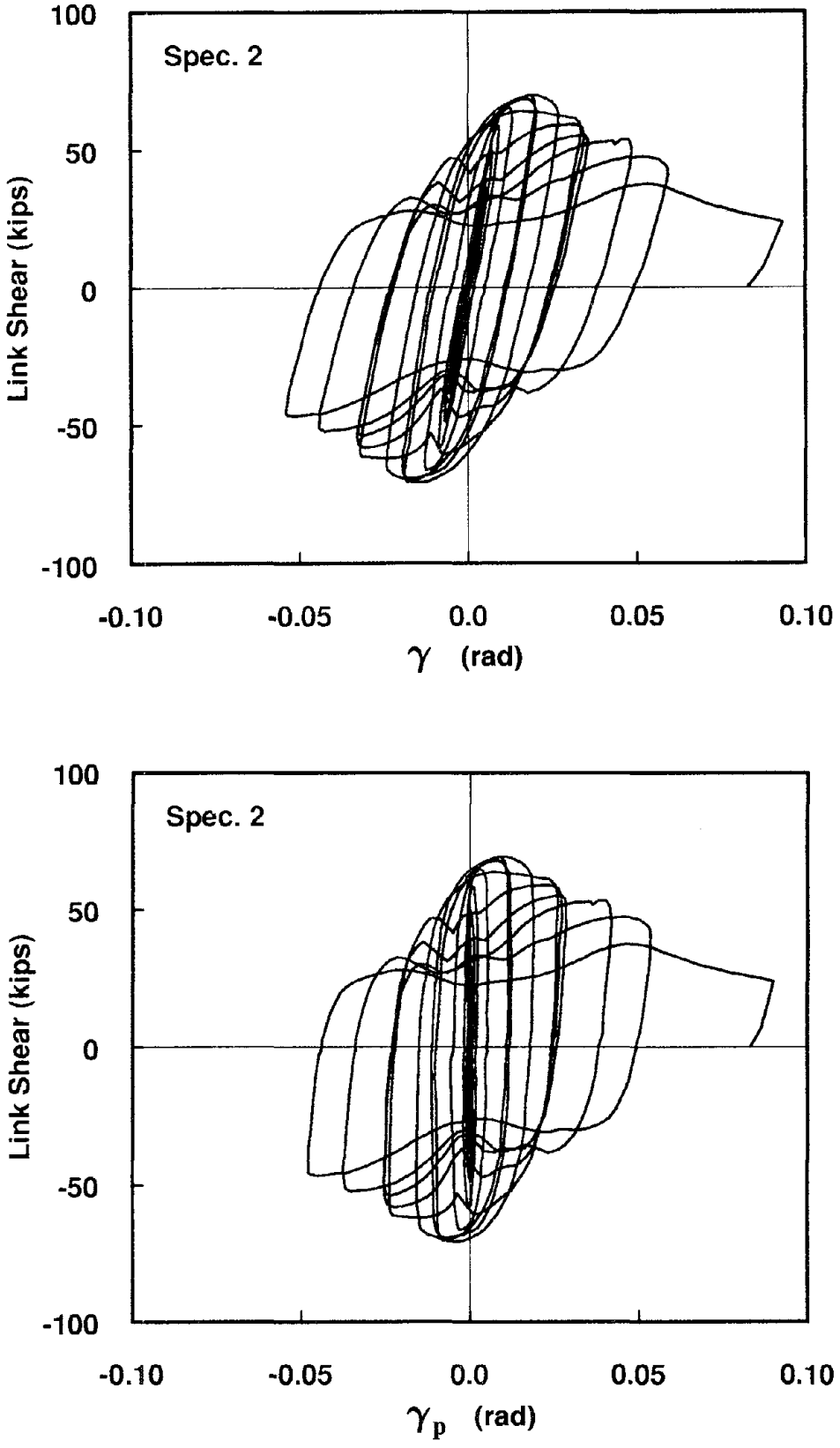

Fig. 3.6 Link Shear vs. Rotation Angle - Specimen 2

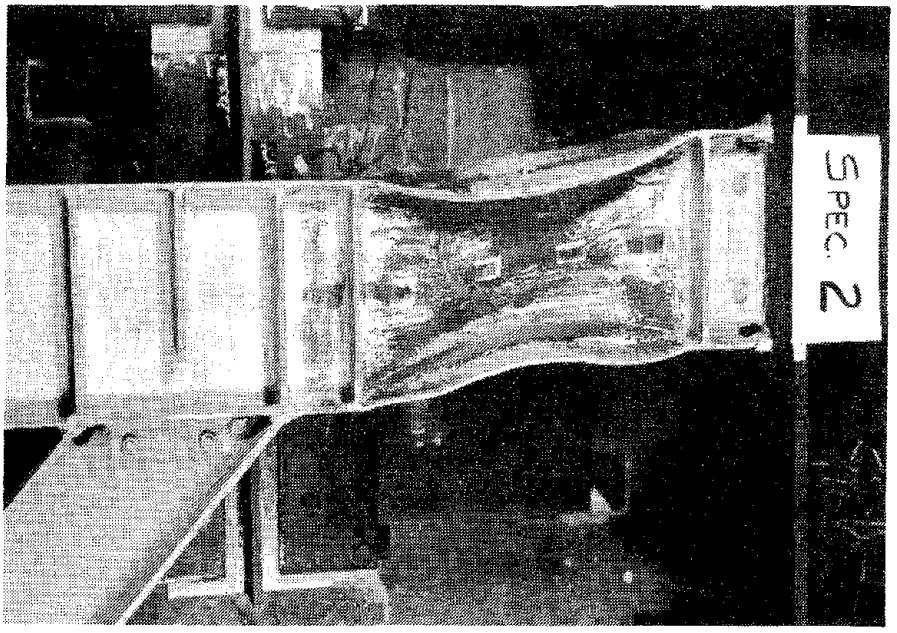

(a) Link Region - After Testing

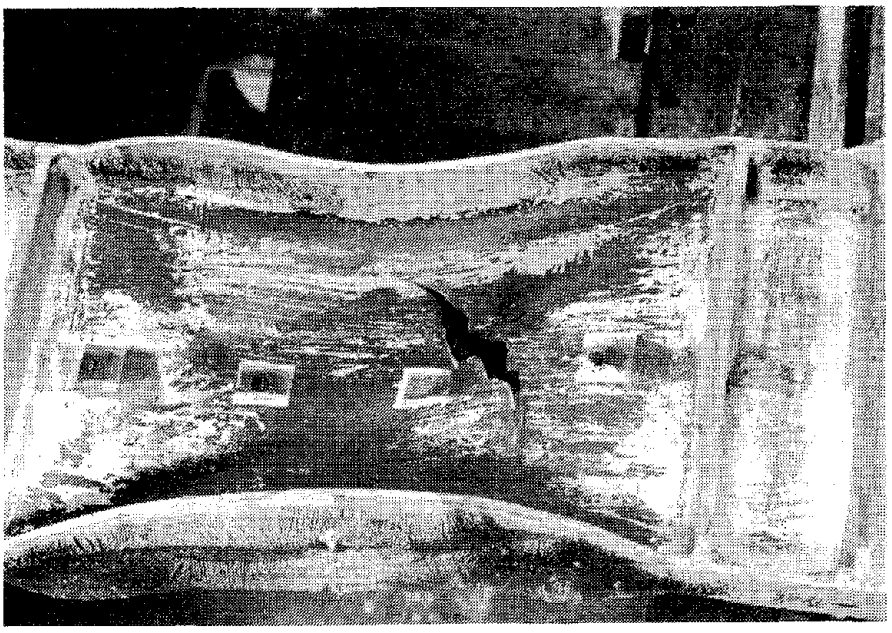

(b) Central Panel of Link - After Testing

Fig. 3.7 Specimen 2

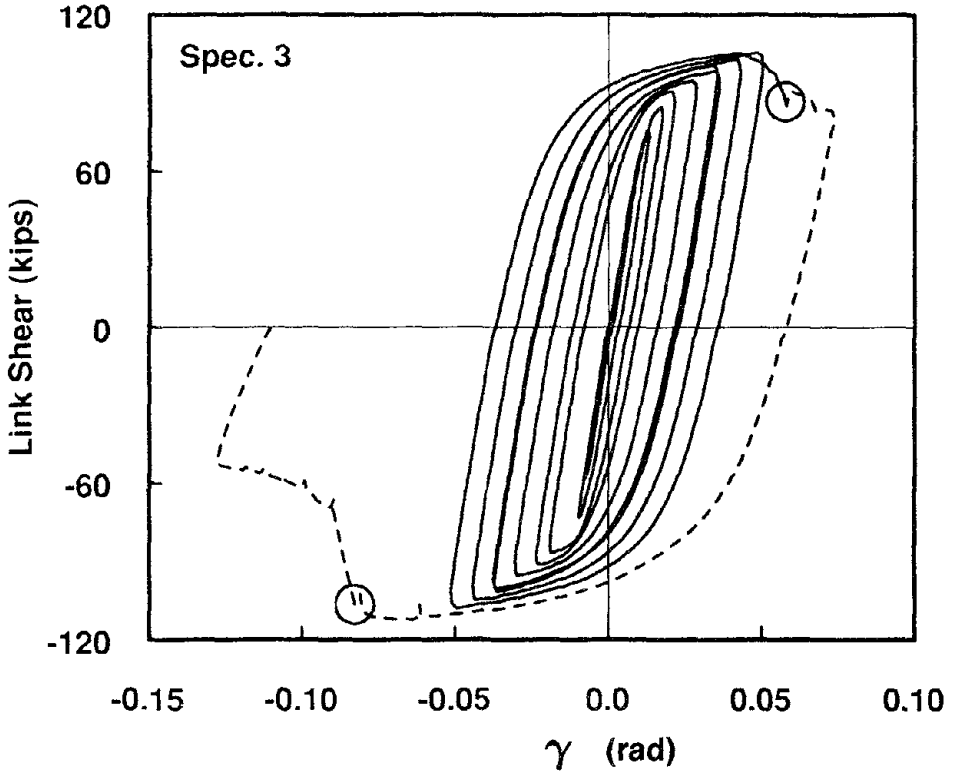

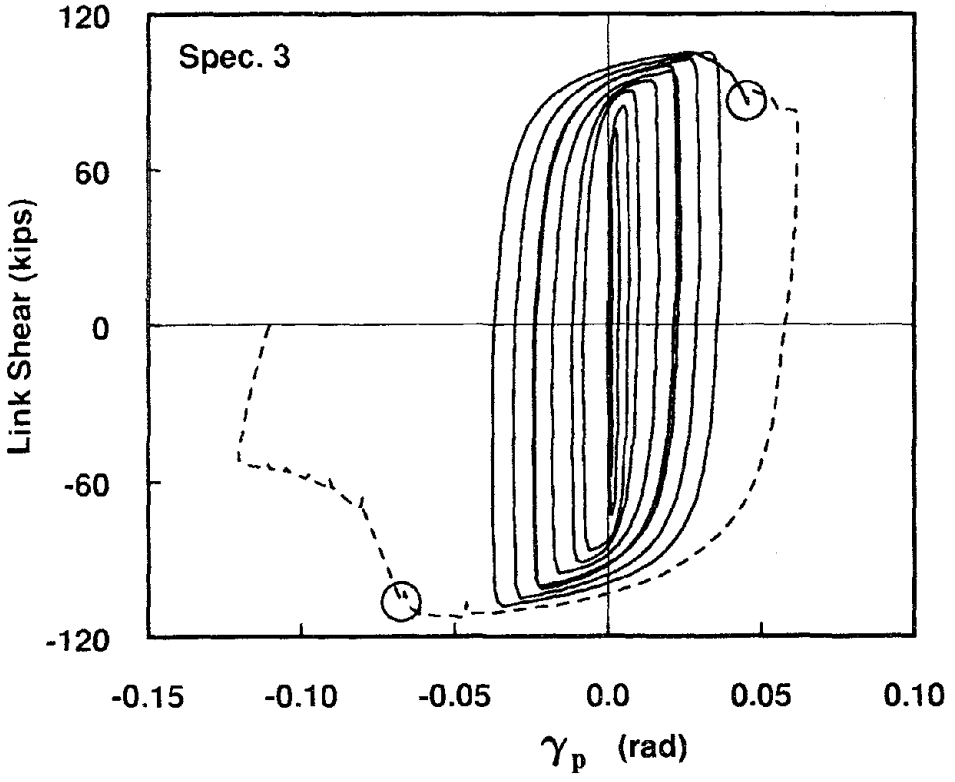

Fig. 3.8 Link Shear vs. Rotation Angle - Specimen 3

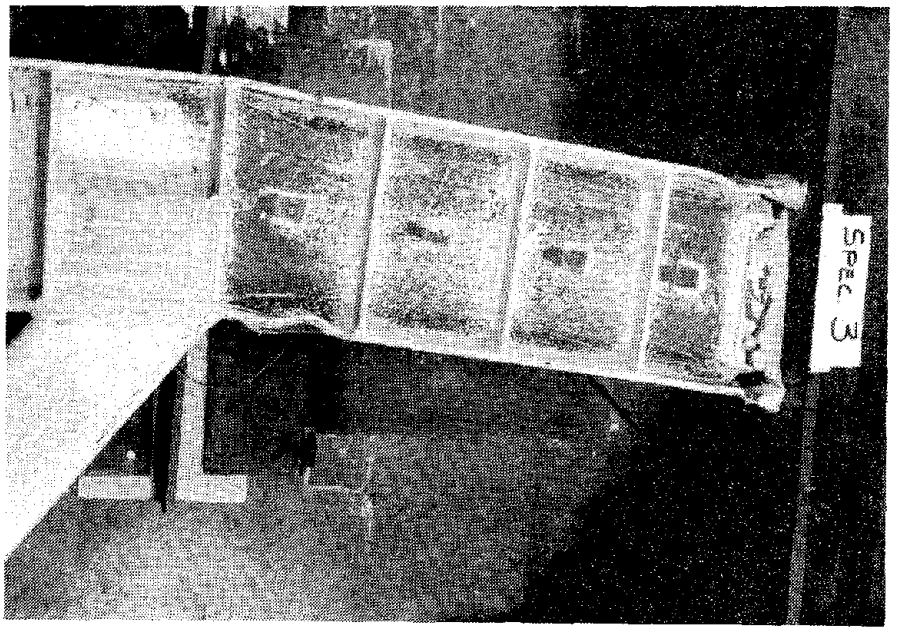

(a) Link Region - After Testing

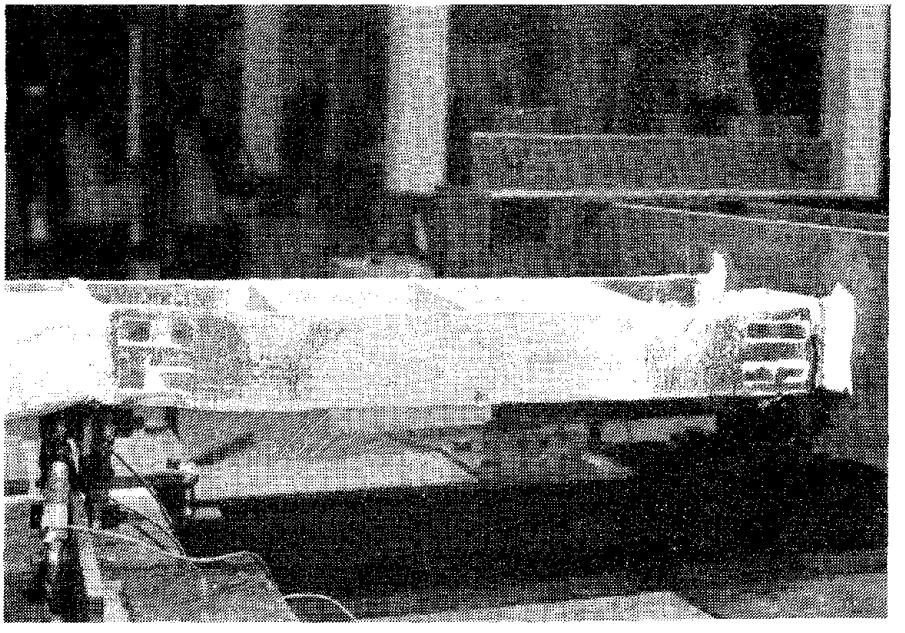

(b) West Flange of Link - After Testing

Fig. 3.9 Specimen 3

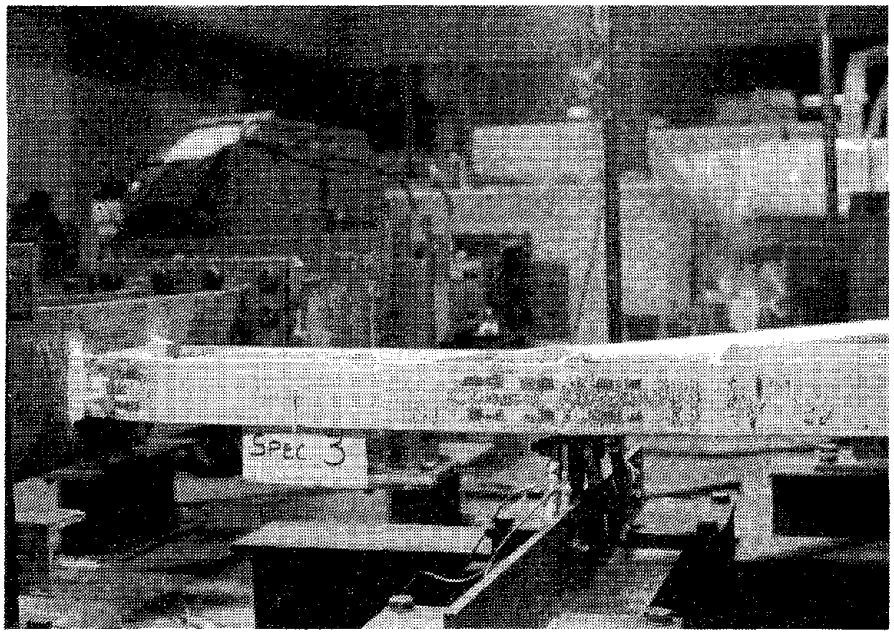

(c) East Flange of Link and Brace Connection Panel - After Testing

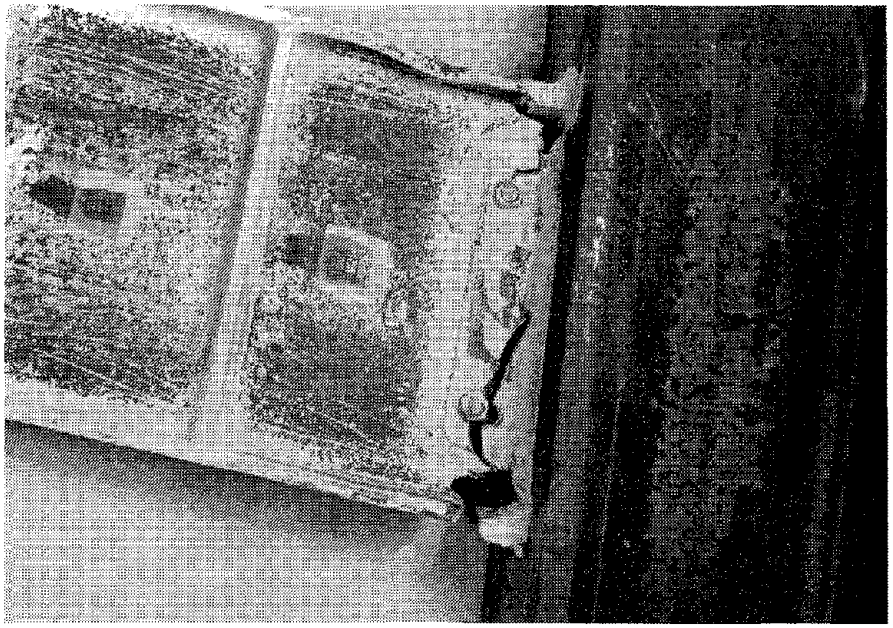

(d) Link-Column Connection - After Testing

Fig. 3.9 Specimen 3 (cont.)

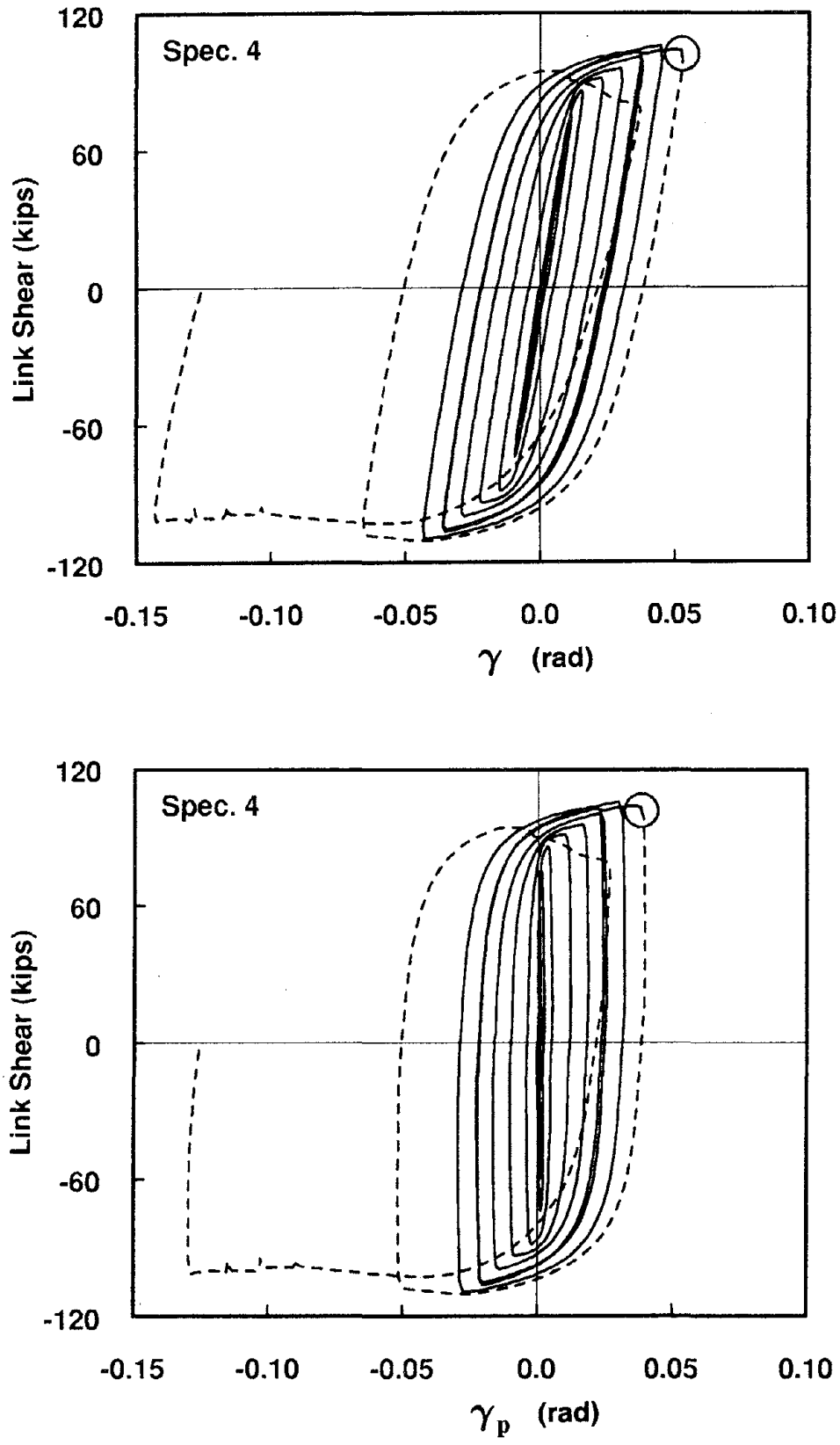

Fig. 3.10 Link Shear vs. Rotation Angle - Specimen 4

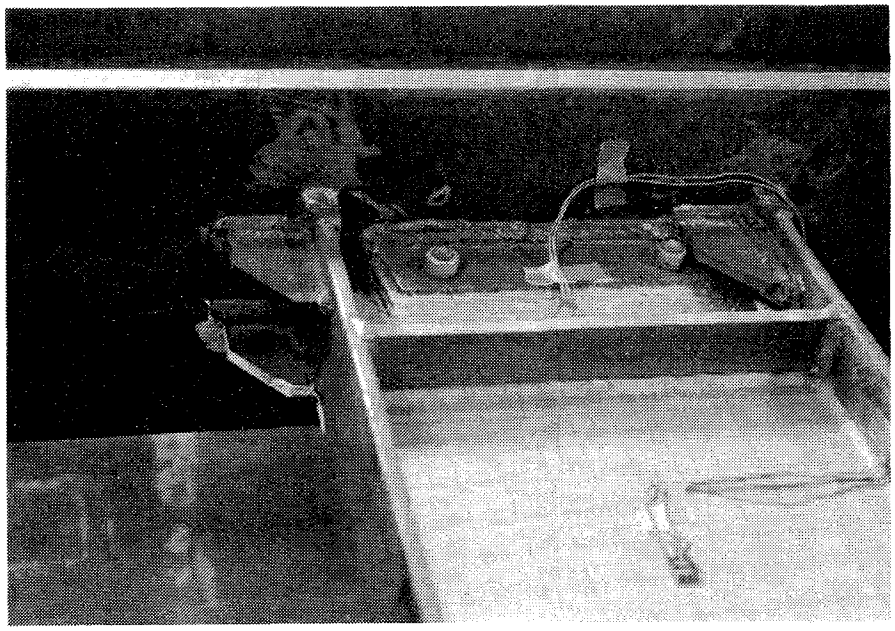

(a) Link-Column Connection - Before Testing

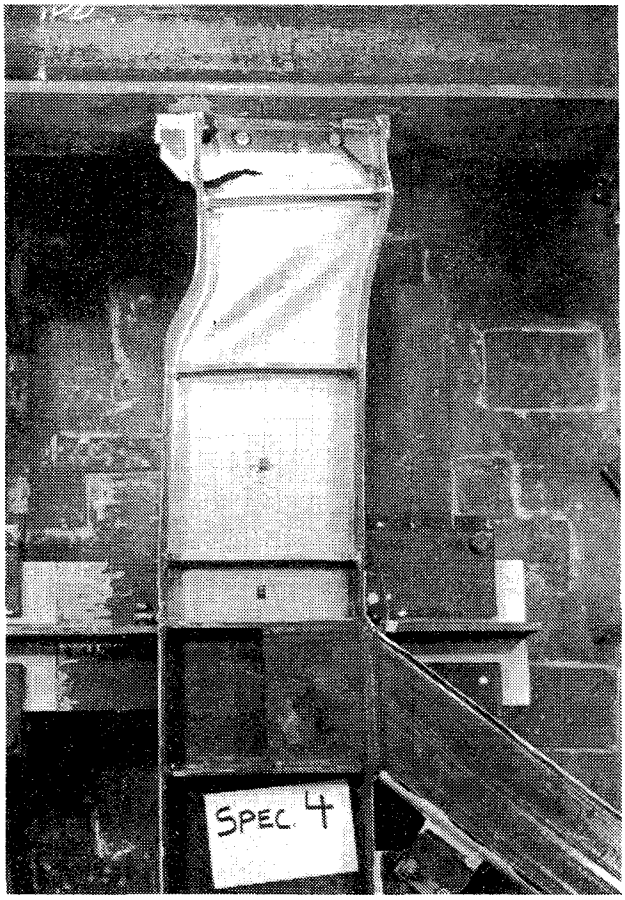

(b) Link Region - After Testing

Fig. 3.11 Specimen 4

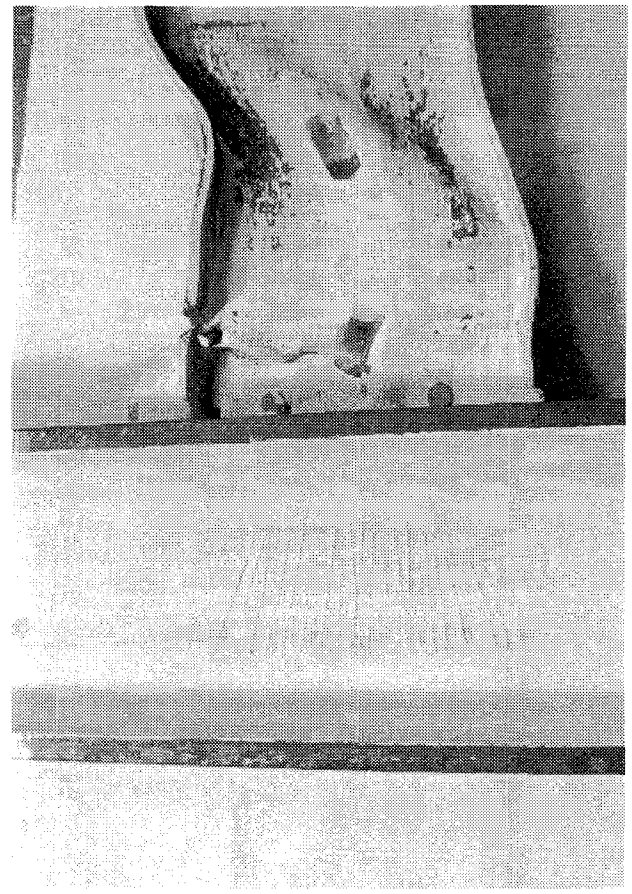

(d) Link-Column Connection (Far Side) - After Testing

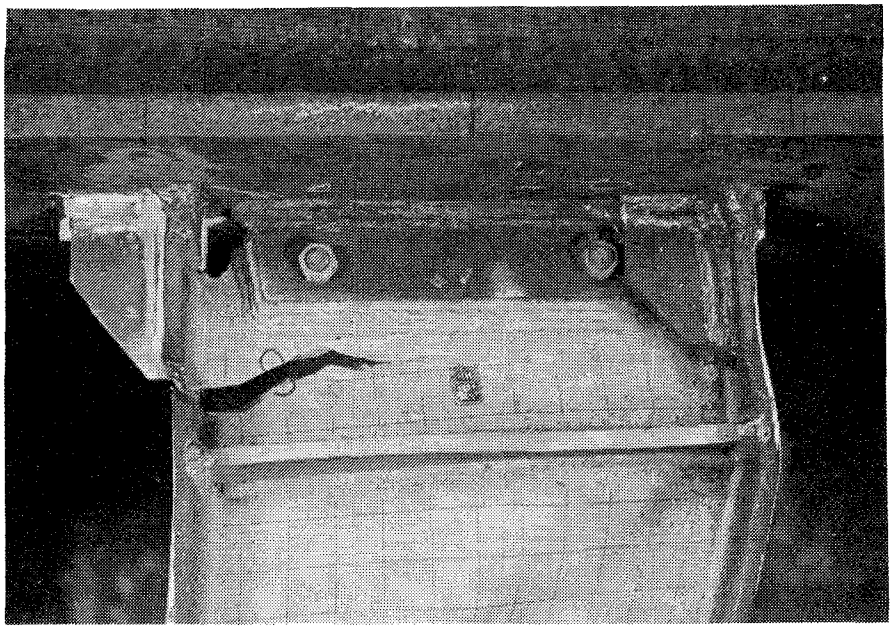

(c) Link-Column Connection (Near Side) - After Testing

Fig. 3.11 Specimen 4 (cont.)

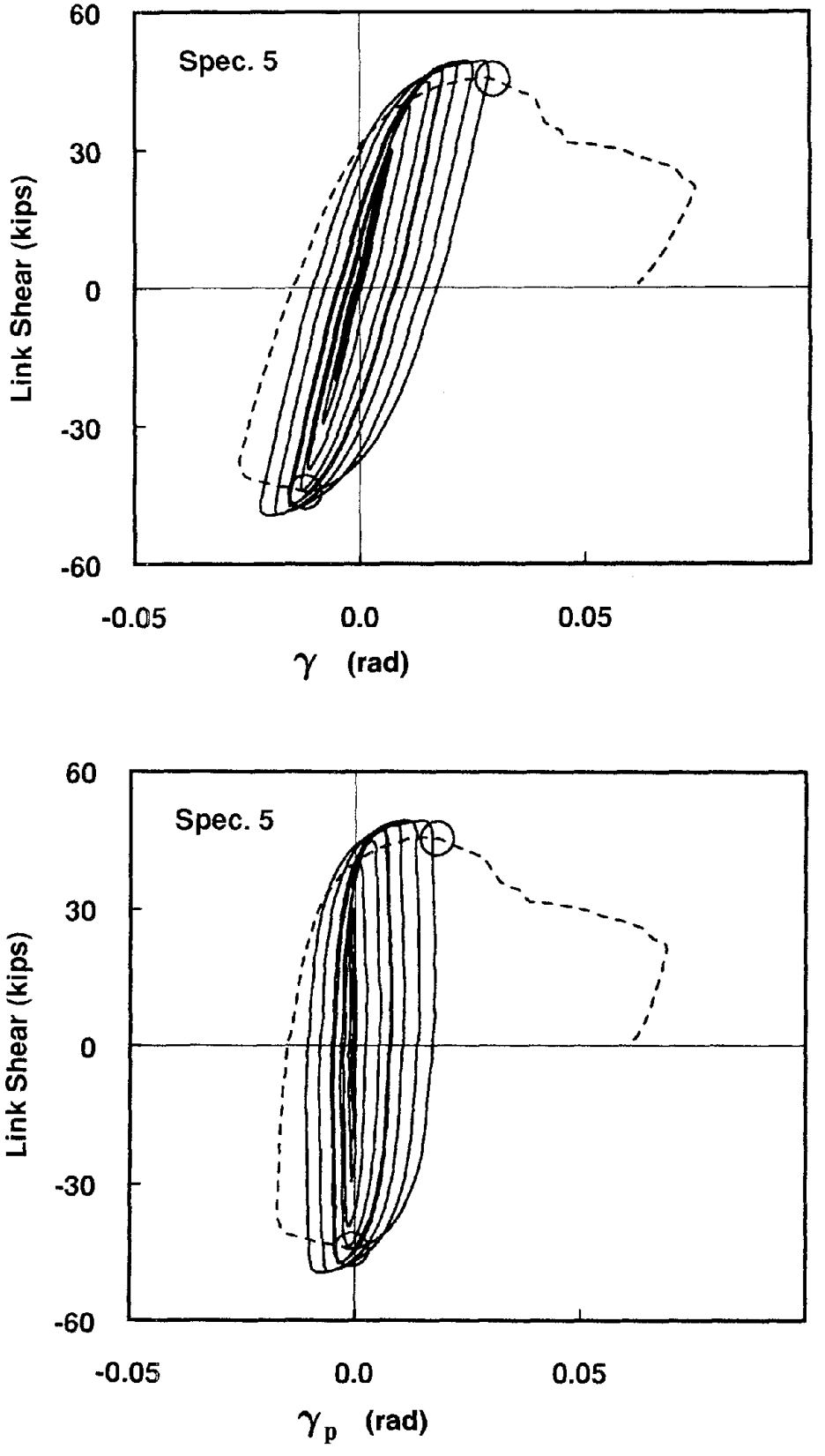

Fig. 3.12 Link Shear vs. Rotation Angle - Specimen 5

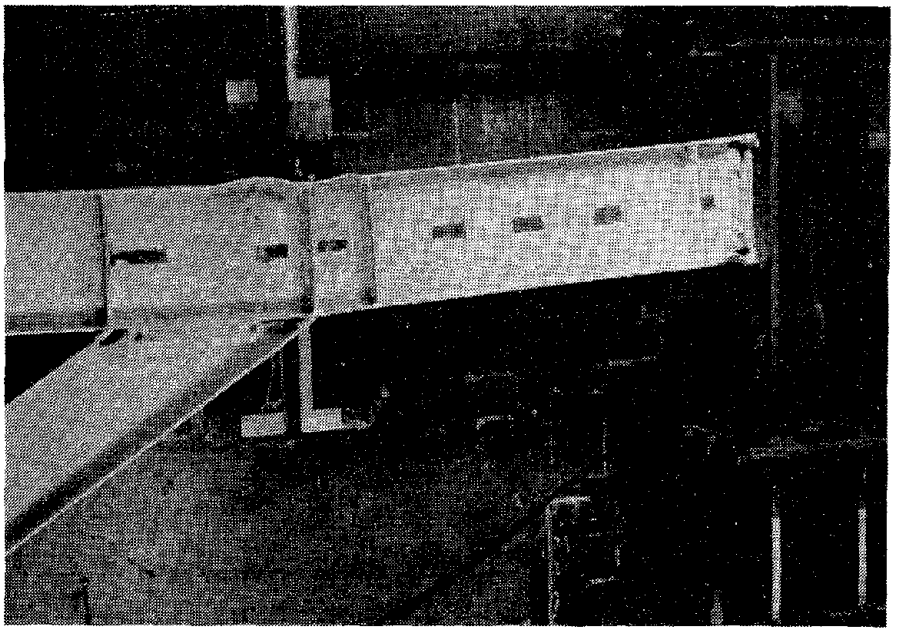

(a) Link Region - After Testing

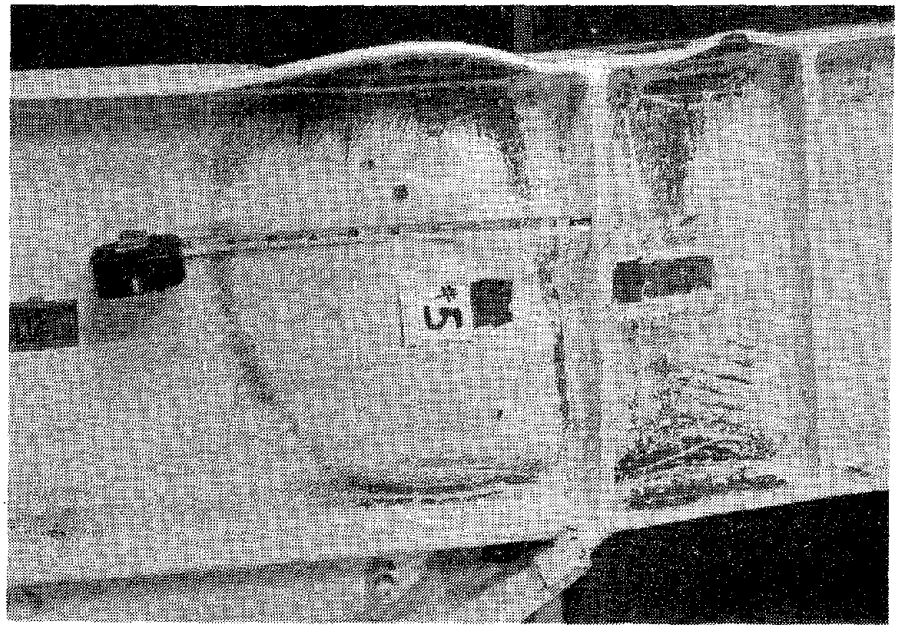

(b) Brace Connection Panel - After Testing

Fig. 3.13 Specimen 5

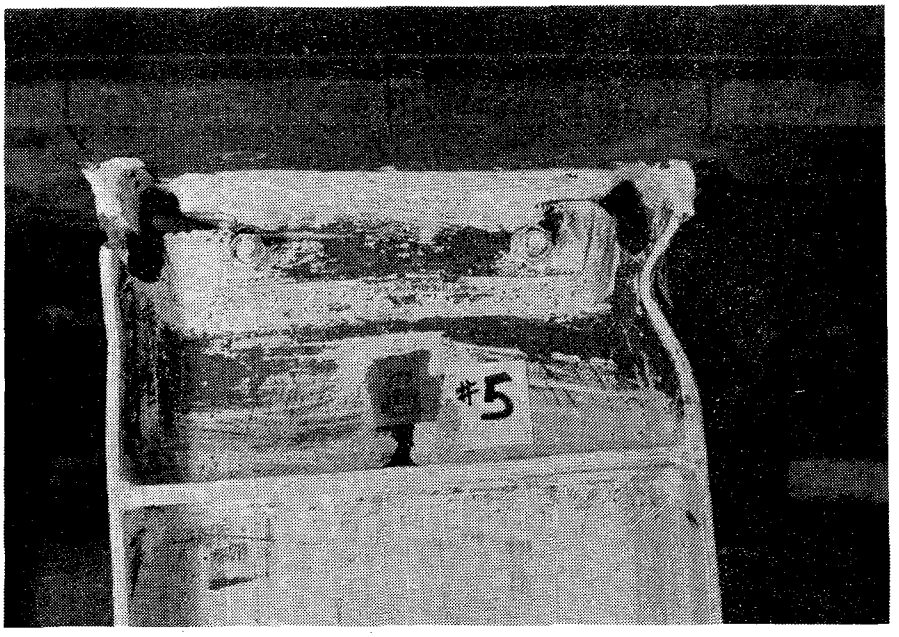

(d) Link-Column Connection - After Testing

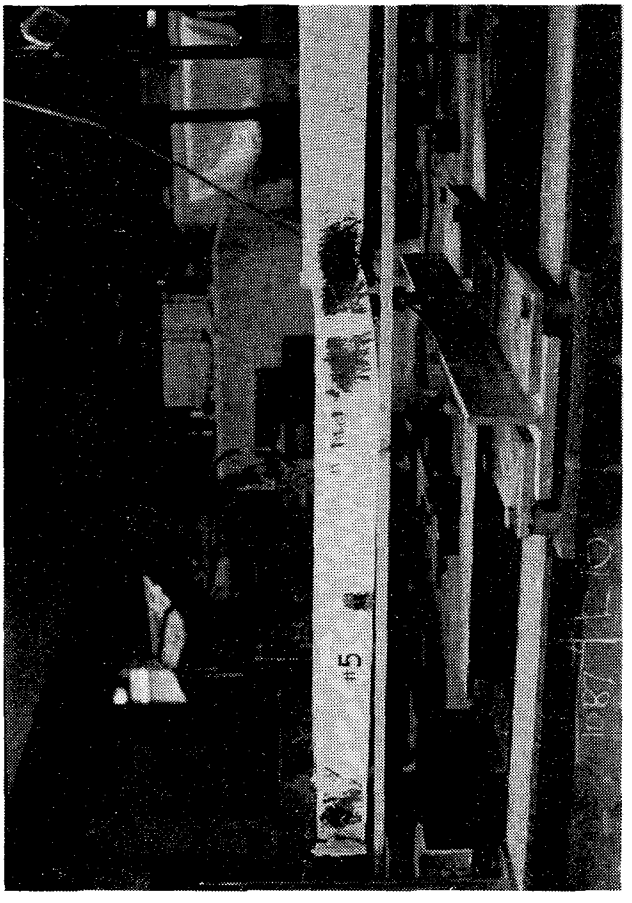

(c) View Looking Towards East Flange - After Testing

Fig. 3.13 Specimen 5 (cont.)

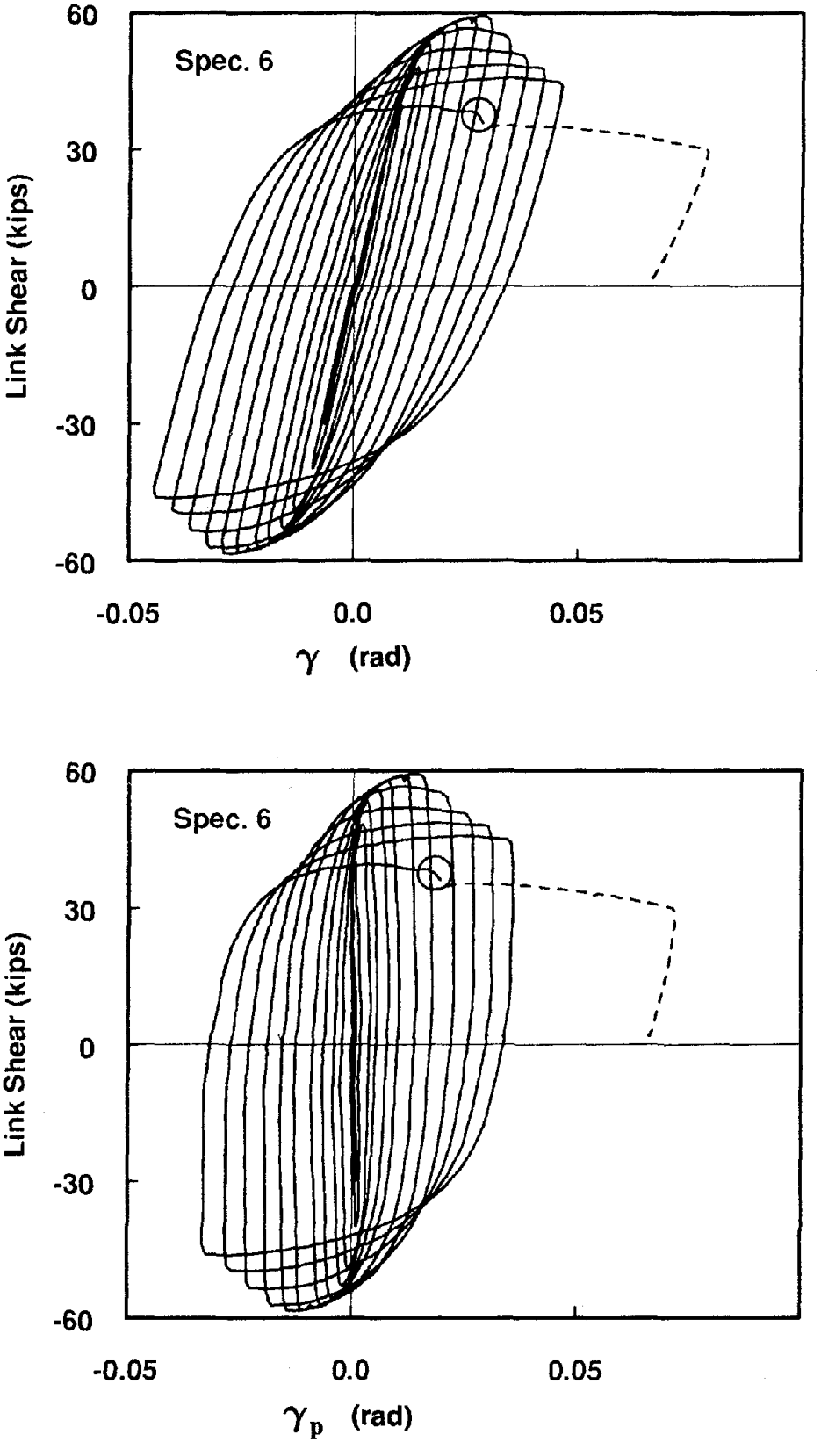

Fig. 3.14 Link Shear vs. Rotation Angle - Specimen 6

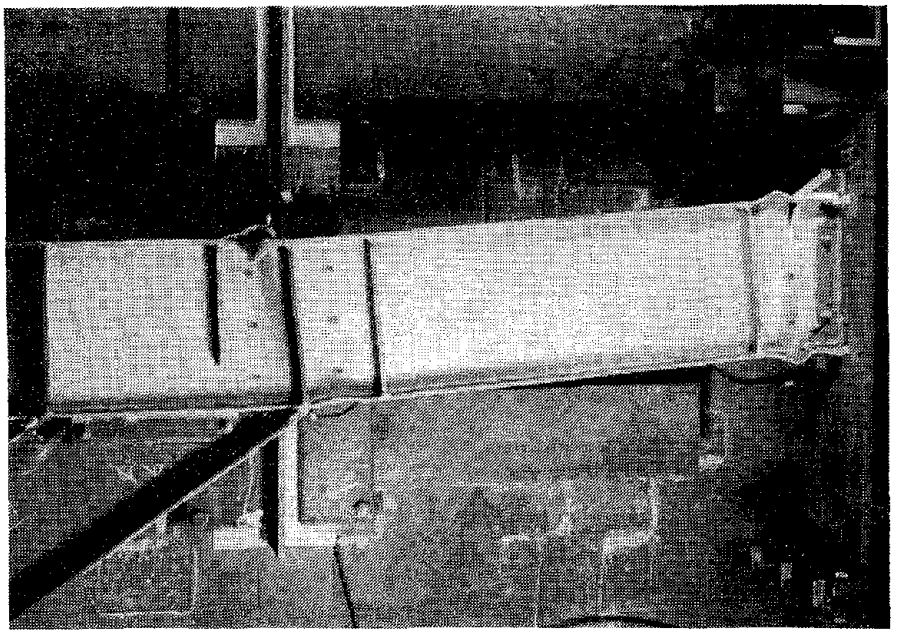

(a) Link Region - After Testing

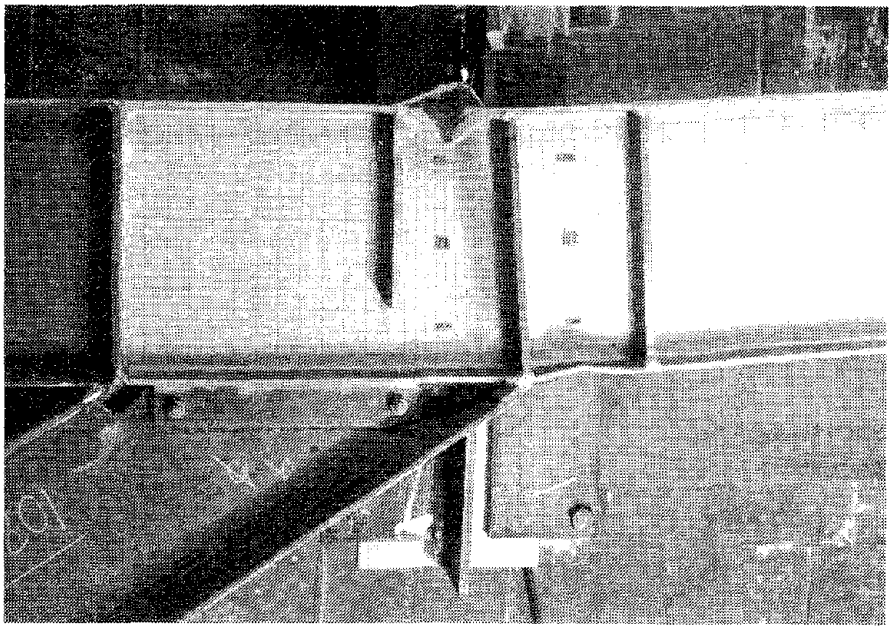

(b) Brace Connection Panel - After Testing

Fig. 3.15 Specimen 6

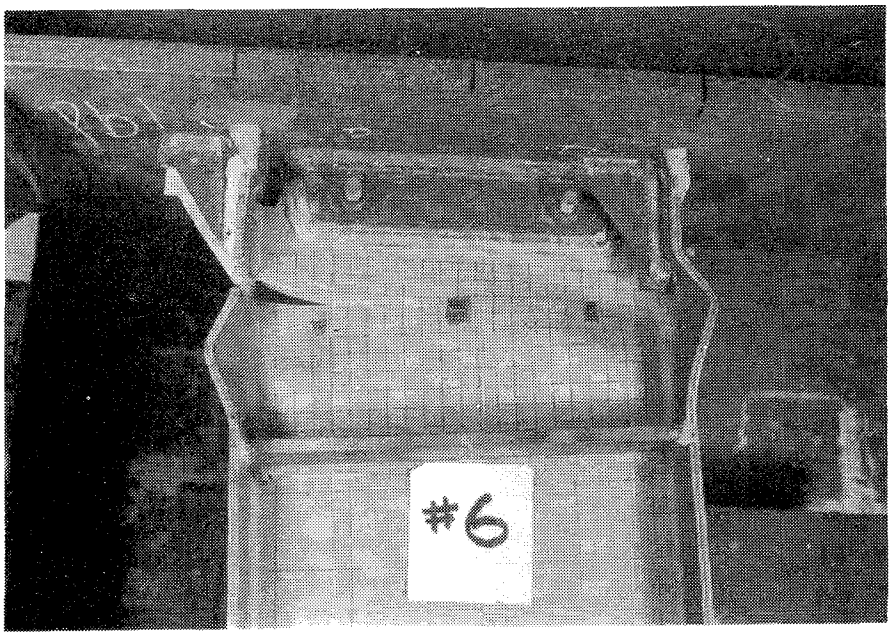

(d) Link-Column Connection - After Testing

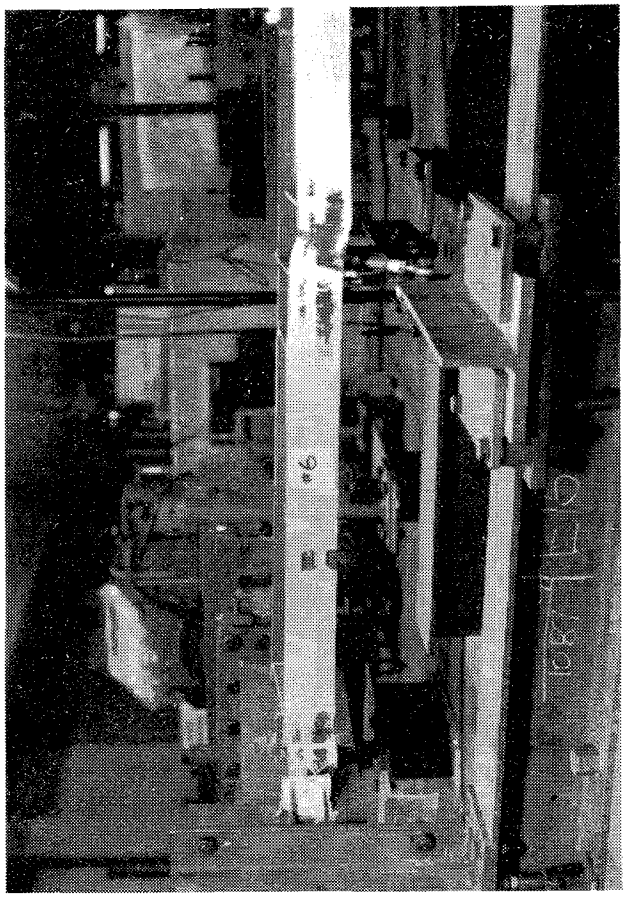

(c) View Looking Towards East Flange - After Testing

Fig. 3.15 Specimen 6 (cont.)

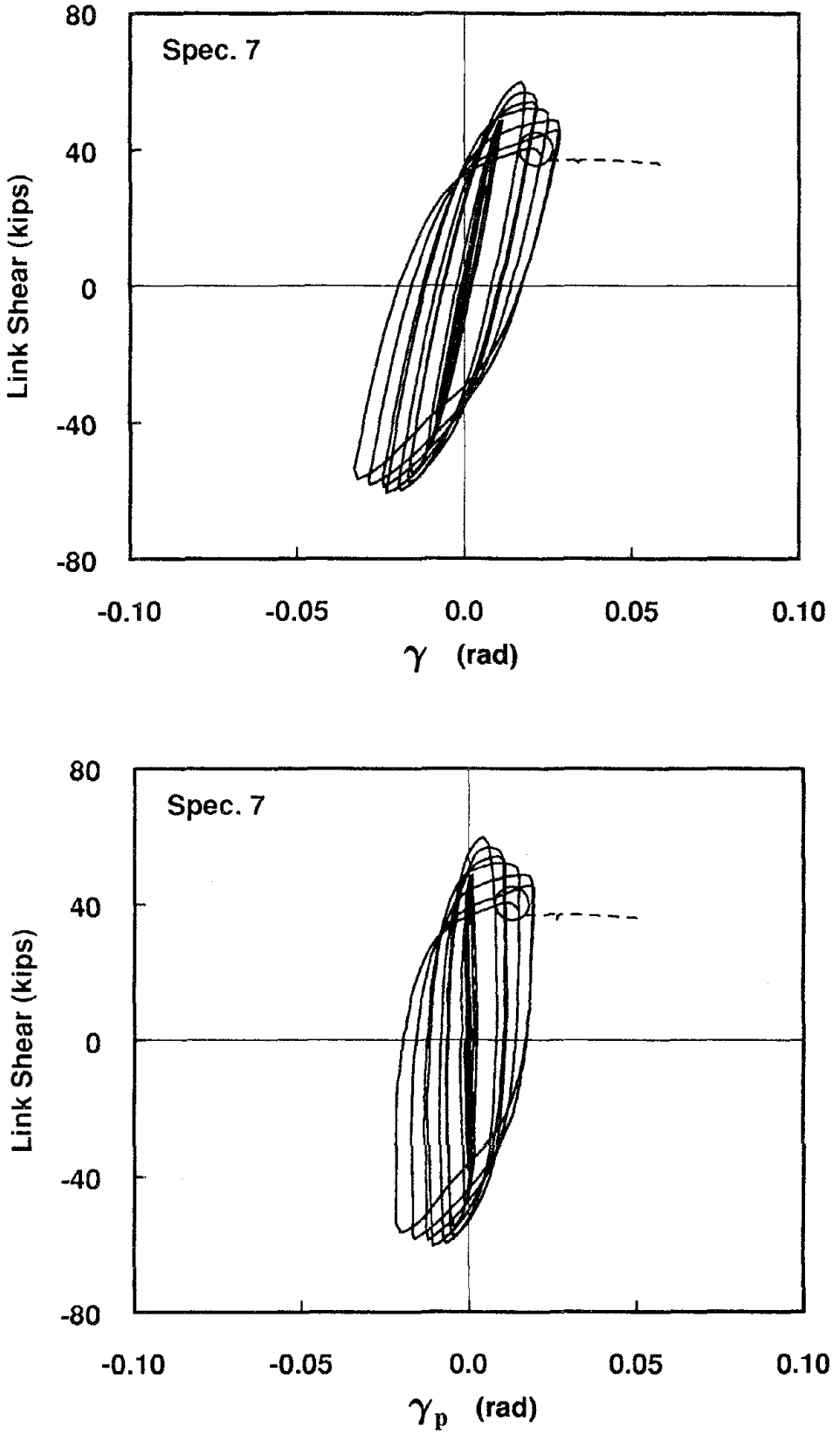

Fig. 3.16 Link Shear vs. Rotation Angle - Specimen 7

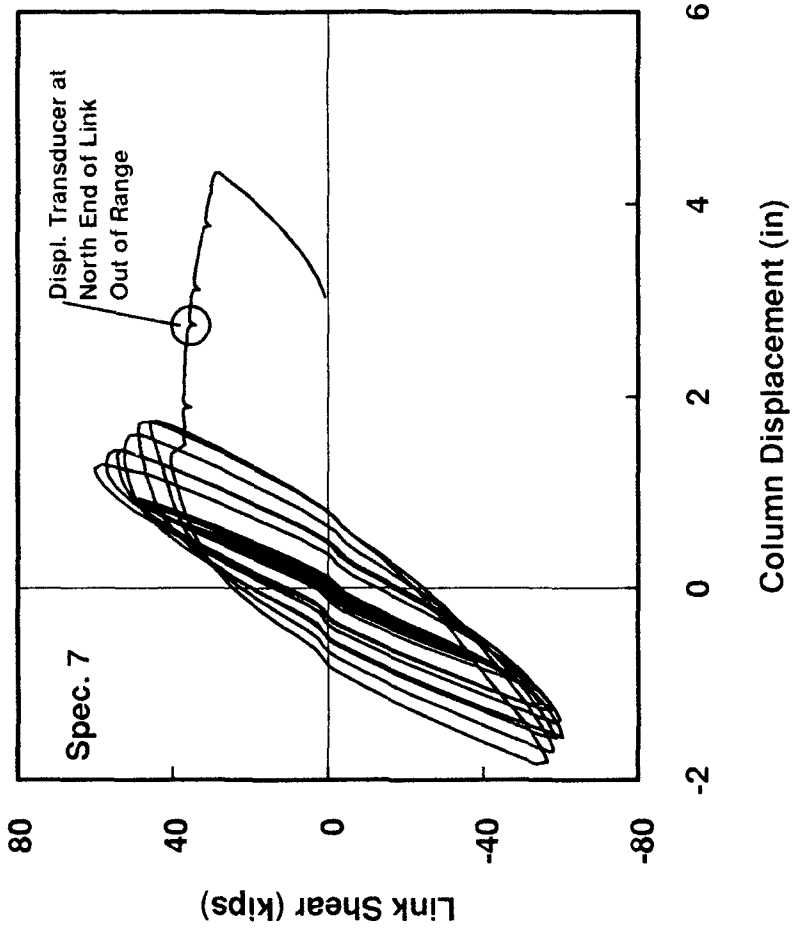

Fig. 3.17 Link Shear vs. Column Displacement - Specimen 7

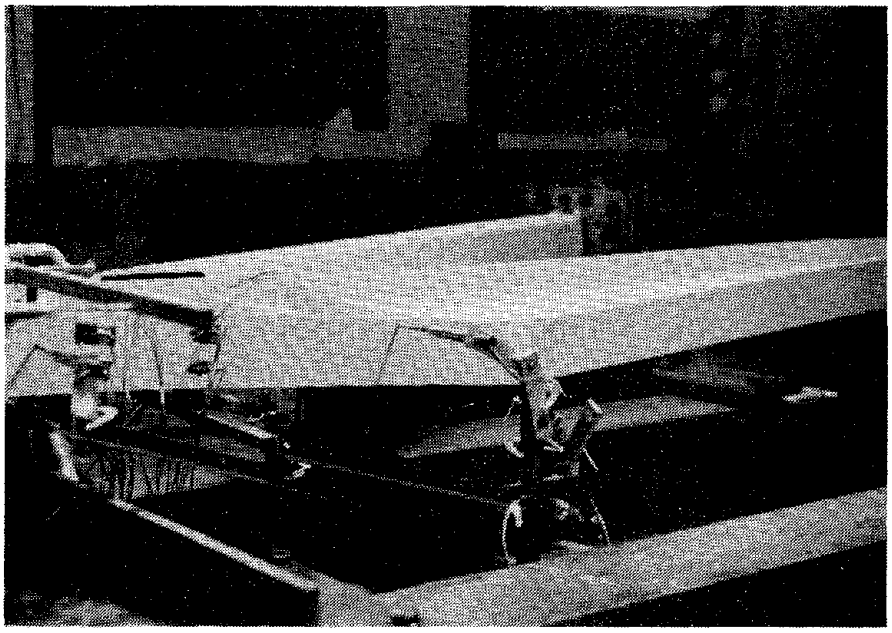

(a) View Looking Towards East Flange of Beam - Cycle 10E

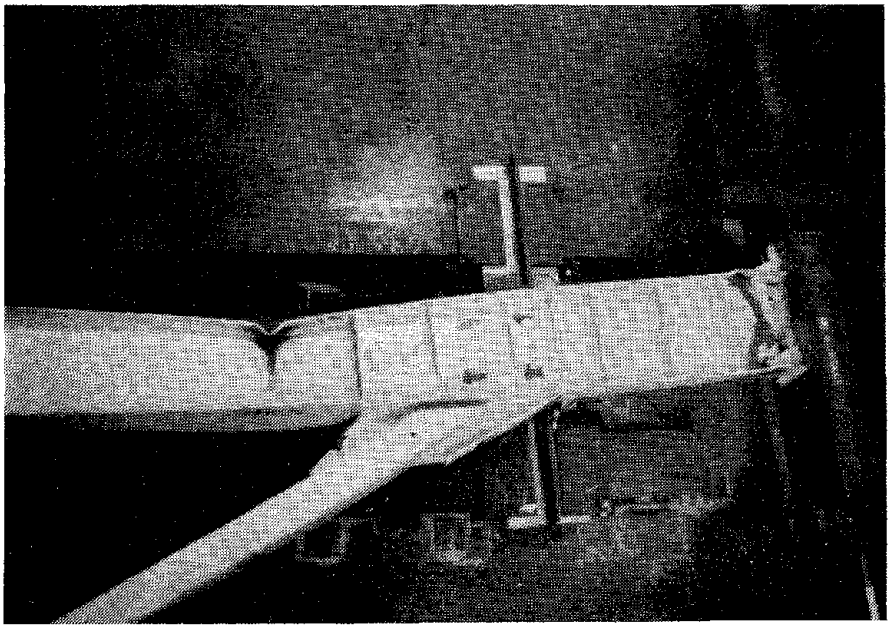

(b) Overall View - After Testing

Fig. 3.18 Specimen 7

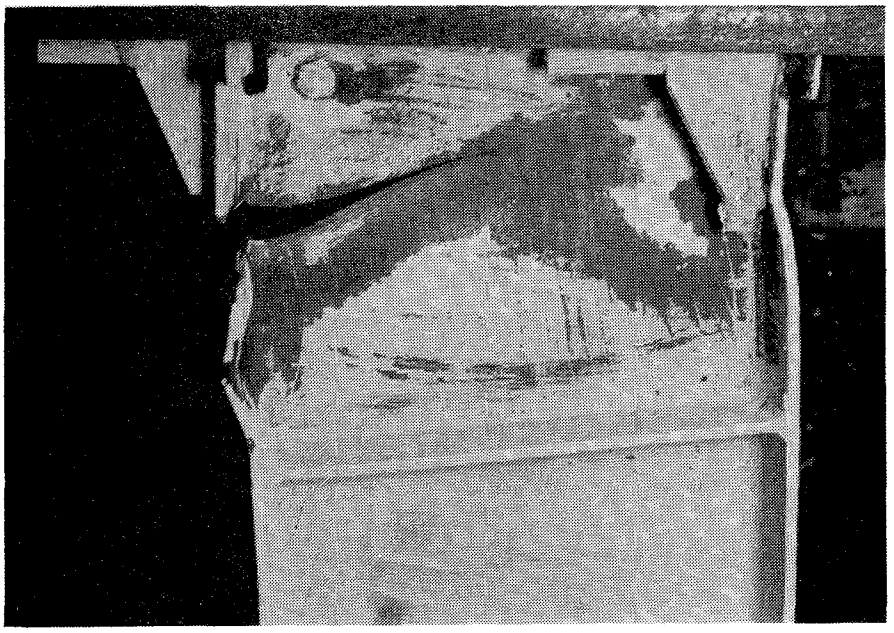

(d) Link-Column Connection - After Testing

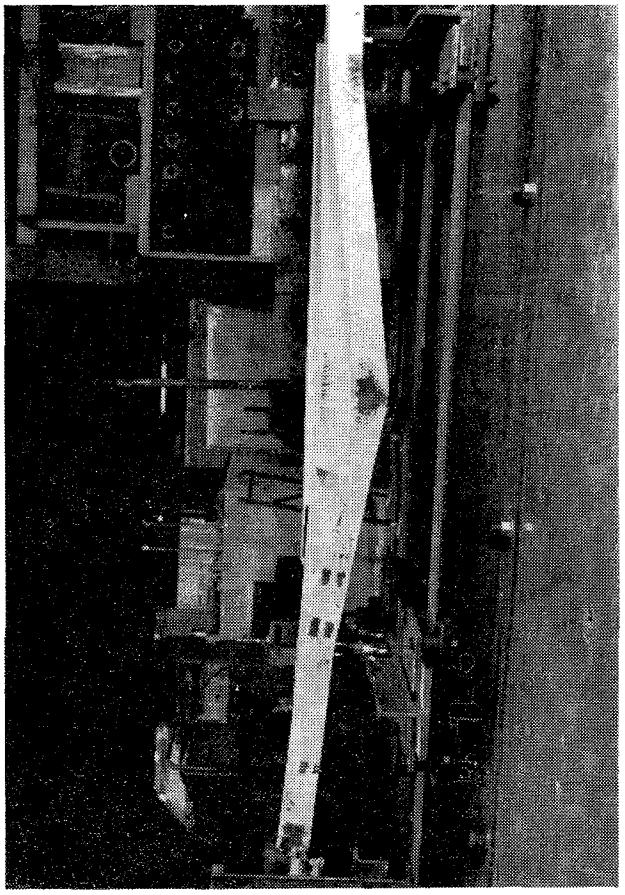

(c) View Looking Towards East Flange of Beam - After Testing

Fig. 3.18 Specimen 7 (cont.)

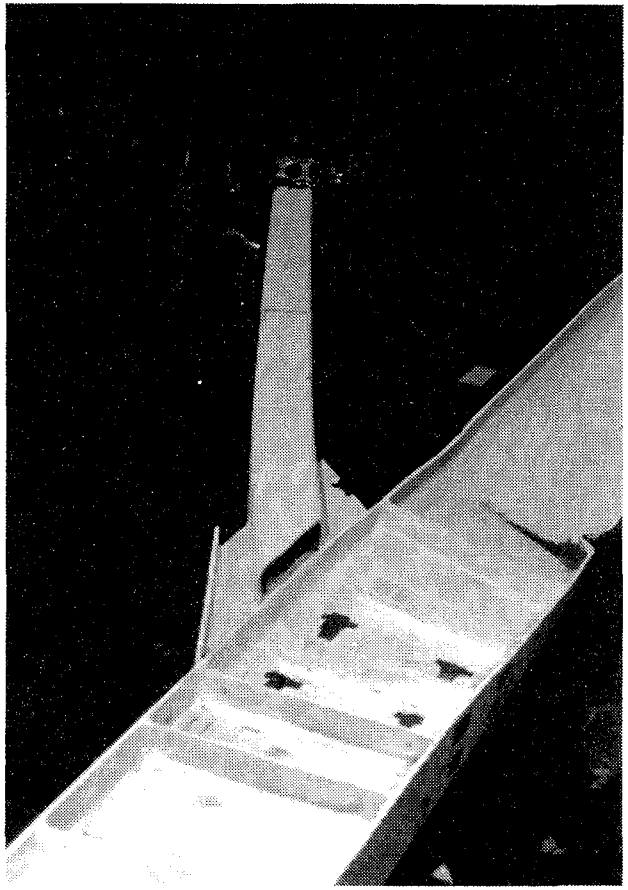

(e) View Looking Towards Brace - After Testing (Note bend in brace)

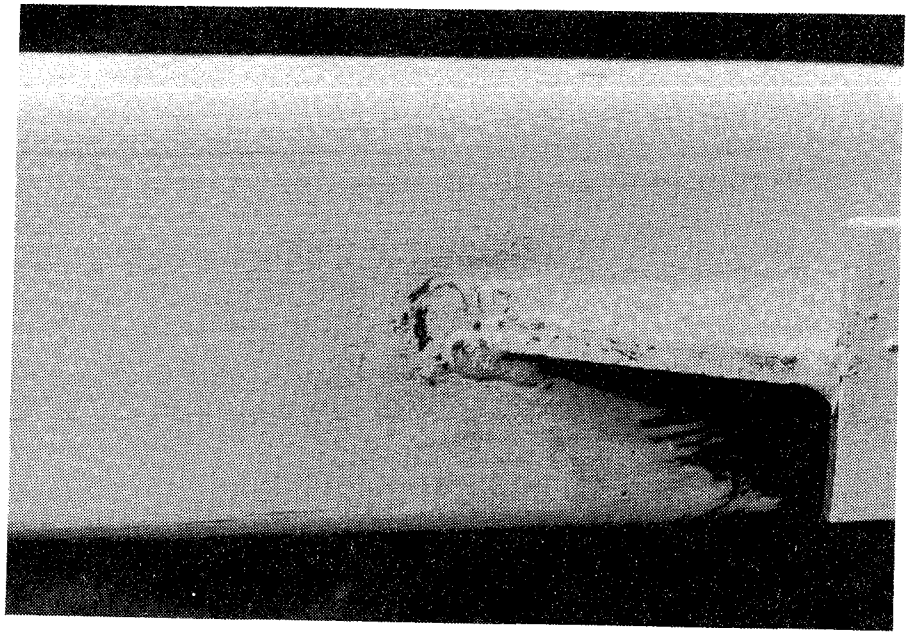

(f) Junction of Gusset Plate and South Flange of Brace - After Testing (Note small crack)

Fig. 3.18 Specimen 7 (cont.)

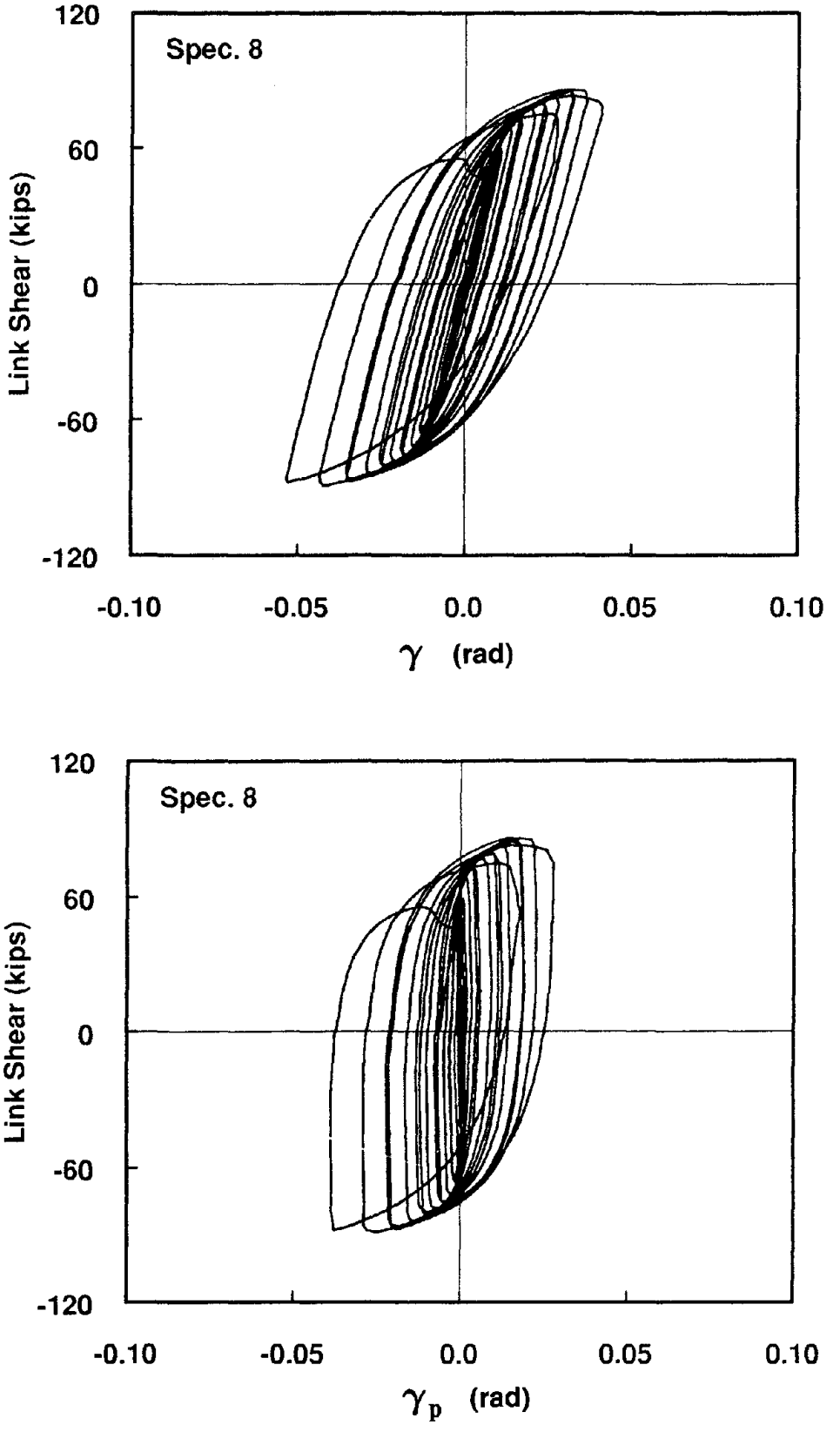

Fig. 3.19 Link Shear vs. Rotation Angle - Specimen 8

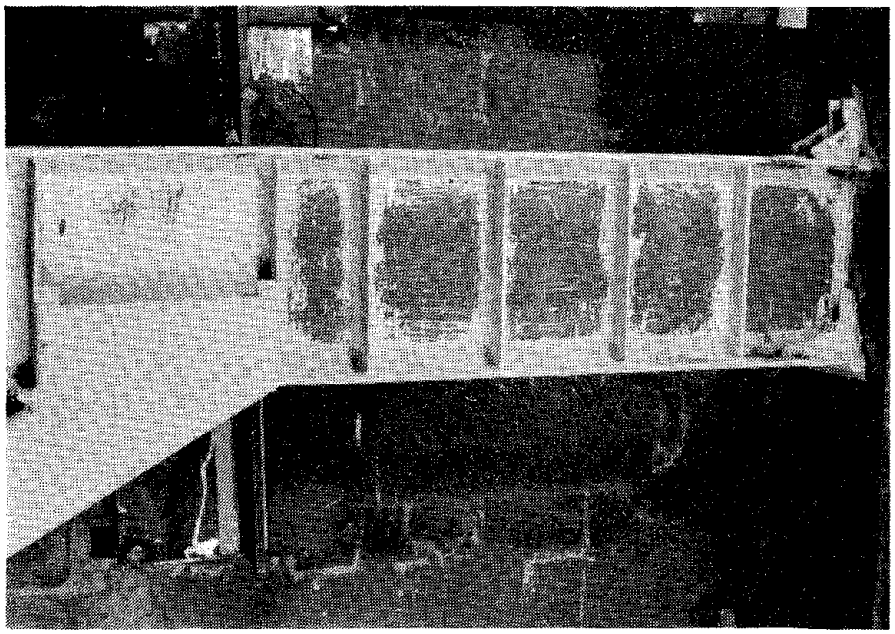

(a) Link Region - After Testing

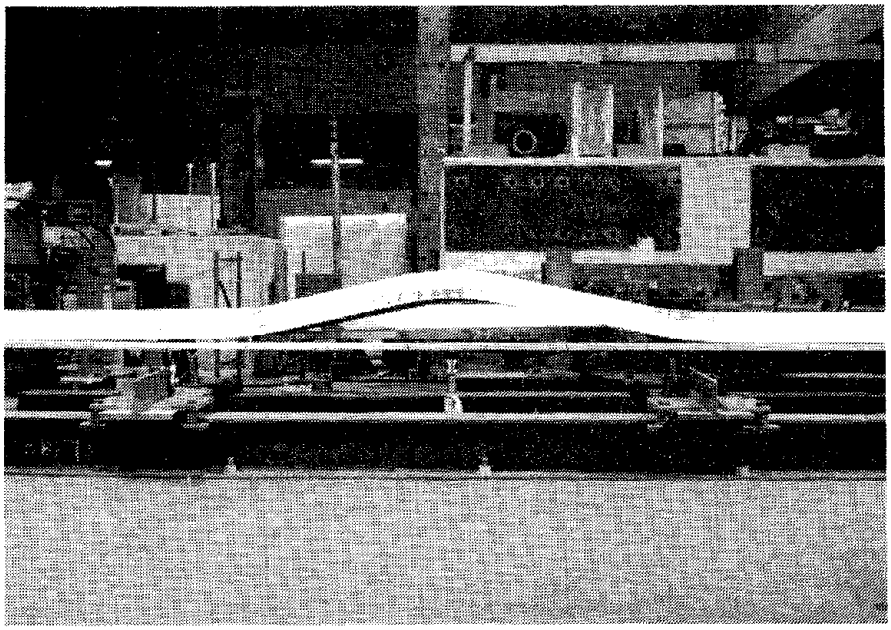

(b) View Looking Towards East Flange - After Testing

Fig. 3.20 Specimen 8

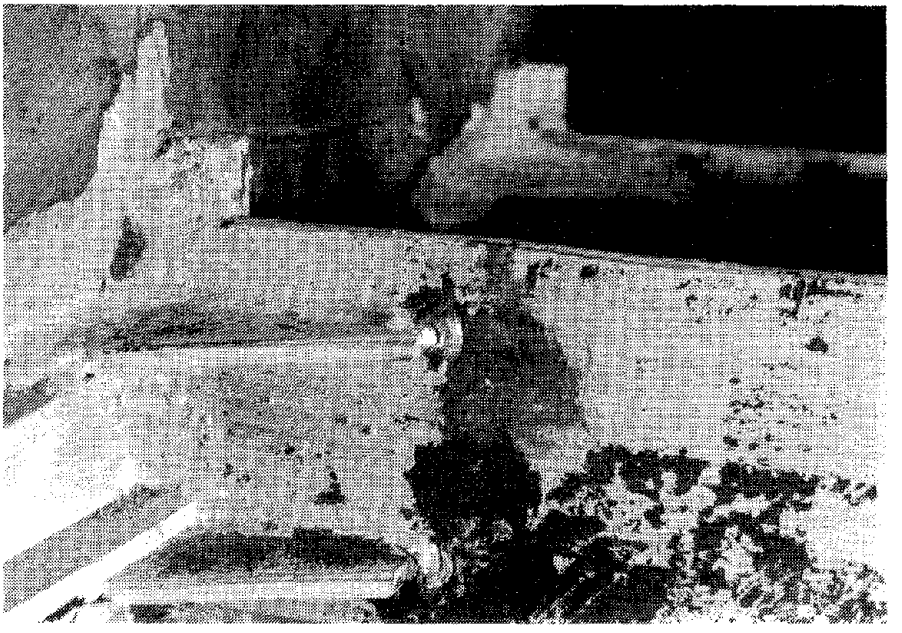

(c) East Flange of Link Near Column- After Testing
(Note cracks in flange at ends of ribs)

Fig. 3.20 Specimen 8 (cont.)

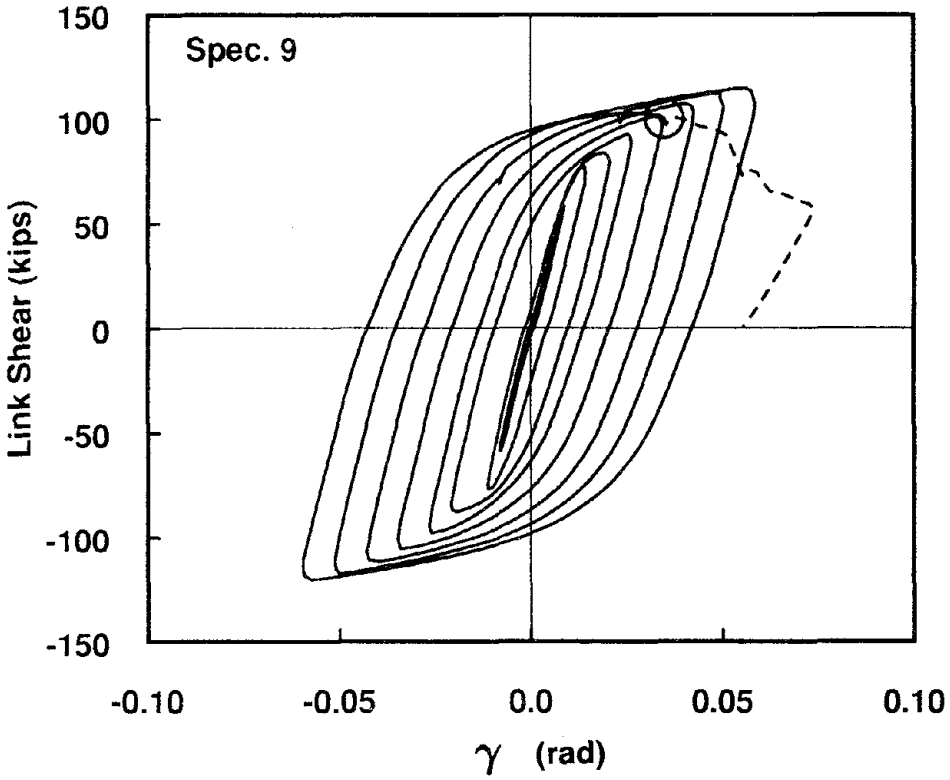

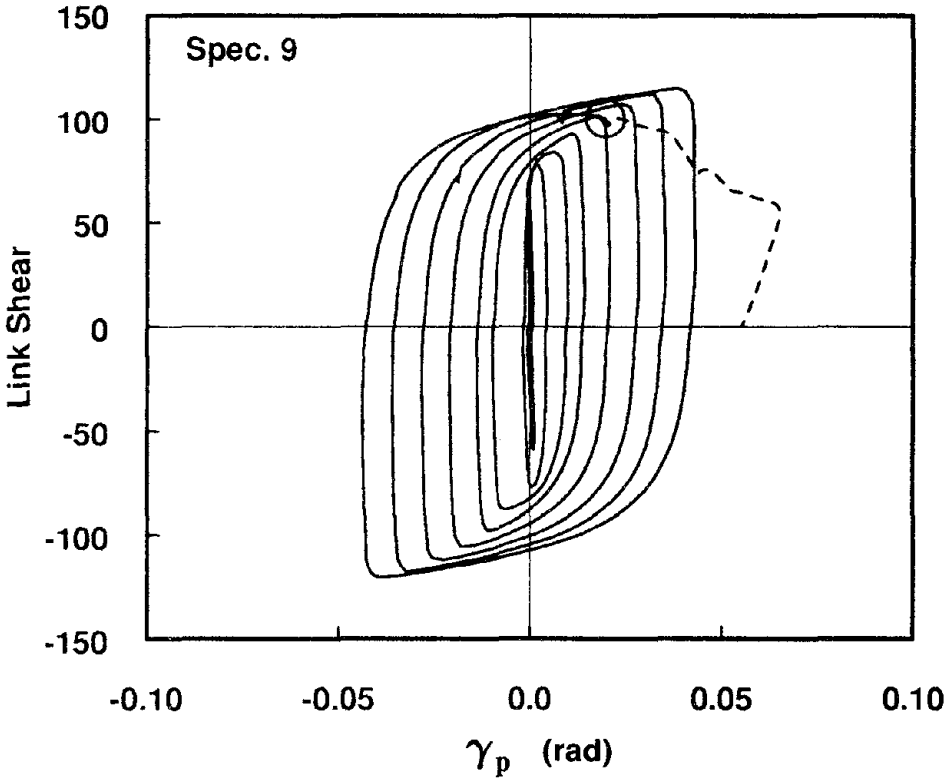

Fig. 3.21 Link Shear vs. Rotation Angle - Specimen 9

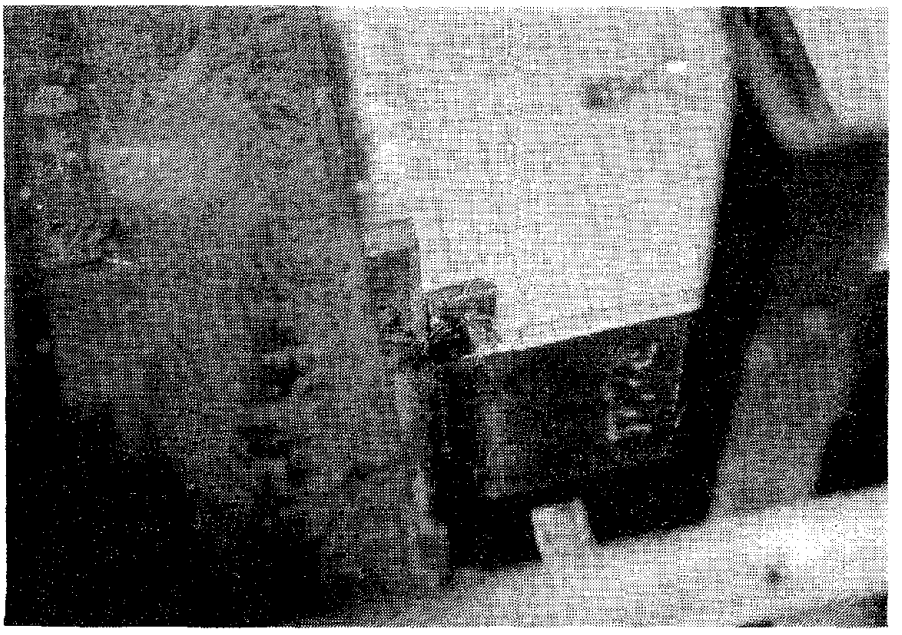

(a) Southeast Link Flange - Cycle 10E
(Note initiation of crack)

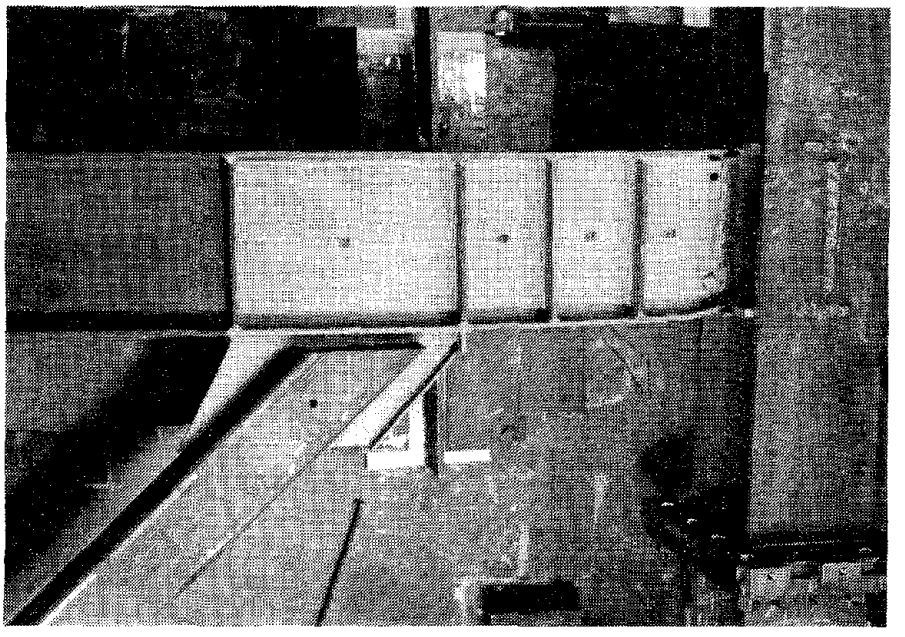

(b) Link Region - After Testing

Fig. 3.22 Specimen 9

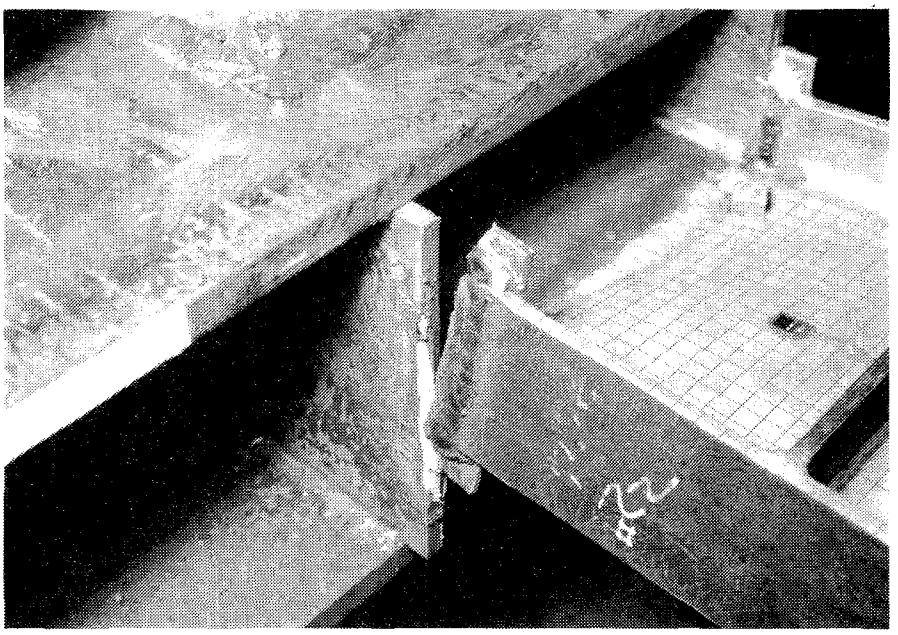

(d) Link-Column Connection - After Testing

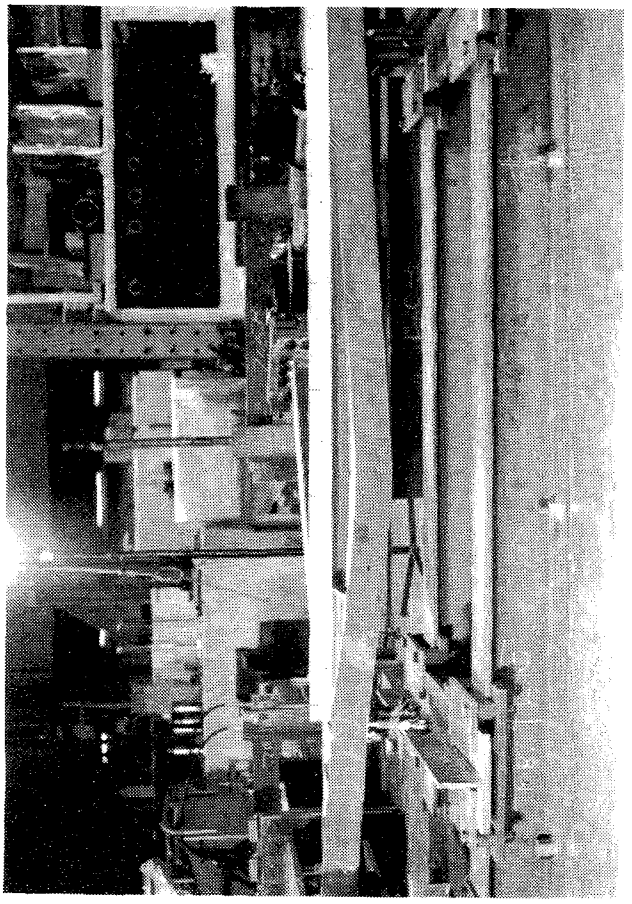

(c) View Looking Towards East Flange - After Testing

Fig. 3.22 Specimen 9 (cont.)

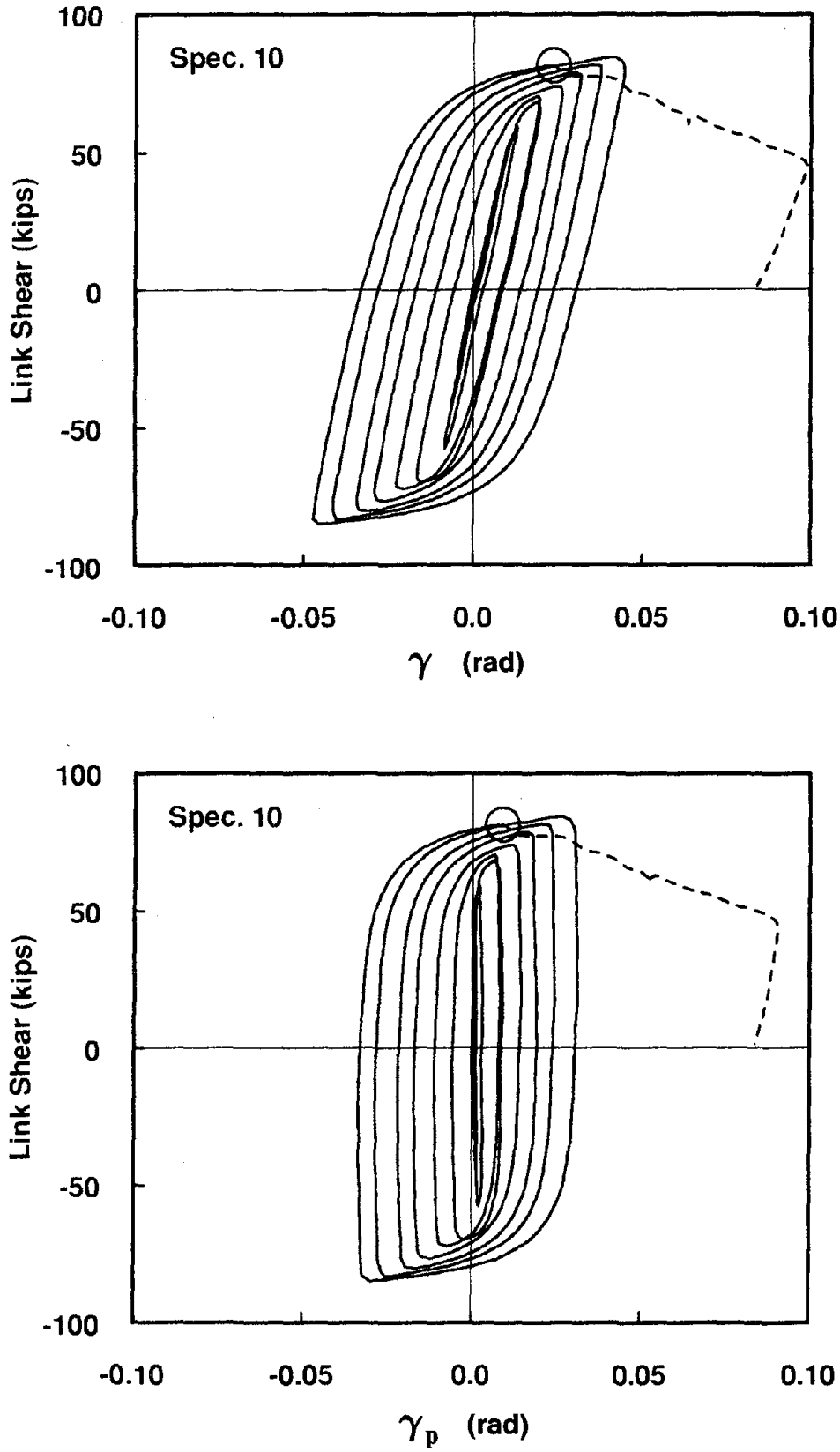

Fig. 3.23 Link Shear vs. Rotation Angle - Specimen 10

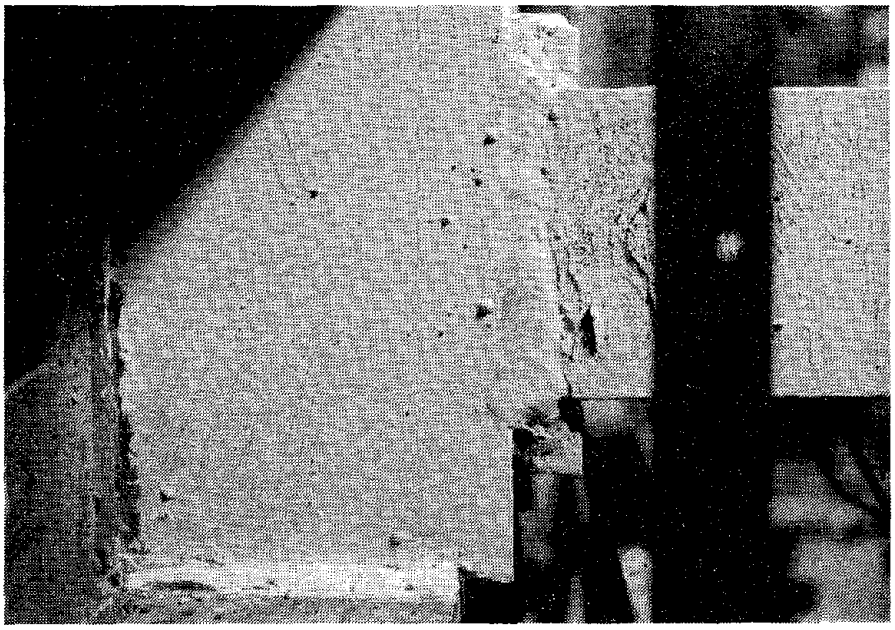

(a) Crack in Southeast Link Flange - Cycle 10E

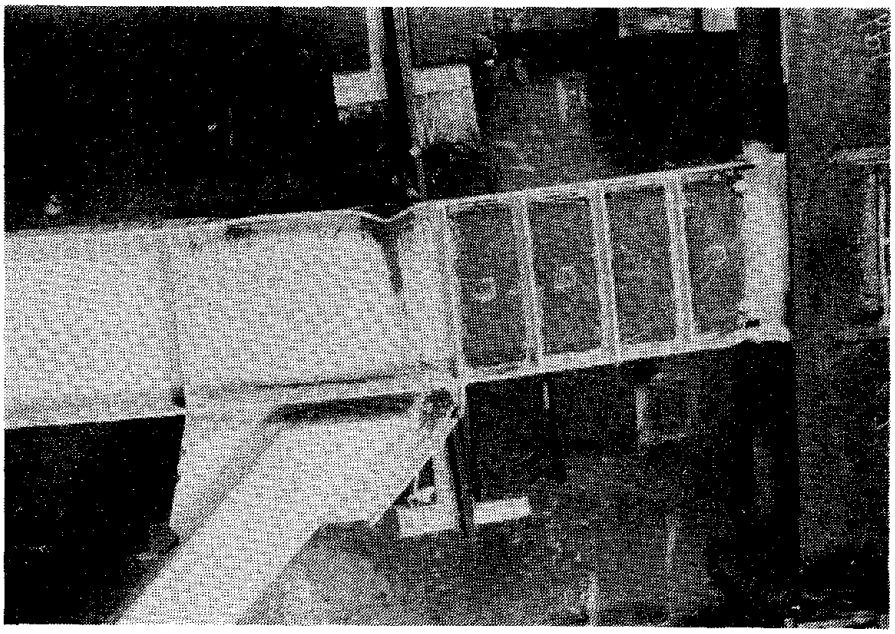

(b) Link Region - After Testing

Fig. 3.24 Specimen 10

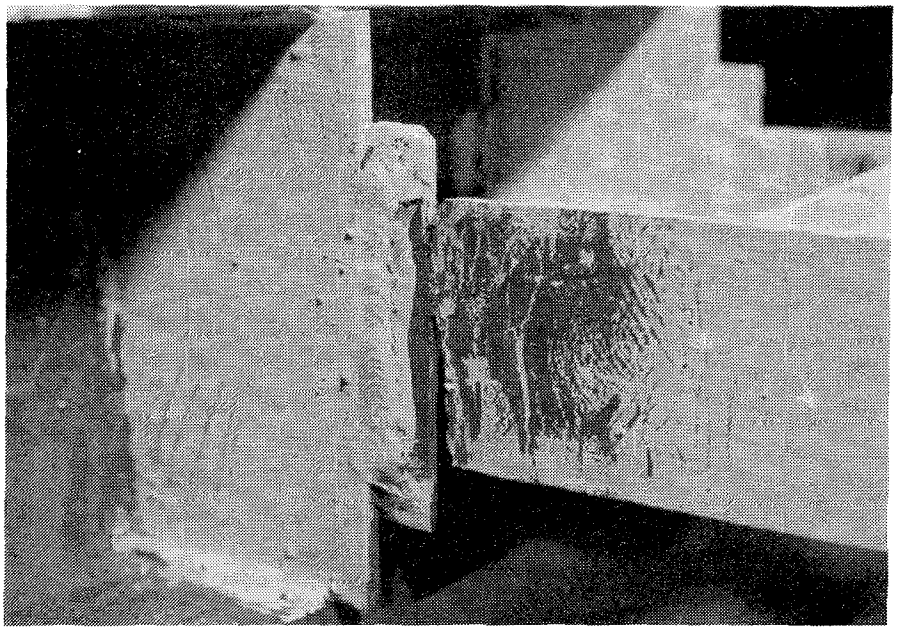

(d) Link-Column Connection - After Testing

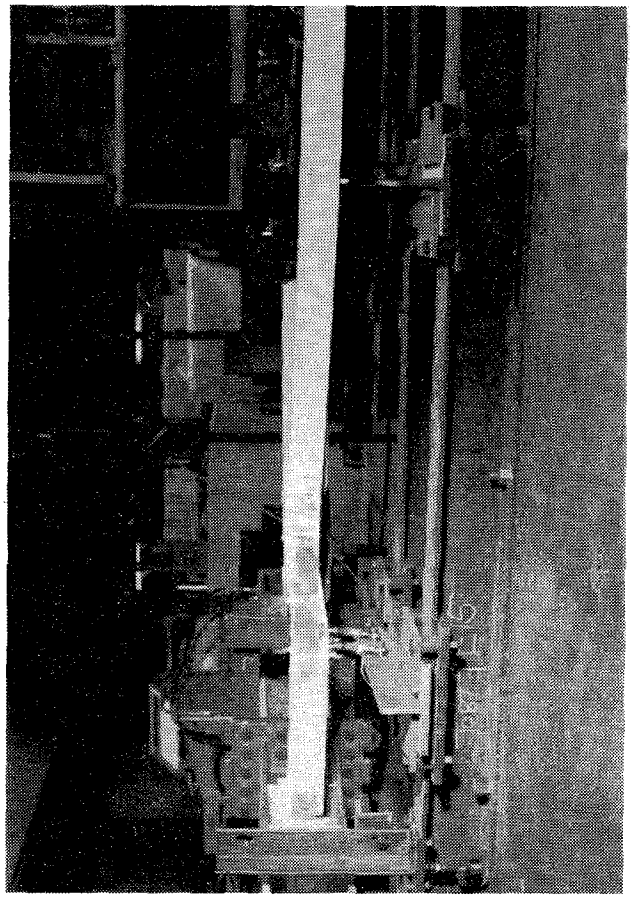

(c) View Looking Towards East Flange - After Testing

Fig. 3.24 Specimen 10 (cont.)

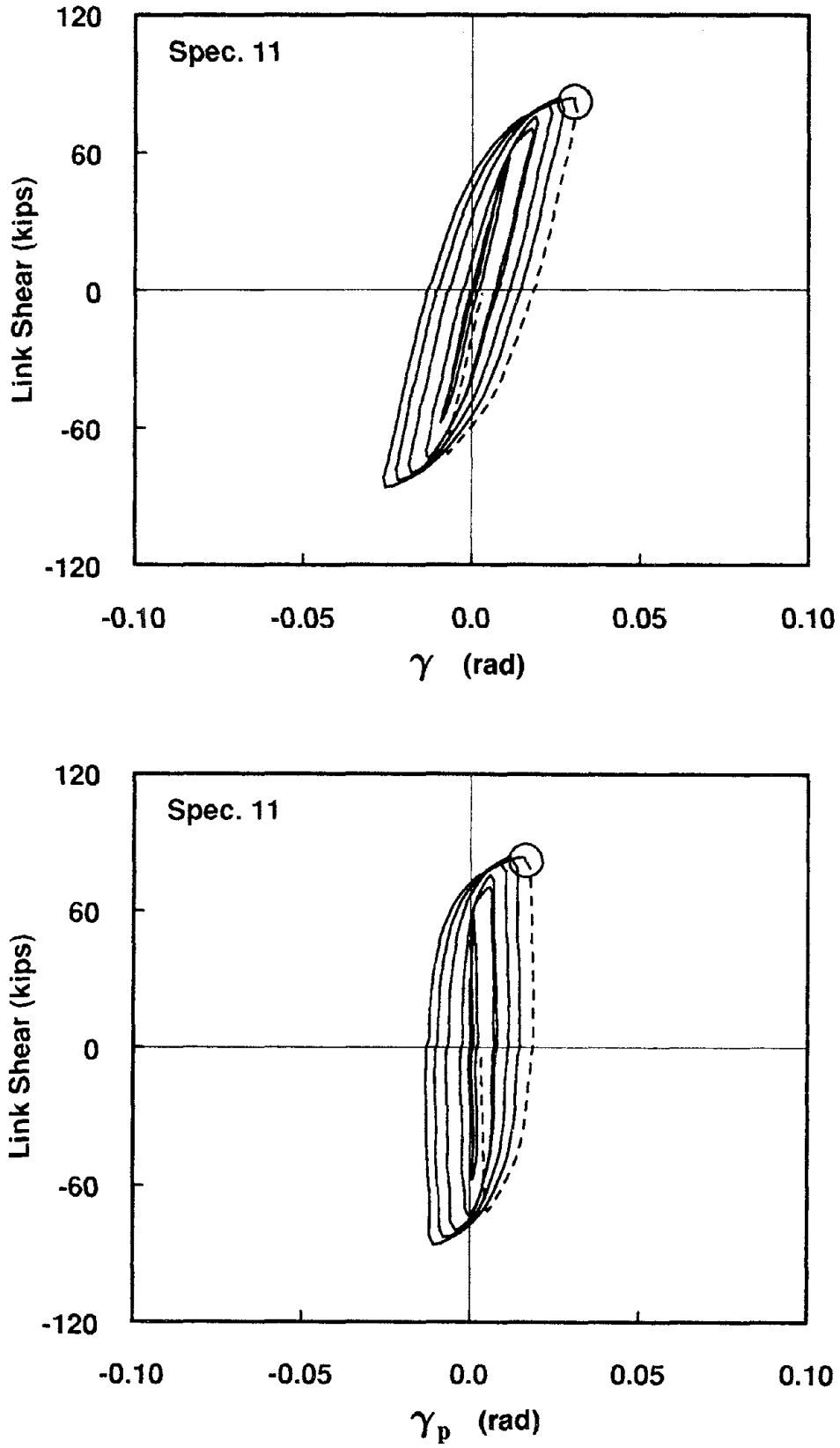

Fig. 3.25 Link Shear vs. Rotation Angle - Specimen 11

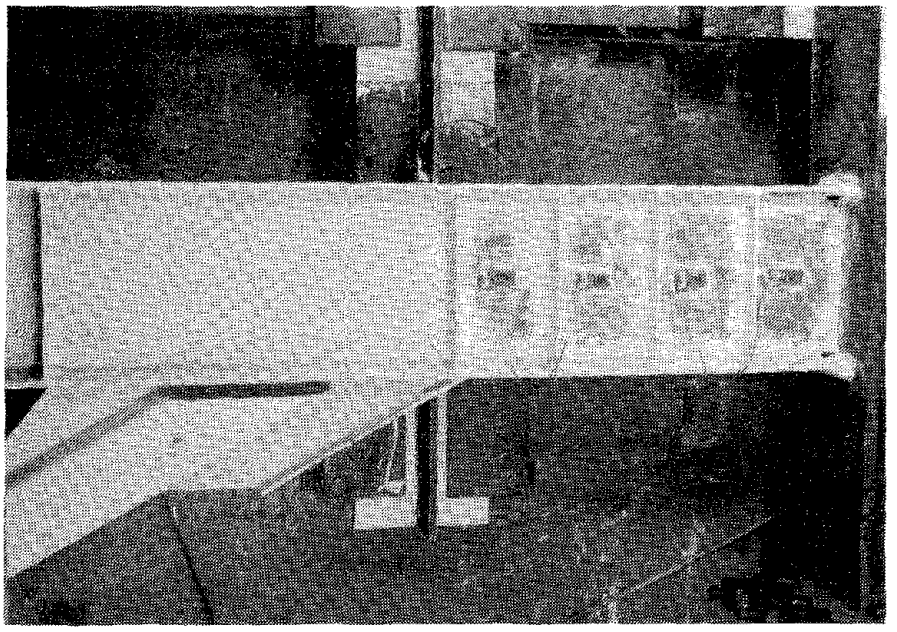

(a) Link Region - After Testing

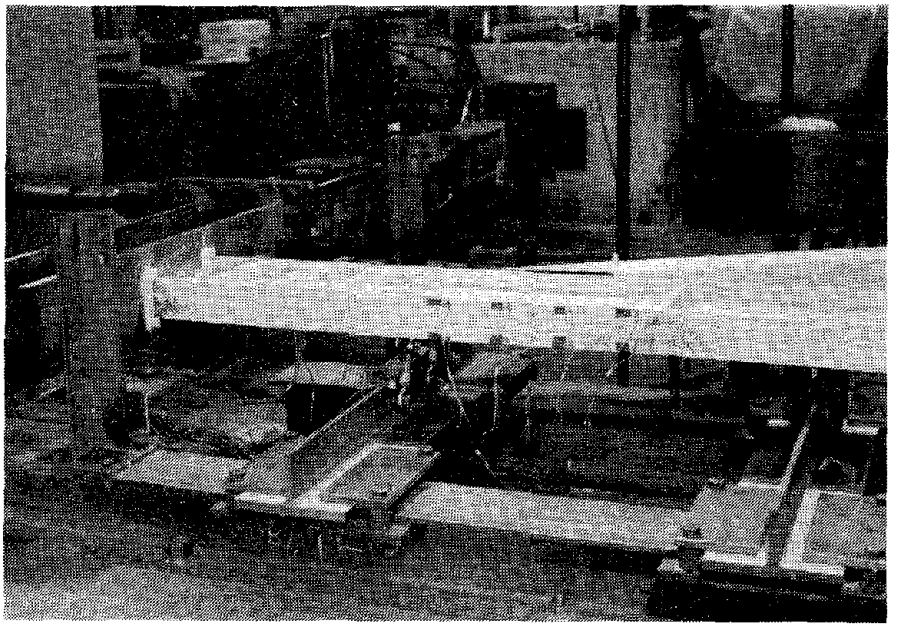

(b) View Looking Towards East Flange - After Testing

Fig. 3.26 Specimen 11

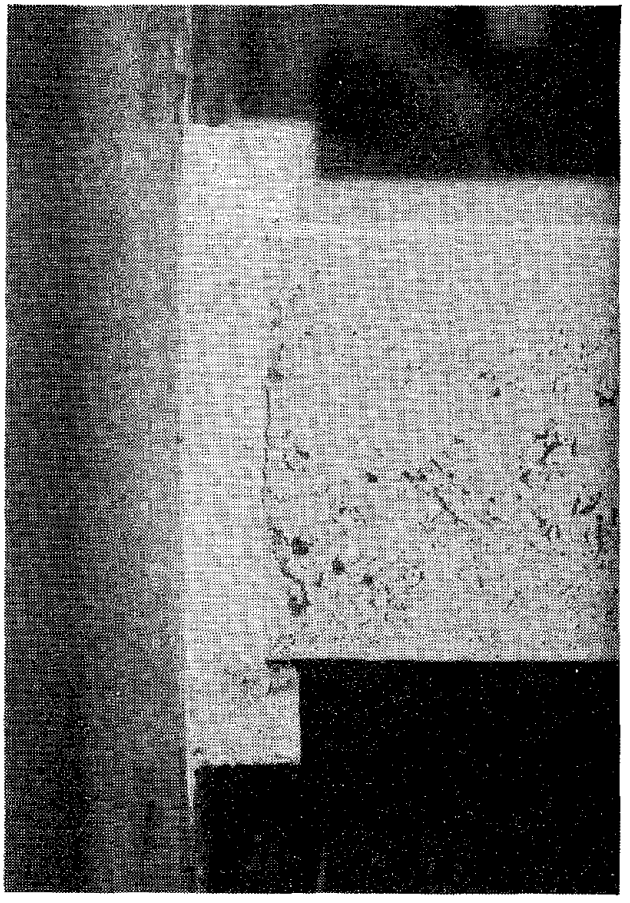

(c) Crack in Southeast Link Flange - After Testing

Fig. 3.26 Specimen 11 (cont.)

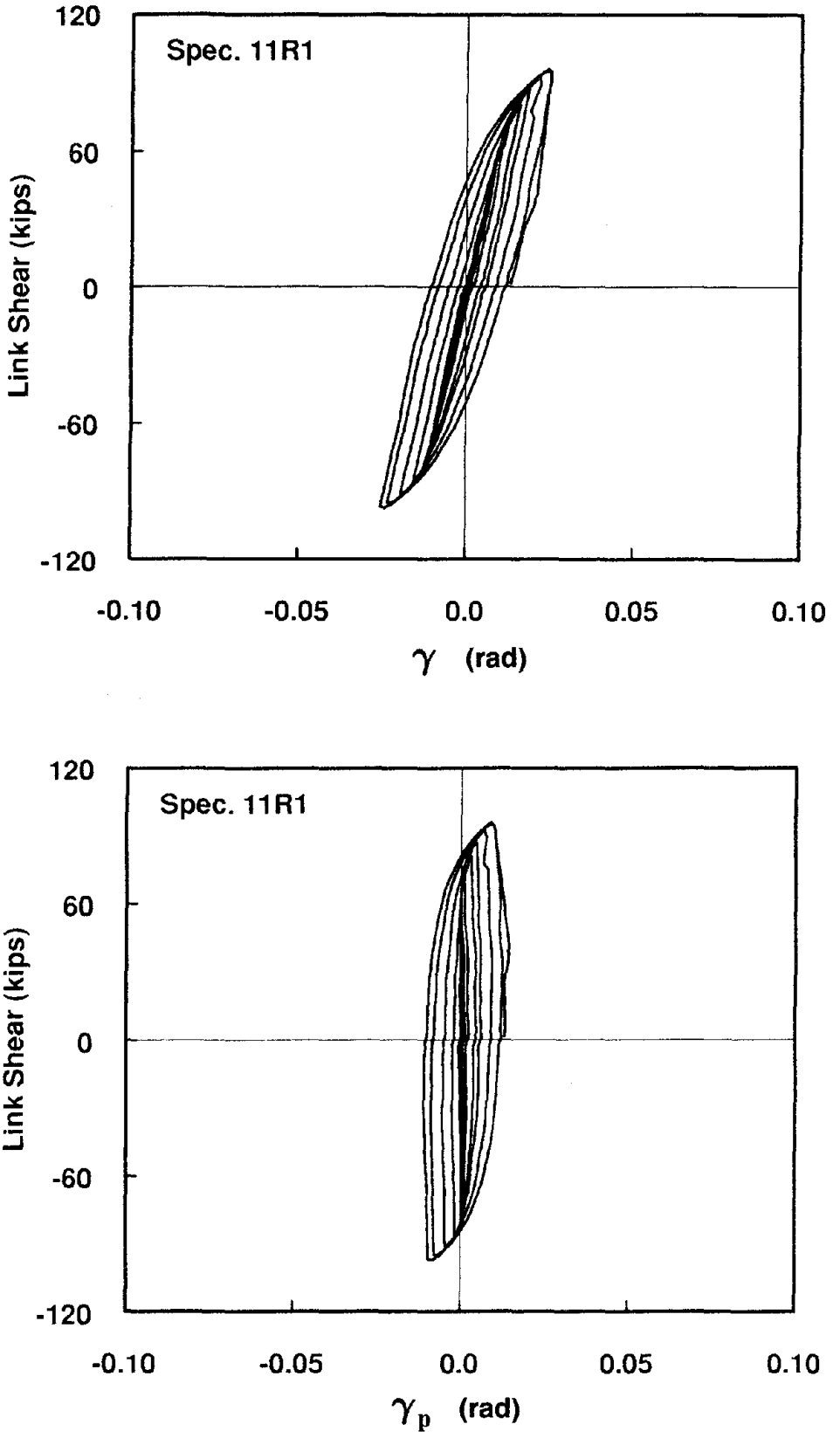

Fig. 3.27 Link Shear vs. Rotation Angle - Specimen 11R1

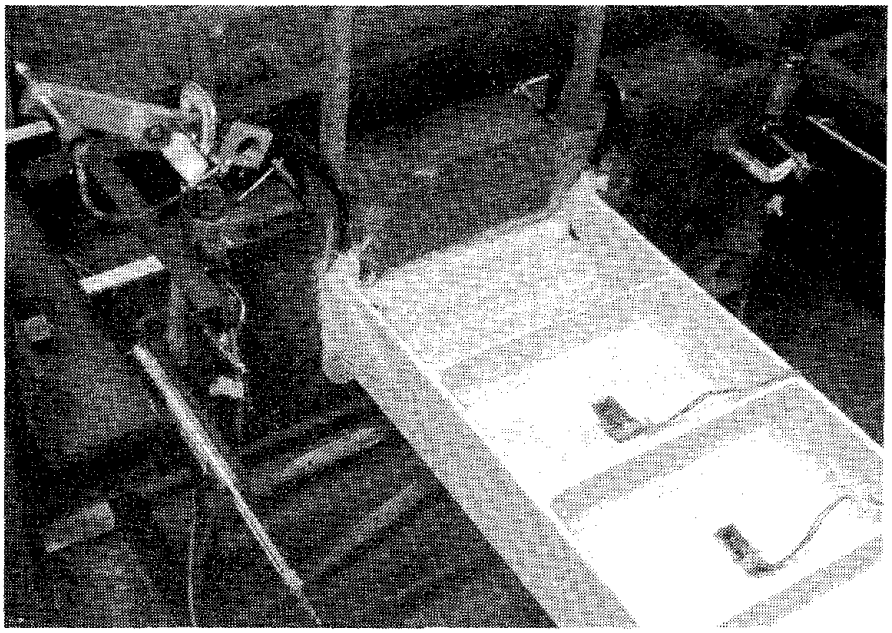

(a) Modified Link-Column Connection - Before Testing

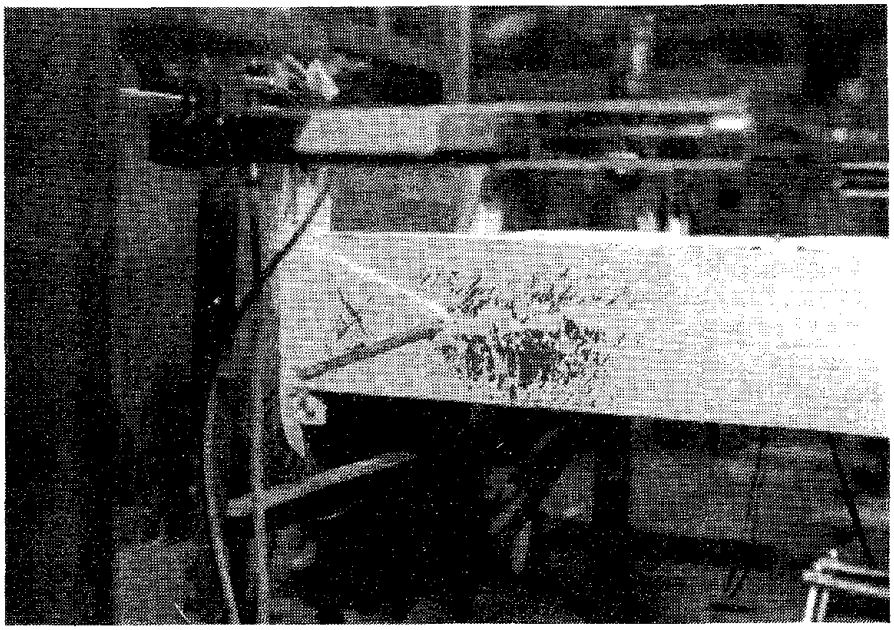

(b) Southeast link Flange - After Testing

Fig. 3.28 Specimen 11R1

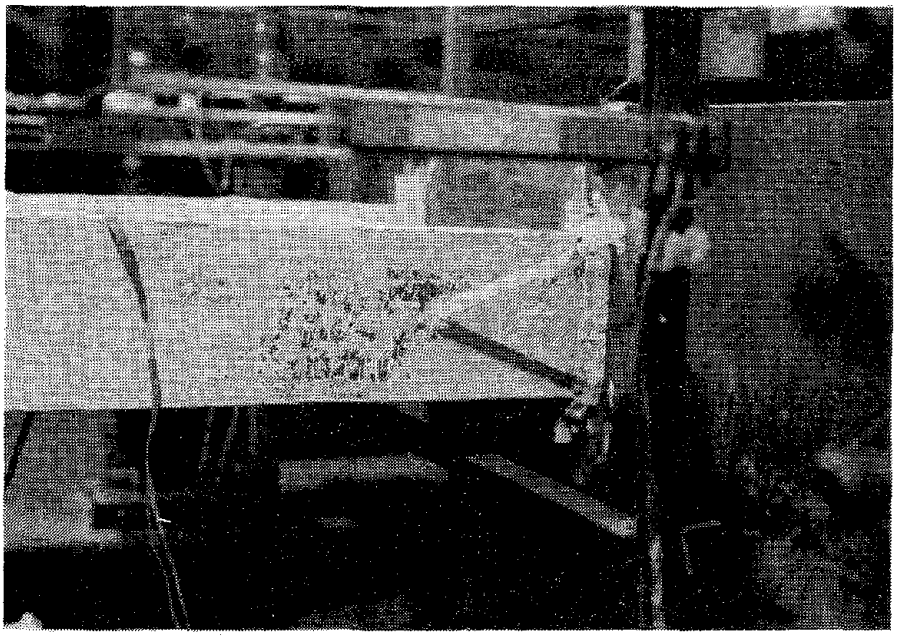

(c) Southwest link Flange - After Testing

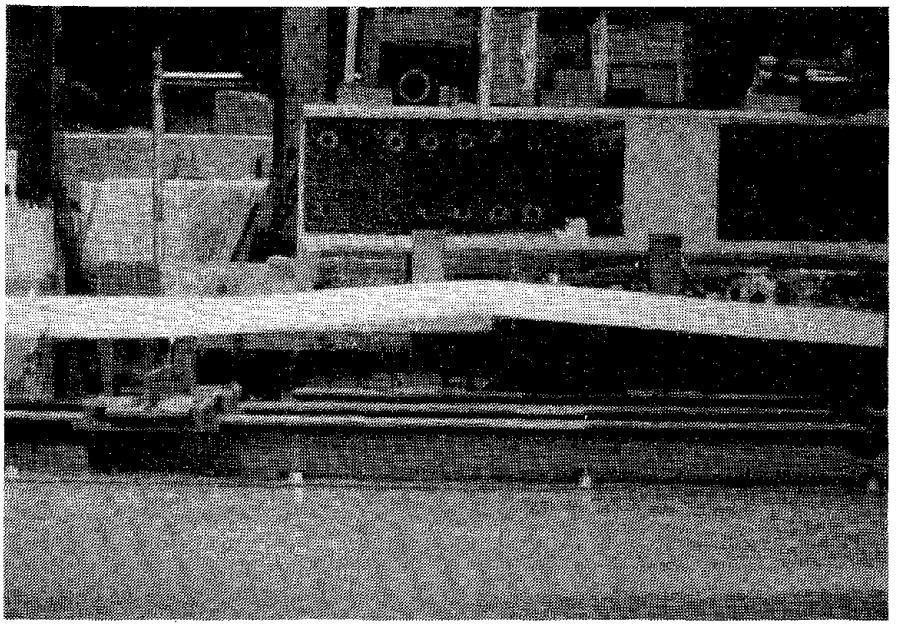

(d) View Looking Towards East Flange of Beam - After Testing

Fig. 3.28 Specimen 11R1 (cont.)

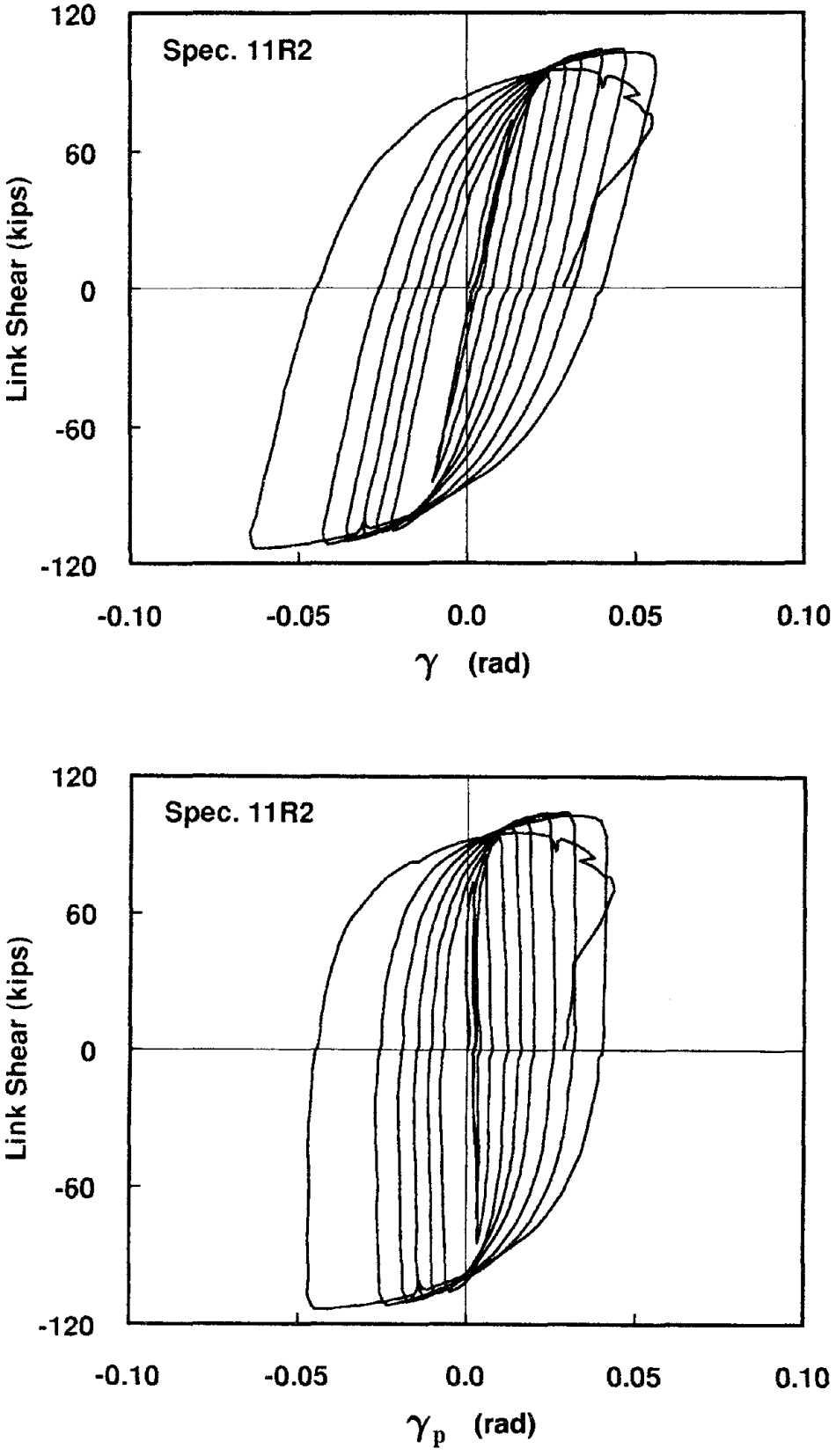

Fig. 3.29 Link Shear vs. Rotation Angle - Specimen 11R2

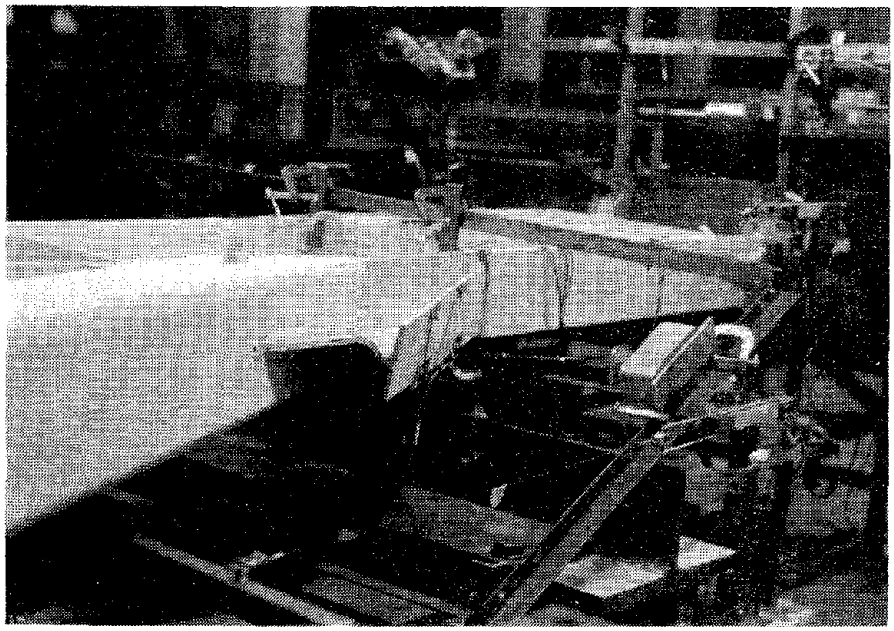

(a) Buckle in Brace Connection Gusset Plate - Cycle 8W

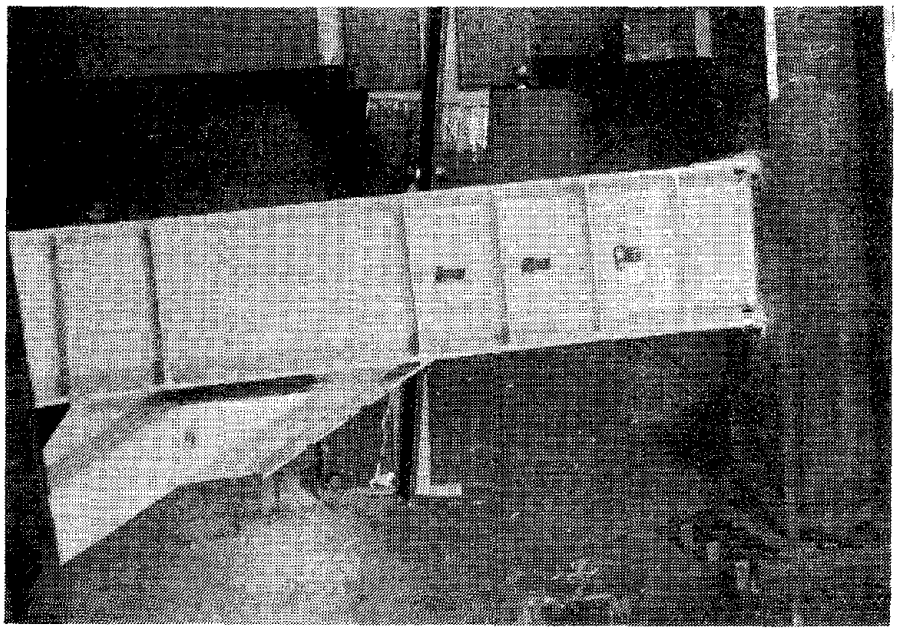

(b) Link Region - After Testing

Fig. 3.30 Specimen 11R2

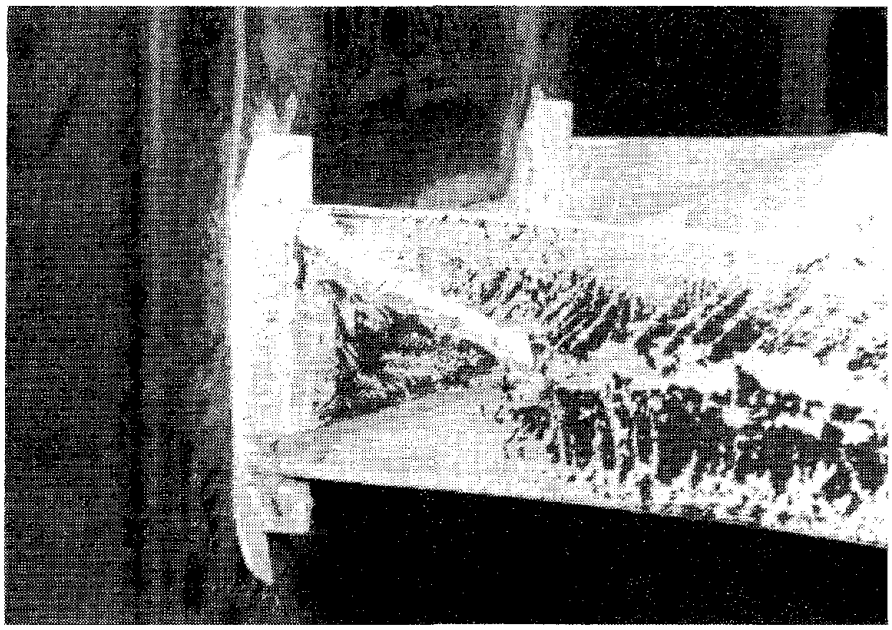

(c) Southeast link Flange - After Testing

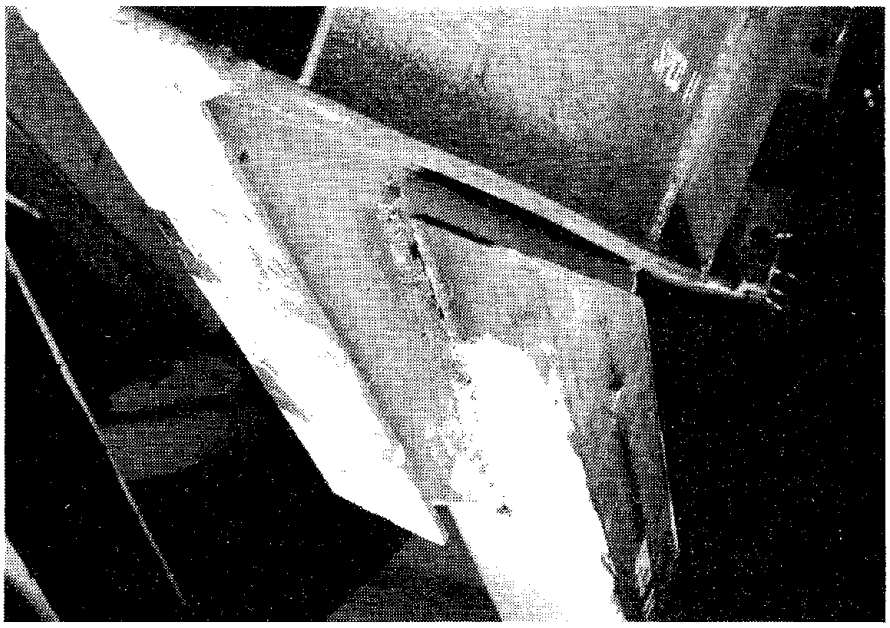

(d) Brace Connection - After Testing (Note separation of Brace and Gusset Plate)

Fig. 3.30 Specimen 11R2 (cont.)

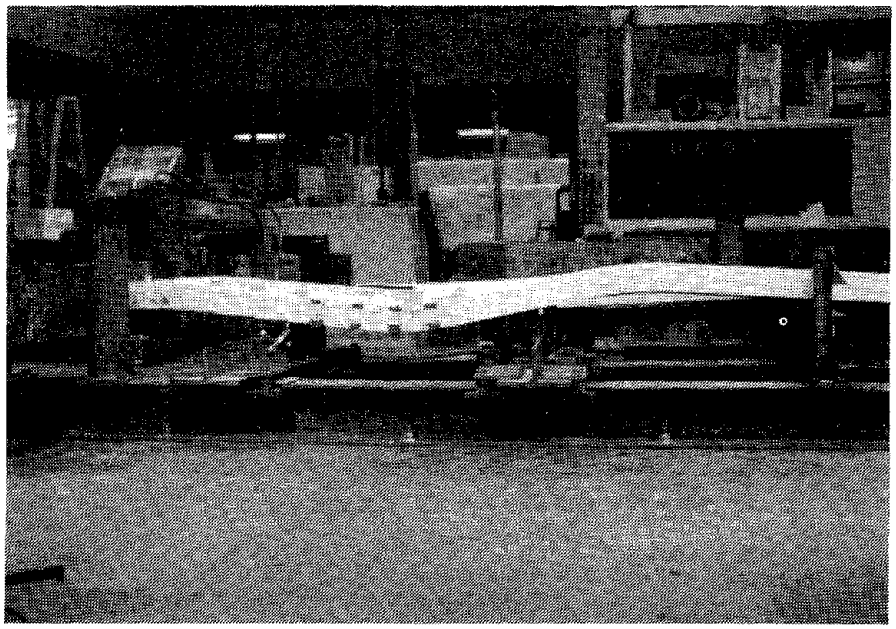

(e) View Looking Towards East Flange of Beam - After Testing

Fig. 3.30 Specimen 11R2 (cont.)

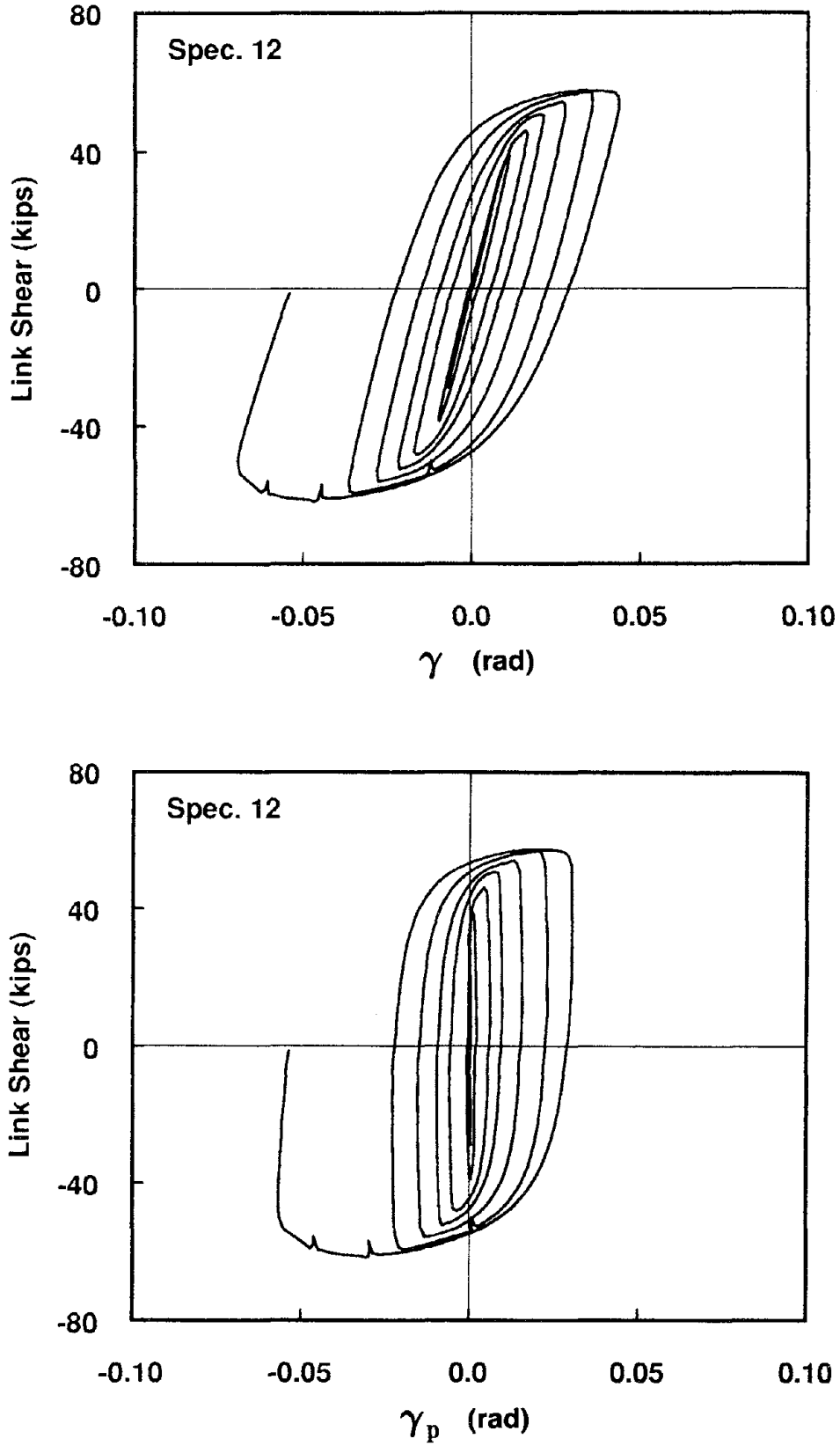

Fig. 3.31 Link Shear vs. Rotation Angle - Specimen 12

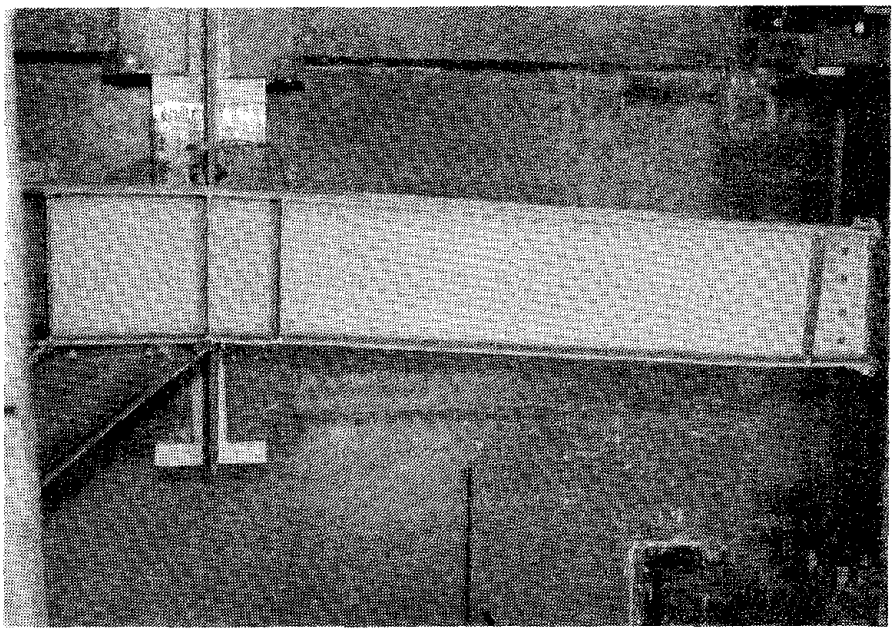

(a) Link Region - After Testing

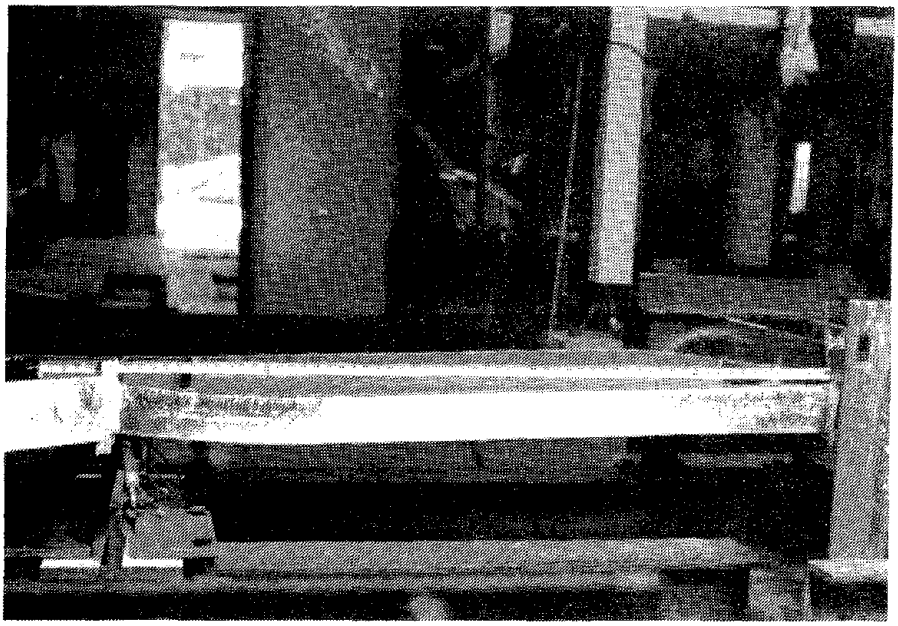

(b) View Looking Towards West Flange of Link - After Testing

Fig. 3.32 Specimen 12

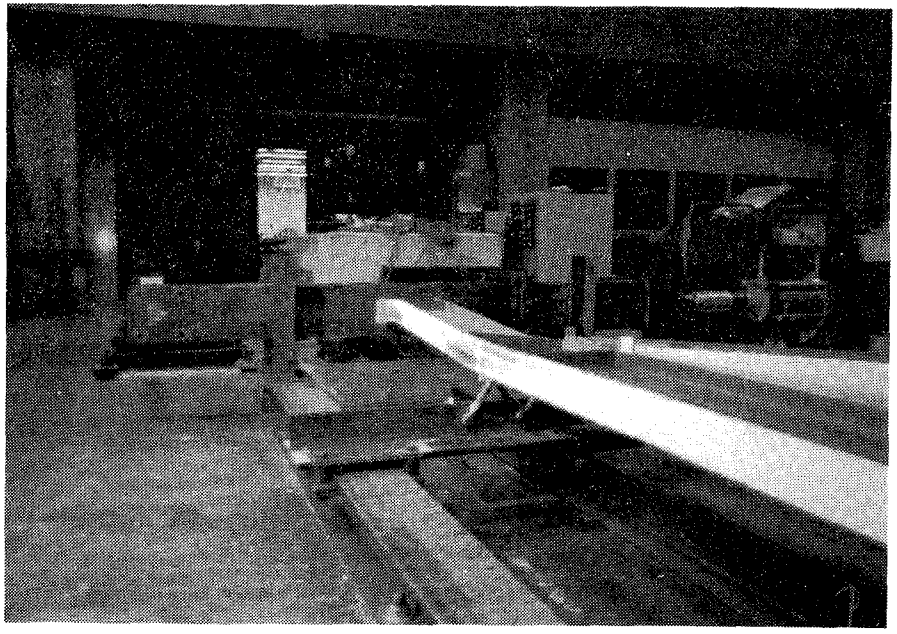

(c) View Looking Towards East Flange of Link - After Testing

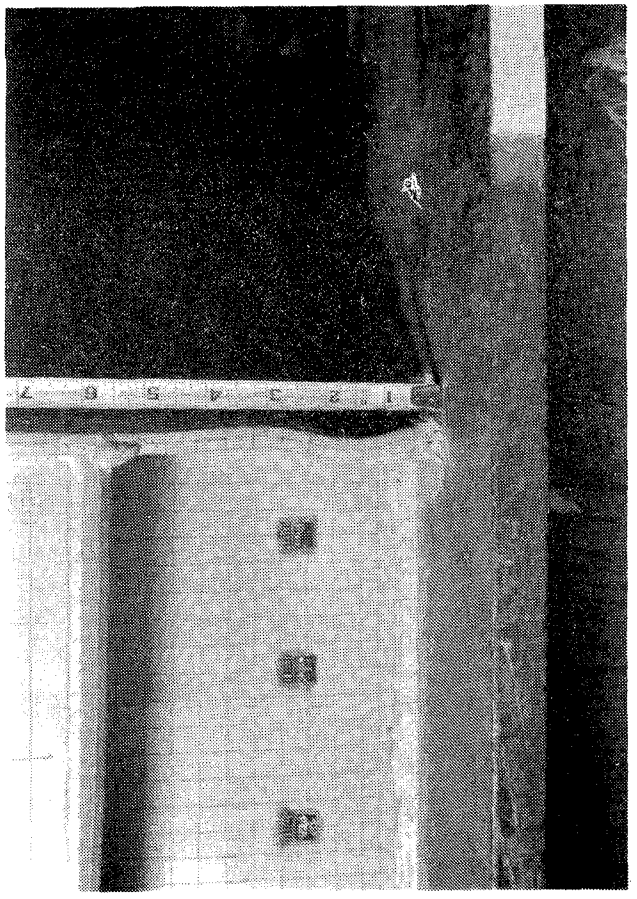

(d) Southeast Link Flange at Column - After Testing

Fig. 3.32 Specimen 12 (cont.)

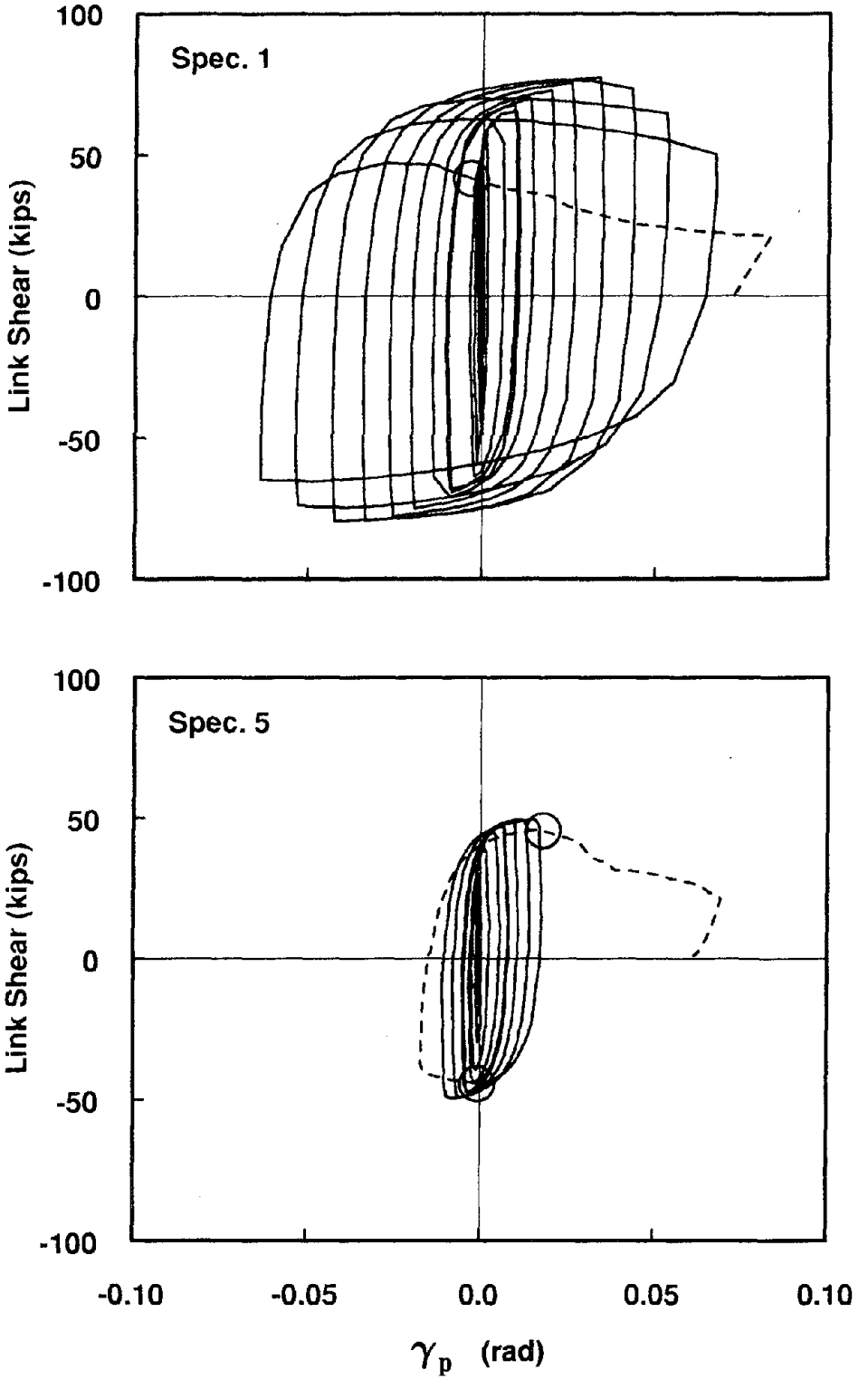

Fig. 3.33 Comparison of Hysteretic Response of Specimens 1 and 5 Effect of Increasing Link Length

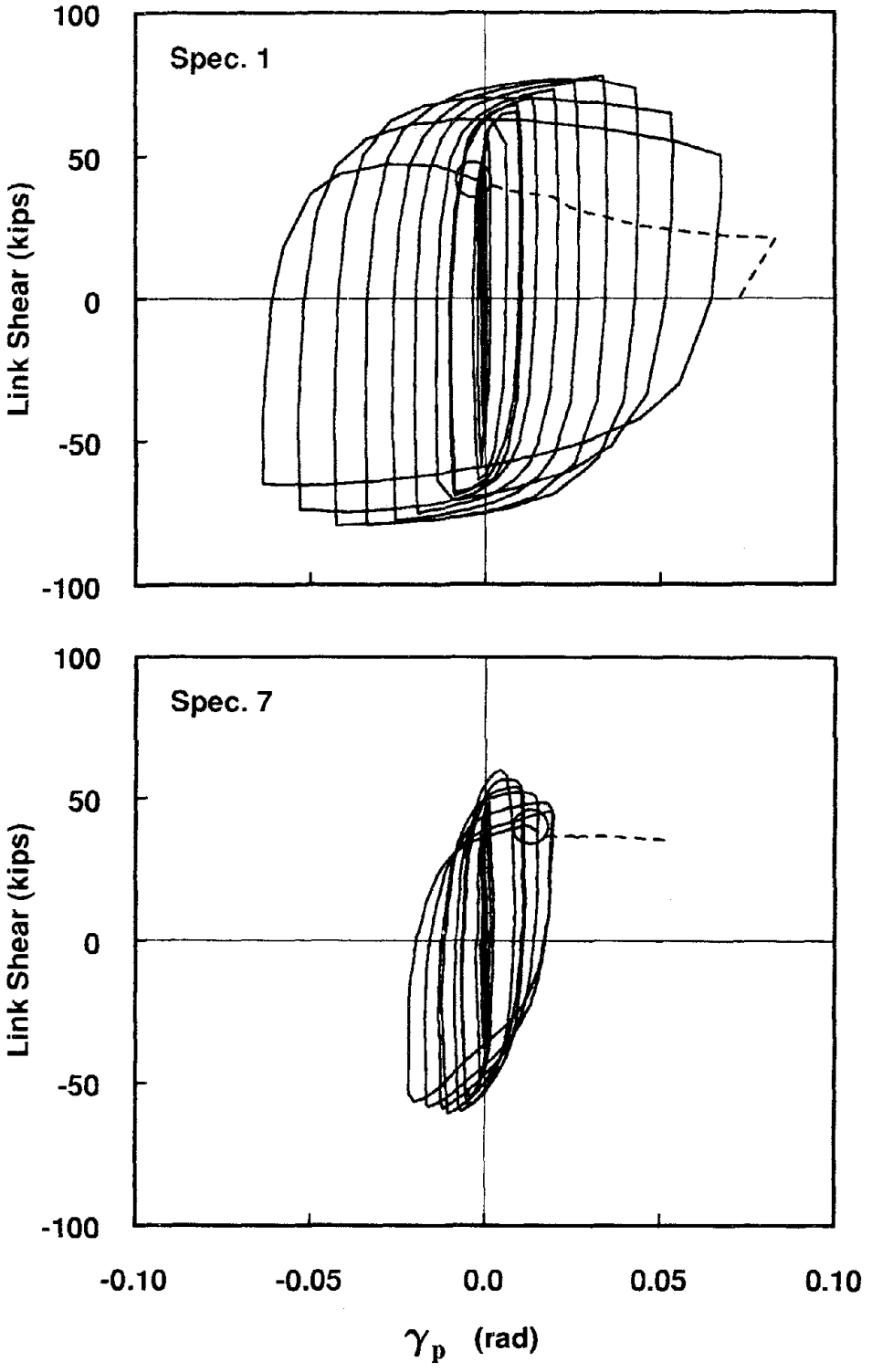

Fig. 3.34 Comparison of Hysteretic Response of Specimens 1 and 7 Effect of Beam Yielding and Instability

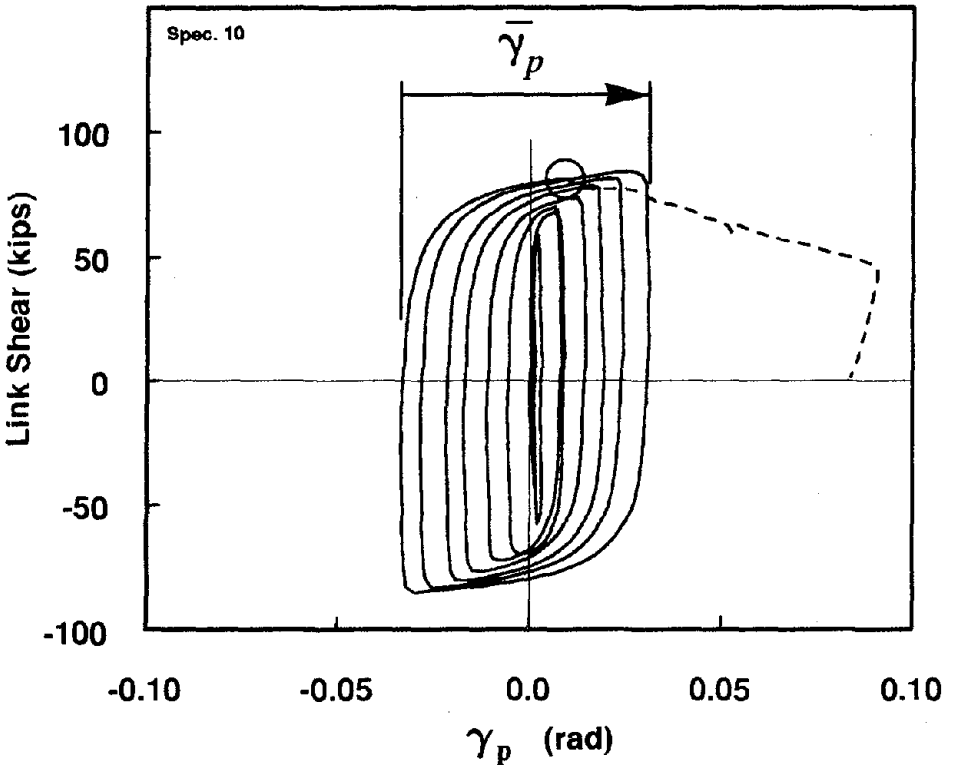

Fig. 3.35 Definition of $\bar{\gamma}_p$

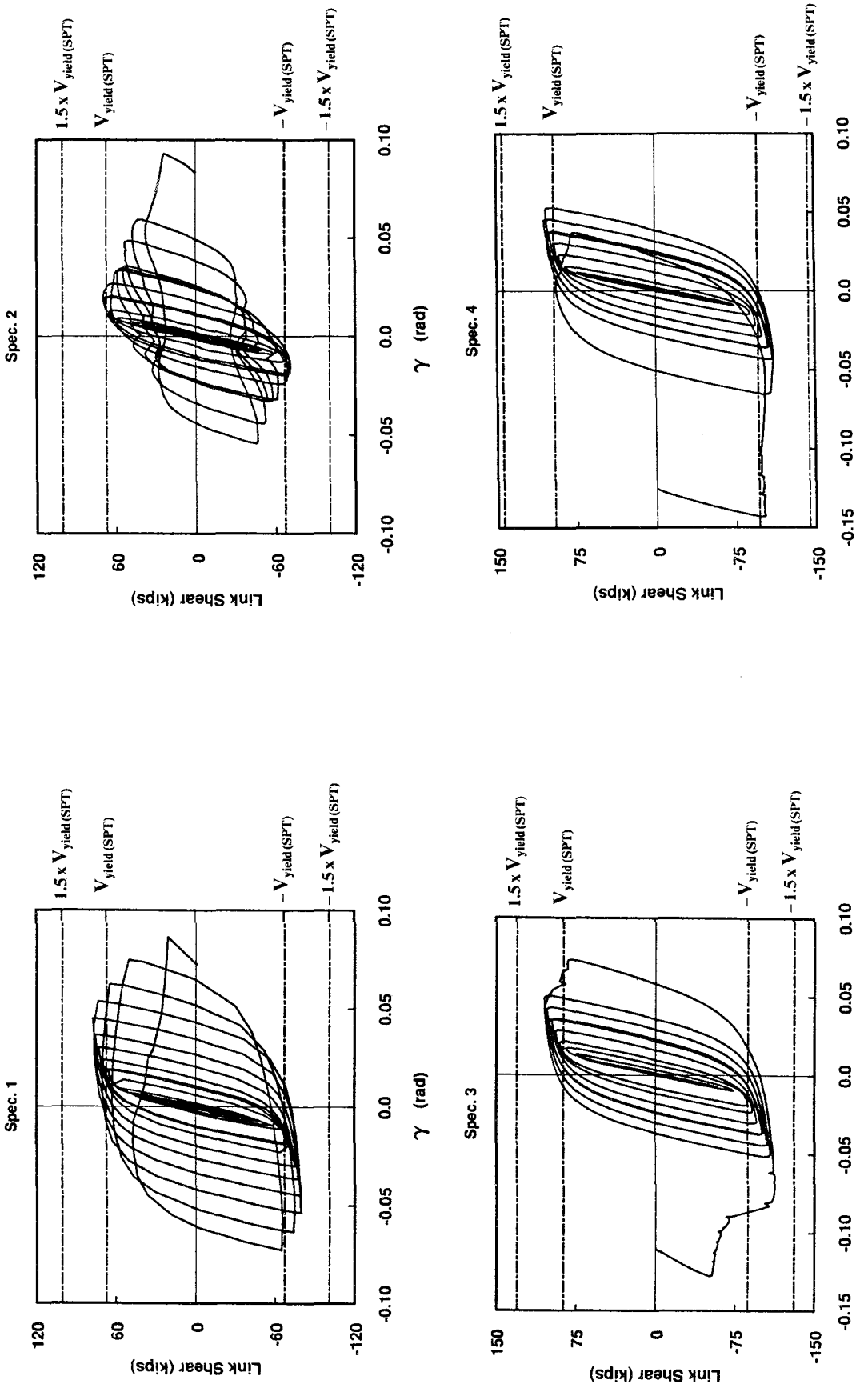

Fig. 4.1 Link Shear-Rotation Response Compared with Link Yield and Ultimate Shear Strength for Simple Plastic Theory

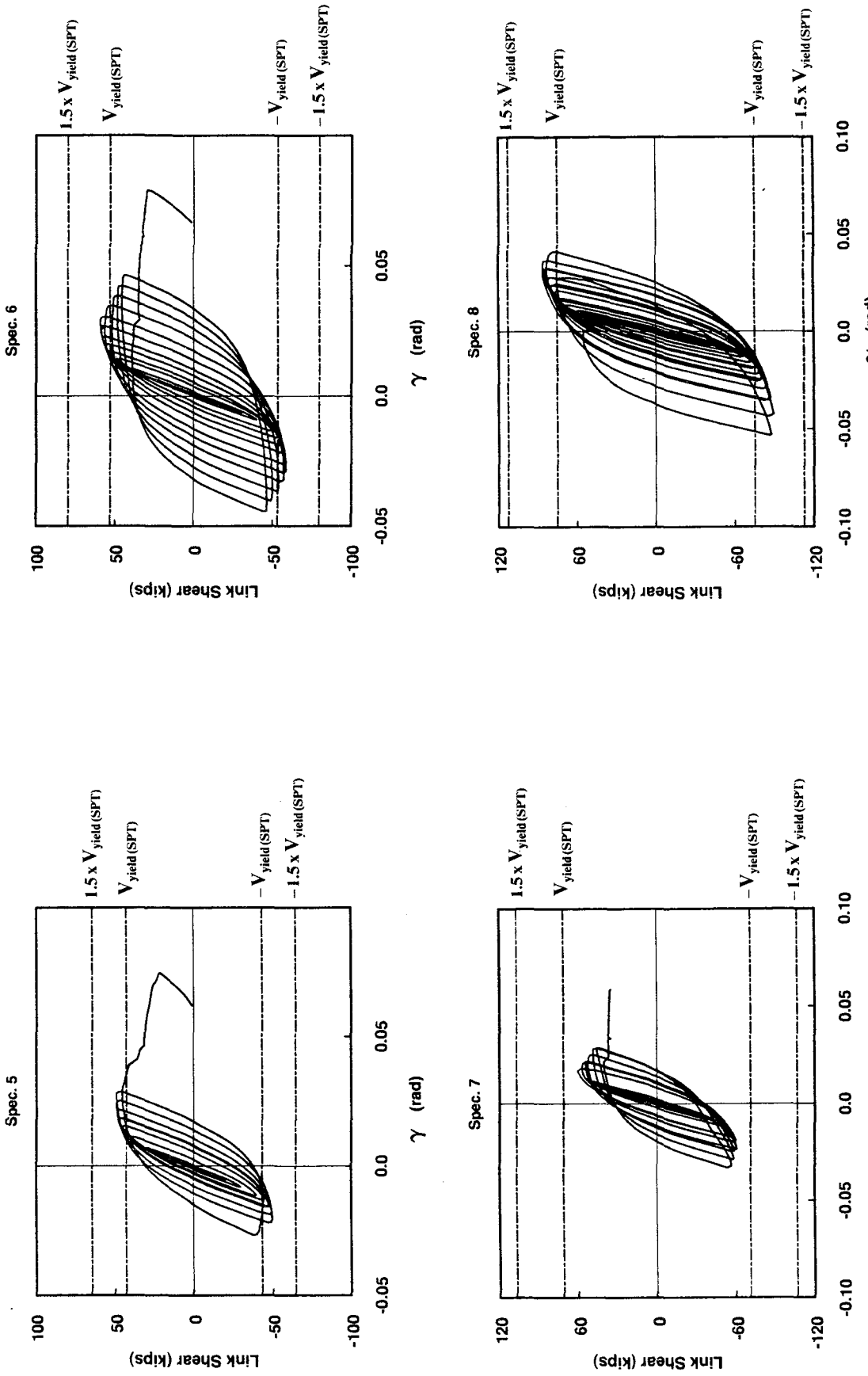

Fig. 4.1 Link Shear-Rotation Response Compared with Link Yield and Ultimate Shear Strength for Simple Plastic Theory (cont.)

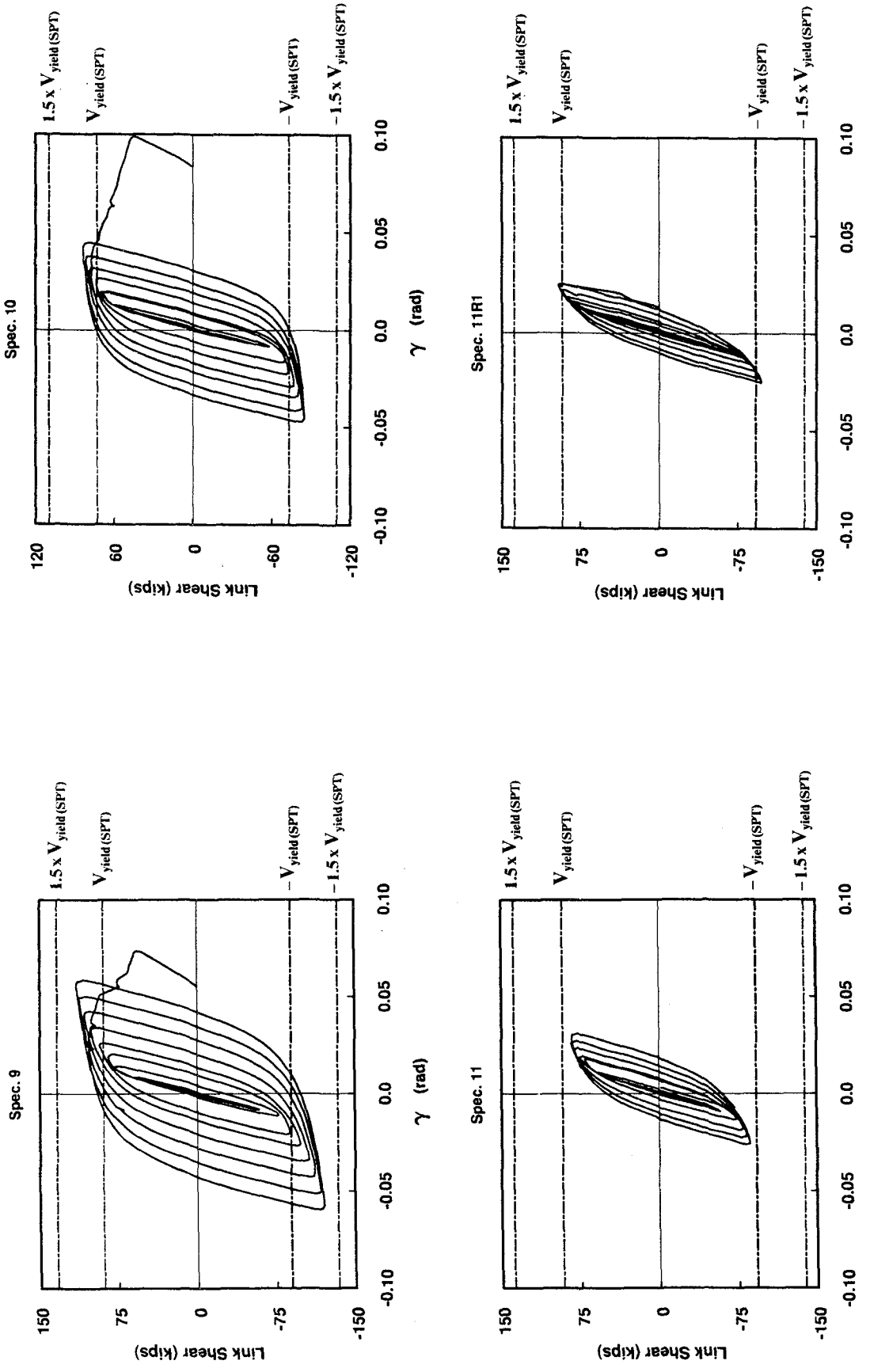

Fig. 4.1 Link Shear-Rotation Response Compared with Link Yield and Ultimate Shear Strength for Simple Plastic Theory (cont.)

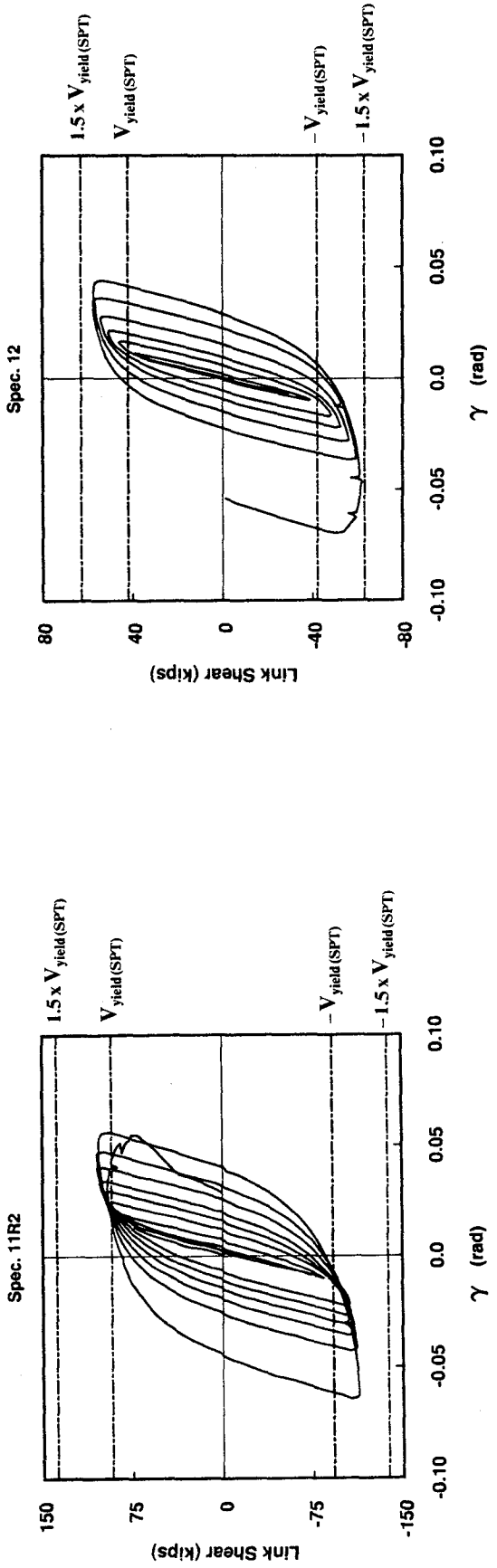

Fig. 4.1 Link Shear-Rotation Response Compared with Link Yield and Ultimate Shear Strength for Simple Plastic Theory (cont.)

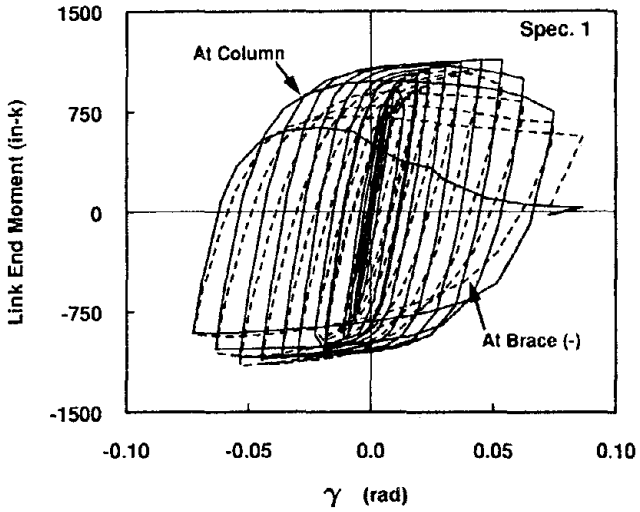

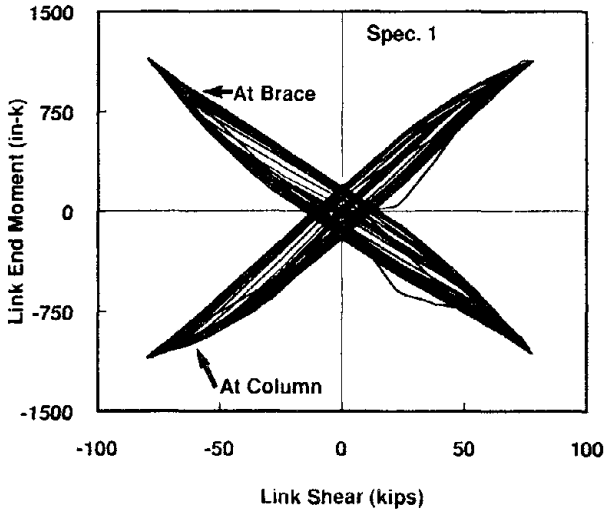

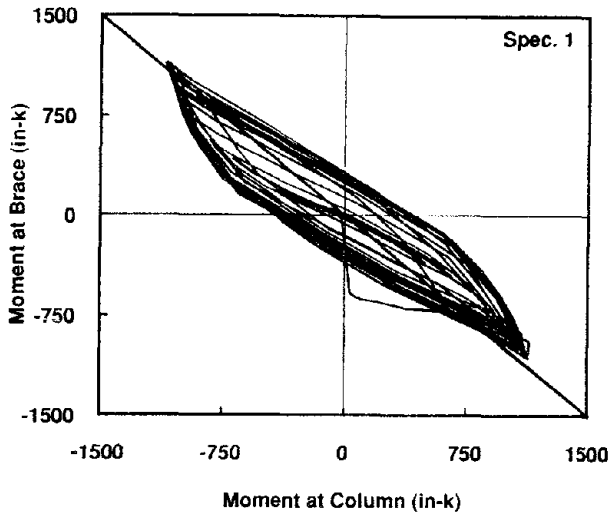

Fig. 4.2 Link End Moments

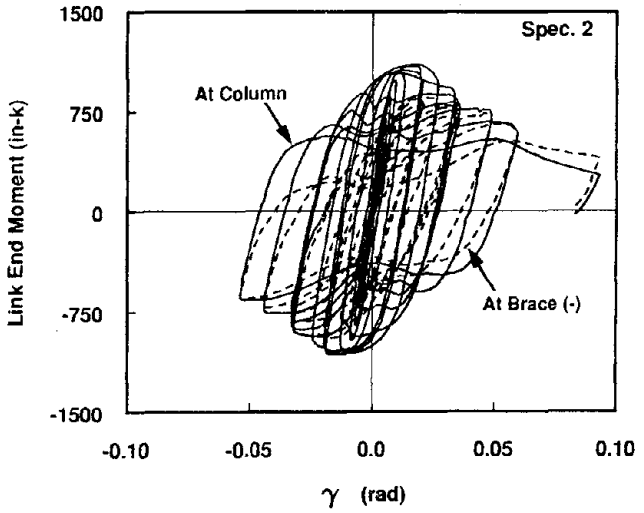

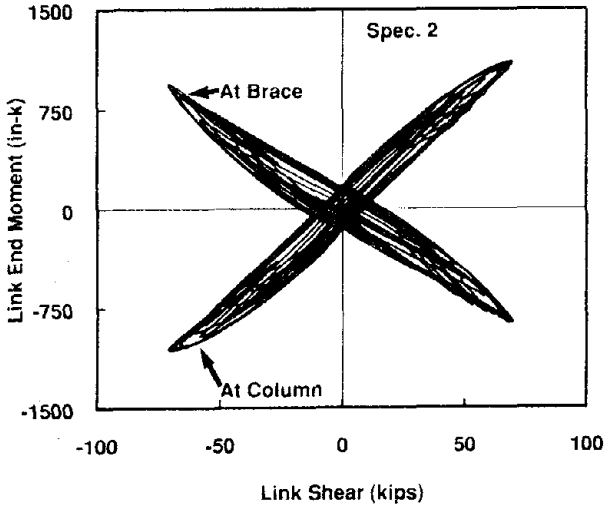

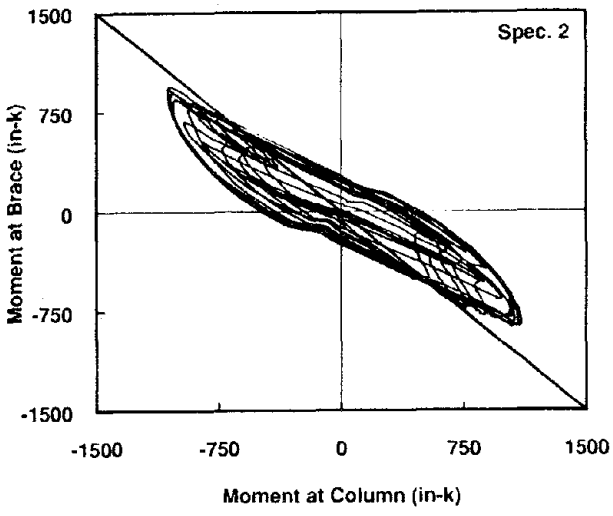

Fig. 4.2 Link End Moments (cont.)

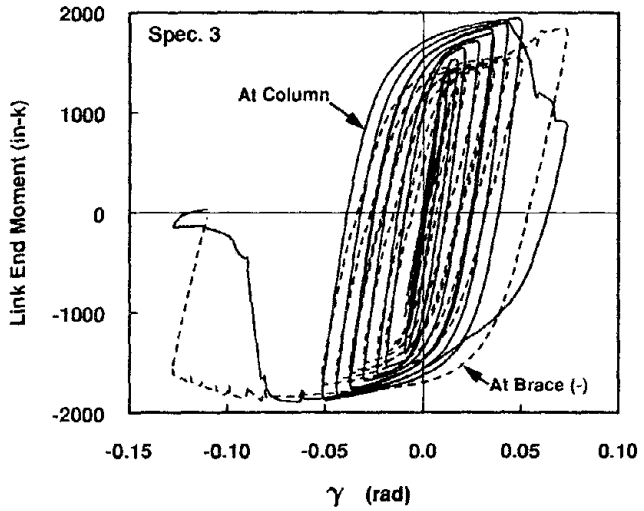

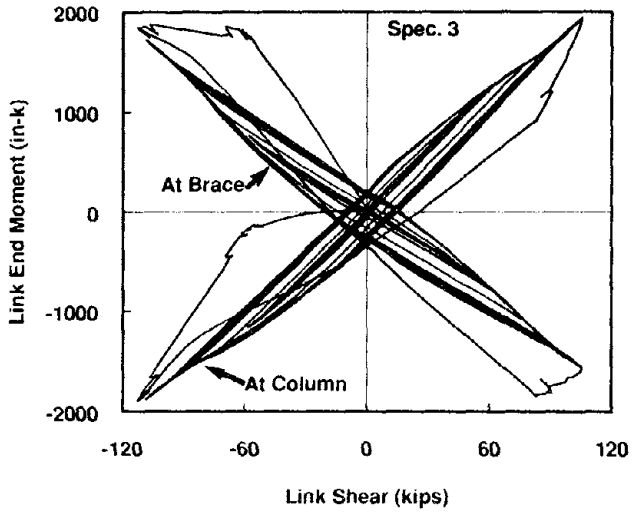

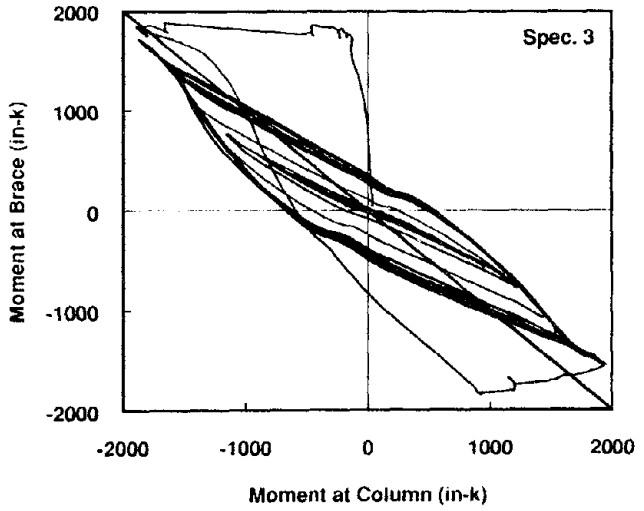

Fig. 4.2 Link End Moments (cont.)

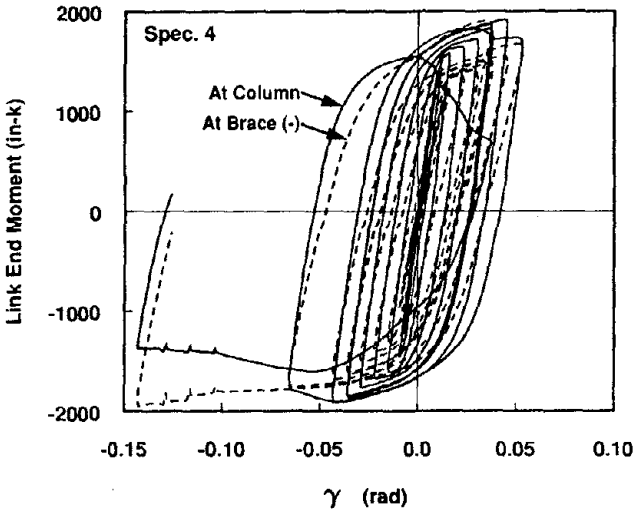

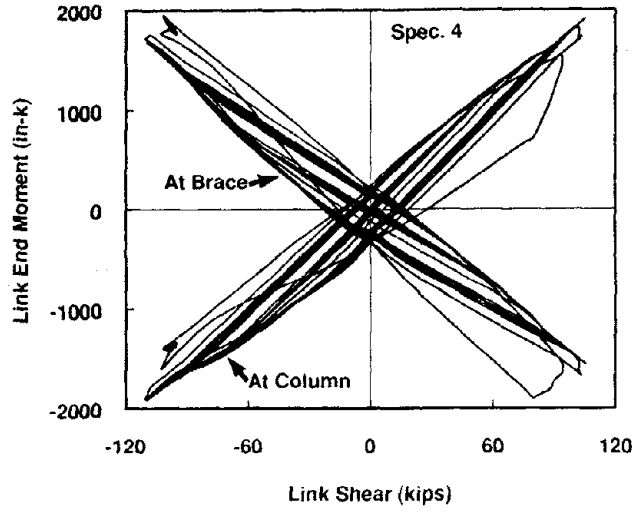

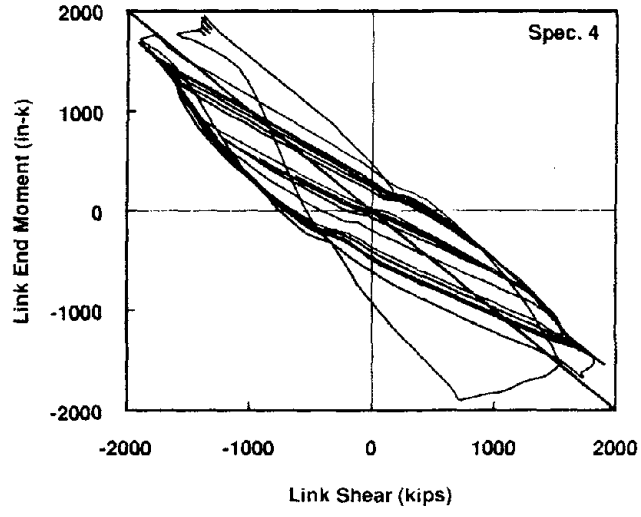

Fig. 4.2 Link End Moments (cont.)

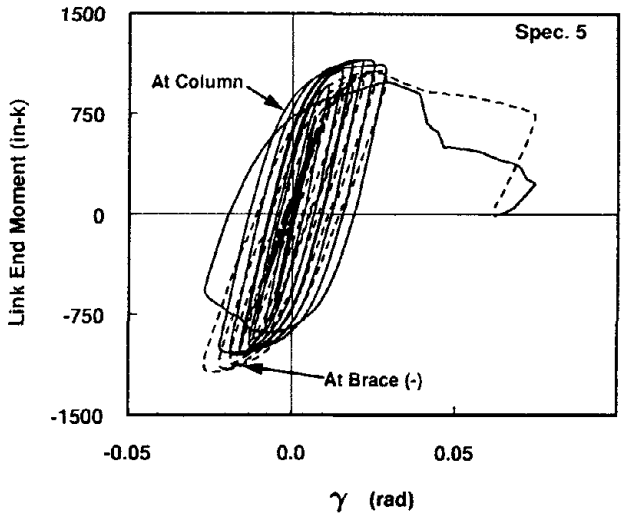

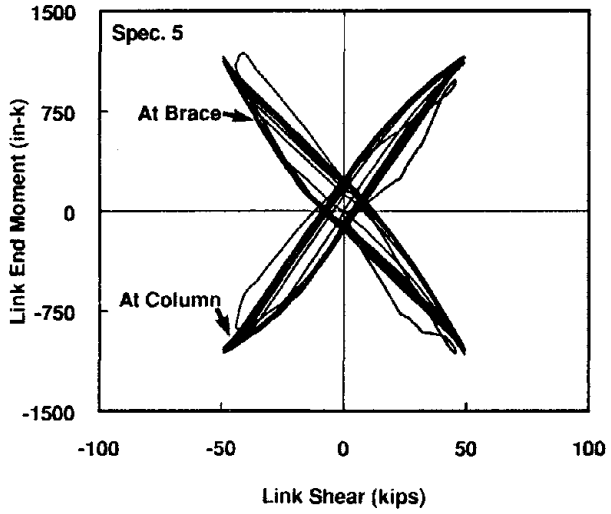

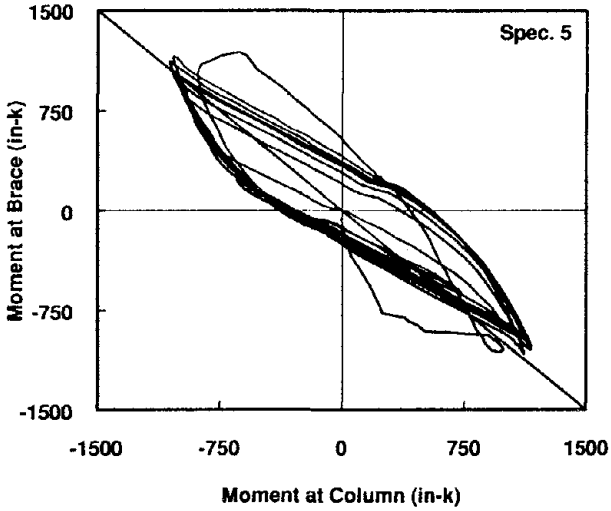

Fig. 4.2 Link End Moments (cont.)

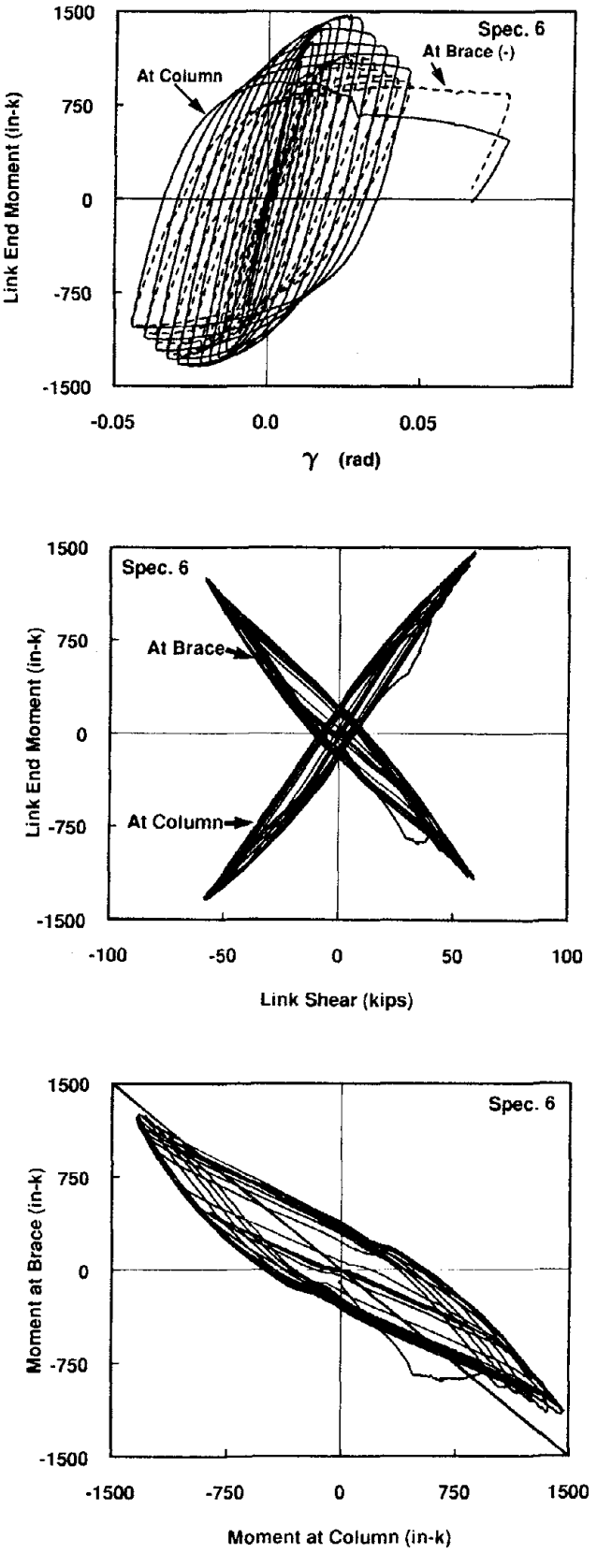

Fig. 4.2 Link End Moments (cont.)

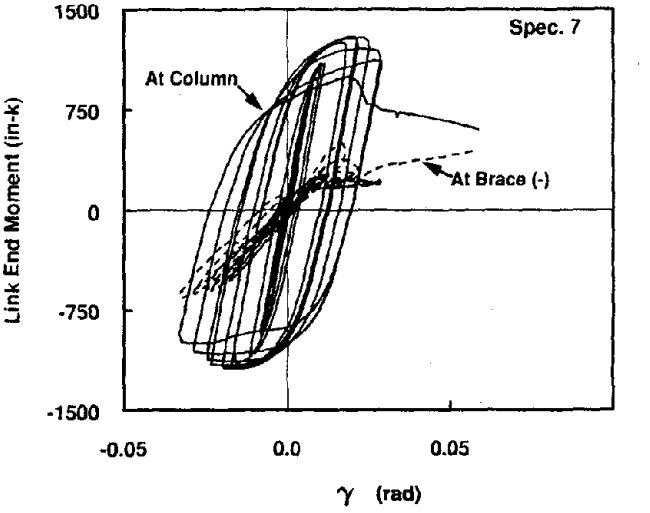

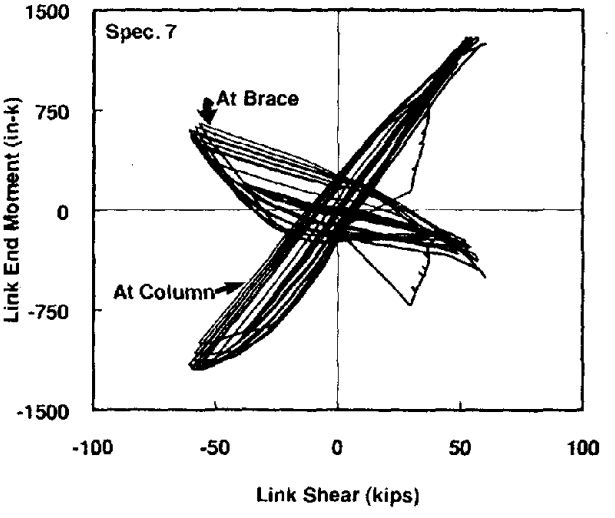

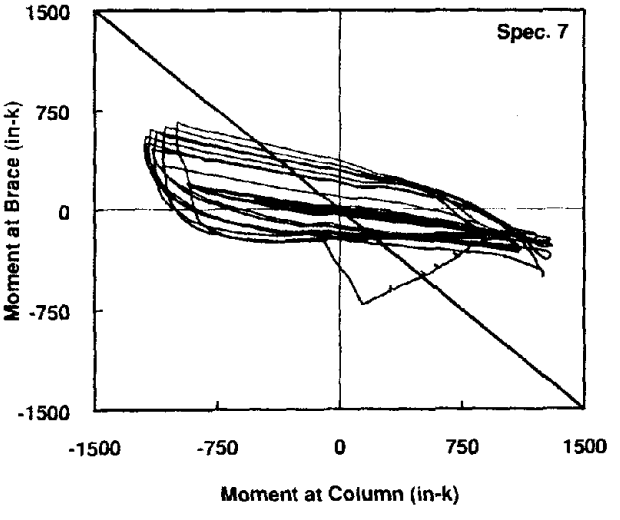

Fig. 4.2 Link End Moments (cont.)

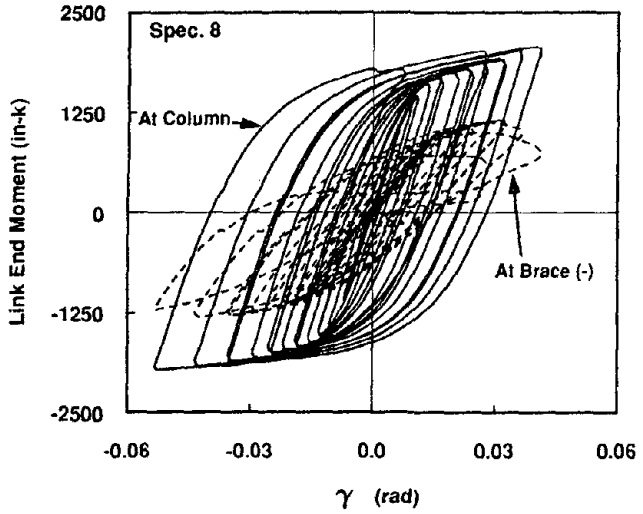

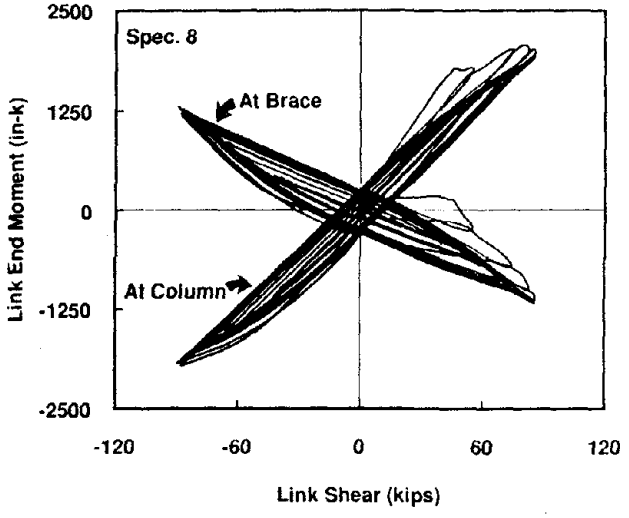

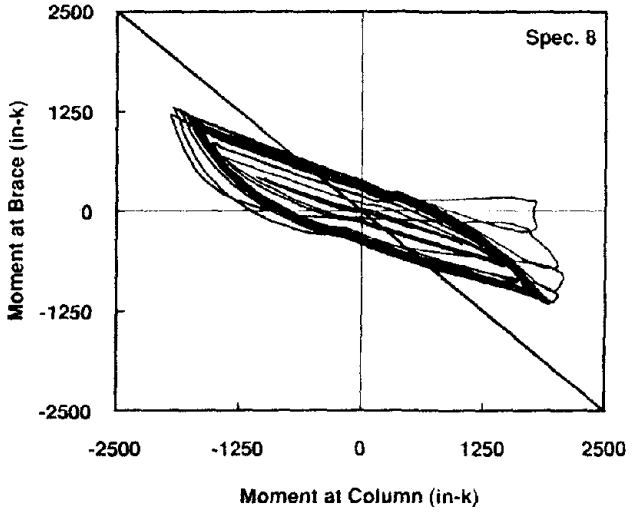

Fig. 4.2 Link End Moments (cont.)

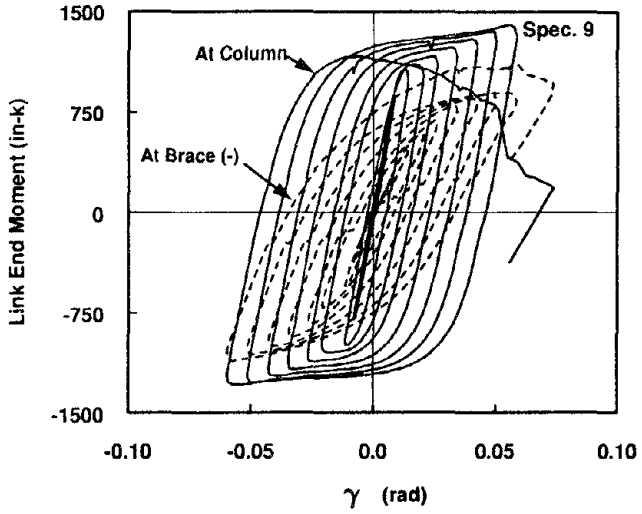

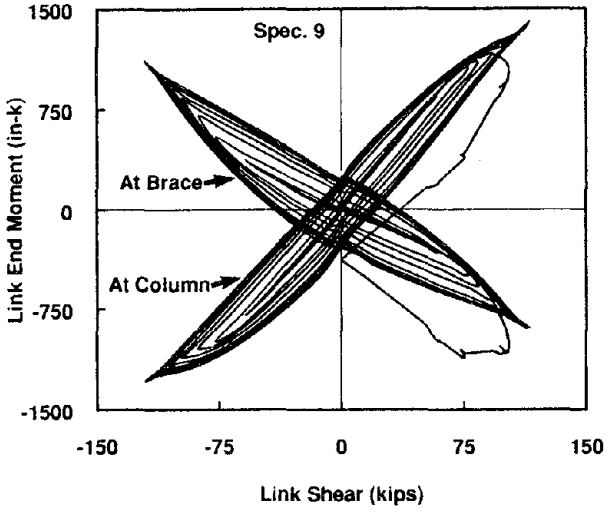

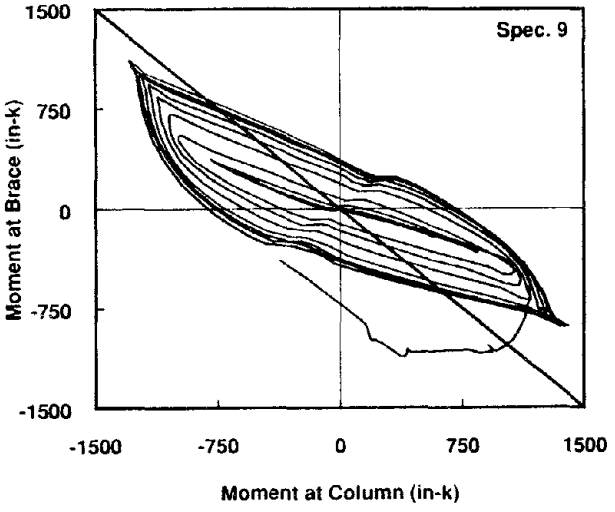

Fig. 4.2 Link End Moments (cont.)

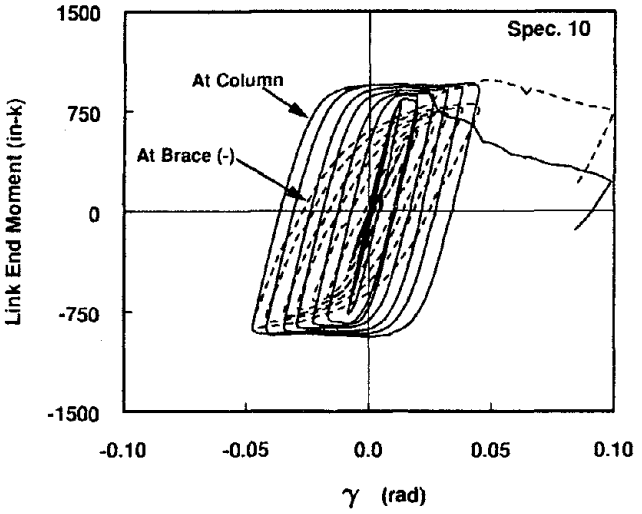

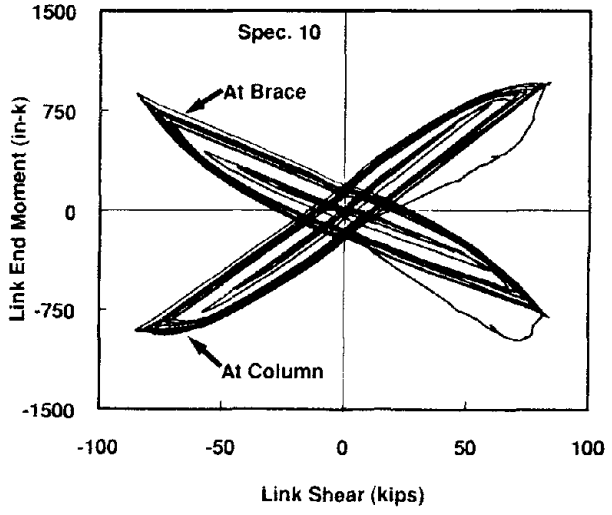

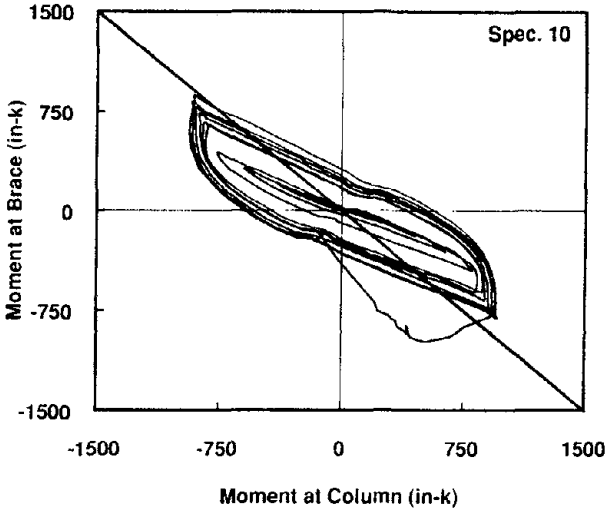

Fig. 4.2 Link End Moments (cont.)

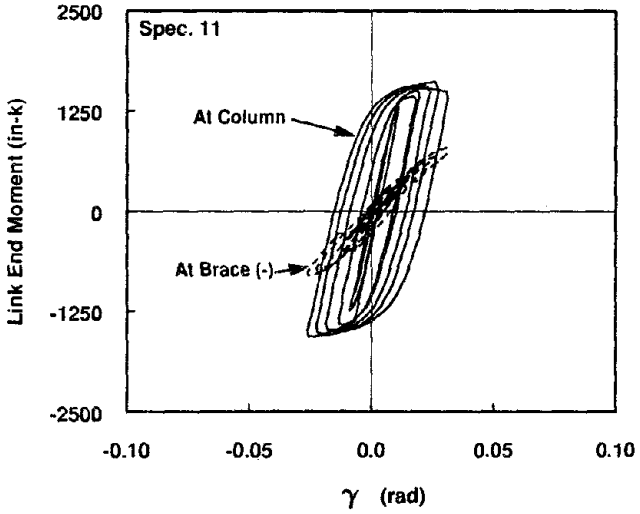

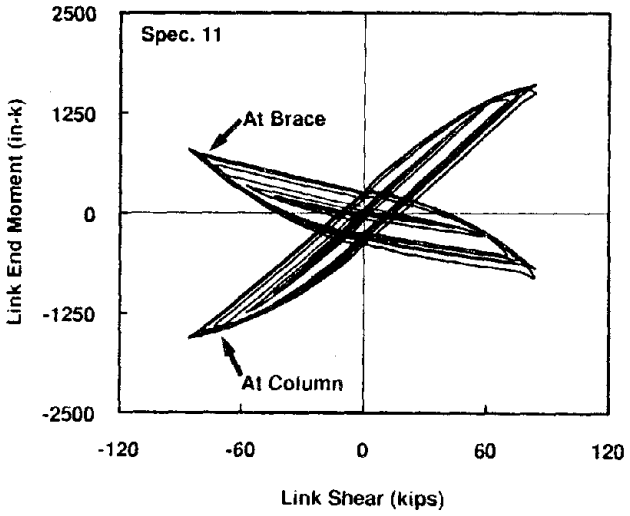

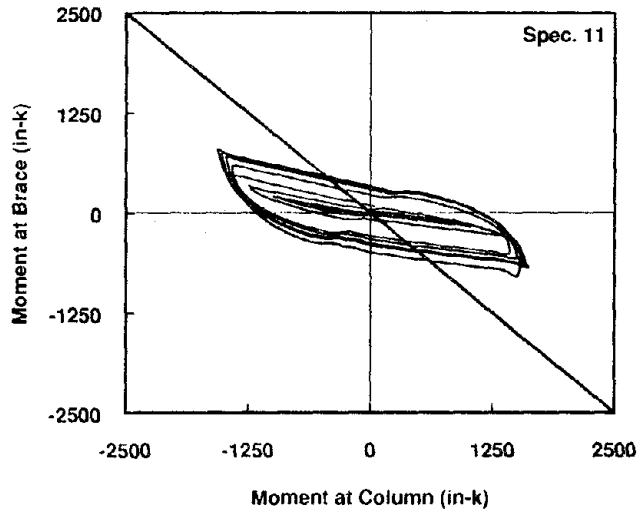

Fig. 4.2 Link End Moments (cont.)

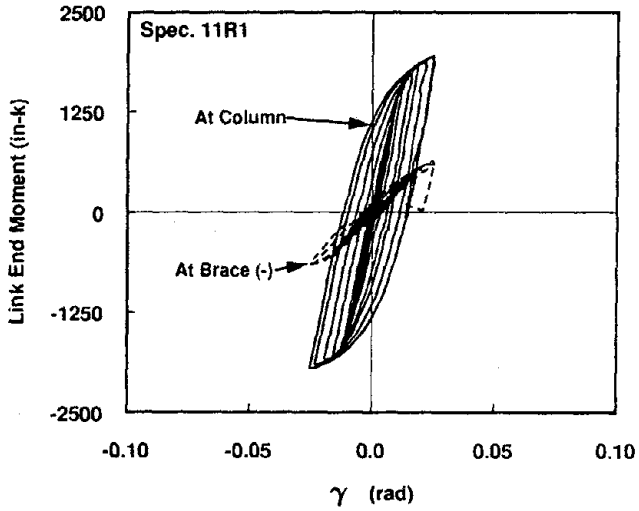

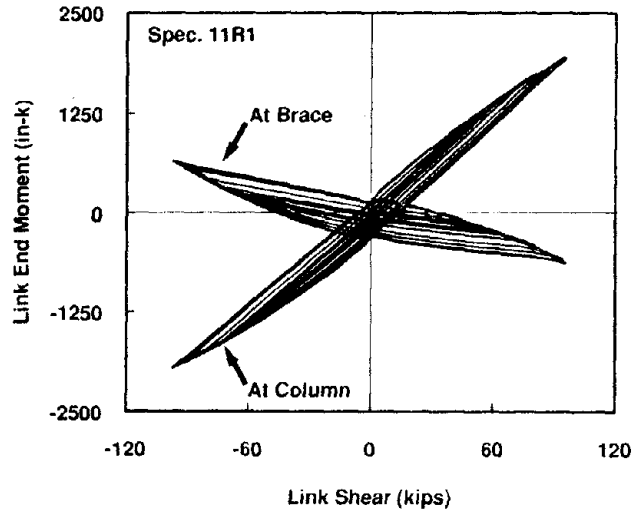

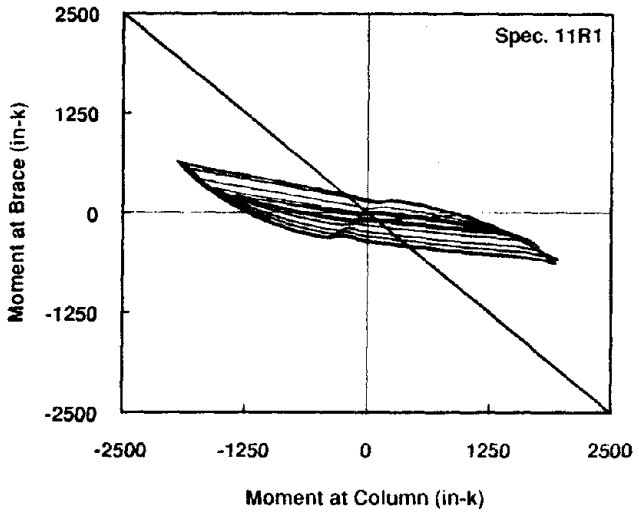

Fig. 4.2 Link End Moments (cont.)

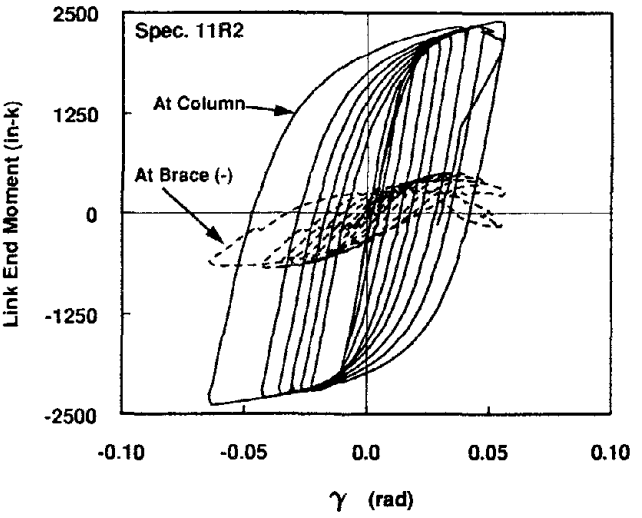

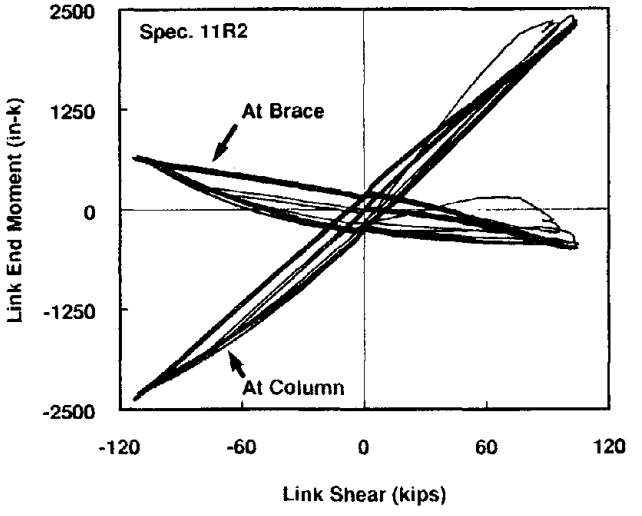

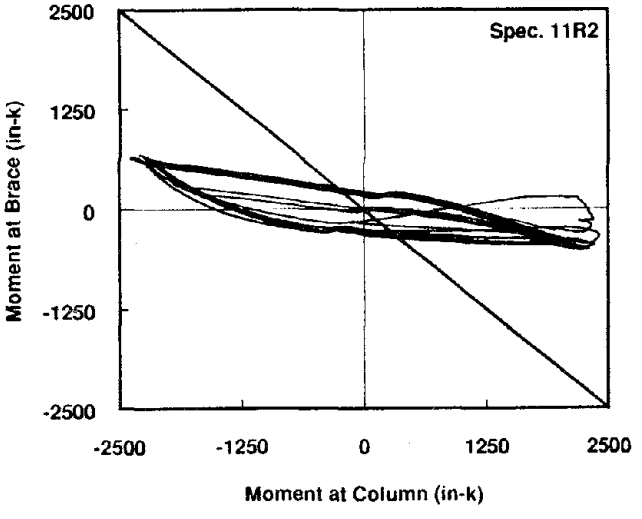

Fig. 4.2 Link End Moments (cont.)

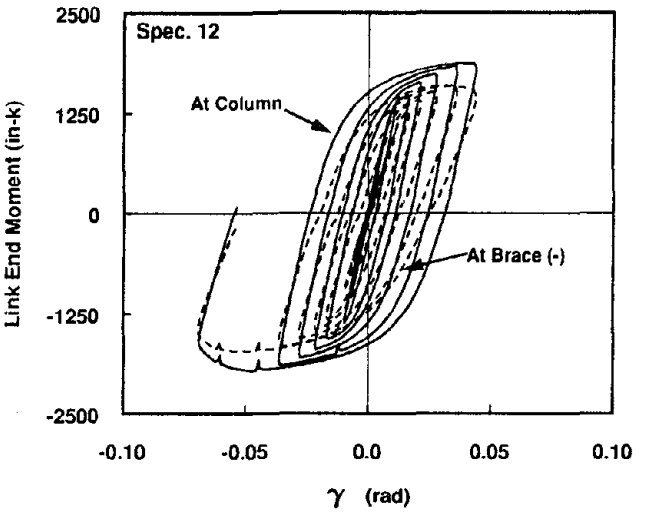

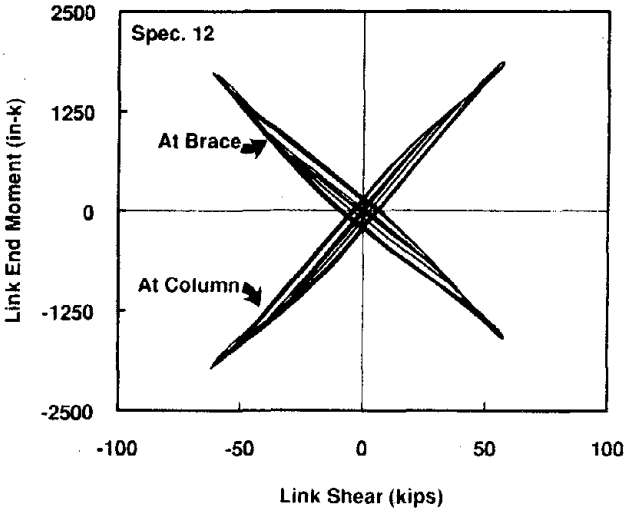

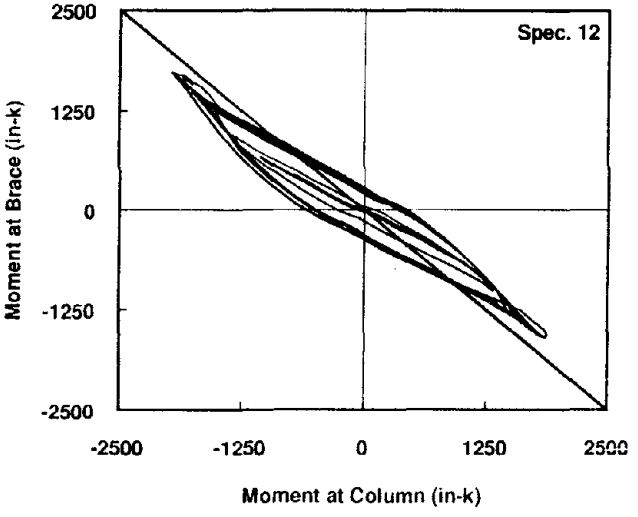

Fig. 4.2 Link End Moments (cont.)

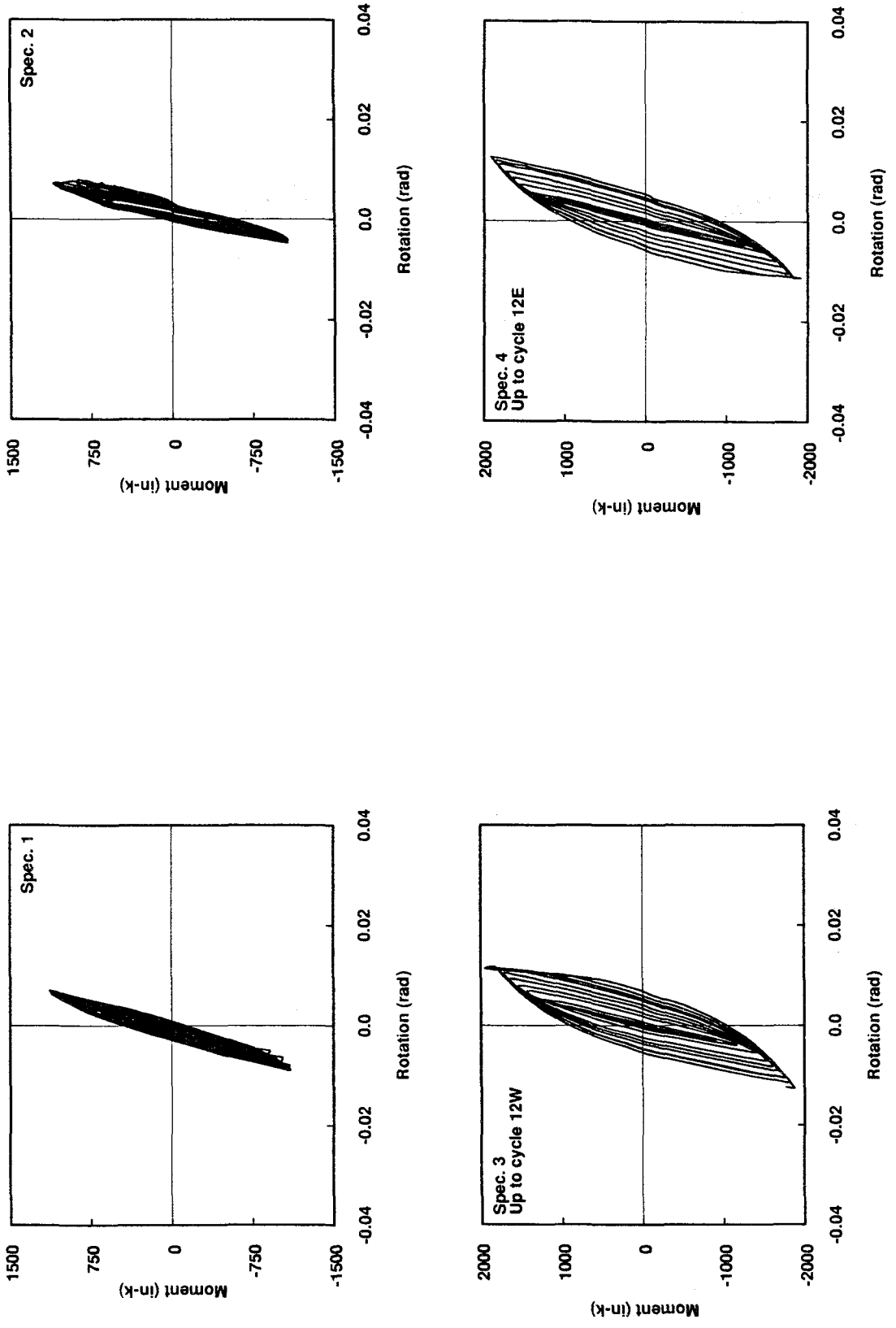

Fig. 4.3 Link End Moment vs. Link End Rotation at Column End of Link

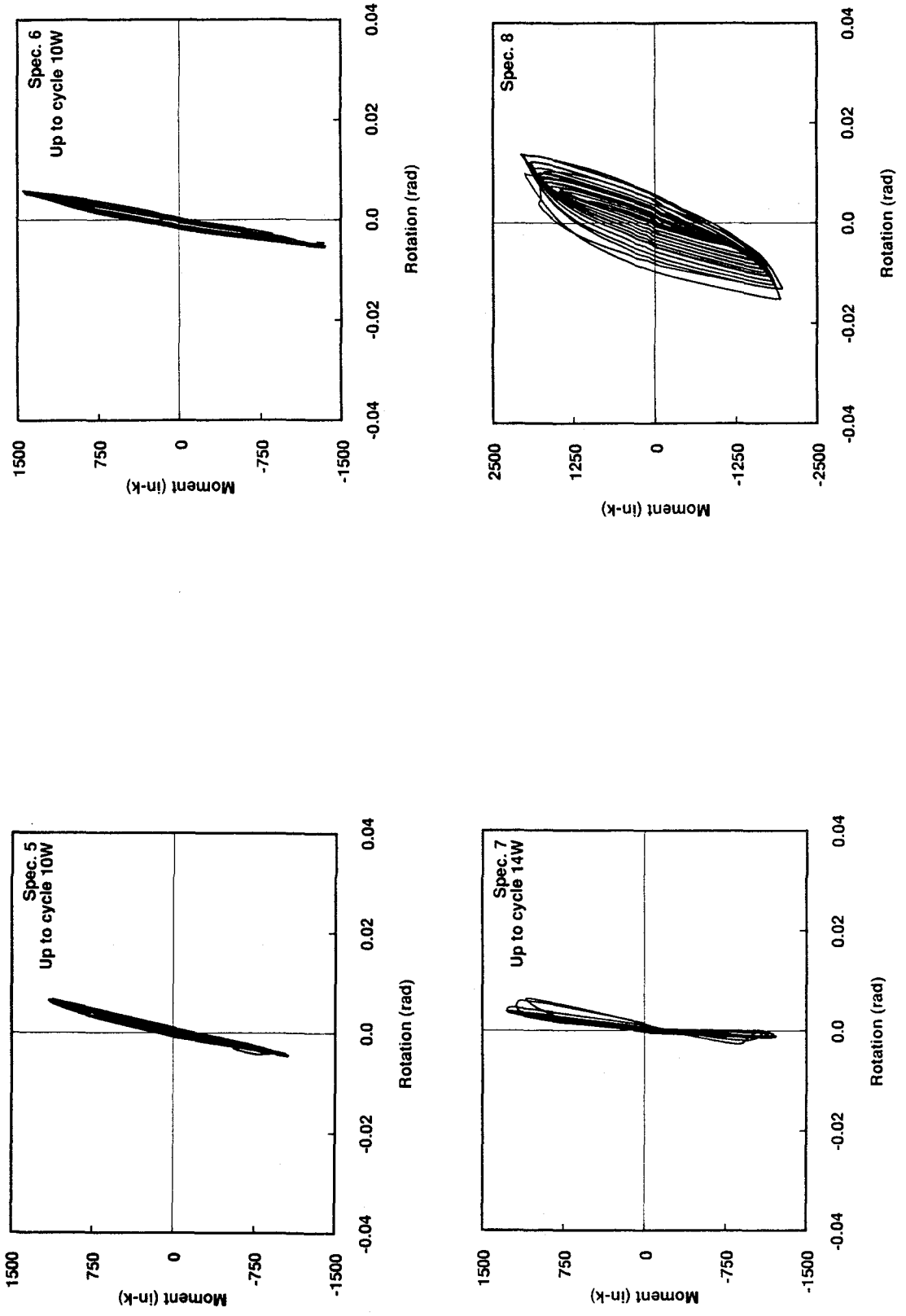

Fig. 4.3 Link End Moment vs. Link End Rotation at Column End of Link (cont.)

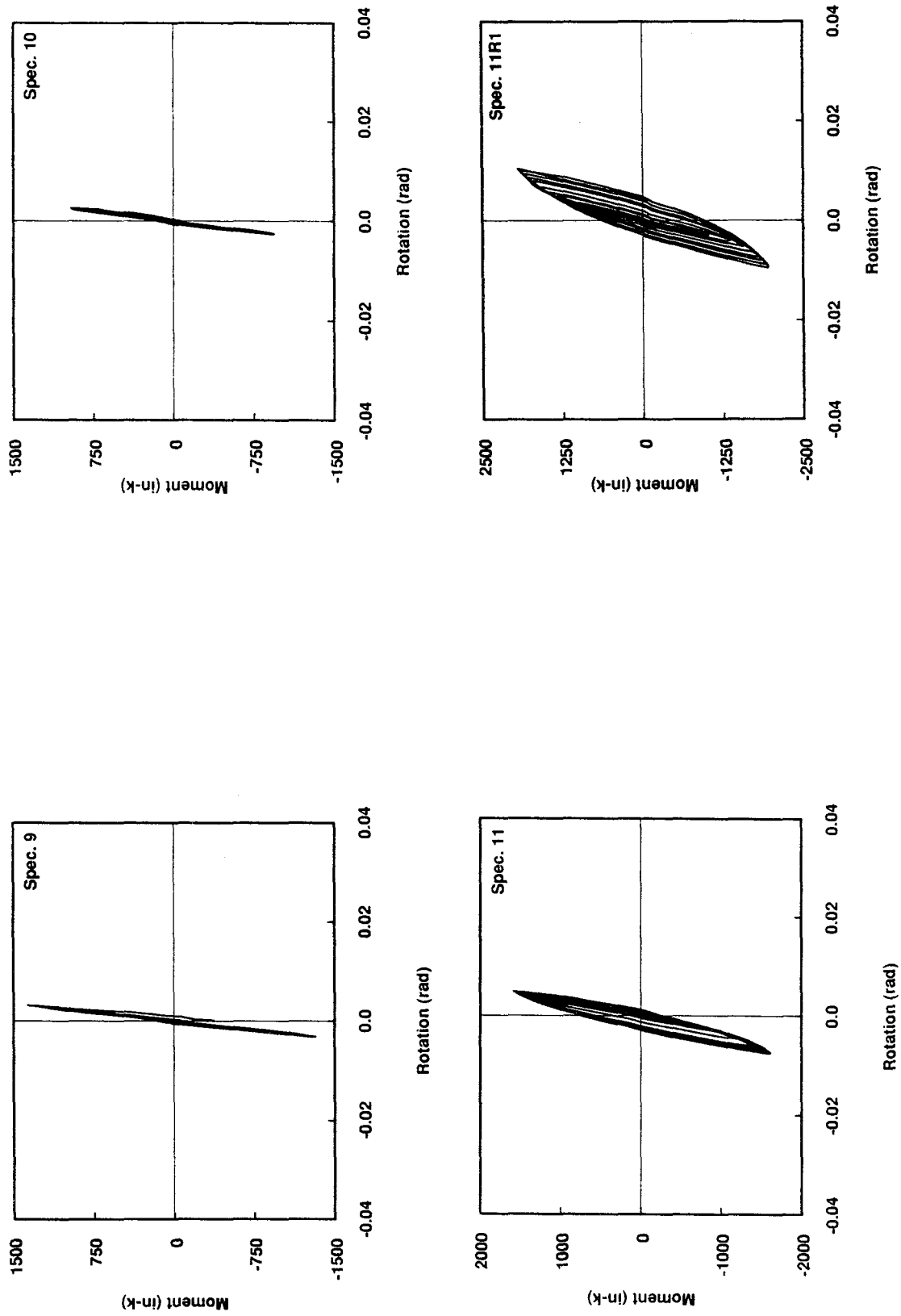

Fig. 4.3 Link End Moment vs. Link End Rotation at Column End of Link (cont.)

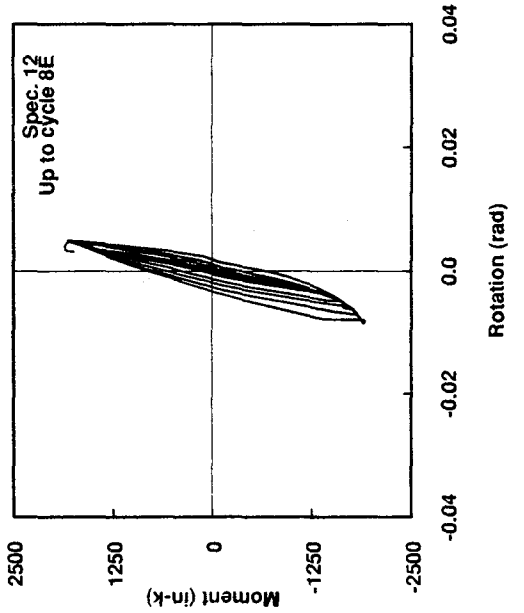

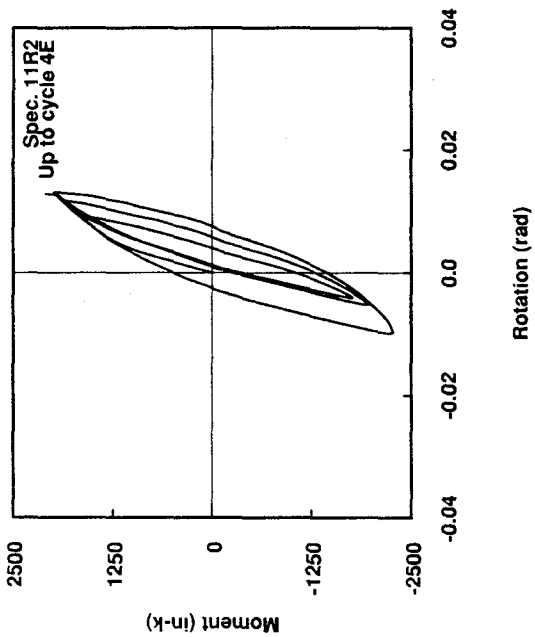

Fig. 4.3 Link End Moment vs. Link End Rotation at Column End of Link (cont.)

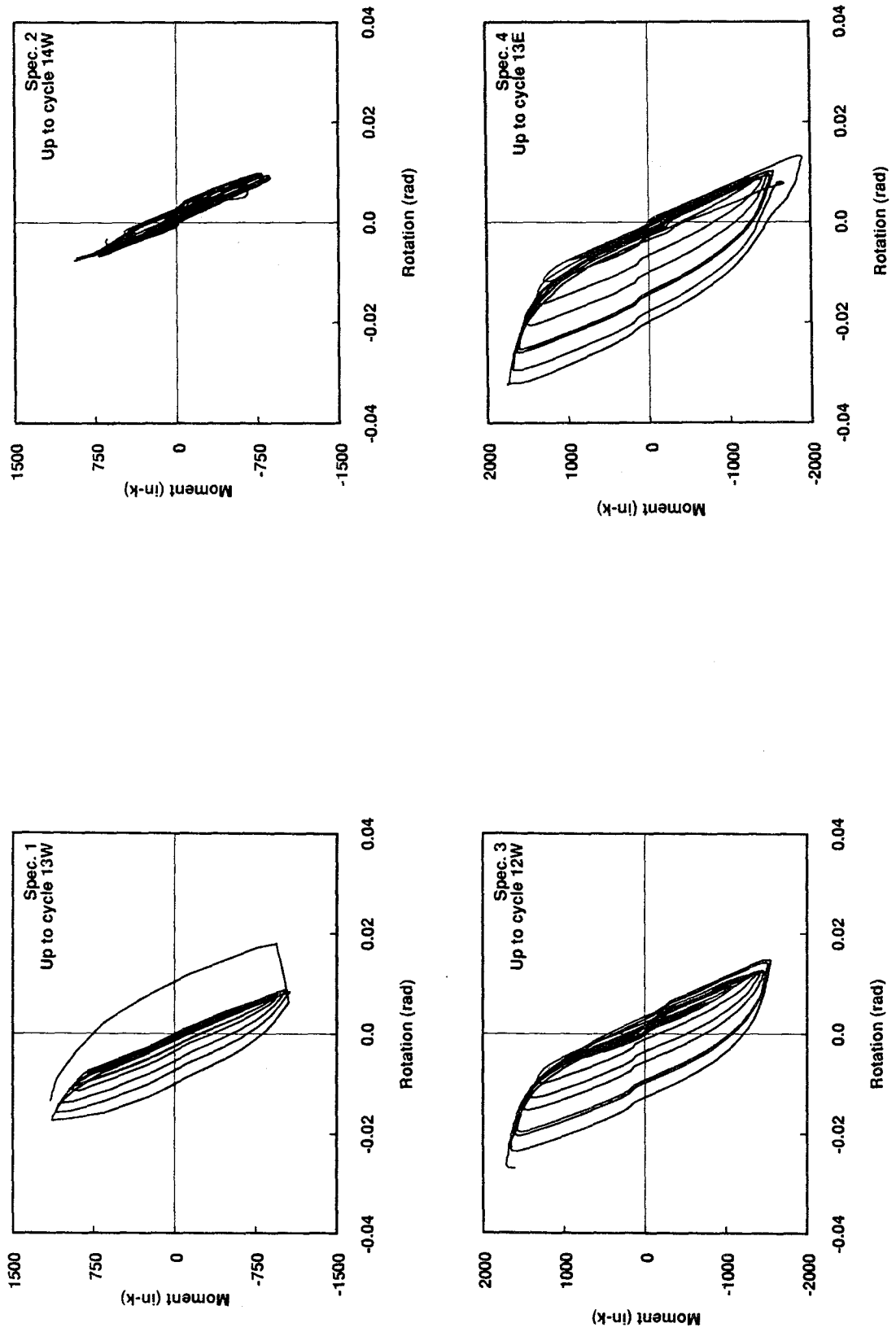

Fig. 4.4 Link End Moment vs. Link End Rotation at Brace End of Link

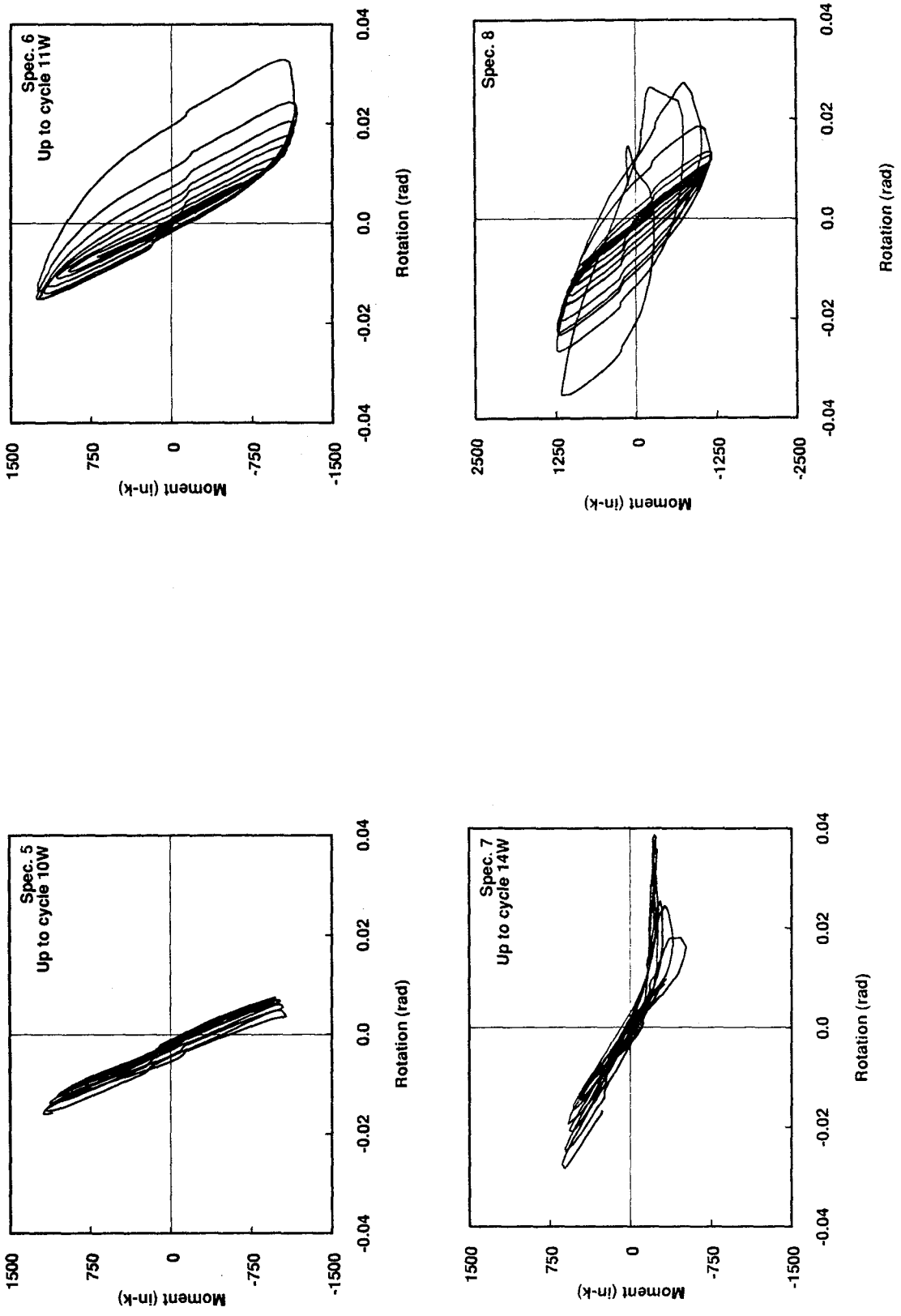

Fig. 4.4 Link End Moment vs. Link End Rotation at Brace End of Link (cont.)

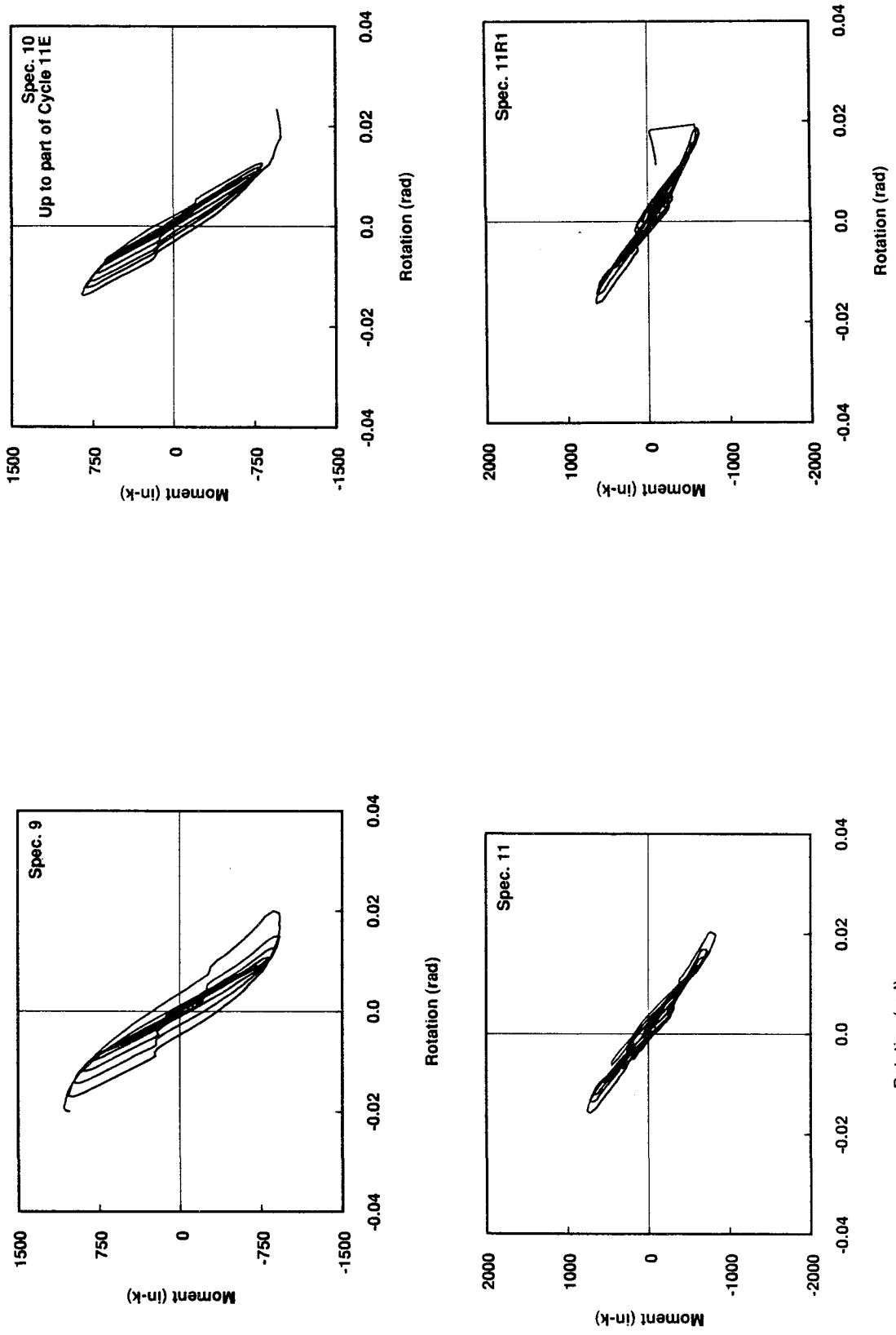

Fig. 4.4 Link End Moment vs. Link End Rotation at Brace End of Link (cont.)

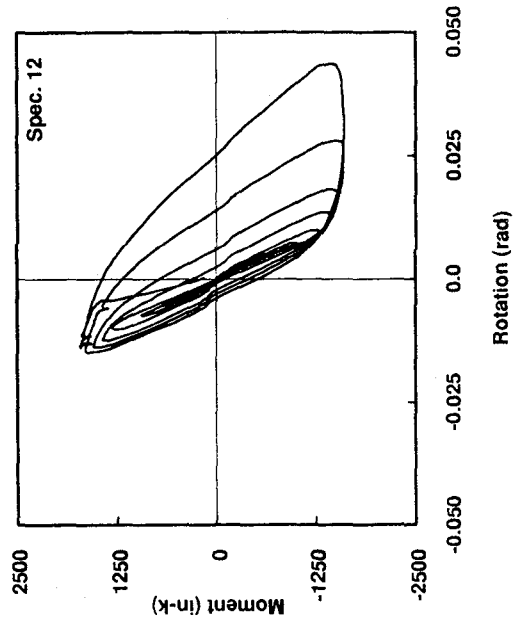

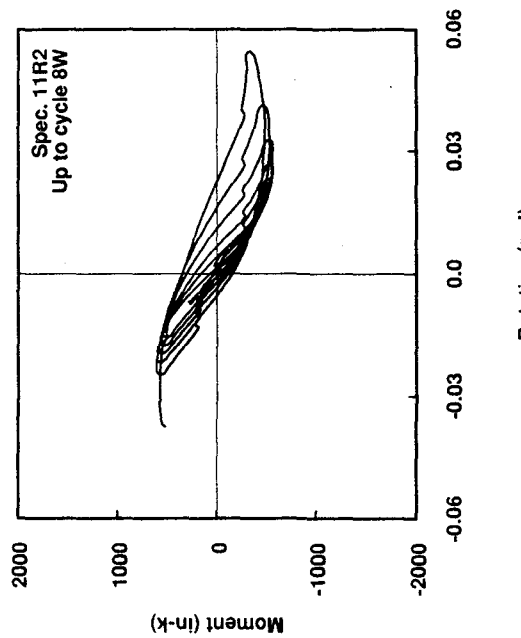

Fig. 4.4 Link End Moment vs. Link End Rotation at Brace End of Link (cont.)

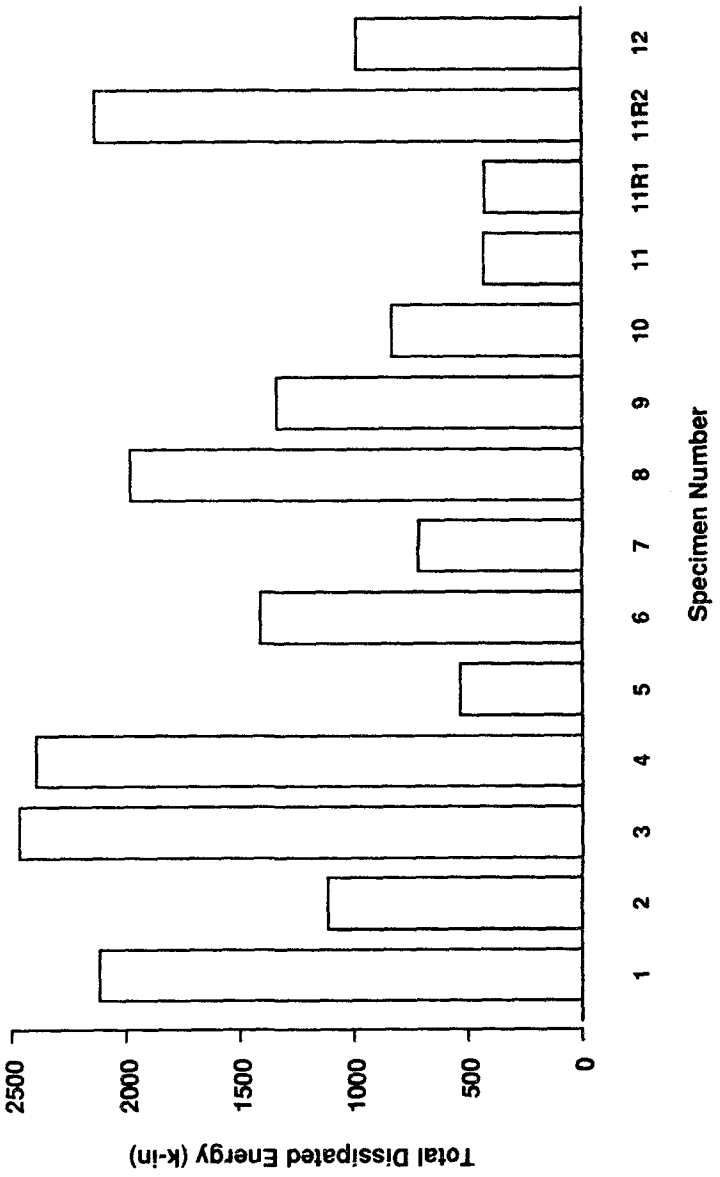

Fig. 4.5 Total (Unnormalized) Energy Dissipated by Test Specimens

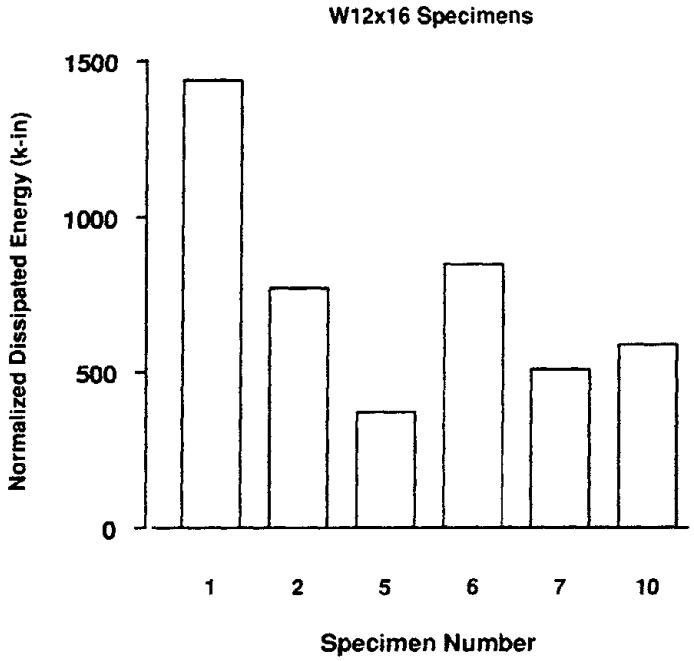

Fig. 4.6 Normalized Energy Dissipated by W12×16 Specimens

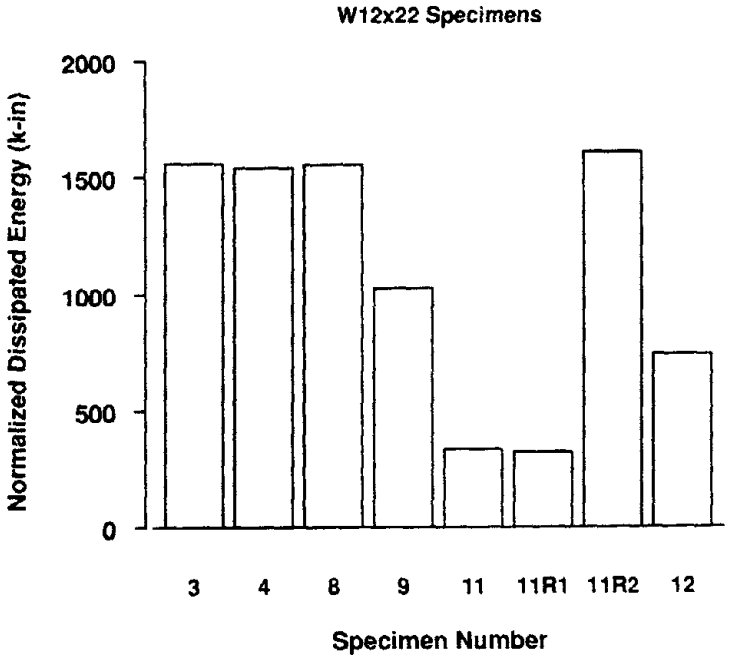

Fig. 4.7 Normalized Energy Dissipated by W12×22 Specimens

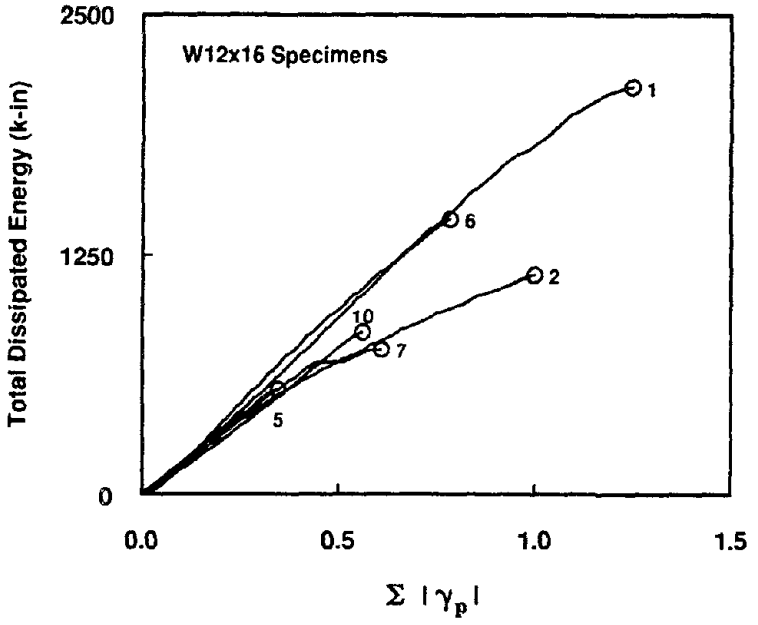

Fig. 4.8 Total (Unnormalized) Energy Dissipated vs. Cumulative Link Plastic Rotation Angle for W 12×16 Specimens

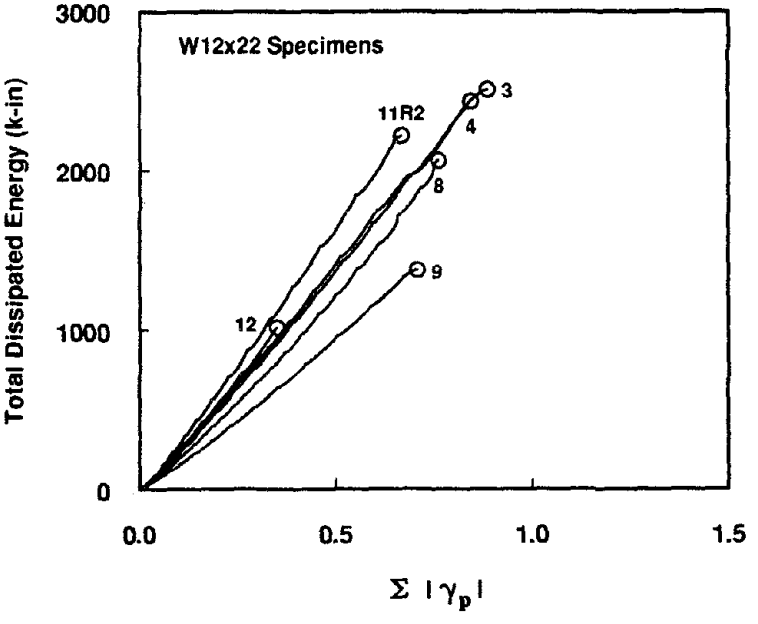

Fig. 4.9 Total (Unnormalized) Energy Dissipated vs. Cumulative Link Plastic Rotation Angle for W 12×22 Specimens

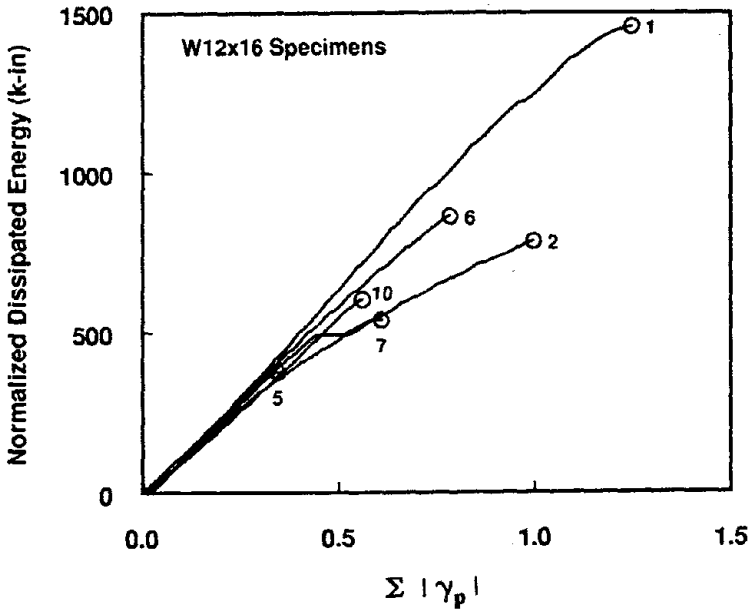

Fig. 4.10 Normalized Energy Dissipated vs. Cumulative Link Plastic Rotation Angle for W 12×16 Specimens

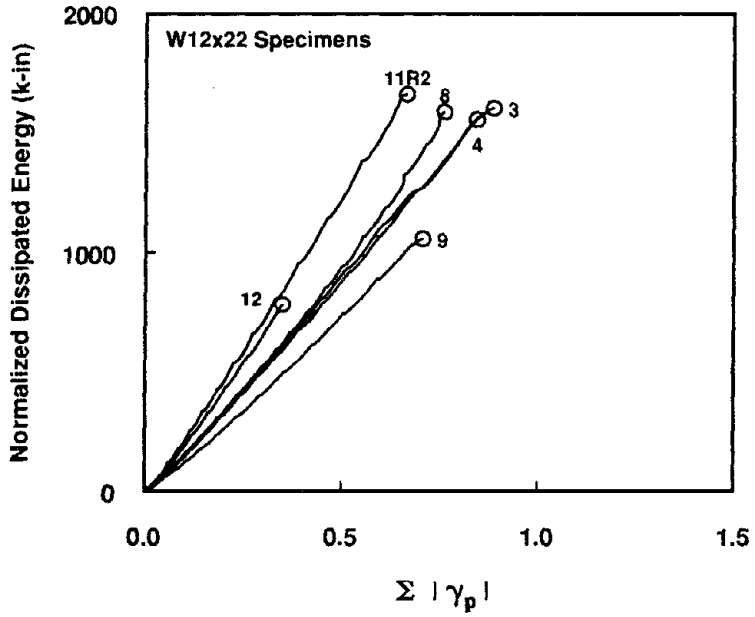

Fig. 4.11 Normalized Energy Dissipated vs. Cumulative Link Plastic Rotation Angle for W 12×22 Specimens

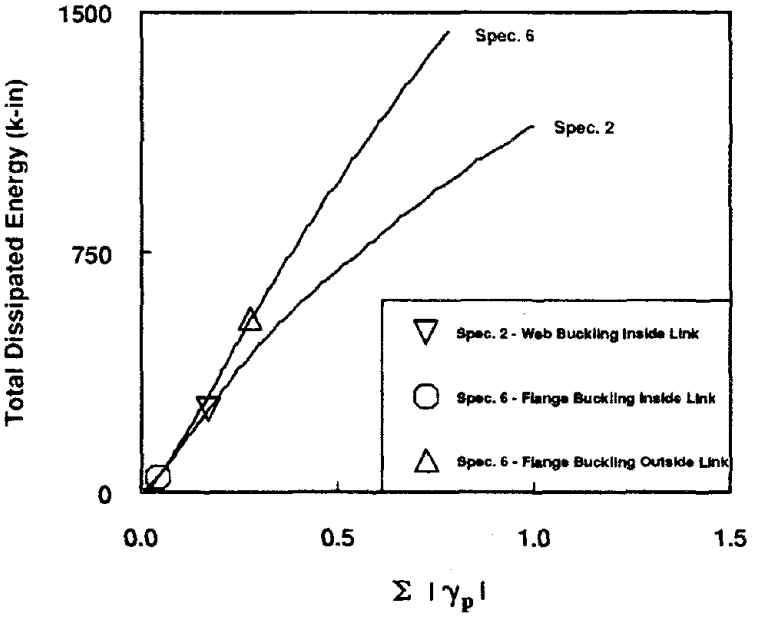

Fig. 4.12 Effect of Flange and Web Buckling on Energy Dissipation

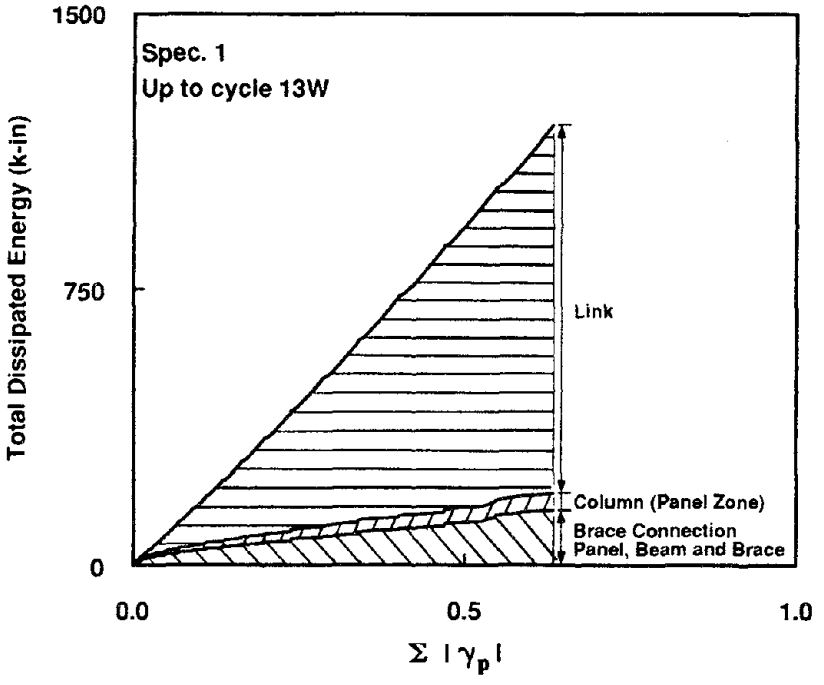

Fig. 4.13 Distribution of Energy Dissipation in Specimen 1

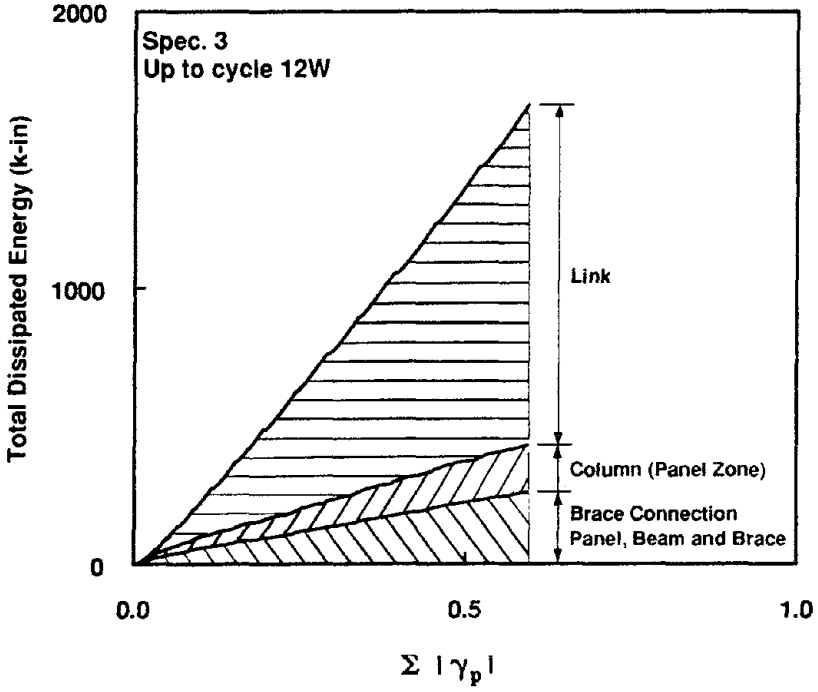

Fig. 4.14 Distribution of Energy Dissipation in Specimen 3

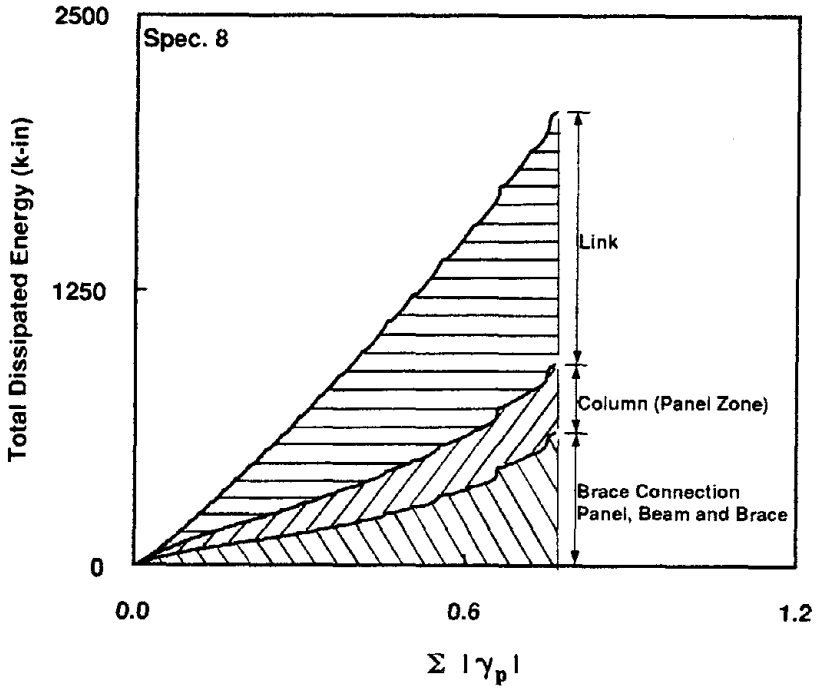

Fig. 4.15 Distribution of Energy Dissipation in Specimen 8

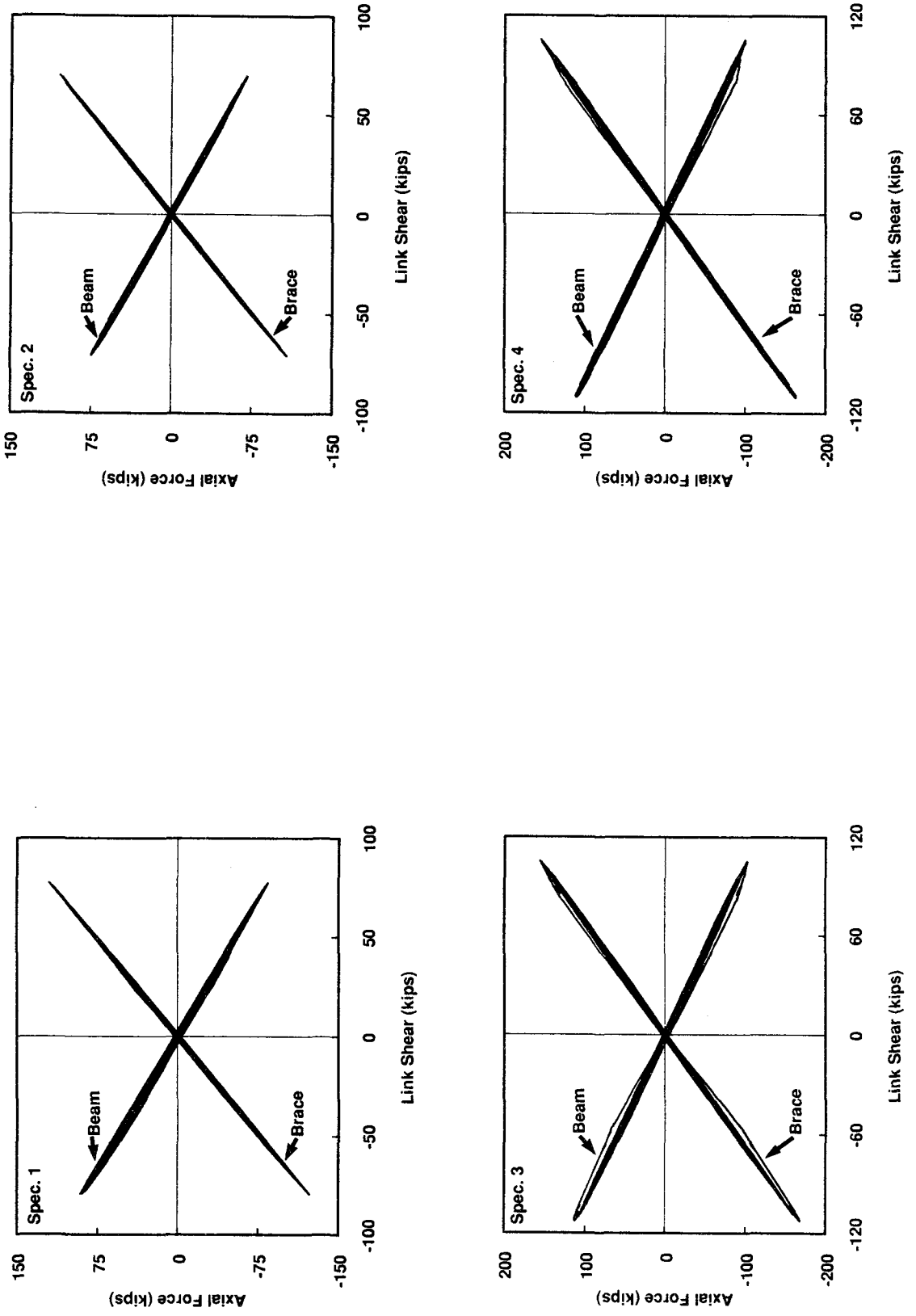

Fig. 4.16 Axial Force in Beam and Brace vs. Shear Force in Link

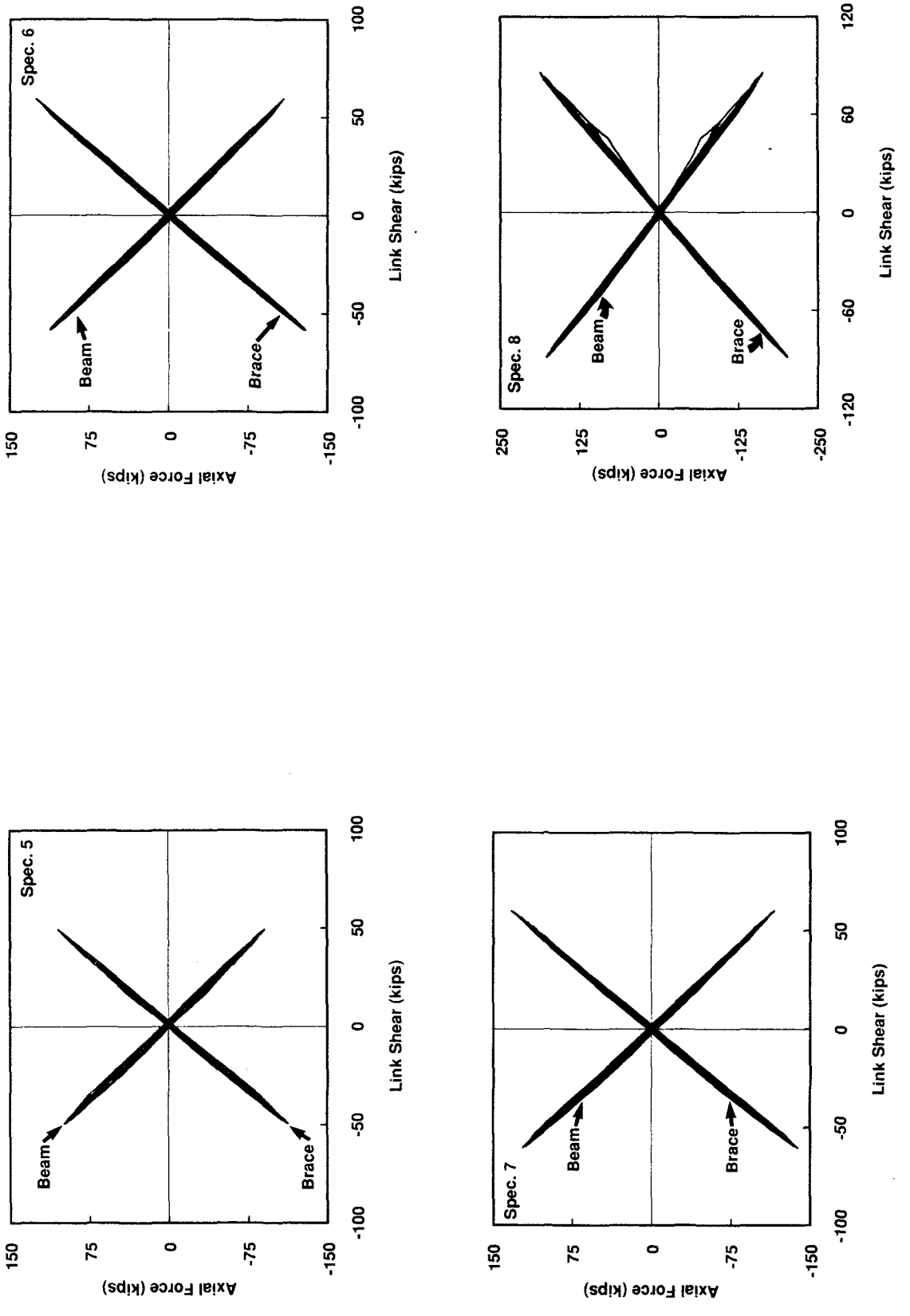

Fig. 4.16 Axial Force in Beam and Brace vs. Shear Force in Link (cont.)

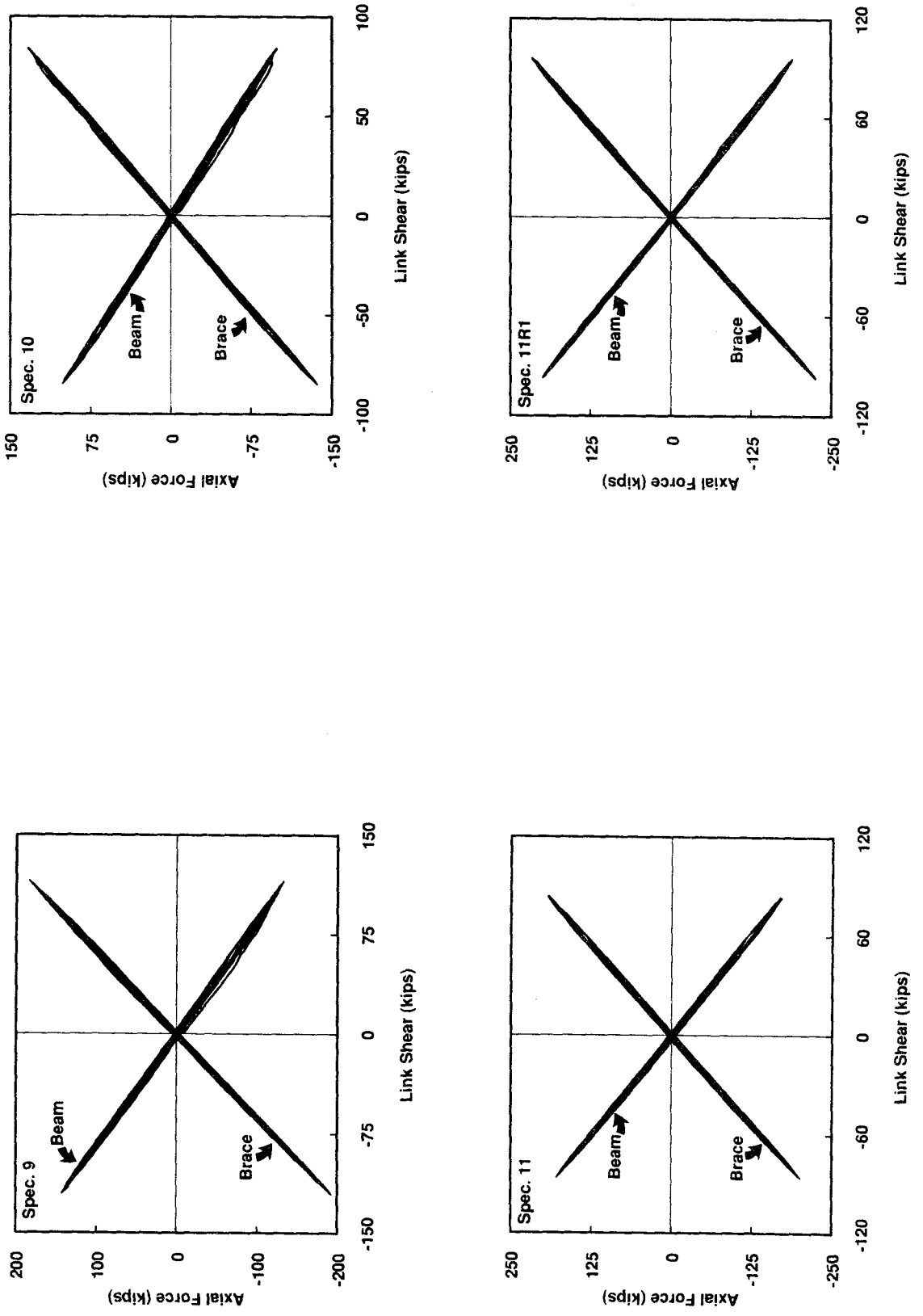

Fig. 4.16 Axial Force in Beam and Brace vs. Shear Force in Link (cont.)

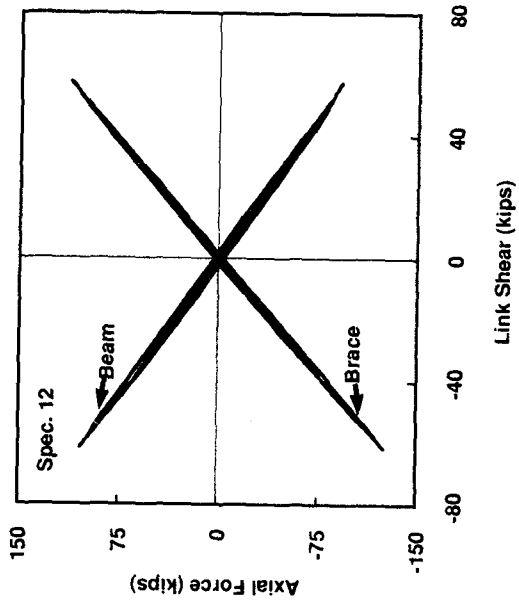

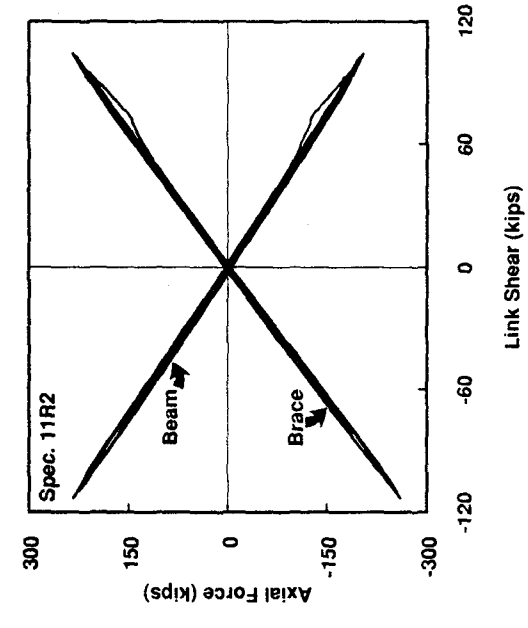

Fig. 4.16 Axial Force in Beam and Brace vs. Shear Force in Link (cont.)

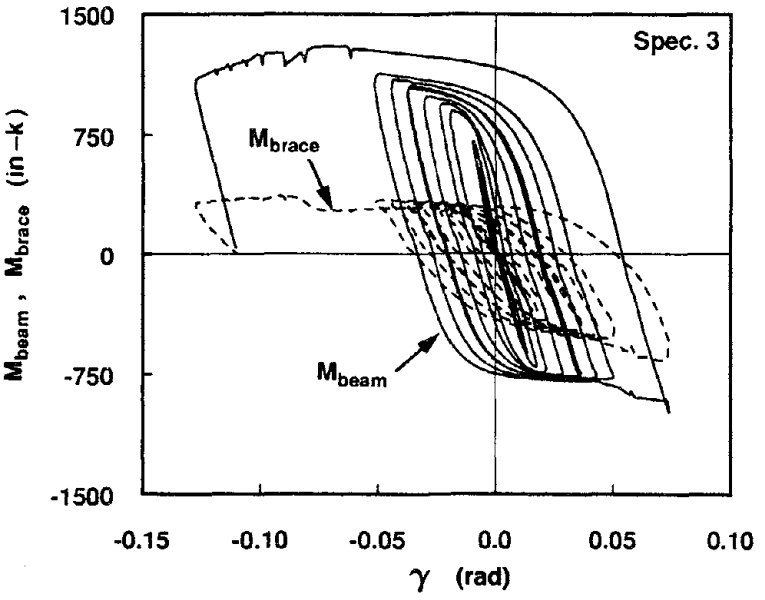

Fig. 4.17 Specimen 3 - Beam and Brace Bending Moments

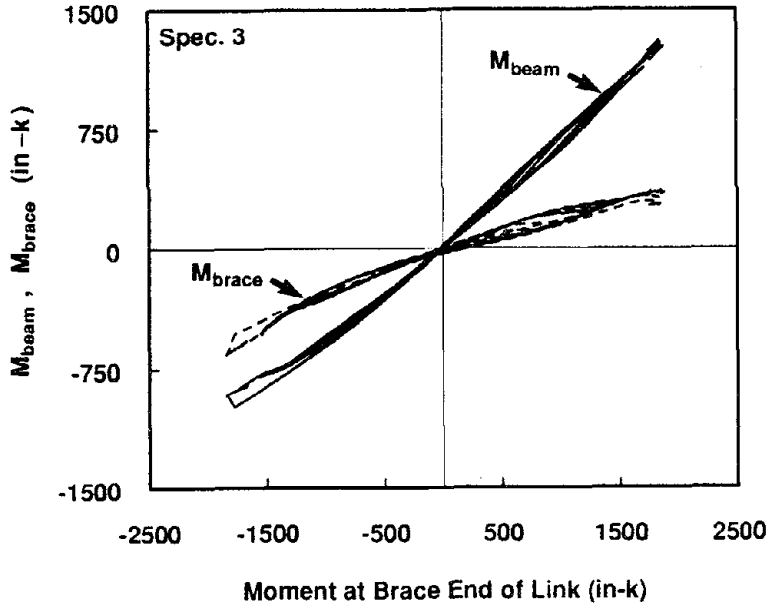

Fig. 4.18 Specimen 3 - Distribution of Link End Moment to Beam and Brace

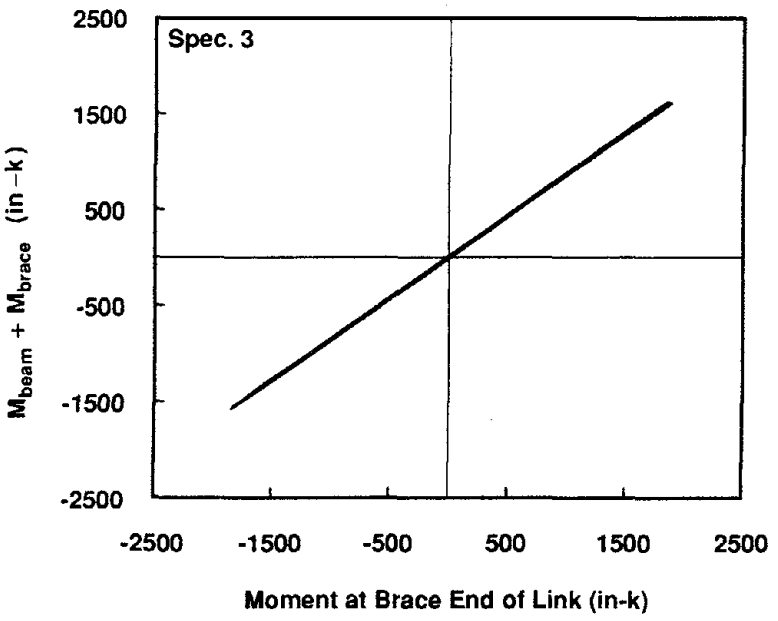

Fig. 4.19 Specimen 3 - Link End Moment vs. Sum of Beam and Brace Moments

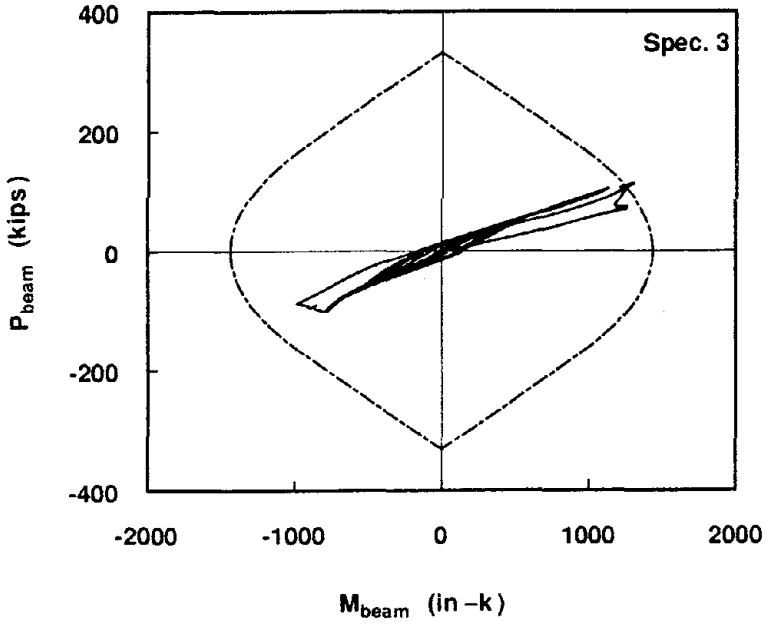

Fig. 4.20 Specimen 3 - Moment vs. Axial Force in Beam

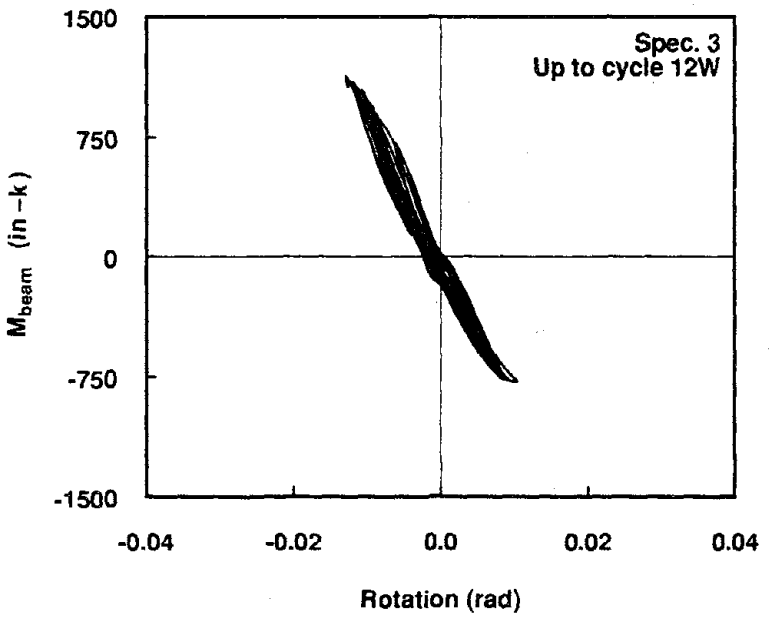

Fig. 4.21 Specimen 3 - Moment vs. Rotation at End of Beam

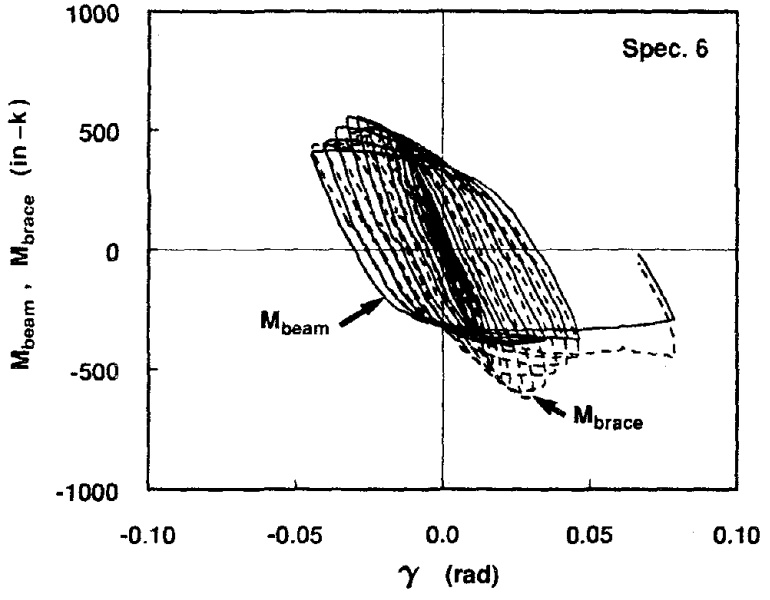

Fig. 4.22 Specimen 6 - Beam and Brace Bending Moments

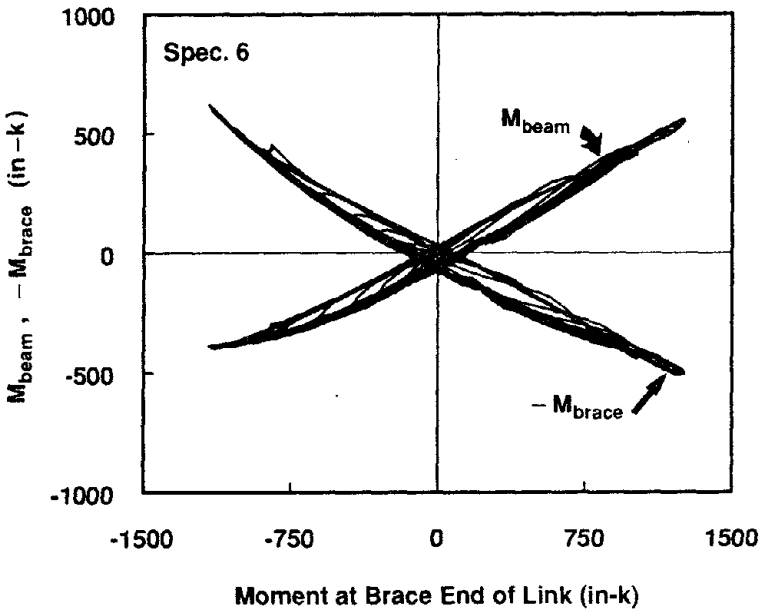

Fig. 4.23 Specimen 6 - Distribution of Link End Moment to Beam and Brace

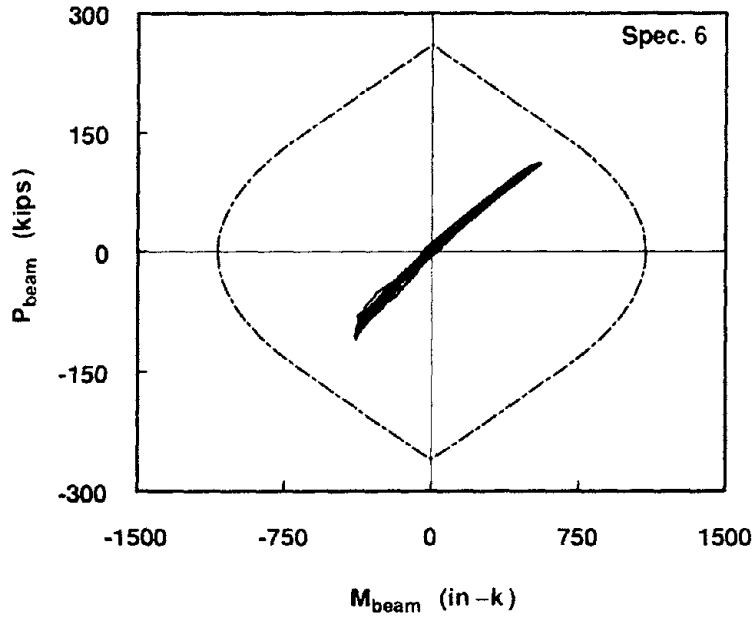

Fig. 4.24 Specimen 6 - Moment vs. Axial Force in Beam

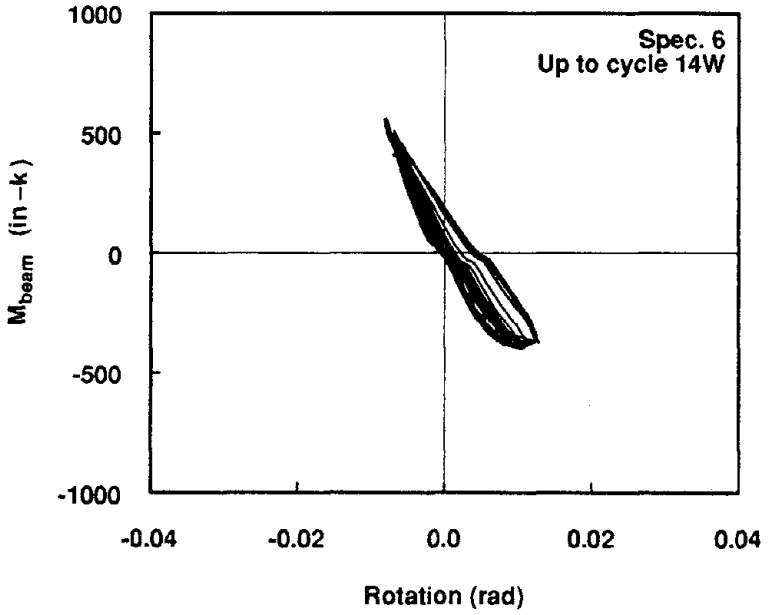

Fig. 4.25 Specimen 6 - Moment vs. Rotation at End of Beam

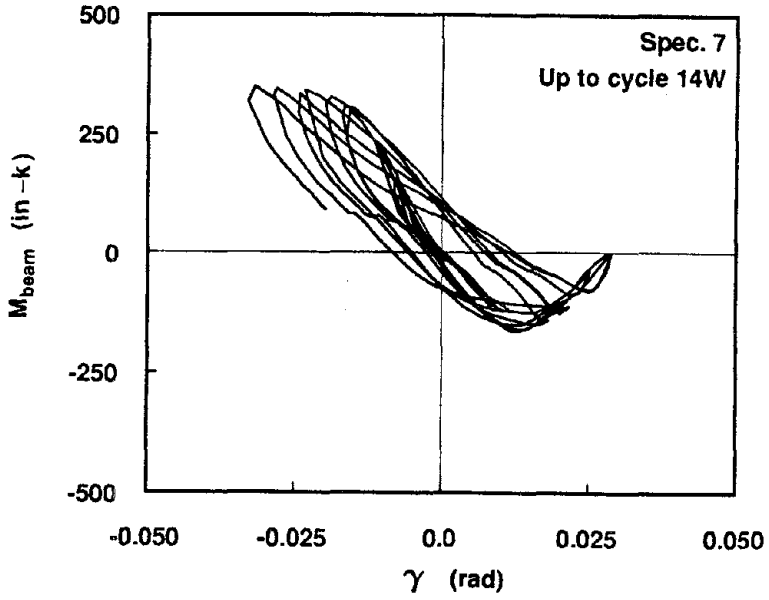

Fig. 4.26 Specimen 7 - Beam Bending Moment

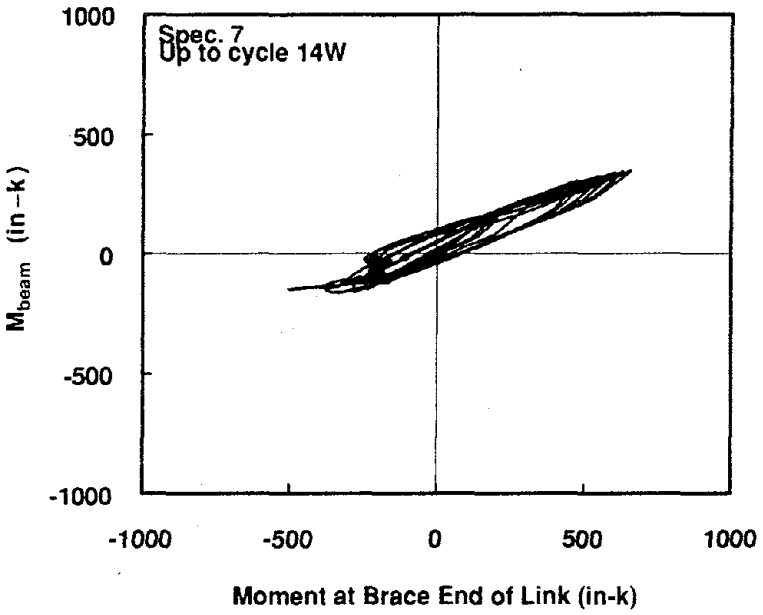

Fig. 4.27 Specimen 7 - Distribution of Link End Moment to Beam

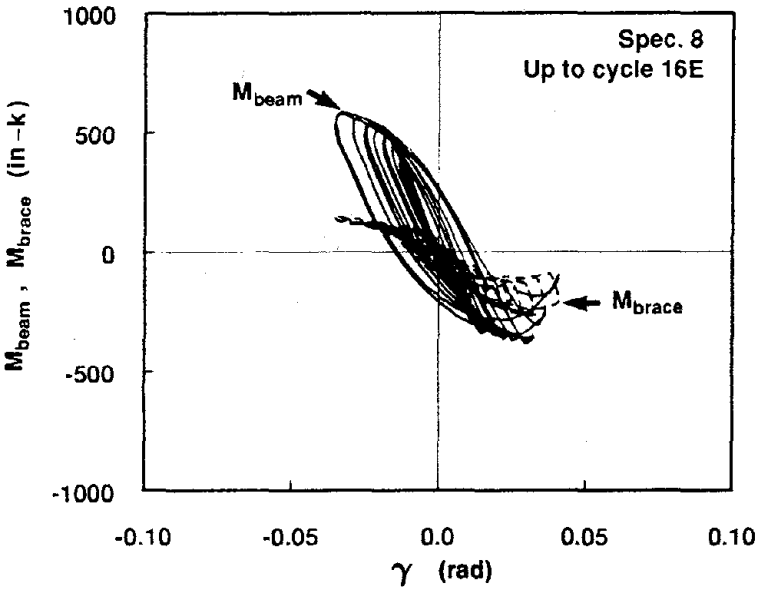

Fig. 4.28 Specimen 8 - Beam and Brace Bending Moments

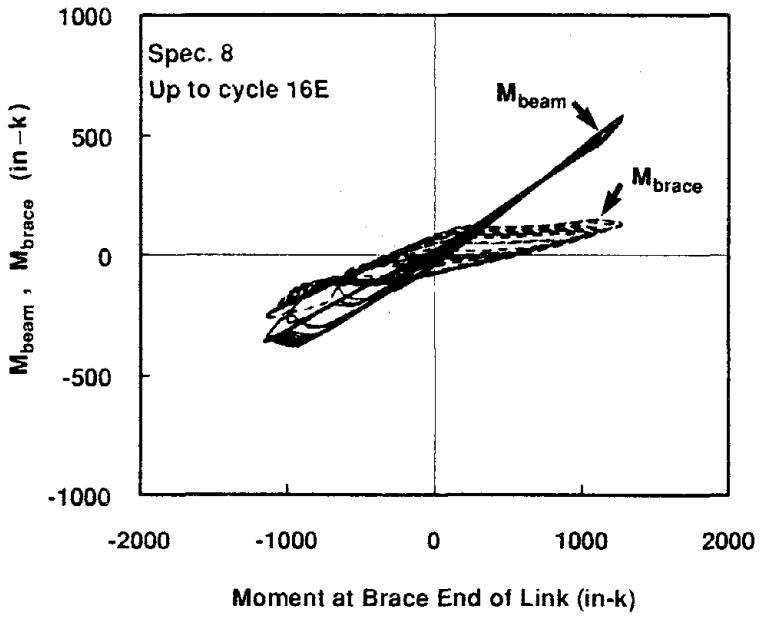

Fig. 4.29 Specimen 8 - Distribution of Link End Moment to Beam and Brace

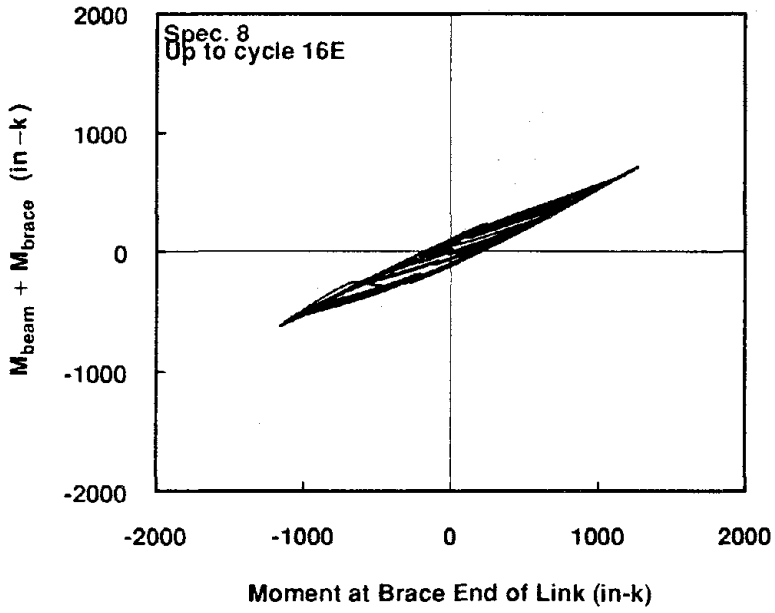

Fig. 4.30 Specimen 8 - Link End Moment vs. Sum of Beam and Brace Moments

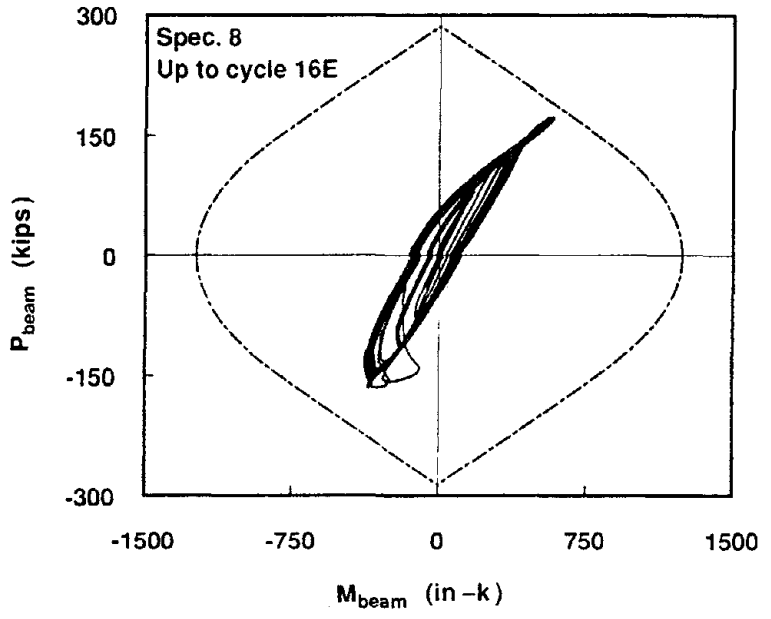

Fig. 4.31 Specimen 8 - Moment vs. Axial Force in Beam

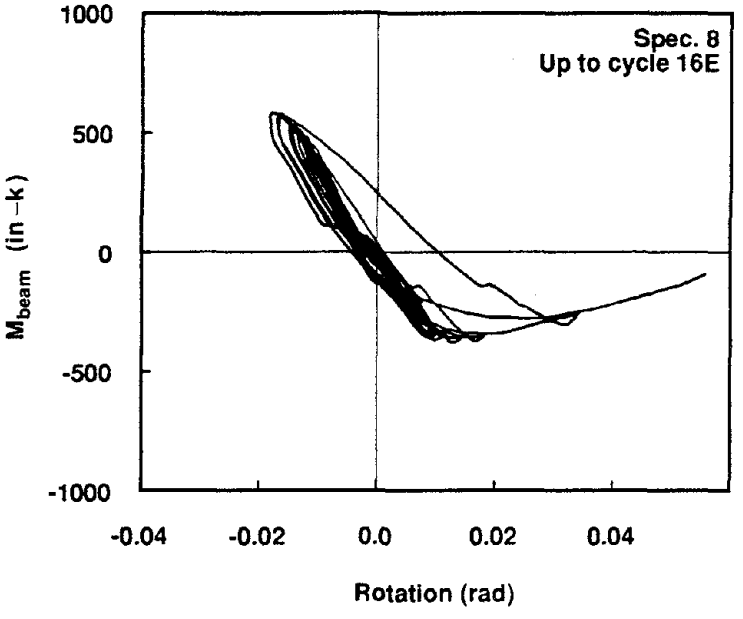

Fig. 4.32 Specimen 8 - Moment vs. Rotation at End of Beam

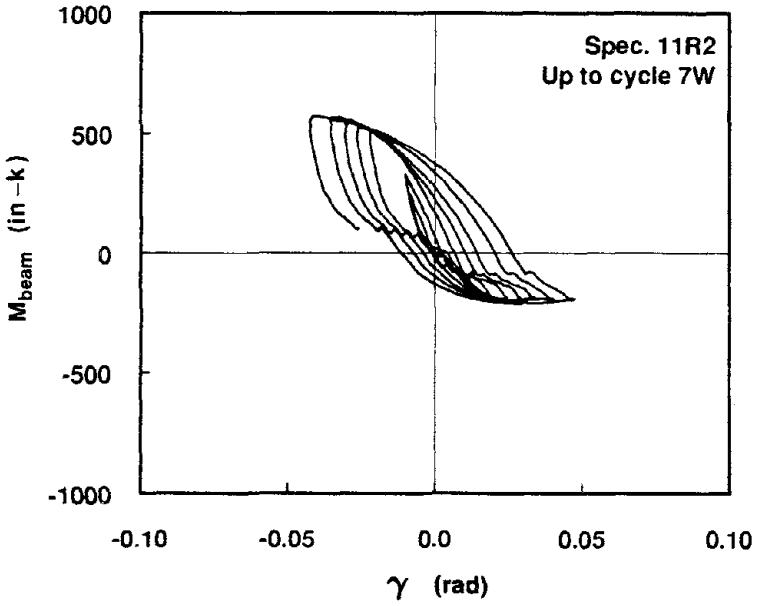

Fig. 4.33 Specimen 11R2 - Beam Bending Moment

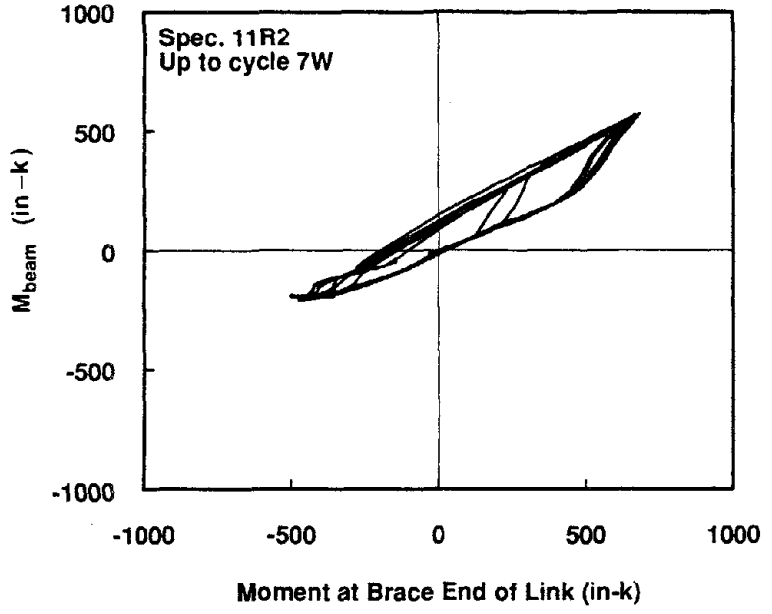

Fig. 4.34 Specimen 11R2 - Distribution of Link End Moment to Beam

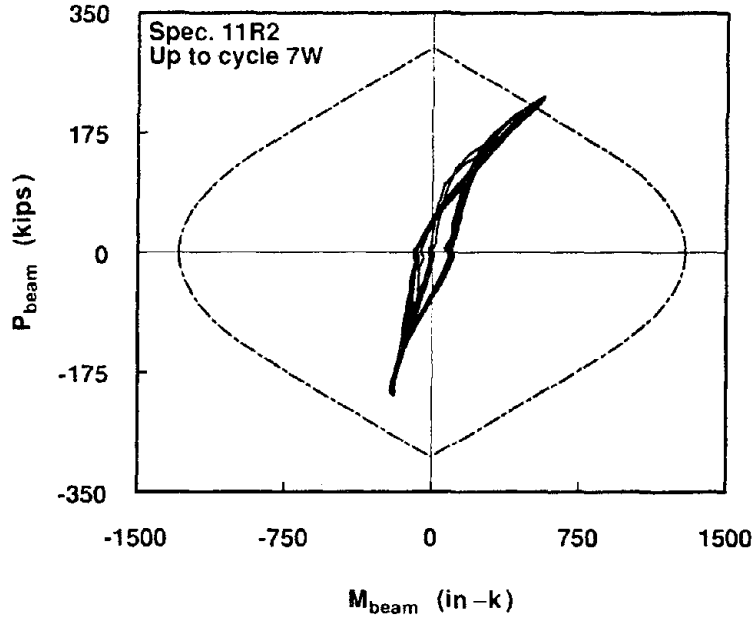

Fig. 4.35 Specimen 11R2 - Moment vs. Axial Force in Beam

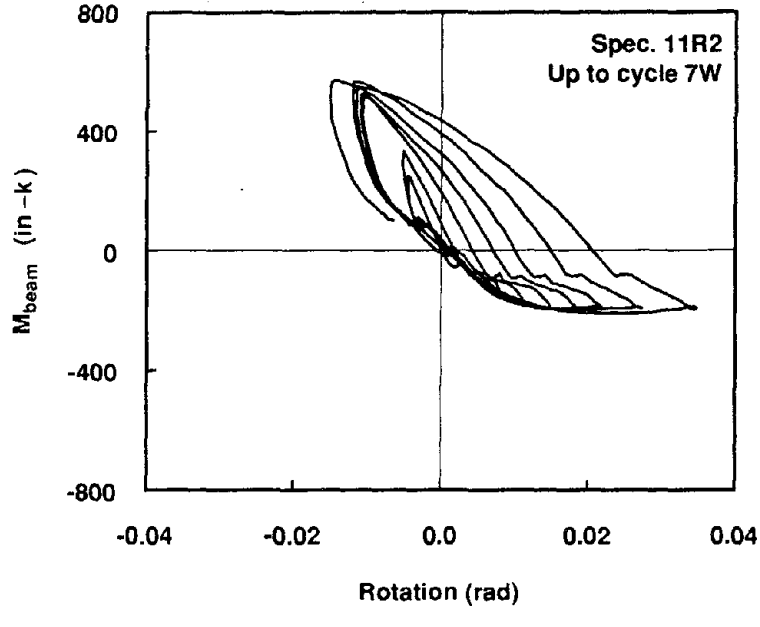

Fig. 4.36 Specimen 11R2 - Moment vs. Rotation at End of Beam

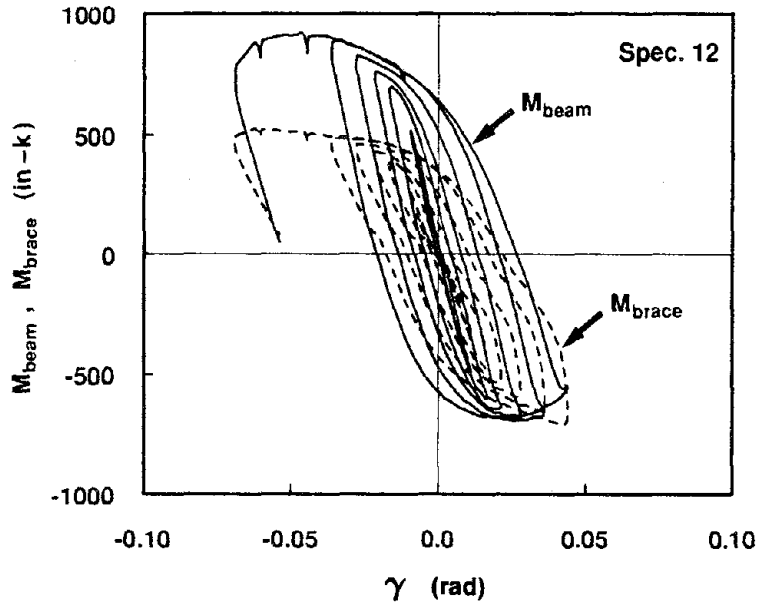

Fig. 4.37 Specimen 12 - Beam and Brace Bending Moments

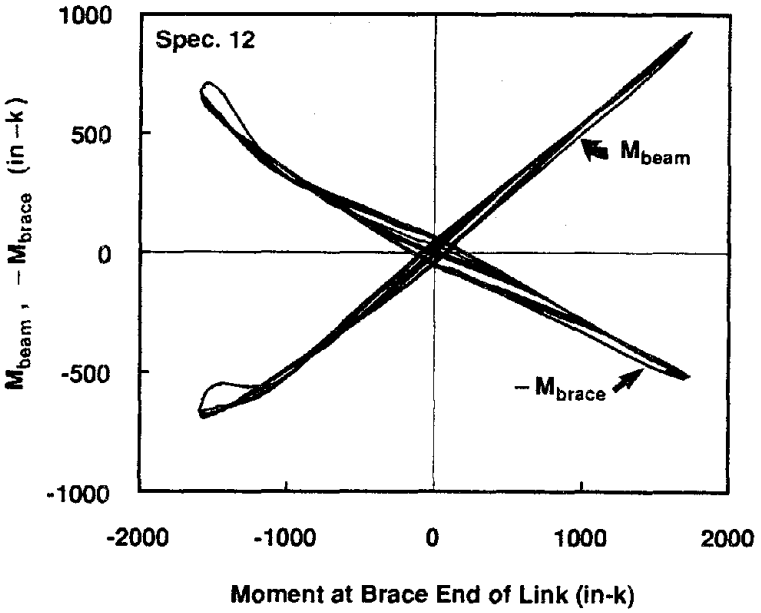

Fig. 4.38 Specimen 12 - Distribution of Link End Moment to Beam and Brace

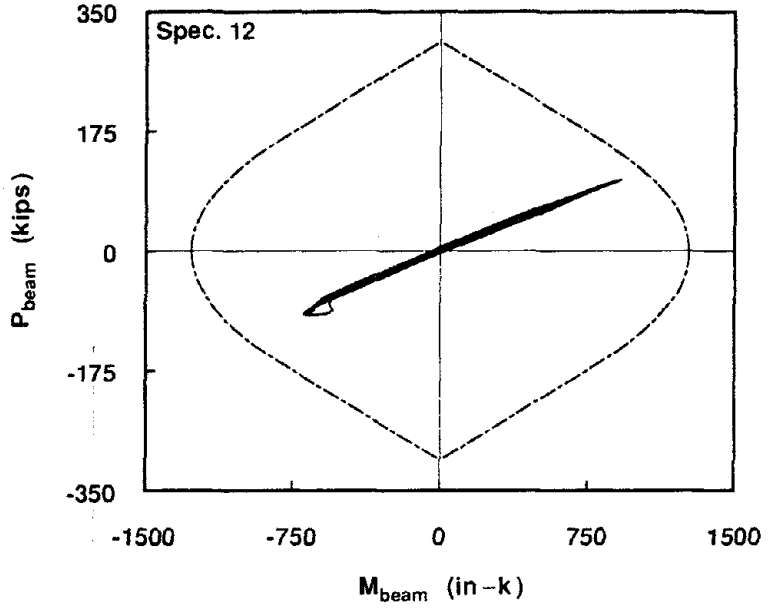

Fig. 4.39 Specimen 12 - Moment vs. Axial Force in Beam

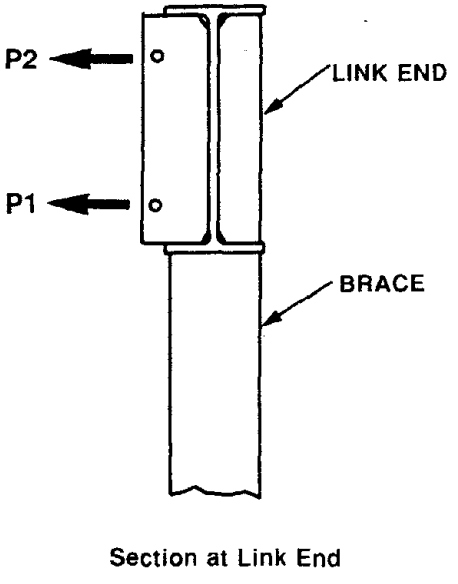

Fig. 4.40 Definition of Out-of-Plane Force Resultants at the Link End Lateral Support

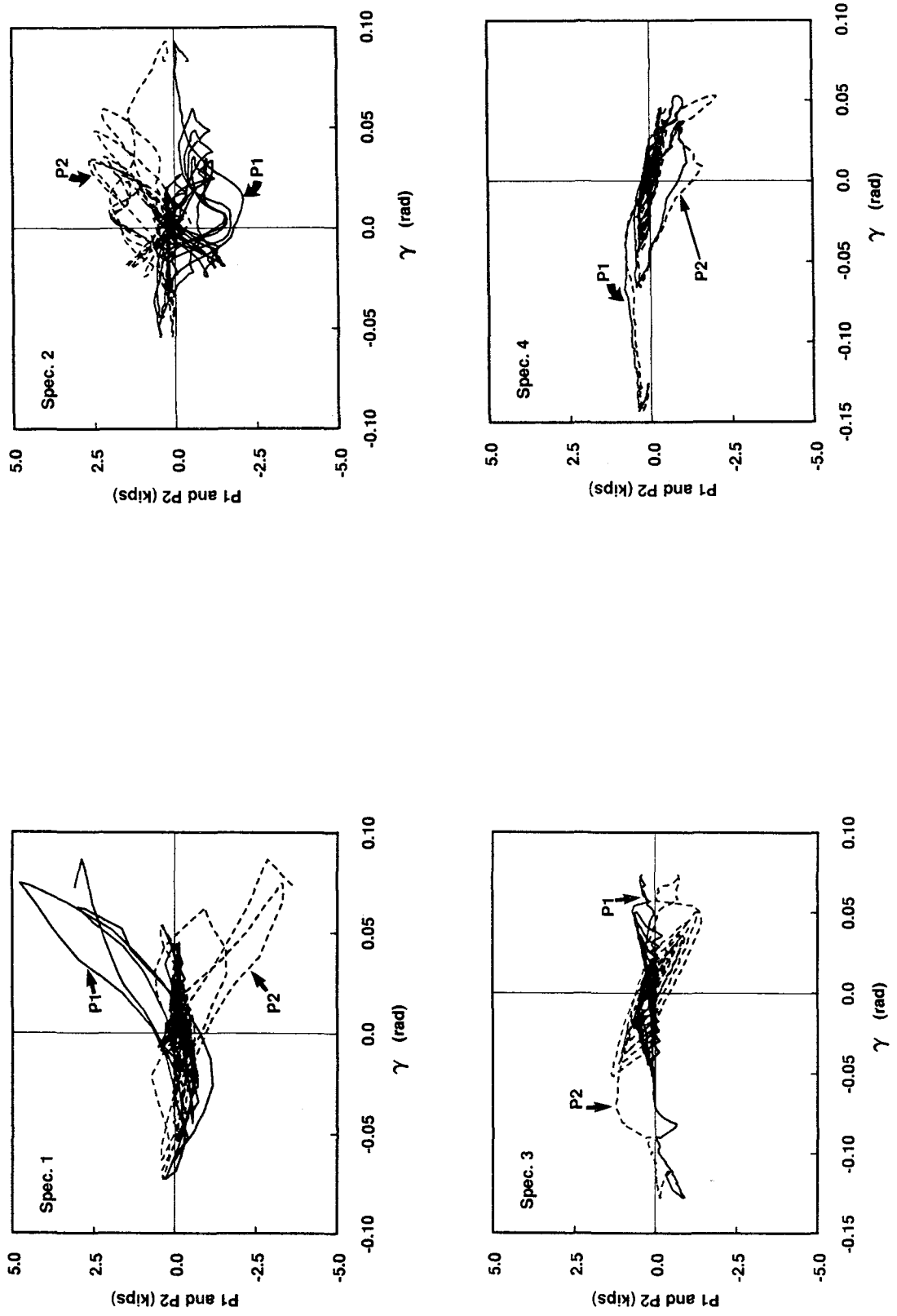

Fig. 4.41 Out-of-Plane Forces at the Link End Lateral Support

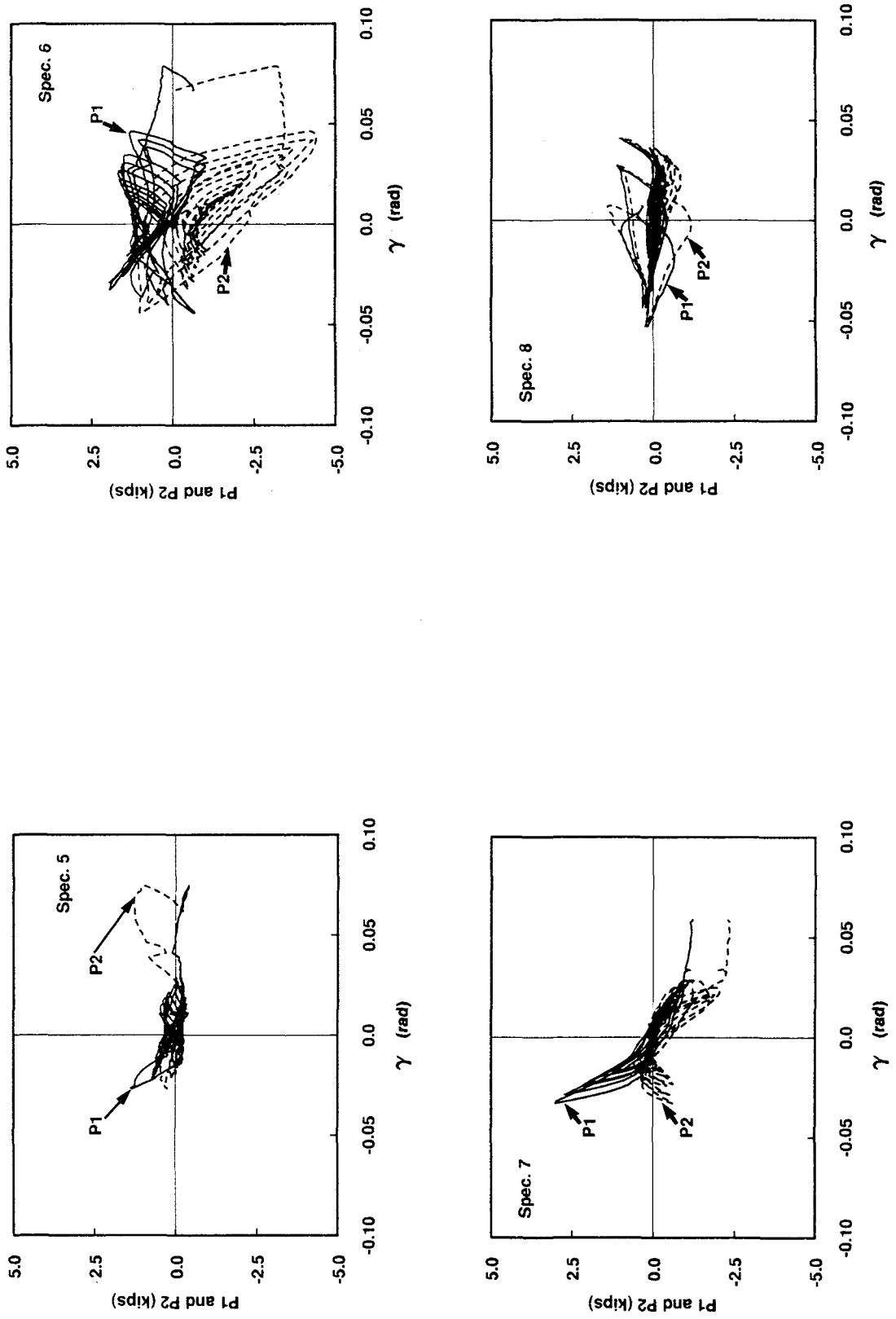

Fig. 4.41 Out-of-Plane Forces at the Link End Lateral Support (cont.)

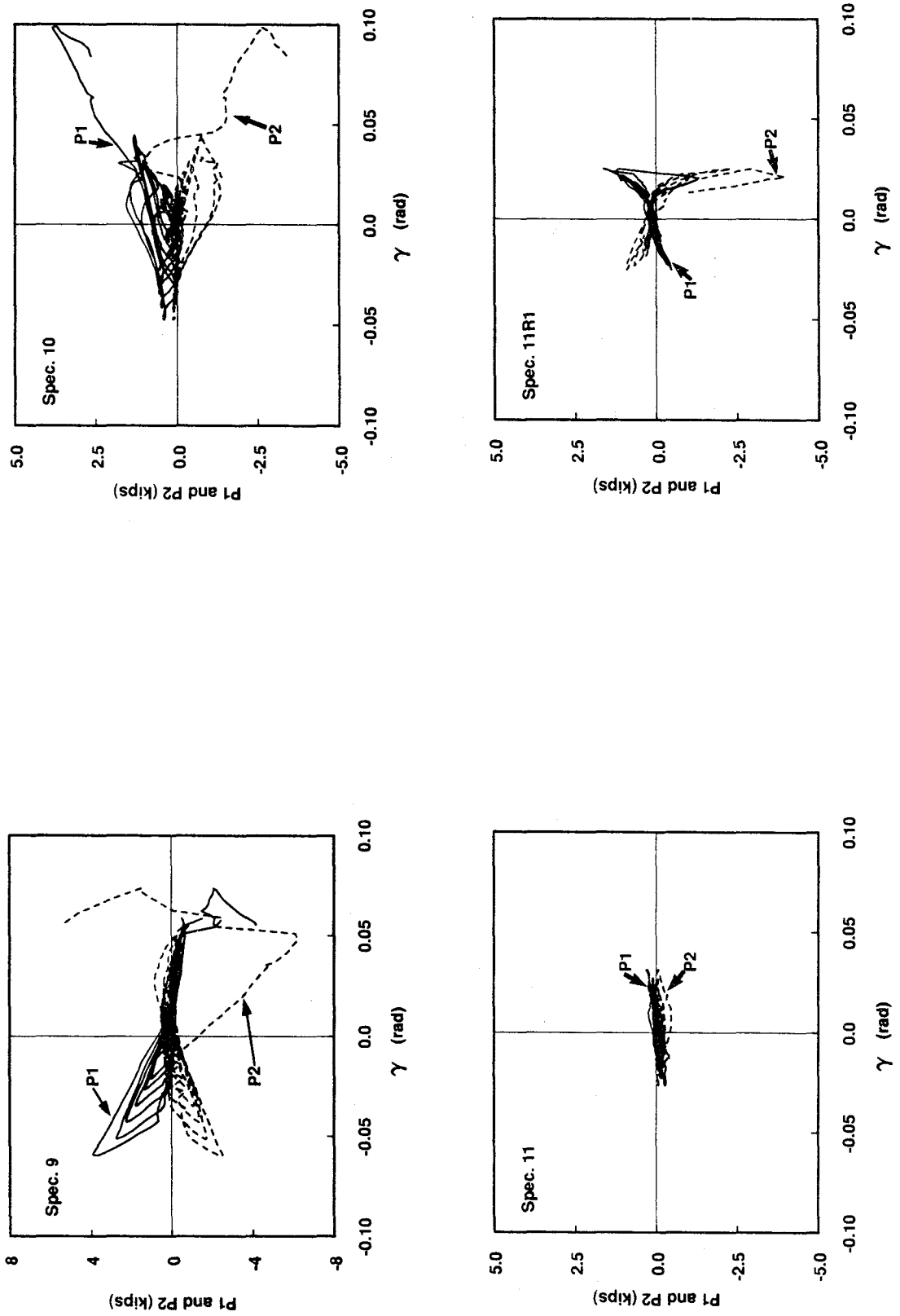

Fig. 4.41 Out-of-Plane Forces at the Link End Lateral Support (cont.)

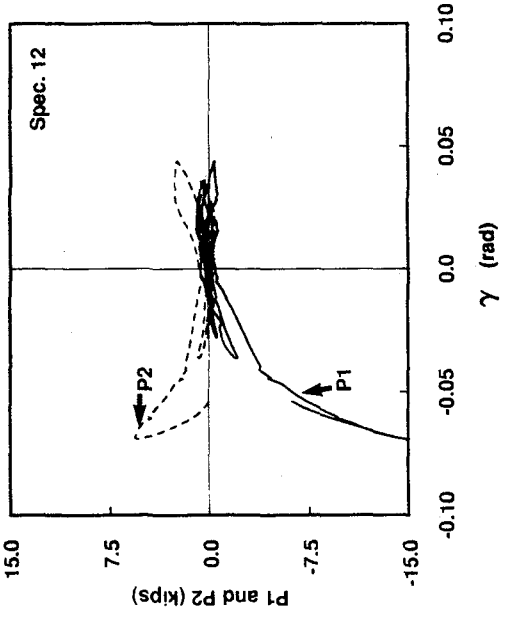

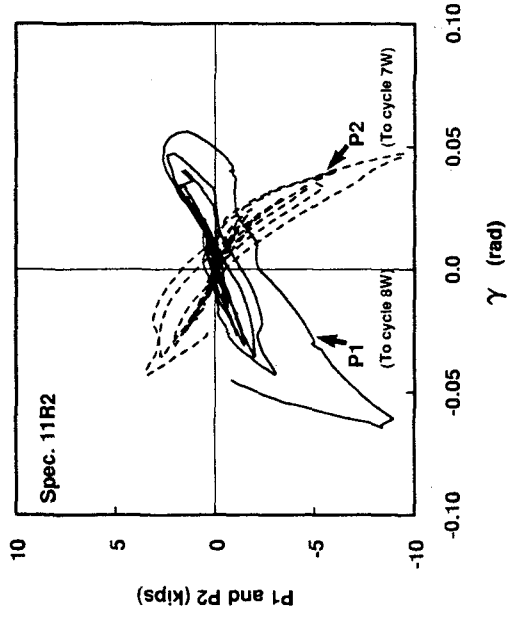

Fig. 4.41 Out-of-Plane Forces at the Link End Lateral Support (cont.)

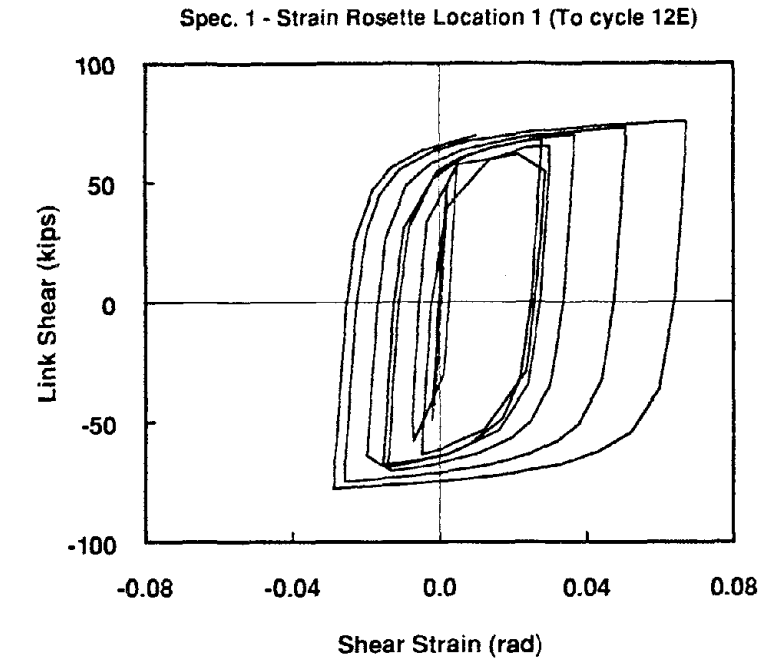

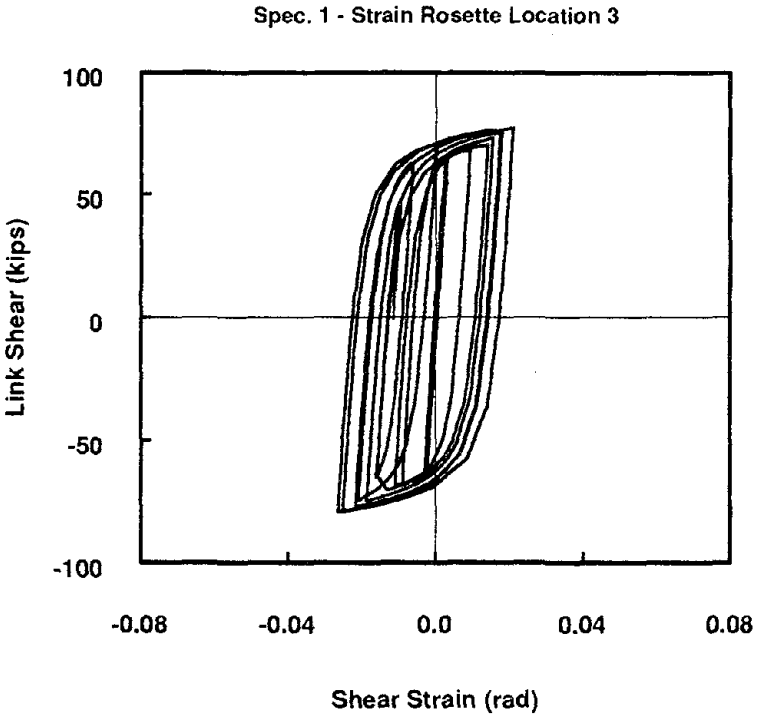

Fig. 4.42 Specimen 1 - Shear Strain Measurements from Rosette Location Nos. 1 and 3

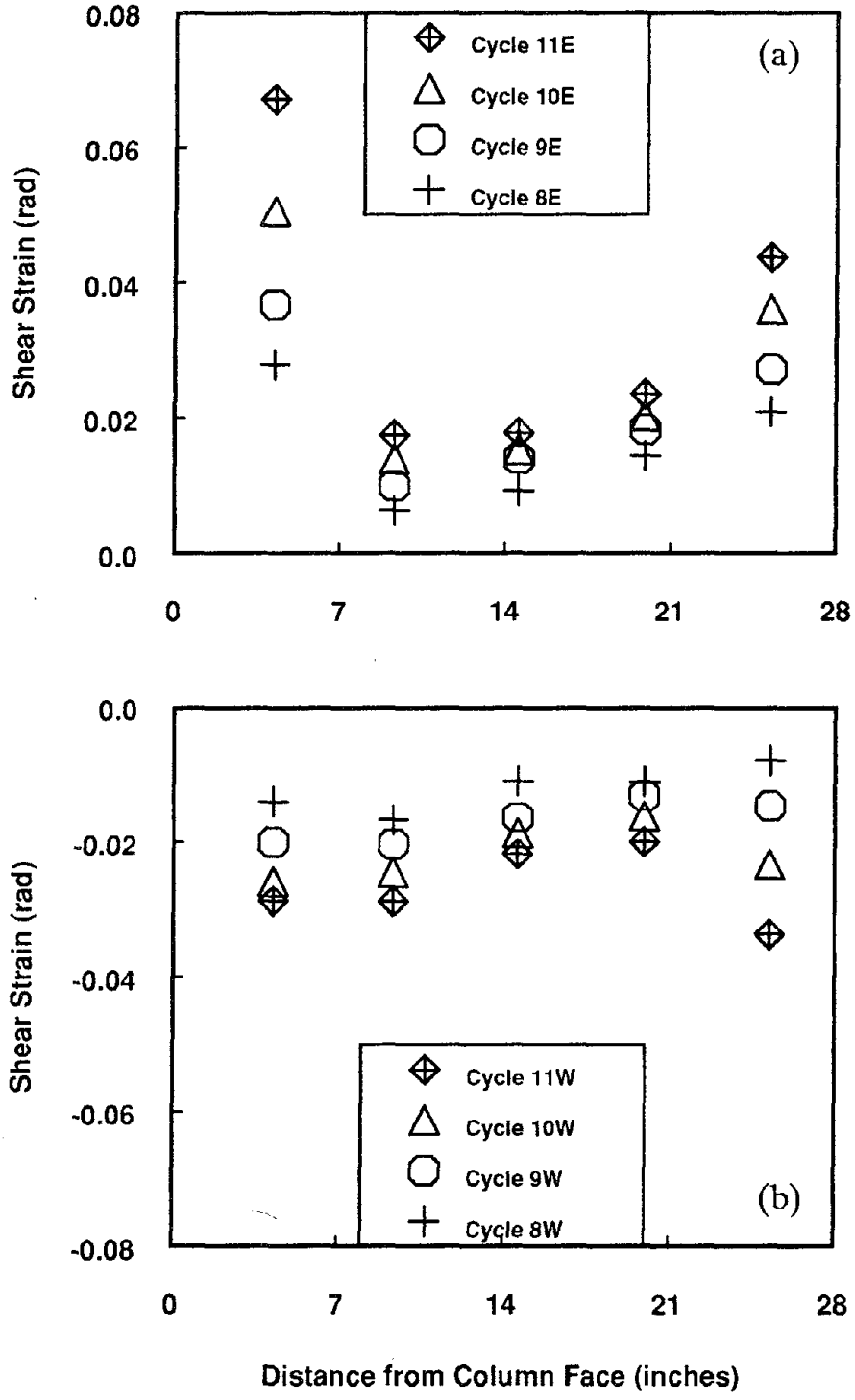

Fig. 4.43 Specimen 1 - Shear Strain Measurements Along Link Centerline at the Peak of Selected Load Cycles
(a) East Load Cycles
(b) West Load Cycles

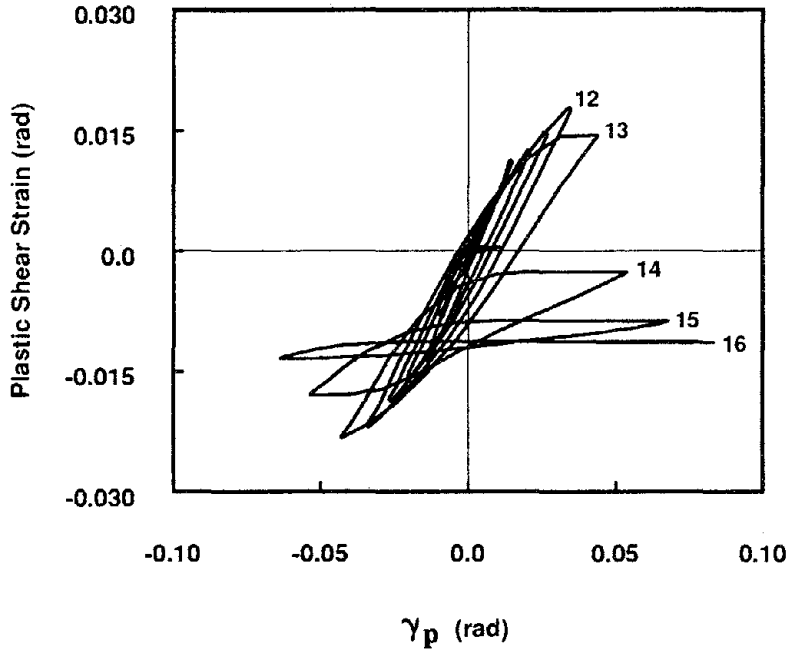

Fig. 4.44 Specimen 1 - Plastic Shear Strain at Rosette Location No. 3

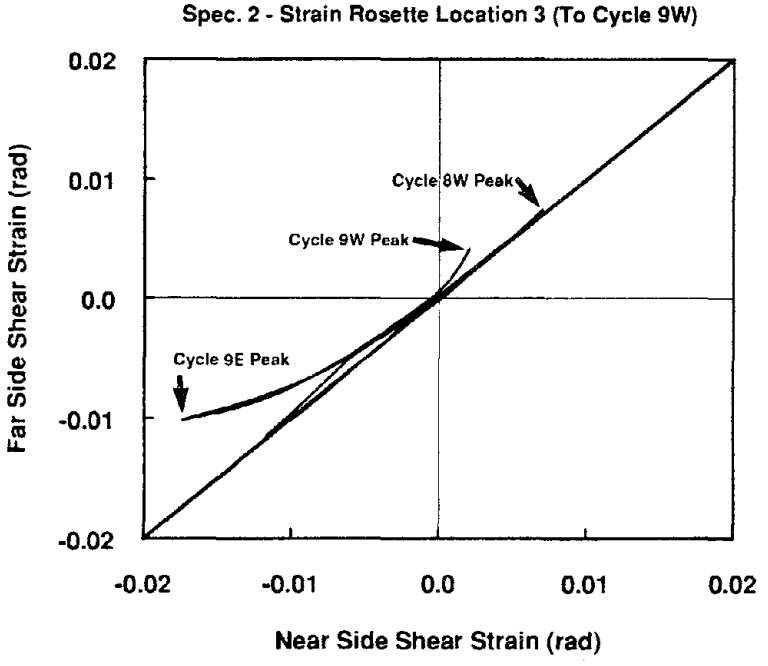

Fig. 4.45 Specimen 2 - Shear Strain Measured on Opposite Sides of the Link Web at Rosette Location No. 3 (11 inches from column face)

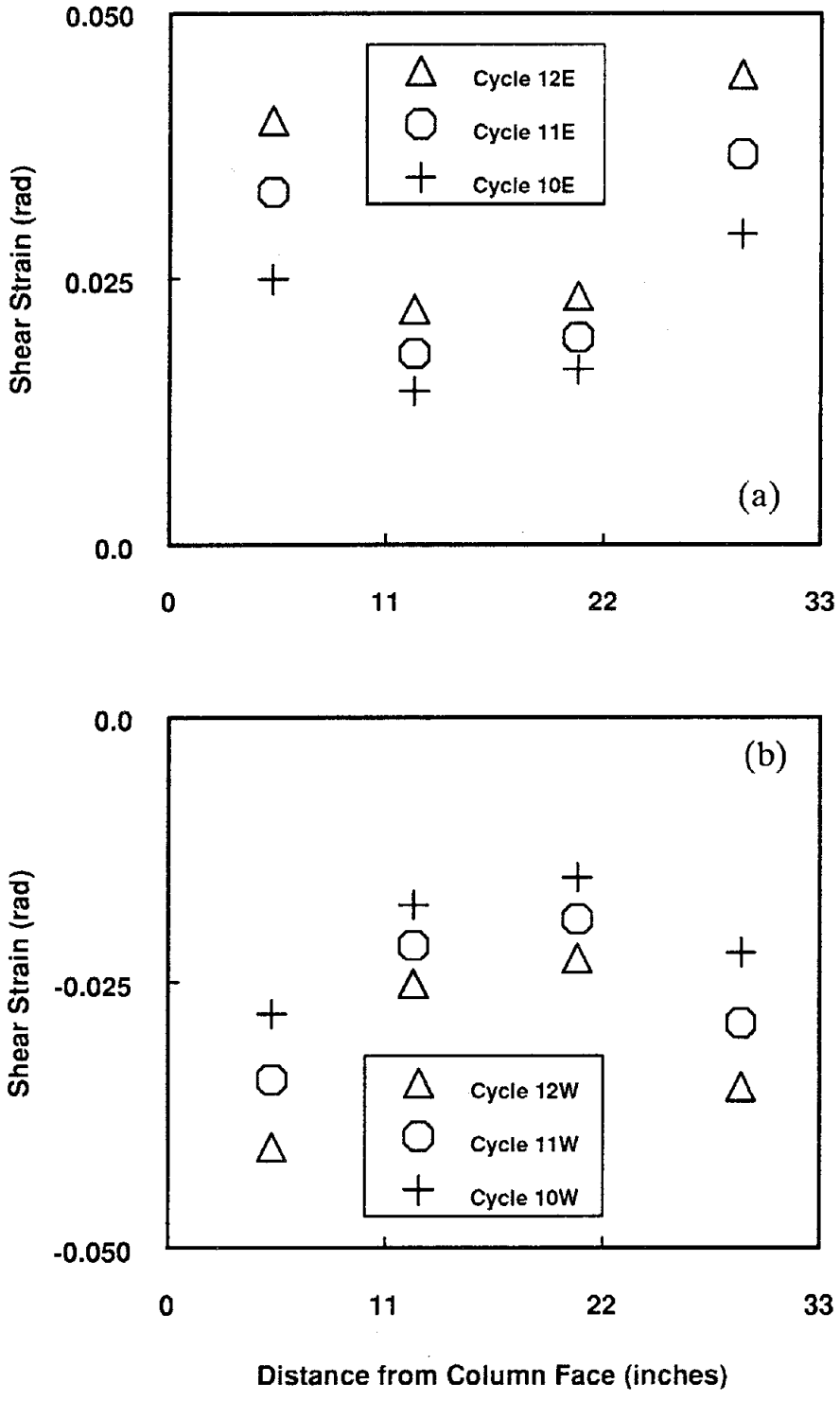

Fig. 4.46 Specimen 3 - Shear Strain Measurements Along Link Centerline at the Peak of Selected Load Cycles
(a) East Load Cycles
(b) West Load Cycles

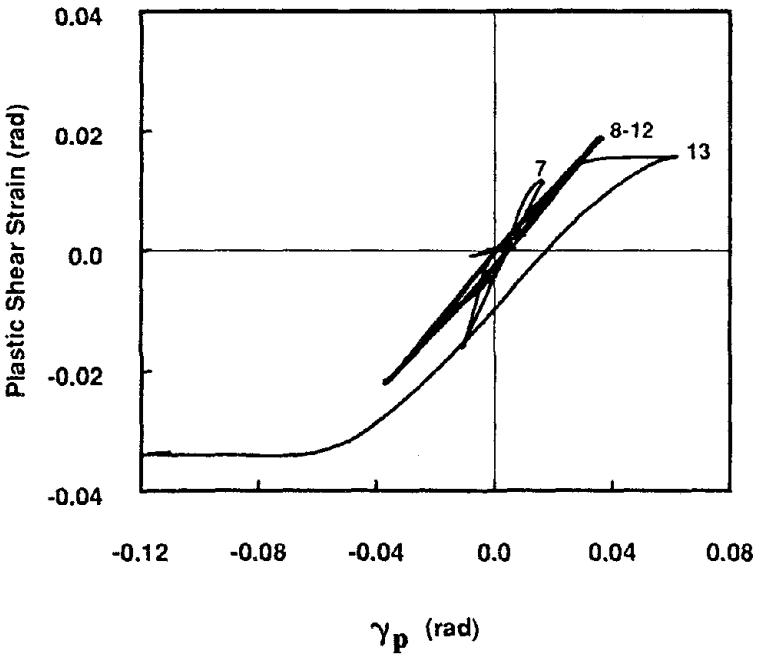

Fig. 4.47 Specimen 3 - Plastic Shear Strain at Rosette Location No. 2

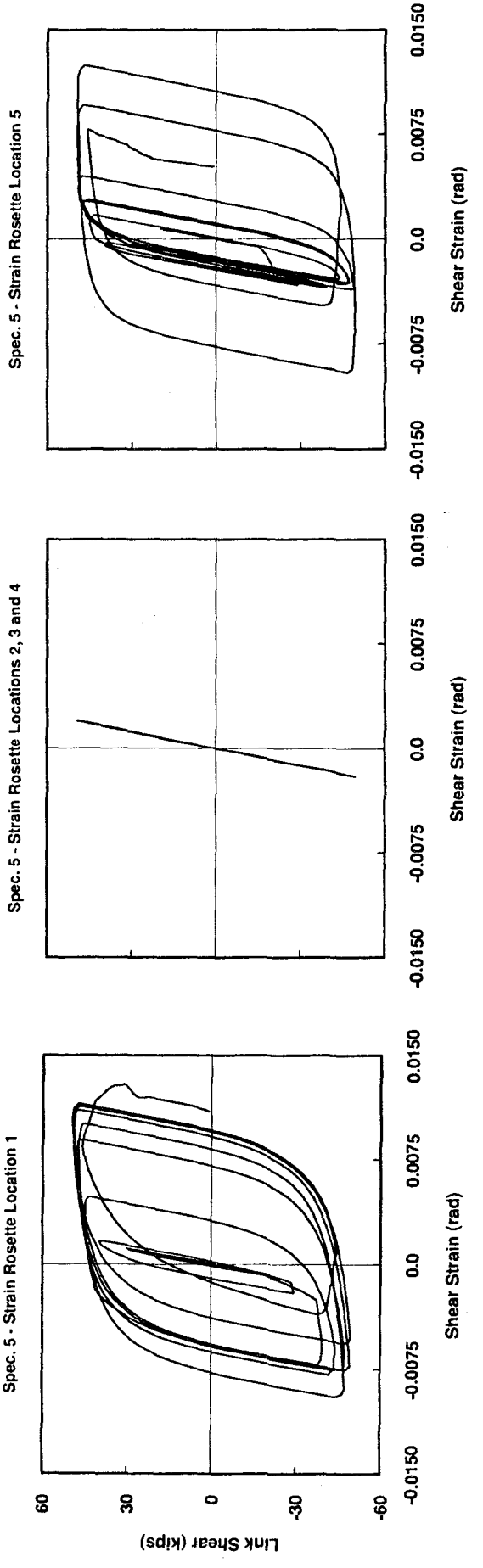

Fig. 4.48 Specimen 5 - Shear Strain Measurements from Rosette Location Nos. 1 to 5

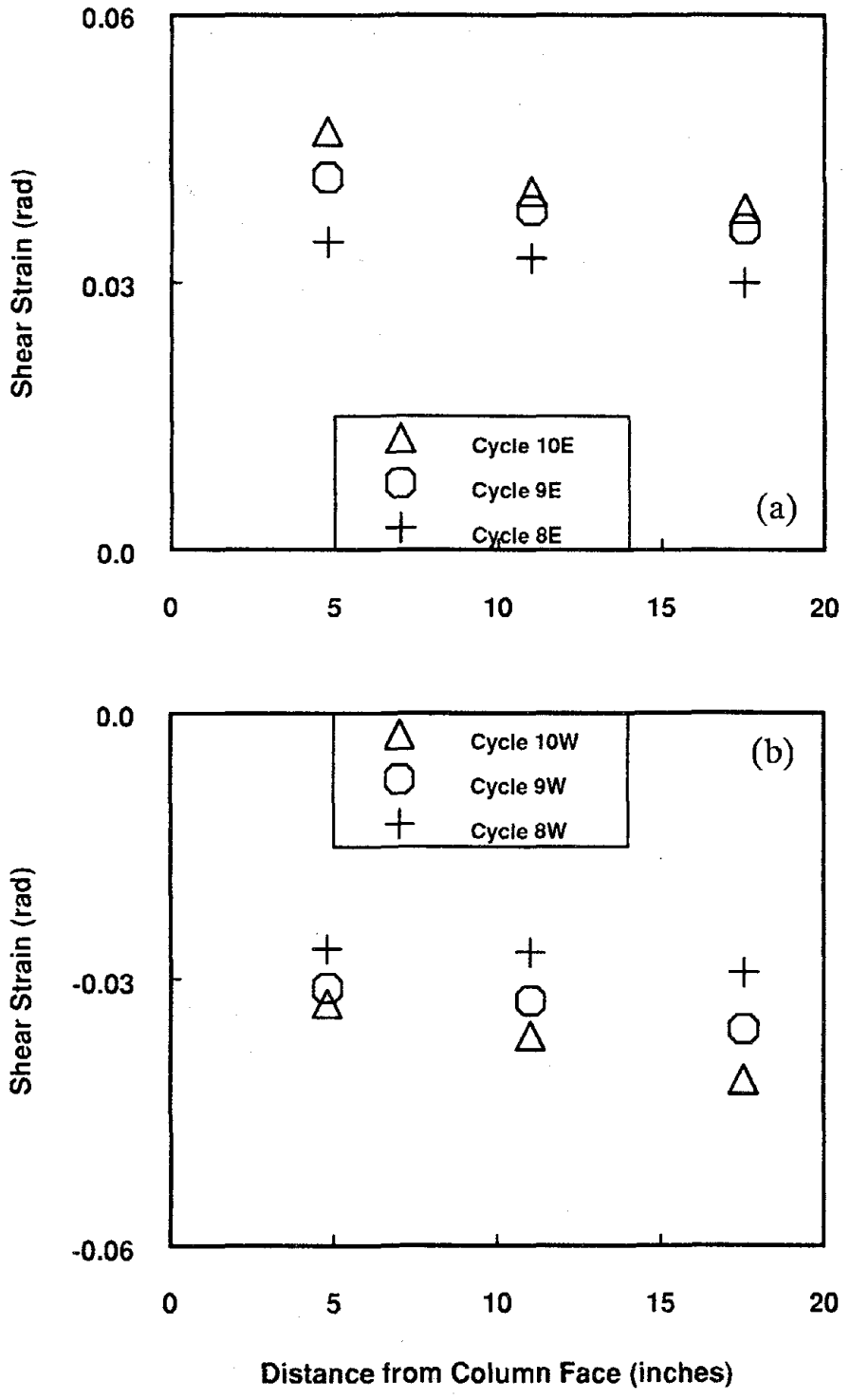

Fig. 4.49 Specimen 9 - Shear Strain Measurements Along Link Centerline at the Peak of Selected Load Cycles
(a) East Load Cycles
(b) West Load Cycles

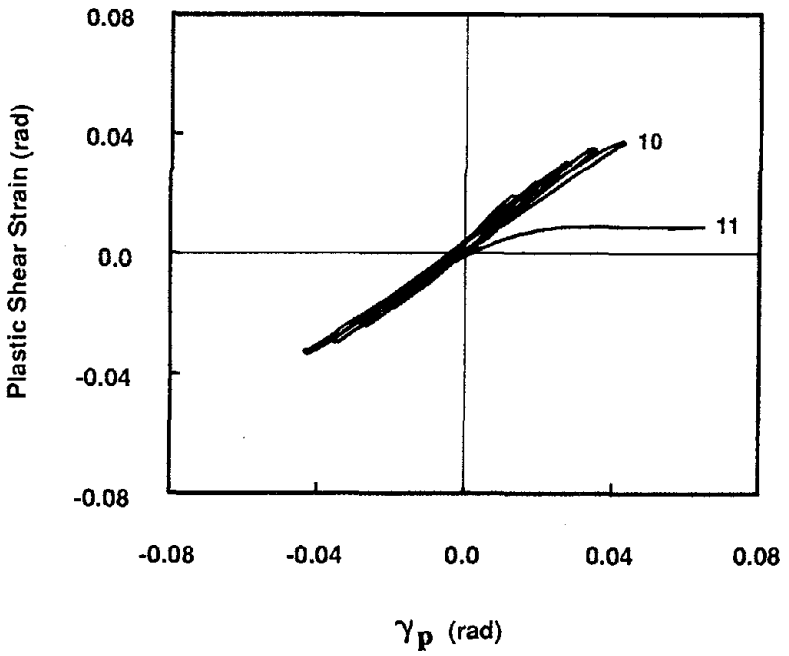

Fig. 4.50 Specimen 9 - Plastic Shear Strain at Rosette Location No. 2

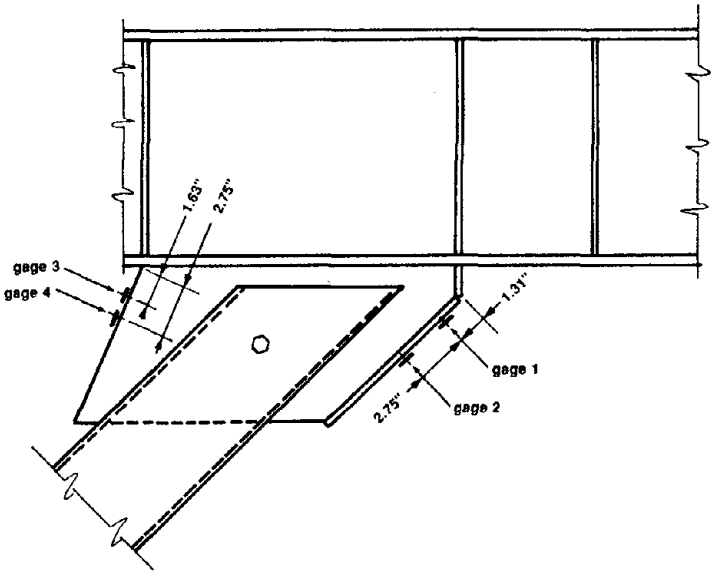

Fig. 4.51 Specimen 9 - Location of Strain Gages on Brace Connection

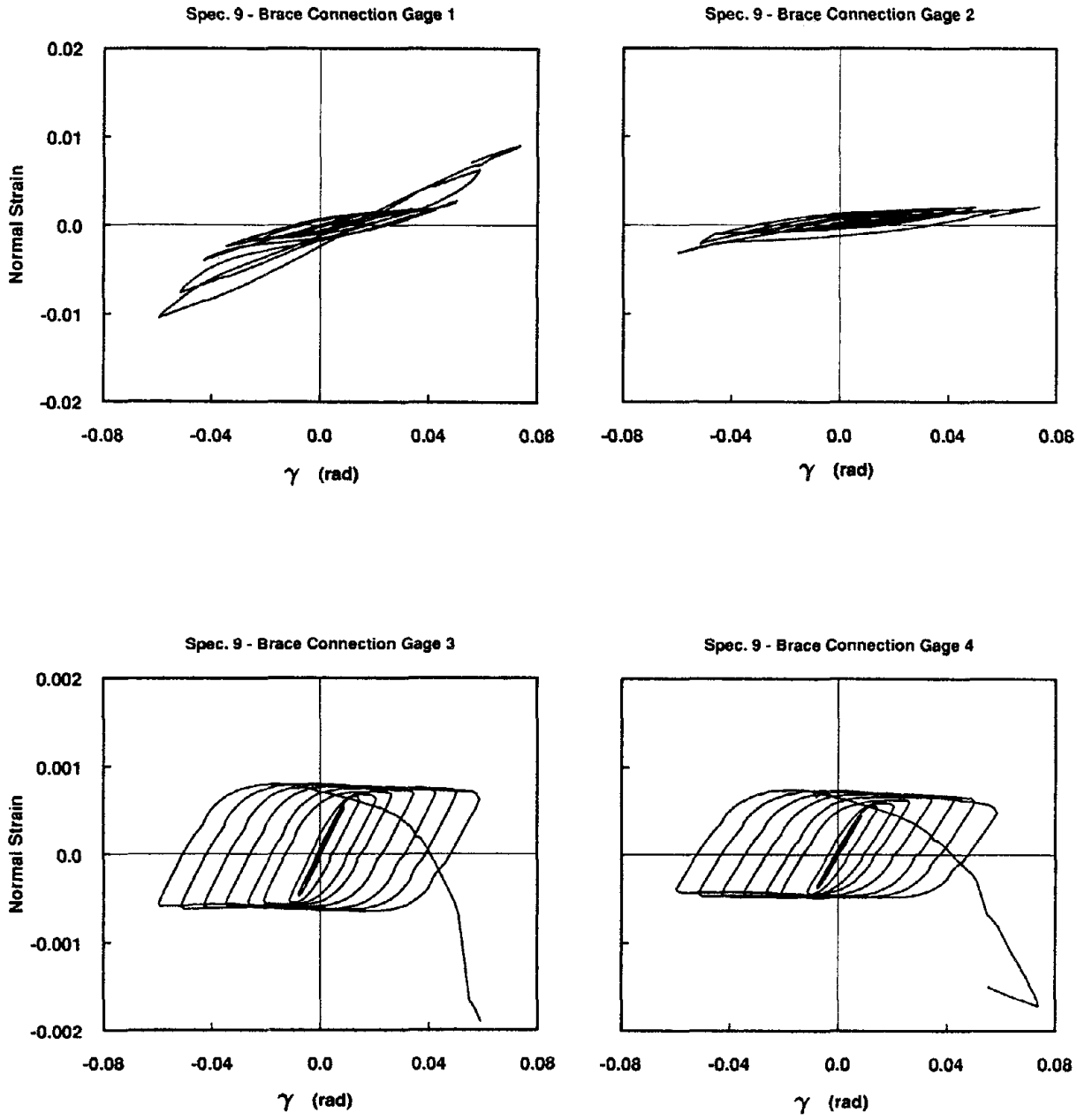

Fig. 4.52 Specimen 9 - Normal Strain Measurements from Gages on Brace Connection

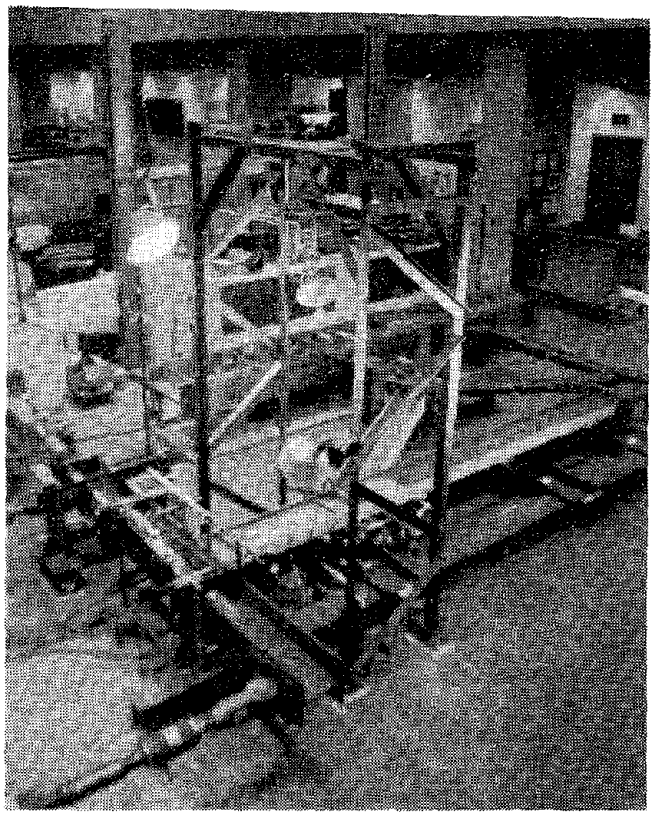

Fig. 5.1 View of Overall Test Setup with Photogrammetry Camera in Place

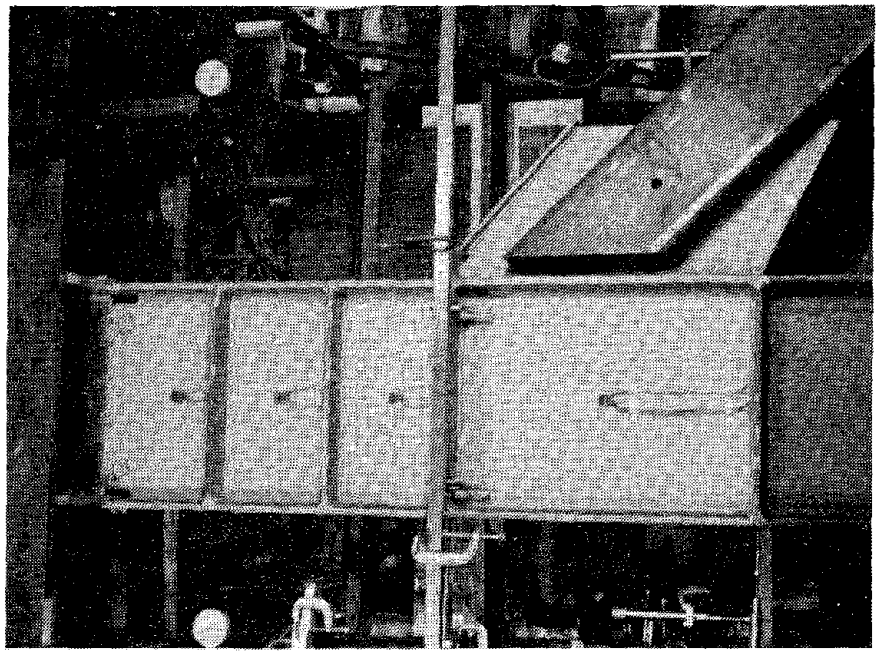

Fig. 5.2 Photogrammetric Grid on Specimen 9 in the Initial Undeformed Position

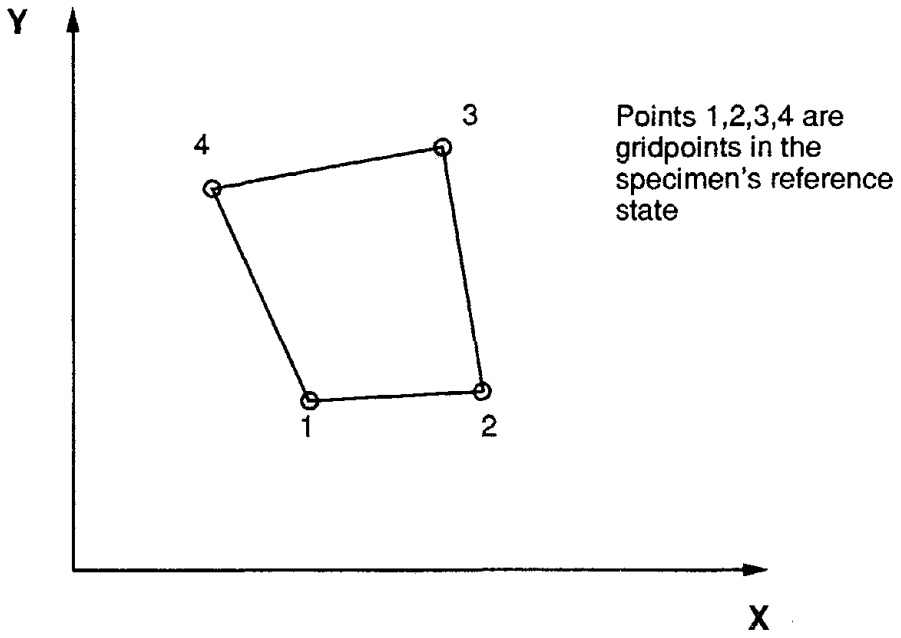

(a) Element in Specimen Coordinate System

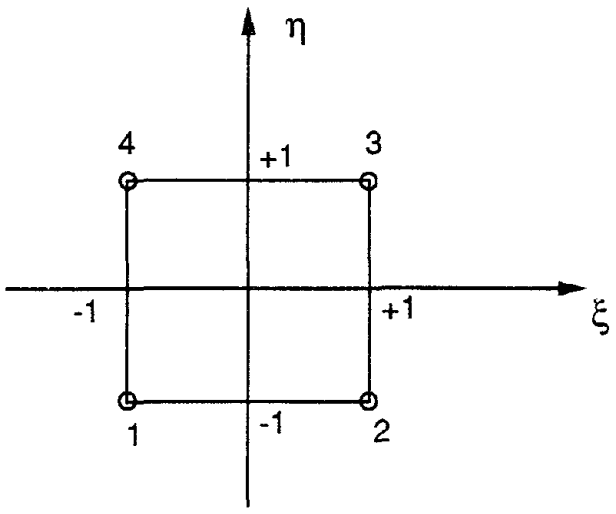

(b) Element in Normalized Coordinate System

Fig. 5.3 Typical "Element" for Use in Computing Shear Strains From Gridpoint Displacements

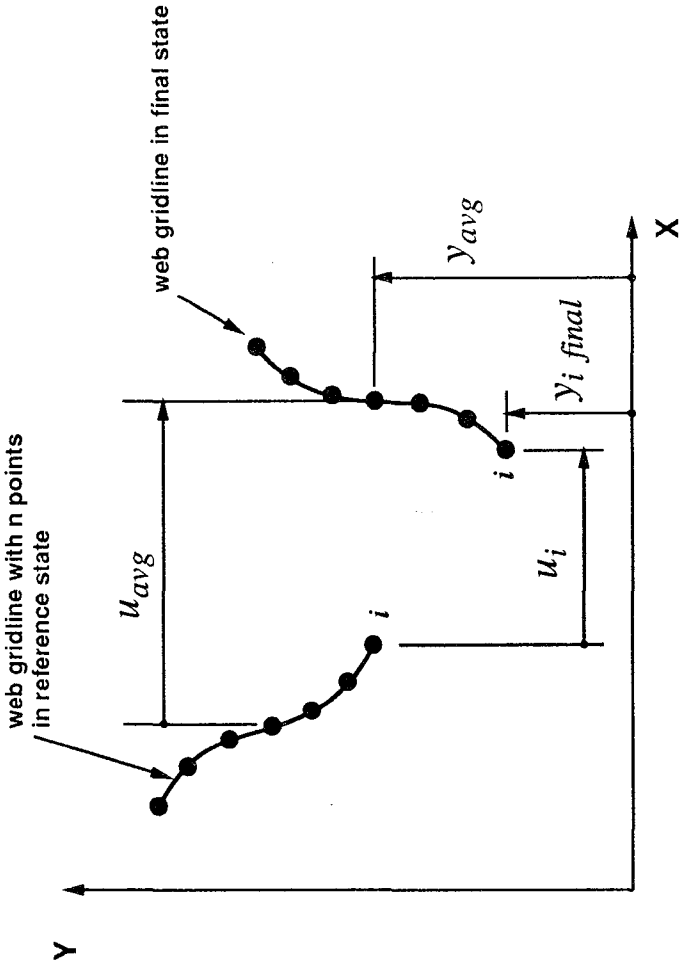

$$u_{avg} = \frac{1}{n}\sum_{i=1}^{n} u_i \qquad y_{avg} = \frac{1}{n}\sum_{i=1}^{n} y_{i\ final}$$

Fig. 5.4 Definition of Terms Used to Compute Average Rotation of Web Gridlines

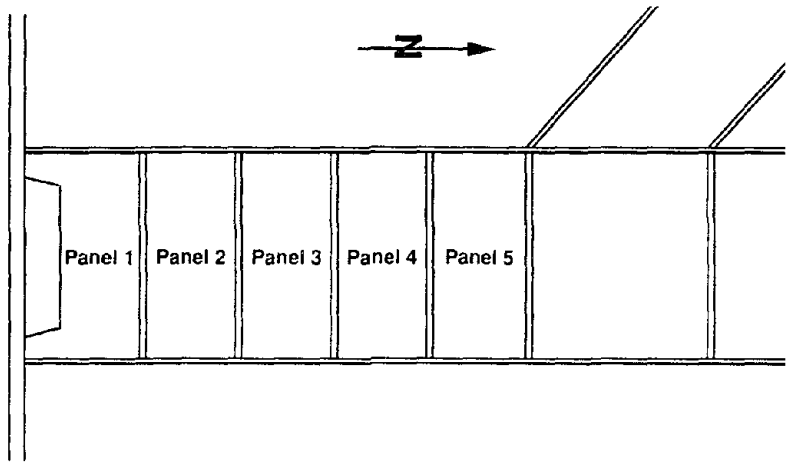

(a) Specimen 1

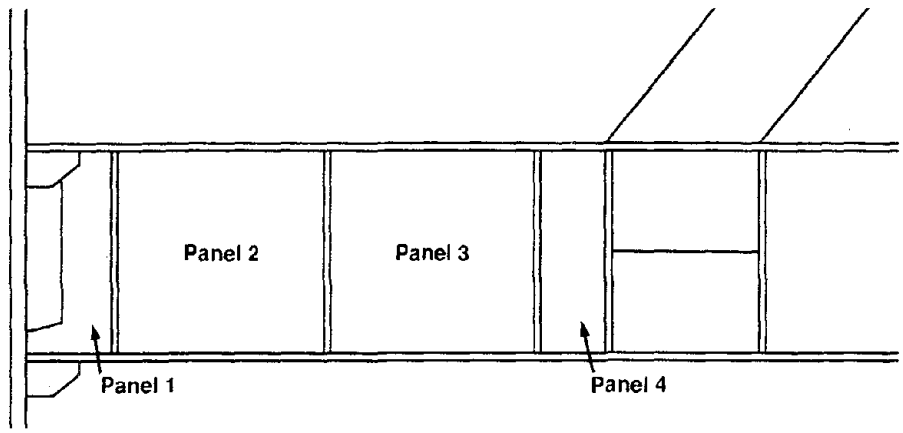

(b) Specimen 4

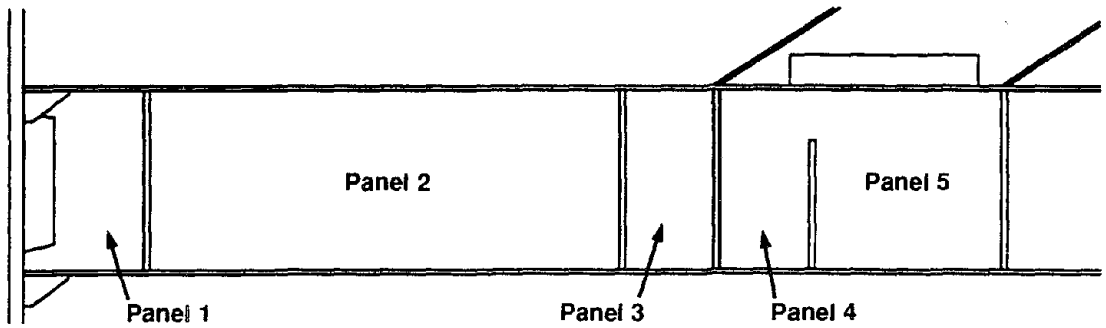

(c) Specimen 6

Fig. 5.5 Panel Designations for Test Specimens

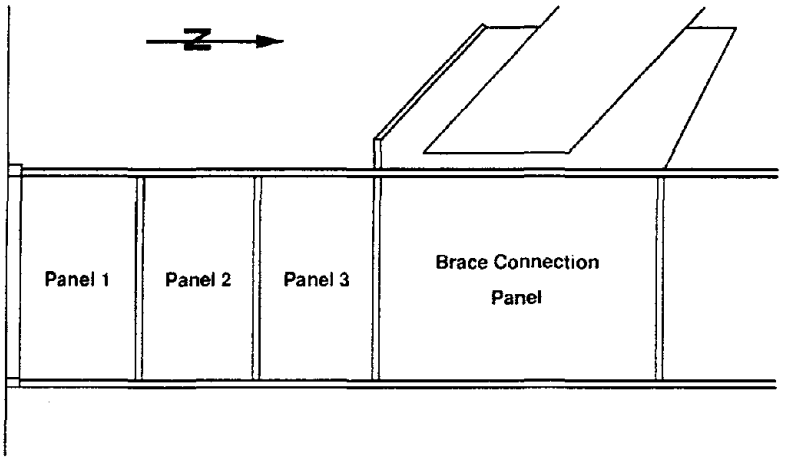

(d) Specimen 9

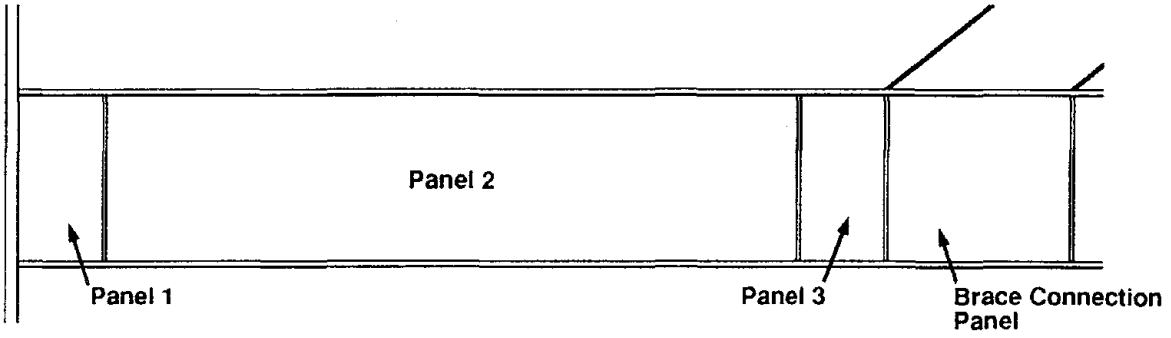

(e) Specimen 12

Fig. 5.5 Panel Designations for Test Specimens (cont)

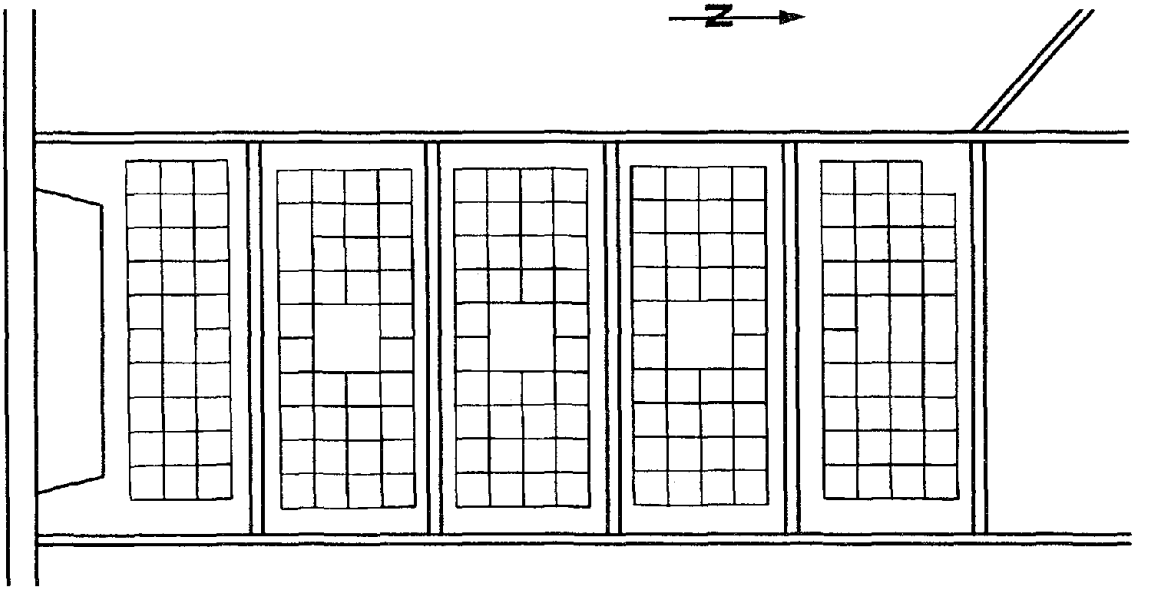

Fig. 5.6 Specimen 1 - Undeformed Gridlines

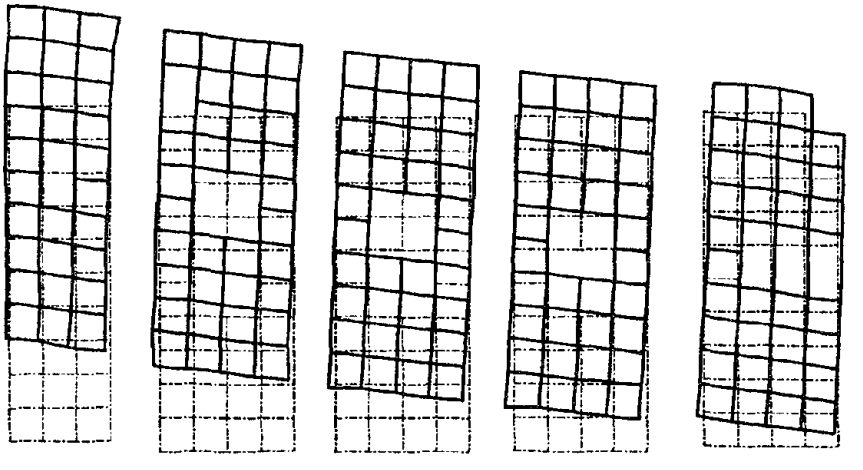

(a) Reference State: Unloaded Specimen at Start of Test
Final State: Peak Deformation at End of Cycle 4W
(Displacements Amplified 5X)

Fig. 5.7 Specimen 1 - Deformed Gridlines

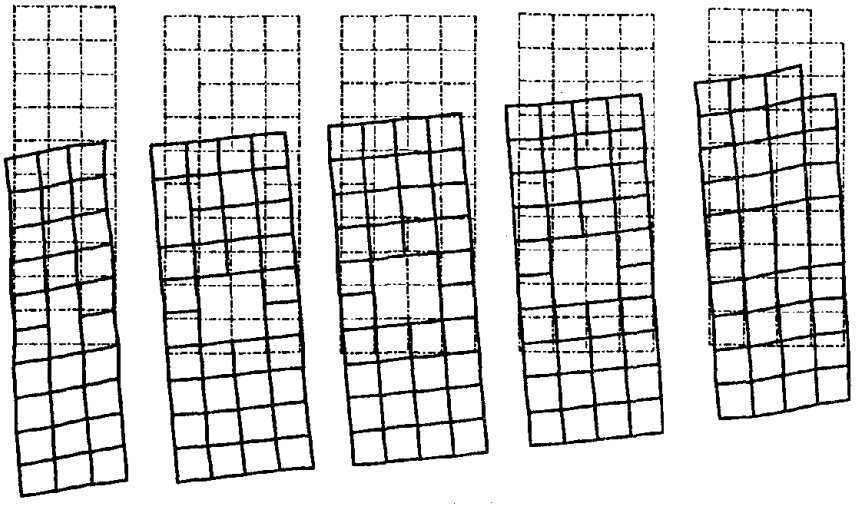

(b) Reference State: Unloaded Specimen at Start of Cycle 7E
Final State: Peak Deformation at End of Cycle 7E
(Displacements Amplified 5X)

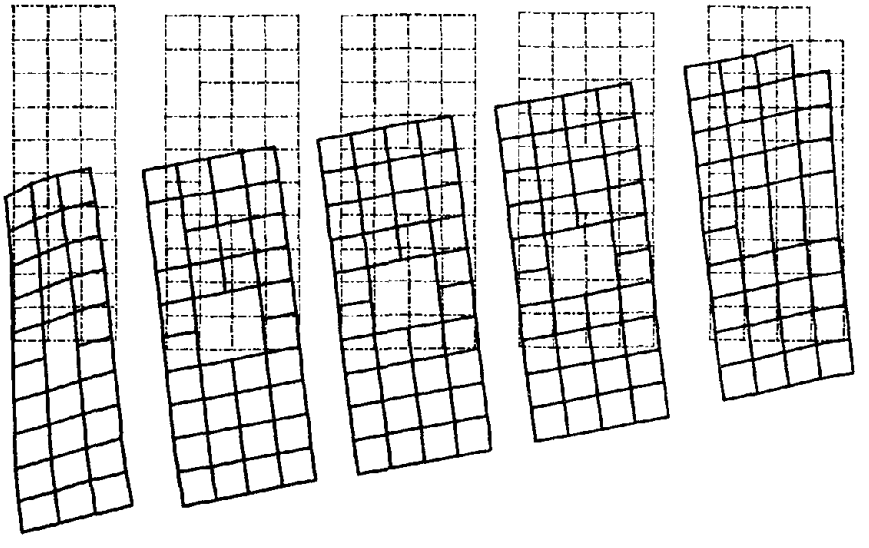

(c) Reference State: Unloaded Specimen at Start of Cycle 13E
Final State: Peak Deformation at End of Cycle 13E
(Displacements Amplified 2X)

Fig. 5.7 Specimen 1 - Deformed Gridlines (cont)

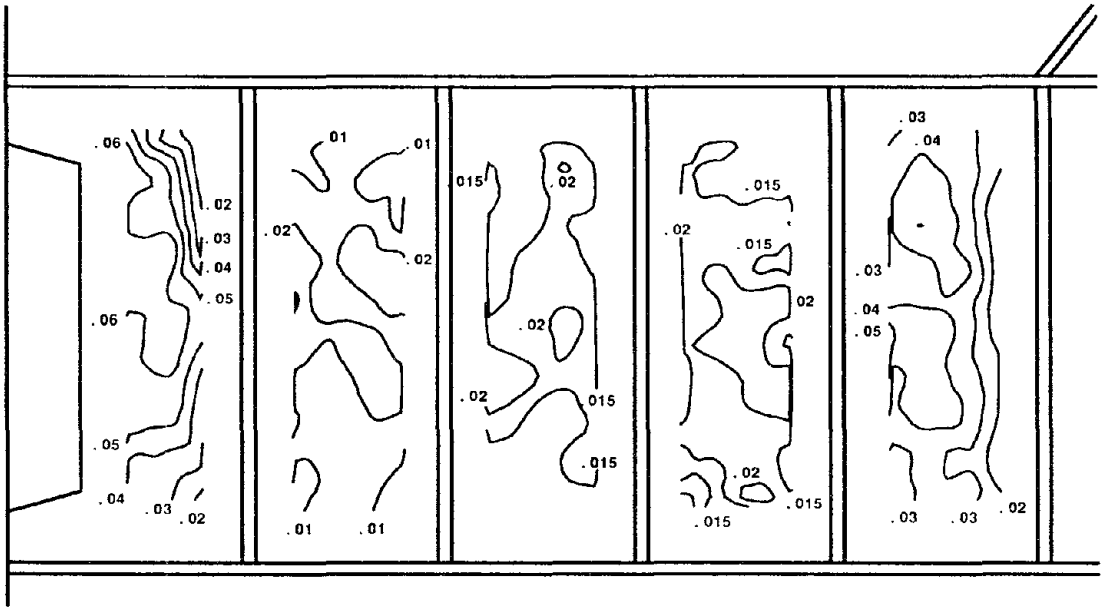

(a) Reference State: Unloaded Specimen at Start of Test
Final State: Peak Deformation at End of Cycle 11E

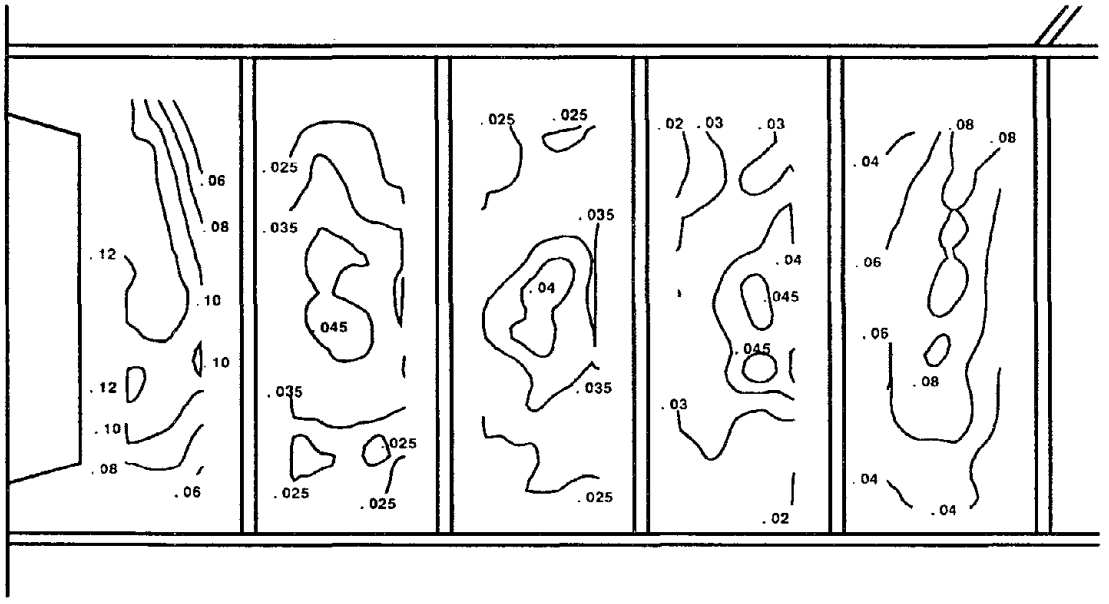

(b) Reference State: Unloaded Specimen at Start of Cycle 13E
Final State: Peak Deformation at End of Cycle 13E

Fig. 5.8 Specimen 1 - Shear Strain Contours

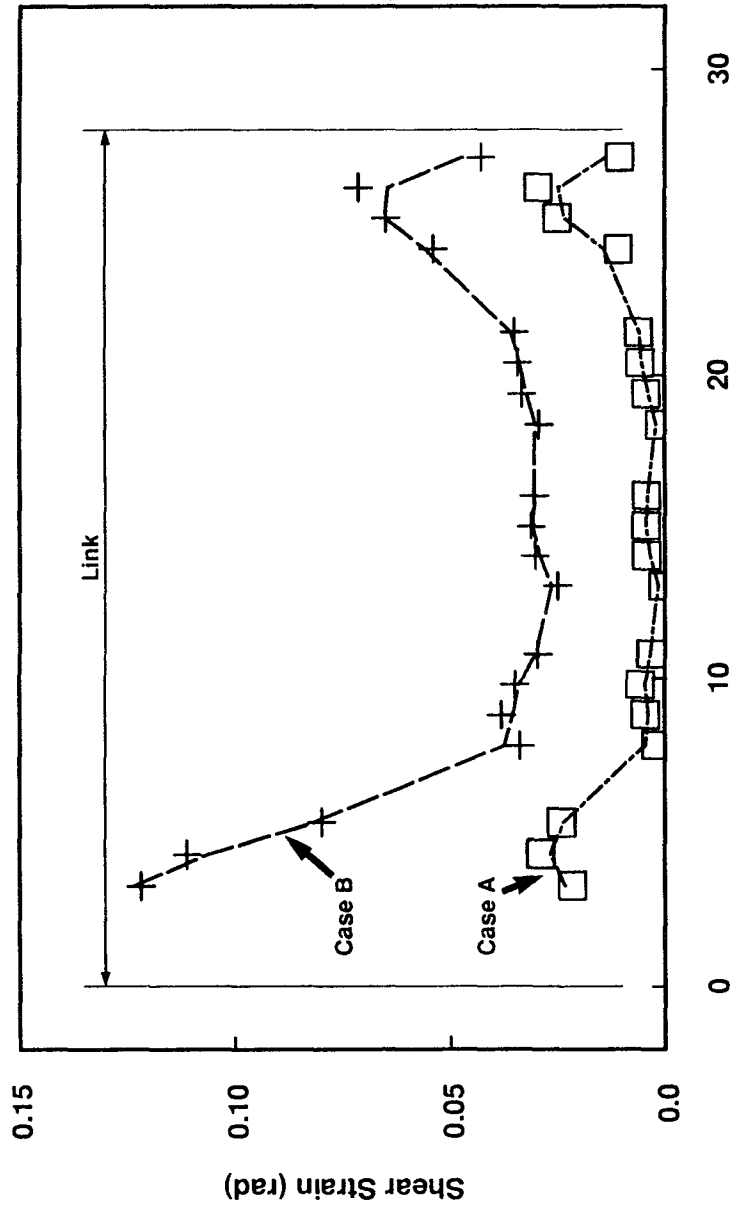

Fig. 5.9 Specimen 1 - Distribution of Average Shear Strain Along Length of Link

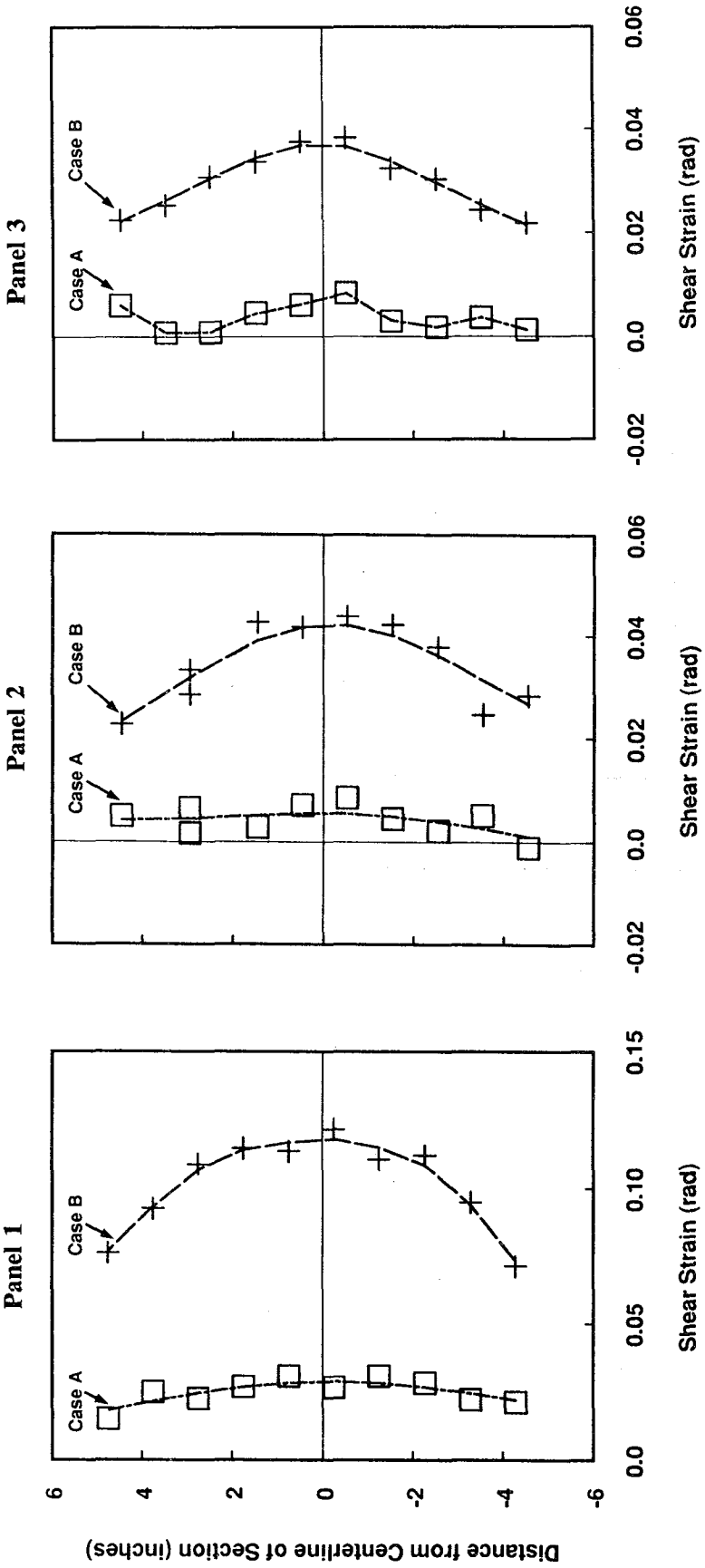

Case A - Reference state: Unloaded specimen at start of cycle 7E
Final state: Peak Deformation at end of cycle 7E
Case B - Reference state: Unloaded specimen at start of cycle 13E
Final state: Peak Deformation at end of cycle 13E

Fig. 5.10 Specimen 1 - Distribution of Average Shear Strain Over Depth of Web

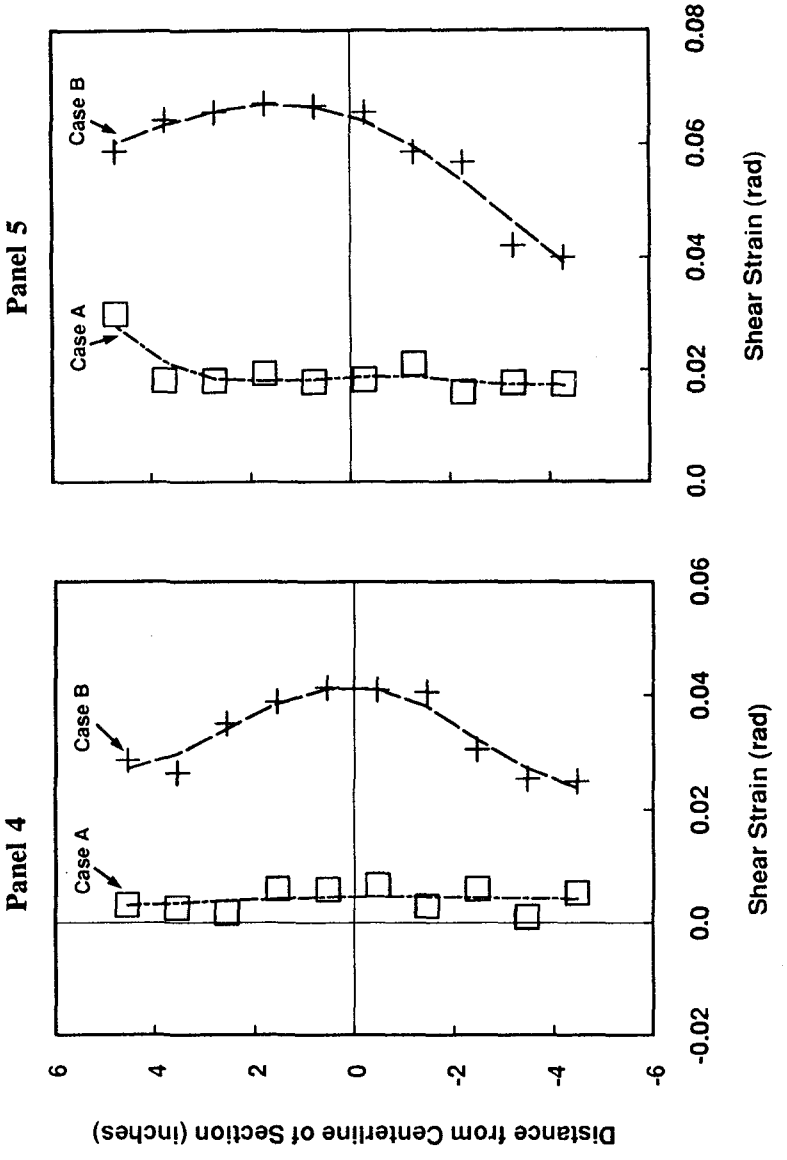

Fig. 5.10 Specimen 1 - Distribution of Average Shear Strain Over Depth of Web (cont)

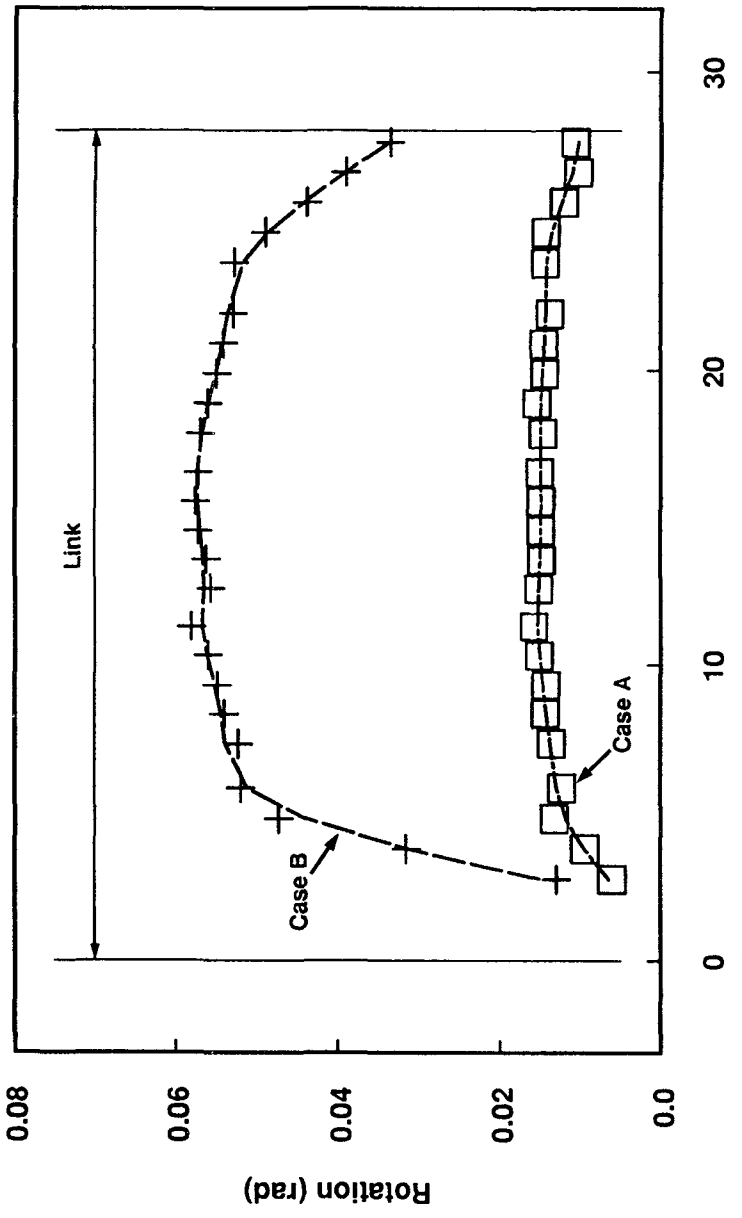

Fig. 5.11 Specimen 1 - Average Rotation of Web Gridlines

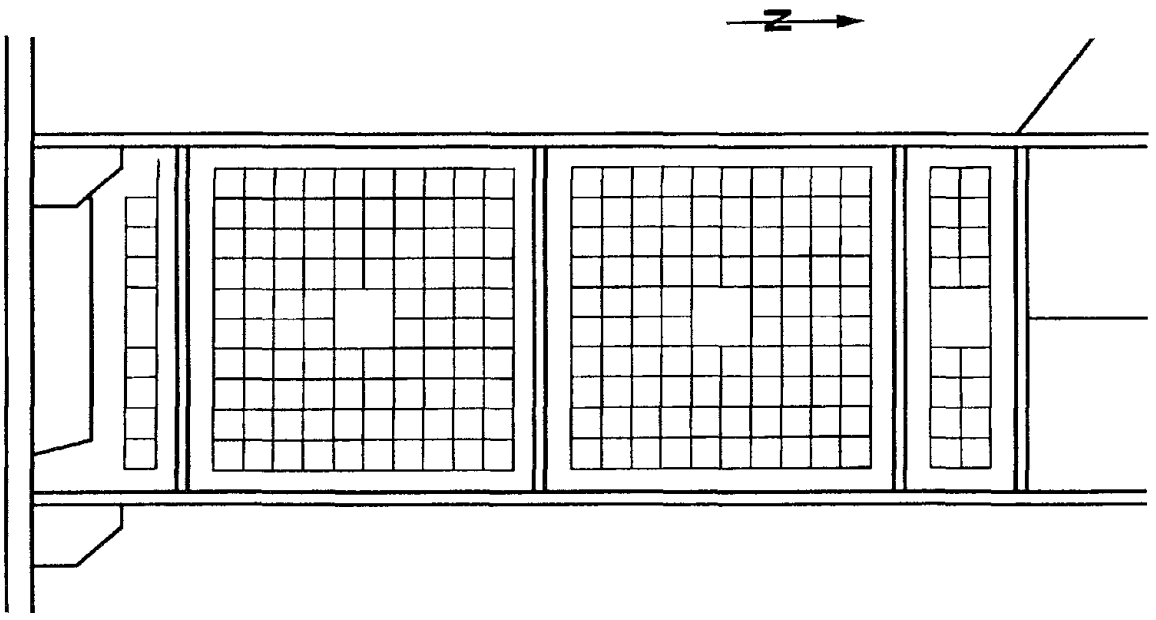

Fig. 5.12 Specimen 4 - Undeformed Gridlines

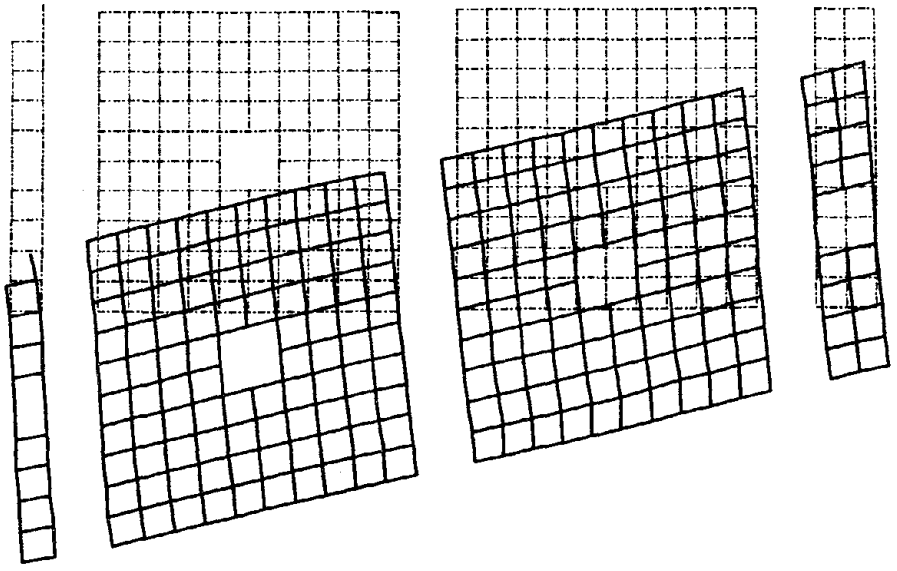

(a) Reference State: Unloaded Specimen at Start of Cycle 8E
Final State: Peak Deformation at End of Cycle 8E
(Displacements Amplified 5X)

Fig. 5.13 Specimen 4 - Deformed Gridlines

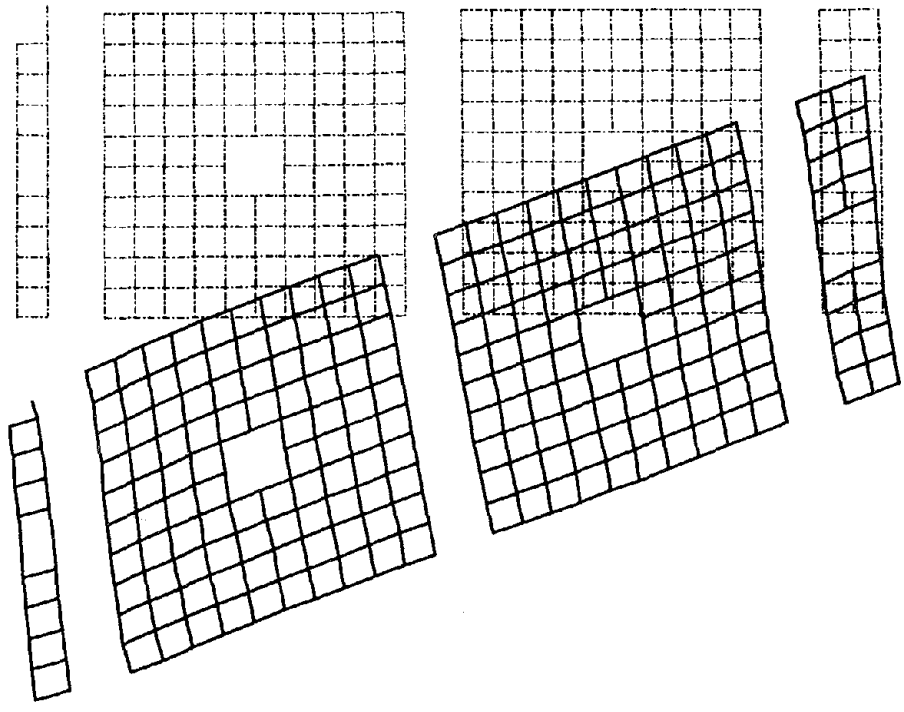

(b) Reference State: Unloaded Specimen at Start of Cycle 11E
Final State: Peak Deformation at End of Cycle 11E
(Displacements Amplified 5X)

Fig. 5.13 Specimen 4 - Deformed Gridlines (cont)

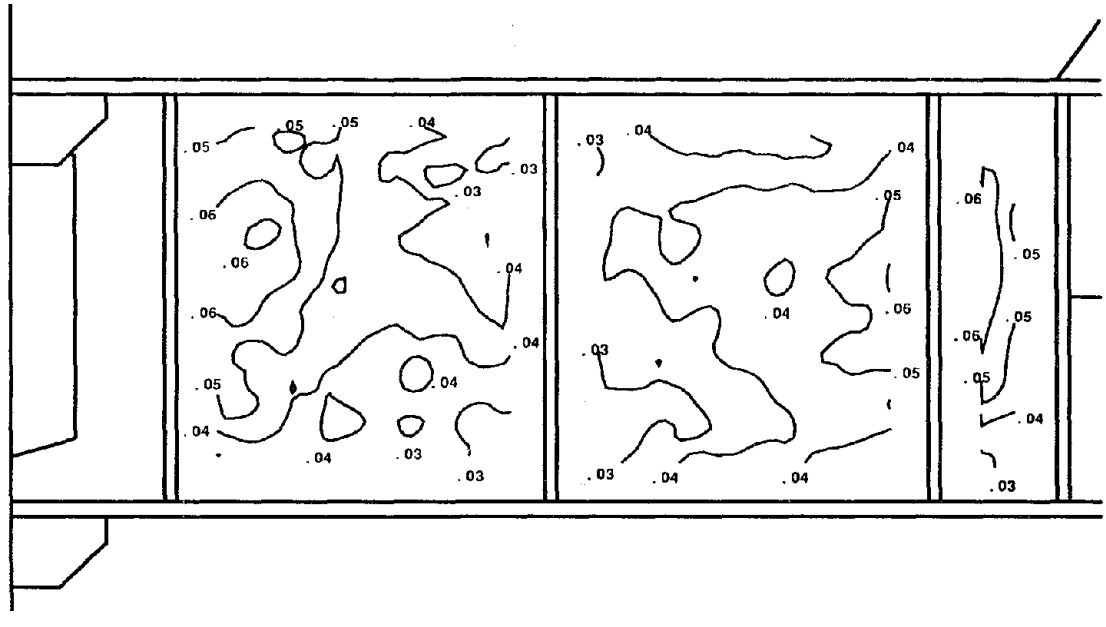

Fig. 5.14 Specimen 4 - Shear Strain Contours
Reference State: Unloaded Specimen at Start of Cycle 11E
Final State: Peak Deformation at End of Cycle 11E

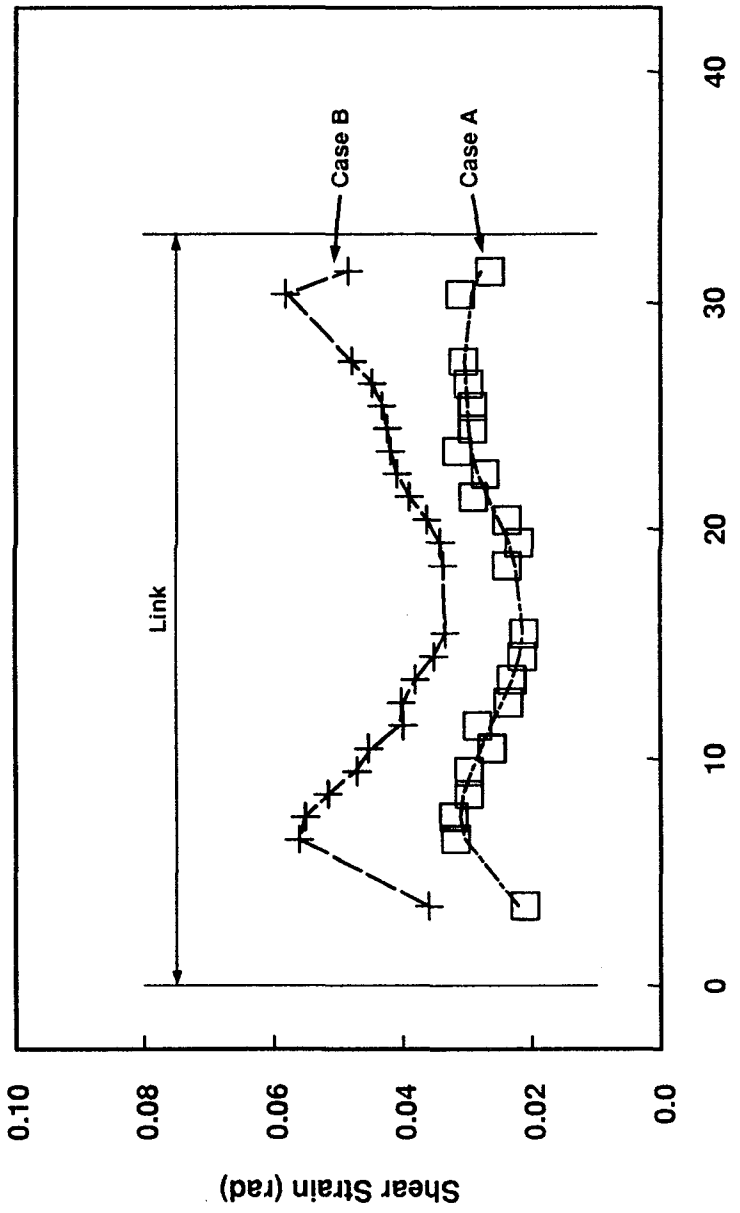

Fig. 5.15 Specimen 4 - Distribution of Average Shear Strain Along Length of Link

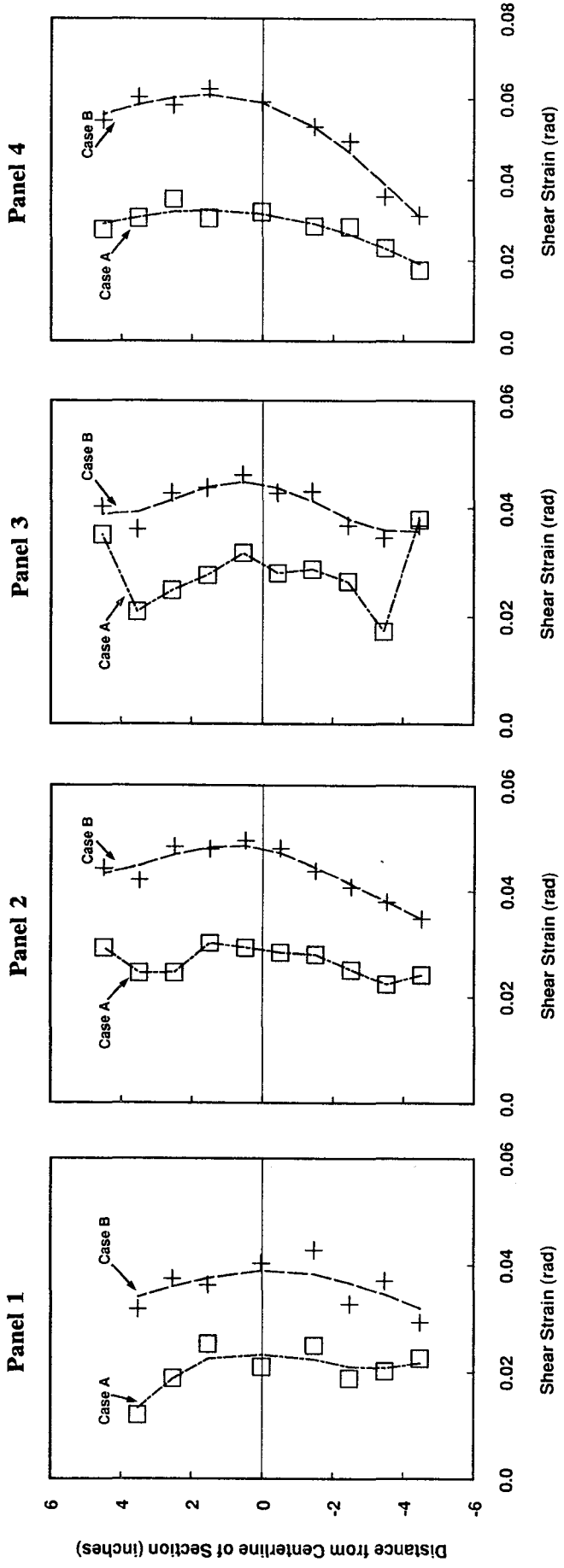

Case A - Reference state: Unloaded specimen at start of cycle 8E
Final state: Peak Deformation at end of cycle 8E
Case B - Reference state: Unloaded specimen at start of cycle 11E
Final state: Peak Deformation at end of cycle 11E

Fig. 5.16 Specimen 4 - Distribution of Average Shear Strain Over Depth of Web

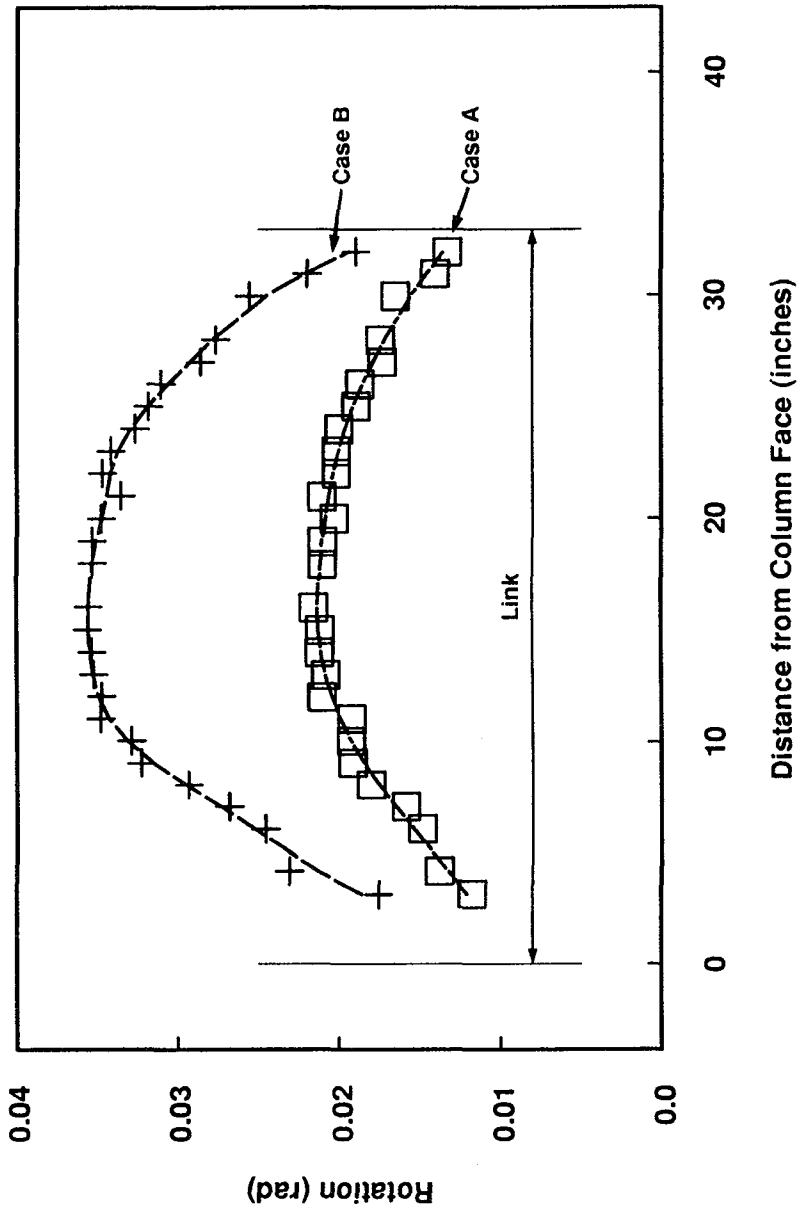

Fig. 5.17 Specimen 4 - Average Rotation of Web Gridlines

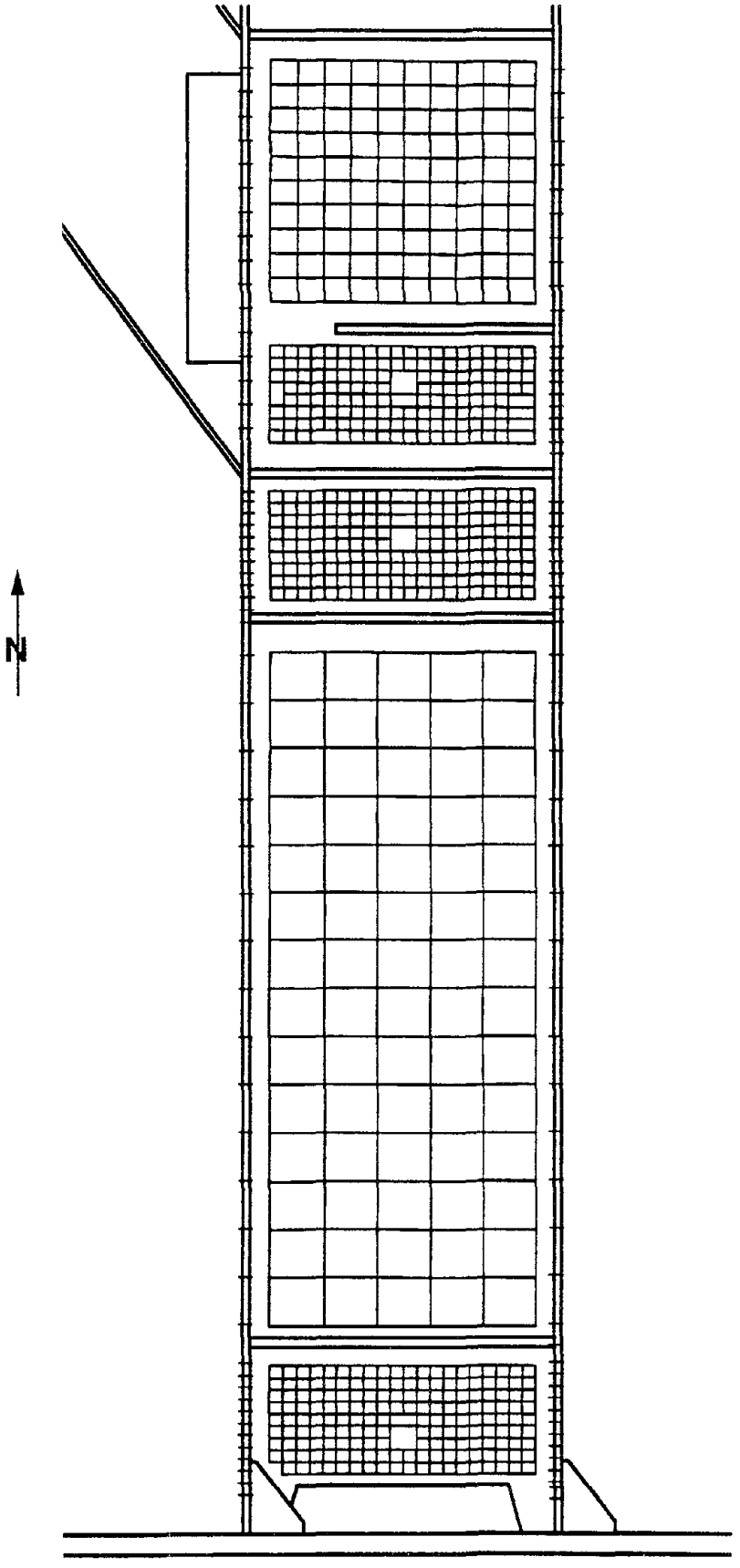

Fig. 5.18 Specimen 6 - Undeformed Gridlines

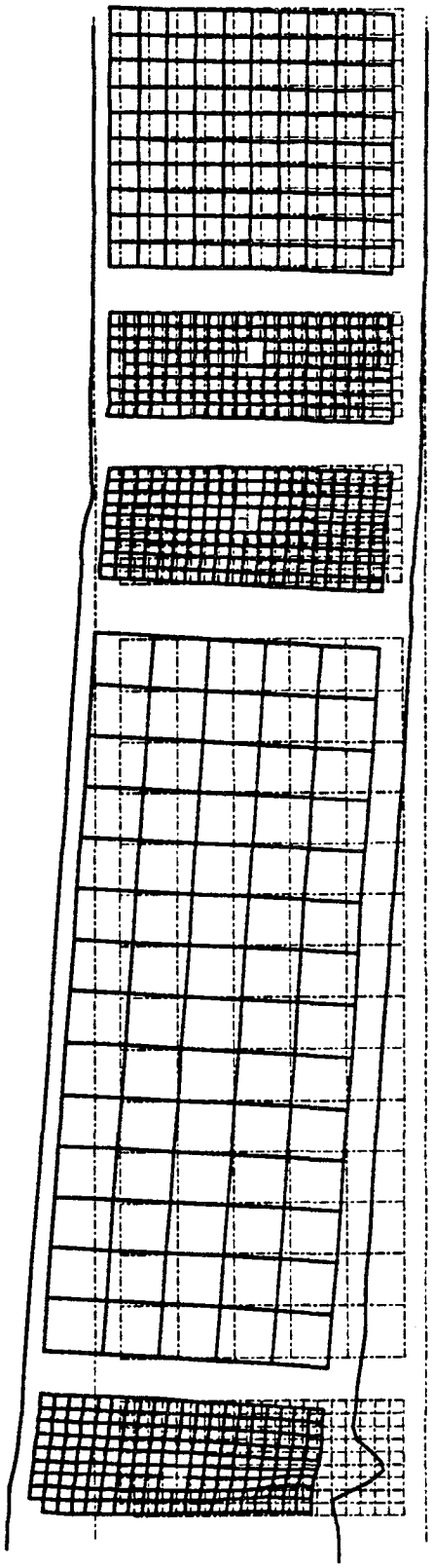

(a) Reference State: Unloaded Specimen at Start of Test
Final State: Unloaded Specimen at Start of Cycle 10E
(Displacements Amplified 5X)

Fig. 5.19 Specimen 6 - Deformed Gridlines

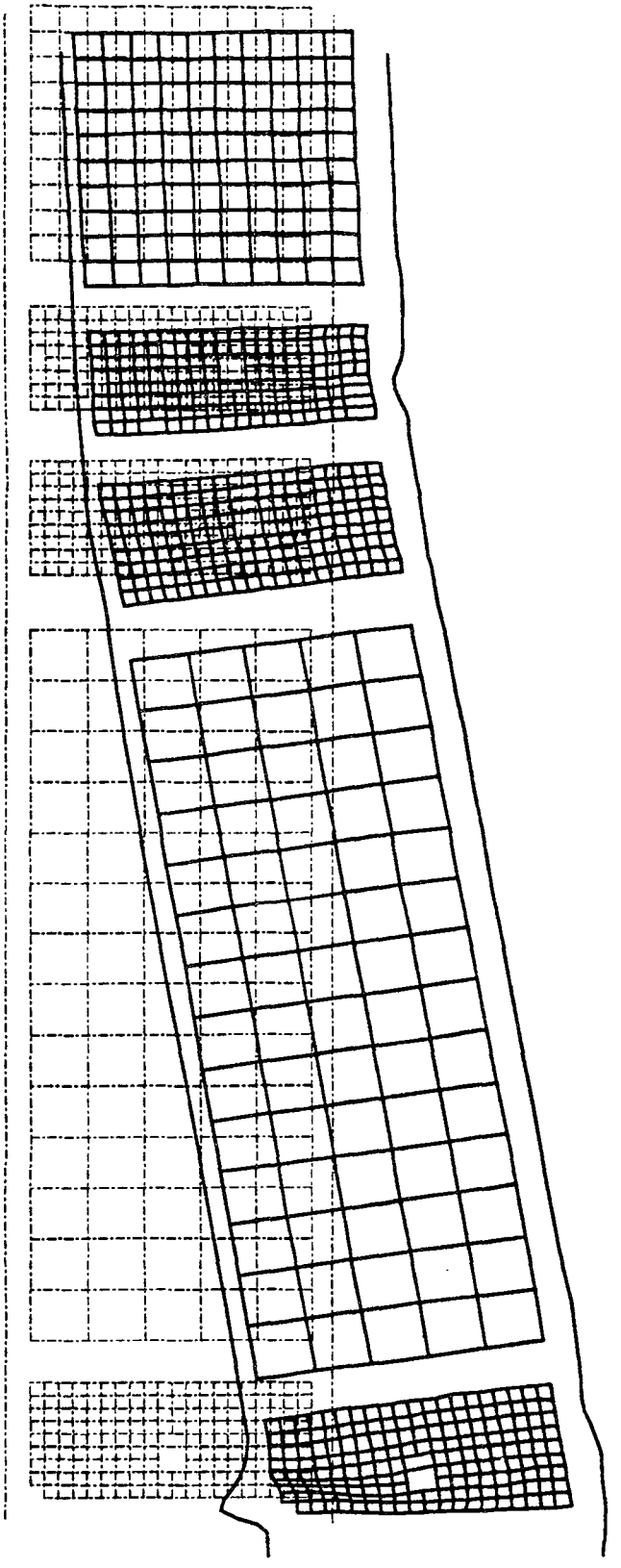

(b) Reference State: Unloaded Specimen at Start of Test
Final State: Peak Deformation at End of Cycle 10E
(Displacements Amplified 5X)

Fig. 5.19 Specimen 6 - Deformed Gridlines (cont)

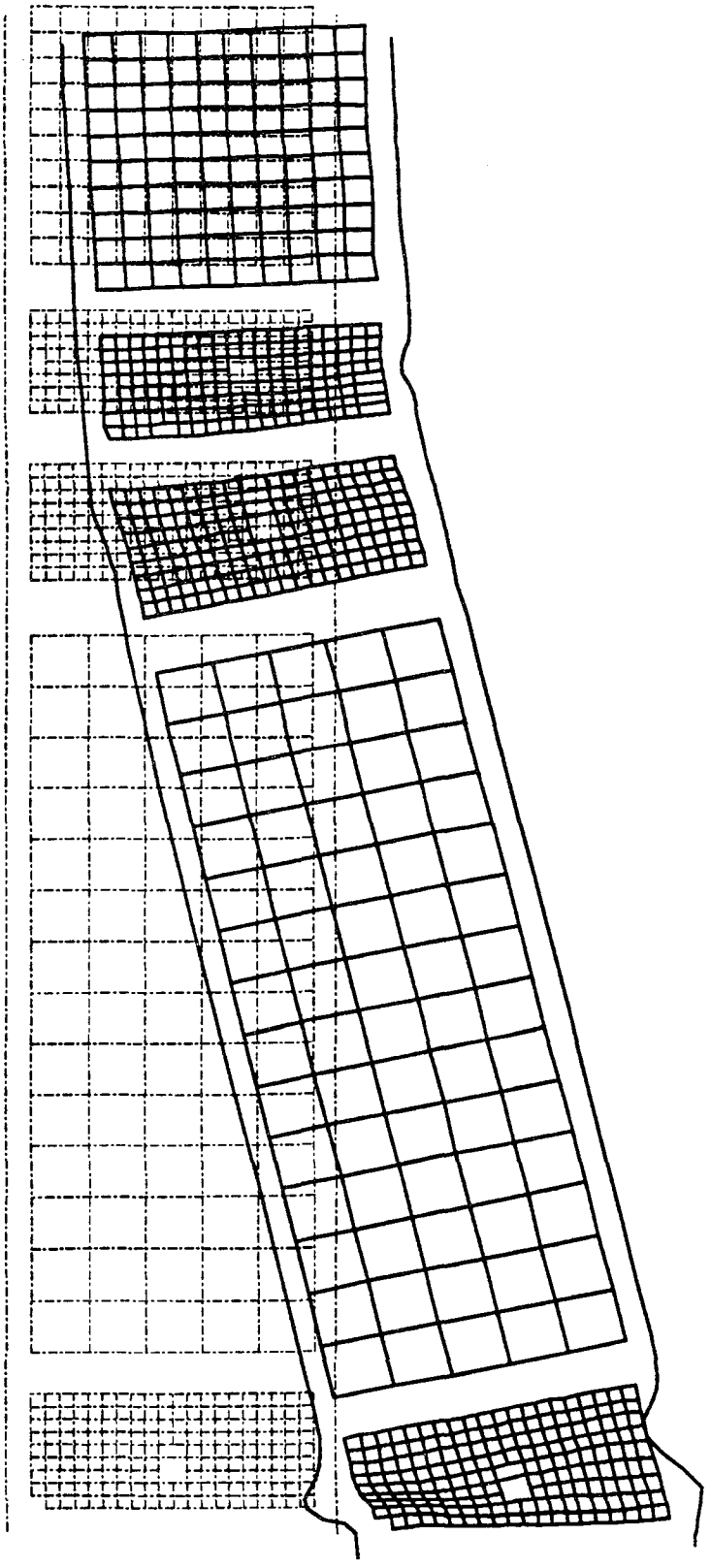

(c) Reference State: Unloaded Specimen at Start of Cycle 10E
Final State: Peak Deformation at End of Cycle 10E
(Displacements Amplified 5X)

Fig. 5.19 Specimen 6 - Deformed Gridlines (cont)

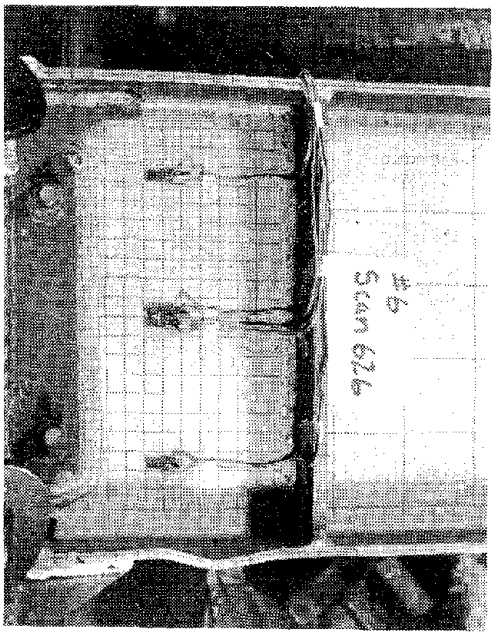

Fig. 5.20 Specimen 6 - Photograph of Column End of Link at Start of Cycle 10E

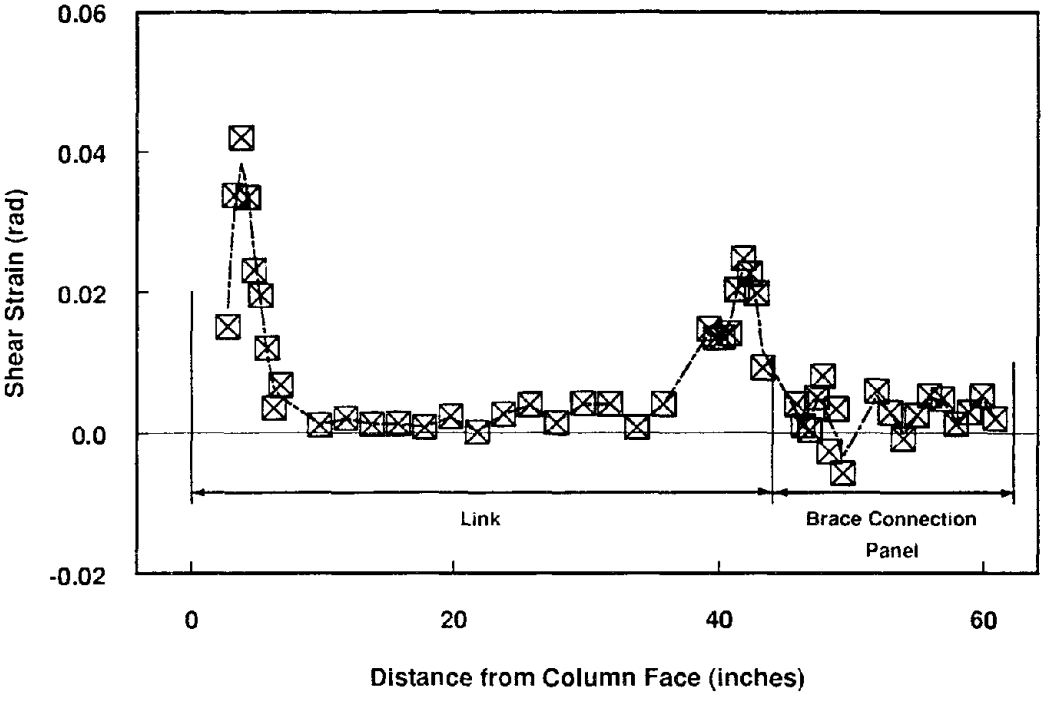

Fig. 5.21 Specimen 6 - Distribution of Average Shear Strain Along Length of Link and Brace Connection Panel
Reference State: Unloaded Specimen at Start of Cycle 10E
Final State: Peak Deformation at End of Cycle 10E

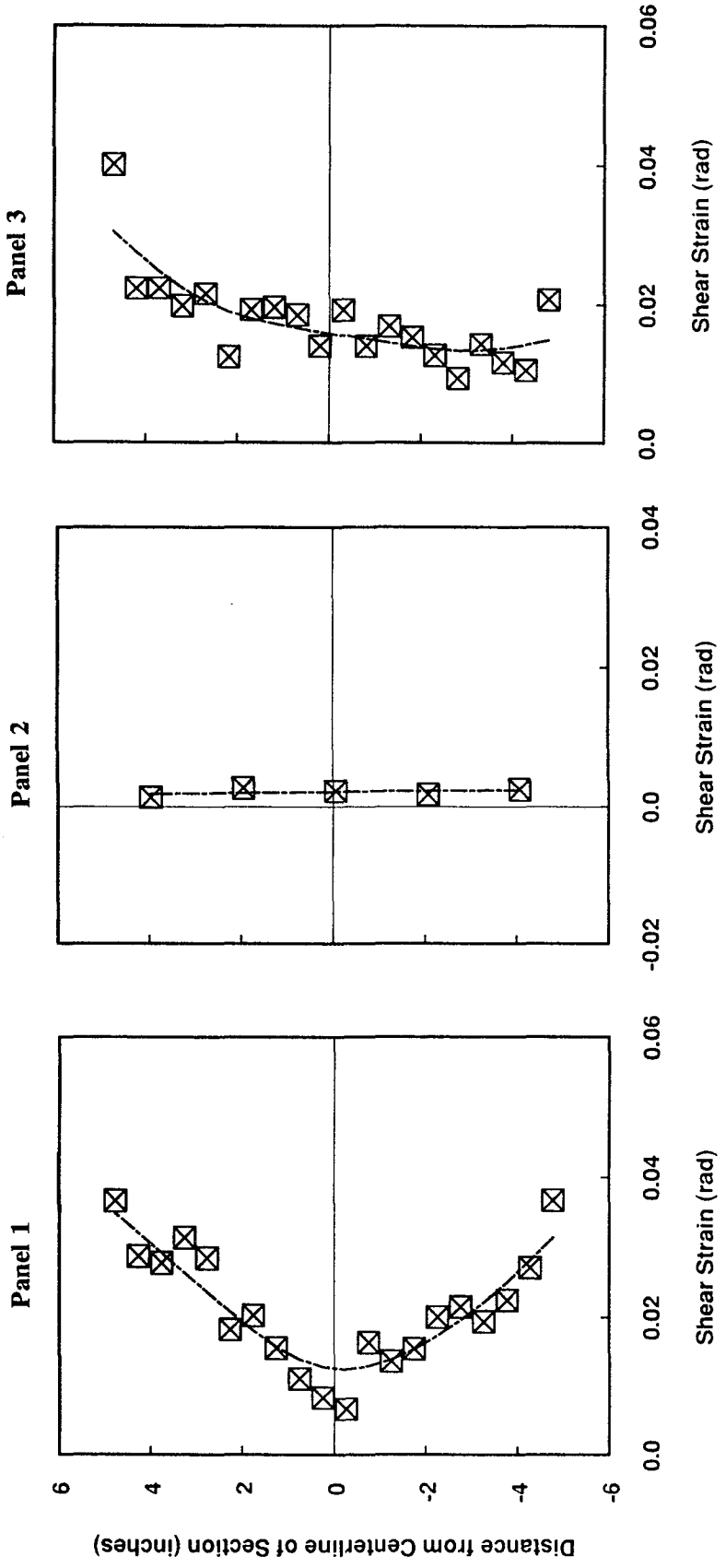

Fig. 5.22 Specimen 6 - Distribution of Average Shear Strain Over Depth of Web
Reference State: Unloaded Specimen at Start of Cycle 10E
Final State: Peak Deformation at End of Cycle 10E

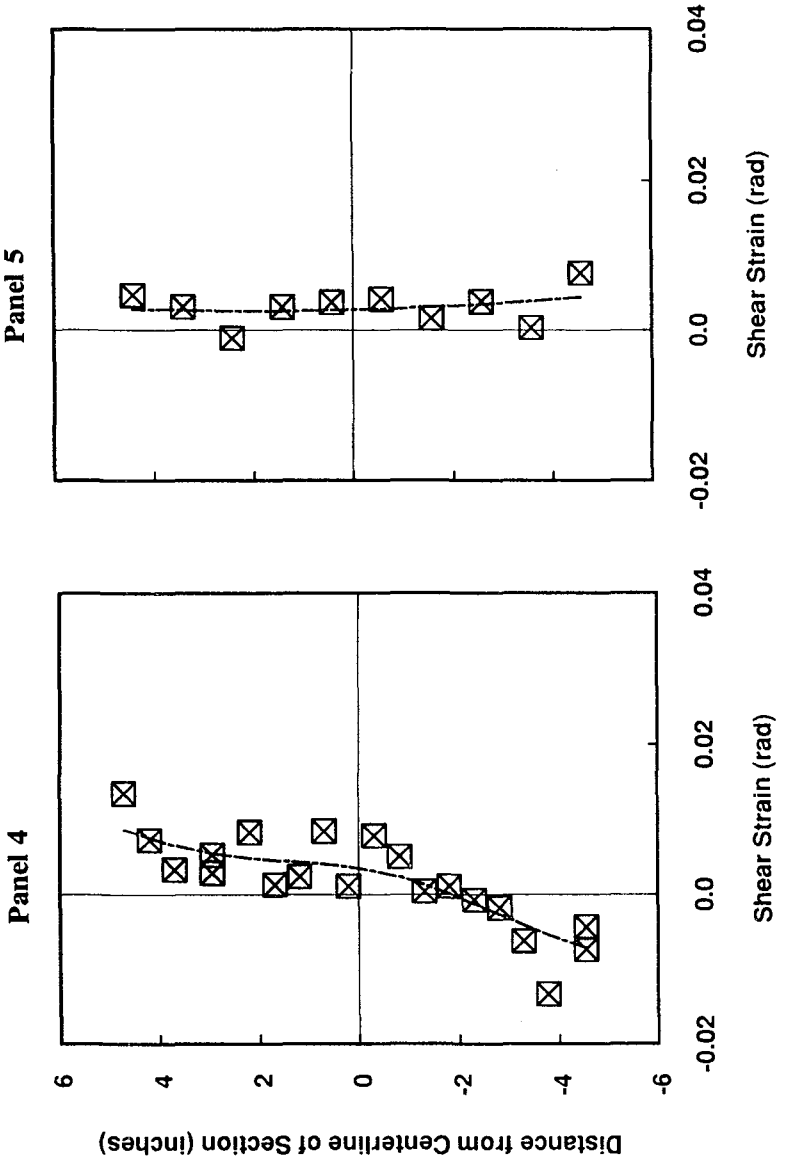

Fig. 5.22 Specimen 6 - Distribution of Average Shear Strain Over Depth of Web (cont)

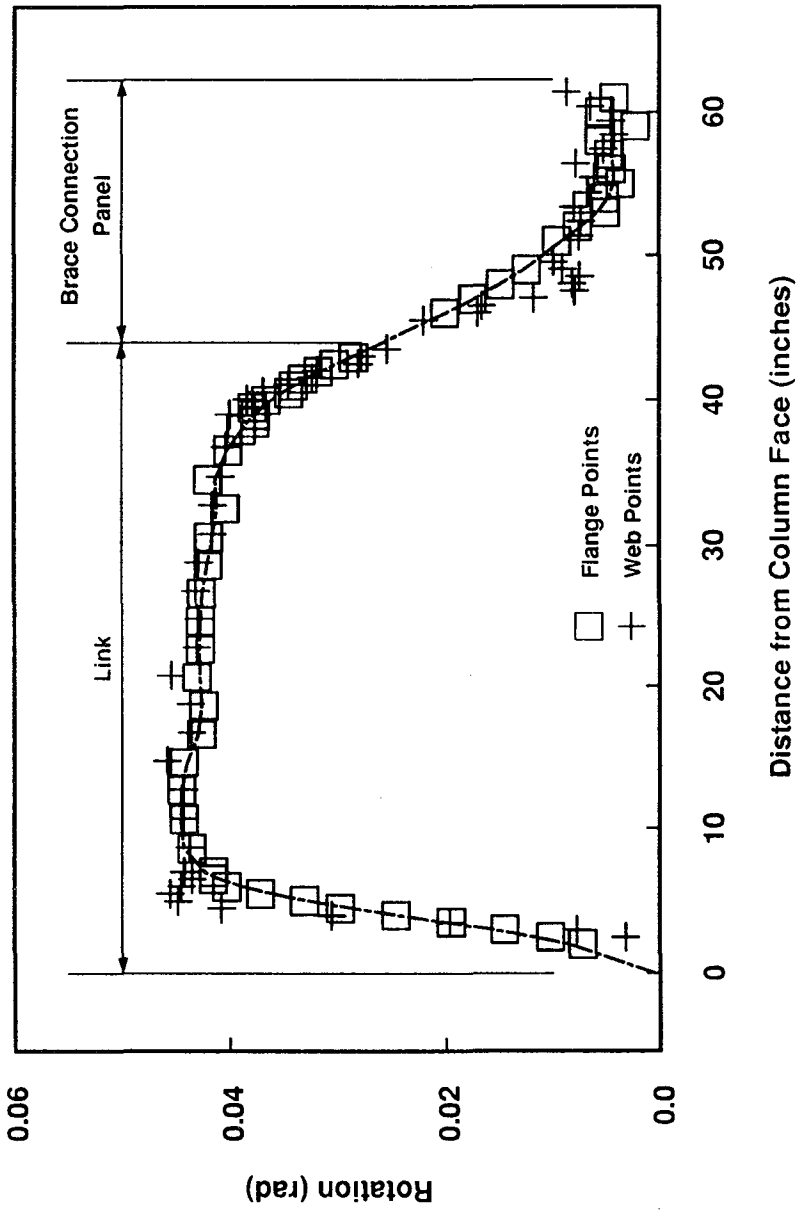

Fig. 5.23 Specimen 6 - Average Rotation of Web Gridlines and Rotation of Flange Gridpoints
Reference State: Unloaded Specimen at Start of Cycle 10E
Final State: Peak Deformation at End of Cycle 10E

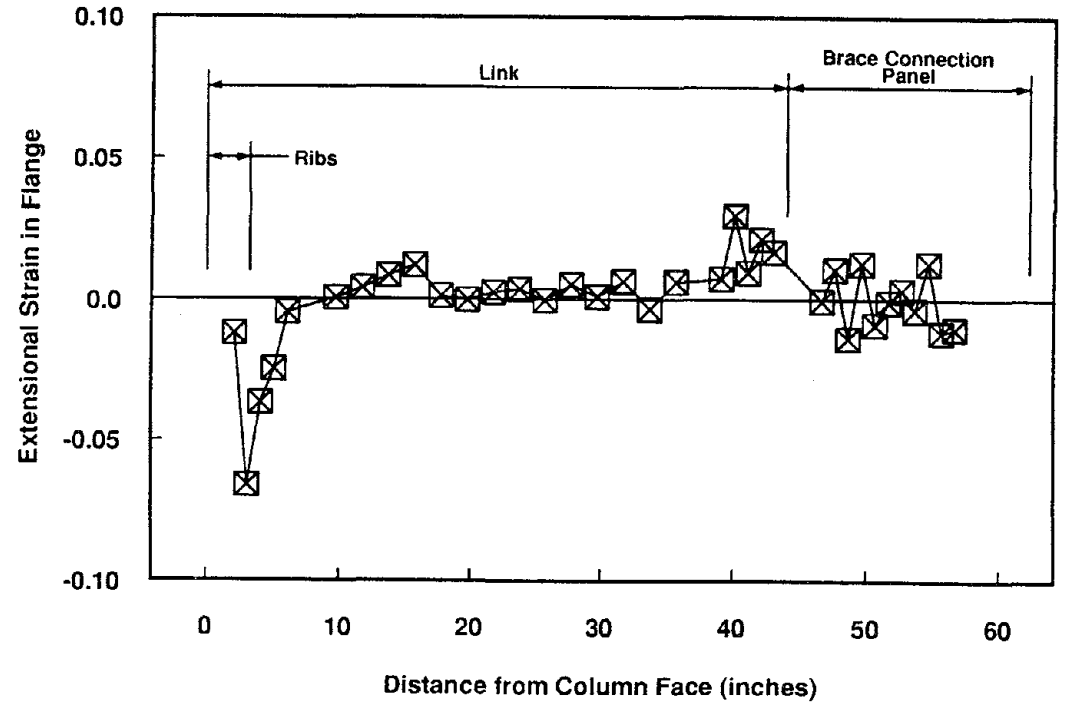

(a) West Flange

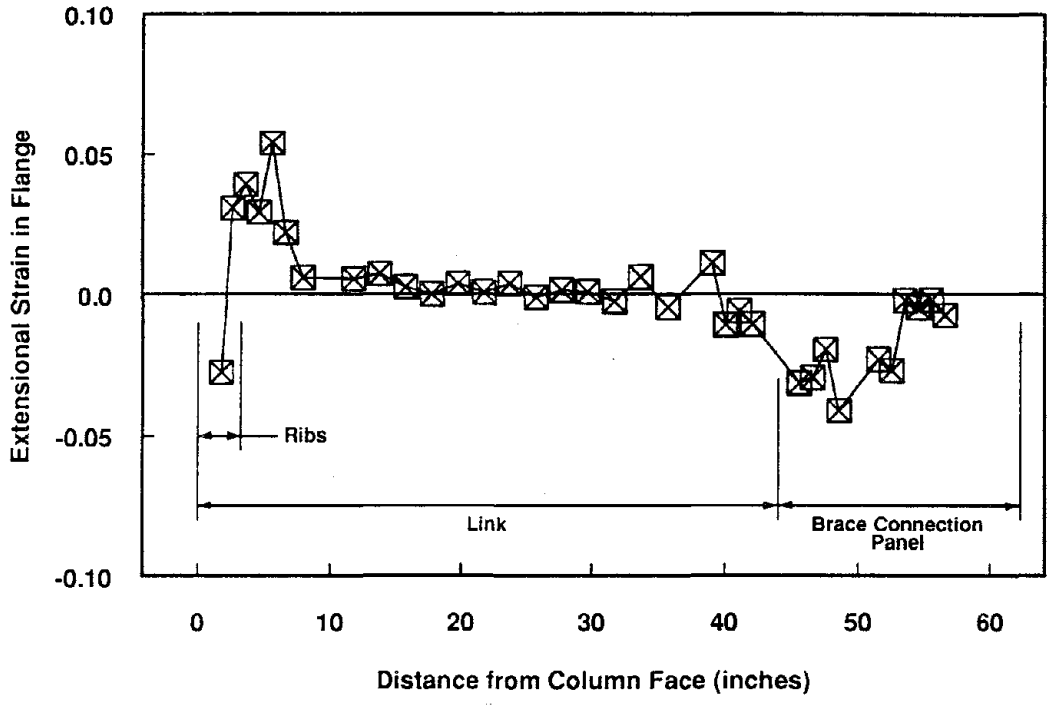

(b) East Flange

Fig. 5.24 Specimen 6 - Extensional Strain Measured from Flange Gridpoints
Reference State: Unloaded Specimen at Start of Cycle 10E
Final State: Peak Deformation at End of Cycle 10E

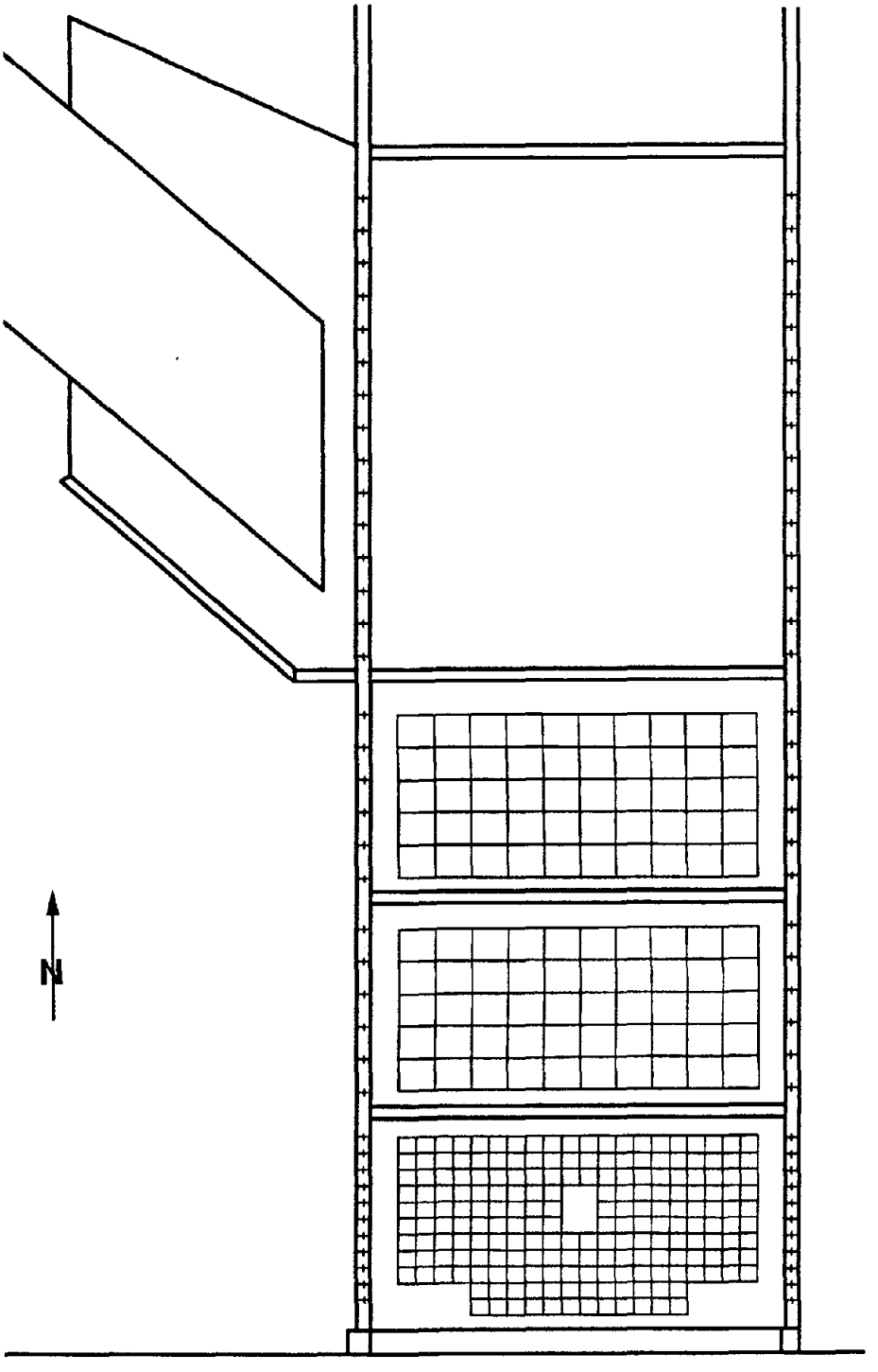

Fig. 5.25 Specimen 9 - Undeformed Gridlines

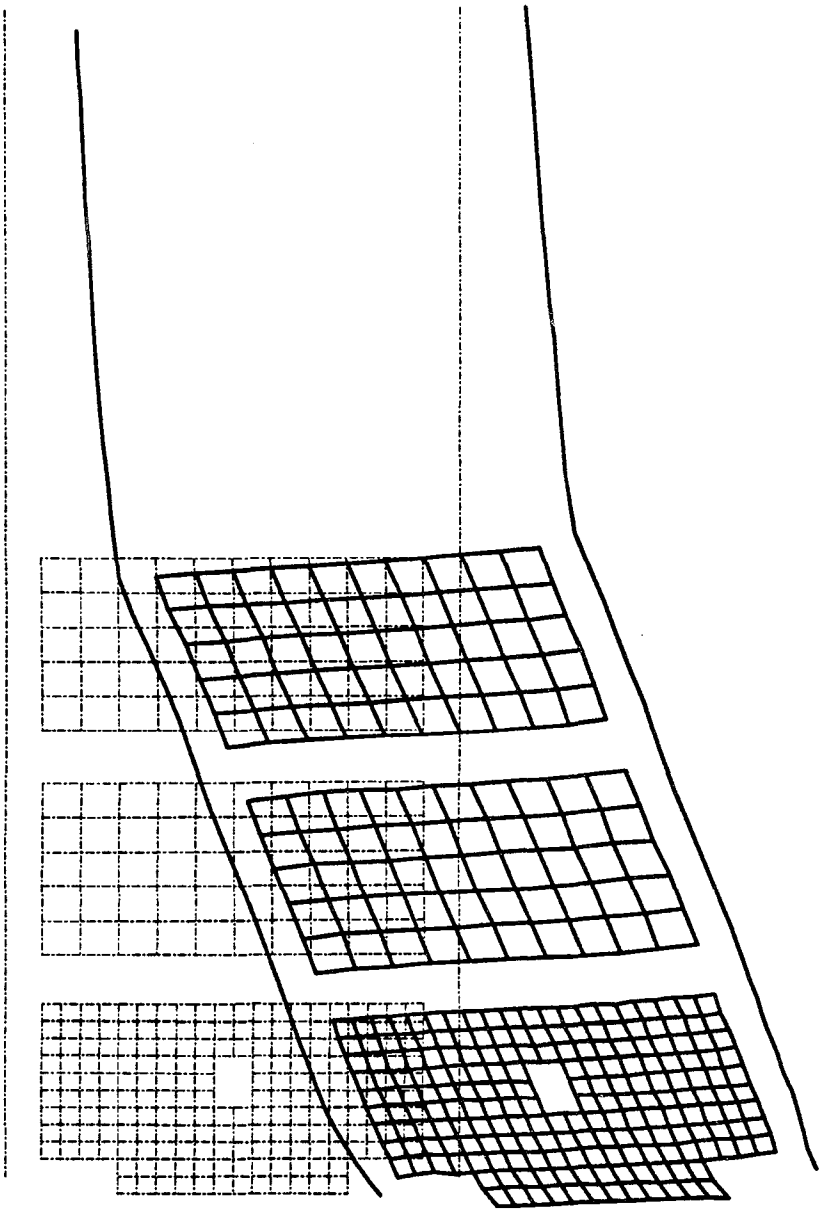

Fig. 5.26 Specimen 9 - Deformed Gridlines
Reference State: Unloaded Specimen at Start of Cycle 9E
Final State: Peak Deformation at End of Cycle 9E

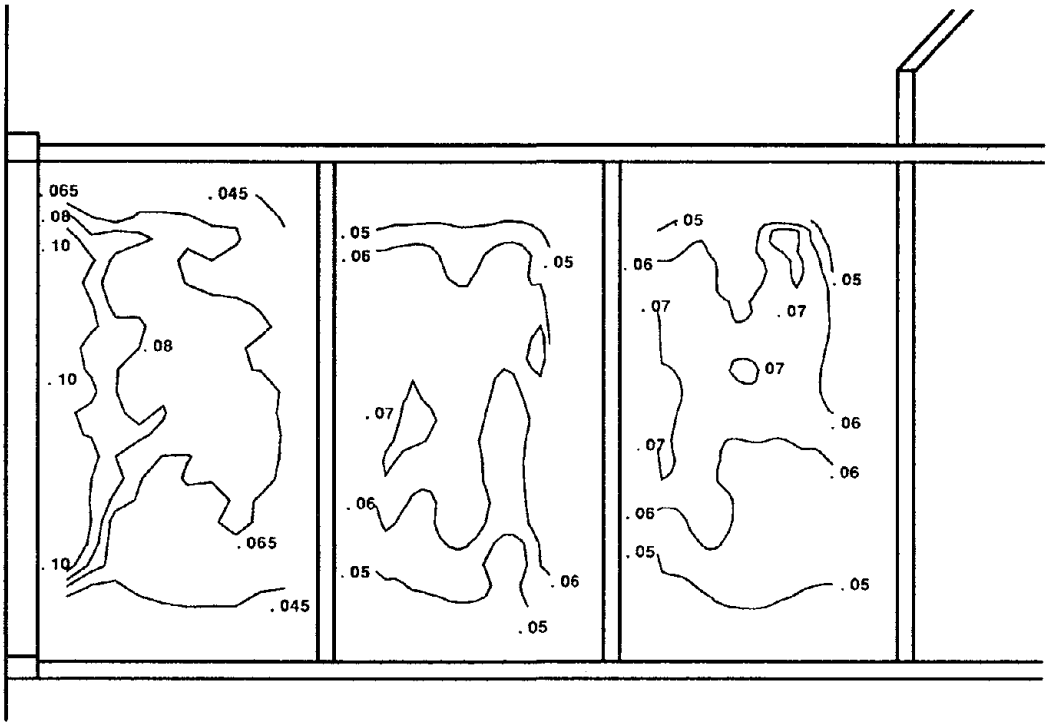

Fig. 5.27 Specimen 9 - Shear Strain Contours
Reference State: Unloaded Specimen at Start of Cycle 9E
Final State: Peak Deformation at End of Cycle 9E

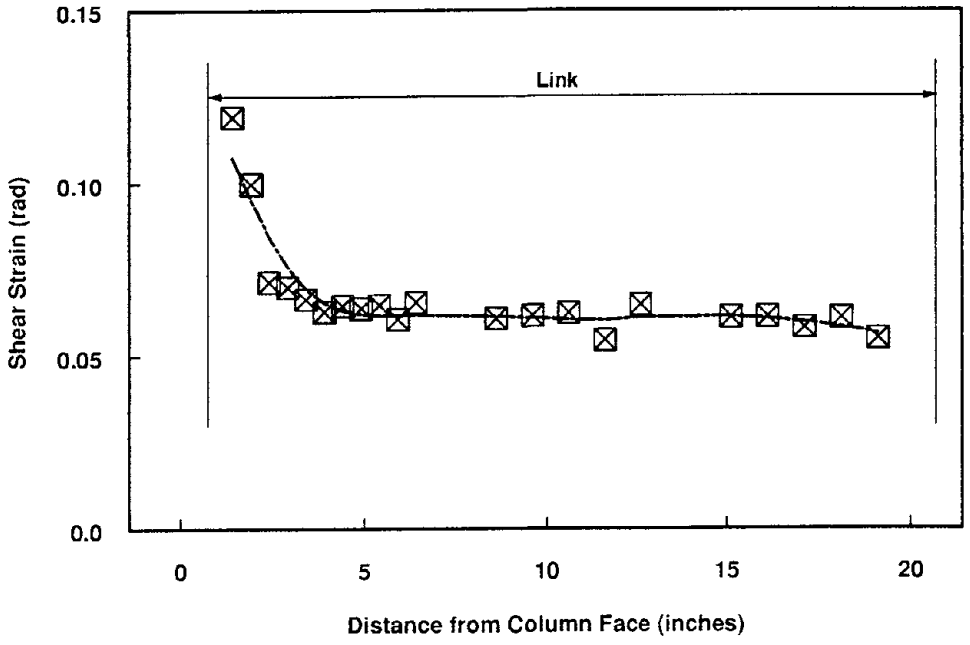

Fig. 5.28 Specimen 9 - Distribution of Average Shear Strain Along Length of Link
Reference State: Unloaded Specimen at Start of Cycle 9E
Final State: Peak Deformation at End of Cycle 9E

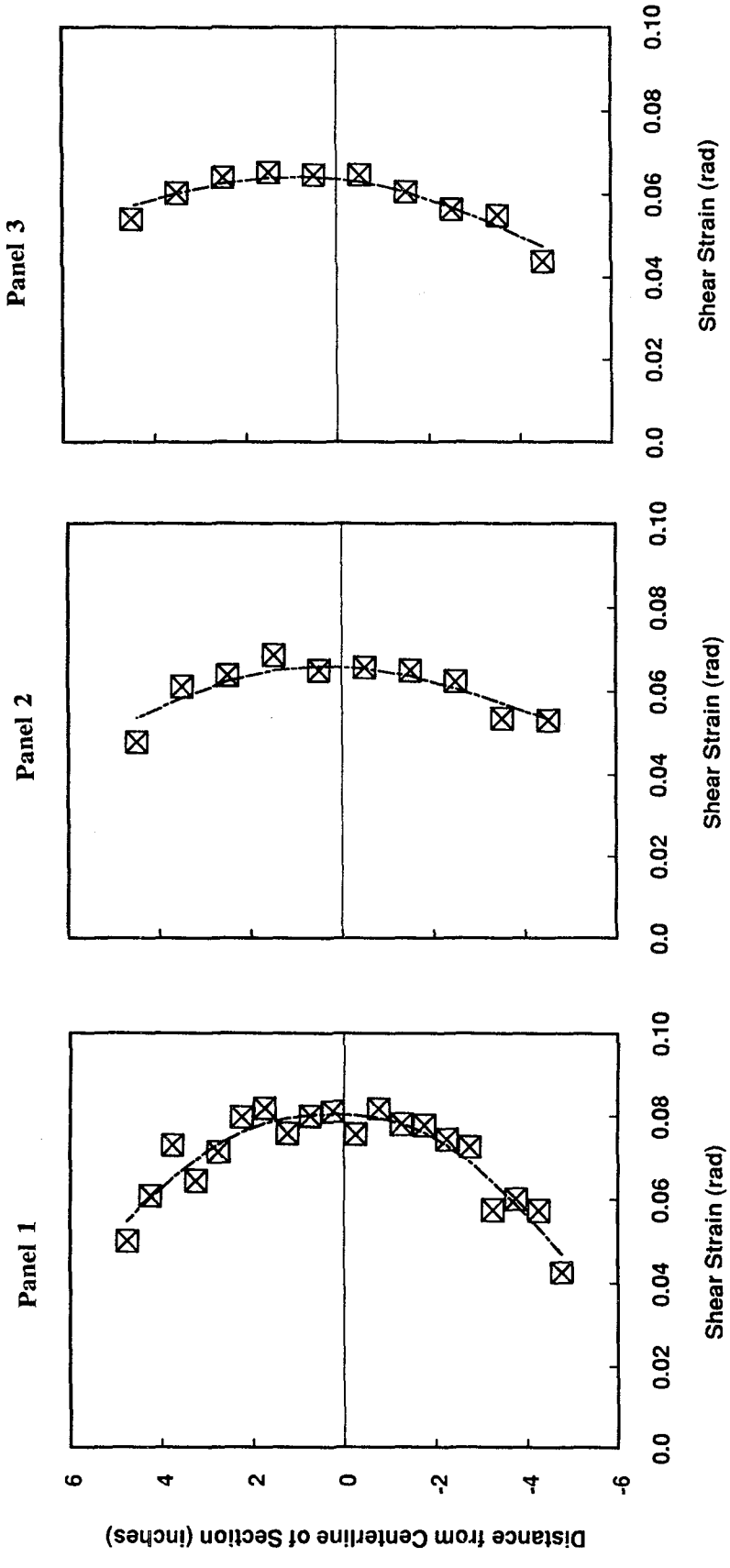

Fig. 5.29 Specimen 9 - Distribution of Average Shear Strain Over Depth of Web
Reference State: Unloaded Specimen at Start of Cycle 9E
Final State: Peak Deformation at End of Cycle 9E

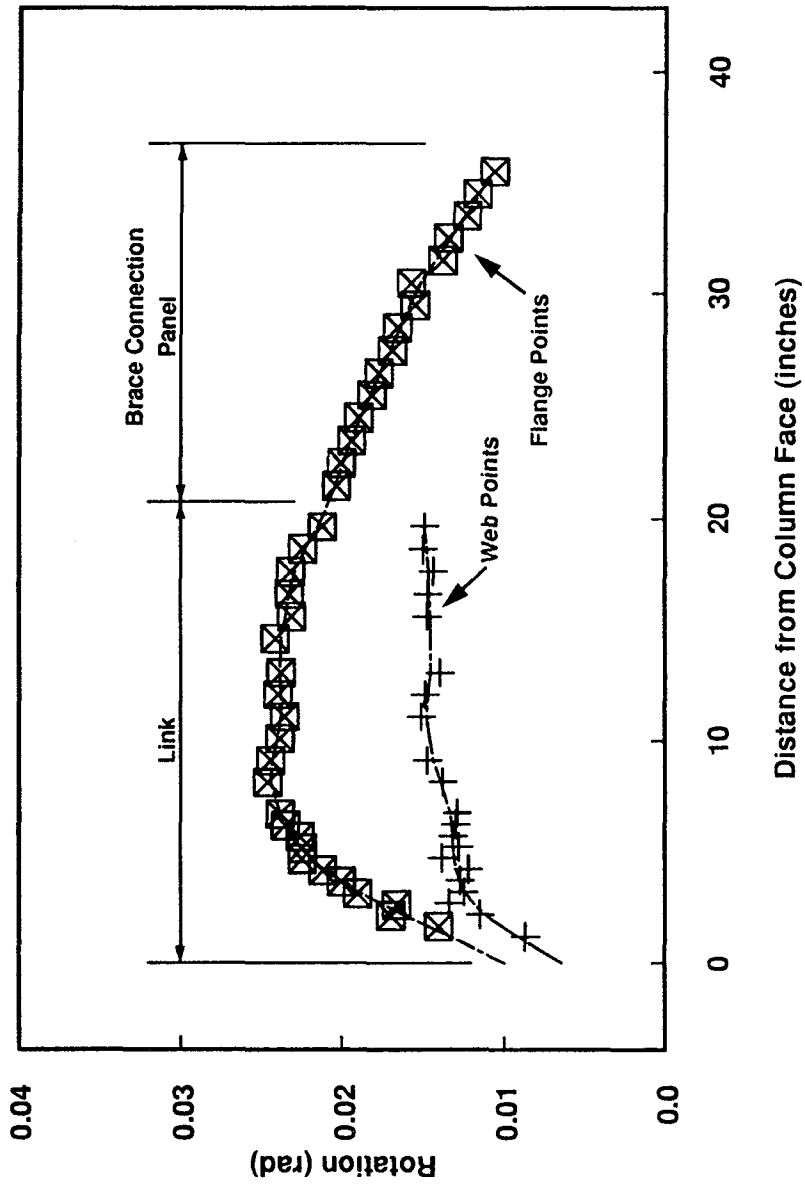

Fig. 5.30 Specimen 9 - Average Rotation of Web Gridlines and Rotation of Flange Gridpoints
Reference State: Unloaded Specimen at Start of Cycle 9E
Final State: Peak Deformation at End of Cycle 9E

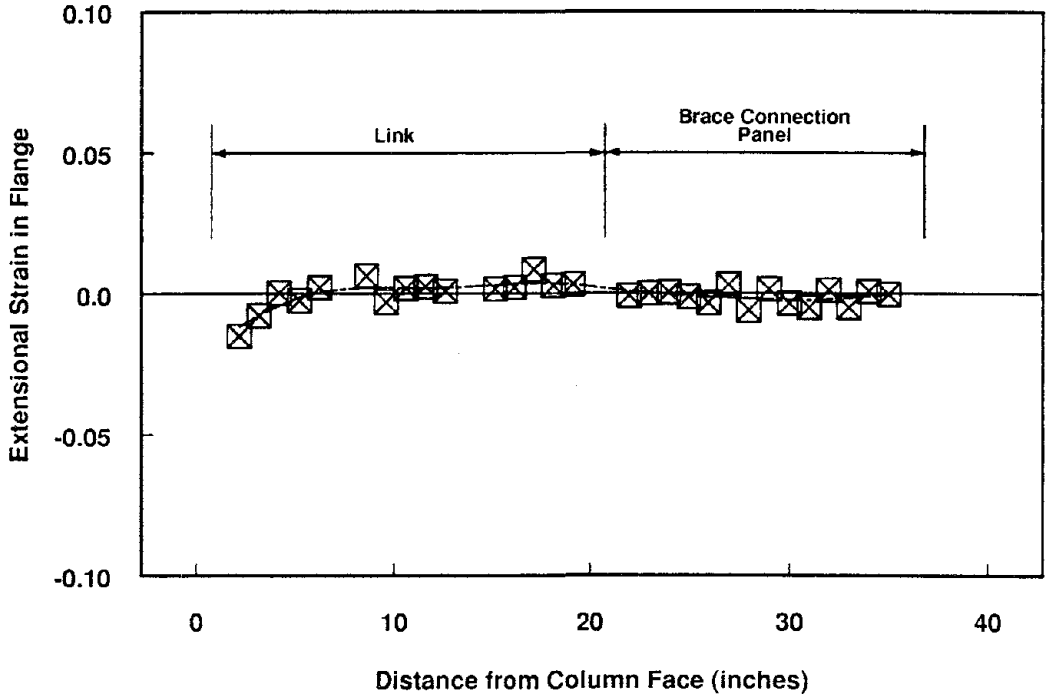

(a) West Flange

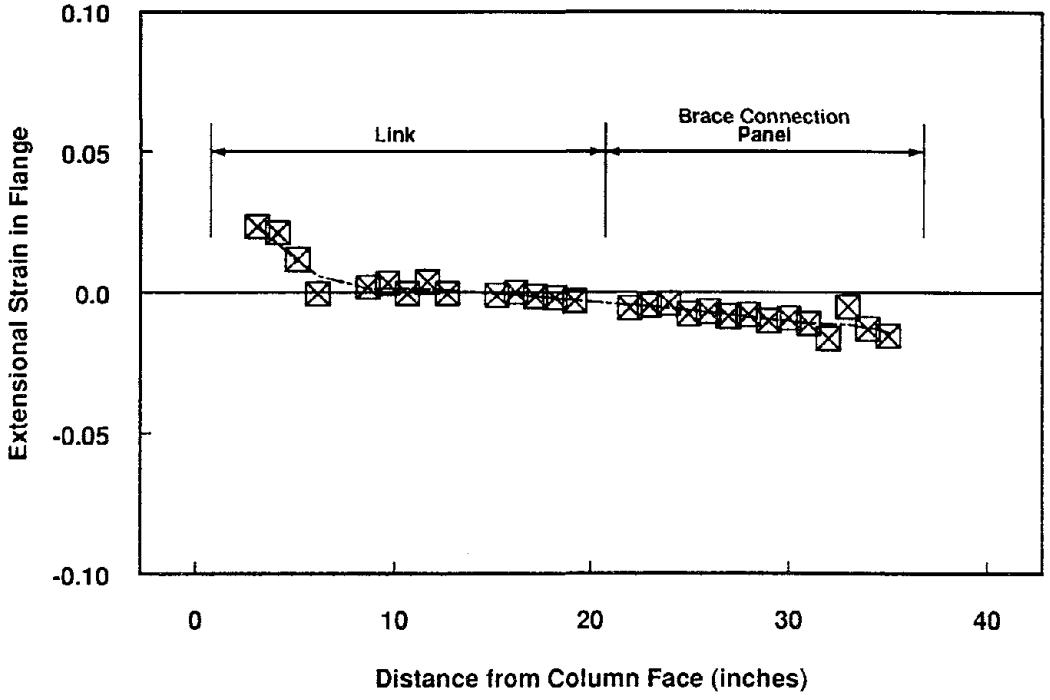

(b) East Flange

Fig. 5.31 Specimen 9 - Extensional Strain Measured from Flange Gridpoints
Reference State: Unloaded Specimen at Start of Cycle 9E
Final State: Peak Deformation at End of Cycle 9E

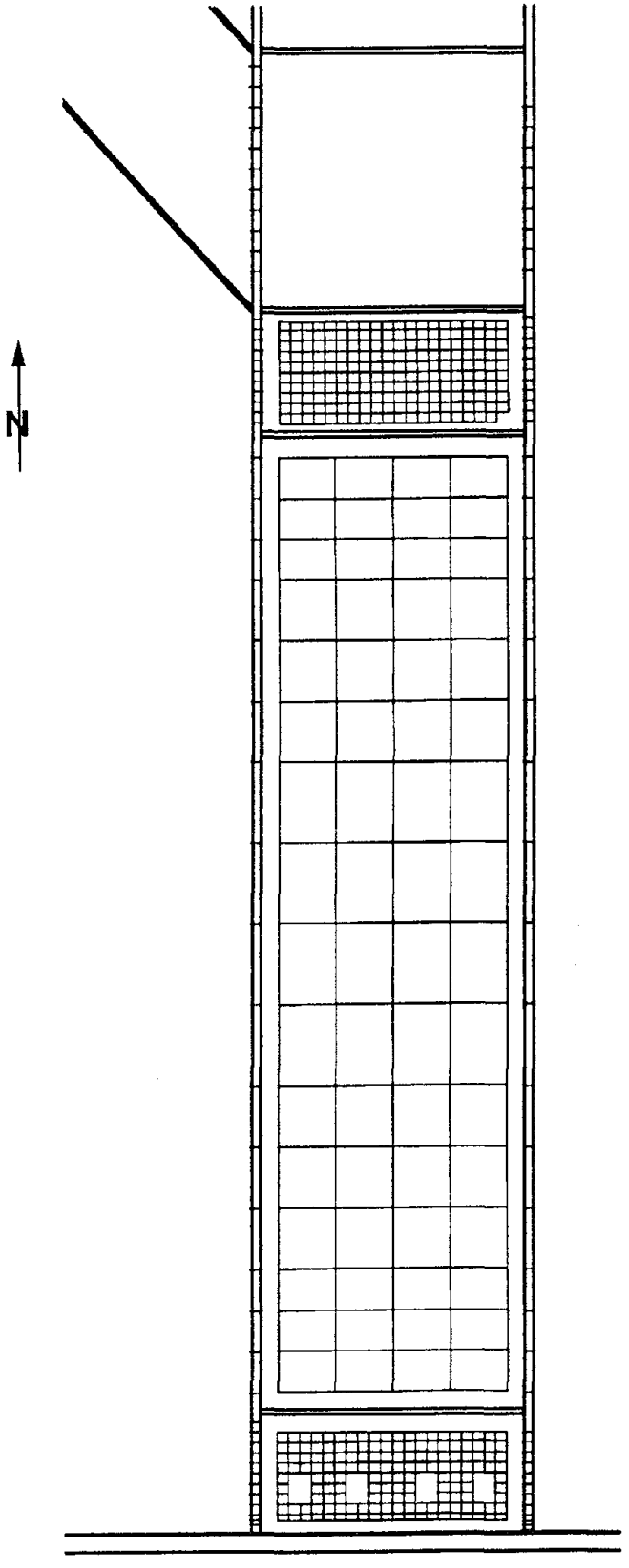

Fig. 5.32 Specimen 12 - Undeformed Gridlines

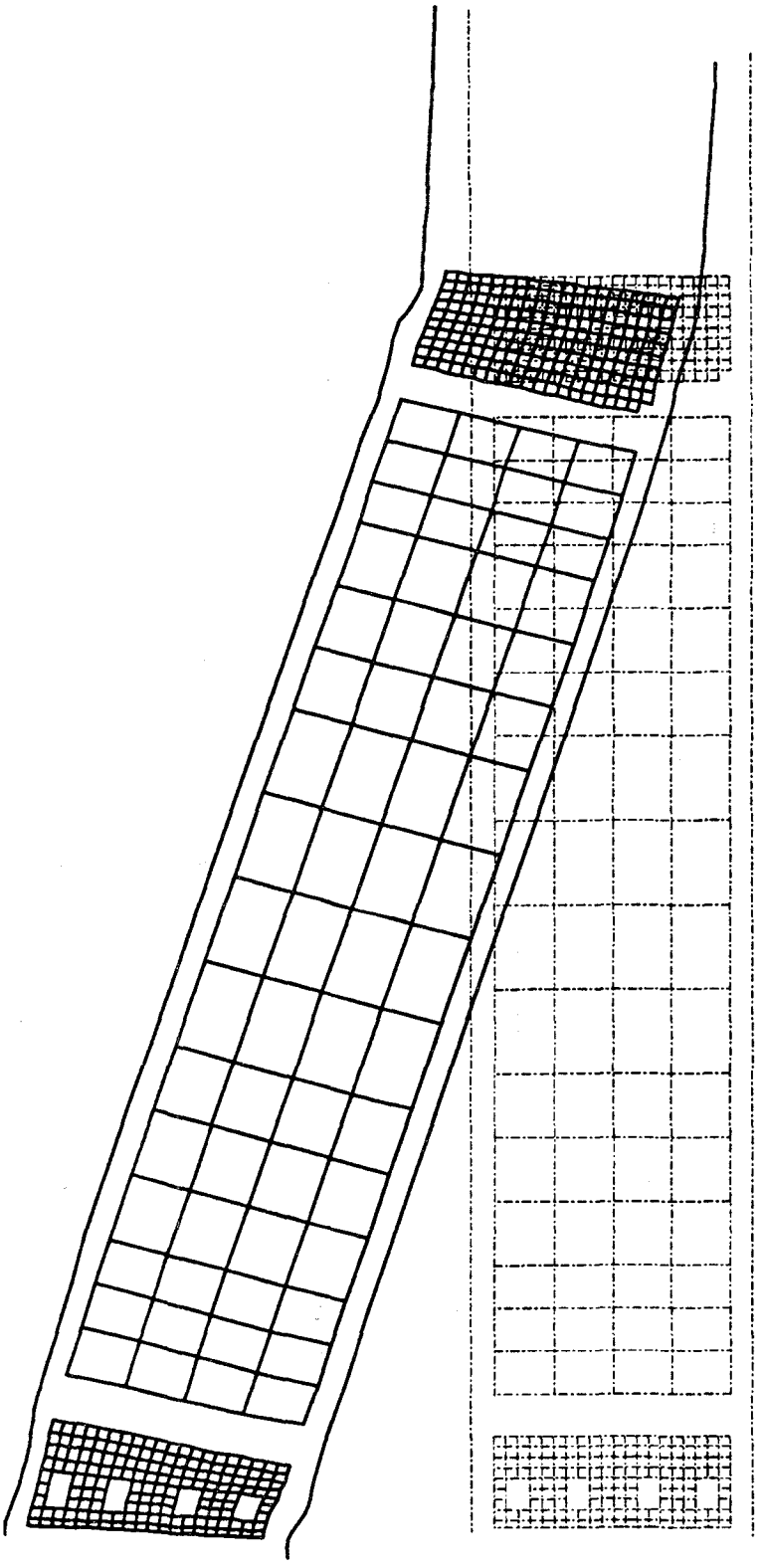

Fig. 5.33 Specimen 12 - Deformed Gridlines
Reference State: Unloaded Specimen at Start of Cycle 7W
Final State: Peak Deformation at End of Cycle 7W

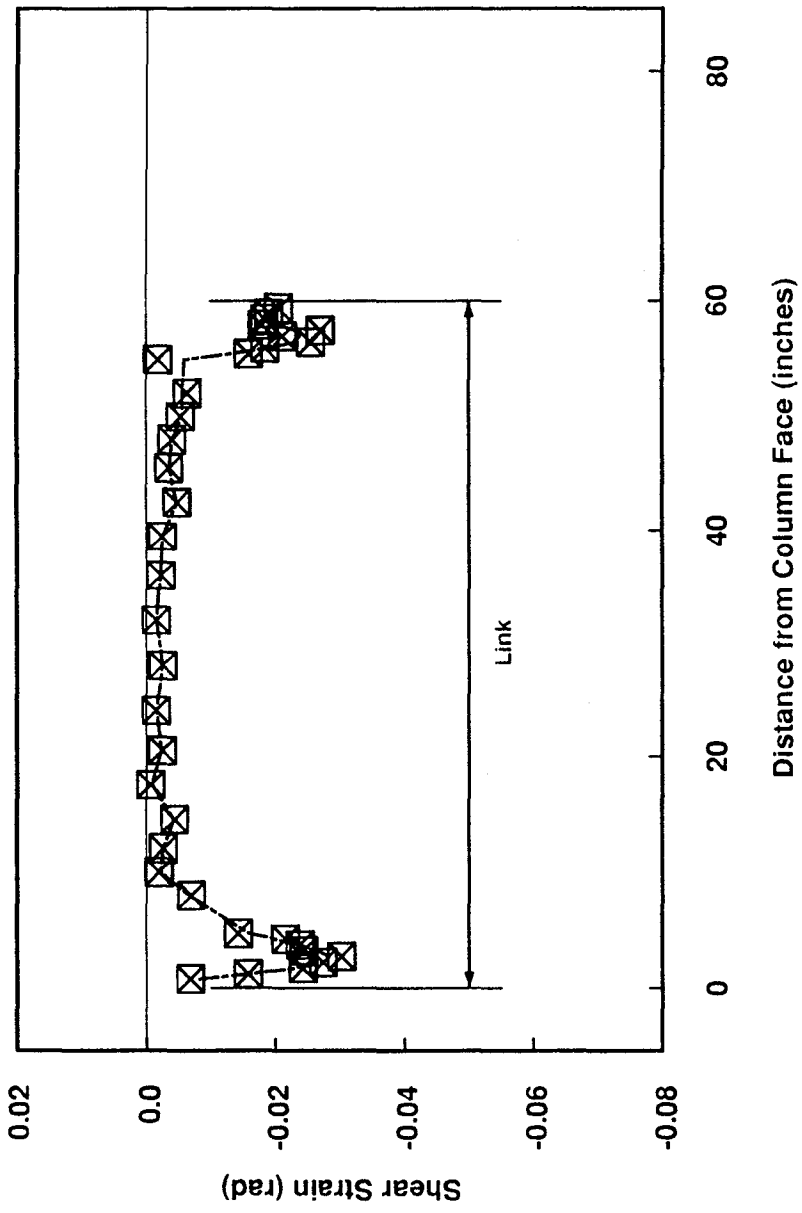

Fig. 5.34 Specimen 12 - Distribution of Average Shear Strain Along Length of Link
Reference State: Unloaded Specimen at Start of Cycle 7W
Final State: Peak Deformation at End of Cycle 7W

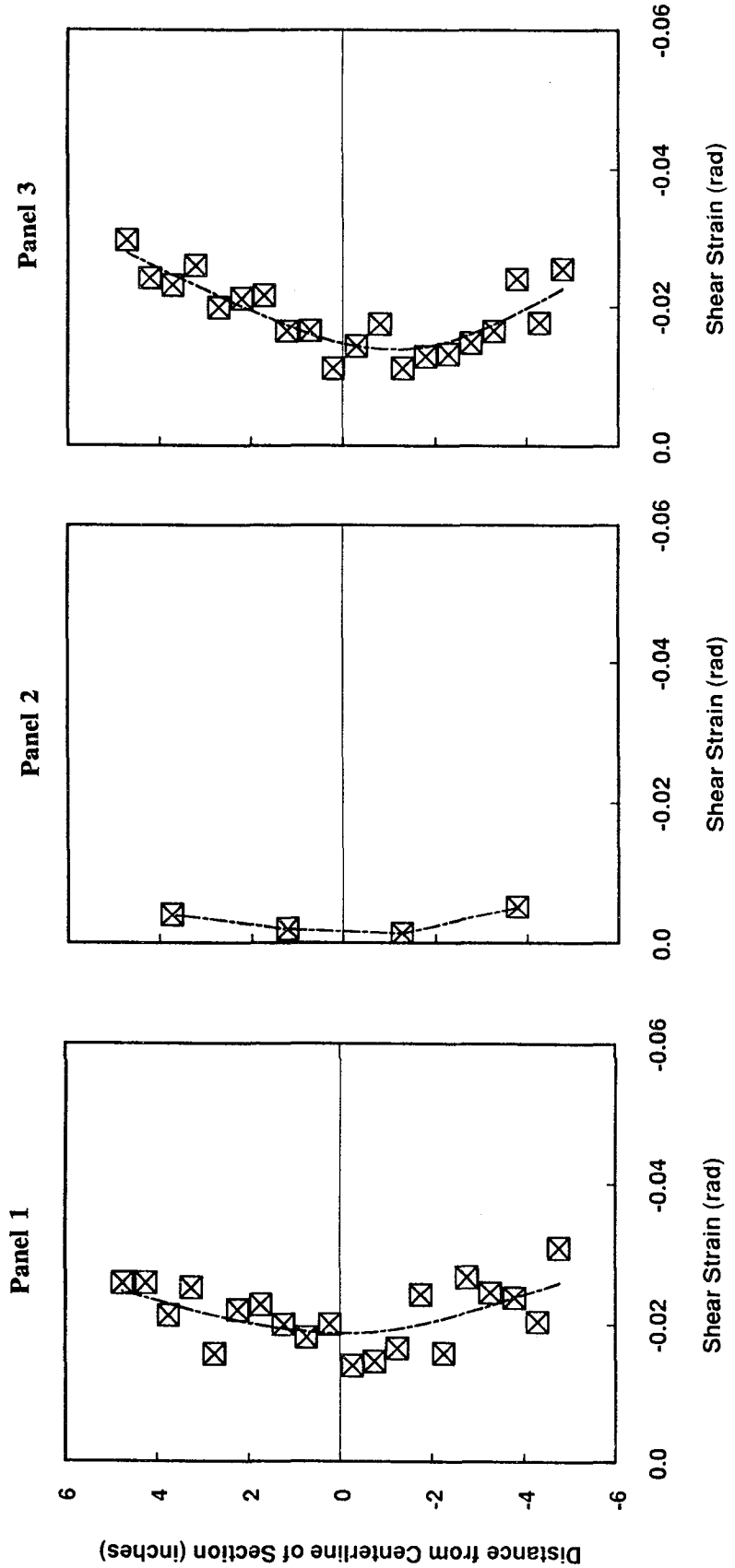

Fig. 5.35 Specimen 12 - Distribution of Average Shear Strain Over Depth of Web
Reference State: Unloaded Specimen at Start of Cycle 7W
Final State: Peak Deformation at End of Cycle 7W

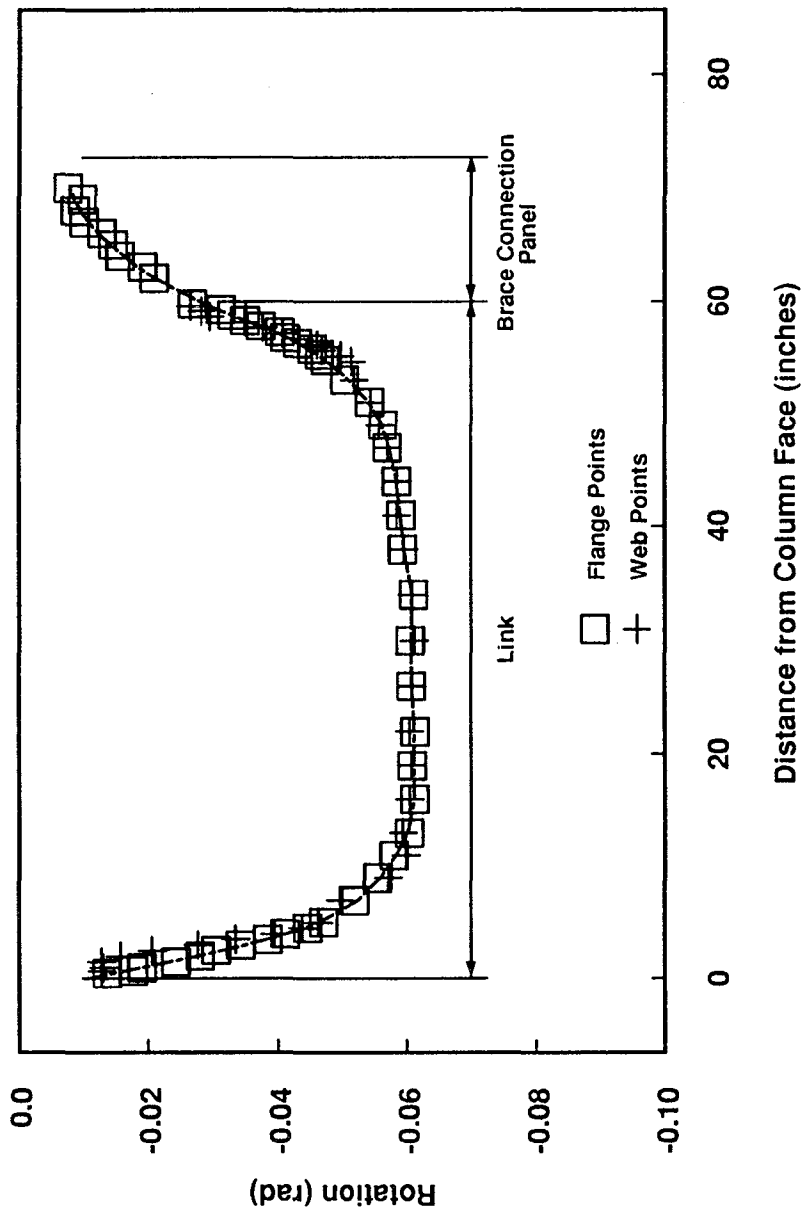

Fig. 5.36 Specimen 12 - Average Rotation of Web Gridlines and Rotation of Flange Gridpoints
Reference State: Unloaded Specimen at Start of Cycle 7W
Final State: Peak Deformation at End of Cycle 7W

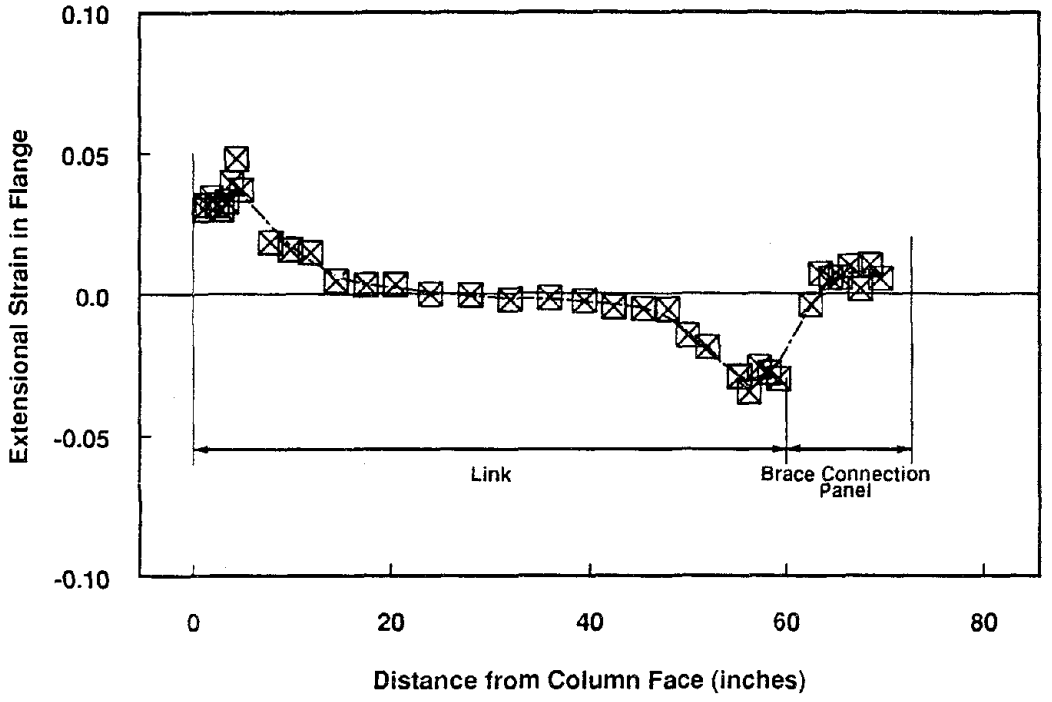

(a) West Flange

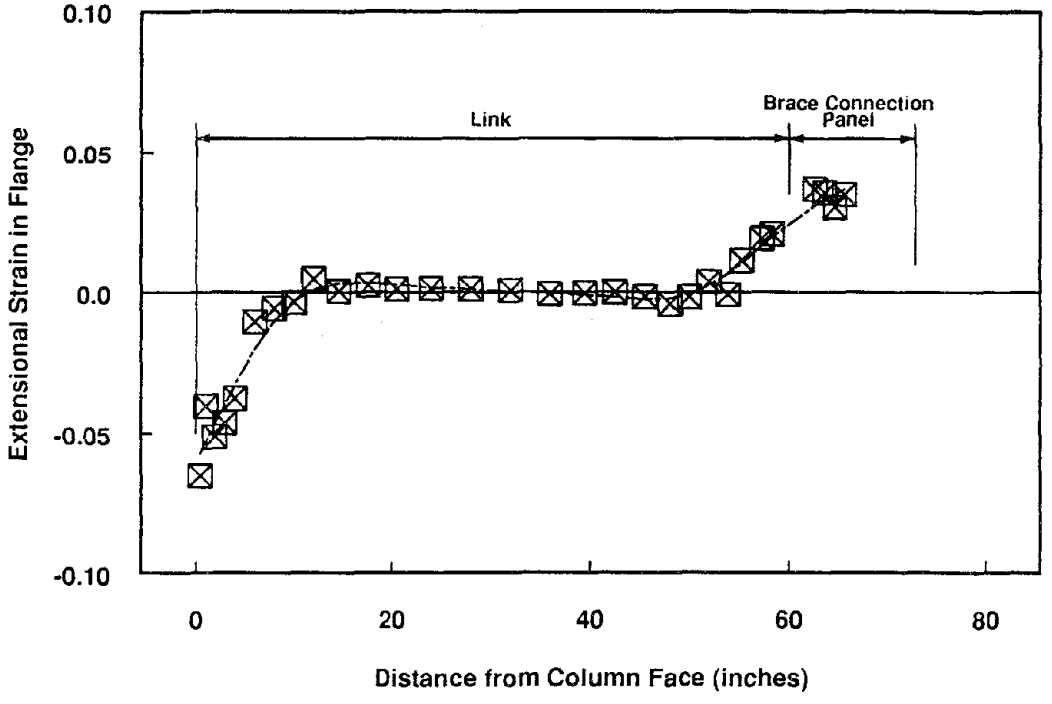

(b) East Flange

Fig. 5.37 Specimen 12 - Extensional Strain Measured from Flange Gridpoints
Reference State: Unloaded Specimen at Start of Cycle 7W
Final State: Peak Deformation at End of Cycle 7W

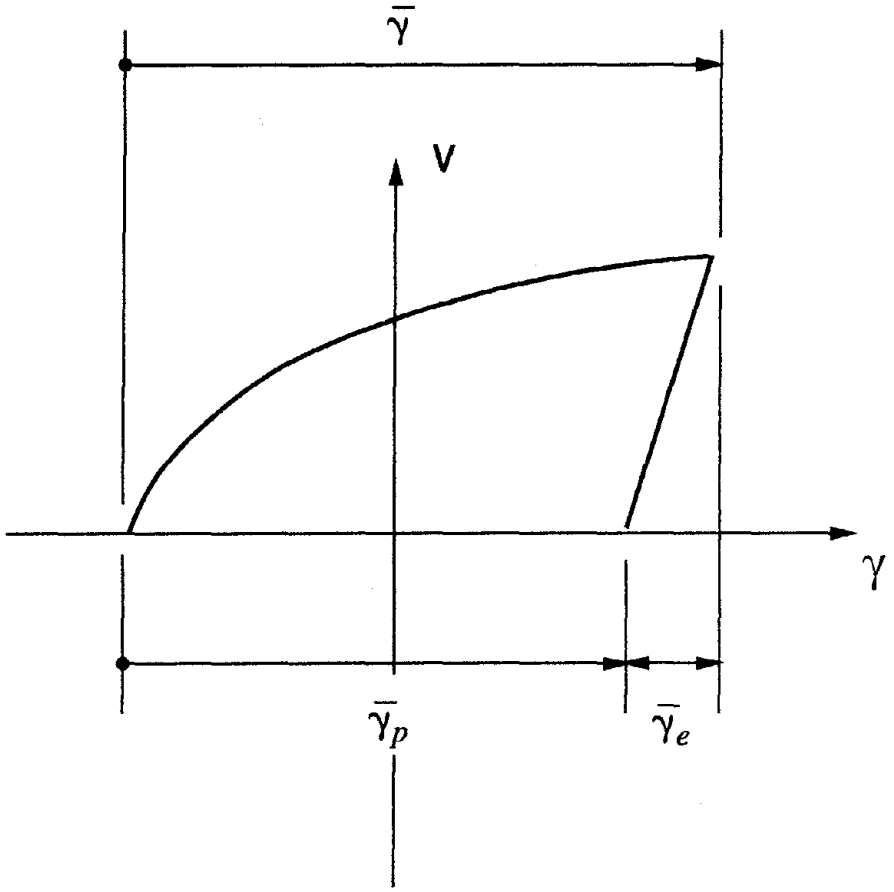

Fig. 5.38 Definition of $\bar{\gamma}$

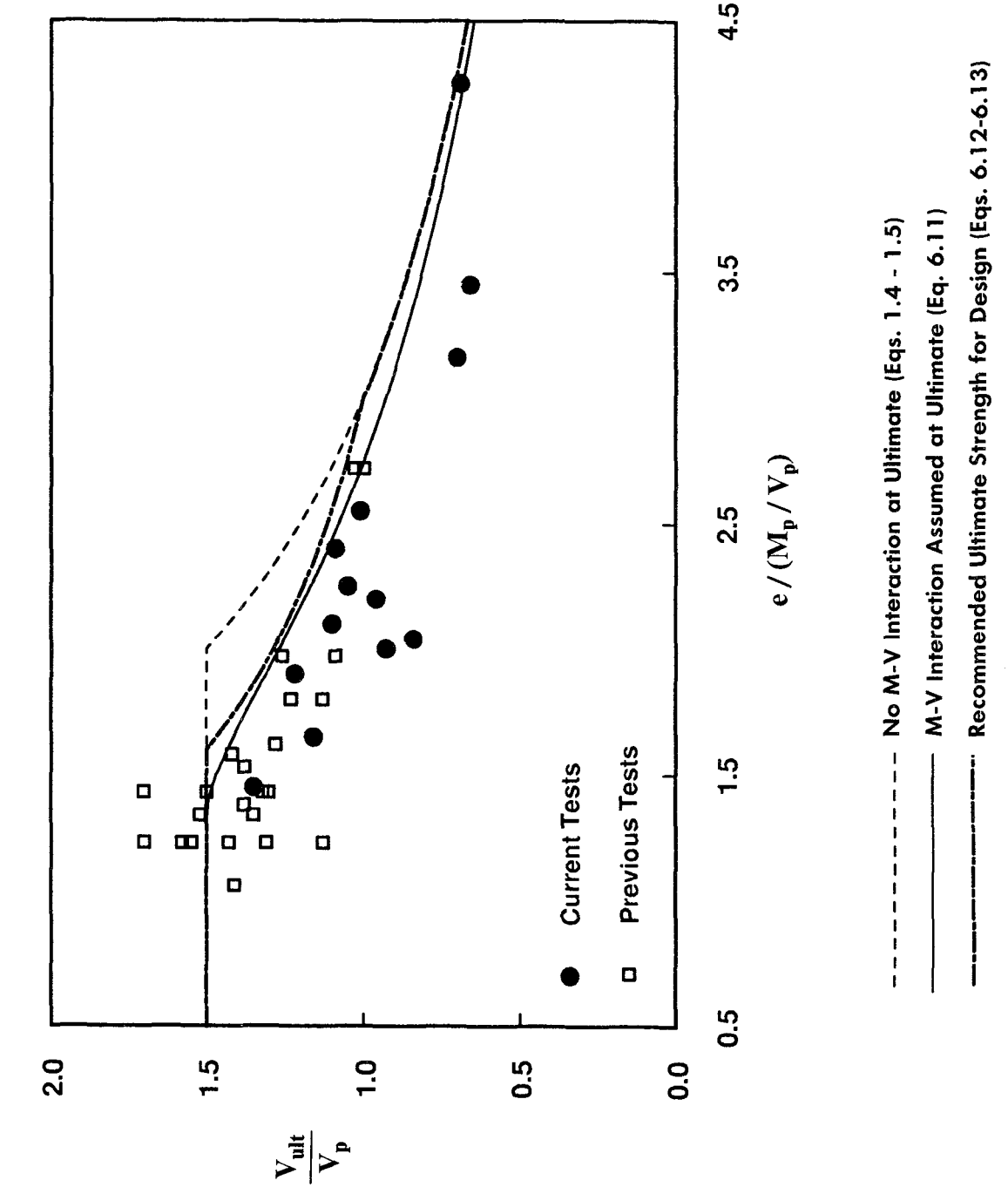

Fig. 6.1 Link Ultimate Shear Strength

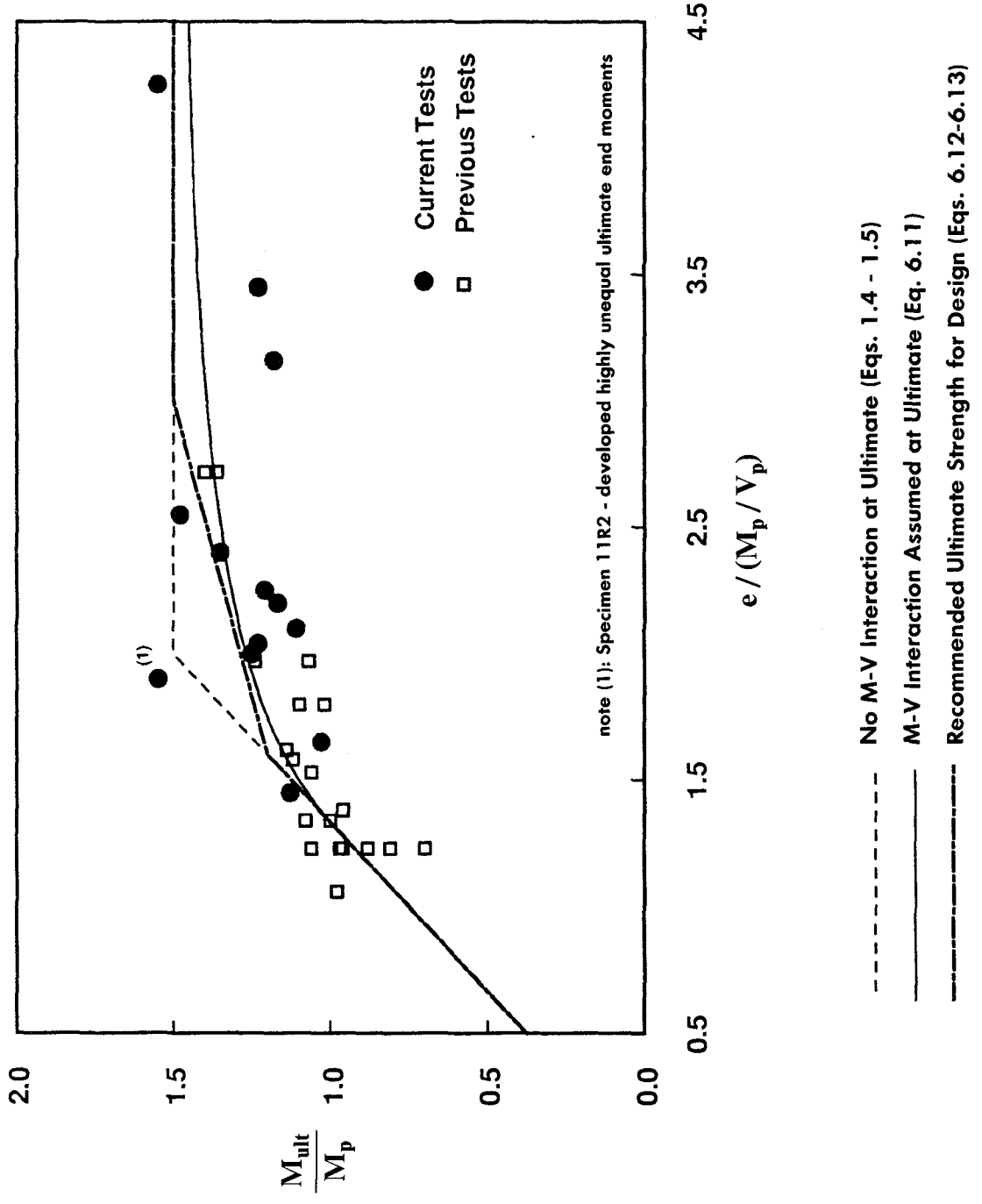

Fig. 6.2 Link Ultimate End Moments

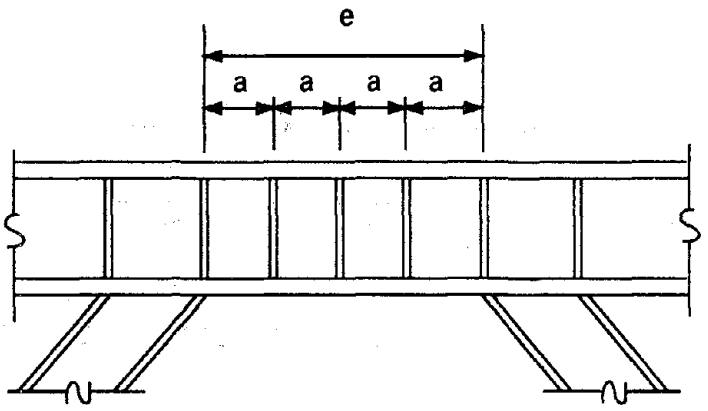

Spacing "a" should not exceed the following [from Ref. 20]:

$$a = 29\,t_w - \frac{d}{5} \quad \text{for} \quad \gamma_p = \pm .09 \text{ rad}$$

$$a = 38\,t_w - \frac{d}{5} \quad \text{for} \quad \gamma_p = \pm .06 \text{ rad}$$

$$a = 56\,t_w - \frac{d}{5} \quad \text{for} \quad \gamma_p = \pm .03 \text{ rad or less}$$

interpolate to determine "a" for intermediate values of γ_p

(a) Short Links ($e \leq 1.6 M_p / V_p$)

Fig. 6.3 Suggested Link Stiffener Spacing Criteria

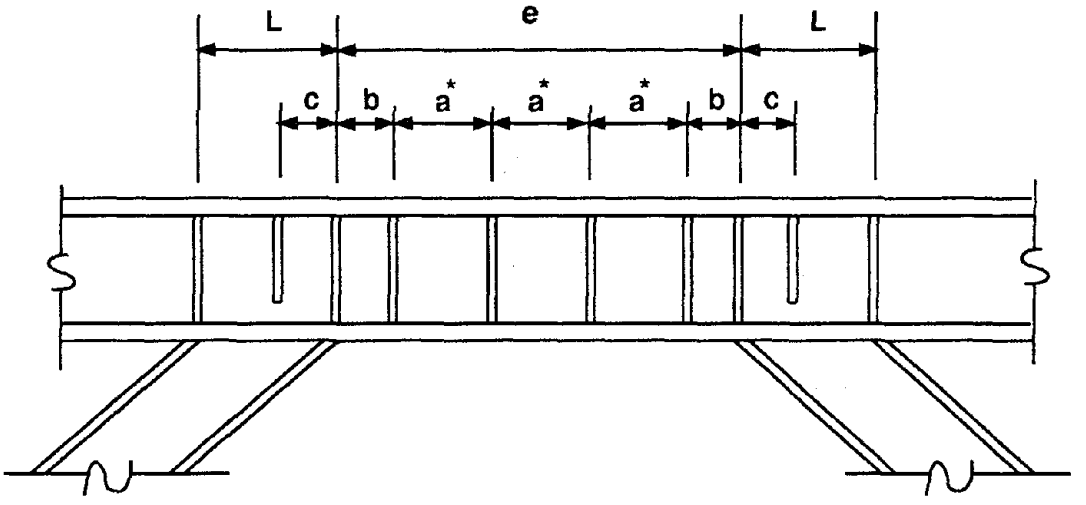

$$a^* = a \qquad \text{for} \quad e = 1.6\frac{M_p}{V_p}$$

$$a^* = \frac{3}{2}\left[\frac{M_p}{V_p} - b_f\right] \qquad \text{for} \quad e = 3\frac{M_p}{V_p}$$

interpolate to determine a^* for $1.6\frac{M_p}{V_p} \le e \le 3\frac{M_p}{V_p}$

$$b = \text{lesser of} \begin{cases} a^* \\ 1\tfrac{1}{2}\, b_f \end{cases}$$

$$c = \text{lesser of} \begin{cases} 1\tfrac{1}{2}\, b_f \\ \tfrac{1}{2}\, L \end{cases}$$

L = Length of Brace Connection Panel

(b) Intermediate Links ($1.6M_p/V_p < e \le 3M_p/V_p$)

Fig. 6.3 Suggested Link Stiffener Spacing Criteria (cont)

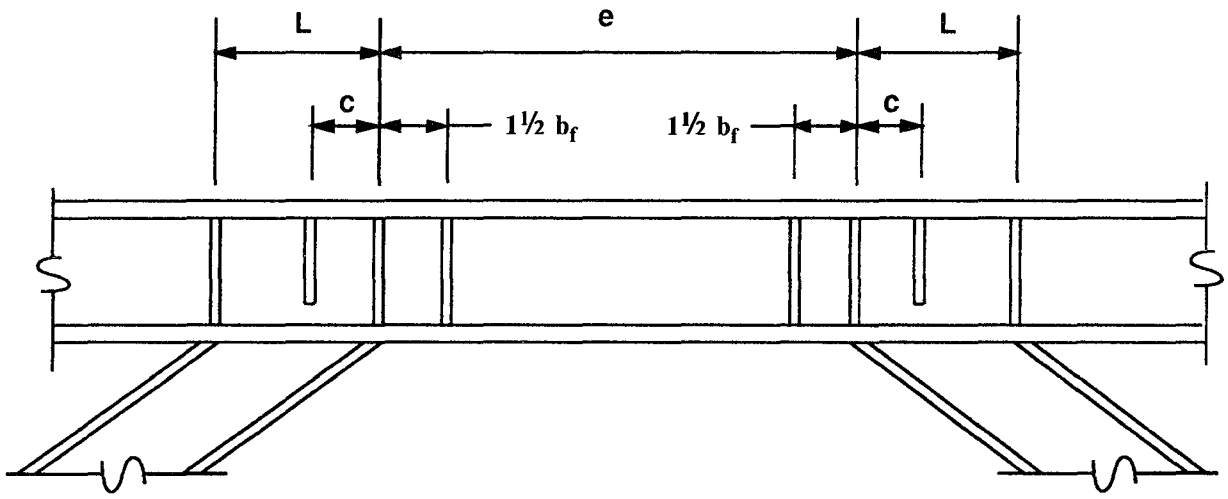

$$c = \text{lesser of} \begin{cases} 1\frac{1}{2}\, b_f \\ \frac{1}{2}\, L \end{cases}$$

L = Length of Brace Connection Panel

(c) Very Long Links ($e > 3M_p / V_p$)

Fig. 6.3 Suggested Link Stiffener Spacing Criteria (cont)

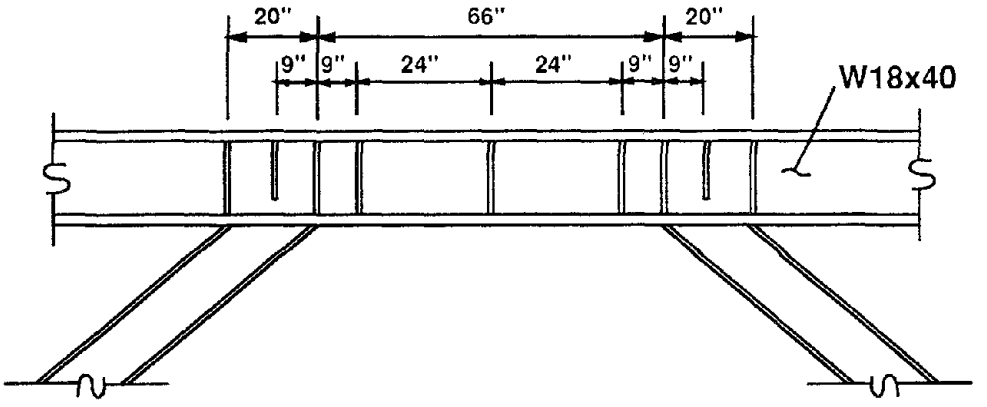

Fig. 6.4 Results of Stiffener Spacing Example

EARTHQUAKE ENGINEERING RESEARCH CENTER REPORT SERIES

EERC reports are available from the National Information Service for Earthquake Engineering(NISEE) and from the National Technical Information Service(NTIS). Numbers in parentheses are Accession Numbers assigned by the National Technical Information Service; these are followed by a price code. Contact NTIS, 5285 Port Royal Road, Springfield Virginia, 22161 for more information. Reports without Accession Numbers were not available from NTIS at the time of printing. For a current complete list of EERC reports (from EERC 67-1) and availablity information, please contact University of California, EERC, NISEE, 1301 South 46th Street, Richmond, California 94804.

UCB/EERC-80/01 "Earthquake Response of Concrete Gravity Dams Including Hydrodynamic and Foundation Interaction Effects," by Chopra, A.K., Chakrabarti, P. and Gupta, S., January 1980, (AD-A087297)A10.

UCB/EERC-80/02 "Rocking Response of Rigid Blocks to Earthquakes," by Yim, C.S., Chopra, A.K. and Penzien, J., January 1980, (PB80 166 002)A04.

UCB/EERC-80/03 "Optimum Inelastic Design of Seismic-Resistant Reinforced Concrete Frame Structures," by Zagajeski, S.W. and Bertero, V.V., January 1980, (PB80 164 635)A06.

UCB/EERC-80/04 "Effects of Amount and Arrangement of Wall-Panel Reinforcement on Hysteretic Behavior of Reinforced Concrete Walls," by Iliya, R. and Bertero, V.V., February 1980, (PB81 122 525)A09.

UCB/EERC-80/05 "Shaking Table Research on Concrete Dam Models," by Niwa, A. and Clough, R.W., September 1980, (PB81 122 368)A06.

UCB/EERC-80/06 "The Design of Steel Energy-Absorbing Restrainers and their Incorporation into Nuclear Power Plants for Enhanced Safety (Vol 1a): Piping with Energy Absorbing Restrainers: Parameter Study on Small Systems," by Powell, G.H., Oughourlian, C. and Simons, J., June 1980.

UCB/EERC-80/07 "Inelastic Torsional Response of Structures Subjected to Earthquake Ground Motions," by Yamazaki, Y., April 1980, (PB81 122 327)A08.

UCB/EERC-80/08 "Study of X-Braced Steel Frame Structures under Earthquake Simulation," by Ghanaat, Y., April 1980, (PB81 122 335)A11.

UCB/EERC-80/09 "Hybrid Modelling of Soil-Structure Interaction," by Gupta, S., Lin, T.W. and Penzien, J., May 1980, (PB81 122 319)A07.

UCB/EERC-80/10 "General Applicability of a Nonlinear Model of a One Story Steel Frame," by Sveinsson, B.I. and McNiven, H.D., May 1980, (PB81 124 877)A06.

UCB/EERC-80/11 "A Green-Function Method for Wave Interaction with a Submerged Body," by Kioka, W., April 1980, (PB81 122 269)A07.

UCB/EERC-80/12 "Hydrodynamic Pressure and Added Mass for Axisymmetric Bodies.," by Nilrat, F., May 1980, HYPAM, (PB81 122 343)A08.

UCB/EERC-80/13 "Treatment of Non-Linear Drag Forces Acting on Offshore Platforms," by Dao, B.V. and Penzien, J., May 1980, (PB81 153 413)A07.

UCB/EERC-80/14 "2D Plane/Axisymmetric Solid Element (Type 3-Elastic or Elastic-Perfectly Plastic)for the ANSR-II Program," by Mondkar, D.P. and Powell, G.H., July 1980, (PB81 122 350)A03.

UCB/EERC-80/15 "A Response Spectrum Method for Random Vibrations," by Der Kiureghian, A., June 1981, (PB81 122 301)A03.

UCB/EERC-80/16 "Cyclic Inelastic Buckling of Tubular Steel Braces," by Zayas, V.A., Popov, E.P. and Mahin, S.A., June 1981, (PB81 124 885)A10.

UCB/EERC-80/17 "Dynamic Response of Simple Arch Dams Including Hydrodynamic Interaction," by Porter, C.S. and Chopra, A.K., July 1981, (PB81 124 000)A13.

UCB/EERC-80/18 "Experimental Testing of a Friction Damped Aseismic Base Isolation System with Fail-Safe Characteristics," by Kelly, J.M., Beucke, K.E. and Skinner, M.S., July 1980, (PB81 148 595)A04.

UCB/EERC-80/19 "The Design of Steel Energy-Absorbing Restrainers and their Incorporation into Nuclear Power Plants for Enhanced Safety (Vol.1B): Stochastic Seismic Analyses of Nuclear Power Plant Structures and Piping Systems Subjected to Multiple Supported Excitations," by Lee, M.C. and Penzien, J., June 1980, PSAP, (PB82 201 872)A08.

UCB/EERC-80/20 "The Design of Steel Energy-Absorbing Restrainers and their Incorporation into Nuclear Power Plants for Enhanced Safety (Vol 1C): Numerical Method for Dynamic Substructure Analysis," by Dickens, J.M. and Wilson, E.L., June 1980.

UCB/EERC-80/21 "The Design of Steel Energy-Absorbing Restrainers and their Incorporation into Nuclear Power Plants for Enhanced Safety (Vol 2): Development and Testing of Restraints for Nuclear Piping Systems," by Kelly, J.M. and Skinner, M.S., June 1980.

UCB/EERC-80/22 "3D Solid Element (Type 4-Elastic or Elastic-Perfectly-Plastic) for the ANSR-II Program," by Mondkar, D.P. and Powell, G.H., July 1980, (PB81 123 242)A03.

UCB/EERC-80/23 "Gap-Friction Element (Type 5) for the Ansr-II Program," by Mondkar, D.P. and Powell, G.H., July 1980, (PB81 122 285)A03.

UCB/EERC-80/24 "U-Bar Restraint Element (Type 11) for the ANSR-II Program," by Oughourlian, C. and Powell, G.H., July 1980, (PB81 122 293)A03.

UCB/EERC-80/25 "Testing of a Natural Rubber Base Isolation System by an Explosively Simulated Earthquake," by Kelly, J.M., August 1980, (PB81 201 360)A04.

UCB/EERC-80/26 "Input Identification from Structural Vibrational Response," by Hu, Y., August 1980, (PB81 152 308)A05.

UCB/EERC-80/27 "Cyclic Inelastic Behavior of Steel Offshore Structures," by Zayas, V.A., Mahin, S.A. and Popov, E.P., August 1980, (PB81 196 180)A15.

UCB/EERC-80/28 "Shaking Table Testing of a Reinforced Concrete Frame with Biaxial Response," by Oliva, M.G., October 1980, (PB81 154 304)A10.

UCB/EERC-80/29 "Dynamic Properties of a Twelve-Story Prefabricated Panel Building," by Bouwkamp, J.G., Kollegger, J.P. and Stephen, R.M., October 1980, (PB82 138 777)A07.

UCB/EERC-80/30 "Dynamic Properties of an Eight-Story Prefabricated Panel Building," by Bouwkamp, J.G., Kollegger, J.P. and Stephen, R.M., October 1980, (PB81 200 313)A05.

UCB/EERC-80/31 "Predictive Dynamic Response of Panel Type Structures under Earthquakes," by Kollegger, J.P. and Bouwkamp, J.G., October 1980, (PB81 152 316)A04.

UCB/EERC-80/32 "The Design of Steel Energy-Absorbing Restrainers and their Incorporation into Nuclear Power Plants for Enhanced Safety (Vol 3): Testing of Commercial Steels in Low-Cycle Torsional Fatigue," by Spanner, P., Parker, E.R., Jongewaard, E. and Dory, M., 1980.

UCB/EERC-80/33 "The Design of Steel Energy-Absorbing Restrainers and their Incorporation into Nuclear Power Plants for Enhanced Safety (Vol 4): Shaking Table Tests of Piping Systems with Energy-Absorbing Restrainers," by Stiemer, S.F. and Godden, W.G., September 1980, (PB82 201 880)A05.

UCB/EERC-80/34 "The Design of Steel Energy-Absorbing Restrainers and their Incorporation into Nuclear Power Plants for Enhanced Safety (Vol 5): Summary Report," by Spencer, P., 1980.

UCB/EERC-80/35 "Experimental Testing of an Energy-Absorbing Base Isolation System," by Kelly, J.M., Skinner, M.S. and Beucke, K.E., October 1980, (PB81 154 072)A04.

UCB/EERC-80/36 "Simulating and Analyzing Artificial Non-Stationary Earth Ground Motions," by Nau, R.F., Oliver, R.M. and Pister, K.S., October 1980, (PB81 153 397)A04.

UCB/EERC-80/37 "Earthquake Engineering at Berkeley - 1980," by , September 1980, (PB81 205 674)A09.

UCB/EERC-80/38 "Inelastic Seismic Analysis of Large Panel Buildings," by Schricker, V. and Powell, G.H., September 1980, (PB81 154 338)A13.

UCB/EERC-80/39 "Dynamic Response of Embankment, Concrete-Gavity and Arch Dams Including Hydrodynamic Interation," by Hall, J.F. and Chopra, A.K., October 1980, (PB81 152 324)A11.

UCB/EERC-80/40 "Inelastic Buckling of Steel Struts under Cyclic Load Reversal.," by Black, R.G., Wenger, W.A. and Popov, E.P., October 1980, (PB81 154 312)A08.

UCB/EERC-80/41 "Influence of Site Characteristics on Buildings Damage during the October 3,1974 Lima Earthquake," by Repetto, P., Arango, I. and Seed, H.B., September 1980, (PB81 161 739)A05.

UCB/EERC-80/42 "Evaluation of a Shaking Table Test Program on Response Behavior of a Two Story Reinforced Concrete Frame," by Blondet, J.M., Clough, R.W. and Mahin, S.A., December 1980, (PB82 196 544)A11.

UCB/EERC-80/43 "Modelling of Soil-Structure Interaction by Finite and Infinite Elements," by Medina, F., December 1980, (PB81 229 270)A04.

UCB/EERC-81/01 "Control of Seismic Response of Piping Systems and Other Structures by Base Isolation," by Kelly, J.M., January 1981, (PB81 200 735)A05.

UCB/EERC-81/02 "OPTNSR- An Interactive Software System for Optimal Design of Statically and Dynamically Loaded Structures with Nonlinear Response," by Bhatti, M.A., Ciampi, V. and Pister, K.S., January 1981, (PB81 218 851)A09.

UCB/EERC-81/03 "Analysis of Local Variations in Free Field Seismic Ground Motions," by Chen, J.-C., Lysmer, J. and Seed, H.B., January 1981, (AD-A099508)A13.

UCB/EERC-81/04 "Inelastic Structural Modeling of Braced Offshore Platforms for Seismic Loading," by Zayas, V.A., Shing, P.-S.B., Mahin, S.A. and Popov, E.P., January 1981, INEL4, (PB82 138 777)A07.

UCB/EERC-81/05 "Dynamic Response of Light Equipment in Structures," by Der Kiureghian, A., Sackman, J.L. and Nour-Omid, B., April 1981, (PB81 218 497)A04.

UCB/EERC-81/06 "Preliminary Experimental Investigation of a Broad Base Liquid Storage Tank," by Bouwkamp, J.G., Kollegger, J.P. and Stephen, R.M., May 1981, (PB82 140 385)A03.

UCB/EERC-81/07 "The Seismic Resistant Design of Reinforced Concrete Coupled Structural Walls," by Aktan, A.E. and Bertero, V.V., June 1981, (PB82 113 358)A11.

UCB/EERC-81/08 "Unassigned," by Unassigned, 1981.

UCB/EERC-81/09 "Experimental Behavior of a Spatial Piping System with Steel Energy Absorbers Subjected to a Simulated Differential Seismic Input," by Stiemer, S.F., Godden, W.G. and Kelly, J.M., July 1981, (PB82 201 898)A04.

UCB/EERC-81/10 "Evaluation of Seismic Design Provisions for Masonry in the United States," by Sveinsson, B.I., Mayes, R.L. and McNiven, H.D., August 1981, (PB82 166 075)A08.

UCB/EERC-81/11 "Two-Dimensional Hybrid Modelling of Soil-Structure Interaction," by Tzong, T.-J., Gupta, S. and Penzien, J., August 1981, (PB82 142 118)A04.

UCB/EERC-81/12 "Studies on Effects of Infills in Seismic Resistant R/C Construction," by Brokken, S. and Bertero, V.V., October 1981, (PB82 166 190)A09.

UCB/EERC-81/13 "Linear Models to Predict the Nonlinear Seismic Behavior of a One-Story Steel Frame," by Valdimarsson, H., Shah, A.H. and McNiven, H.D., September 1981, (PB82 138 793)A07.

UCB/EERC-81/14 "TLUSH: A Computer Program for the Three-Dimensional Dynamic Analysis of Earth Dams," by Kagawa, T., Mejia, L.H., Seed, H.B. and Lysmer, J., September 1981, (PB82 139 940)A06.

UCB/EERC-81/15 "Three Dimensional Dynamic Response Analysis of Earth Dams," by Mejia, L.H. and Seed, H.B., September 1981, (PB82 137 274)A12.

UCB/EERC-81/16 "Experimental Study of Lead and Elastomeric Dampers for Base Isolation Systems," by Kelly, J.M. and Hodder, S.B., October 1981, (PB82 166 182)A05.

UCB/EERC-81/17 "The Influence of Base Isolation on the Seismic Response of Light Secondary Equipment," by Kelly, J.M., April 1981, (PB82 255 266)A04.

UCB/EERC-81/18 "Studies on Evaluation of Shaking Table Response Analysis Procedures," by Blondet, J. M., November 1981, (PB82 197 278)A10.

UCB/EERC-81/19 "DELIGHT.STRUCT: A Computer-Aided Design Environment for Structural Engineering," by Balling, R.J., Pister, K.S. and Polak, E., December 1981, (PB82 218 496)A07.

UCB/EERC-81/20 "Optimal Design of Seismic-Resistant Planar Steel Frames," by Balling, R.J., Ciampi, V. and Pister, K.S., December 1981, (PB82 220 179)A07.

UCB/EERC-82/01 "Dynamic Behavior of Ground for Seismic Analysis of Lifeline Systems," by Sato, T. and Der Kiureghian, A., January 1982, (PB82 218 926)A05.

UCB/EERC-82/02 "Shaking Table Tests of a Tubular Steel Frame Model," by Ghanaat, Y. and Clough, R.W., January 1982, (PB82 220 161)A07.

UCB/EERC-82/03 "Behavior of a Piping System under Seismic Excitation: Experimental Investigations of a Spatial Piping System supported by Mechanical Shock Arrestors," by Schneider, S., Lee, H.-M. and Godden, W. G., May 1982, (PB83 172 544)A09.

UCB/EERC-82/04 "New Approaches for the Dynamic Analysis of Large Structural Systems," by Wilson, E.L., June 1982, (PB83 148 080)A05.

UCB/EERC-82/05 "Model Study of Effects of Damage on the Vibration Properties of Steel Offshore Platforms," by Shahrivar, F. and Bouwkamp, J.G., June 1982, (PB83 148 742)A10.

UCB/EERC-82/06 "States of the Art and Pratice in the Optimum Seismic Design and Analytical Response Prediction of R/C Frame Wall Structures," by Aktan, A.E. and Bertero, V.V., July 1982, (PB83 147 736)A05.

UCB/EERC-82/07 "Further Study of the Earthquake Response of a Broad Cylindrical Liquid-Storage Tank Model," by Manos, G.C. and Clough, R.W., July 1982, (PB83 147 744)A11.

UCB/EERC-82/08 "An Evaluation of the Design and Analytical Seismic Response of a Seven Story Reinforced Concrete Frame," by Charney, F.A. and Bertero, V.V., July 1982, (PB83 157 628)A09.

UCB/EERC-82/09 "Fluid-Structure Interactions: Added Mass Computations for Incompressible Fluid," by Kuo, J.S.-H., August 1982, (PB83 156 281)A07.

UCB/EERC-82/10 "Joint-Opening Nonlinear Mechanism: Interface Smeared Crack Model," by Kuo, J.S.-H., August 1982, (PB83 149 195)A05.

UCB/EERC-82/11 "Dynamic Response Analysis of Techi Dam," by Clough, R.W., Stephen, R.M. and Kuo, J.S.-H., August 1982, (PB83 147 496)A06.

UCB/EERC-82/12 "Prediction of the Seismic Response of R/C Frame-Coupled Wall Structures," by Aktan, A.E., Bertero, V.V. and Piazzo, M., August 1982, (PB83 149 203)A09.

UCB/EERC-82/13 "Preliminary Report on the Smart 1 Strong Motion Array in Taiwan," by Bolt, B.A., Loh, C.H., Penzien, J. and Tsai, Y.B., August 1982, (PB83 159 400)A10.

UCB/EERC-82/14 "Seismic Behavior of an Eccentrically X-Braced Steel Structure," by Yang, M.S., September 1982, (PB83 260 778)A12.

UCB/EERC-82/15 "The Performance of Stairways in Earthquakes," by Roha, C., Axley, J.W. and Bertero, V.V., September 1982, (PB83 157 693)A07.

UCB/EERC-82/16 "The Behavior of Submerged Multiple Bodies in Earthquakes," by Liao, W.-G., September 1982, (PB83 158 709)A07.

UCB/EERC-82/17 "Effects of Concrete Types and Loading Conditions on Local Bond-Slip Relationships," by Cowell, A.D., Popov, E.P. and Bertero, V.V., September 1982, (PB83 153 577)A04.

UCB/EERC-82/18 "Mechanical Behavior of Shear Wall Vertical Boundary Members: An Experimental Investigation," by Wagner, M.T. and Bertero, V.V., October 1982, (PB83 159 764)A05.

UCB/EERC-82/19 "Experimental Studies of Multi-support Seismic Loading on Piping Systems," by Kelly, J.M. and Cowell, A.D., November 1982.

UCB/EERC-82/20 "Generalized Plastic Hinge Concepts for 3D Beam-Column Elements," by Chen, P. F.-S. and Powell, G.H., November 1982, (PB83 247 981)A13.

UCB/EERC-82/21 "ANSR-II: General Computer Program for Nonlinear Structural Analysis," by Oughourlian, C.V. and Powell, G.H., November 1982, (PB83 251 330)A12.

UCB/EERC-82/22 "Solution Strategies for Statically Loaded Nonlinear Structures," by Simons, J.W. and Powell, G.H., November 1982, (PB83 197 970)A06.

UCB/EERC-82/23 "Analytical Model of Deformed Bar Anchorages under Generalized Excitations," by Ciampi, V., Eligehausen, R., Bertero, V.V. and Popov, E.P., November 1982, (PB83 169 532)A06.

UCB/EERC-82/24 "A Mathematical Model for the Response of Masonry Walls to Dynamic Excitations," by Sucuoglu, H., Mengi, Y. and McNiven, H.D., November 1982, (PB83 169 011)A07.

UCB/EERC-82/25 "Earthquake Response Considerations of Broad Liquid Storage Tanks," by Cambra, F.J., November 1982, (PB83 251 215)A09.

UCB/EERC-82/26 "Computational Models for Cyclic Plasticity, Rate Dependence and Creep," by Mosaddad, B. and Powell, G.H., November 1982, (PB83 245 829)A08.

UCB/EERC-82/27 "Inelastic Analysis of Piping and Tubular Structures," by Mahasuverachai, M. and Powell, G.H., November 1982, (PB83 249 987)A07.

UCB/EERC-83/01 "The Economic Feasibility of Seismic Rehabilitation of Buildings by Base Isolation," by Kelly, J.M., January 1983, (PB83 197 988)A05.

UCB/EERC-83/02 "Seismic Moment Connections for Moment-Resisting Steel Frames.," by Popov, E.P., January 1983, (PB83 195 412)A04.

UCB/EERC-83/03 "Design of Links and Beam-to-Column Connections for Eccentrically Braced Steel Frames," by Popov, E.P. and Malley, J.O., January 1983, (PB83 194 811)A04.

UCB/EERC-83/04 "Numerical Techniques for the Evaluation of Soil-Structure Interaction Effects in the Time Domain," by Bayo, E. and Wilson, E.L., February 1983, (PB83 245 605)A09.

UCB/EERC-83/05 "A Transducer for Measuring the Internal Forces in the Columns of a Frame-Wall Reinforced Concrete Structure," by Sause, R. and Bertero, V.V., May 1983, (PB84 119 494)A06.

UCB/EERC-83/06 "Dynamic Interactions Between Floating Ice and Offshore Structures," by Croteau, P., May 1983, (PB84 119 486)A16.

UCB/EERC-83/07 "Dynamic Analysis of Multiply Tuned and Arbitrarily Supported Secondary Systems," by Igusa, T. and Der Kiureghian, A., July 1983, EADHI, (PB84 118 272)A11.

UCB/EERC-83/08 "A Laboratory Study of Submerged Multi-body Systems in Earthquakes," by Ansari, G.R., June 1983, (PB83 261 842)A17.

UCB/EERC-83/09 "Effects of Transient Foundation Uplift on Earthquake Response of Structures," by Yim, C.-S. and Chopra, A.K., June 1983, (PB83 261 396)A07.

UCB/EERC-83/10 "Optimal Design of Friction-Braced Frames under Seismic Loading," by Austin, M.A. and Pister, K.S., June 1983, (PB84 119 288)A06.

UCB/EERC-83/11 "Shaking Table Study of Single-Story Masonry Houses: Dynamic Performance under Three Component Seismic Input and Recommendations," by Manos, G.C., Clough, R.W. and Mayes, R.L., July 1983, (UCB/EERC-83/11)A08.

UCB/EERC-83/12 "Experimental Error Propagation in Pseudodynamic Testing," by Shiing, P.B. and Mahin, S.A., June 1983, (PB84 119 270)A09.

UCB/EERC-83/13 "Experimental and Analytical Predictions of the Mechanical Characteristics of a 1/5-scale Model of a 7-story R/C Frame-Wall Building Structure," by Aktan, A.E., Bertero, V.V., Chowdhury, A.A. and Nagashima, T., June 1983, (PB84 119 213)A07.

UCB/EERC-83/14 "Shaking Table Tests of Large-Panel Precast Concrete Building System Assemblages," by Oliva, M.G. and Clough, R.W., June 1983, (PB86 110 210/AS)A11.

UCB/EERC-83/15 "Seismic Behavior of Active Beam Links in Eccentrically Braced Frames," by Hjelmstad, K.D. and Popov, E.P., July 1983, (PB84 119 676)A09.

UCB/EERC-83/16 "System Identification of Structures with Joint Rotation," by Dimsdale, J.S., July 1983, (PB84 192 210)A06.

UCB/EERC-83/17 "Construction of Inelastic Response Spectra for Single-Degree-of-Freedom Systems," by Mahin, S. and Lin, J., June 1983, (PB84 208 834)A05.

UCB/EERC-83/18 "Interactive Computer Analysis Methods for Predicting the Inelastic Cyclic Behaviour of Structural Sections," by Kaba, S. and Mahin, S., July 1983, (PB84 192 012)A06.

UCB/EERC-83/19 "Effects of Bond Deterioration on Hysteretic Behavior of Reinforced Concrete Joints," by Filippou, F.C., Popov, E.P. and Bertero, V.V., August 1983, (PB84 192 020)A10.

UCB/EERC-83/20 "Analytical and Experimental Correlation of Large-Panel Precast Building System Performance," by Oliva, M.G., Clough, R.W., Velkov, M. and Gavrilovic, P., November 1983.

UCB/EERC-83/21 "Mechanical Characteristics of Materials Used in a 1/5 Scale Model of a 7-Story Reinforced Concrete Test Structure," by Bertero, V.V., Aktan, A.E., Harris, H.G. and Chowdhury, A.A., October 1983, (PB84 193 697)A05.

UCB/EERC-83/22 "Hybrid Modelling of Soil-Structure Interaction in Layered Media," by Tzong, T.-J. and Penzien, J., October 1983, (PB84 192 178)A08.

UCB/EERC-83/23 "Local Bond Stress-Slip Relationships of Deformed Bars under Generalized Excitations," by Eligehausen, R., Popov, E.P. and Bertero, V.V., October 1983, (PB84 192 848)A09.

UCB/EERC-83/24 "Design Considerations for Shear Links in Eccentrically Braced Frames," by Malley, J.O. and Popov, E.P., November 1983, (PB84 192 186)A07.

UCB/EERC-84/01 "Pseudodynamic Test Method for Seismic Performance Evaluation: Theory and Implementation," by Shing, P.-S.B. and Mahin, S.A., January 1984, (PB84 190 644)A08.

UCB/EERC-84/02 "Dynamic Response Behavior of Kiang Hong Dian Dam," by Clough, R.W., Chang, K.-T., Chen, H.-Q. and Stephen, R.M., April 1984, (PB84 209 402)A08.

UCB/EERC-84/03 "Refined Modelling of Reinforced Concrete Columns for Seismic Analysis," by Kaba, S.A. and Mahin, S.A., April 1984, (PB84 234 384)A06.

UCB/EERC-84/04 "A New Floor Response Spectrum Method for Seismic Analysis of Multiply Supported Secondary Systems," by Asfura, A. and Der Kiureghian, A., June 1984, (PB84 239 417)A06.

UCB/EERC-84/05 "Earthquake Simulation Tests and Associated Studies of a 1/5th-scale Model of a 7-Story R/C Frame-Wall Test Structure," by Bertero, V.V., Aktan, A.E., Charney, F.A. and Sause, R., June 1984, (PB84 239 409)A09.

UCB/EERC-84/06 "R/C Structural Walls: Seismic Design for Shear," by Aktan, A.E. and Bertero, V.V., 1984.

UCB/EERC-84/07 "Behavior of Interior and Exterior Flat-Plate Connections subjected to Inelastic Load Reversals," by Zee, H.L. and Moehle, J.P., August 1984, (PB86 117 629/AS)A07.

UCB/EERC-84/08 "Experimental Study of the Seismic Behavior of a Two-Story Flat-Plate Structure," by Moehle, J.P. and Diebold, J.W., August 1984, (PB86 122 553/AS)A12.

UCB/EERC-84/09 "Phenomenological Modeling of Steel Braces under Cyclic Loading," by Ikeda, K., Mahin, S.A. and Dermitzakis, S.N., May 1984, (PB86 132 198/AS)A08.

UCB/EERC-84/10 "Earthquake Analysis and Response of Concrete Gravity Dams," by Fenves, G. and Chopra, A.K., August 1984, (PB85 193 902/AS)A11.

UCB/EERC-84/11 "EAGD-84: A Computer Program for Earthquake Analysis of Concrete Gravity Dams," by Fenves, G. and Chopra, A.K., August 1984, (PB85 193 613/AS)A05.

UCB/EERC-84/12 "A Refined Physical Theory Model for Predicting the Seismic Behavior of Braced Steel Frames," by Ikeda, K. and Mahin, S.A., July 1984, (PB85 191 450/AS)A09.

UCB/EERC-84/13 "Earthquake Engineering Research at Berkeley - 1984," by , August 1984, (PB85 197 341/AS)A10.

UCB/EERC-84/14 "Moduli and Damping Factors for Dynamic Analyses of Cohesionless Soils," by Seed, H.B., Wong, R.T., Idriss, I.M. and Tokimatsu, K., September 1984, (PB85 191 468/AS)A04.

UCB/EERC-84/15 "The Influence of SPT Procedures in Soil Liquefaction Resistance Evaluations," by Seed, H.B., Tokimatsu, K., Harder, L.F. and Chung, R.M., October 1984, (PB85 191 732/AS)A04.

UCB/EERC-84/16 "Simplified Procedures for the Evaluation of Settlements in Sands Due to Earthquake Shaking," by Tokimatsu, K. and Seed, H.B., October 1984, (PB85 197 887/AS)A03.

UCB/EERC-84/17 "Evaluation of Energy Absorption Characteristics of Bridges under Seismic Conditions," by Imbsen, R.A. and Penzien, J., November 1984.

UCB/EERC-84/18 "Structure-Foundation Interactions under Dynamic Loads," by Liu, W.D. and Penzien, J., November 1984, (PB87 124 889/AS)A11.

UCB/EERC-84/19 "Seismic Modelling of Deep Foundations," by Chen, C.-H. and Penzien, J., November 1984, (PB87 124 798/AS)A07.

UCB/EERC-84/20 "Dynamic Response Behavior of Quan Shui Dam," by Clough, R.W., Chang, K.-T., Chen, H.-Q., Stephen, R.M., Ghanaat, Y. and Qi, J.-H., November 1984, (PB86 115177/AS)A07.

UCB/EERC-85/01 "Simplified Methods of Analysis for Earthquake Resistant Design of Buildings," by Cruz, E.F. and Chopra, A.K., February 1985, (PB86 112299/AS)A12.

UCB/EERC-85/02 "Estimation of Seismic Wave Coherency and Rupture Velocity using the SMART 1 Strong-Motion Array Recordings," by Abrahamson, N.A., March 1985, (PB86 214 343)A07.

UCB/EERC-85/03 "Dynamic Properties of a Thirty Story Condominium Tower Building," by Stephen, R.M., Wilson, E.L. and Stander, N., April 1985, (PB86 118965/AS)A06.

UCB/EERC-85/04 "Development of Substructuring Techniques for On-Line Computer Controlled Seismic Performance Testing," by Dermitzakis, S. and Mahin, S., February 1985, (PB86 132941/AS)A08.

UCB/EERC-85/05 "A Simple Model for Reinforcing Bar Anchorages under Cyclic Excitations," by Filippou, F.C., March 1985, (PB86 112 919/AS)A05.

UCB/EERC-85/06 "Racking Behavior of Wood-framed Gypsum Panels under Dynamic Load," by Oliva, M.G., June 1985.

UCB/EERC-85/07 "Earthquake Analysis and Response of Concrete Arch Dams," by Fok, K.-L. and Chopra, A.K., June 1985, (PB86 139672/AS)A10.

UCB/EERC-85/08 "Effect of Inelastic Behavior on the Analysis and Design of Earthquake Resistant Structures," by Lin, J.P. and Mahin, S.A., June 1985, (PB86 135340/AS)A08.

UCB/EERC-85/09 "Earthquake Simulator Testing of a Base-Isolated Bridge Deck," by Kelly, J.M., Buckle, I.G. and Tsai, H.-C., January 1986, (PB87 124 152/AS)A06.

UCB/EERC-85/10 "Simplified Analysis for Earthquake Resistant Design of Concrete Gravity Dams," by Fenves, G. and Chopra, A.K., June 1986, (PB87 124 160/AS)A08.

UCB/EERC-85/11 "Dynamic Interaction Effects in Arch Dams," by Clough, R.W., Chang, K.-T., Chen, H.-Q. and Ghanaat, Y., October 1985, (PB86 135027/AS)A05.

UCB/EERC-85/12 "Dynamic Response of Long Valley Dam in the Mammoth Lake Earthquake Series of May 25-27, 1980," by Lai, S. and Seed, H.B., November 1985, (PB86 142304/AS)A05.

UCB/EERC-85/13 "A Methodology for Computer-Aided Design of Earthquake-Resistant Steel Structures," by Austin, M.A., Pister, K.S. and Mahin, S.A., December 1985, (PB86 159480/AS)A10 .

UCB/EERC-85/14 "Response of Tension-Leg Platforms to Vertical Seismic Excitations," by Liou, G.-S., Penzien, J. and Yeung, R.W., December 1985, (PB87 124 871/AS)A08.

UCB/EERC-85/15 "Cyclic Loading Tests of Masonry Single Piers: Volume 4 - Additional Tests with Height to Width Ratio of 1," by Sveinsson, B., McNiven, H.D. and Sucuoglu, H., December 1985.

UCB/EERC-85/16 "An Experimental Program for Studying the Dynamic Response of a Steel Frame with a Variety of Infill Partitions," by Yanev, B. and McNiven, H.D., December 1985.

UCB/EERC-86/01 "A Study of Seismically Resistant Eccentrically Braced Steel Frame Systems," by Kasai, K. and Popov, E.P., January 1986, (PB87 124 178/AS)A14.

UCB/EERC-86/02 "Design Problems in Soil Liquefaction," by Seed, H.B., February 1986, (PB87 124 186/AS)A03.

UCB/EERC-86/03 "Implications of Recent Earthquakes and Research on Earthquake-Resistant Design and Construction of Buildings," by Bertero, V.V., March 1986, (PB87 124 194/AS)A05.

UCB/EERC-86/04 "The Use of Load Dependent Vectors for Dynamic and Earthquake Analyses," by Leger, P., Wilson, E.L. and Clough, R.W., March 1986, (PB87 124 202/AS)A12.

UCB/EERC-86/05 "Two Beam-To-Column Web Connections," by Tsai, K.-C. and Popov, E.P., April 1986, (PB87 124 301/AS)A04.

UCB/EERC-86/06 "Determination of Penetration Resistance for Coarse-Grained Soils using the Becker Hammer Drill," by Harder, L.F. and Seed, H.B., May 1986, (PB87 124 210/AS)A07.

UCB/EERC-86/07 "A Mathematical Model for Predicting the Nonlinear Response of Unreinforced Masonry Walls to In-Plane Earthquake Excitations," by Mengi, Y. and McNiven, H.D., May 1986, (PB87 124 780/AS)A06.

UCB/EERC-86/08 "The 19 September 1985 Mexico Earthquake: Building Behavior," by Bertero, V.V., July 1986.

UCB/EERC-86/09 "EACD-3D: A Computer Program for Three-Dimensional Earthquake Analysis of Concrete Dams," by Fok, K.-L., Hall, J.F. and Chopra, A.K., July 1986, (PB87 124 228/AS)A08.

UCB/EERC-86/10 "Earthquake Simulation Tests and Associated Studies of a 0.3-Scale Model of a Six-Story Concentrically Braced Steel Structure," by Uang, C.-M. and Bertero, V.V., December 1986, (PB87 163 564/AS)A17.

UCB/EERC-86/11 "Mechanical Characteristics of Base Isolation Bearings for a Bridge Deck Model Test," by Kelly, J.M., Buckle, I.G. and Koh, C.-G., 1987.

UCB/EERC-86/12 "Effects of Axial Load on Elastomeric Isolation Bearings," by Koh, C.-G. and Kelly, J.M., November 1987.

UCB/EERC-87/01 "The FPS Earthquake Resisting System: Experimental Report," by Zayas, V.A., Low, S.S. and Mahin, S.A., June 1987.

UCB/EERC-87/02 "Earthquake Simulator Tests and Associated Studies of a 0.3-Scale Model of a Six-Story Eccentrically Braced Steel Structure," by Whittaker, A., Uang, C.-M. and Bertero, V.V., July 1987.

UCB/EERC-87/03 "A Displacement Control and Uplift Restraint Device for Base-Isolated Structures," by Kelly, J.M., Griffith, M.C. and Aiken, I.D., April 1987.

UCB/EERC-87/04 "Earthquake Simulator Testing of a Combined Sliding Bearing and Rubber Bearing Isolation System," by Kelly, J.M. and Chalhoub, M.S., 1987.

UCB/EERC-87/05 "Three-Dimensional Inelastic Analysis of Reinforced Concrete Frame-Wall Structures," by Moazzami, S. and Bertero, V.V., May 1987.

UCB/EERC-87/06 "Experiments on Eccentrically Braced Frames with Composite Floors," by Ricles, J. and Popov, E., June 1987.

UCB/EERC-87/07 "Dynamic Analysis of Seismically Resistant Eccentrically Braced Frames," by Ricles, J. and Popov, E., June 1987.

UCB/EERC-87/08 "Undrained Cyclic Triaxial Testing of Gravels-The Effect of Membrane Compliance," by Evans, M.D. and Seed, H.B., July 1987.

UCB/EERC-87/09 "Hybrid Solution Techniques for Generalized Pseudo-Dynamic Testing," by Thewalt, C. and Mahin, S.A., July 1987.

UCB/EERC-87/10 "Ultimate Behavior of Butt Welded Splices in Heavy Rolled Steel Sections," by Bruneau, M., Mahin, S.A. and Popov, E.P., July 1987.

UCB/EERC-87/11 "Residual Strength of Sand from Dam Failures in the Chilean Earthquake of March 3, 1985," by De Alba, P., Seed, H.B., Retamal, E. and Seed, R.B., September 1987.

UCB/EERC-87/12 "Inelastic Seismic Response of Structures with Mass or Stiffness Eccentricities in Plan," by Bruneau, M. and Mahin, S.A., September 1987.

UCB/EERC-87/13 "CSTRUCT: An Interactive Computer Environment for the Design and Analysis of Earthquake Resistant Steel Structures," by Austin, M.A., Mahin, S.A. and Pister, K.S., September 1987.

UCB/EERC-87/14 "Experimental Study of Reinforced Concrete Columns Subjected to Multi-Axial Loading," by Low, S.S. and Moehle, J.P., September 1987.

UCB/EERC-87/15 "Relationships between Soil Conditions and Earthquake Ground Motions in Mexico City in the Earthquake of Sept. 19, 1985," by Seed, H.B., Romo, M.P., Sun, J., Jaime, A. and Lysmer, J., October 1987.

UCB/EERC-87/16 "Experimental Study of Seismic Response of R. C. Setback Buildings," by Shahrooz, B.M. and Moehle, J.P., October 1987.

UCB/EERC-87/17 "The Effect of Slabs on the Flexural Behavior of Beams," by Pantazopoulou, S.J. and Moehle, J.P., October 1987.

UCB/EERC-87/18 "Design Procedure for R-FBI Bearings," by Mostaghel, N. and Kelly, J.M., November 1987.

UCB/EERC-87/19 "Analytical Models for Predicting the Lateral Response of R C Shear Walls: Evaluation of their Reliability," by Vulcano, A. and Bertero, V.V., November 1987.

UCB/EERC-87/20 "Earthquake Response of Torsionally-Coupled Buildings," by Hejal, R. and Chopra, A.K., December 1987.

UCB/EERC-87/21 "Dynamic Reservoir Interaction with Monticello Dam," by Clough, R.W., Ghanaat, Y. and Qiu, X-F., December 1987.

UCB/EERC-87/22 "Strength Evaluation of Coarse-Grained Soils," by Siddiqi, F.H., Seed, R.B., Chan, C.K., Seed, H.B. and Pyke, R.M., December 1987.

UCB/EERC-88/01 "Seismic Behavior of Concentrically Braced Steel Frames," by Khatib, I., Mahin, S.A. and Pister, K.S., January 1988.

UCB/EERC-88/02 "Experimental Evaluation of Seismic Isolation of Medium-Rise Structures Subject to Uplift," by Griffith, M.C., Kelly, J.M., Coveney, V.A. and Koh, C.G., January 1988.

UCB/EERC-88/03 "Cyclic Behavior of Steel Double Angle Connections," by Astaneh-Asl, A. and Nader, M.N., January 1988.

UCB/EERC-88/04 "Re-evaluation of the Slide in the Lower San Fernando Dam in the Earthquake of Feb. 9, 1971," by Seed, H.B., Seed, R.B., Harder, L.F. and Jong, H.-L., April 1988.

UCB/EERC-88/05 "Experimental Evaluation of Seismic Isolation of a Nine-Story Braced Steel Frame Subject to Uplift," by Griffith, M.C., Kelly, J.M. and Aiken, I.D., May 1988.

UCB/EERC-88/06 "DRAIN-2DX User Guide.," by Allahabadi, R. and Powell, G.H., March 1988.

UCB/EERC-88/07 "Cylindrical Fluid Containers in Base-Isolated Structures," by Chalhoub, M.S. and Kelly, J.M. , April 1988.

UCB/EERC-88/08 "Analysis of Near-Source Waves: Separation of Wave Types using Strong Motion Array Recordings," by Darragh, R.B., June 1988.

UCB/EERC-88/09 "Alternatives to Standard Mode Superposition for Analysis of Non-Classically Damped Systems," by Kusainov, A.A. and Clough, R.W., June 1988.

UCB/EERC-88/10 "The Landslide at the Port of Nice on October 16, 1979," by Seed, H.B., Seed, R.B., Schlosser, F., Blondeau, F. and Juran, I., June 1988.

UCB/EERC-88/11 "Liquefaction Potential of Sand Deposits Under Low Levels of Excitation," by Carter, D.P. and Seed, H.B., August 1988.

UCB/EERC-88/12 "Nonlinear Analysis of Reinforced Concrete Frames Under Cyclic Load Reversals," by Filippou, F.C. and Issa, A., September 1988.

UCB/EERC-88/13 "Earthquake-Resistant Design of Building Structures: An Energy Approach," by Uang, C.-M. and Bertero, V.V., September 1988.

UCB/EERC-88/14 "An Experimental Study of the Behavior of Dual Steel Systems," by Whittaker, A.S. , Uang, C.-M. and Bertero, V.V., September 1988.

UCB/EERC-88/15 "Dynamic Moduli and Damping Ratios for Cohesive Soils," by Sun, J.I., Golesorkhi, R. and Seed, H.B., August 1988.

UCB/EERC-88/16 "Reinforced Concrete Flat Plates Under Lateral Load: An Experimental Study Including Biaxial Effects," by Pan, A. and Moehle, J., November 1988.

UCB/EERC-88/17 "Earthquake Engineering Research at Berkeley - 1988," November 1988.

UCB/EERC-88/18 "Use of Energy as a Design Criterion in Earthquake-Resistant Design," by Uang, C.-M. and Bertereo, V.V., November 1988.

UCB/EERC-88/19 "Steel Beam-Column Joints in Seismic Moment Resisting Frames," by Tsai, K.-C. and Popov, E.P., September 1988.

UCB/EERC-89/01 "Behavior of Long Links in Eccentrically Braced Frames," by Engelhardt, M.D. and Popov, E.P., January 1989.